FOSSIL ENERGY

DOE/BC/14869-8
(OSTI ID: 750148)

GYPSY FIELD PROJECT IN RESERVOIR CHARACTERIZATION

Final Report
June 1997-September 1998

By
John P. Castagna
Daniel J. O'Meara, Jr.

Date Published: January 2000

Work Performed Under Contract No. DE-FG22-95BC14869

University of Oklahoma
Norman,Oklahoma

National Petroleum Technology Office
U. S. DEPARTMENT OF ENERGY
Tulsa, Oklahoma

DOE/BC/14869-8
Distribution Category UC-122

Gypsy Field Project in Reservoir Characterization

By
John P. Castagna
Daniel J. O'Meara, Jr.

January 2000

Work Performed Under Contract No. DE-FG22-95BC14869

Prepared for
U.S. Department of Energy
Assistant Secretary for Fossil Energy

Robert E. Lemmon, Program Manager
National Petroleum Technology Office
P.O. Box 3628
Tulsa, OK 74101

Prepared by
University of Oklahoma
Center for Reservoir Characterization
1000 Asp Avenue, Room 114
Norman, OK 73019

Table of Contents

ABSTRACT

The objectives of this study were to investigate the effects of geological modeling strategies, well location, and reservoir boundary conditions on the scale-up of petrophysical properties. The Gypsy formation was used as the experimental site because detailed information was available from 22 wells. Three models for Gypsy formation were developed and used in the scale-up study.

A methodology for scale-up was developed, in which transmissibility, instead of permeability, was scaled up. Special consideration was given to the pinch-out grid blocks in the system in order to obtain a representative flow simulation. After a linear scale-up was conducted between the grid blocks, a scale-up on productivity index, or PI scale-up, was performed to consider the radial flow around the wellbore. Two hypothetical models, a layer-cake model and a pinch-out model were used to illustrate the application of the methodology. Successful scale-up results were obtained after a PI scale-up technique around the wellbore was applied.

The effects of geological modeling on scale-up were studied by conducting scale-up on the three models for Gypsy formation. The effects of well location and boundary condition on scale-up were studied using different production-injection scenarios and boundary conditions. It was observed that channel model and lithofacies model resulted in similar scale-up results, but flow unit model resulted in large errors. It was observed that in order to obtain a successful scale-up, not only should the fine-scale model be as homogeneous as possible in the vertical direction for each geological unit upscaled, but

the model also should have a good communication in horizontal direction. Well location and boundary conditions have significant effects on scale-up. Line-drive scenario produced the better scale-up results compared to nine-spot and five-spot scenarios, due to closer resemblance to linear flow. No-flow boundary condition produced the better scale-up results compared to bottom-water drive and edge-water drive.

Gypsy Field Project in Reservoir Characterization:
Report for the Period
June 1997 - September 1998

OBJECTIVES

The overall objective of this project is to use the extensive Gypsy Field laboratory and data as a focus for developing and testing reservoir characterization methods that are targeted at improved recovery of conventional oil.

This report describes progress since project report DOE/BC/14970-7 and covers the period June 1997 - September 1998 and represents one year of funding originally allocated for the year 1996.

During the course of the work previously performed, high resolution geophysical and outcrop data revealed the importance of fractures at the Gypsy site. In addition, personnel changes and alternative funding (OCAST and oil company support of various kinds) allowed us to leverage DOE contributions and focus more on geophysical characterization. The new emphases resulted in the following division of sub-projects:

1. Upscaling: A flow-based upscaling method is used to identify regions of flow activity and for guiding optimal configuration of gridblock boundaries in the resulting low-resolution models.

2. Geophysical Characterization and Flow Simulation: High-resolution geophysical techniques calibrated with outcrop data, are used to construct reservoir models with and without permeable fractures. Reservoir simulations are analyzed to assess the importance of fracture characterization in determining sweep efficiency.

3. Seismic Attribute Analysis: Well data is used to calibrate the extraction of 3D seismic attributes. New algorithms for spectral analysis using wavelet transforms and wavelet extraction are developed for this purpose.

4. Modeling Sedimentary Environments: Mathematical methods for construction of geological models are developed and evaluated. These include sensitivity and resolution techniques coupled with multi-resolution analysis.

All of these efforts are closely interlinked and focus on use of data from both the Gypsy outcrop and pilot sites. They (1) target improved recovery of conventional oil through better reservoir characterization, and (2) develop methods which can be used to extend the life of producing fields or to make small fields economic.

SUMMARY

This final report contains four sections corresponding to the four subprojects: (1) Upscaling, (2) Geophysical Characterization, (3) Seismic Attribute Analysis, and (4) Modeling Sedimentary Environments. The major conclusions for these projects are summarized here and detailed reports in the form of theses, papers, and progress reports are provided as appendices. The first two subprojects are essentially complete while the latter two are in progress and will be continued if further funding is obtained.

Upscaling (Dan O'Meara, Anuj Gupta, and Wei Wang): A methodology was developed whereby transmissibilities rather than permeabilities are scaled up. The effects of geological modeling strategies, well locations, and reservoir boundary conditions on the success of this method were investigated. It was determined that a scale-up of productivity index was needed to account for radial flow around the well bore. Upscaling for channel and lithofacies reservoir models worked well, however, flow unit upscaling resulted in large errors. It was observed that the more homogeneous and laterally communicative the reservoir, the better the upscaling results. Well locations and boundary conditions also significantly effect the success of the upscaling procedure.

This work is documented in detail in Appendix A which is a dissertation by Wei Wang entitled "Strategies of Geological Modeling and Scale-Up in Reservoir Simulation". Appendix B is a paper by Wei Wang and Anuj Gupta entitled "Strategies of Geological Modeling and Heterogeneity of Formation" presented at the 3rd Young Academy Conference of the Scientific Association of China.

Geophysical Characterization of Flow Simulation (Roger Young, Matthias Mueller, Zhengen Deng, and Victoria French): Ground penetrating radar (GPR) and seismic data define channel boundaries and a fracture set near the Gypsy outcrop site. Borehole lithology logs show that both geophysical methods image the same boundary between two sandstone channels. 3D dip-filtering and coherence of a migrated 3D GPR survey clearly map the channel boundary. Depth slices of instantaneous frequency show a prominent fracture set that correlates with the orientation of fractures measured at the outcrop.

The geophysically defined fractures were included in a 3D earth model constructed by upscaling matrix properties defined by laboratory permeability and porosity measurements of core from shallow boreholes. Matrix and fracture flow are made to occur in separate, but interacting cells. Waterflood simulations shows that the fracture-assisted permeability can improve or impede sweep efficiency, depending on the placement of the wells.

Appendix C is an expanded abstract of a paper presented by Roger Young at the 1998 Annual SEG Convention entitled "Geophysical Site Characterization for 3D Flow Simulation at the Gypsy Outcrop Site, Oklahoma".

Appendix D is a paper by Roger Young and others published in the June 1997 issue of The Leading Edge entitled "3D Dip Filtering and Coherence Applied to GPR Data: A Study."

Appendix E is a report by Victoria French on fracture analysis at the Gypsy outcrop site.

Appendix F contains selected excerpts from a thesis by Zhengan Deng entitled "The Application of Ground Penetrating radar for Geological Characterization in Three Dimensions at the Gypsy Outcrop Site, Northeastern Oklahoma, USA".

Appendix G contains excerpts from a thesis by Matthias Mueller entitled "Detection and Modeling of Fractures and Their Influence on Flow Simulation at the Gypsy Site, Oklahoma".

Seismic Attribute Analysis (Bill Lamb, John Castagna, Ray Brown, Dirk Seifert, Xia Li):

During the report period we focussed on seismic attenuation and dispersion as reservoir characterization attributes which are theoretically related to pore fluid properties, lithology, petrophysical properties, and stratigraphic relationships. We have developed new algorithms for high resolution spectral analysis and attenuation/dispersion measurement from 3D seismic data in the vicinity of a borehole and are currently applying them to the Gypsy data.

Appendix H is a report by Xia Li describing the wavelet transform spectral analysis algorithm and is titled "Application of Ricker Wavelet in Wavelet Transform".

Appendix I is a progress report by Bill Lamb entitled "Absorption and Dispersion from Gypsy data."

Appendix J is the final form published in Geophysics of material previously reported by Ray Brown and Dirk Seifert entitled "Velocity Dispersion: A Tool for Characterizing Reservoir Rocks".

We intend to continue developing attenuation and dispersion as seismic reservoir characterization attributes.

Modeling Depositional Environments (Luther White and Ying-jun Jin): This project uses the Gypsy data as a prototype reservoir for the development of mathematical methods for constructing geological reservoir models. The goals for the study are to (1) include multi-resolution analysis in inverse and geostatistical methods, and (2) to couple multi-resolution analysis with sensitivity and resolution techniques to investigate, in a more precise way, the detail in estimated reservoir mappings supported by various types of data.

Appendix K by Luther White provides the theoretical basis for the proposed methodology.

Appendix L is a report by Luther White entitled "Differentiability of Interior Regularized Output Least Squares Estimators with Respect to Data for Parabolic Systems". This constitutes a key step in the study of resolution properties of model-based estimation test problems.

Appendix M is a report by Ying-jun Jin and Luther White entitled "Resolution of Regularized Output Least Squares Estimators for Elliptic and Parabolic Problems" which describes the study of interior optimal regularized output least squares estimators with respect to perturbations of coefficients used in posing numerical test problems for finite element approximations of parabolic problems.

This work is continuing with the application of multi-resolution analysis to the Gypsy data a primary objective of future activities.

Appendix A

Strategies of Geological Modeling and Scale-Up

in Reservoir Simulation

by

Wei Wang

A dissertation submitted to the graduate faculty of the University of Oklahoma, 1998.

CHAPTER I

INTRODUCTION

Detailed reservoir descriptions are now possible with the development of geological and engineering reservoir characterization techniques that both honor and integrate information from core analysis, well logs, well tests, geological and geophysical data. The purpose of such description is to provide an accurate quantitative physical model of the reservoir that can be used by a numerical reservoir simulator to predict oil and gas recoveries under various production scenarios.

However, the detailed reservoir description models with millions of grid blocks cannot be directly incorporated into reservoir simulators because of their intensive computational cost. Despite advances in computer technology, most commercial reservoir simulators are limited to fewer than 10,000 grid blocks, basically 100 times less than the detailed geological models. Scale-up techniques are needed to bridge the gap between fine-scale and coarse-scale models.

Scale-up techniques have been developed in recent years. One limitation of these scale-up methods is that they concentrate only on the mathematics of combining petrophysical properties of finer grid blocks, while giving little consideration to the heterogeneity of geological and structural details. These methods choose coarse-grid cell boundaries independent of the distribution of reservoir properties, i.e., averaging reservoir properties within layers or channels without considering the effect of

heterogeneity on fluid flow and scale-up. Such 'layer or channel scale-up' may average out the effects of extreme values of reservoir properties, such as thin continuous communicating layers, large flow barriers, or partially communicating faults. Therefore, in order to obtain reliable results in scale-up for reservoir simulation, not only is it very important to use a reliable mathematical method for the calculation of average value of reservoir properties for the upscaled grid blocks, but also to find an effective method to determine the boundaries of upscaled grid blocks. A successful scale-up result can be obtained with the combination of reliable mathematical scale-up methodology and detailed description of formation heterogeneity.

1.1 Objectives of the Study

Reservoir properties, such as permeability and porosity, are heterogeneous and their values can change in three dimensions of space. Based on the processes of deposition and diagenesis of formation, the variation of these properties in the vertical direction is more abrupt compared to the variation in the horizontal direction. The purpose of this study is to evaluate the issues surrounding scale up in the vertical direction of the reservoir and to develop new methodologies for scale up modeling.

The objectives of this study are:

(1) To develop an improved vertical layering method for scale-up in reservoir simulation using information typically available from well logging and core analysis.

(2) To develop an effective scale-up methodology that can be used in reservoir simulation.

(3) To investigate the effects of geological modeling, well location, production-injection scenario, and boundary condition on scale-up.

1.2 Contents of the Study

Seven chapters are included in this study. Chapter II contains a brief literature review on the classification of reservoir heterogeneity and scale, development of reservoir description techniques as well as scale-up techniques.

Chapter III includes the development of three different models for Gypsy formation and the analysis of the heterogeneity of these three models.

Chapter IV discusses the strategies of transmissibility scale-up developed and used in this study. Two different hypothetical models are used to illustrate the methodology. Further improvement in scale-up is accomplished by considering the scale-up around wellbore area using PI scale-up method. Successful scale-up results are obtained and displayed in this Chapter.

Chapter V presents the application of the scale-up methodology developed in Chapter IV to three Gypsy models. Scale-up results demonstrated that strategies of geological modeling have significant effects on scale-up.

Chapter VI studies the effects of well location, production-injection scenario, and boundary condition of reservoir on scale-up. Relative error is used as criterion to evaluate the effects of various strategies on scale-up.

Chapter VII presents the conclusions of this study and the recommendations for the study in future.

CHAPTER II

RESERVOIR DESCRIPTION AND SCALE-UP

In order to obtain successful scale-up results, three concepts are very important. They are: (1) reservoir scale and heterogeneity; (2) reservoir description; and (3) scale-up techniques. The following is a review of each of these concepts.

2.1 Reservoir Scale and Heterogeneity

Reservoir heterogeneity can be characterized at different scales from microscopic to large scale. Flow phenomena observed at a given scale of heterogeneity exhibits different features compared to those observed at other scales. During reservoir characterization, all available measurements are used, including core scale of laboratory measurements, the scale of well test data, and the scale of seismic and production data. Reservoir description is a combined effort of discretizing the reservoir into subunits, such as layers and then grid blocks, and assigning values to all pertinent physical properties for these blocks. For this purpose, data from several scales and sources are available. Information at each scale results in different accuracy and involves measurement averaging over a different volume of rock (Haldorsen, 1986).

Four conceptual scales of averaging volumes can be classified that exhibit various types of reservoir heterogeneity, and they are: (1) microscopic; (2) macroscopic;

(3) megascopic; (4) and gigascopic. Fig. 2-1 is an illustration of these four scales (Haldorsen, 1986).

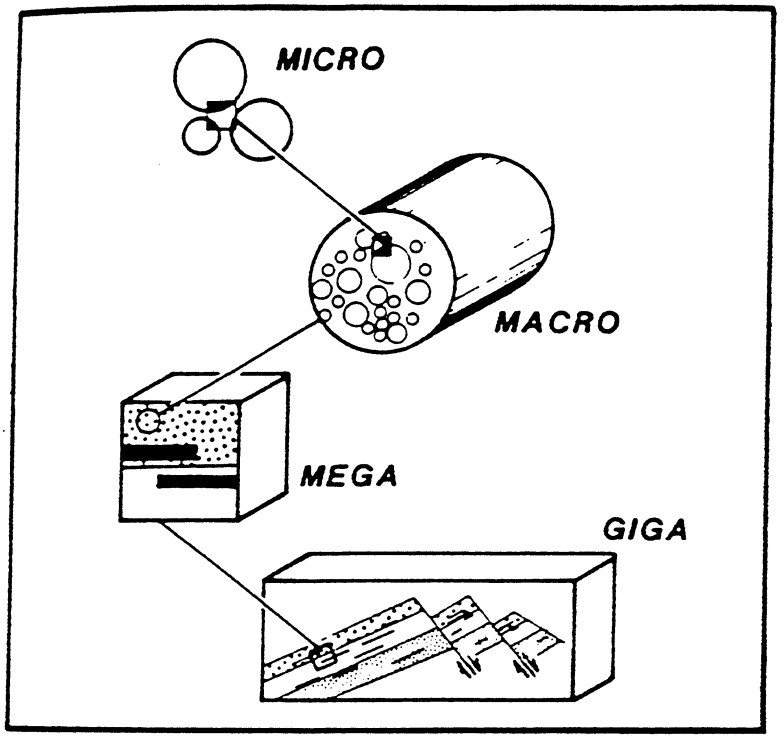

Fig. 2-1 Illustration of Four Conceptual Scales (Haldorsen, 1986)

Microscopic is the scale at which pore throats and grain sizes are described. Variability at this scale produces microscopic scale heterogeneity which governs the distribution of fluid saturation in reservoir. The data for this scale can be obtained from Scanning Electron Miscroscope (SEM) analysis, Pore Image Analysis (PIA), and conventional thin section analysis. The study on this scale is often conducted using a network modeling approach, which assumes that the pore throats of porous media

possess different shapes and explicitly incorporates pore wettability effects into a network model in order to quantify flow parameters, to fit experimental data, and to examine the sensitivities of a given process to a variety of phenomena.

Macroscopic is the scale at which core analysis is conducted using core plugs to obtain the properties of the reservoir, such as porosity, permeability, water saturation, capillary pressure, relative permeability, and wettability. From a mechanistic point of view, macroscopic scale corresponds to the viscous-capillary flow regime where gravity forces are considered negligible (Lasseter *et al.*, 1986). This is the most important scale in reservoir study because the continuity equations describing the fluid transport phenomena in porous media are derived based on this scale. The properties of rock within this scale are usually considered to be constant. The data obtained from this scale are used to calibrate the data from well logs and well testing, and used as the input in reservoir simulation. However, the data obtained from this scale are not accurate enough to represent the conditions of reservoir because many factors can affect the measurements, such as pressure, temperature, orientation, and boundary conditions.

Megascopic is the scale at which well logs and well tests are conducted. This scale corresponds to the viscous-capillary-gravity dominated flow regime, in which all three forces play significant roles in determining the dynamic multiphase behavior (Lasseter *et al.*, 1986). Reservoir simulation and scale-up are conducted on this scale, in which reservoir formation is divided into many grid blocks where the variations of rock and fluid properties are averaged or upscaled from macroscopic scale to be assigned as single values to the whole grid block. Because of the limitation of time and computer memory, only thousands of grid blocks can be handled in reservoir simulation. This

means that the grid blocks used in simulation have to be large enough to represent the whole reservoir using only several thousand gird-blocks. Each parameter value, such as permeability and porosity, that is assigned to the large grid blocks is an important consideration. Collin *et al.* (1961) recommended that porosity of reservoir in megascopic scale should be calculated from core data as the volume weighted arithmetic average. The probable error in average porosity is propotional to the inverse square root of the total volume of cores analyzed. Porosity is an intrinsic property of porous medium that is independent of the boundary condition measured. In contrast, the permeability of a heterogenous medium is defined for equivalent homogeneous medium that, with different boundary conditions, would produce different flow movement. Thus, permeability of a porous medium depends on both the boundary conditions and the heterogeneity of the porous medium studied (Begg *et al.*, 1985).

Gigascopic is the scale of total formation that consists of many depositional units and perhaps several depositional environments. The essential features of the gigascopic scale are lateral continuity and vertical communication. Seismic and production data are mostly used to obtain the information on this scale.

To realistically predict reservoir performance, reservoir heterogeneity at various scales must be modeled accurately. Reservoir engineers and geologists should combine efforts to develop a quantitative approach to define the depositional units and the depositional environments of the reservoir in which it was formed. Reservoir engineers must attain efficient means to use these detailed, quantitative, and complex descriptions of reservoirs in reservoir simulation models.

2.2 Reservoir Description

The task of reservoir description is to characterize the physical and chemical properties of porous medium and its pore fluids over a broad range of dimensions from pore throat to whole reservoir. The purpose of such descriptions is to provide an accurate quantitative physical model of the reservoir that can be translated for use in numerical reservoir simulation models to predict oil and gas reservoirs under various production scenarios (Forgotson, 1991).

In the past, reservoir description for simulation has evolved from simple to quite complex models. Past reservoir simulation studies treated the reservoir as a package of superimposed subhomogeneous layers, or layer cakes, in which reservoir properties, such as porosity and permeability, were assigned constant values based on the data points obtained from core measurements. Because of the discontinuity of sand bodies of variable thickness or the occurrence of major lateral permeability contrast, this was often an over-simplification. In recent years, 3-D heterogeneous geological models were developed, in which each layer was horizontally divided into many grid blocks with different petrophysical properties, in order to improve that simplification.

Four major studies are included in conventional reservoir description. These are: (1) rock studies to define lithology, depositional environment of the reservoir, and correlations of rock properties; (2) framework studies that establish the structure continuity of reservoir and nonreservoir rock and gross thickness; (3) reservoir quality studies to determine the variation of rock properties (permeability, porosity); and (4) integration studies that yield maps of porosity, permeability, and formation thickness across the reservoir (Willhite, 1986).

Rock studies are used to identify the rock types for both reservoir and nonreservoir rocks that make up the reservoir intervals and to interpret the depositional origin of the intervals using information from cutting, cores, well logs, and routine core-analysis data. This information is fundamental in predicting reservoir continuity and thickness patterns and variation in pore-space properties. Typical output developed at this level of analysis are core-description graphs and porosity-permeability cross-plots (Harris and Hewitt, 1977).

Framework studies determine the geometric configuration of the trap and the vertical and lateral distribution of the rock types that were identified in rock studies. Framework studies begin by mapping the gross structure from well and seismic data to define the areal and vertical extent of the deposit. It is important to identify aquifer and estimate aquifer size in framework studies because it is a measure of the capacity of reservoir to maintain reservoir pressure under primary production. The principal activity in framework studies is the determination of areas and vertical limits and the continuity of reservoir and nonreservoir zones.

Reservoir quality studies utilize well logs, core analysis, and well test data to ascertain pore-space attributes and distributions. Special core analysis and petrophysical studies may be required to identify the pay zone and to predict fluid saturation distribution (Harris and hewitt, 1977).

Integration studies are the epitome of the total effort, because both data and professional experience must be used to complete the description activity satisfactorily. Porosity and/or permeability maps can be combined with net-thickness maps to provide the pore-volume or transmissibility maps needed in reservoir simulation. Reservoir

simulation techniques can then be used to match reservoir history and predict future performance.

In reservoir description, the tasks for geologists are to identify and describe the mineralogy, texture, grain size, bedding and flow structures, depositional sequences and the geometry of genetically related depositional units, using the information from seismic, outcrop, and cores, and finally to produce a conceptual geological mode. The tasks of petrophysicists are to measure and provide the information of porosity, permeability, fluid saturation, and well logs. Finally, reservoir engineers need to combine all of the available information from exploration, drilling, reservoir engineering and production data to build up a discrete geological model used to predict the performance of the reservoir for different production scenarios.

The most common method to determine if a model is adequately describing a reservoir is to match the reservoir's performance history. Reservoir engineers have found it difficult to use a geological model developed by conventional methods to match the history of a reservoir. The geological models developed by conventional methods are too coarse and too homogeneous to match reservoir performance, because it did not reflect the vertical and lateral variations of reservoir heterogeneity. Reservoirs are so complex and heterogeneous that it is impossible to have a geological model to describing them absolutely. Numerous techniques for improved reservoir characterization were developed in 1980's.

Reservoir characterization is a detailed quantitative description of the physical and chemical properties of a porous medium and its contained fluids. The present emphasis on reservoir characterization is to integrate geological, geophysical, and

engineering data at many scales, in order to obtain a more comprehensive understanding of the distribution of reservoir rock and fluid properties.

Two distinct approaches to the determination of lateral reservoir properties are being developed. The first approach is called deterministic and the second approach is called geostatistical.

Deterministic method is used to determine the distribution of reservoir properties for systems with small well spacing and reasonably simple reservoir architecture. Deterministic weighting weights the data based on the distance from the well to the center of the cell being calculated. This method honors the data at the well locations. The following equation is used in the interpolation to derive the cell value (Landmark, 1995):

$$V = \frac{\sum_{i=1}^{n} W(r_i, R).Z_i}{\sum_{i=1}^{n} W(r_i, R)} \qquad (2\text{-}1)$$

where:

V = final cell value,

W = the weighting function,

r = the distance from the interpolated point,

R = the search radius,

n = total number of well values used,

Z = well value.

The weighting function W in the equation is represented by the following equation:

$$W(r,R) = (1 - r/R)^2 . (R/r)^X \qquad (2\text{-}2)$$

where:

X = power factor.

Values R and x reflect the heterogeneity of a reservoir, and they need to be determined experimentally for a specific reservoir. R should be determined based on the well spacing, distance of wells from the boundary of the reservoir, and the distribution area of the layer studied.

When the well spacing is very large and reservoir architecture is very complex, a deterministic correlation may be not enough to describe the reservoir heterogeneity. In this case, a statistical approach is more appropriate to use to develop a more accurate configuration of reservoir architecture (Weber *et al.* 1990).

Geostatistical method was developed based on the discovery that many earth-science variables present two main characteristics: there is some randomness in their behavior, but at the same time there is some continuity (Dubrule *et al.*, 1986). This means that knowing the value at one point x gives some information about the values in the neighborhood of x (continuity), but not enough to exactly predict what these values are (randomness). Geostatistics takes into account the randomness by considering the value Z(x) at point x as the realization for a random variable Z(x). The continuity is represented by a variogram $\gamma(h)$, which is a measure of the difference between values estimated as a function of distance of separation. For a certain reservoir, a variogram correlation for the variable studied is first generated using the available data. This correlation is then applied to represent the degree of continuity of the variable in the specific reservoir. Geostatistical method is especially useful for the estimation of

reservoir properties during the development of reservoir in early stages, when limited data is available.

Variations of reservoir property in the vertical direction can be determined by combining the information from well logs and core analysis. Openhole logs, frequently gamma ray and induction/resistivity, may identify the stratigraphic sequences or depositional units that are consistent with seismic interpretations.

Several methods have been proposed and used for subdividing a sedimentary interval for reservoir description. Statistical techniques based on the variations of permeability have been used by previous investigators to zone the reservoir into layers. Testerman (1962) proposed a statistical reservoir 'zonation technique' using permeability data from a sedimentary interval to identify and describe naturally occurring zones in a reservoir. First, the interval was divided into two zones and then into three zones. The subdivision of additional zones continued until the zones had minimum variation in permeability internally and maximum variation between zones. The problem with this method is that it does not take into account the geological attributes that control reservoir zonation.

With the advance in facies modeling, sedimentological studies have introduced facies-zones, and facies associations as flow units for reservoir sublayering. A facies is a three-dimensional body of rock having the same environmental as determined from characteristics such as external and internal geometry, sedimentary structures, lithology, organic content, stratigraphic relations, and associated sedimentary facies (Finley and Tyler, 1986).

Rodriguez *et al.* (1988) characterized facies units by identifying major changes in the related depositional sequences using porosity and permeability values. In their study, eight facies were first identified using the type of lithology, sedimentary structures, sedimentary textures, and amount of bioturbation. Facies were then grouped into four facies assemblages or sedimentary units, according to attributes such as, the first appearance of conglomeratic sand with erosive basal contact with the underlying Paleocene carbonate sequence, presence of a very fine-grained sand sequence with continuous shales intercalations, and the first appearance of an heterolithic sand/shale sequence with considerable thickness.

In recent years, the concept of hydraulic or flow unit was introduced as a method of subdividing a sedimentary interval for reservoir description. The term 'flow unit' has different definitions depending on its application. A flow unit is defined as a volume of reservoir rock that is continuous laterally and vertically and has similar averages of those rock properties that affect fluid flow. It represents an assemblage of facies having similar characteristics. The significance of dividing the sedimentary intervals into flow units is that each flow unit usually reflects a specific depositional environment and characteristics of fluid flow (Ti *et al.*, 1995). A compelling reason for describing reservoirs in terms of depositional units is that units formed in the same depositional environment have similar characteristics (Lasseter *et al.* 1986). Thus in reservoir simulation, each flow unit can be treated as a layer or a vertical gridblock (Weber and Geuns, 1990). Continuous flow units with similar properties can be upscaled into one layer to reduce the amount of memory and computing time needed without adversely

affecting the accuracy of simulation results, in order to obtain the optimum layering for reservoir simulation.

Scuta (1997) used injected and produced volumes of oil and water, oil-water contact map, and time-lapse injectivity profiles, to interpret flow unit in a complex carbonate reservoir using sequence-stratigraphic concepts as well as, the interpreted structural evolution for Vacuum Field in New Mexico. A 3-D geological model was built to understand and visualize the three-dimensional distribution of properties. This model was later upscaled for reservoir simulation by first summing and averaging porosity in each layer, and then ranking and grouping the layers with similar ranks. Various parameters were used to determine the optimal layering scheme that would maintain the structure and detail of the geological model for reservoir simulation.

Hearn *et al.* (1986) defined a flow unit as a zone that is continuous over a defined volume of the reservoir, has similar averages of these rock properties that affects fluid flow, and has similar bedding characteristics. The distribution of flow unit is related to the facies distribution, but flow unit boundaries do not necessarily coincide with facies boundaries. They used the concept of flow unit in the simulation of Hartzog Draw Field. In their study, flow units were defined based on the range of porosity and permeability distribution as shown in Fig. 2-2.

Slatt and Hopkins (1988) developed a flow unit model which integrated detailed geological and petrophysical properties to provide a more comprehensive understanding of reservoir architecture and heterogeneity within Balmoral Field. Five flow units were defined using measurements of porosity, permeability, grain-size, capillary pressure curves, and various geological properties. This flow unit model is considered to be the

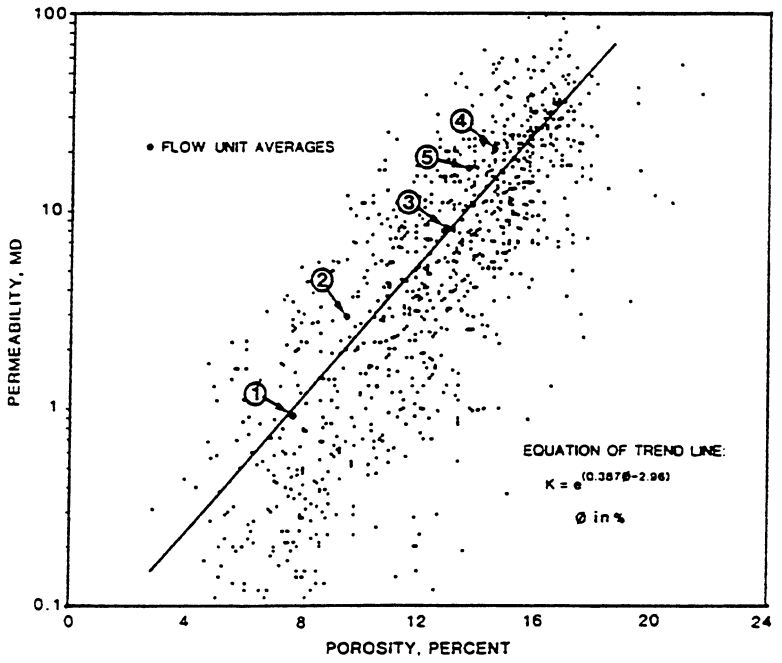

Fig. 2-2 Classification of Flow Units by Permeability and Porosity ((Hearn *et al.*, 1986)

most complex model, because it incorporates a variety of geological and petrophysical parameters and it provides the most comprehensive description for simulation studies.

Ti *et al.* (1995) developed a quantitative way to classify a reservoir into distinct flow units. Sedimentary intervals of the cored wells were divided into major zones on the basis of core description information. The major zones were further subdivided into subzones to allow less variation in geologic and petrophysical properties within each subzone and more variation between the subzones. On the basis of the transmissibility, storativity, and net-to-gross-thickness data, the subzones were classified into four distinct fluid flow units by use of the statistical method of cluster analysis.

Understanding the complex variations in pore geometry within different lithofacies is the key to improving reservoir description and subsequently, reservoir exploration (Amaefule *et al.*, 1993). The variations in pore geometrical attributes can be used to identify distinct zones or hydraulic flow units with similar fluid-flow characteristics. Amaefule *et al.* (1993) proposed a methodology to identify and characterize hydraulic flow units based on a modified Kozeny-Carmen equation using the mean hydraulic radius. A hydraulic unit is defined as the representative elementary volume of total reservoir rock within which geological and petrophysical properties that affect fluid flow are internally consistent. Hydraulic units are related to geologic facies distribution, but do not necessarily coincide with facies boundaries (Hearn *et al.*, 1984). According to their proposed method, a log-log plot of RQI versus ϕ_z, which are defined in the following equations, for the same flow unit with an ideal pore geometry should follow a straight line.

$$\text{RQI}=0.0314\sqrt{\frac{k}{\phi}} \tag{2-3}$$

$$\phi_z=\left(\frac{\phi}{1-\phi}\right) \tag{2-4}$$

k is permeability in mD, ϕ is porosity in fraction. Fig. 2-3 illustrates a log-log plot of RQI versus ϕ_z for East Texas.

Shedid (1997) extended Amaefule's method to represent a real porous medium system in a generalized form. A log-log plot of RQI versus ϕ formed a straight line with a slope of $\frac{(C_2+1)m-1}{2}$ and an intercept of $\left(0.0314\sqrt{C_1}*\sqrt{\frac{R_{ti}}{aR_w}}\right)$. C_1 and C_2 are

coefficients of permeability equation and porosity exponent, respectively; m is porosity exponent; a is the coefficient in Archie's equation; R_{ti} is the true formation resistivity at irreducible water saturation; and R_w is formation water resistivity. For a real porous medium system, the slope is not unity, but a function of the coefficients and porosity exponent. The intercept of the plot is a function of the coefficient of permeability equation, formation water resistivity, and true formation resistivity.

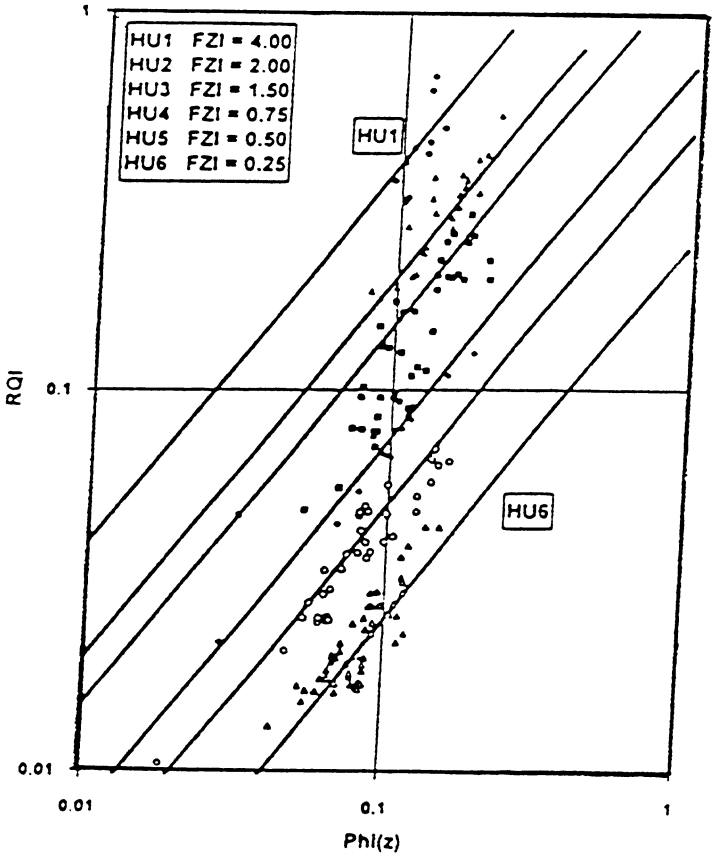

Fig. 2-3 Log-Log Plot of RQI versus ϕ_z for East Texas (Amaefule *et al.*, 1993)

2.3 Scale-up Techniques

Two categories of scale-up techniques have been developed: single-phase scale-up and two-phase scale-up. Single-phase scale-up focuses on preserving the gross feature of flow on the simulation grid and calculates an effective permeability, which can result in the same total flow rate of fluids through the coarse, homogeneous block as that obtained from the fine heterogeneous blocks. Scale-up of two phase flow is more complicated than single-phase flow since it involves not only absolute permeability but also relative permeability and capillary pressure. In this study, only one phase flow was studied. Therefore, only one phase scale-up is discussed below.

2.3.1 Scale-up for Linear Flow

Numerous methods for scale-up of single phase flow have been developed, including average method (arithmetic/geometric/harmonic) (Cardwell and Parsons, 1945; Begg *et al.*, 1989), tensor method (Pickup *et al.*, 1992; Aasum *et al.* 1993; King, 1993 & 1994; Pickup and Sorbie, 1994(a); Pickup and Sorbie, 1994(b)), transmissibility scale-up (White and Horne, 1987; Peaceman, 1996), renormalization technique (King, 1989; Gautier and Natinger, 1994; Christie *et al.*, 1995; King *et al.*, 1993; Hearn *et al.*, 1984), and pressure-solver method (Begg and King, 1985; Begg *et al.*, 1989).

The simplest method for calculating average permeability of porous medium is the average method. Begg *et al.* (1989) calculated the average permeability for different rocks using three average methods and determined that harmonic and arithmetic methods gave the lowest and highest values of average permeability. Geometric method provided average values between the values from harmonic and arithmetic methods.

White and Horne (1987) presents an algorithm to compute transmissibility using permeability heterogeneity and anisotropy at fine scale. In his proposed method, the transmissibility for coarse-scale grid blocks were treated as a tensor, and, for a 2-D simulation, the flux across the +x face of coarse-scale grid block was expressed as:

$$q_{i+1/2,j} = -\left[T^{xx}_{i+1/2,j}\Delta p_{x,i+1/2,j} + T^{xy}_{i+1/2,j}\Delta p_{y,i+1/2,j}\right] \tag{2-5}$$

Where:

$q_{i+1/2,j}$ = flux between two grid blocks,

$T^{xx}_{i+1/2,j}$ = normal transmissibility between two grid blocks,

$T^{xy}_{i+1/2,j}$ = cross transmissibility between two grid blocks,

$\Delta p_{x,i+1/2,j}$ = pressure difference between two grid blocks in x direction,

$\Delta p_{y,i+1/2,j}$ = pressure difference between two grid blocks in y direction.

Similarly, the expression of flux in y direction can be also expressed as Eq. (2-5). The well to well-block transmissibility is determined by the following equation:

$$Q = T_b\left(p_{i,j} - p_b\right) \tag{2-6}$$

where:

Q = total flow rate of well,

T_b = transmissibility of well to wellblock,

$p_{i,j}$ = wellblock pressure,

p_b = wellbore pressure.

In order to solve for both normal and across transmissibilities, at least two distinct boundary conditions must be set. The pressures and fluxes for coarse-scale grid blocks were obtained by averaging and summing the pressures and fluxes from fine-scale

simulations with different boundary conditions. Least-squares method was then used to estimate the transmissibilities between coarse-scale grid blocks and between well to wellblock. It was demonstrated that the general tensor scaling procedure can give accurate, efficient production estimate on a coarse grid.

Peaceman (1996) proposed a methodology in which six half-block transmissibilities for each coarse grid-block were calculated by directly solving the finite-difference equations for pressure in each of six half-blocks. Uniform pressures are applied at two opposite faces and no-flow boundary conditions are applied at the other four faces when solving the finite-difference equation. An illustration of the half block is provided in Fig. 2-4.

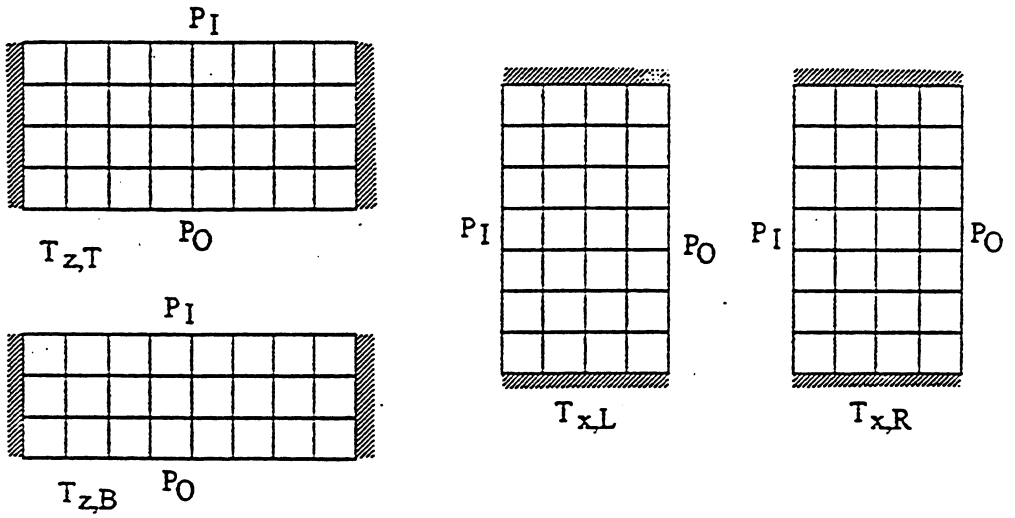

Fig. 2-4 Schematic of Half Block Transmissibility (Peaceman, 1996)

Tensor method takes effective permeability of reservoir as a full tensor with elements k_{xx}, k_{xy}, k_{xz}, k_{yy}, k_{yx}, k_{yz}, k_{zx}, k_{zy}, and k_{zz} to represent the heterogeneity and anisotropy of reservoir formation. Aasum *et al.* (1993) developed an analytical method to calculate effective permeability tensor for a grid block by accounting for small scale heterogeneity within the grid block. The method honors both location and orientation of the small scale heterogeneity. Pickup and Sorbie (1994b) developed a new two-phase scale-up method based on tensor permeabilities. The method was validated when it accurately reproduced fine grid calculations using tensors on a coarser grid. Tensor method is significantly more accurate than other scale-up methods, but it greatly increases the computation time needed for simulation. Therefore, it still cannot be directly incorporated into a commercial reservoir simulator without significantly slowing down computation time.

Renormalization Technique for effective permeability was pioneered by King (1993). The idea of the renormalization method is to replace a single scale-up step from the fine grid to the coarse grid with a series of steps which transits from fine grid to coarse grid through a series of increasingly coarse intermediate grids (Christie *et al.*, 1995). The approach works by taking a large problem and breaking it down into a hierarchy of manageable problems (Christie, 1996). In the application of the method, King *et al.* (1993) used a resistor-network analogy for the direct expression of effective permeability. The effective permeability of a small group of cells was first calculated and then put back in place of the original fine group of cells. The process can be repeated for many levels and provides a quick estimation of effective permeability. Renormalization method provided comparable results to that of simulation results. The

technique is valid for situations with large permeability variation or with a finite fraction of non-reservoir rock (Christie, 1996).

Begg and King (1985) described a pressure-solver method for the scale-up of single-phase flow similar to the method of Kyte and Berry (1975). The method was developed based on the principle that the effective permeability, k_e, of a heterogeneous medium is the permeability of an equivalent homogeneous medium that, for the same boundary conditions, would give the same flux. Therefore, it depends on both the boundary conditions and the distribution of heterogeneity, and the volume being considered. In this method, the effective permeability for coarse grid block was calculated to produce the same flow rate as for the fine-grid blocks. The results obtained using this method depend on the assumptions and specific boundary conditions made. Fig. 2-5 is an illustration of pressure-solver method.

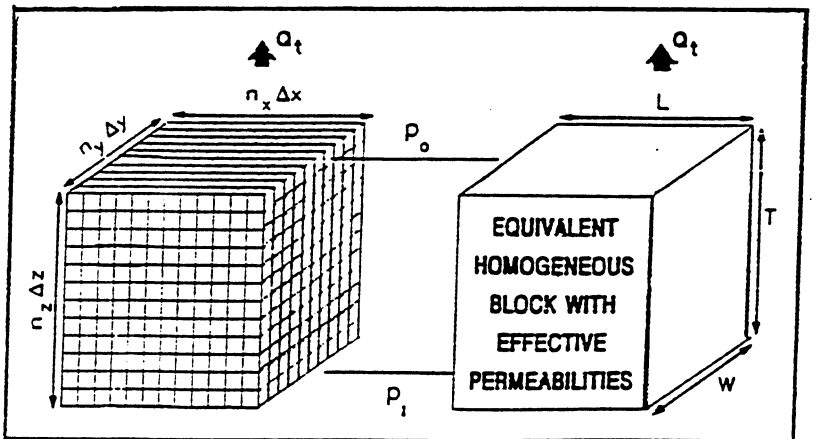

Fig. 1—Illustration of pressure-solver method.

Fig. 2-5 Illustration Of Pressure-Solver Method (Begg *et al.*, 1989)

2.3.2 Scale-up for Radial Flow Near Wellbore

As discussed earlier, the scale-up on permeability or transmissibility is only suitable for a linear flow condition when grid blocks do not contain wells. For the grid blocks in which production well or injection wells are located, the method discussed previously may not be appropriate to obtain a satisfactory result in scale-up.

The flow region in a reservoir can be divided into two types: a radial flow region with a high pressure gradient and a linear flow region with a low pressure gradient. The radial flow region is usually more important in production forecasting, because it is directly related to the wells.

Several authors have proposed methods for scale-up at the wellbore or in the vicinity of wells that consider the characteristics of radial flow. Soeriawinata and Kelkar (1996) presented an analytical method to calculate effective permeability for a coarse-grid wellblock from fine-grid permeabilities. The wellblock was divided into many rays, as shown in Fig. 2-6. Two kinds of reservoir conditions were considered: (1) no communication along the θ and z directions and (2) communication in θ direction. In the first reservoir condition, the permeability for each ray was calculated using the following equation:

$$K_{ray} = \frac{\sum_{i=1}^{nb_{ray}} ln\left(\frac{r_{f,i}}{r_{n,i}}\right)}{\sum_{i=1}^{nb_{ray}} \frac{ln\left(\frac{r_{f,i}}{r_{n,i}}\right)}{k_i}} \qquad (2\text{-}7)$$

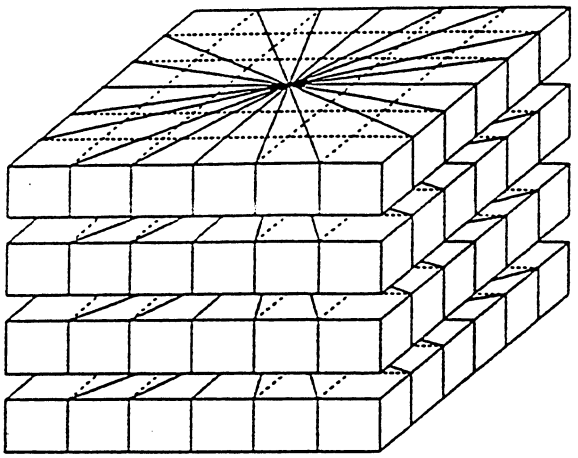

Fig. 2-6 Illustration of Wellblock Divided into Rays (Soeriawinta and kelkar, 1996)

The permeability for each layer was calculated as the weighted arithmetic average as follows:

$$K_{layer} = \frac{\sum_{j=1}^{n_{ray}} k_{ray,j} w_{ray,j}}{\sum_{j=1}^{n_{ray}} w_{ray,j}} \tag{2-8}$$

$$w_{ray,j} = \sum_{i=1}^{nb_{ray}} ln\left(\frac{r_{f,i}}{r_{n,i}}\right)_j \tag{2-9}$$

where:

k_{ray} =permeability for the ray (mD),

$r_{f,i}$ = farthest point from i-th block to the well (ft),

$r_{n,i}$ = nearest point from i-th block to the well (ft),

nb_{ray} = total number of blocks in a ray,

k_{layer} = permeability for the layer (mD),

n_{ray} = total number of ray,

$w_{ray,\,j}$ = weighting coefficient of the i-th ray.

The permeability of the wellblock was determined using a thickness average method. Eq. 2-7 reflects the averaging procedure for parallel beds with radial flow. The results of coarse grid simulations with the permeabilities upscaled through the new well-block approach were comparable to the results of the fine grid simulation with initial permeability distributions. This method can only be used for scale-up of permeability.

Ding (1995) proposed a scale-up procedure to calculate the equivalent coarse grid transmissibility for the linear flow region based on the results of simulation on fine grid. For radial flow in the vicinity of a well, the transmissibility was scaled-up by using an imposed well condition. A numerical productivity index (PI) for wellblocks in coarse gird was defined as follows:

$$PI_c = PI_f(P_f - P_w)/(P_c - P_w) = Q/\left(P_c - P_w\right) \tag{2-10}$$

where:

PI_c = productivity index of coarse grid (bbl/day/psi),

PI_f = productivity index of fine gird (bbl/day/psi),

P_f = wellblock pressure of fine grid (psi),

P_c = wellblock pressure of coarse grid (psi),

P_w = wellbore pressure (psi),

Q = flow rate (bbl/day).

If well production rate, wellblock pressure, and wellbore pressure are known, the productivity index for a coarse-scale grid block can be calculated using Eq. 2-10. Ding (1995) tested single-phase incompressible flow by conducting a simulation with a fine-scale model, which was used as the reference solution. Then scale-up was conducted using a standard procedure developed by Begg *et al.* (1989). The second scale-up method used included the standard procedure for linear flow pattern and the procedure for radial flow pattern. Fig. 2-7 illustrates the flow rates obtained from three different simulations for each individual well (nine wells in total). The errors caused by the new scale-up procedure including a radial flow region are generally lower than the error caused by standard procedure. Therefore, it was concluded that scale-up for radial flow is very important in a overall scale-up process.

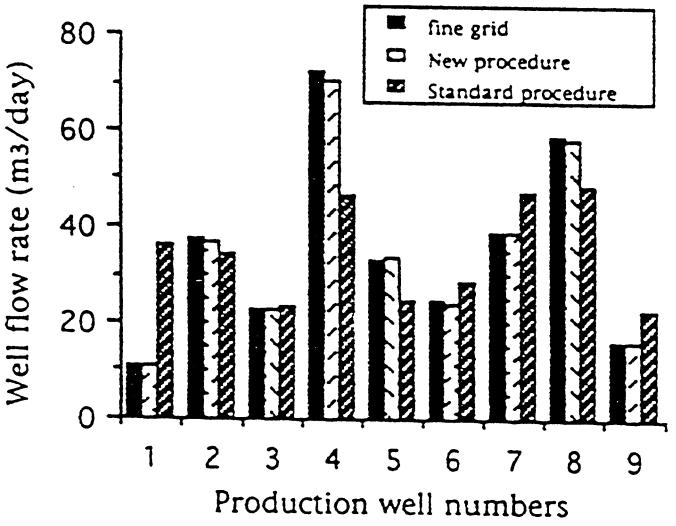

Fig. 2-7 Comparison of Well Flow Rates from Fine-Scale Simulation and Two Different Scale-up Procedures (Ding, 1995)

CHAPTER III

DEVELOPMENT OF GYPSY GEOLOGICAL MODELS

The Gypsy formation was chosen as the experimental site to develop three different geological models, which are used in later chapters to conduct the scale up and study the effects of geological modeling, boundary conditions, and well locations on scale up.

The Gypsy formation is a non-oil bearing formation located in northeastern Oklahoma near Lake Keystone, as shown in Fig. 3-1. It was chosen as the experimental site for this study because of the extensive data available from 22 wells in the formation. Data were collected from these 22 wells by BP Exploration between 1989 to 1992 and 1,056 core samples have been acquired and studied (Doyle and Sweet, 1992). Data available include permeability, porosity, and lithofacies, that were measured and identified at one foot intervals or smaller, when there was a significant change in rock properties within one foot interval.

3.1 Geology of Gypsy Formation

Gypsy sandstone is an informal name for the lowermost interval of the upper Pennsylvanian Vamoosa Formation. Gypsy formation was deposited as a mixed load meanderbelt system and the sediment transport direction was dominantly west to northwest (Doyle and Sweet, 1992).

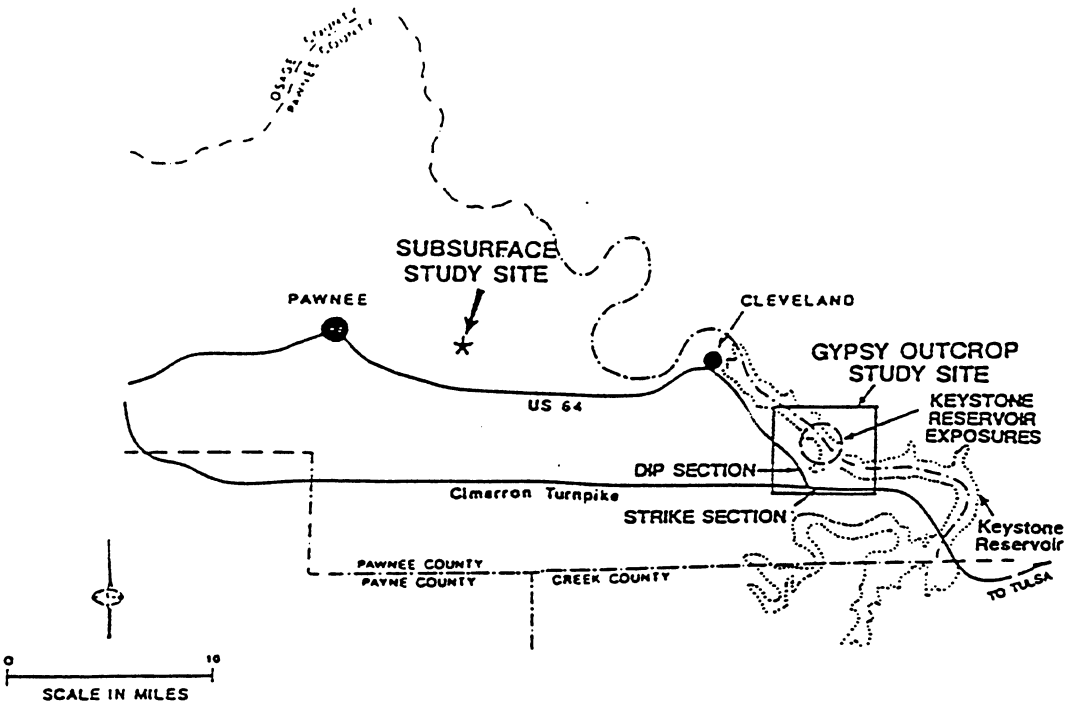

Fig. 3-1 Location of Gypsy Formation (Doyle and Sweet, 1992)

Six channels and one crevasse-splay, in total seven channels, were identified within the Gypsy Outcrop formation. Channel sandbodies are subparallel and trend north to northwest, ranging from 6 to 21 ft thick and 150 to 560 ft wide. Isopach maps of net thickness for the seven channels present in Gypsy formation, which were generated in this study using software Geographix, are provided as Figs. 3-2 to 3-8. The modeling area is 1181 feet wide and 1410 feet long. The lower contact of each channel sandbody is erosional, and upper contacts may be erosional with younger channels or conformable with floodplain deposits. All of the channels are surrounded or partially subdivided by floodplain deposits that are dominantly composed of impermeable mudstone and siltstone.

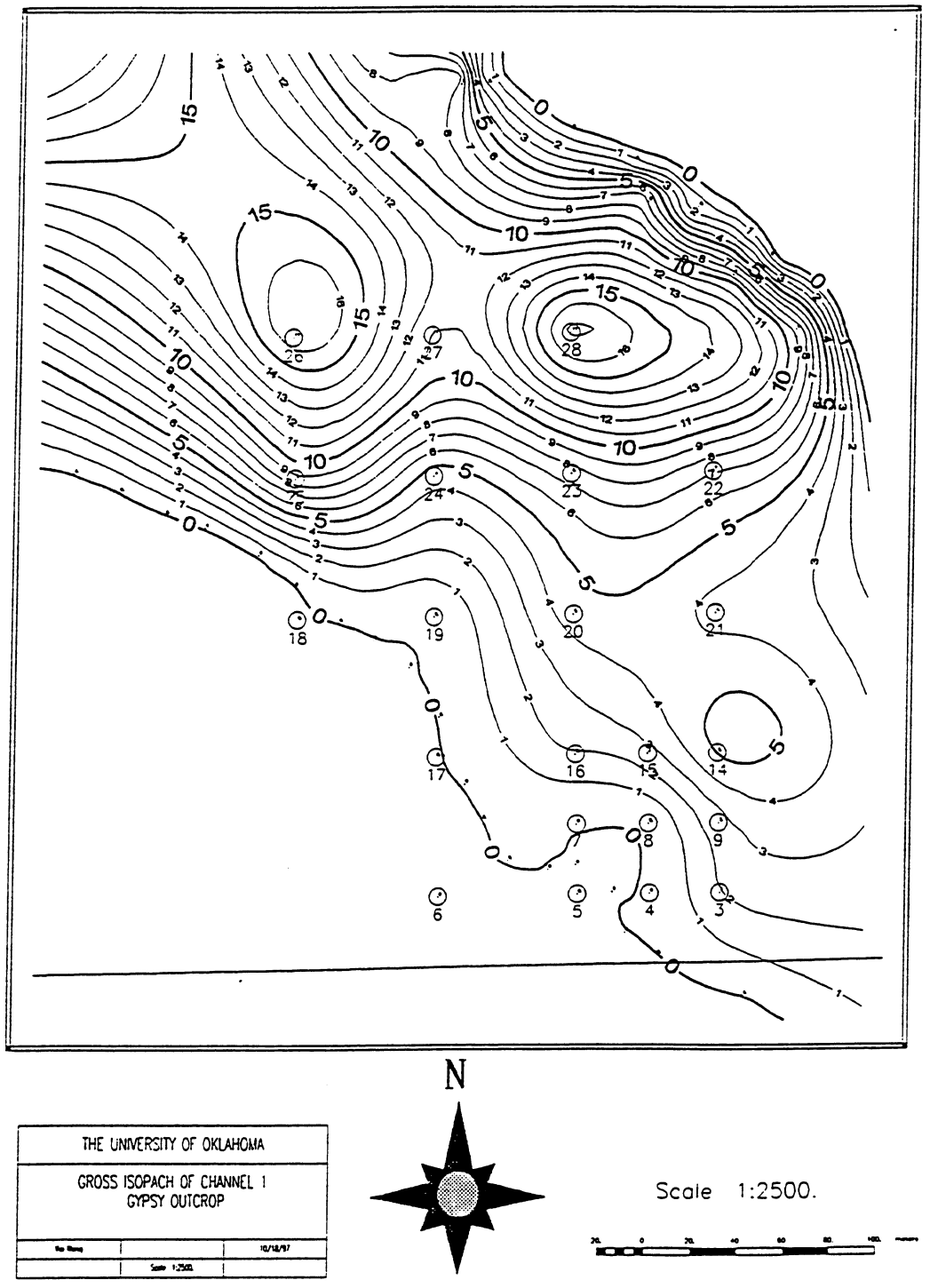

Fig. 3-2 Gross Isopach of Channel 1 In Gypsy Formation

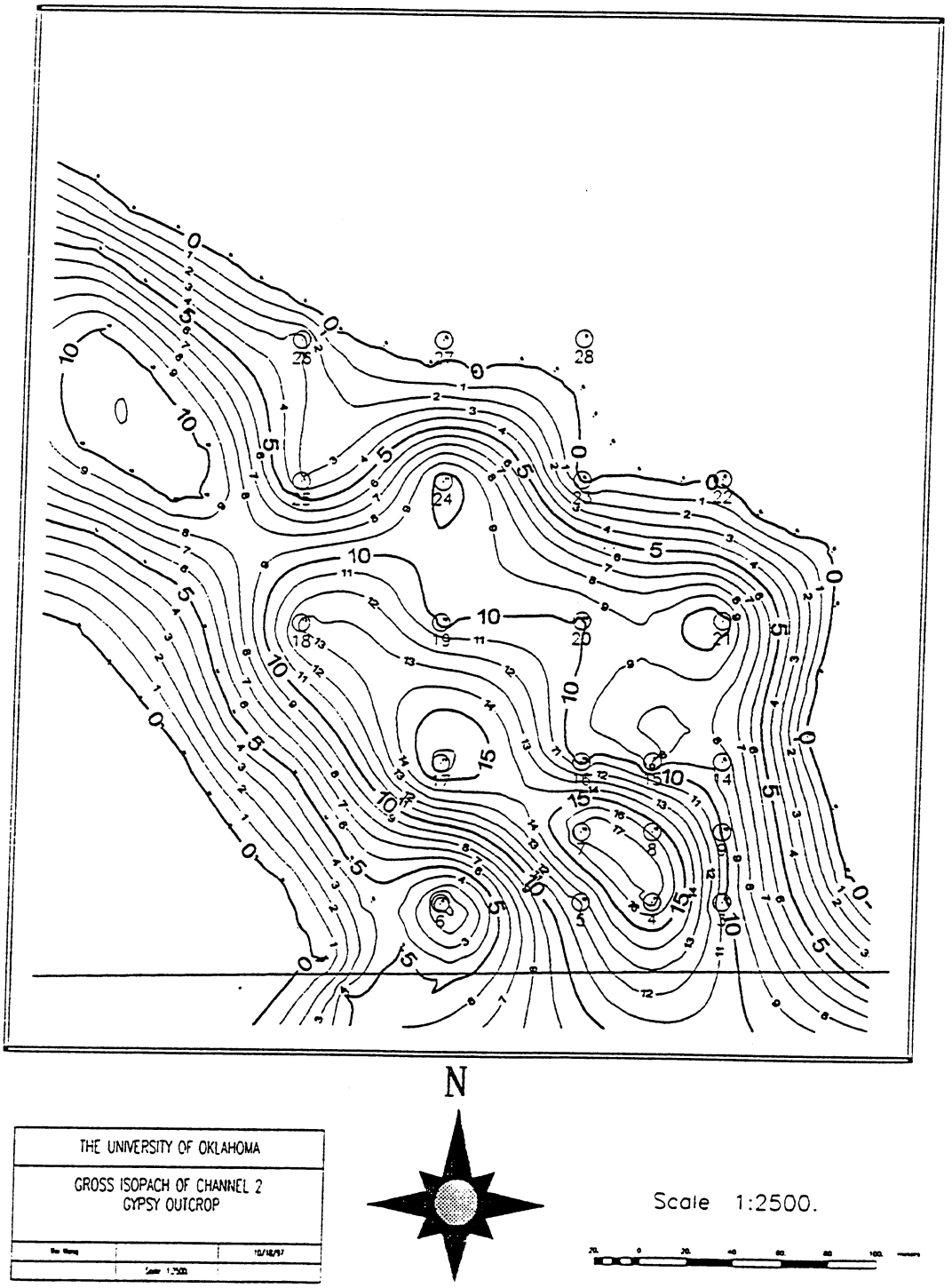

Fig. 3-3 Gross Isopach of Channel 2 In Gypsy Formation

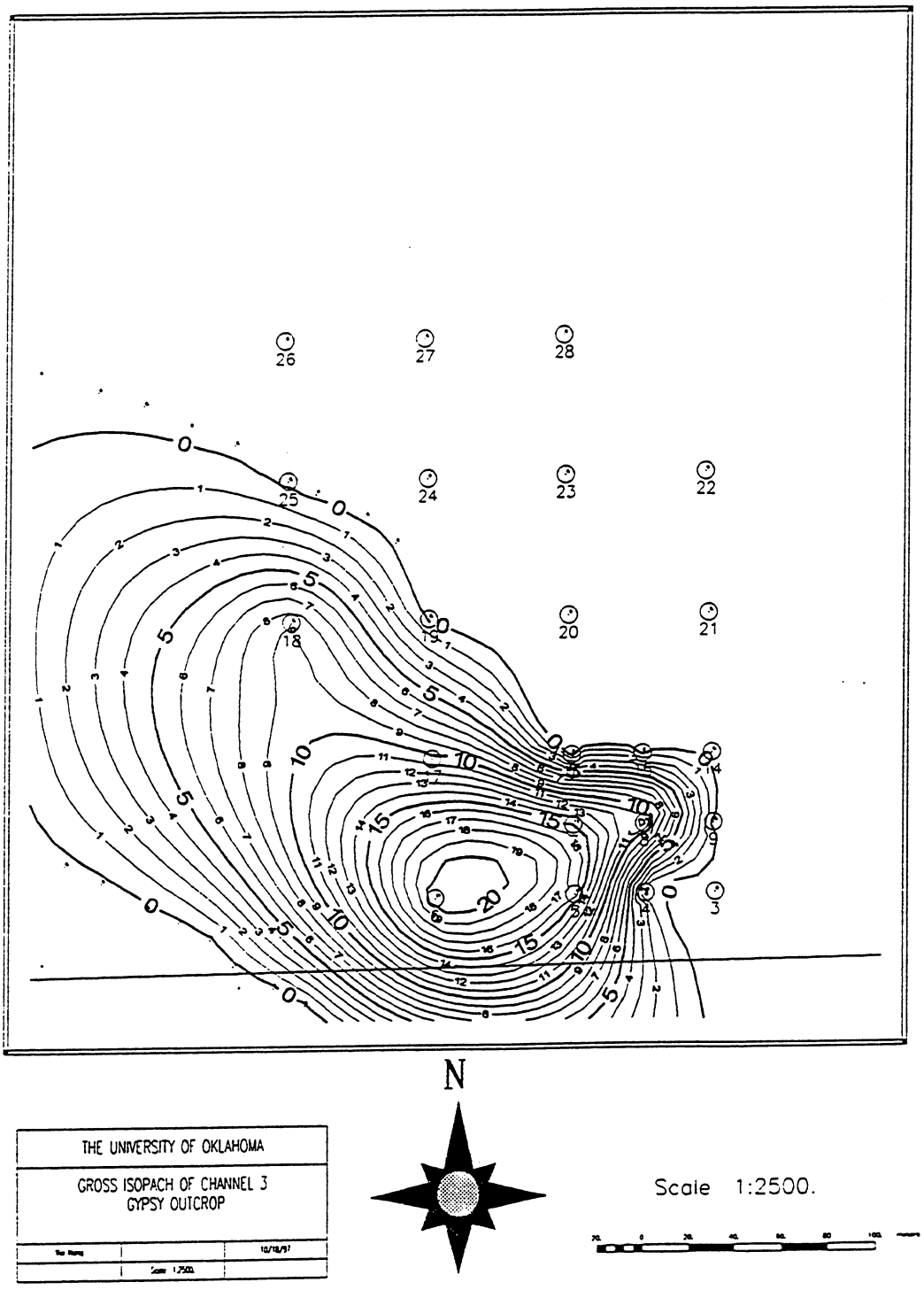

Fig. 3-4 Gross Isopach of Channel 3 In Gypsy Formation

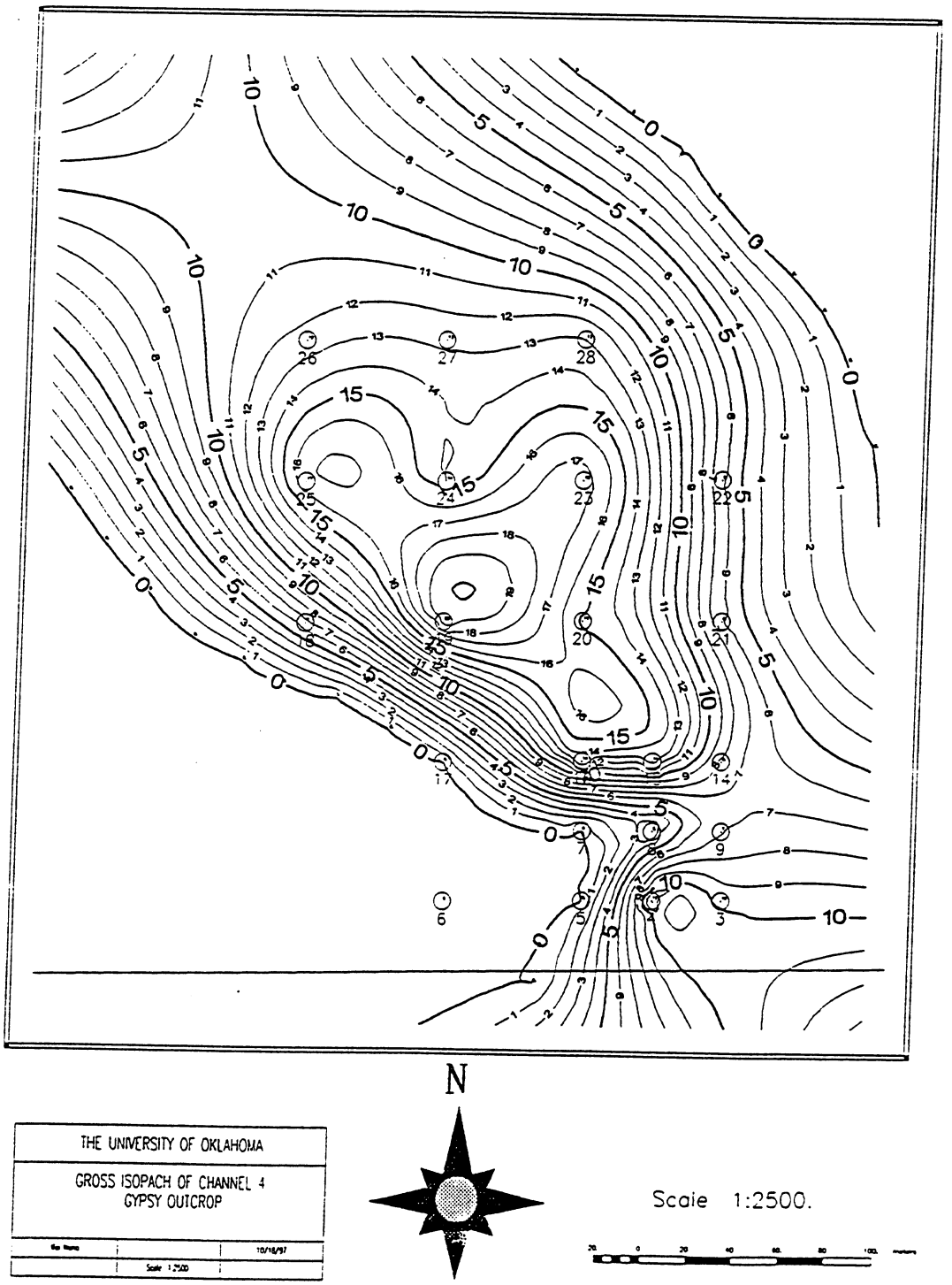

Fig. 3-5 Gross Isopach of Channel 4 In Gypsy Formation

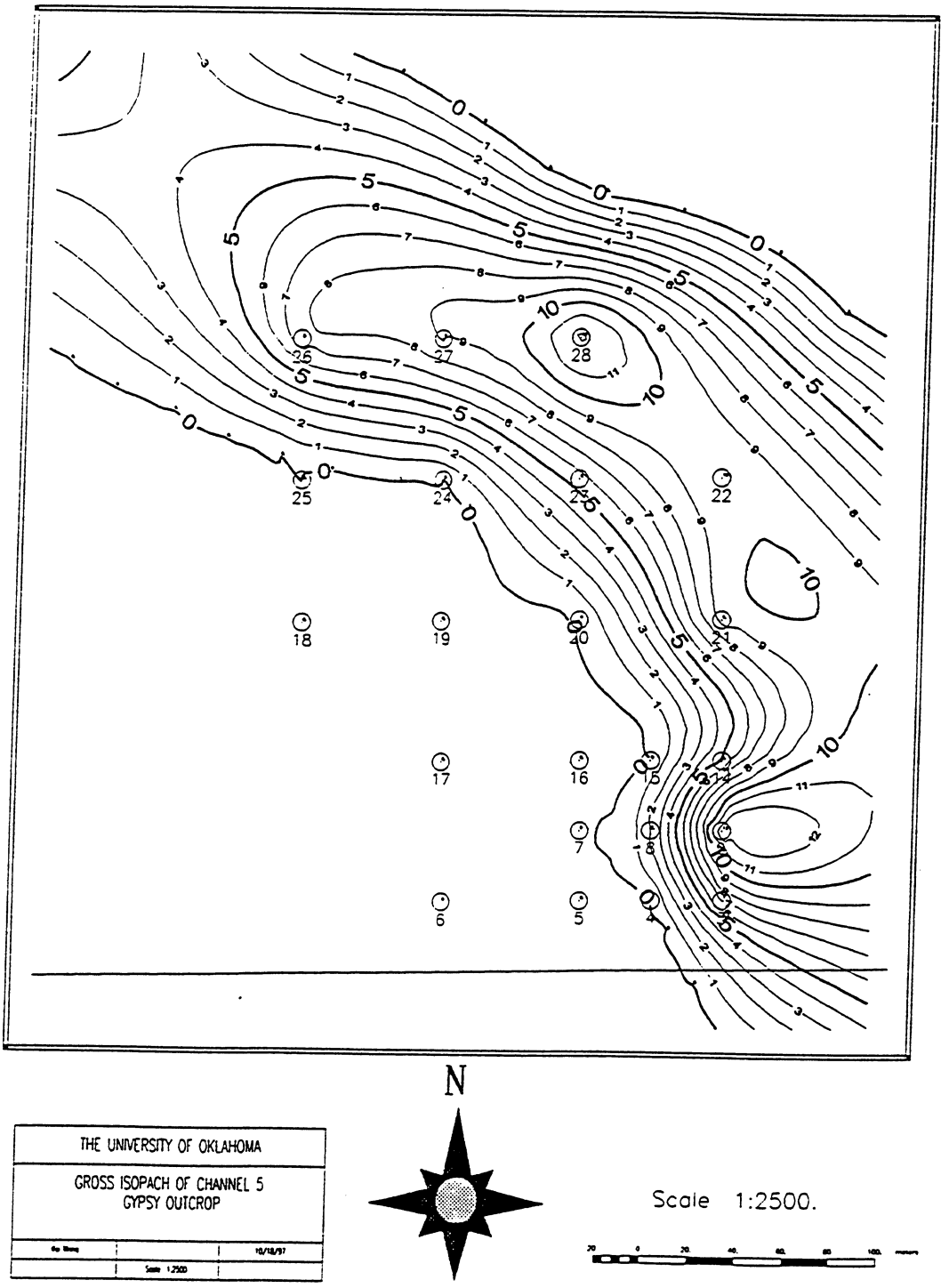

Fig. 3-6 Gross Isopach of Channel 5 In Gypsy Formation

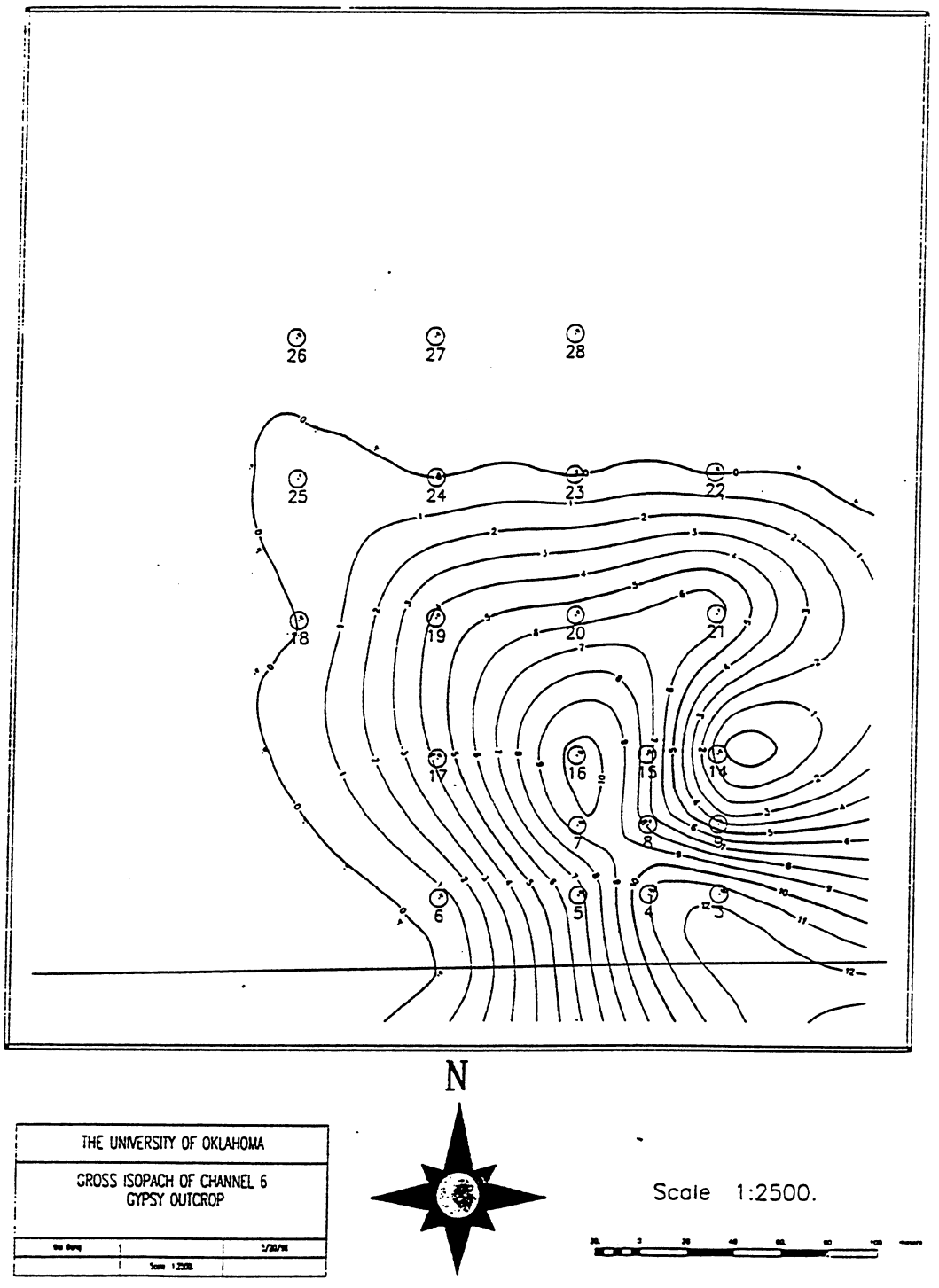

Fig. 3-7 Gross Isopach of Channel 6 In Gypsy Formation

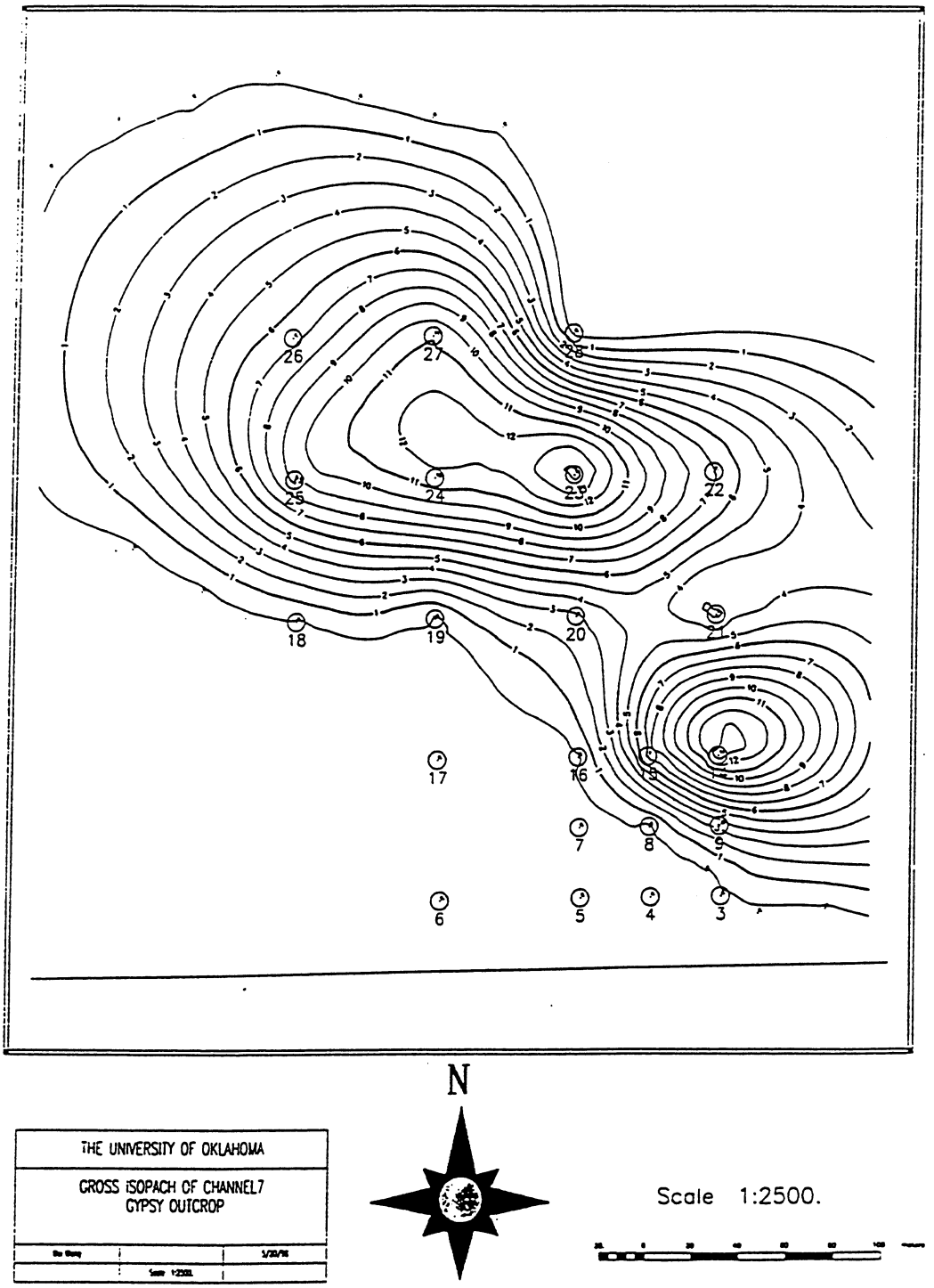

Fig. 3-8 Gross Isopach of Channel 7 In Gypsy Formation

As stated earlier, the Gypsy formation is well documented, including 1,056 cores analyzed and described from 22 wells. Five sandstone lithofacies identified within Gypsy sandbodies, are mudclast, cross-beds, plane-beds, ripple-beds, and overbank. In addition, some core samples represent soft sediment deformation and unidentifiable sedimentary structures. The lateral extent of lithofacies has been determined to be less than 100 ft (Doyle *et al.*, 1992). A typical lithofacies sequence within an individual channel sandbody of the Gypsy sandstone is illustrated in Fig. 3-9. Most core descriptions in 22 wells follow the distribution illustrated in Fig. 3-9 in the vertical direction, except some cross-beds and plane-beds occur interchangeably within one channel.

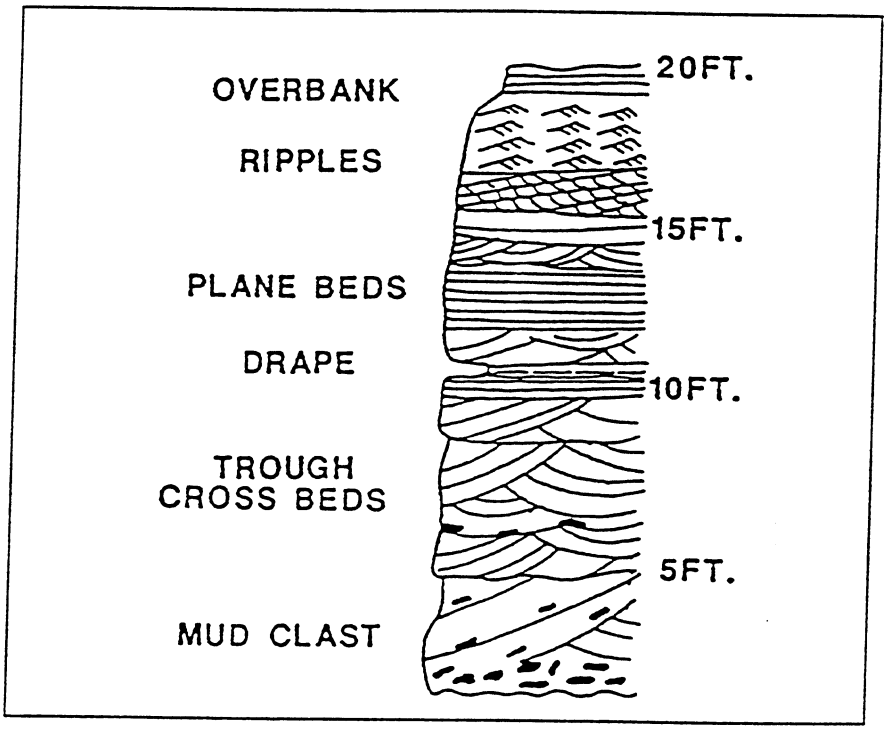

Fig. 3-9 Typical Lithofacies Sequence in Gypsy Formation ((Doyle and Sweet, 1992)

Mudclast sandstone is more extensively developed in the lower channels than in the higher ones. The characteristic grains of this facies are cobble to medium sand-size intraclasts of red, green, and/or grey mudstone. The individual facies is typically 1 to 3 ft thick. **Cross-Beds** sandstone is composed of 0.3 to 3 ft thick sets of cross-bedding. The grain size is very fine to medium sand with some coarse sand and granule-size intraclasts observed on foreset laminations. **Plane-beds** sandstone is fine to very fine grained sandstone with a planar bedding thickness ranging from 0.5 to 3 ft. **Ripple-beds** sandstone is fine to very fine sandstone and often interlaminated with mudstone and siltstone. **Overbank** is mainly composed of impermeable mudstone and siltstone ranging 4.5 to 13 ft thick (Doyle and Sweet, 1992).

Using porosity and permeability data from the 22 wells, a relationship was plotted as in Fig. 3-10. It was observed that cross-beds, plane-beds, and mudstone exhibit better correlation as compared to ripple-beds and mudclast. Cross-beds and plane-beds exhibit the best reservoir quality and also show similar trend in this plot. Overbank presents the lowest values of porosity and permeability. The properties of ripple-beds fall between cross-beds, plane-beds and overbank. Mudclast is the most heterogeneous lithofacies in the Gypsy formation and exhibits a wide distribution of properties as shown in Fig. 3-10. Table 3-1 lists the statistical characteristics for the five lithofacies in the Gypsy formation.

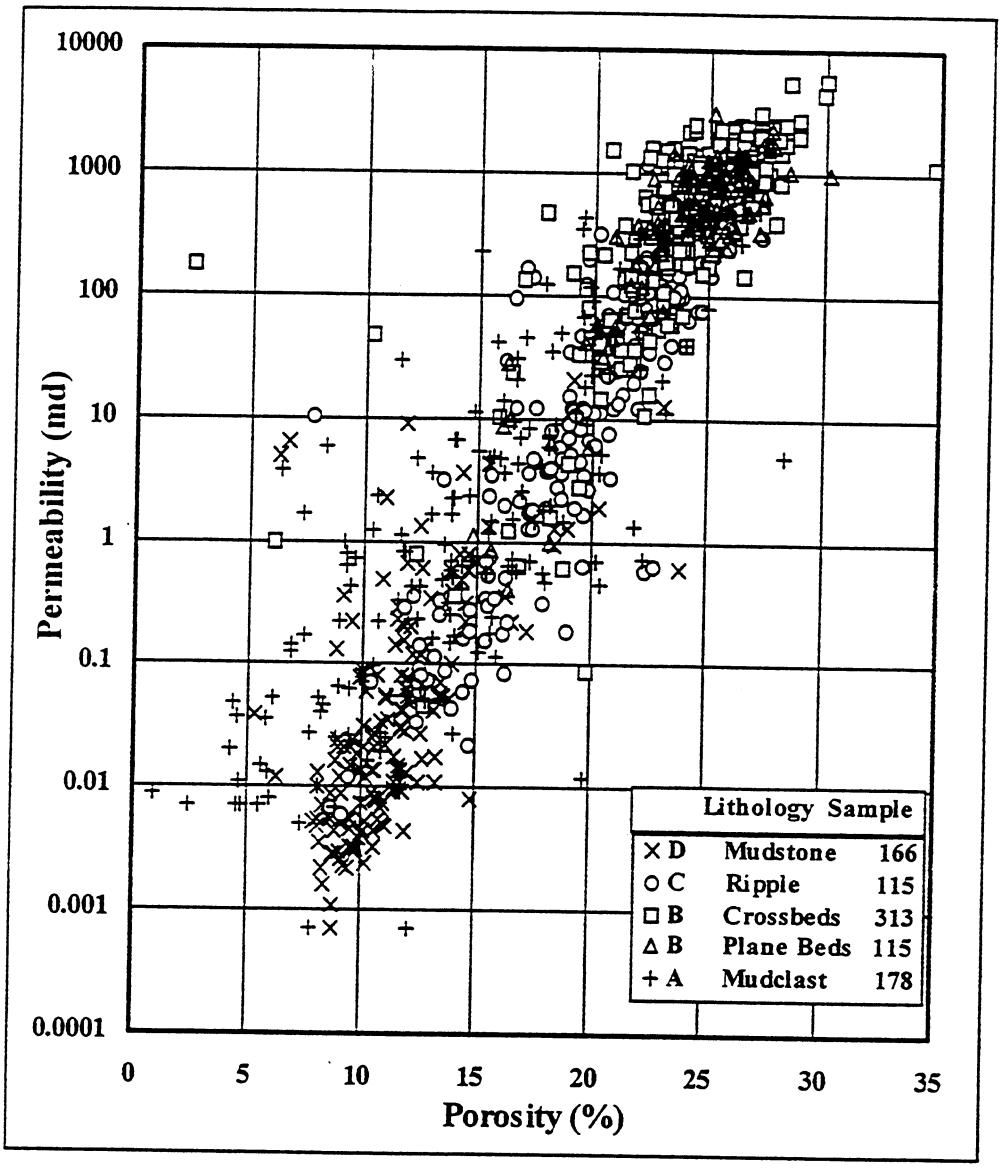

Fig. 3-10 Cross Plot of Permeability and Porosity for Gypsy Formation

Table 3-1 Statistical Characteristics of the Different Lithofacies In Gypsy Formation

Lithofacies	ϕ (%) Mean	ϕ (%) Standard Deviation	k (mD) Mean	k (mD) Standard Deviation
Mudstone	11.38	2.78	0.52	2.15
Ripple-bed	19.47	3.93	88.08	190.92
Cross-bed	24.23	3.24	871.90	779.59
Plane-bed	24.12	2.84	658.68	520.77
Musclast	15.04	5.80	60.43	170.11

3.2 Channel Model

Landmark's Stratigraphic Geocellular Modeling (SGM) was used to develop the geological models in this study. SGM is used to model heterogeneous rock and fluid properties in three dimensions for geological analysis and visualization. Incorporating grided subsurface horizons and well data from all available sources, SGM can generate a comprehensive 3-D geological model at finer resolution to better assist the petroleum engineer in understanding reservoir characteristics. SGM uses stratigraphic patterns to generate a three-dimensional framework for geological models. The surface maps representing the distribution of layers in space were generated by Geographix.

The structural behavior of Gypsy sandbodies was determined in BP's Integrated Reservoir Description Project in 1989 (Doyle and Sweet, 1992) by observing and analyzing the outcrops and core samples from 22 well bores. Table 3-2 shows the top and bottom elevation of seven channels observed in 22 wells.

Table 3-2. Correlation of Channels in the Gypsy Formation

Well	S. E.	T7	B7	T6	B6	T5	B5	T4
3	885.9	.	.	878.4	866.8	866.1	857.7	857.6
4	882.1	.	.	875.5	864.3	.	.	863.9
5	878.0	.	.	872.4	866.1	.	.	.
6	866.1	.	.		865.7	.	.	.
7	887.8	.	.	875.7	865.8	.	.	.
8	893.1	.	.	876.9	869.7	869.4	867.4	866.3
9	891.1	877.9	874.6	874.6	870.8	870.8	858	858
14	887.7	879.5	865.9			864.6	859.5	859.4
15	896.7	877.5	870.2	870.2	862.6	.	.	862
16	896.0	.	.	875.6	865.2	.	.	860.7
17	879.1	.	.	876	871.8	.	.	.
18	867.8	.	.			.	.	863.1
19	889.5	.	.	874.8	870.5	.	.	861.7
20	900.4	875.3	872.5	872.5	867	.	.	861.8
21	878.1	878.1	875.4	875.4	868.7	868	858.7	858.6
22	871.2	870.6	863.5	.	.	863.5	853.7	853.6
23	892.4	881.3	866.9	.	.	866.9	861.3	861.3
24	897.0	879.7	868	.	.	.	.	862
25	877.5	875.4	866.1	866	864.9	.	.	861.5
26	880.5		873.9	.	.	873.9	866.2	866.1
27	896.5	883	872.1	.	.	872.1	863	862.9
28	878.7	.	.	.	.	878.7	866.6	865.4
Well	**B4**	**T3**	**B3**	**T2**	**B2**	**T1**	**B1**	**Tallant**
3	848	.	.	847.9	837.7	837.7	835.6	830.7
4	851.7	.	.	851.7	834.3	.	.	828.9
5	.	863	846.5	846.5	834.6	.	.	827
6	.	864.9	843.9			.	.	828.5
7	.	863.8	848.8	848.8	830.8	.	.	828.8
8	864.4	864.3	851.9	851.9	836.1	.	.	829.6
9	851.1	.	.	851	841.1	841.1	838.5	830.3
14	851.7	.	.	851.6	842.9	842.8	837.4	832
15	848.5	.	.	848.5	840.5	840.5	837.8	829.6
16	846.7	.	.	846.7	837.1	837	834.9	829.1
17	.	861.3	851	850.9	834.6	.	.	828.1
18	856.4	856.4	847.4	847.3	834	.	.	828.3
19	842.1	.	.	842.1	832.5	.	.	822.6
20	847	.	.	846.9	836.8	836.7	832.1	824.2
21	852.5	.	.	852.5	841.6	841.6	837.9	832.7
22	847.5	.	.	.	.	847.5	840.5	834.1
23	843.7	.	.	.	.	843.7	836.2	830.9
24	848	.	.	847.9	837	837	832.7	827.1
25	844.7	.	.	844.7	841.6	841.6	832.7	826.3
26	853.7	.	.	853.6	850.1	850	833.2	825.4
27	850.2	.	.	.	.	850.1	839.2	824.8
28	852.7	.	.	.	.	852.6	835.4	827.9

Note: S.E. - surface elevation, T7 - top of channel 7, B7 - bottom of channel 7, Tallant - bottom of Gypsy formation

Fourteen surface maps, including the tops and bottoms of the seven channels, were generated using Geographix and the data in Table 3-2. The modeling grid system used was 36 by 43, with a grid size of 32.8 feet in both X and Y direction.

These fourteen surface maps were imported into SGM to generate a 3D geological channel model. Permeability and porosity data in 22 wells were used as control points to determine the distribution of reservoir properties.

A deterministic method was used to determine the distribution of reservoir properties, including permeability and porosity. One important parameter, which effects the heterogeneity of geological model, is the search radius, R, which determines how many wells are included when the properties of grid blocks are calculated. There exists a minimum and a maximum values of R. The minimum value of R is the smallest one that does not create null values, and the maximum value of R is the one that still provides the best characterization of reservoir heterogeneity. To determine a value of R applicable for Gypsy formation, several R values were used to generate 3-D models. The statistical characteristics of the heterogeneity of the model were then compared with the one obtained from core analysis. Statistical mean and standard deviation were used to evaluate the validity of a R value used.

Figs. 3-11 to 3-14 illustrate the statistical characteristics of the channel model when three different R values were used as compared to the statistical characteristics from core analysis. The minimum search radius for the channel model of Gypsy formation was determined to be 534 ft, because null values were observed when a value of R less than 534 ft was used. The geological models become more

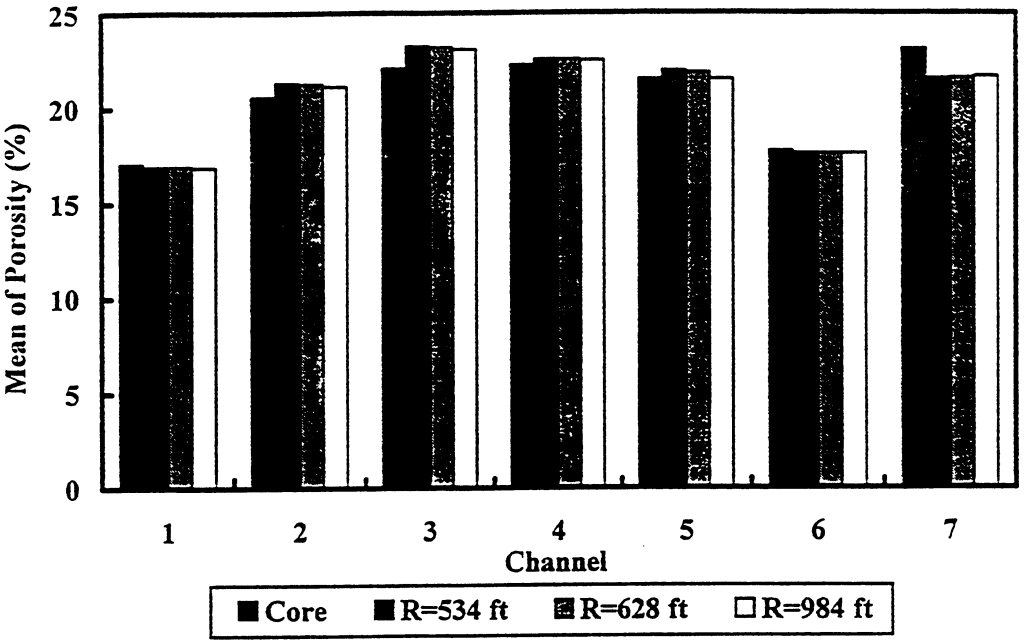

Fig. 3-11 Statistical Mean of Prosity for Channel Model

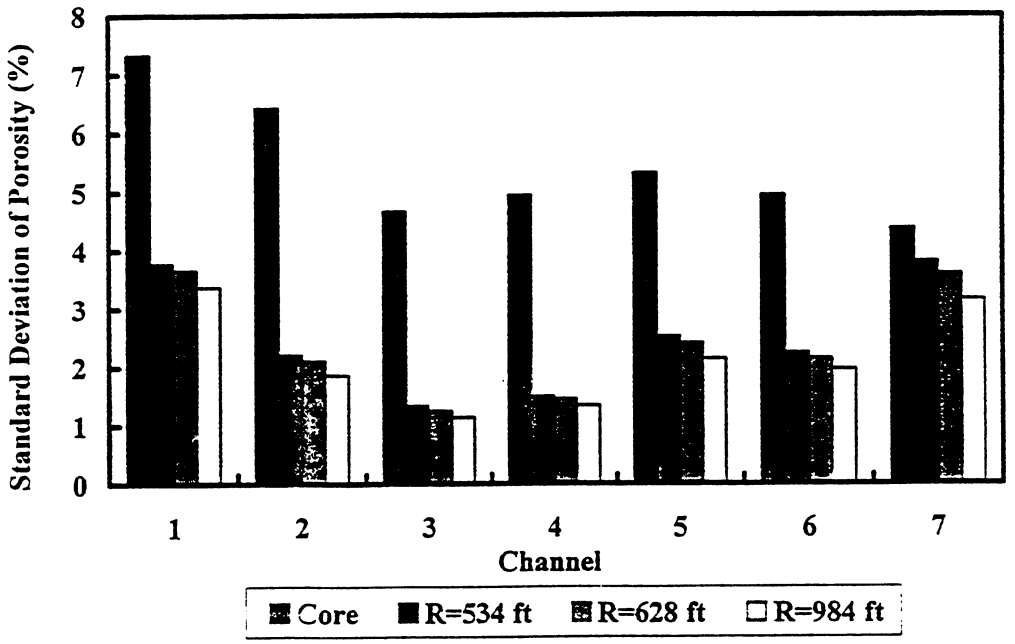

Fig. 3-12 Standard Deviation of Porosity for Channel Model

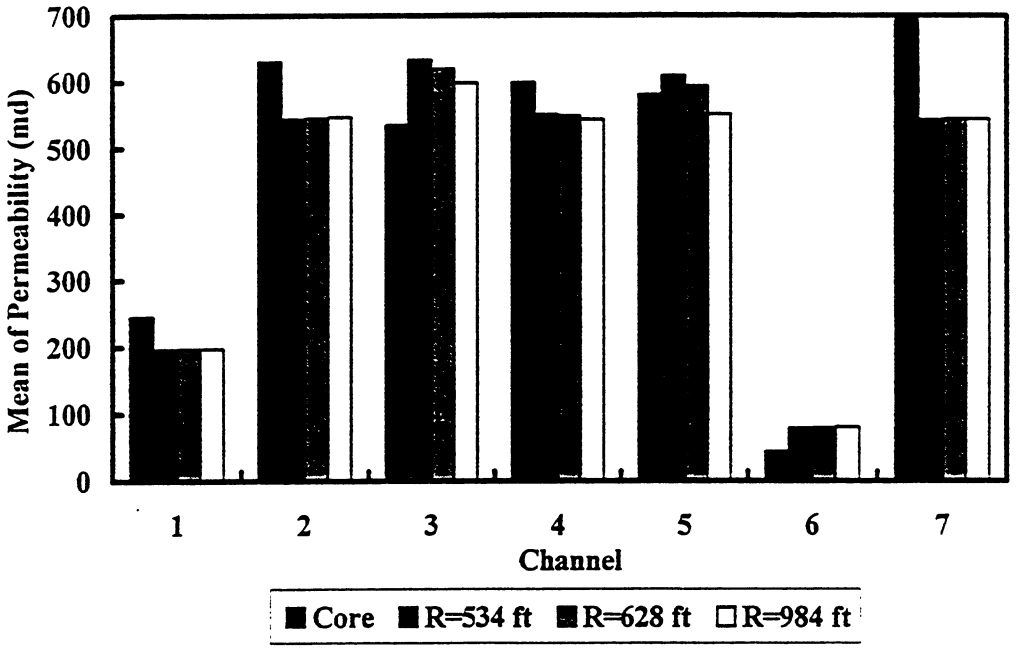

Fig. 3-13 Statistical Mean of Permeability for Channel Model

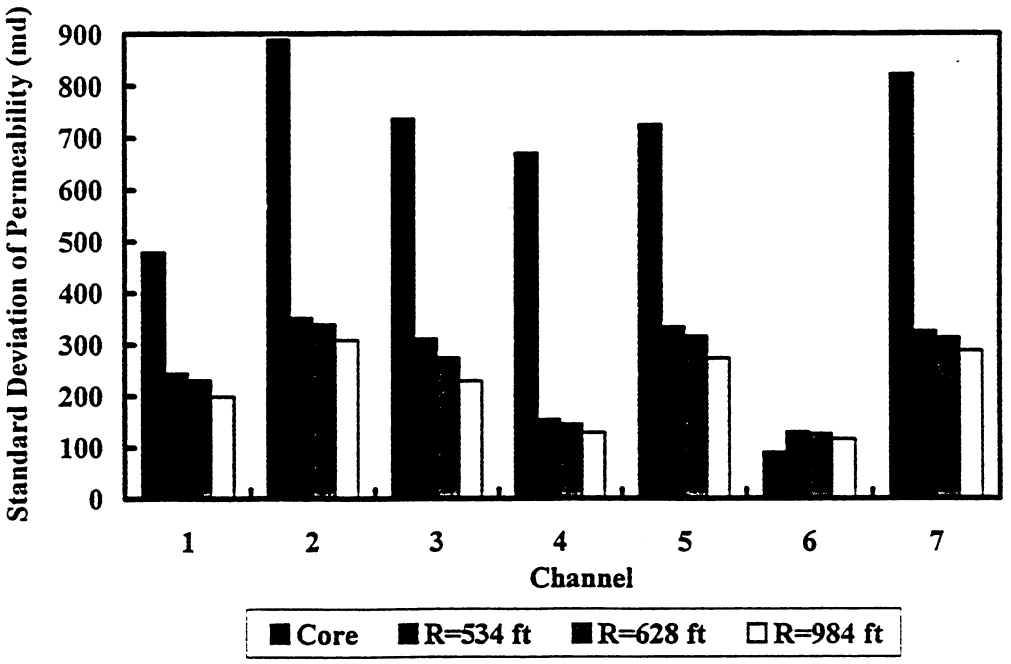

Fig. 3-14 Standard Deviation of Permeability for Channel Model

homogeneous as R increases, as is apparent from smaller values of the standard deviations for porosity and permeability with increasing R values. This is consistent with the principle of deterministic algorithms. Even though 534 ft is probably not small enough to characterize the statistical variations in the properties of Gypsy formation, null value did occur when smaller R values were used. Therefore, 534 ft was determined to be the optimum R value for Gypsy channel model. It can be observed that the mean and standard deviation of porosity are not very sensitive to R values, but the mean and standard deviation of permeability are very sensitive to R values used.

Fig. 3-15 is the cross sectional view of coarse-scale Gypsy channel model, in which different colors represent different channels from channel 1 to 7. The deep blue color represents the mudstone and siltstone between channels. Pinch-out can be obviously observed in all seven channels.

3.3 Lithofacies Model

To develop a lithofacies model, initial identification of lithofacies layers is necessary. The channel boundaries may not intersect such lithofacies layers because floodplain or mudstone layers exist that acts as a flow barrier between channels, even though they are not continuous over the whole formation area. It is very important that a lateral correlation of each lithofacies unit between wells exists and such correlation is mappable. Therefore, it was required in this study that each individual lithofacies within a channel must occur in at least two wells. If it exists in only one well and its thickness is less than one foot, it was ignored and combined with an adjacent

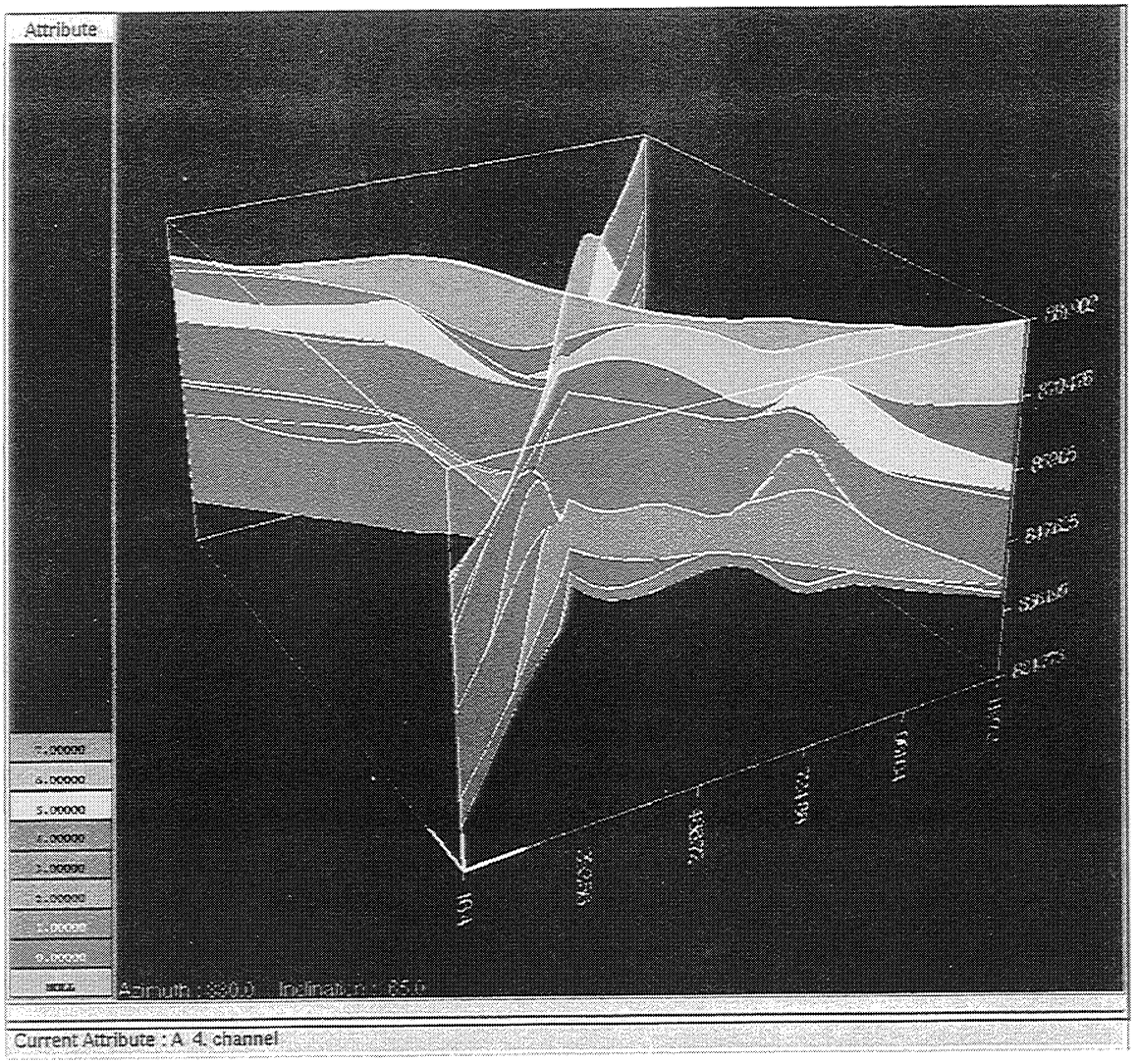

Fig. 3-15 Cross-Sectional View of Gypsy Channel Model

ithofacies unit that demonstrates similar properties. Observing the distribution of lithofacies in 22 wells, it is apparent that five kinds of lithofacies are present and follow the sequence of overbank, ripple-bed, plane-beds, cross-beds, and mudclast, from top to bottom, except that plane-beds and cross-beds occur interchangeably in some wells. Because cross-beds and plane-beds possess similar rock properties, as shown in Fig. 3-10, they were combined and treated as one lithofacies unit. Hence, there were only four significant lithofacies units in each individual channel in the lithofacies model. In total, 22 lithofacies units were identified in the Gypsy formation. Therefore, there are 28 layers in lithofacies model, including 22 lithofacies layers and six barriers between channels. The top and bottom positions of each lithofacies unit in the study area were determined and listed in Table 3-3.

Based on the correlation of lithofacies in Table 3-1, fifteen surface maps were generated using Geographix in addition to the fourteen surface maps generated in channel model, or a total of 29 surface maps were used to generate a 3-D lithofacies model. The search radius, R, was determined to be 890 ft for lithofacies model. Fig. 3-16 is the cross-sectional view of the lithofacies model for Gypsy formation. As for channel model, different colors represent different lithofacies units from 1 to 22 in the model. It can be observed that each channel was divided into 2 to 4 lithofacies units, which was indicated by the boundary lines in the model.

Table 3-3 Correlation of Lithofacies Units in the Gypsy Formation

WELL	SURFACE	T7C	T7B	T7A	B7	T6D	T6C	B6	T5C	T5B	T5A	B5	T4D	T4C	T4B	T4A
3	885.9					878.4		866.8		864.86	858.73	857.7			857.6	
4	882.1						875.5	864.3						863.9	858.95	
5	878						872.4	866.1								
6	866.1						866.1	865.7								
7	887.8						875.7	865.8								
8	893.1					876.9	872.45	869.7	869.4			867.4		866.3		
9	891.1	877.9	876.7		874.6	874.6	874.1	870.8	870.8	865.2		858		858	855.175	
14	887.7	879.5	871.7	867.3	865.9					864.6		859.5		859.4	854.9	
15	896.7	877.5	874.2		870.2		870.2	862.6							862	
16	896						875.6	865.2							860.7	847.125
17	879.1						876	871.8						863.1	862.775	
18	867.8													861.7	861.25	846.375
19	889.5						874.8	870.5							861.8	
20	900.4		875.3		872.5	872.5		867				858.7		858.6	855.1	
21	878.1		878.1		875.4		875.4	866.7	868	861.875		853.7				853.6
22	871.2			870.6	863.5					863.5	857.2	861.3	861.3	861.025	858.4	848.4
23	892.4		881.3	868.4	866.9				866.9	863.4				862	857.85	
24	897		879.7		868									861.5	859.5	848.5
25	877.5		875.4		866.1		866	864.9				866.2	866.1	865.05	863.5	855.05
26	880.5		880.5		873.9					873.9		863			862.9	
27	886.5		883		872.1					872.1	864.375	866.6		865.6	863.7	
28	878.7									878.7						
WELL	SURFACE	B4	T3C	T3B	B3	T2D	T2C	T2B	T2A	B2	T1D	T1C	T1B	T1A	B1	TALLANT
3	885.9	848						847.9	841.4	837.7				837.7	835.6	830.7
4	882.1	851.7						851.7	840.3	834.3						828.9
5	878			863	846.5			846.5	841	834.6						827
6	866.1		864.9	859.1	843.9											828.5
7	887.8		863.8	860.55	848.8			848.8	837.8	830.8						828.8
8	893.1	864.4	864.3	860.5	851.9	851.9		851.1	843.55	836.1						829.6
9	891.1	851.1						851	843.37	841.1				841.1	838.5	830.3
14	887.7	851.7					851.6	850.55	845.05	842.9		842.8		841.45	837.4	832
15	896.7	848.5						848.5	842.7	840.5				840.5	837.8	829.6
16	896	846.7						846.7	842	837.1				837	834.9	829.1
17	879.1		861.3	859.05	851			850.9	842.95	834.1						828.1
18	867.8	856.4	856.4	855.11	847.4			847.3	839.565	834						828.3
19	889.5	842.1						842.1	838.5	832.5						822.6
20	900.4	847						846.9	840.35	836.8			836.7	834.425	832.1	824.2
21	878.1	852.5						852.5	847.45	841.6				841.6	837.9	832.7
22	871.2	847.5									847.5			844.2	840.5	834.1
23	892.4	843.7											843.7	839.4	836.2	830.9
24	897	848				847.9	844.125	842.125	840.7	837				837	832.7	827.1
25	877.5	844.7					844.7		843	841.6		841.6		837.5	832.7	826.3
26	880.5	853.7						853.6		850.1	850	847.575	838.225	835.4	833.2	825.4
27	886.5	850.2											850.1	842.5	839.2	824.8
28	878.7	852.7											852.6	842.7	835.4	827.9

- A - Mudclast B - Crossbeds and Planebeds C - Ripple D - Overbank
- T7C - Top of lithofacies C in channel 7 B6 - Bottom of channel 6 Surface - surface of Gypsy formation Tallant - bottom of Gypsy formation

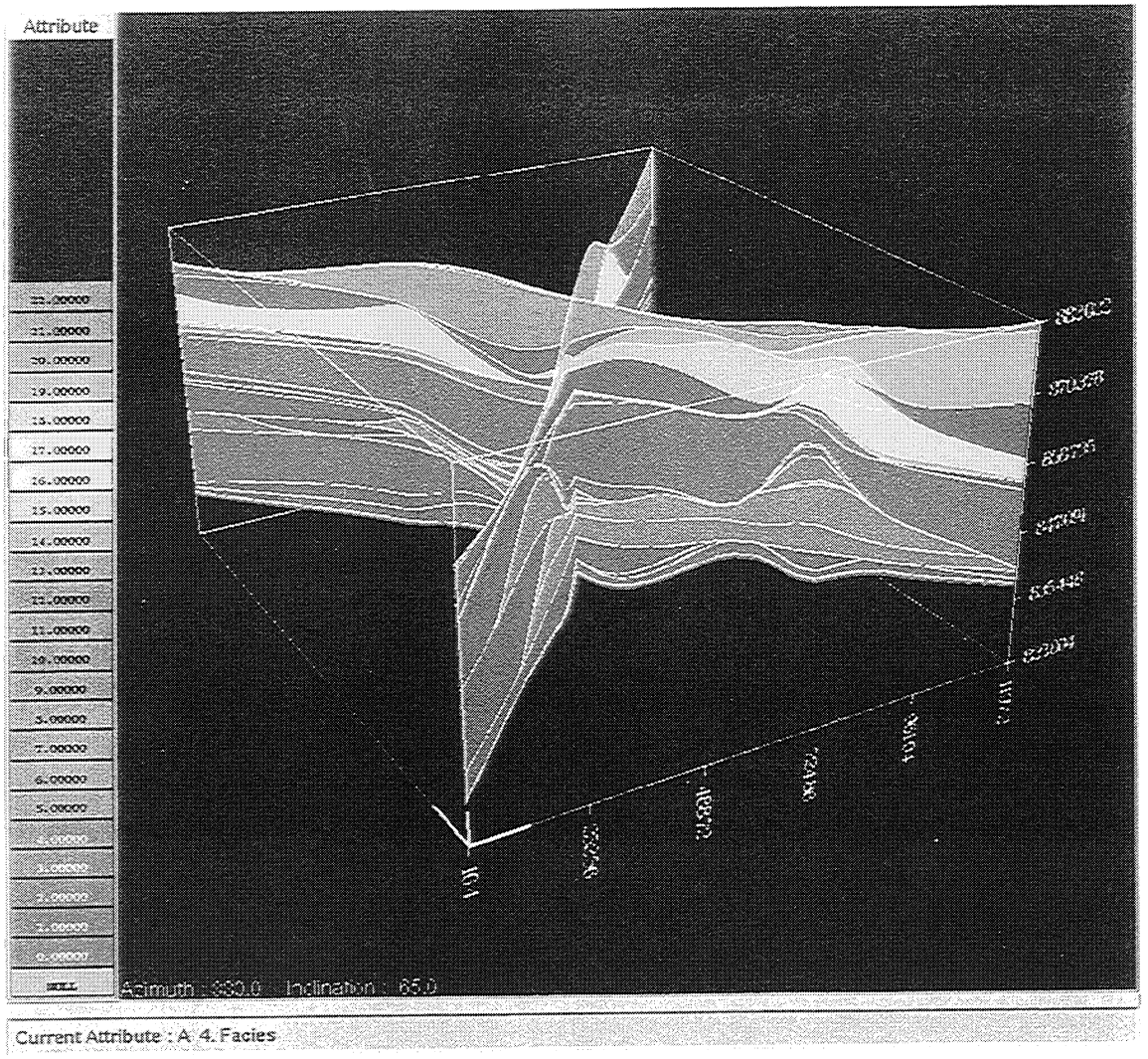

Fig. 3-16 Cross-Sectional View of Gypsy Lithofacies Model

3.4 Flow Unit Model

The concept of flow unit has been discussed in Chapter II. In this study, the definition of hydraulic flow unit, which was proposed by Amaefule *et al.* (1993) and extended by Shedid (1997), will be used to identify the possible flow units for Gypsy formation.

The channel model consists of only thirteen layers, including sandbodies and barriers between channels. The lithofacies model is probably the most accurate model we can obtain, however, the number of layers is twice as many as the channel model. In a practical reservoir simulation study, it would be prohibitively expensive to use so many layers. Therefore, it is of significant benefit to develop a geological model that use less layers than lithofacies model, yet provides satisfactory results in reservoir simulation and scale-up. The flow unit concept offers a possible approach that may accomplish such a geological model.

Flow units can only be obtained by combining some continuous layers or lithofacies units. As mentioned previously, lithofacies unit is probably the most homogeneous unit we can obtain based on the information available, but the boundaries of channels are not crossable, because barriers exist between channels. Therefore, this study focused on identifying the lithofacies units in the same channel that could be combined to form the same flow unit.

As stated previously, there are four lithofacies in Gypsy formation. In total, 22 lithofacies units were identified. Observing the distribution of lithofacies in 22 wells, overbank occurs on the tops of channel 1, 2, 4, and 6 only (only one well has overbank deposits in channel 5, it was combined with the adjacent lithofacies).

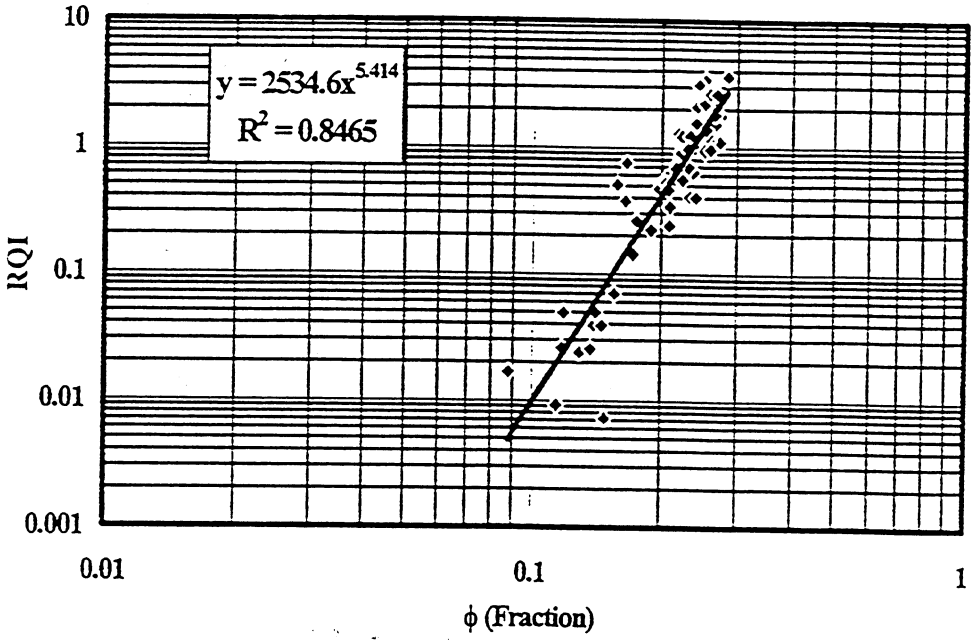

Fig. 3-21 Log-Log Plot of RQI vs ϕ for Flow Unit #5

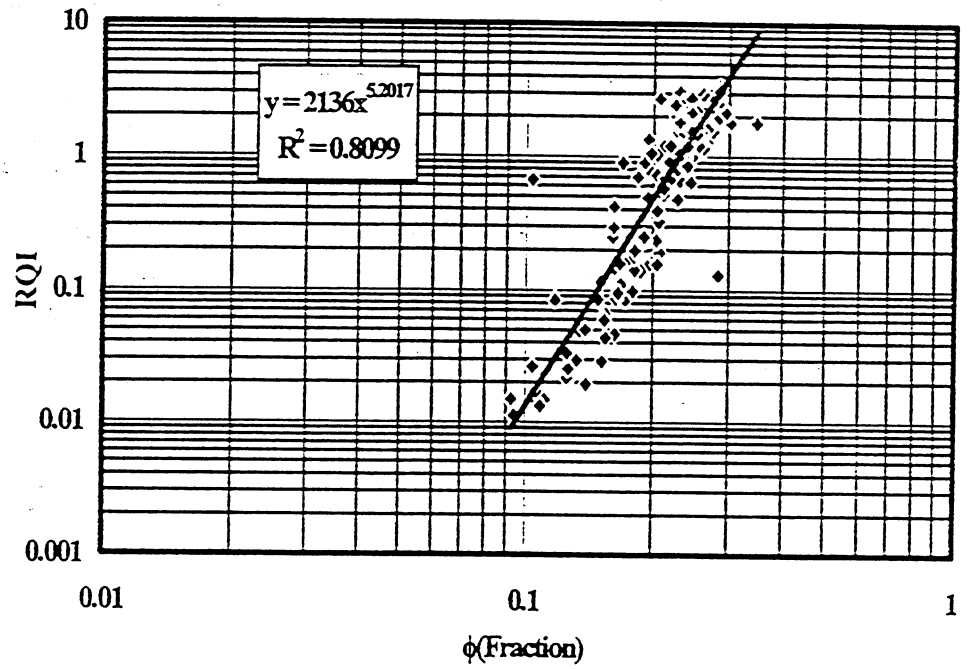

Fig. 3-22 Log-Log Plot of RQI vs ϕ for Flow Unit #6

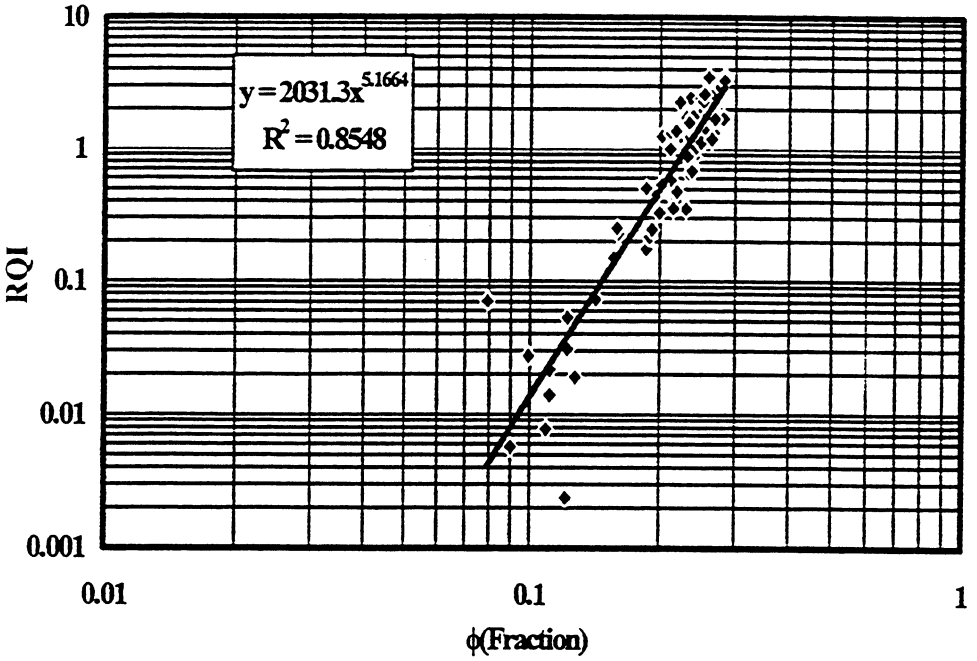

Fig. 3-23 Log-Log Plot of RQI vs ϕ for Flow Unit #7

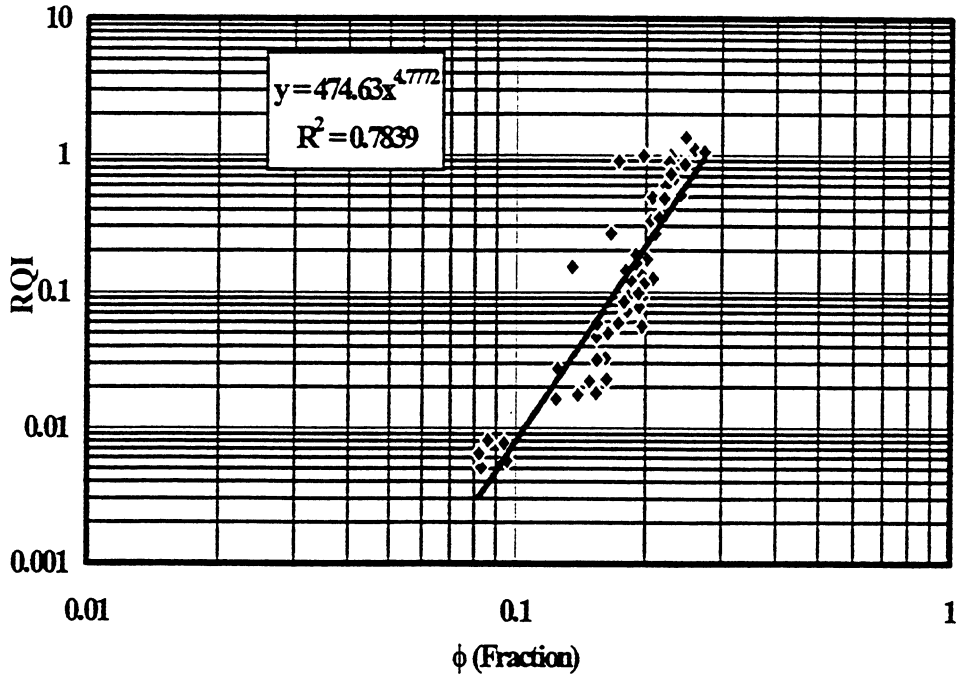

Fig. 3-24 Log-Log Plot of RQI vs ϕ for Flow Unit #8

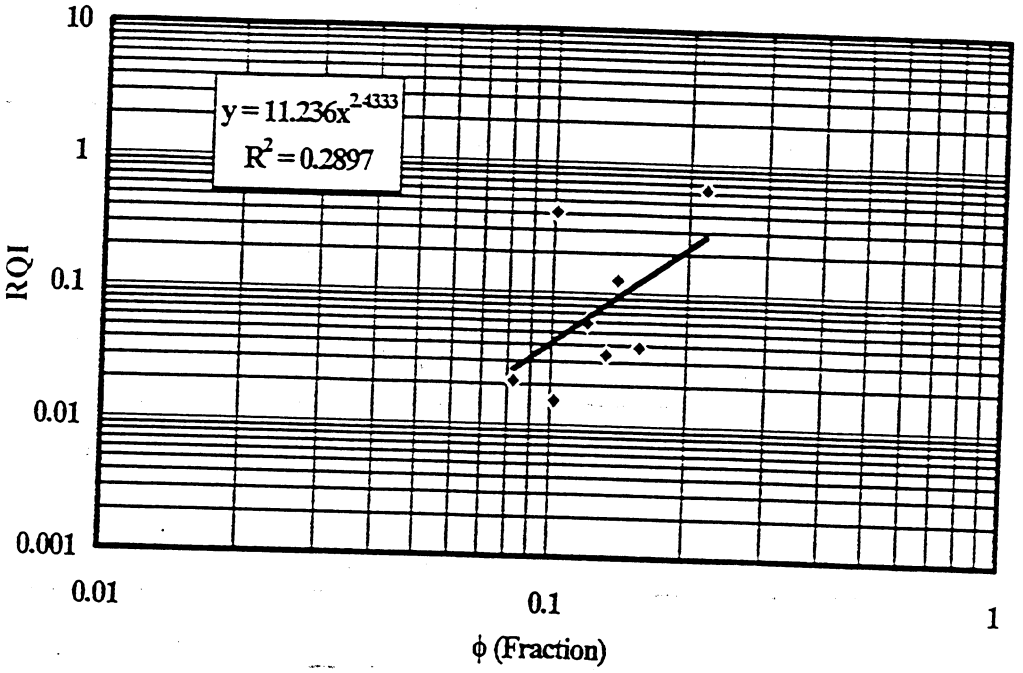

Fig. 3-25 Log-Log Plot of RQI vs ϕ for Flow Unit #9

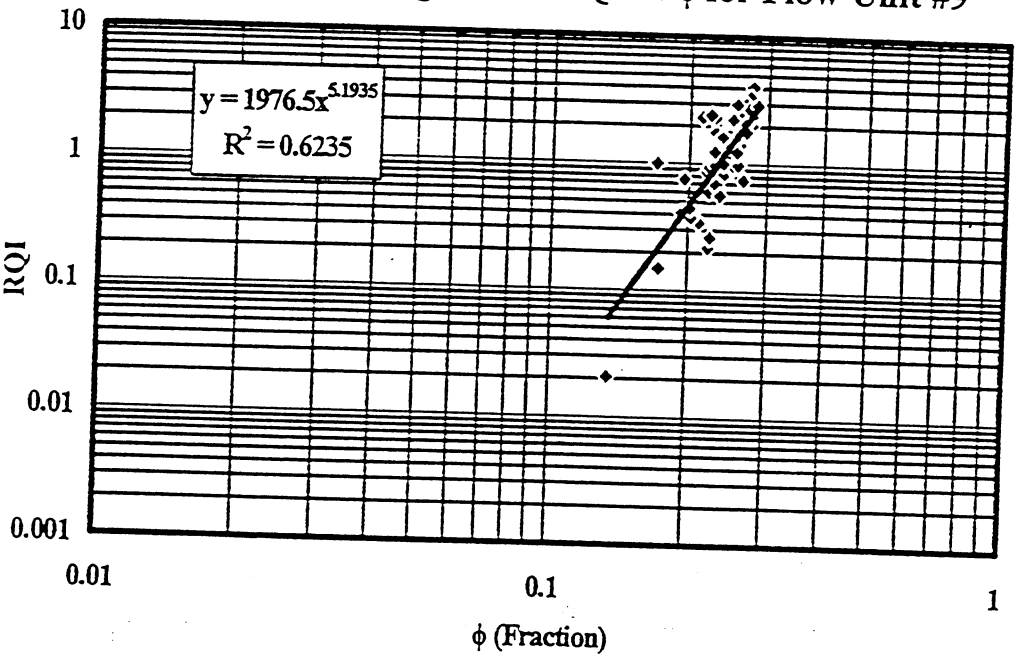

Fig. 3- 26 Log-Log Plot of RQI vs ϕ for Flow Unit #10

Table 3-4 Identification of Flow Units in the Gypsy Formation

Channel	Facies	Flowunit	Slope	FZI
7	C	10	5.1935	1976.5
	B			
	A	9	2.4333	11.236
6	C	8	4.7772	474.63
5	C	7	5.1664	2031.3
	B			
	A			
4	C	6	5.2017	2136
	B			
	A			
3	C	5	5.414	2534.6
	B			
2	C	4	5.3878	2846
	B			
	A	3	2.3112	10.786
1	C	2	5.6055	2655.1
	B			
	A	1	2.0966	6.7215

3.5 Heterogeneity Analysis of the Three Geological Models

Fig. 3-28 is the illustration for the three models, where each column lists the contents of the channel model, the lithofacies model and the flow unit model. Table 3-5 is the summary of the three geological models.

Table 3-5 Summary of the Three Geological Models

Geological Model	Total layer	Permeable Layer	Total Grid (X*Y*Z)
Channel	13	7	19656
Lithofacies	28	22	42336
Flowunit	16	10	24192

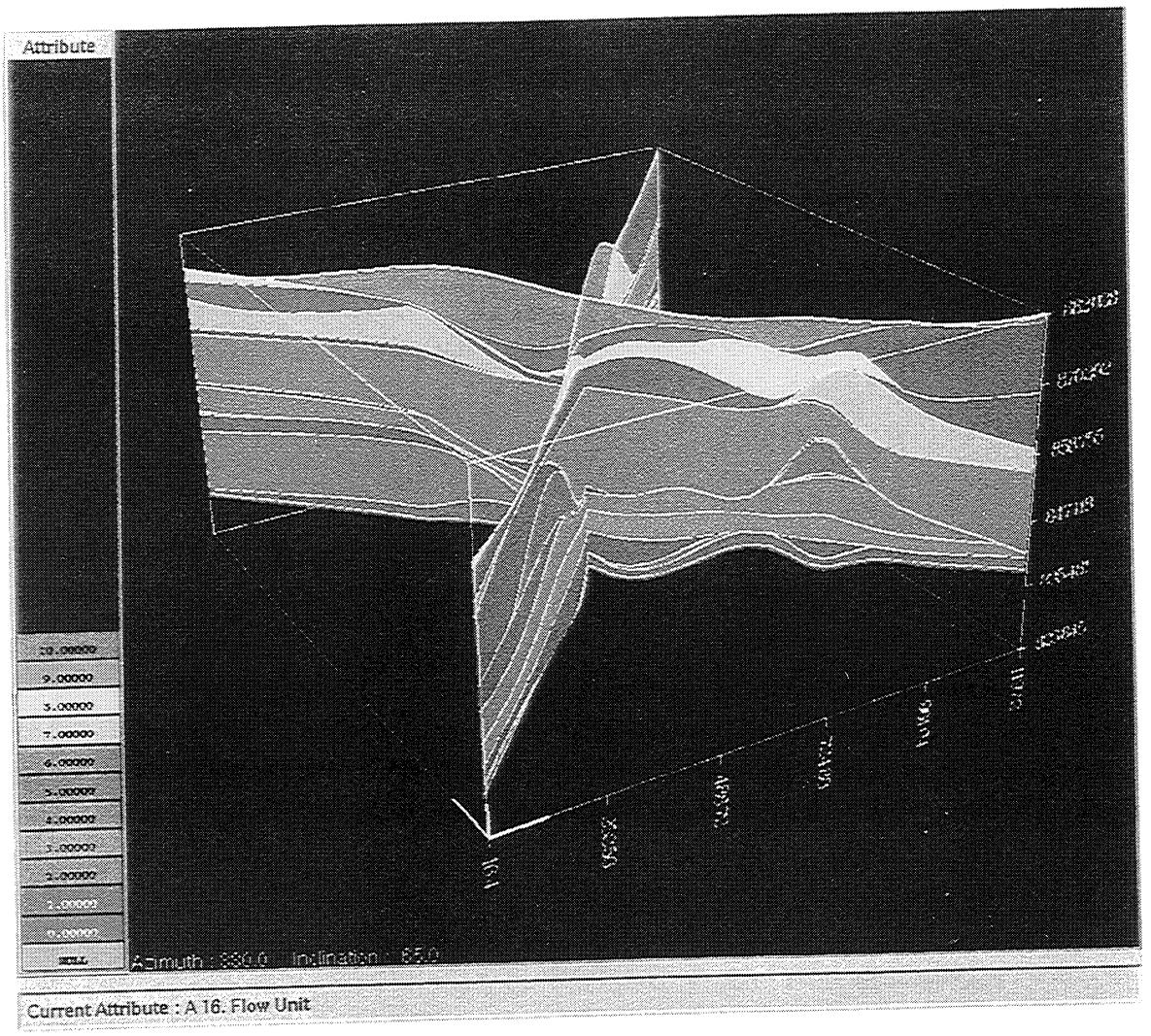

Fig. 3-27 Cross-Sectional View of Gypsy Flowunit Model

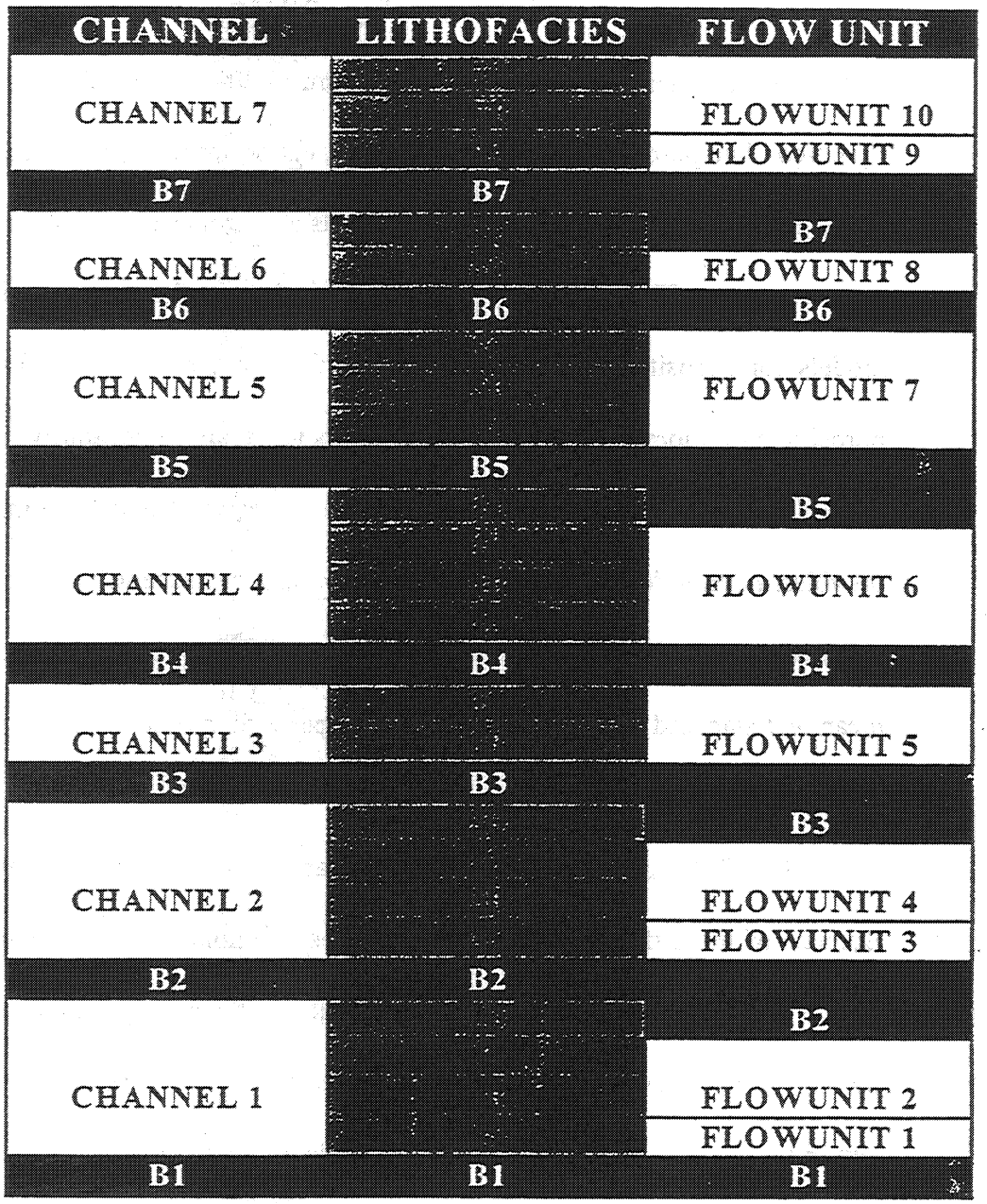

Fig. 3-28 Illustration of Three Geological Models for the Gypsy Formation

The statistical characteristics for the properties of lithofacies model and flowunit model are provided in Figs. 3-29 to 3-36. The statistical characteristics for channel model were provided earlier Figs. 3-11 to 3-14. When comparing the statistical characteristics of porosity and permeability for the three models, it was observed that porosity was more accurately characterized than permeability. The averages of porosity determined by the models are similar to that obtained from core measurements. The differences of standard deviations from core measurement and models for porosity are much smaller than that for permeability. This is because porosity has more homogeneous characteristics than permeability in the Gypsy formation. Comparing the three models, it was observed that the lithofacies model provided a better description than the other two models, except for the permeability of mudstone in the lithofacies model had a unreasonably greater deviation in both its mean and standard deviation because of its sparse distribution. It, therefore, was not presented in the plot.

In SGM, only one search radius, R, can be used for all layers in each model. Because of the different distribution in channels, lithofacies, and flowunits, this may lead to the homogenization during the generation of the geological models. To prevent this error, it is recommended that different search radius, R, should be used for each unit in the generation of geological models if deterministic method is used.

Different strategies of geological modeling can lead to different characteristics of heterogeneity for the models. When comparing the three models generated in this study, the lithofacies model produce more accurate characterization than channel model and flowunit model. In the deterministic method, the search radius, R, has a

significant effect on the heterogeneity of geological model. The extent of heterogeneity decreased with increasing values of R.

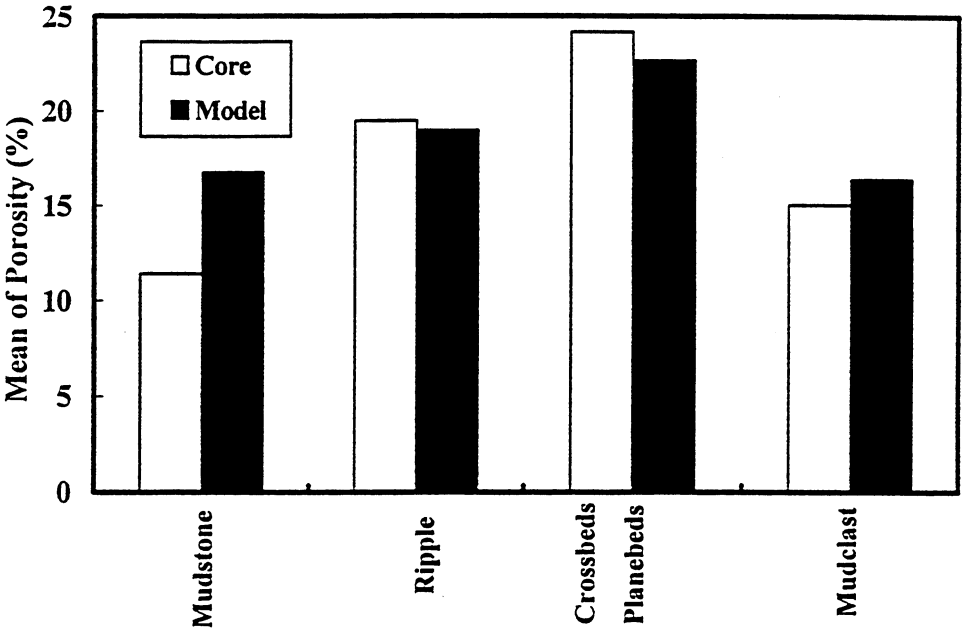

Fig. 3-29 Statistical Mean of Porosity for Lithofacies Model

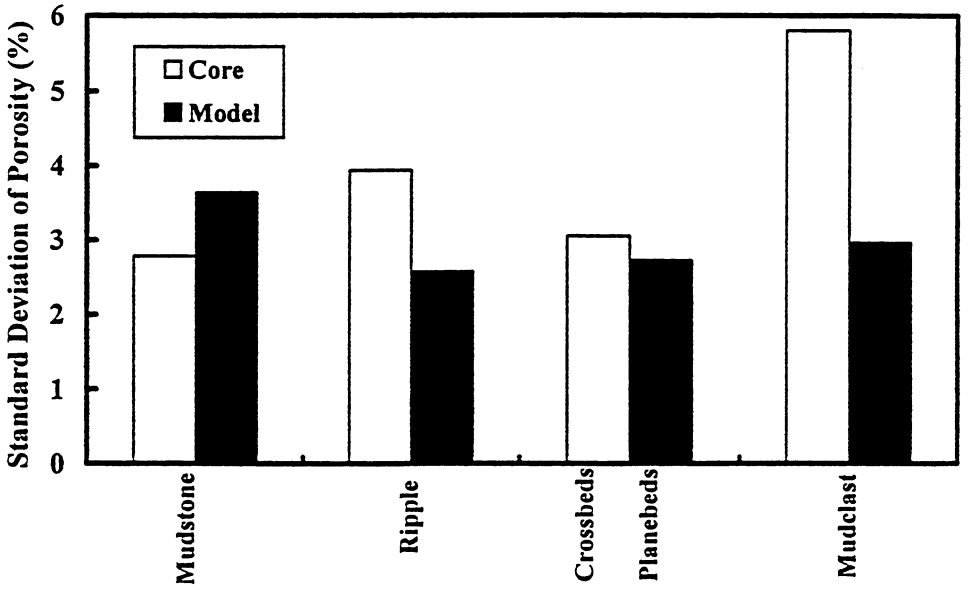

Fig. 3-30 Standard Deviation of Porosity for Lithofacies Model

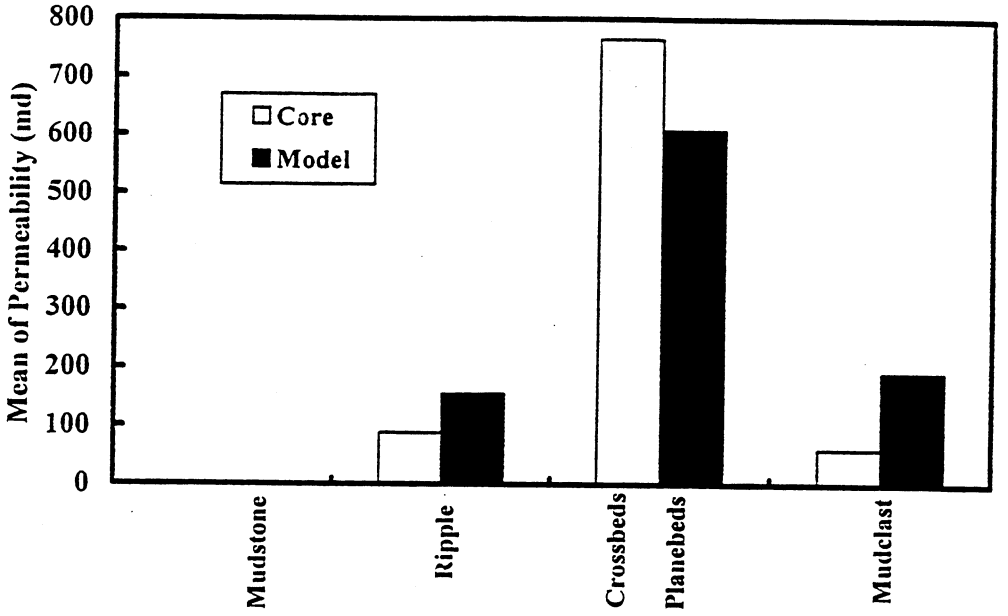

Fig. 3-31 Statistical Mean of Permeability for Lithofacies Model

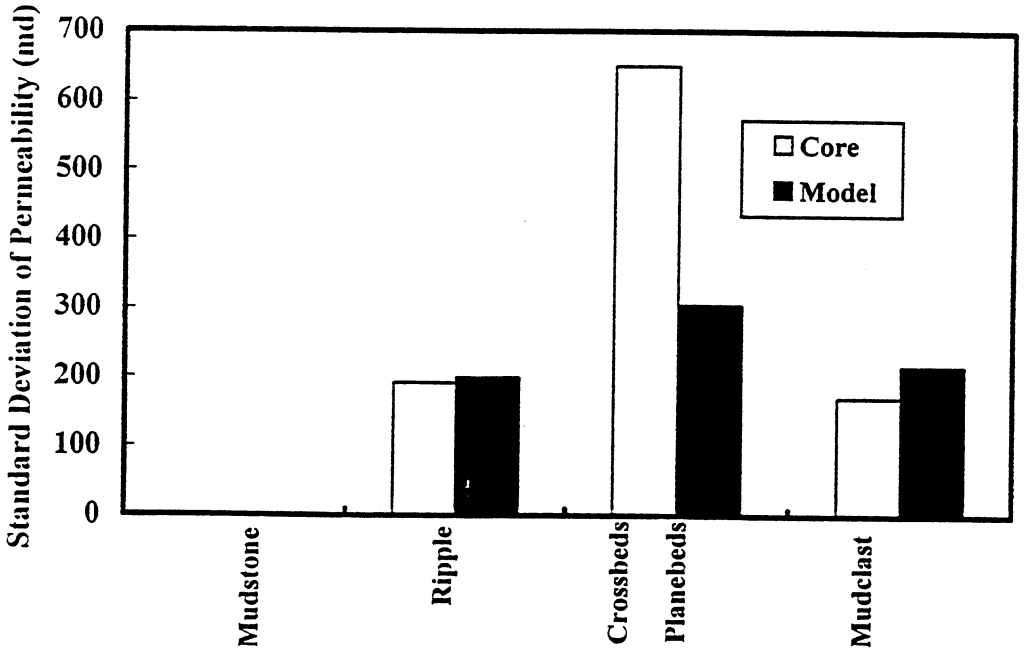

Fig. 3-32 Standard Deviation of Permeability for Lithofacies Model

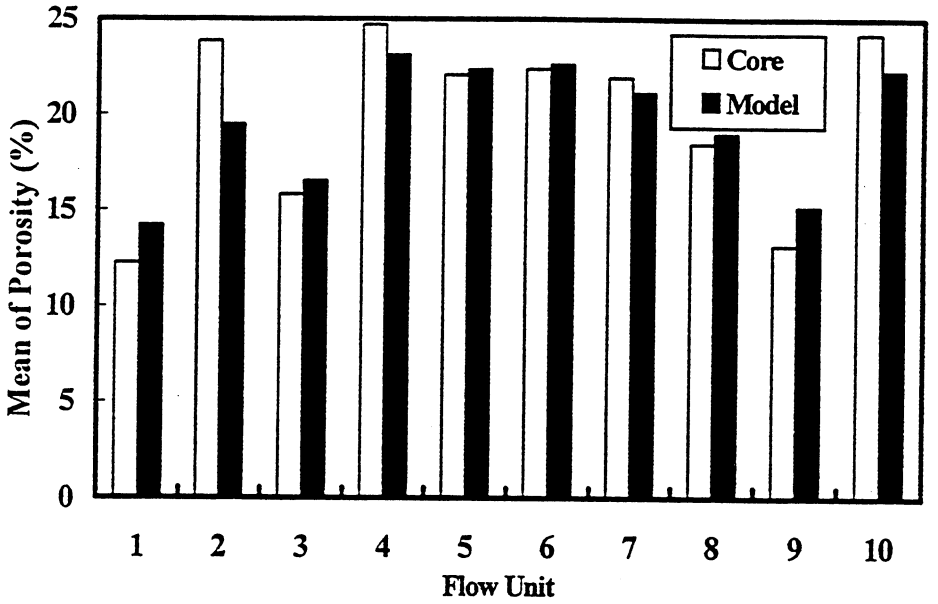

Fig. 3-33 Statistical Mean of Porosity for Flow Unit Model

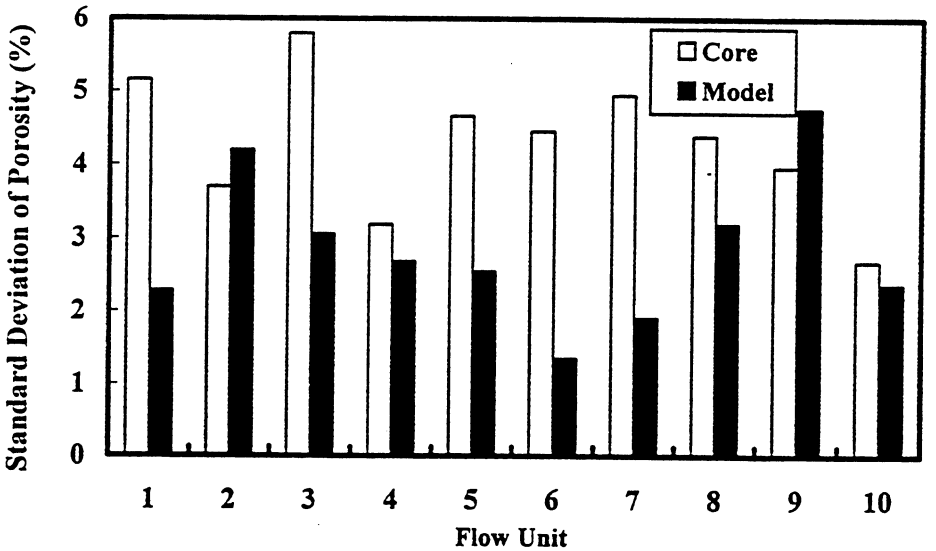

Fig. 3-34 Standard Deviation of Porosity for Flow Unit Model

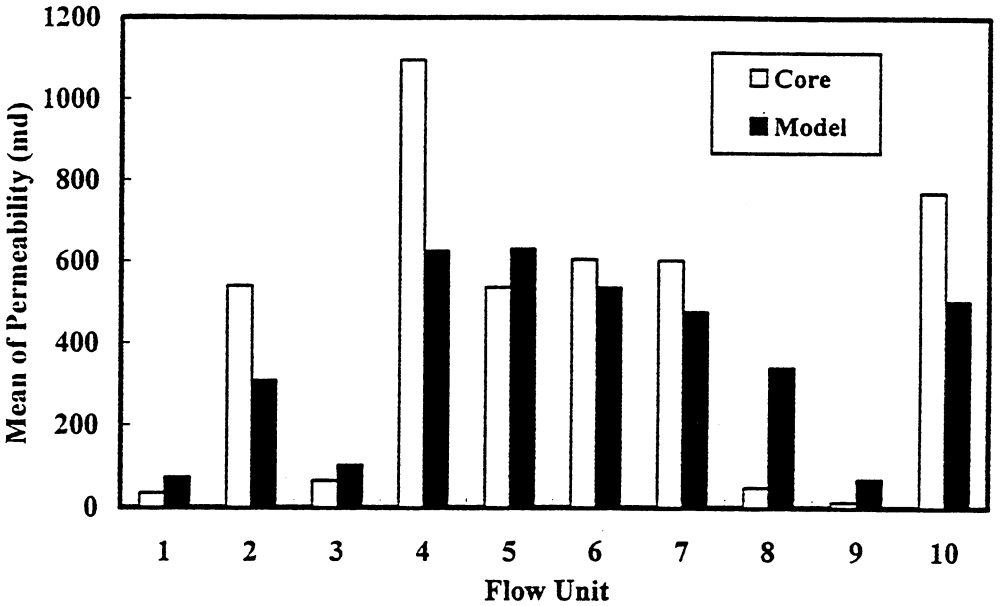

Fig. 3-35 Statistical Mean of Permeability for Flowunit Model

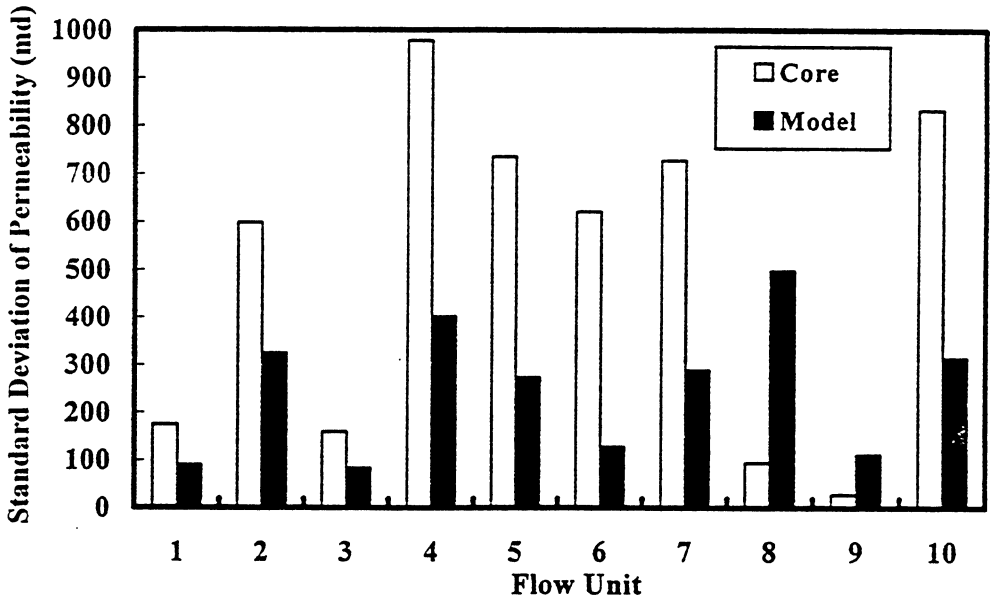

Fig. 3-36 Standard Deviation of Permeability for Flowunit Model

CHAPTER IV

STRATEGIES OF SCALE - UP

In this chapter, the strategies of scale-up developed in this study will be discussed. Two hypothetical geological models are used to illustrate the application of these scale-up strategies.

4.1 Scale-up of Transmissibility for Single Phase Flow

In Chapter II, scale-up methods developed in literature have been reviewed. In summary, the scale-up for equivalent properties of heterogeneous porous medium can be classified into two kinds of categories. The first consists of determining the effective permeability according to spatial distribution or correlation. It provides the average effective properties for porous medium that is independent of the flow conditions of reservoir, and this is a purely mathematical scale-up strategy. The second consists of providing the equivalent permeability so that the flow rate from simulation on coarse grid is comparable to those from fine grid. The boundary conditions imposed on the fine grid, which is used to determine the equivalent properties on the coarse grid, can significantly influence the scaling-up results (Ding, 1995).

In the second category of scale-up, most work has concentrated on the scale-up of effective permeability. The purpose of permeability scale-up is to preserve the gross features of flow on a coarse grid and to match them to a fine gird in reservoir simulation. The algorithm calculates an 'effective permeability' that will result in the same total

flow of single-phase fluid through the coarse, homogeneous block as that obtained from fine heterogeneous block (Christie, 1996)

Even though effective permeability is used as the input in reservoir simulation, what is required in simulator to solve the partial differential equation is the transmissibility from the center of one grid block to the center of adjacent grid block, as shown in Fig. 4-1. Many scale-up methods concentrate on keeping the heterogeneity trend in coarse-scale model the same as in fine-scale model. However, the same heterogeneity trend may not produce the same simulation results in the two different scales.

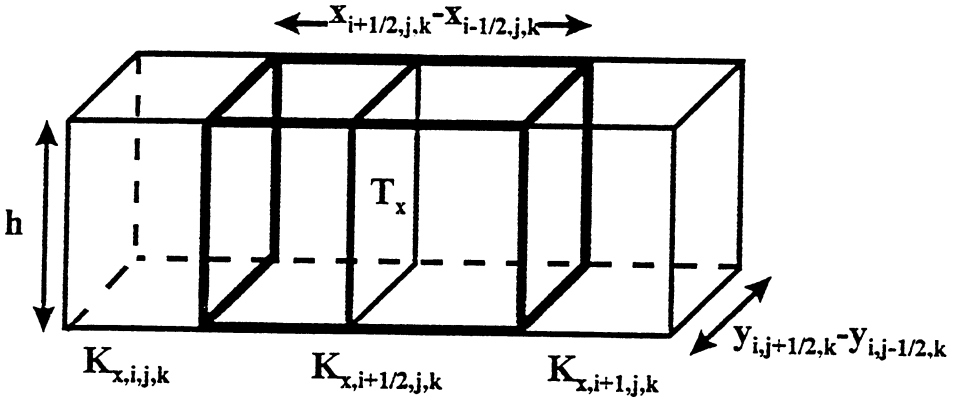

Fig. 4-1 Illustration of Transmissibility (T_x) in Reservoir Simulation

Eqs. 4-1 to 4-3 are used to define transmissibility in reservoir simulation in x, y, and z directions, respectively.

$$(T_x)_{i+1/2,j,k} = \frac{(k_x)_{i+1/2,j,k}\left(\Delta z_{i,j,k} + \Delta z_{i+1,j,k}\right)\left(\Delta y_{i,j,k} + \Delta y_{i+1,j,k}\right)}{4\left(x_{i+1,j,k} - x_{i,j,k}\right)} \qquad (4\text{-}1)$$

$$(T_y)_{i,j+1/2,k} = \frac{(k_y)_{i,j+1/2,k}(\Delta x_{i,j,k} + \Delta x_{i,j+1,k})(\Delta z_{i,j,k} + \Delta z_{i,j+1,k})}{4(y_{i,j+1,k} - y_{i,j,k})} \qquad (4\text{-}2)$$

$$(T_z)_{i,j,k+1/2} = \frac{(k_z)_{i,j,k+1/2}(\Delta x_{i,j,k} + \Delta x_{i,j,k+1})(\Delta y_{i,j,k} + \Delta y_{i,j,k+1})}{4(z_{i,j,k+1} - z_{i,j,k})} \qquad (4\text{-}3)$$

where:

T_x, T_y, T_z = transmissibility in x, y, and z directions (ft. mD),

k_x, k_y, k_z = average permeabilities of the two-half grid blocks that are neighbors (mD),

$\Delta x, \Delta y, \Delta z$ = length of grid block in x, y, and z directions (ft),

x, y, z = dimensions of grid block (ft).

When the dimensions of the grid blocks in three dimensions are variables, the average permeability of two-half grid blocks ($k_x)_{i+1/2,j,k}$, $(k_y)_{i,j+1/2,k}$, $(k_z)_{i,j,k+1/2}$ in Eq. 4-1 to 4-3 can be calculated by the following equations:

$$(k_x)_{i+1\ 2,j,k} = \frac{2(k_x)_{i,j,k}(k_x)_{i+1,j,k}(x_{i+1,j,k} - x_{i,j,k})\Delta y_{i,j,k}\Delta z_{i,j,k}\Delta y_{i+1,,k}\Delta z_{i+1,j,k}}{\left[(k_x)_{i,j,k}\Delta x_{i+1,j,k}\Delta y_{i,j,k}\Delta z_{i,j,k} + (k_x)_{i+1,j,k}\Delta x_{i,j,k}\Delta y_{i+1,j,k}\Delta z_{i+1,j,k}\right]} \frac{4}{\left(\Delta y_{i,j,k} + \Delta y_{i+1,j,k}\right)\left(\Delta z_{i,j,k} + \Delta z_{i+1,j,k}\right)} \qquad (4-4)$$

$$(k_y)_{i,j+1\ 2,k} = \frac{2(k_y)_{i,j,k}(k_y)_{i,j+1,k}(y_{i,j+1,k} - y_{i,j,k})\Delta x_{i,j,k}\Delta z_{i,j,k}\Delta x_{i,j+1,k}\Delta z_{i,j+1,k}}{\left[(k_y)_{i,j,k}\Delta x_{i,j,k}\Delta y_{i,j+1,k}\Delta z_{i,j,k} + (k_y)_{i,j+1,k}\Delta x_{i,j+1,k}\Delta y_{i,j,k}\Delta z_{i,j+1,k}\right]} \frac{4}{\left(\Delta x_{i,j,k} + \Delta x_{i,j+1,k}\right)\left(\Delta z_{i,j,k} + \Delta z_{i,j+1,k}\right)} \qquad (4-5)$$

$$(k_z)_{i,j,k+1\ 2} = \frac{2(k_z)_{i,j,k}(k_z)_{i,j,k+1}(z_{i,j,k+1} - z_{i,j,k})\Delta x_{i,j,k}\Delta y_{i,j,k}\Delta x_{i,j,k+1}\Delta y_{i,j,k+1}}{\left[(k_z)_{i,j,k}\Delta x_{i,j,k}\Delta y_{i,j,k}\Delta z_{i,j,k+1} + (k_z)_{i,j,k+1}\Delta x_{i,j,k+1}\Delta y_{i,j,k+1}\Delta z_{i,j,k}\right]} \frac{4}{\left(\Delta x_{i,j,k} + \Delta x_{i,j,k+1}\right)\left(\Delta y_{i,j,k} + \Delta z_{i,j,k+1}\right)} \qquad (4-6)$$

In reservoir simulation, partial differential equations are solved simultaneously in 3-D. For one phase flow, there are no capillary and gravity effects. It was assumed that Darcy's Law is still valid for the flow between two grid blocks in any directions as follows:

$$Q_{x,i+1/2,j,k} = \frac{(k_x M)_{i+1/2,j,k}(\Delta y_{i,j,k} + \Delta y_{i+1,j,k})(\Delta z_{i,j,k} + \Delta z_{i+1,j,k})(\Phi_{i+1,j,k} - \Phi_{i,j,k})}{4\left(x_{i+1,j,k} - x_{i,j,k}\right) / 0.001127} \quad (4\text{-}7)$$

$$Q_{y,i,j+1/2,k} = \frac{(k_y M)_{i,j+1/2,k}(\Delta x_{i,j,k} + \Delta x_{i,j+1,k})(\Delta z_{i,j,k} + \Delta z_{i,j+1,k})(\Phi_{i,j+1,k} - \Phi_{i,j,k})}{4\left(y_{i,j+1,k} - y_{i,j,k}\right) / 0.001127} \quad (4\text{-}8)$$

$$Q_{z,i,j,k+1/2} = \frac{(k_z M)_{i,j,k+1/2}(\Delta x_{i,j,k} + \Delta x_{i,j,k+1})(\Delta y_{i,j,k} + y_{i,j,k+1})(\Phi_{i,j,k+1} - \Phi_{i,j,k})}{4\left(z_{i,j,k+1} - z_{i,j,k}\right) / 0.001127} \quad (4\text{-}9)$$

where:

Q_x, Q_y, Q_z = flow rate in x, y, and z directions, respectively (STB/day),

M = mobility of the fluid and can be expressed as: $M = \frac{k_r}{B\mu}$,

k_r = relative permeability of fluid (dimensionless),

B = formation volume factor (rb/stb),

μ = viscosity (cp),

Φ = potential of grid block (psi).

Using T_x, T_y, and T_z to replace the terms in Eqs. 4-7 to 4-9, respectively, the following relationships were obtained :

$$Q_{x,i+1/2,j,k} = 0.001127(T_x M)_{i+1/2,j,k}(\Phi_{i+1,j,k} - \Phi_{i,j,k}) \quad (4\text{-}10)$$

$$Q_{y,i,j+1/2,k} = 0.001127(T_y M)_{i,j+1/2,k}(\Phi_{i,j+1,k} - \Phi_{i,j,k}) \quad (4\text{-}11)$$

$$Q_{z,i,j,k+1/2} = 0.001127(T_z M)_{i,j,k+1/2}(\Phi_{i,j,k+1} - \Phi_{i,j,k}) \tag{4-12}$$

Hence, the transimissibilities T_x, T_y, and T_z can be calculated as:

$$T_{x,i+1/2,j,k} = \frac{Q_{x,i+1/2,j,k}}{0.001127(M)_{i+1/2,j,k}(\Phi_{i+1,j,k} - \Phi_{i,j,k})} \tag{4-13}$$

$$T_{y,i,j+1/2,k} = \frac{Q_{y,i,j+1/2,k}}{0.001127(M)_{i,j+1/2,k}(\Phi_{i,j+1,k} - \Phi_{i,j,k})} \tag{4-14}$$

$$T_{z,i,j,k+1/2} = \frac{Q_{z,i,j,k+1/2}}{0.001127(M)_{i,j,k+1/2}(\Phi_{i,j,k+1} - \Phi_{i,j,k})} \tag{4-15}$$

As mentioned above, the purpose of scale-up for single phase flow is to preserve the gross features of flow on the simulation grid, i.e., to match the flow rates from fine-scale model with coarse-scale model. The flow rate for each grid block of fine-scale model, which is the target of study, can be simply obtained from the output of a simulation for a fine-scale model. If the potentials for each grid block of a coarse-scale model are obtained, the transmissibilities, T_x, T_y, and T_z can be calculated using Eqs. 4-13 to 4-15, which should lead to the same flow rates as in the fine-scale model. In reservoir simulation, it is possible to either input permeability for each grid block or directly input transmissibilities. Therefore, one possible approach for scale-up is to use permeability as an input in fine-scale simulation and transmissibility as an input in coarse-scale simulation in order to match the flow rates. Average pressure for each coarse-scale grid block can be obtained using pore volume average on a fine-scale gird-block pressure. The potential for coarse-scale grid block can be calculated by considering the elevation difference between two grid blocks.

In this study, only the scale-up in the vertical direction was considered, meaning only to combine the layers in vertical direction, but keep the dimensions in the horizontal direction the same in both fine scale and coarse scale. As shown in Fig. 4-2, the total flow rate for the coarse-scale grid block in x and y directions is simply the sum of the flow rates of the fine-scale grid blocks in vertical direction. In the z direction, the flow rate for coarse-scale grid block is equal to the flow rate of fine-scale grid block at the boundary of upscaled zone or layer. The potentials of coarse-scale grid block can be calculated using the following equation:

$$\Phi_{i,j,k} = \frac{\sum_{z=1}^{n} v\phi p}{\sum_{z=1}^{n} v\phi} + 0.4335 * \left(E_{i,j,k} - E_{datum}\right)\rho_f \qquad (4\text{-}16)$$

Where,

Φ = potential of grid block (i,j,k) (psi),

v = volume of fine-scale grid block (ft^3),

ϕ = porosity of fine-scale grid block (fraction),

p = pressure of fine-scale grid block (psi),

E_{datum} = elevation of reference datum (ft),

$E_{i,j,k}$ = elevation of grid block (i,j,k) (ft),

ρ_f = density of fluid in reservoir (g/cm^3),

n = number of layers upscaled.

4.2 Scale-Up on Hypothetical Reservoir Models

In this section, a hypothetical geological model was used to apply the methodology discussed in section 4.1. First, a layer-cake model without pitch-out was

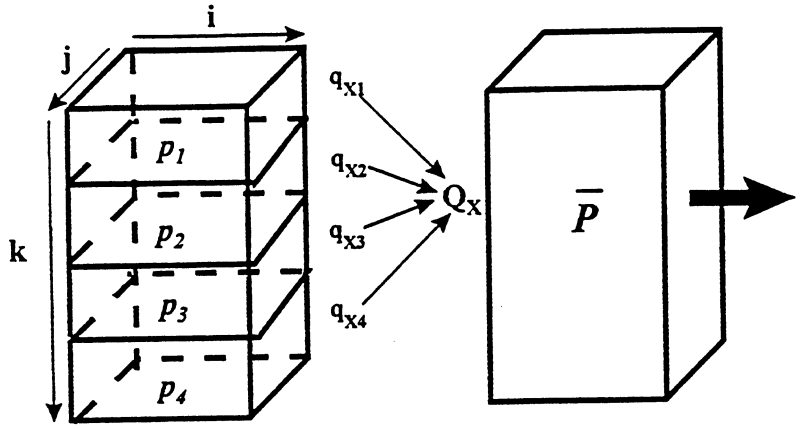

Fig. 4-2 Illustration of Upscaled Flow Rate and Pressure

considered and then pitch-out was included in the second model. Normal distributions for porosity and permeability were assumed in the hypothetical models.

4.2.1 Description of the Hypothetical Reservoir Model

A 17-layer fine-scale hypothetical reservoir model was used to illustrate the application of scale-up described in section 4.1. The reservoir was assumed to be located at depth between 8450 to 8510 feet. The modeling area was 270x270 ft^2 with a grid system of 9x9x17 in x, y, and z directions, respectively. The porosity and permeability of the model was assumed to be randomly and normally distributed and generated using the tool for data analysis in MS Excel. The statistical properties of the model are provided in Table 4-1.

In the model, layers 6 and 12 were designed to serve as barriers between layers 5, and 7, and, 11 and 13, which have very low porosity and permeabilities, as shown in

Table 4-1. The 17-layer fine-scale model was scaled up into a 5-layer coarse-scale model, (i.e., layer 1 to 5, 7 to 11, and 12 to 17 was scaled up to become layer 1, 3, and 5 in coarse-scale model, respectively). In this particular model, no pitch-out exists meaning no zero thickness in any grid blocks.

Five wells were created, as shown in Fig. 4-3, to perform this hypothetical simulation, in which one injection well is located at the center of the model and four production wells are at the four corners of the model. Fig. 4-4 is a three dimensional view of permeability distribution of the model. The properties of reservoir fluid and several important parameters of reservoir used in the simulation are provided in Table 4-2.

Table 4 -1 Statistical Characteristics of Hypothetical Layer-Cake Model

Fine Scale (Layer)	Coarse Scale (Layer)	ϕ Mean (%)	ϕ Standard Deviation (%)	k Mean (mD)	k Standard Deviation (mD)
1 - 5	1	24.13	5.04	688.13	437.11
6	2	8.20	6.02	0.012	0.0031
7 - 11	3	18.08	3.81	96.34	65.73
12	4	7.77	7.83	0.015	0.0045
13 - 17	5	25.00	3.15	1091.97	698.39

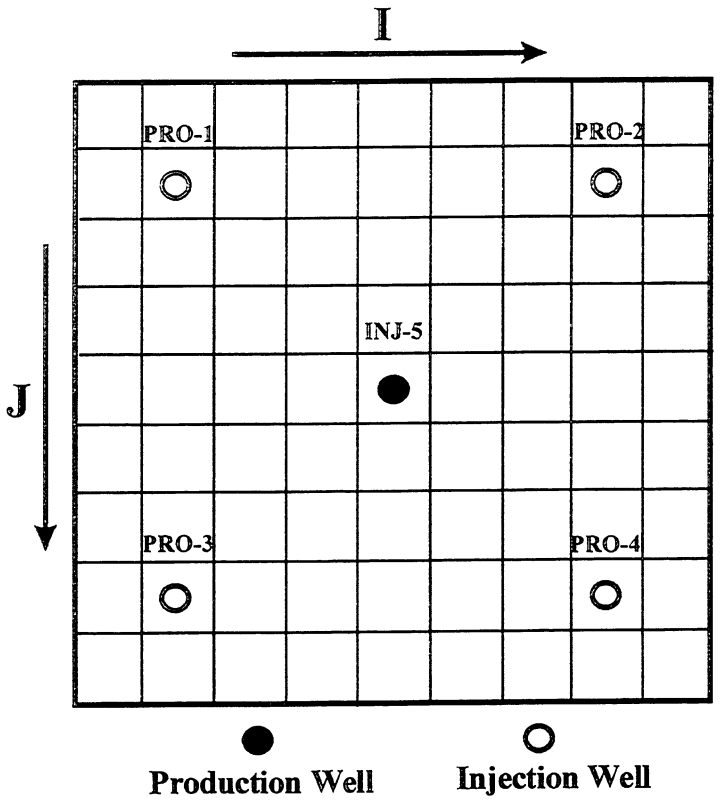

Fig. 4-3 Well Pattern Used for Hypothetical Model #1

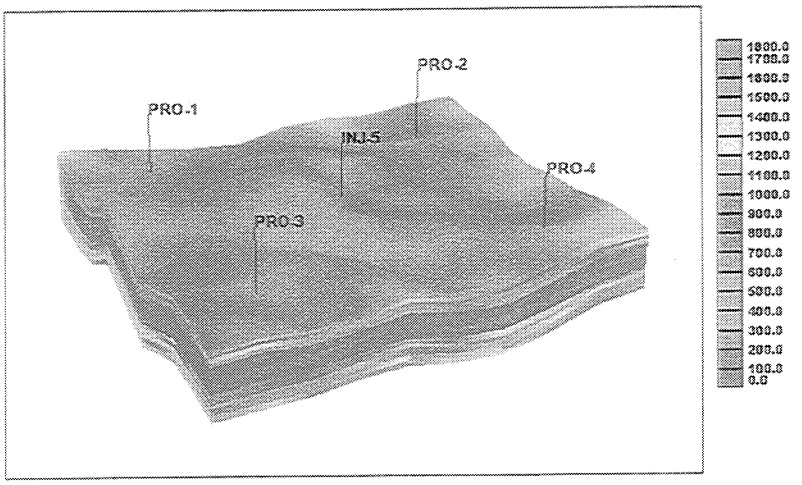

Fig.4-4 3-D View of Permeability Distribution for Model #1

Table 4-2 Properties of Reservoir Fluid and Reservoir Parameters Used in the Reservoir Simulation for Model #1

Parameter	Unit	Value
Water Density	gm/cc	1.0
Water Volume Factor	rb/stb	1.0
Water Viscosity	cp	1.0
Water Compressibility	psi^{-1}	$3x10^{-6}$
Pore Compressibility	psi^{-1}	$4x10^{-6}$
Reservoir Temperature	°F	180
Standard Temperature	°F	60
Standard Pressure	psi	14.65
P_i (at 8000 ft)	psi	2500
Q_{max} (Production Well)	STB/day	10000
P_{min}(Production Well at 8350 ft)	psi	1000
Q_{max} (Injection Well)	STB/day	2250
P_{max}(Injection Well at 8350 ft)	psi	10000

4.2.2 Test for the Validity of Transmissibility Calculation

To test the validity of the scale-up strategy, transmissibility, T_X, T_Y, and T_Z of fine-scale grid blocks were calculated using the method proposed in Section 4.1. These values were then compared with the transmissibility obtained from the simulation output as illustrated in Fig. 4-5 to Fig. 4-10. Note that all data are provided in Figs. 4-5, 4-7, and 4-9. Several negative values observed in these three plots occurred when the pressure difference between the two grid blocks was very small. When the potential was calculated, the errors were introduced. In Figs. 4-6, 4-8, and 4-10, only positive values were plotted. Most of the values follow a 45^0 line with a small percentage scattered away from this line. Overall, the plotted data in Figs 4-5 to 4-10 show that the proposed method for calculating transmissibility is valid.

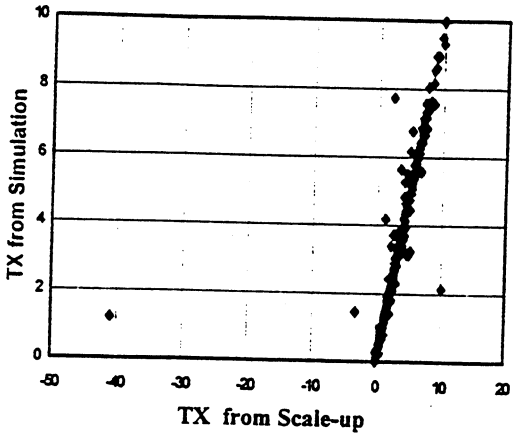

Fig. 4-5 Cross Plot of Transmissibility (T_x) Obtained from Simulation and Scale-up (Include all data)

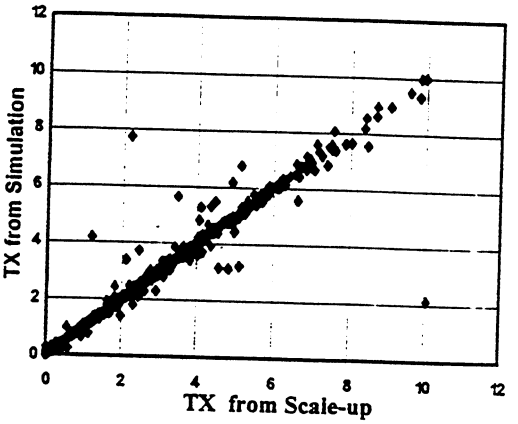

Fig. 4-6 Cross Plot of Transmissibility (T_x) Obtained from Simulation and Scale-up (Only Positive data)

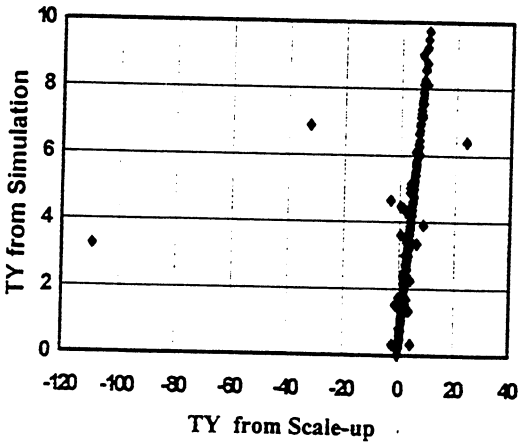

Fig. 4-7 Cross Plot of Transmissibility (T_y) Obtaine from Simulation and Scale-up (Include all data)

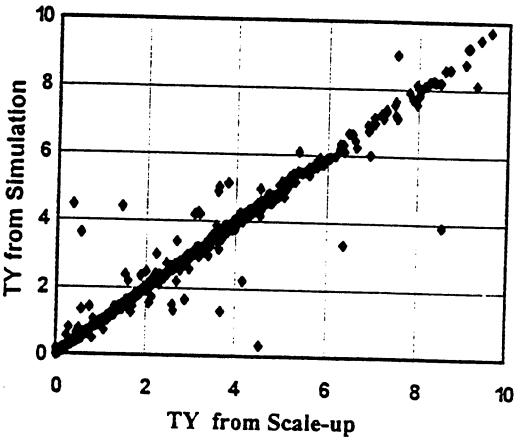

Fig. 4-8 Cross Plot of Transmissibility (T_y) Obtained from Simulation and Scale-up (Only Positive data)

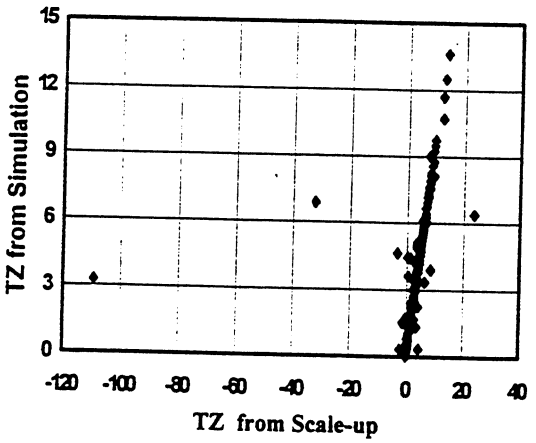

Fig. 4-9 Cross Plot of Transmissibility (T_z) Obtained from Simulation and Scale-up (Include all data)

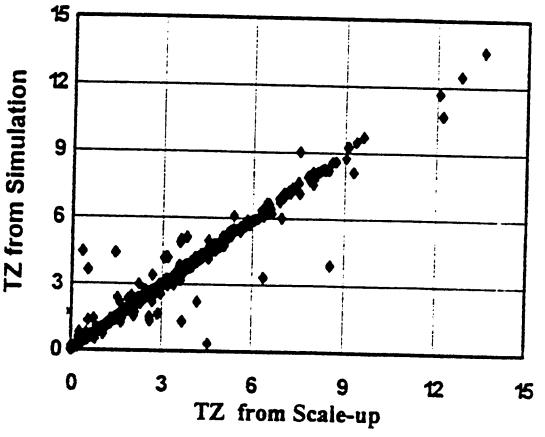

Fig. 4-10 Cross Plot of Transmissibility (T_z) Obtained from Simulation and Scale-up (Only Positive data)

4.2.3 Scale-Up on A Hypothetical Layer-Cake Reservoir Model

Scale-up was conducted by first running single-phase simulation on fine-scale model to obtain the outputs of flow rate and pressure for fine-scale grid blocks. Then the simulation was run on a coarse-scale model using the following reservoir properties: transmissibilities, pore volume, and thickness, obtained from scale-up calculation. Simulation on fine-scale model was run for ten days until stabilized production and injection rates were obtained.

Scale-up was conducted using a FORTRAN program developed in this study. A flow chart of the program is provided in Fig. 4-11. The definitions of the parameters used in the FORTRAN program are provided in Appendix A.

In the calculation, a pore-volume average method was used to calculate the average pressure and porosity for each coarse grid block. Negative values of T_X, T_Y, or T_Z can occur when production rates and potential gradient between two grid blocks have different directions. The potential gradient in x or y directions may sometimes have a zero value. The program automatically checks for these problems during the calculation. When detected, the transmissibility T_x, T_y, or T_z are calculated using Eqs. 4-1 to 4-3. The average permeability K_y for each coarse grid block were calculated from permeability of fine-scale grid blocks using thickness averaging method, and K_Z using harmonic averaging method. In Eqs. 4-1 to 4-3 , the average permeability of two half adjacent coarse grid blocks in x, y, and z directions were calculated using Eqs. 4-4 to 4-6, respectively. Flow rates and pressure in x, y, and z directions for fine-scale were obtained from an output map file. Transmissibility, thickness, and pore volume for coarse-scale model were calculated and input into the coarse-scale simulation model.

Fig. 4-11 Flow Chart of the Program for Scale-up Without Pinch-out

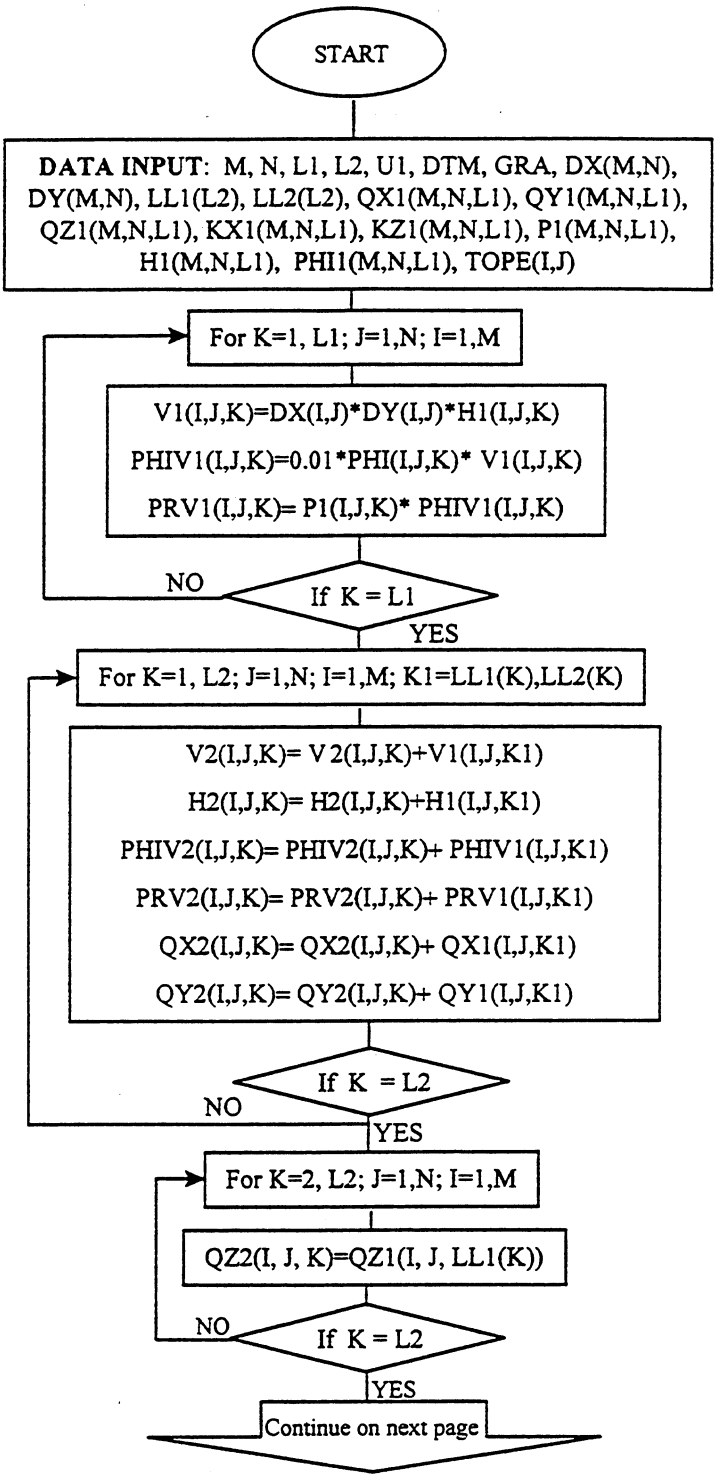

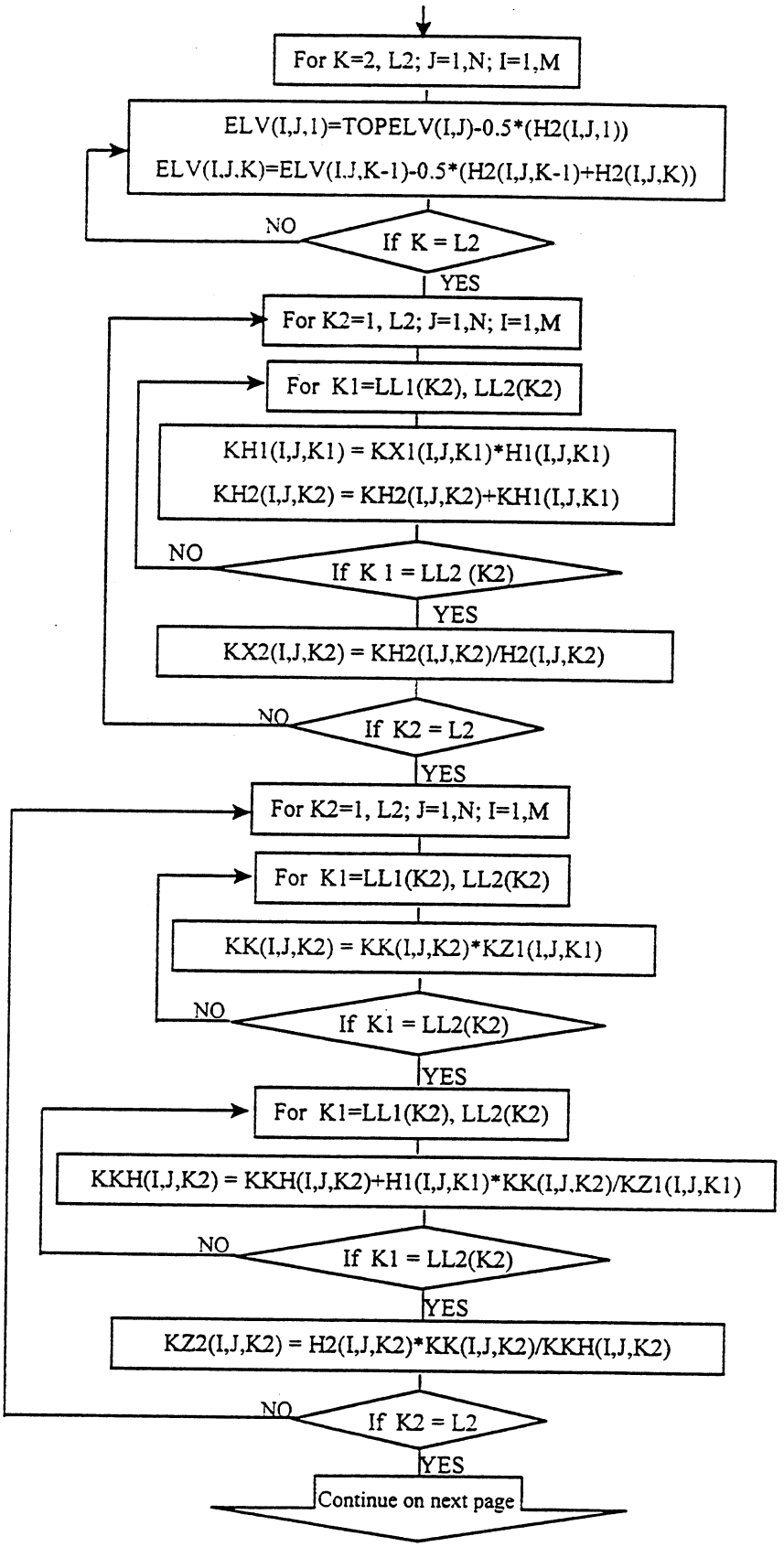
For K=2, L2; J=1,N; I=1,M
ELV(I,J,1)=TOPELV(I,J)-0.5*(H2(I,J,1))
ELV(I,J,K)=ELV(I,J,K-1)-0.5*(H2(I,J,K-1)+H2(I,J,K))
NO
If K = L2
YES
For K2=1, L2; J=1,N; I=1,M
For K1=LL1(K2), LL2(K2)
KH1(I,J,K1) = KX1(I,J,K1)*H1(I,J,K1)
KH2(I,J,K2) = KH2(I,J,K2)+KH1(I,J,K1)
NO
If K 1 = LL2 (K2)
YES
KX2(I,J,K2) = KH2(I,J,K2)/H2(I,J,K2)
NO
If K2 = L2
YES
For K2=1, L2; J=1,N; I=1,M
For K1=LL1(K2), LL2(K2)
KK(I,J,K2) = KK(I,J,K2)*KZ1(I,J,K1)
NO
If K1 = LL2(K2)
YES
For K1=LL1(K2), LL2(K2)
KKH(I,J,K2) = KKH(I,J,K2)+H1(I,J,K1)*KK(I,J,K2)/KZ1(I,J,K1)
NO
If K1 = LL2(K2)
YES
KZ2(I,J,K2) = H2(I,J,K2)*KK(I,J,K2)/KKH(I,J,K2)
NO
If K2 = L2
YES
Continue on next page

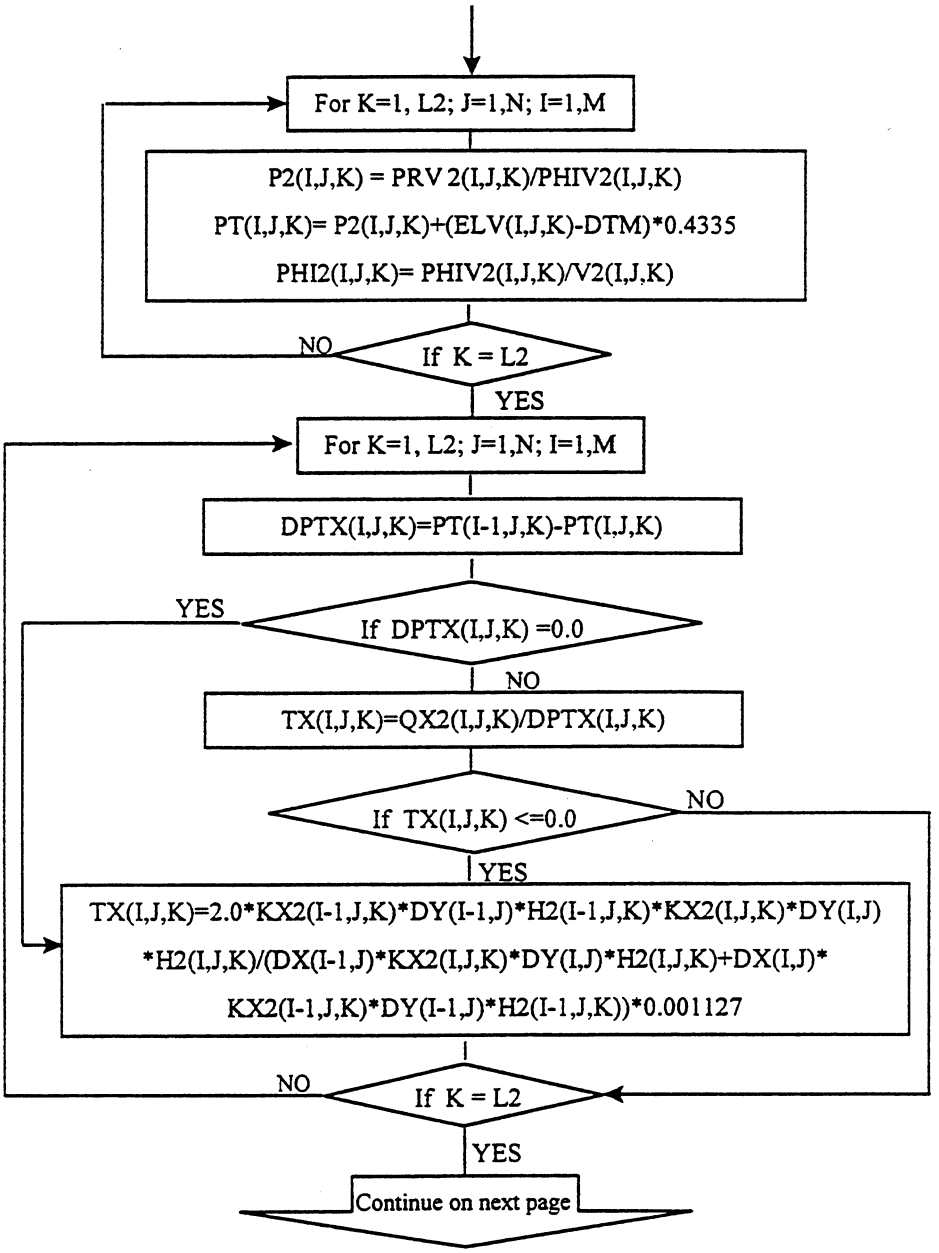
For K=1, L2; J=1,N; I=1,M
P2(I,J,K) = PRV 2(I,J,K)/PHIV2(I,J,K)
PT(I,J,K)= P2(I,J,K)+(ELV(I,J,K)-DTM)*0.4335
PHI2(I,J,K)= PHIV2(I,J,K)/V2(I,J,K)
NO
If K = L2
YES
For K=1, L2; J=1,N; I=1,M
DPTX(I,J,K)=PT(I-1,J,K)-PT(I,J,K)
YES
If DPTX(I,J,K) =0.0
NO
TX(I,J,K)=QX2(I,J,K)/DPTX(I,J,K)
If TX(I,J,K) <=0.0
NO
YES
TX(I,J,K)=2.0*KX2(I-1,J,K)*DY(I-1,J)*H2(I-1,J,K)*KX2(I,J,K)*DY(I,J)
*H2(I,J,K)/(DX(I-1,J)*KX2(I,J,K)*DY(I,J)*H2(I,J,K)+DX(I,J)*
KX2(I-1,J,K)*DY(I-1,J)*H2(I-1,J,K))*0.001127
NO
If K = L2
YES
Continue on next page

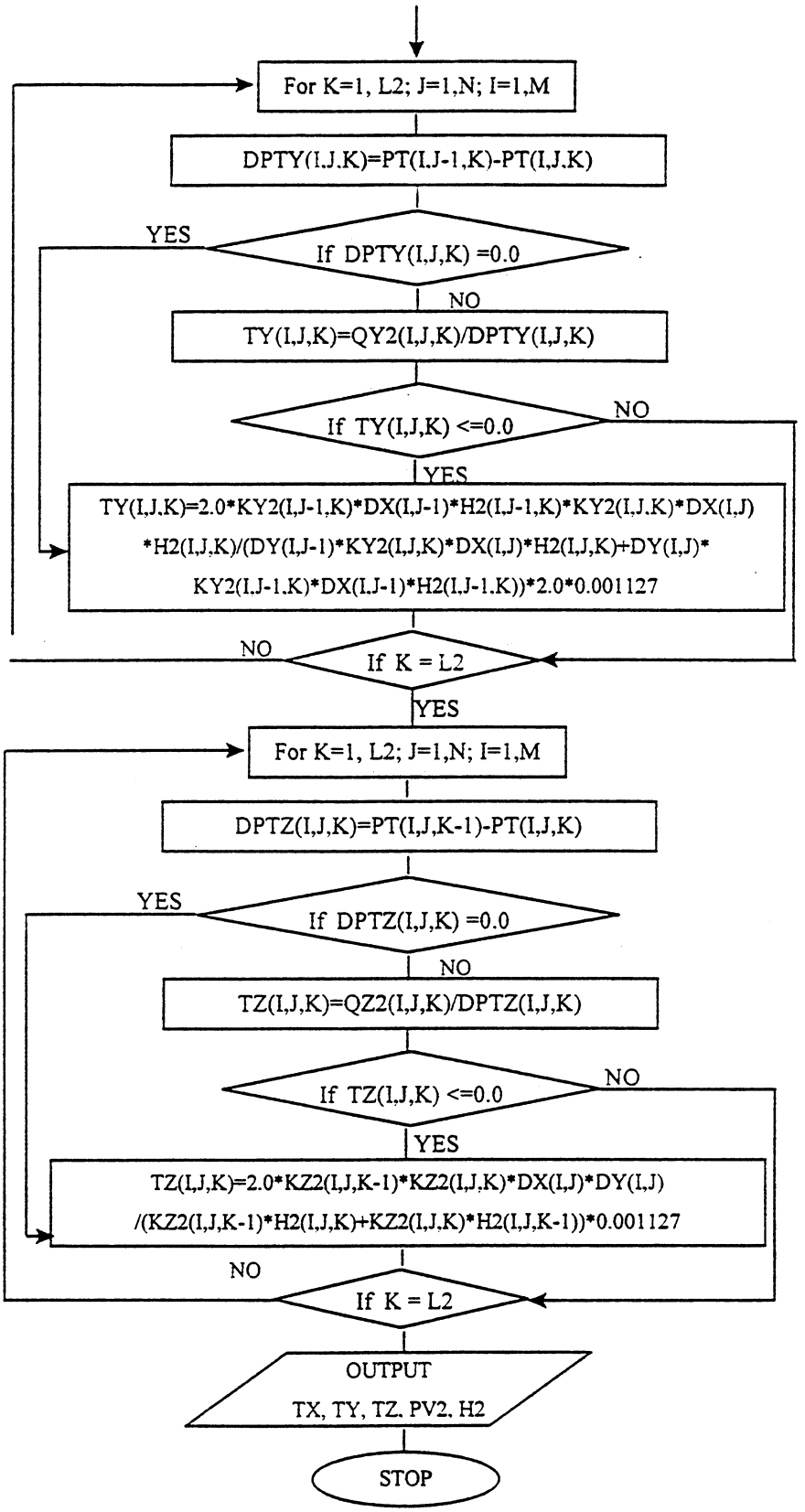
For K=1, L2; J=1,N; I=1,M
DPTY(I,J,K)=PT(I,J-1,K)-PT(I,J,K)
YES
If DPTY(I,J,K) =0.0
NO
TY(I,J,K)=QY2(I,J,K)/DPTY(I,J,K)
If TY(I,J,K) <=0.0
NO
YES
TY(I,J,K)=2.0*KY2(I,J-1,K)*DX(I,J-1)*H2(I,J-1,K)*KY2(I,J,K)*DX(I,J)
*H2(I,J,K)/(DY(I,J-1)*KY2(I,J,K)*DX(I,J)*H2(I,J,K)+DY(I,J)*
KY2(I,J-1,K)*DX(I,J-1)*H2(I,J-1,K))*2.0*0.001127
NO
If K = L2
YES
For K=1, L2; J=1,N; I=1,M
DPTZ(I,J,K)=PT(I,J,K-1)-PT(I,J,K)
YES
If DPTZ(I,J,K) =0.0
NO
TZ(I,J,K)=QZ2(I,J,K)/DPTZ(I,J,K)
If TZ(I,J,K) <=0.0
NO
YES
TZ(I,J,K)=2.0*KZ2(I,J,K-1)*KZ2(I,J,K)*DX(I,J)*DY(I,J)
/(KZ2(I,J,K-1)*H2(I,J,K)+KZ2(I,J,K)*H2(I,J,K-1))*0.001127
NO
If K = L2
OUTPUT
TX, TY, TZ. PV2. H2
STOP

Simulation results, including production rate, cumulative production, injection rate, cumulative injection, and pressure, for both reservoir and individual wells were used to evaluate the results of scale-up. Figs. 4-12 to 4-14 present the scale-up results of water production rate, cumulative water production, and pressure for the reservoir. Injection rate and cumulative injection from fine-scale and coarse-scale simulation are completely consistent and were therefore not presented. Figs. 4-15 to Fig. 4-29 show the scale-up results of water production rate, cumulative water production and injection rates, cumulative water production and injection, and average wellblock pressure for well #1 to Well #5.

It can be observed that:

1. The production of the reservoir went through both depletion and displacement process in only one day period, because the volume of the reservoir is very small and the permeability of the reservoir is high.
2. When scale-up of transmissibility was conducted, production results obtained better match than reservoir and wellblock pressure. The differences in pressure between fine-scale and coarse-scale is quite large.

Analyzing the scale-up procedure and results, the difference of results between fine-scale and coarse-scale simulation could be caused by the error introduced during calculation of transmissibility. However, the main error was probably caused due to the use of scale-up of transmissibility for linear flow to the whole reservoir area. The radial flow around wellbore was not considered. It may not have been correctly upscaled by this simple process. Therefore, scale-up of radial flow around wellbore area was considered in the next section to improve the match.

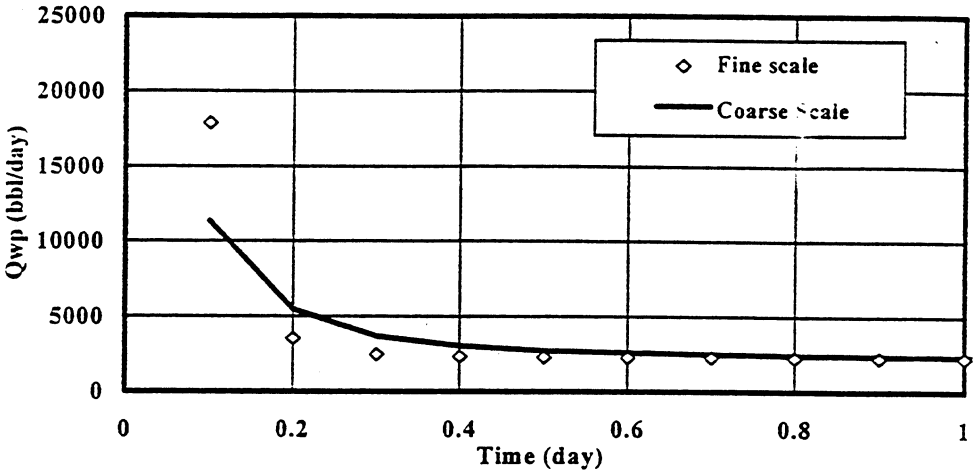

Fig. 4-12 Water Production Rate of Model #1 Without PI Scale-up

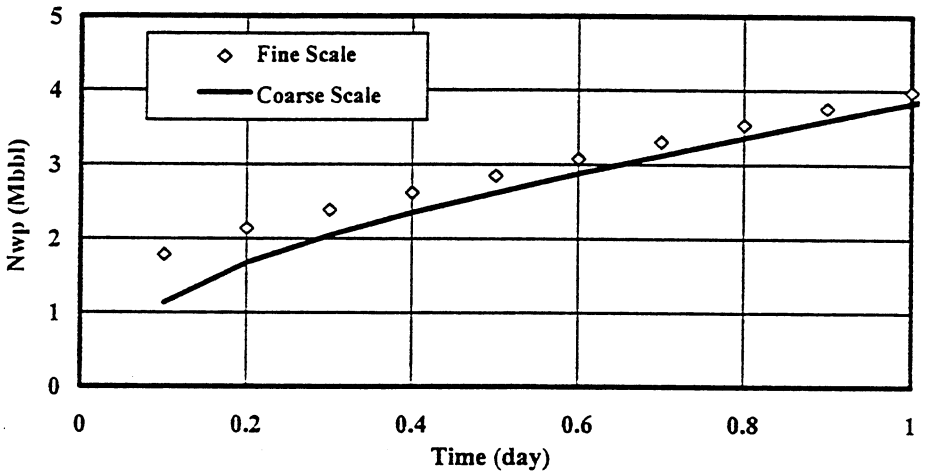

Fig. 4-13 Cum. Water Production of Model #1 Without PI Scale-up

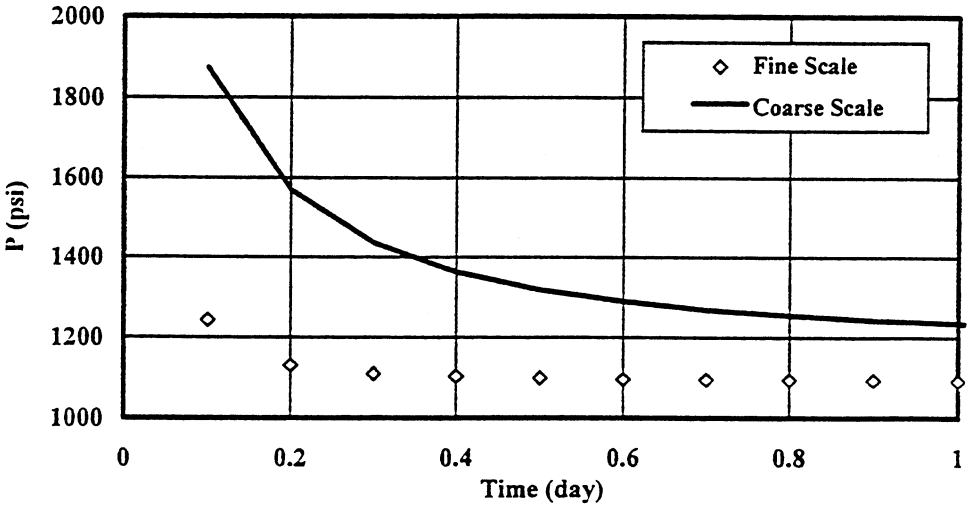

Fig. 4-14 Reservoir Pressure of Model #1 Without PI Scale-up

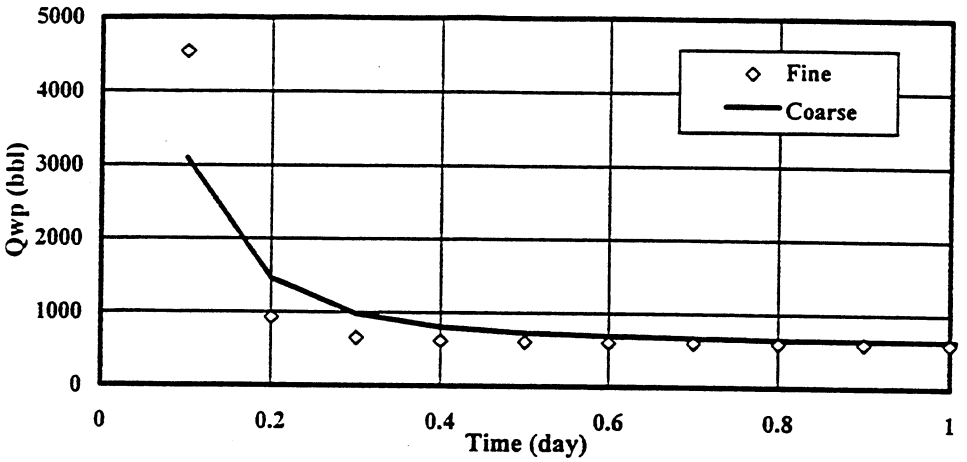

Fig. 4-15 Water Production Rate for Well #1 of Model #1 Without PI Scale-up

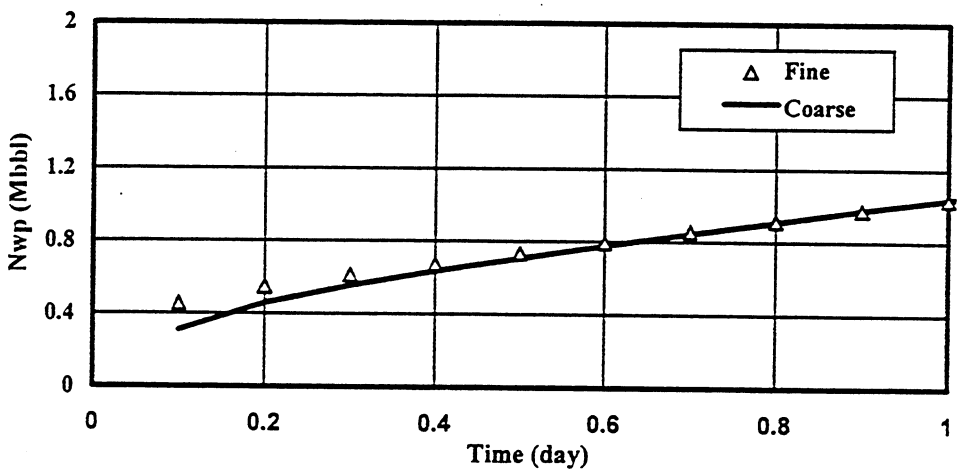

Fig. 4-16 Cum. Water Production for Well #1 of Model #1 Without PI Scale-up

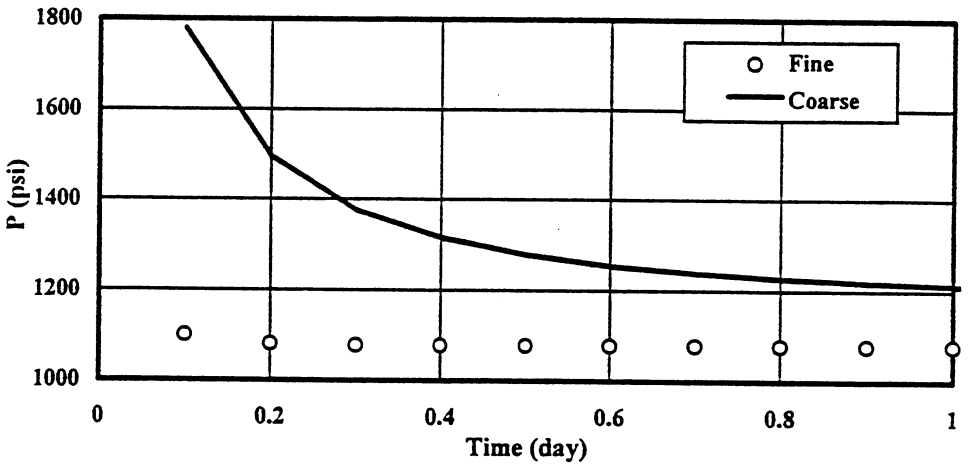

Fig. 4-17 Well Block Pressure for Well #1 of Model #1 Without PI Scale-up

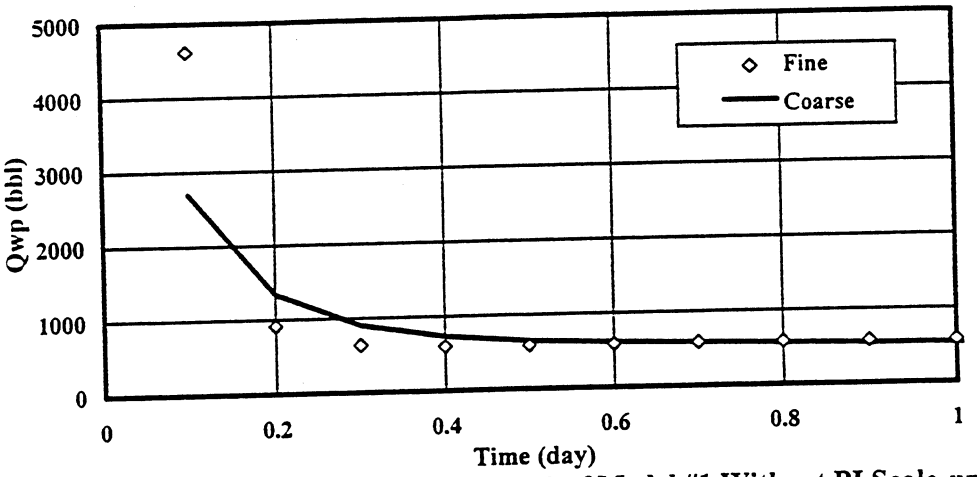

Fig. 4-18 Water Production Rate for Well #2 of Model #1 Without PI Scale-up

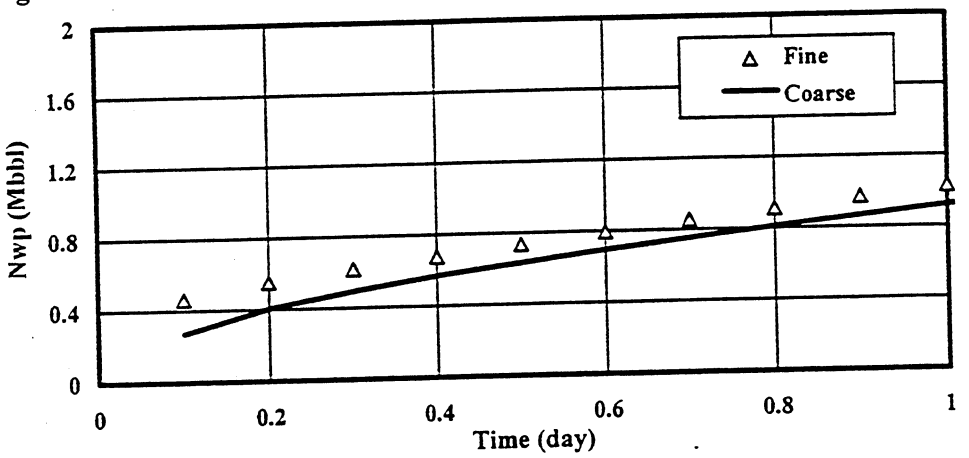

Fig. 4-19 Cum. Water Production for Well #2 of Model #1 Without PI Scale-up

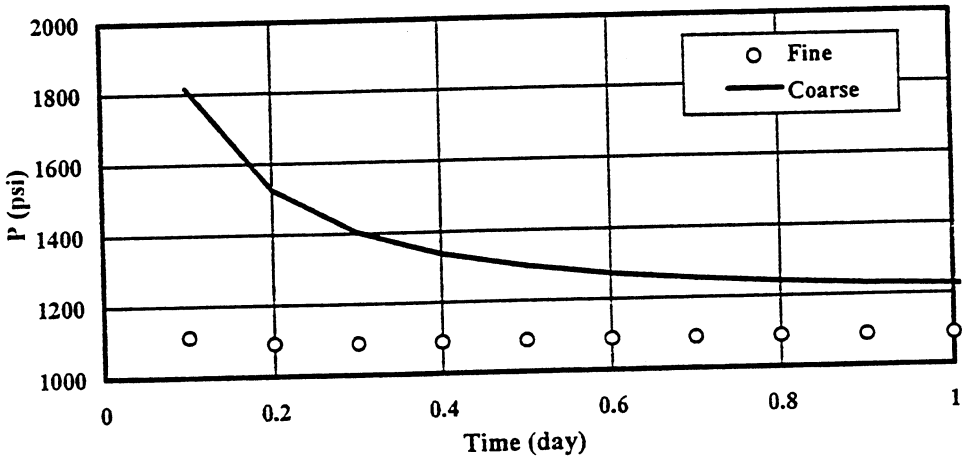

Fig. 4-20 Well Block Pressure for Well #2 of Model #1 Without PI Scale-up

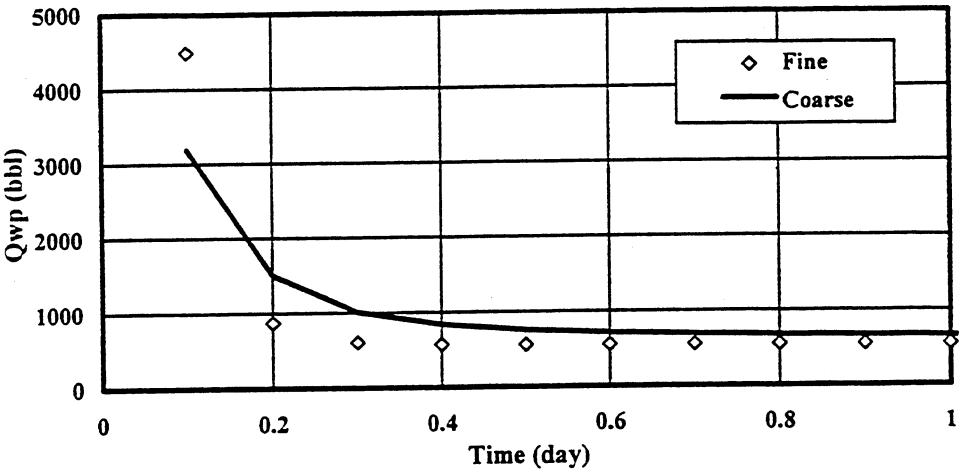

Fig. 4-21 Water Production Rate for Well #3 of Model #1 Without PI Scale-up

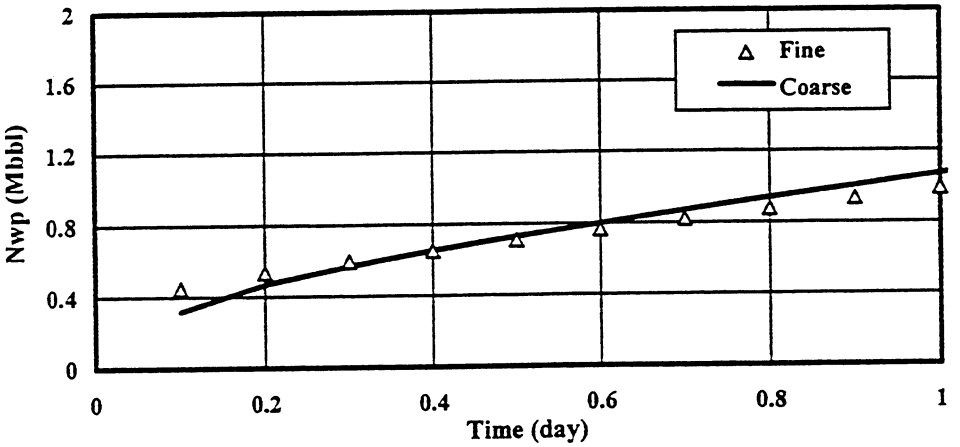

Fig. 4-22 Cum. Water Production for Well #3 of Model #1 Without PI Scale-up

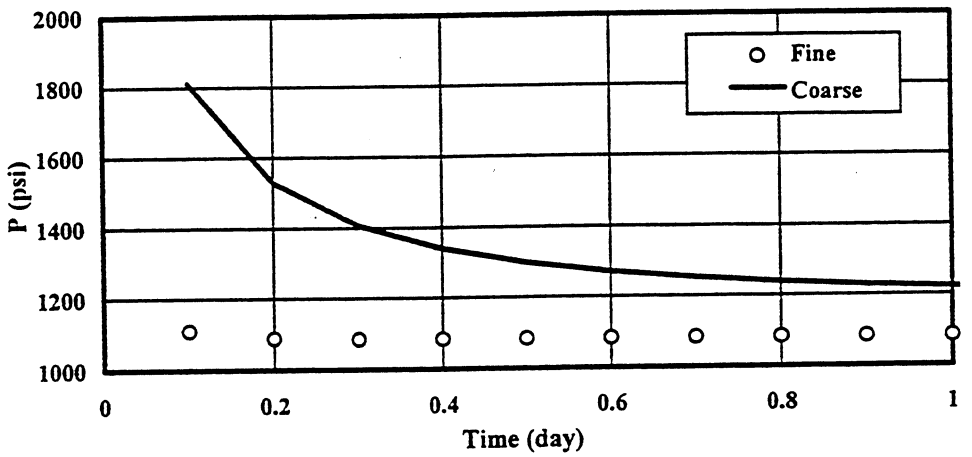

Fig. 4-23 Well Block Pressure for Well #3 of Model #1 Without PI Scale-up

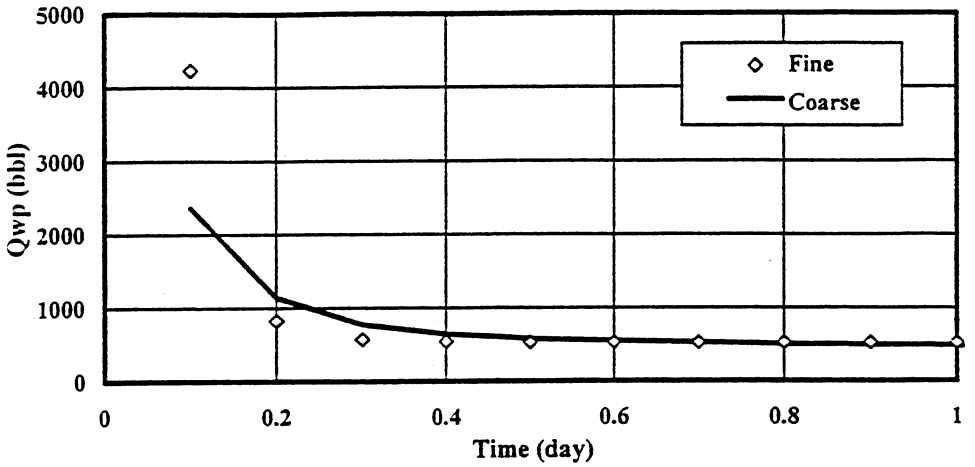

Fig. 4-24 Water Production Rate for Well #4 of Model #1 Without PI Scale-up

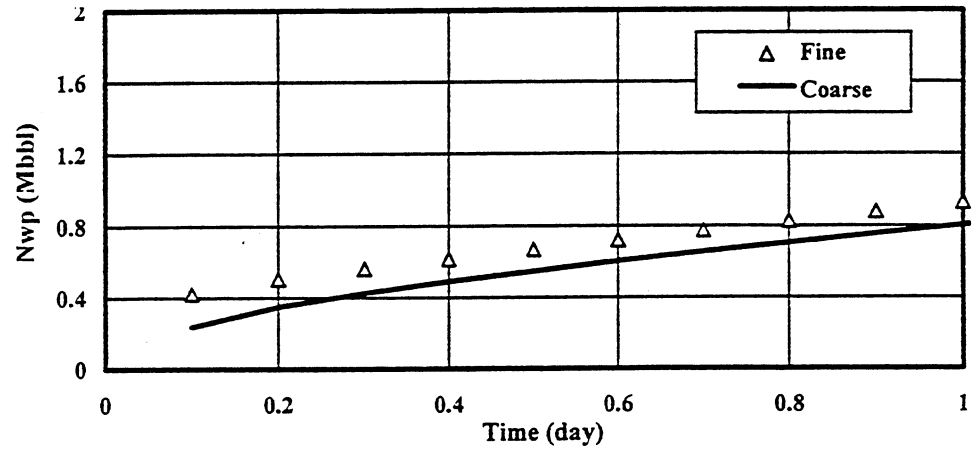

Fig. 4-25 Cum. Water Production for Well #4 of Model #1 Without PI Scale-up

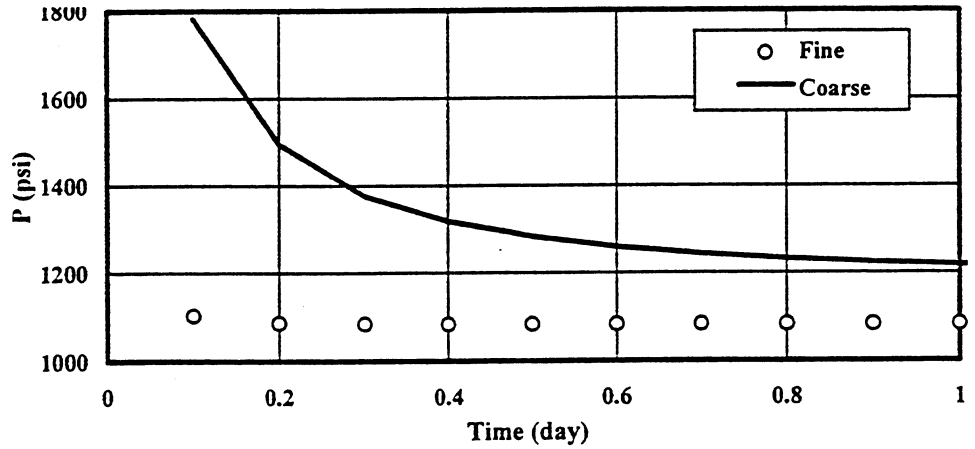

Fig. 4-26 Well Block Pressure for Well #4 of Model #1 Without PI Scale-up

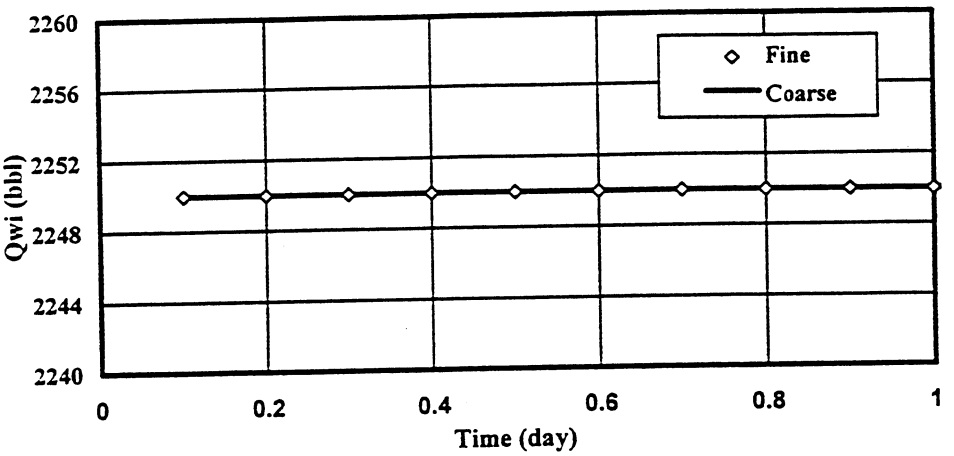

Fig. 4-27 Water Injection Rate for Well #5 of Model #1 Without PI Scale-up

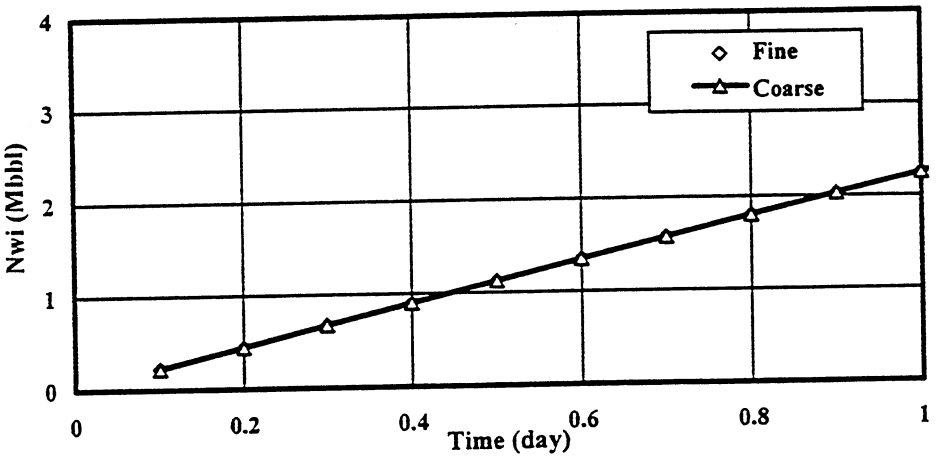

Fig. 4-28 Cum. Water Injection for Well #5 of Model #1 Without PI Scale-up

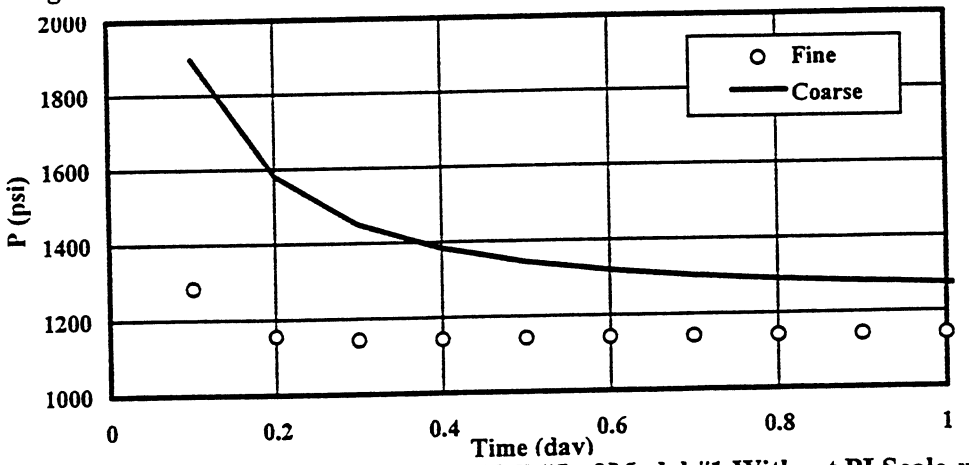

Fig. 4-29 Well Block Pressure for Well #5 of Model #1 Without PI Scale-up

4.3 Scale-up for Radial Flow Around the Wellbore

In Chapter II, the previous studies on the scale-up around wellbore were reviewed. The analytical method proposed by Soeriawinata (1996) calculates effective permeability for a coarse-scale wellblock from fine-scale permeability. This method divides the wellblock into many rays or slices so that the grid block includes some irregular shapes. This method can scale up wellblock permeability without running a reservoir simulation. However, as using arithmetic, harmonic, or geometric methods to calculate average permeability of coarse-scale grid blocks for linear flow, the values obtained are difficult to accept, because of the complex configuration of fluid flow in formation. Still, the results are considered to be a closer approximation to the real reservoir condition than that just using the grid block value along. The concept proposed by Ding (1995) directly relates the well flow rate, which is one of the targets to match, to the parameter used in reservoir simulation. The fluid flow within reservoir is very complex at a microscale. However, the flow at macroscale is of most concern to us, i.e., the flow rate of 'in' and 'out'. Ding's method also scales up transmissibility, and can therefore be easily combined with the scale-up of linear flow conducted previously.

In reservoir simulation, either the well injectivity index or the productivity index is required as input into the simulator in order to reflect the extent of formation damage around the wellbore and the dimension of reservoir and wells. When wellblock and wellbore pressures are known, the flow rate of well can be determined by productivity index. Well injectivity index is dimensionless and can be expressed by the following equation (SGM, 1995):

$$WI = \frac{2\pi}{Ln\left(\frac{r_b}{r_w}\right) + s} \tag{4-17}$$

where:

WI = well injectivity index (dimensionless),

r_b = equivalent radius (Peaceman) of wellblock (ft),

r_w = wellbore radius (ft),

s = skin factor.

The productivity index is related to the well injectivity index by the following equation:

$$PI = WI.\frac{0.001127\sum_{l=1}^{L}\left[\frac{khk_{rw}}{\mu_w B_w}\right]}{gf} \tag{4-18}$$

where:

PI = productivity index (STB/day-psi),

k = permeability of production layer (mD),

h = thickness of production layer (ft),

k_{rw} = relative permeability of water;

μ_w = viscosity of reservoir water (cp),

B_w = volume factor of reservoir water (rb/STB).

gf = geometry factor= $\frac{ln(r_e / r_w)}{ln(r_b / r_w)}$,

r_e = drainage radius (ft),

L = total layer number.

In reservoir simulation, either the well productivity or the injectivity index can be used as input. If the skin factor can be estimated, then the WI can be calculated using Eq. 4-17 and used as input. The simulator will calculate PI for the well using Eq. 4-18. If PI can be estimated by measuring the well flow rate, wellblock pressure, and wellbore pressure, then PI can be directly input into the simulation model. In this study, WI for each well in the fine-scale model was assumed to be 10 for the hypothetical model. For the simulation for coarse-scale model, Eq. 4-18, indicates that the upscaled permeability will effect the calculation of PI, so WI or PI must be considered in scale-up.

Upscaled WI cannot be simply calculated, because the upscaled skin factor is usually unknown. It is possible to calculate the upscaled PI from its definition as follows:

$$PI = \frac{Q_t}{p_g - p_b} \tag{4-19}$$

where:

Q_t = total flow rate of well (STB/day),

p_g = average wellblock pressure (psi),

p_b = bottom hole pressure (psi).

Recalling Eqs. 4-13 to 4-15 for the calculation of upscaled transmissibility of coarse grid blocks, the PI in Eq. 4-19 is, in fact, the transmissibility of wellblock to wellbore. To obtain PI in Eq. 4-19, Q_t can be obtained by simply summing the flow rate in each layer of the wellbore in the fine-scale model to represent the total flow rate of the well. P_g can be obtained using pressure values from fine-scale model and pore volume average method. Fortunately, the simulator outputs this value in the well report, as well as values

for P_b. Therefore, upscaled PI for each well can be calculated using Eq. 4-19 and data from simulation report.

In VIP simulator, only the PI value for each well is required as an input parameter. The program will distribute the PI values for each layer internally based on the permeability and thickness of each layer. Calculated PI for both production wells and injection well in model #1 are listed in Table 4-3. The results of a simulation on the coarse-scale model using the upscaled PI in Table 4-3 are provided in Figs. 4-30 to 4-47 for both reservoir and individual wells. It was observed that significant improvements were obtained after considering the scale-up near the wellbore area. Excellent matches were obtained in all of the plots. Using scale-up near wellbore is important in the overall process, so scale-up around wellbore will be included for all of the models in this study when scale-up is conducted.

Table 4-3 Well Injectivity and Productivity Index Used in the Fine-Scale and Coarse-Scale Simulation for Model #1

Well	WI Fine Scale	PI Coarse Scale
PROD-1	10	227.19
PROD-2	10	217.89
PROD-3	10	262.97
PROD-4	10	250.23
INJE-5	10	254.22

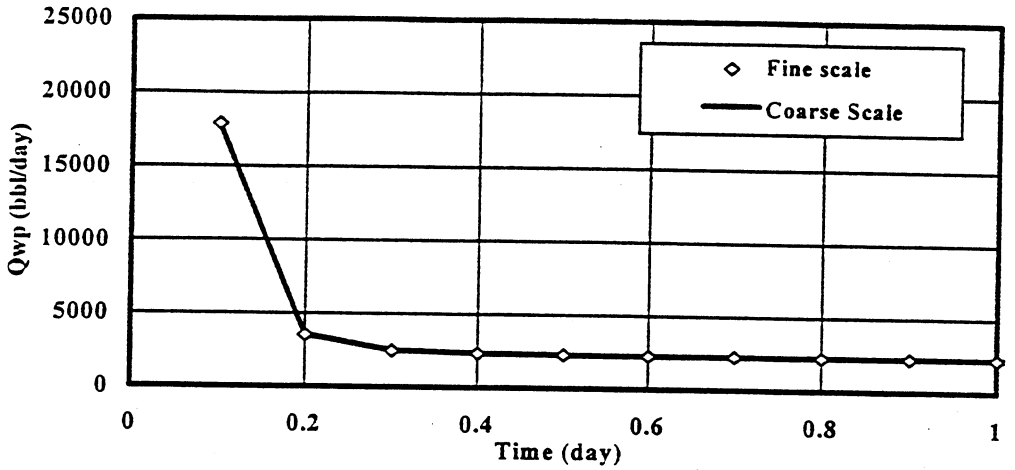

Fig. 4-30 Water Production Rate of Model #1 With PI Scale-up

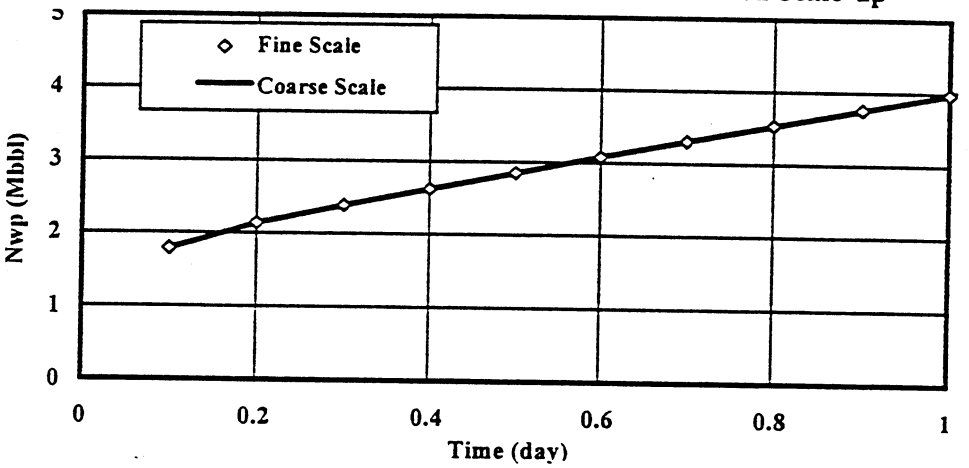

Fig. 4-31 Cum. Water Production of Model #1 With PI Scale-up

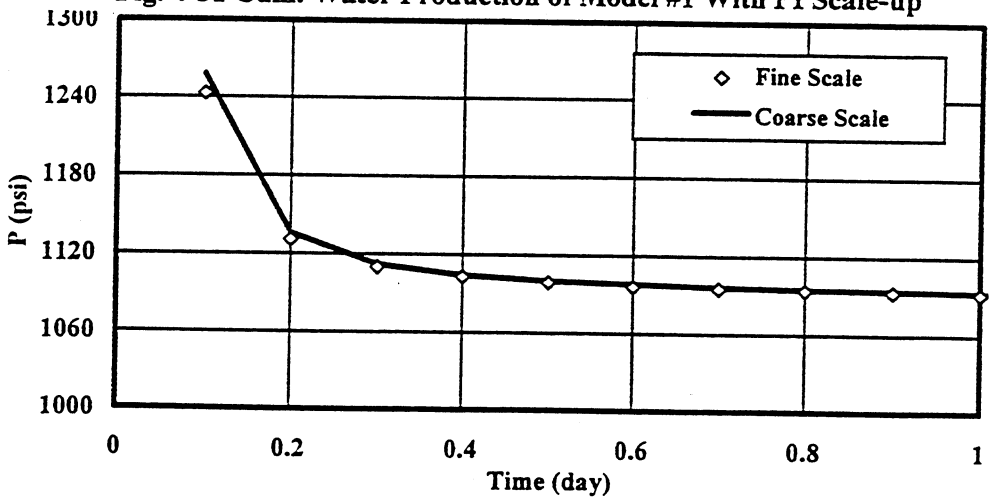

Fig. 4-32 Reservoir Pressure of Model #1 With PI Scale-up

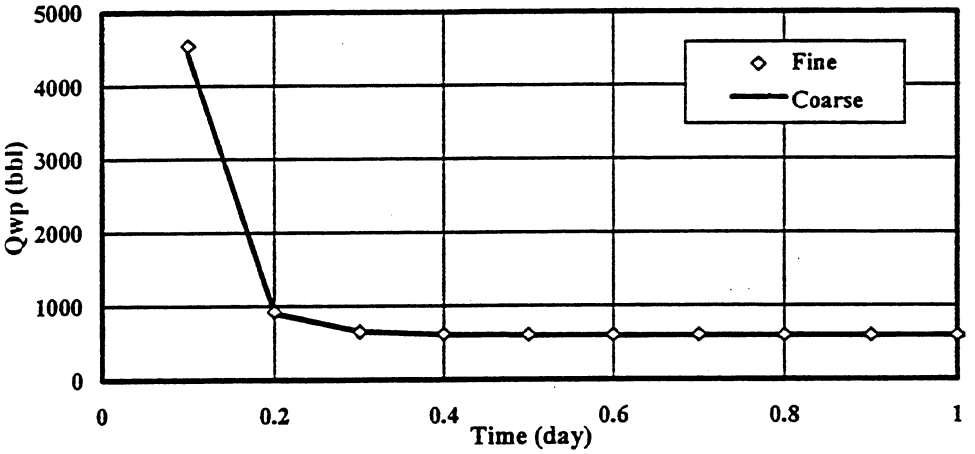

Fig. 4-33 Water Production Rate for Well #1 of Model #1 With PI Scale-up

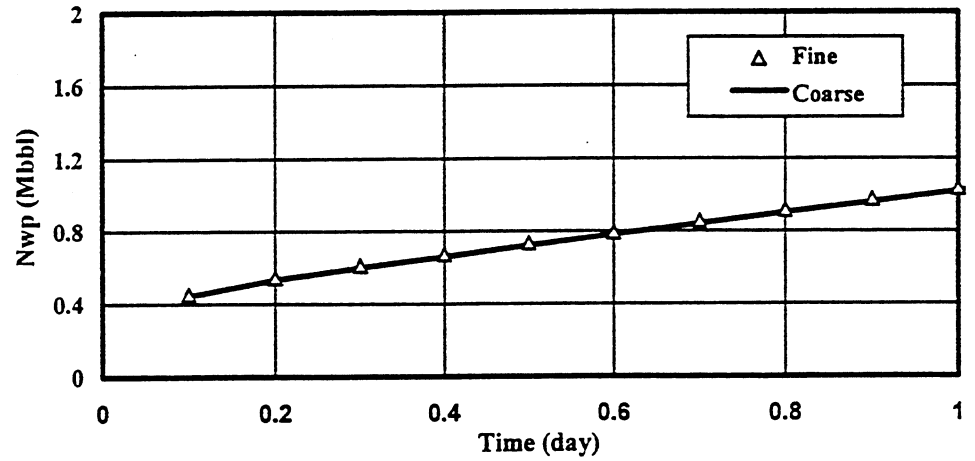

Fig. 4-34 Cum. Water Production for Well #1 of Model #1 With PI Scale-up

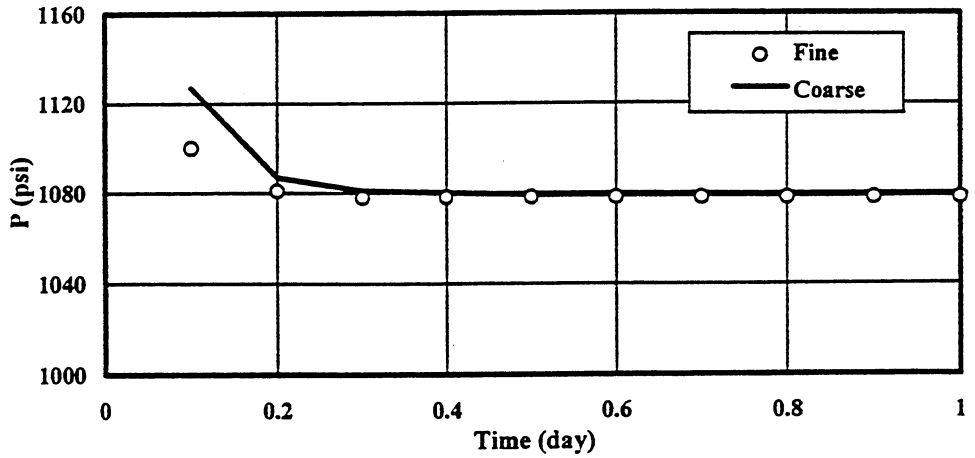

Fig. 4-35 Well Block Pressure for Well #1 of Model #1 With PI Scale-up

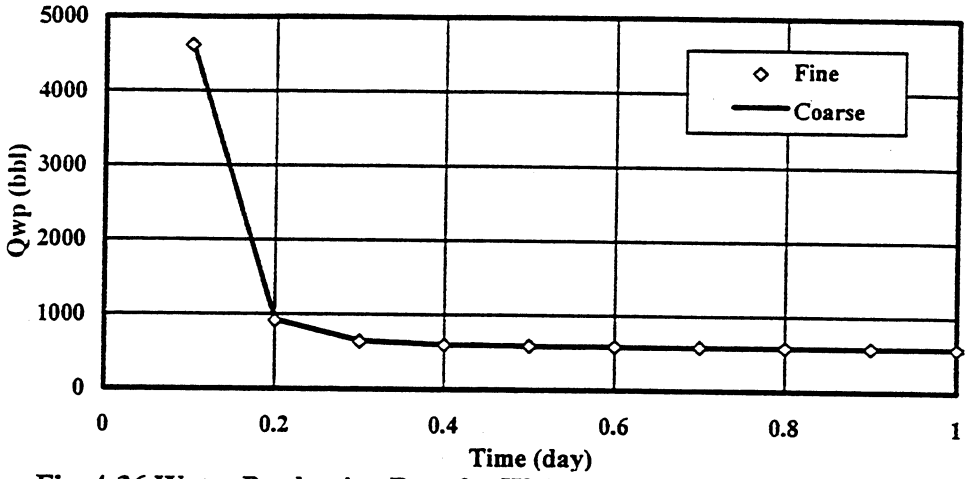

Fig. 4-36 Water Production Rate for Well #2 of Model #1 With PI Scale-up

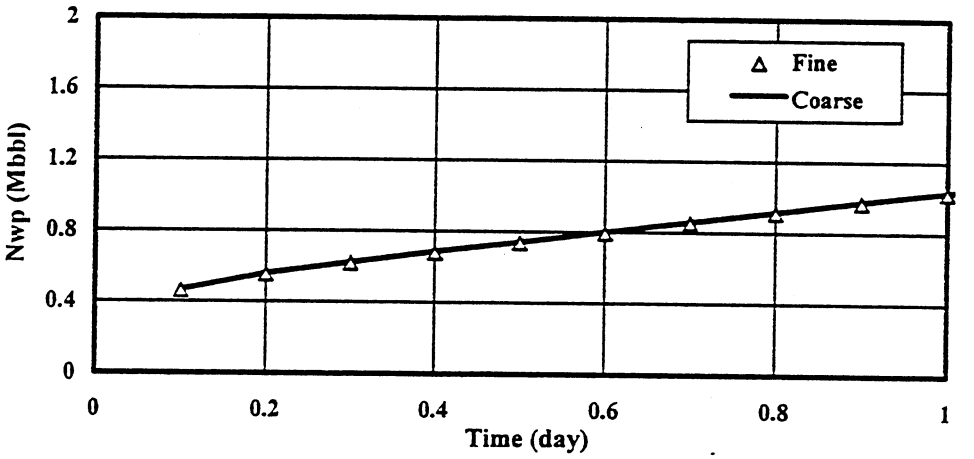

Fig. 4-37 Cum. Water Production for Well #2 of Model #1 With PI Scale-up

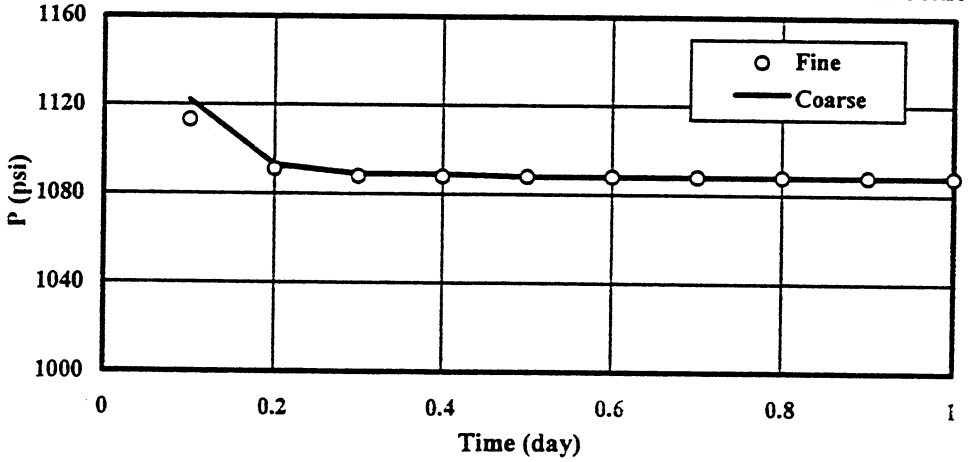

Fig. 4-38 Well Block Pressure for Well #2 of Model #1 With PI Scale-up

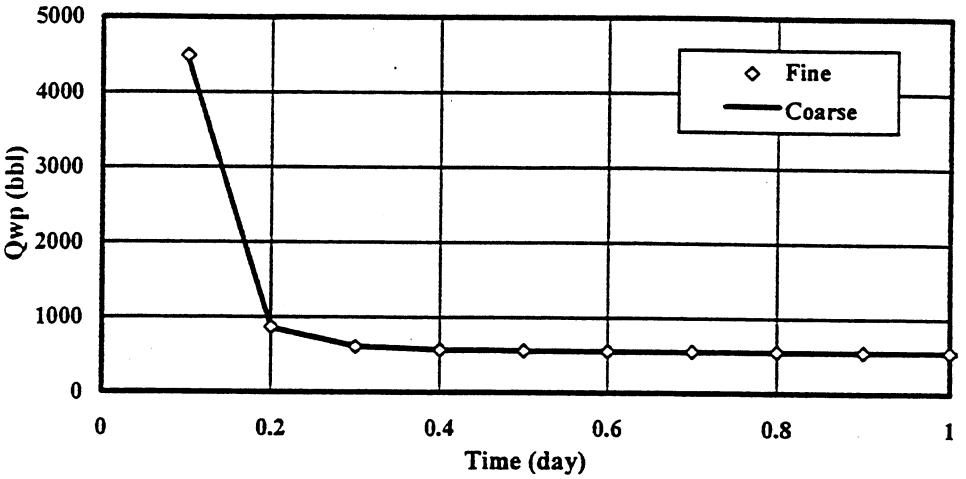

Fig. 4-39 Water Production Rate for Well #3 of Model #1 With PI Scale-up

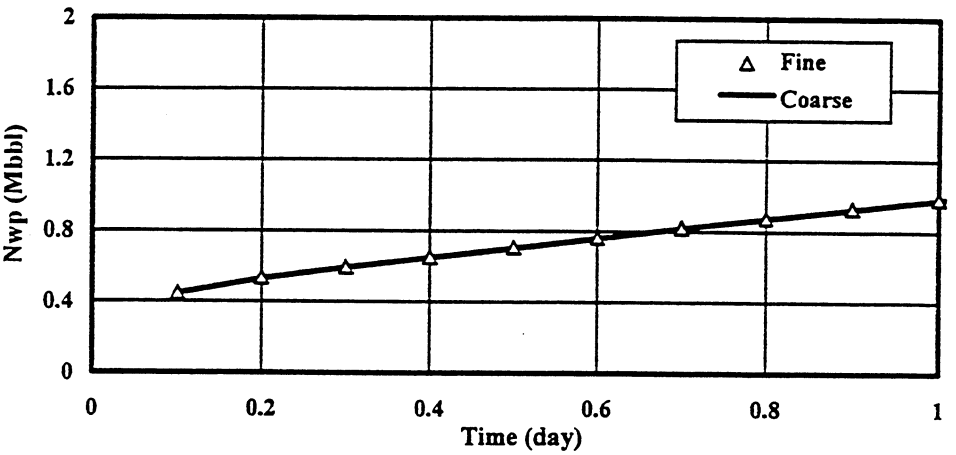

Fig. 4-40 Cum. Water Production for Well #3 of Model #1 With PI Scale-up

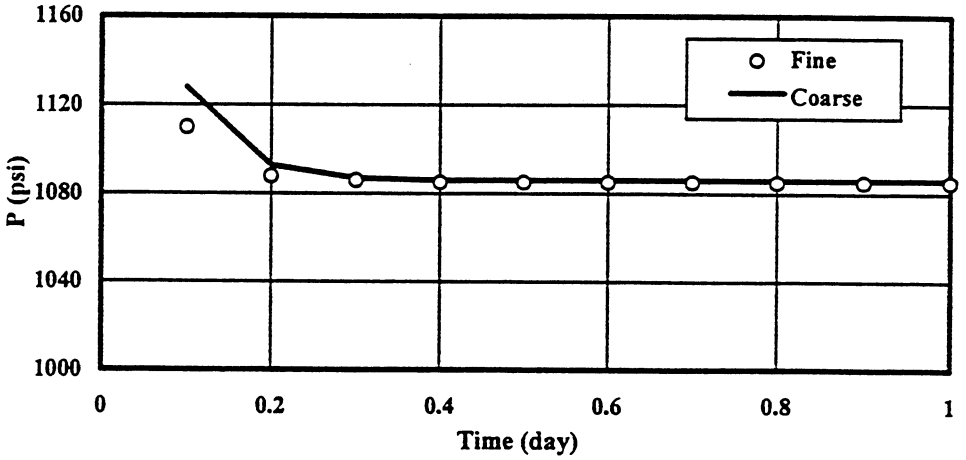

Fig. 4-41 Well Block Pressure for Well #3 of Model #1 With PI Scale-up

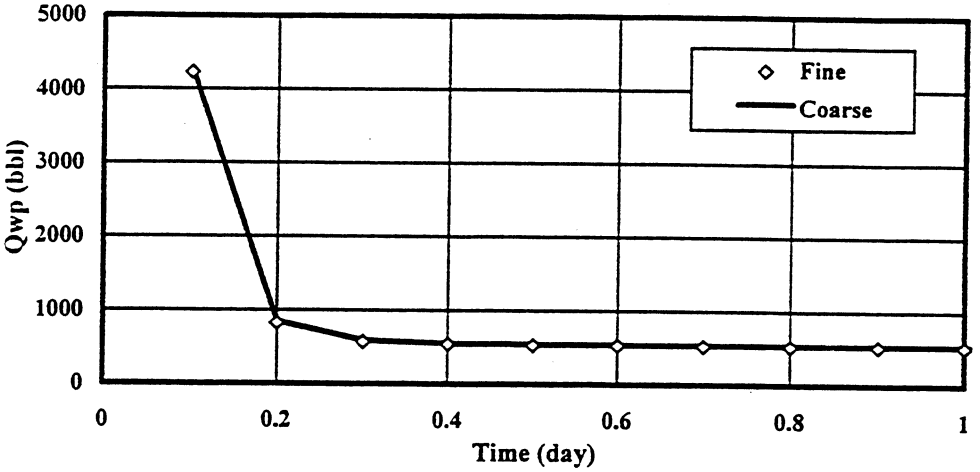

Fig. 4-42 Water Production Rate for Well #4 of Model #1 With PI Scale-up

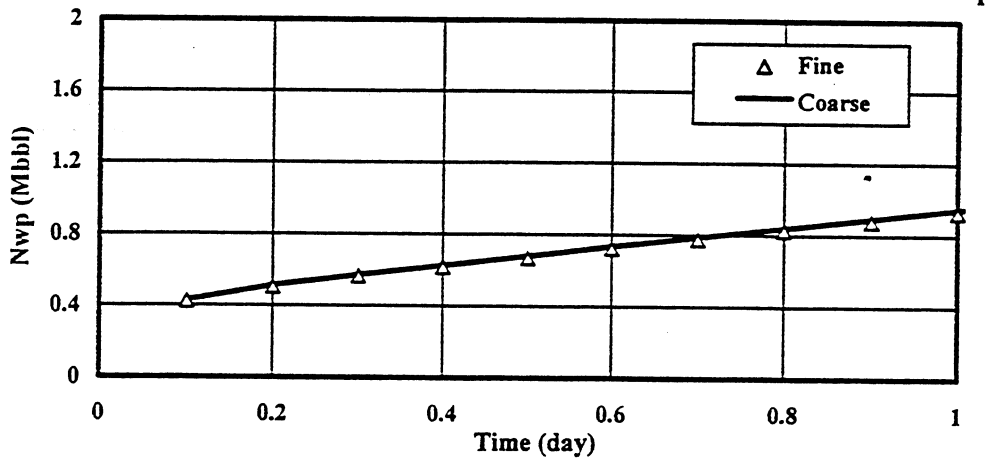

Fig. 4-43 Cum. Water Production for Well #4 of Model #1 With PI Scale-up

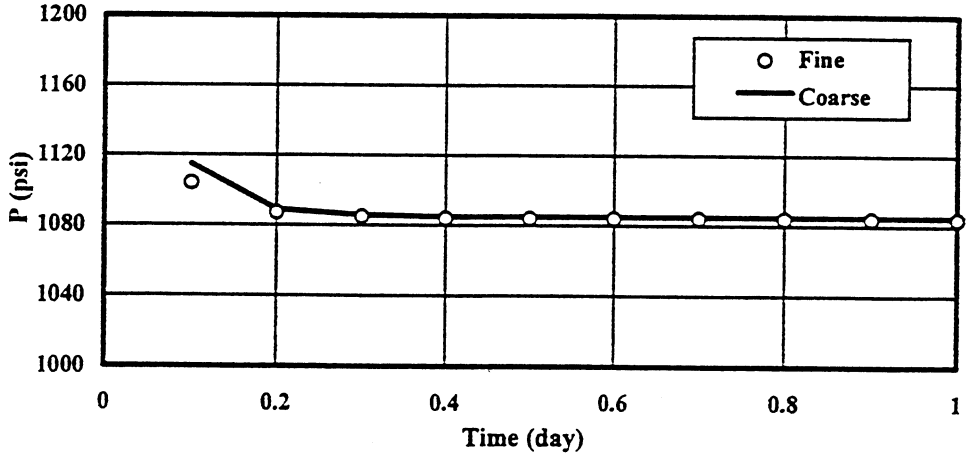

Fig. 4-44 Well Block Pressure for Well #4 of Model #1 With PI Scale-up

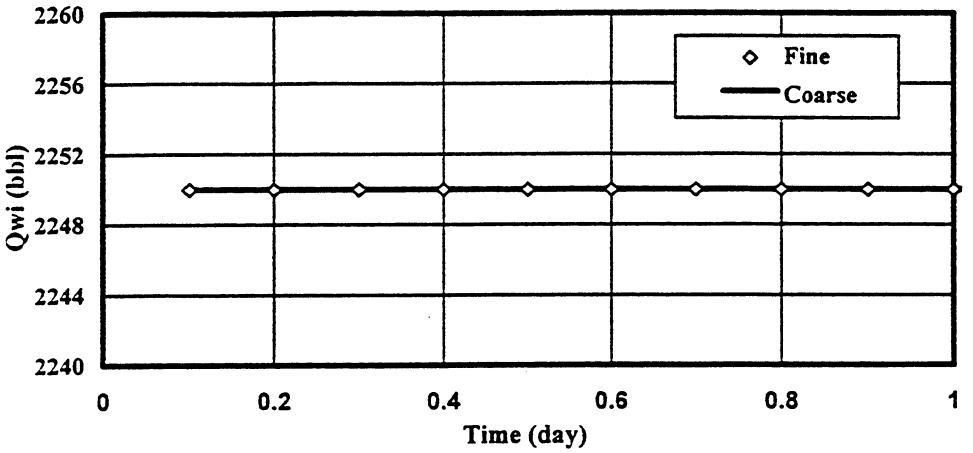

Fig. 4-45 Water Injection Rate for Well #5 of Model #1 With PI Scale-up

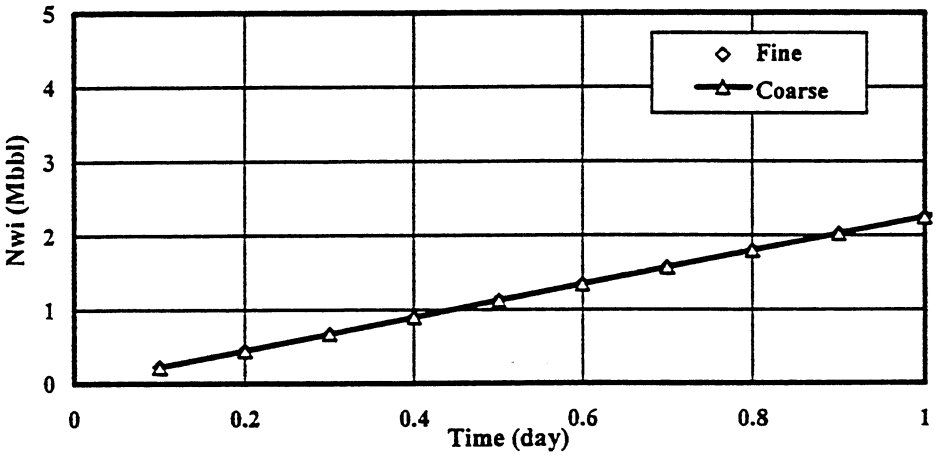

Fig. 4-46 Cum. Water Injection for Well #5 of Model #1 With PI Scale-up

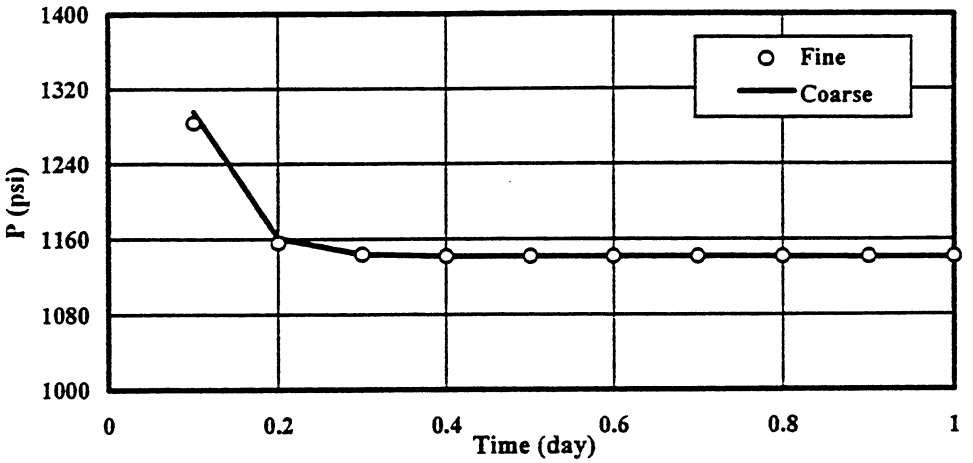

Fig. 4-47 Well Block Pressure for Well #5 of Model #1 With PI Scale-up

4.4 Scale-up on A Hypothetical Reservoir Model with Pinch-Out

In section 4.2, scale-up for a hypothetical layer-cake reservoir without pinch-out was studied and illustrated. Due to the complexity of many depositional environments, the distribution of channels, lithofacies, or flow units may not be continuous over reservoir volume studied, especially in a fine-scale model. The scale-up process described in section 4.2 is inadequate when pinch-outs exist in the reservoir. Therefore, in this section, pinch-out was considered when scale-up is conducted.

4.4.1 Transmissibility for a Reservoir with Pinch-out

In a reservoir simulator, the 3-D continuity equation is solved from left to right in the x direction, from back to front in the y direction, and from top to bottom in the z direction. The transmissibility defined in a simulator for a specified grid-block are applicable to the left, back, and top faces of the grid block in x, y, and z directions, respectively. Therefore, for a reservoir with no flow boundary condition, the horizontal transmissibility, T_x and T_y are zero for grid blocks at boundaries identified with arrows in Fig. 4-48. The vertical transmissibility T_z for the grid blocks on the top layer are zero, if no pinch-out exists in this layer. When pinch-out exists in the top layer, as shown in Fig. 4-49, the vertical transmissibility for the grid blocks are zero at the top of the layer that is pinched out. Fig. 4-49 is a cross-sectional illustration of pinch-out in a geological model, with 9 columns in the x direction and 9 layers in the z direction. Pinch-outs occur in layers 3, 4, 7, and 9 in the vertical direction, and in columns 1, 2, 4, 5 and 9 in the x direction. In column 1, the grid blocks (1, 4), and (1,7) are pinched out. In this illustration, layers 3 and 5, 6 and 8, are connected to each other geologically. In the

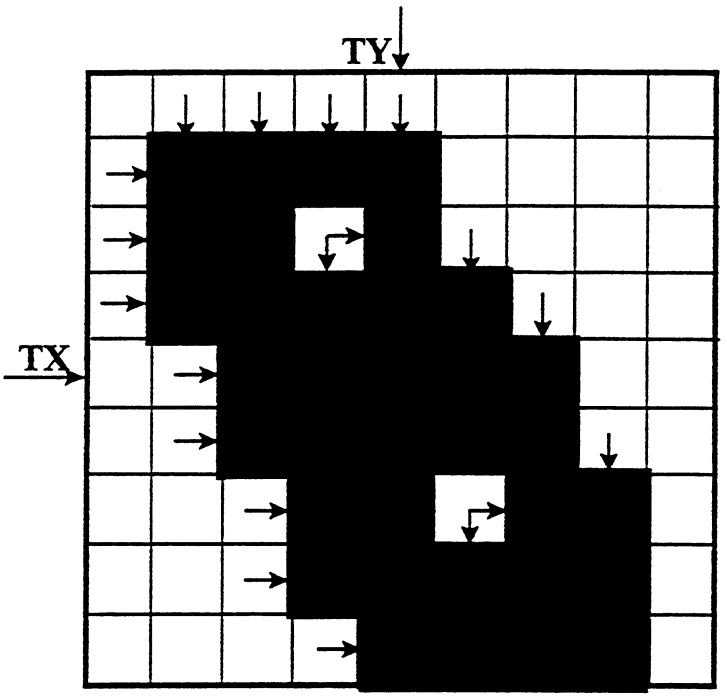

Fig. 4-48 Illustration For the Horizontal View of Pinch-Out In Reservoir Model

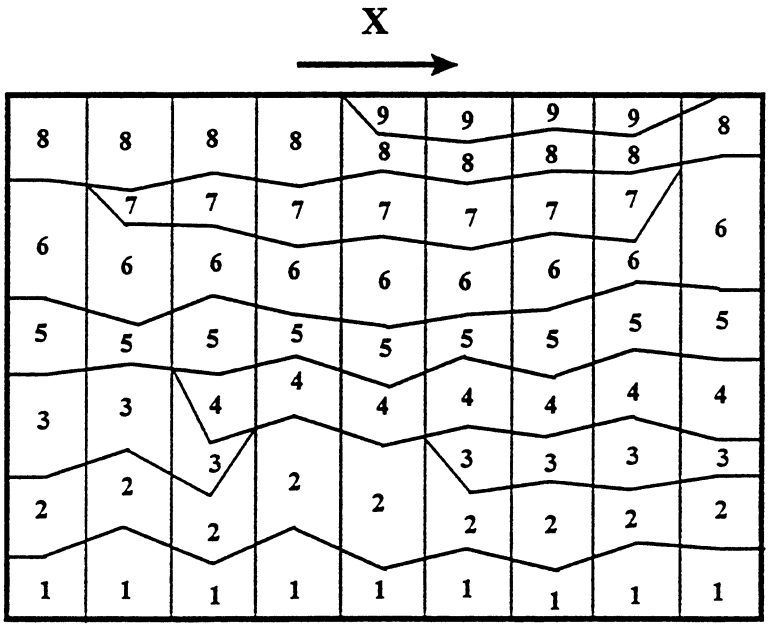

Fig. 4-49 Illustration For the Vertical View of Pinch-Out In Reservoir Model

mathematical model, when the thickness of the grid block is zero, the simulator will automatically assign a vertical transmissibility of zero to the grid block next to the grid block with zero thickness. Therefore, by default, there will be no flow between layers 3 and 5, 6 and 8 in Column 1. If a conventional transmissibility is used in the simulator, an incorrect simulation of fluid flow in the reservoir will occur. To resolve this problem, special considerations are needed for systems with pinch-out when reservoir simulation is conducted.

4.4.2 Simulation Model with Pinch-out

It was assumed that pitch-out exists in the fine-scale model used in section 4.2 from layers 1 to 12 by setting the thickness of the pinch-out grid blocks as zero. Fig. 4-50 is the three dimensional description of permeability for the pinch-out model used in this study. Pinch-out can be observed on top of the model around well #2 and #5, where the top grid blocks were pinched out and lower permeability with blue color for the grid blocks of next layer was presented.

To simulate the pinch-out, a pinch-out option is available in VIP, which automatically detects the pinch-out between two grid blocks and connects two grid blocks with non-zero transmissibility when simulation is conducted. When this option is used, corner-point geometry system of grid block must also be used.

Two areas of concerns indicated that the pinch-out option unsuitable for this study. First, after running the simulation on fine-scale model and obtaining the flow rate and pressure for each grid block, it was found that the flow rates in the z direction

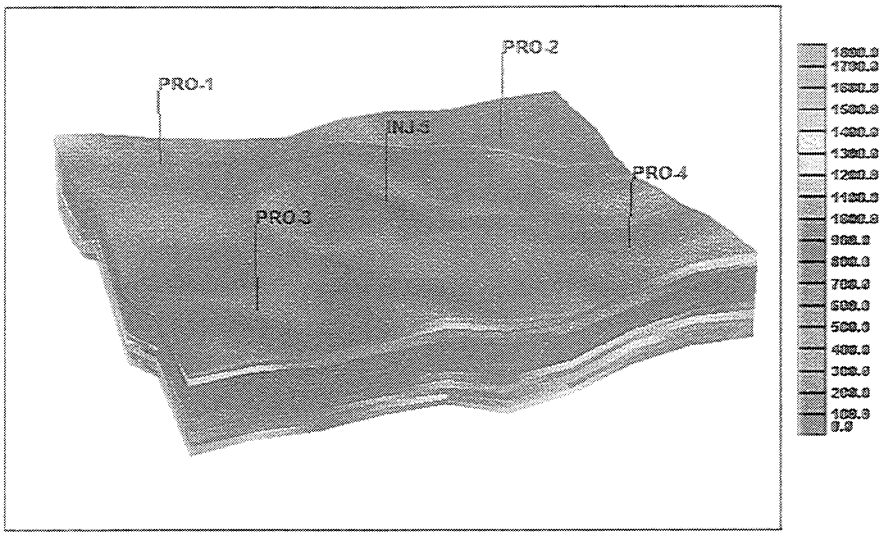

Fig. 4-50 3-D View For the Permeability Distribution of Model #2 With Pinch-out

between two grid blocks, which should have opposite directions, but same values, were incorrect. They were non-zero in negative direction, but zero in positive direction, which means the simulator could not simulate the pinch-out correctly. Second, when the corner-geometry option is used in VIP, the transmissibility option can not be used, i.e., grid-block permeability must be used as input.

Because of these two constraints, it is inappropriate to use the pinch-out option of VIP for this study. A unique characteristic of the pinch-out grid blocks is that there is no horizontal flow, but a direct vertical communication. To reproduce this scenario, it can be assumed that there exists a very thin layer between two grid blocks having pinch-out grid, such that it would not cause significant error in simulation results. Fig. 4-50 is an illustration

illustration for the geological model described in Fig. 4-49, in which the bold lines represent the thin pinch-out grid blocks. It was assumed that the horizontal permeability of these thin layers is zero, so that no horizontal flow occurs in these grid blocks. A high vertical permeability was used to flow rates in vertical direction between the two grid blocks, between which pinch-out exists, to be essentially the same, as in a reservoir with pinch-out. The pore volume of such thin grid blocks should be very small in order to reduce any error in the calculation of reservoir volume. The limitation of material balance in simulation will limit this assumption to some extent, because the pore volumes of these thin grid blocks cannot be so small that a violation in simulation will occur. In this study, the value used for the pinch-out grid blocks were 9999 mD for vertical permeability , 0.01 ft for thickness, and 5% for porosity.

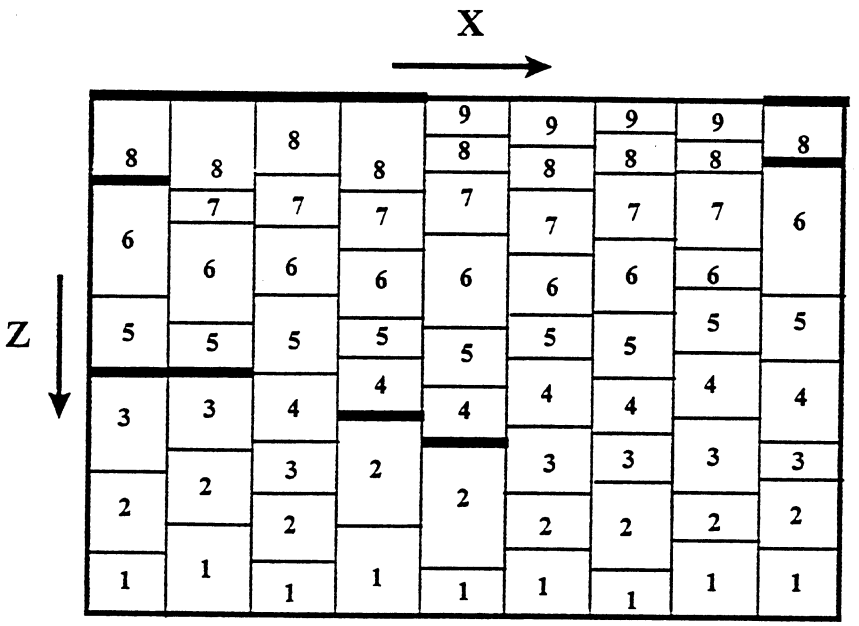

Fig. 4-51 Illustration of Pinch-Out In Mathematical Model

In comparing the pore volume of the real pinch-out model with the pseudo-pinch-out model, an error of 0.4% in pore volume resulted due to this assumption. The common tolerance for pore volume calculation in reservoir simulation is about 5%, so this assumption is reasonable.

4.4.3 Special Considerations for Pinch-out and Results of Scale-up

When pinch-out is used in the model, the process described in section 4.2.3 for scale-up on a reservoir model without pinch-out must be modified. The following special considerations are required:

1. The assumed thin grid blocks must not be included in the calculation of average permeability for coarse grid blocks.
2. When pinch-out exists between two coarse-scale grid blocks in the x or y direction, the transmissibility T_X or T_Y for this pinch-out grid block must be set to be zero.
3. The reservoir volume and pore volume for fine-scale and coarse-scale models, respectively, should be the same, so that the simulation results for fine scale and coarse scale can be compared. Therefore, the thin layers should be accounted for when porosity and thickness for coarse-scale model are calculated.

After taking the above factors into consideration, scale-up was conducted on the pinch-out model. The results are shown in Figs. 4-52 to 4-69 for the reservoir and the five individual wells, respectively. In these figures, both results with PI scale-up and without PI scale-up are displayed. The values of well injectivity index, WI, used for input in fine-scale model and upscaled productivity index PI used for coarse-scale model are listed in Table 4-4.

Table 4-4 Well Injectivity and Productivity Index Used for the Fine-Scale and Coarse-Scale Simulation for Model #2

Well	WI Fine Scale	PI Coarse Scale
PROD-1	10	313.32
PROD-1	10	170.61
PROD-1	10	177.37
PROD-1	10	220.82
INJE-5	10	200.11

It was observed in plots 4-52 to 4-69 for scale-up on pinch-out model #2 that:

1. As in model #1, significant improvements were obtained after PI scale-up was considered for both water production and reservoir pressure. PI scale-up was shown again to be a very important component of the overall scale-up procedure.
2. As for model #1, water production predictions matched better than reservoir pressure without PI scale-up. After PI scale-up, successful matches were obtained in all the plots.

In summary, scale-up was conducted on two hypothetical models. A successful scale-up result was obtained. The scale-up methodology presented in this chapter was then applied to Gypsy models and are described in Chapter V.

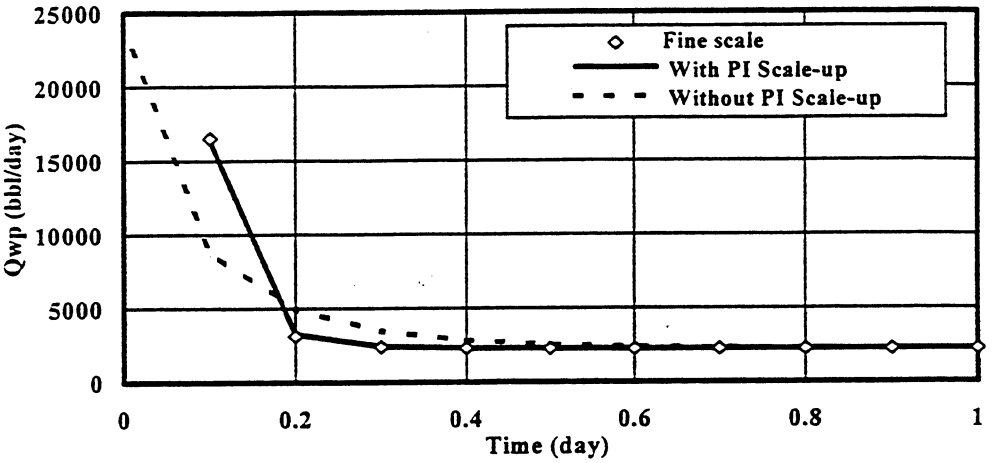

Fig. 4-52 Water Production Rate of Model #2

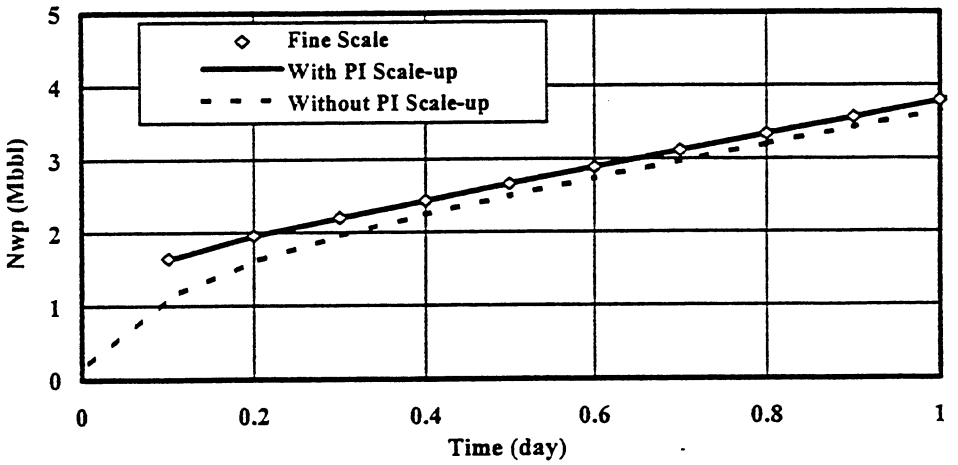

Fig. 4-53 Cum. Water Production of Model #2

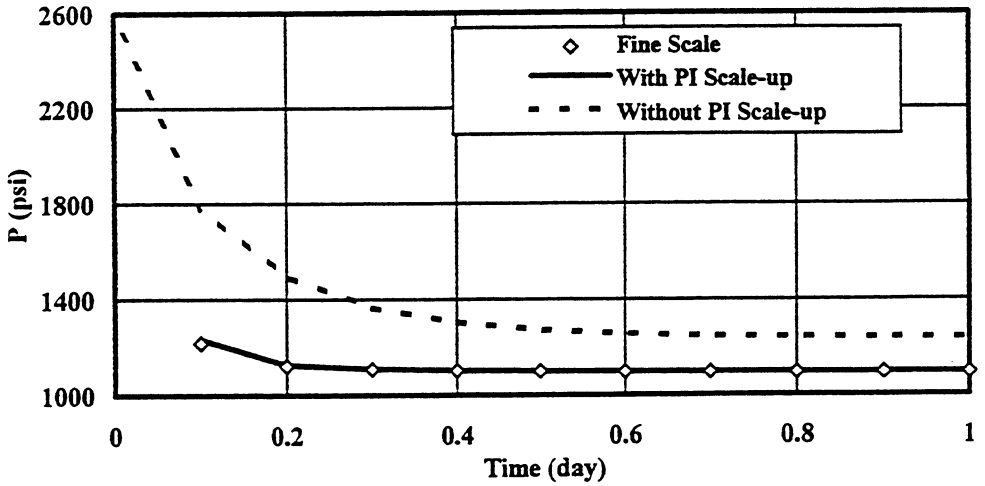

Fig. 4-54 Reservoir Pressure of Model #2

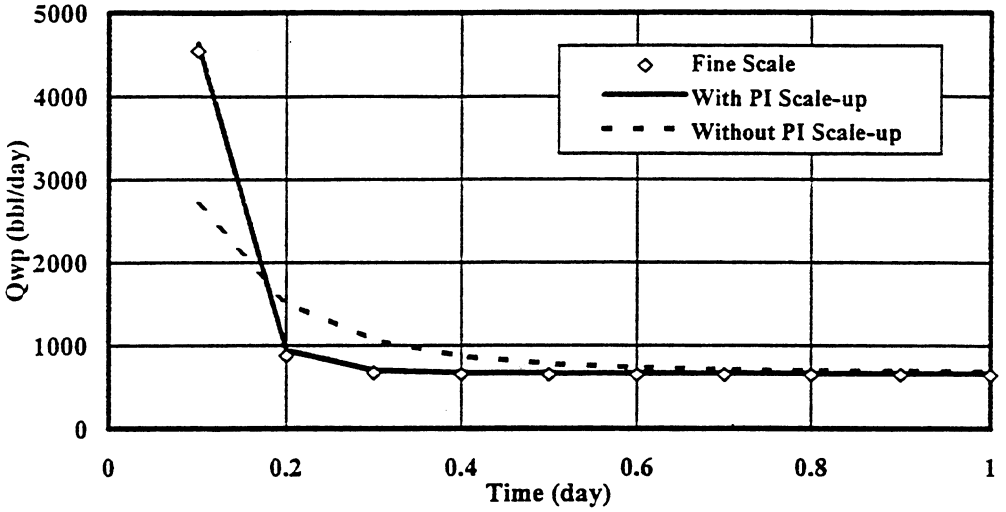

Fig. 4-55 Water Production Rate for Well #1 of Model #2

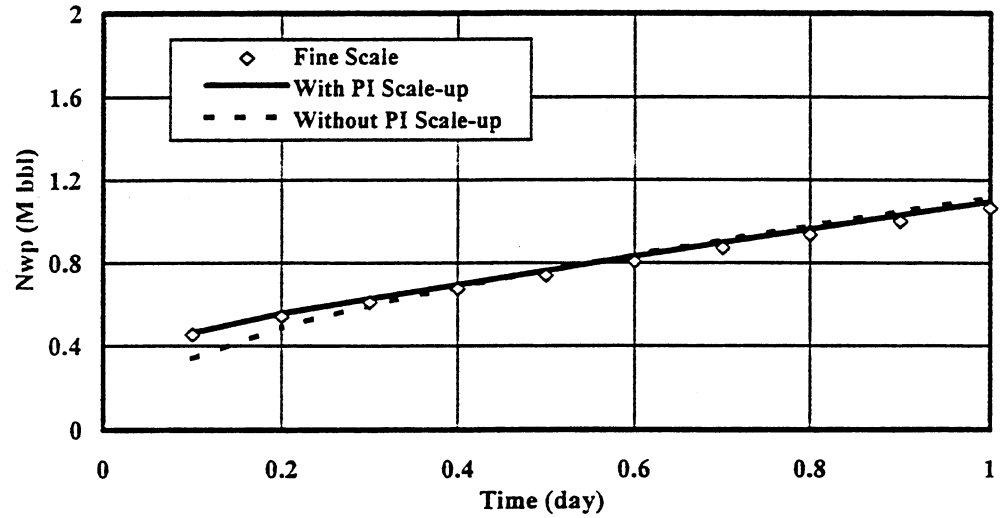

Fig. 4-56 Cum. Water Production for Well #1 of Model #2

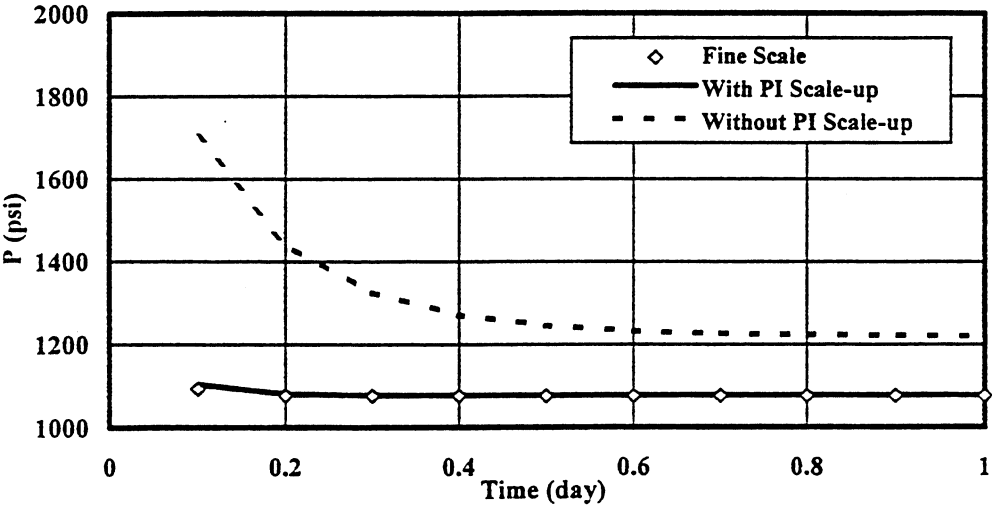

Fig. 4-57 Well Block Pressure for Well #1 of Model #2

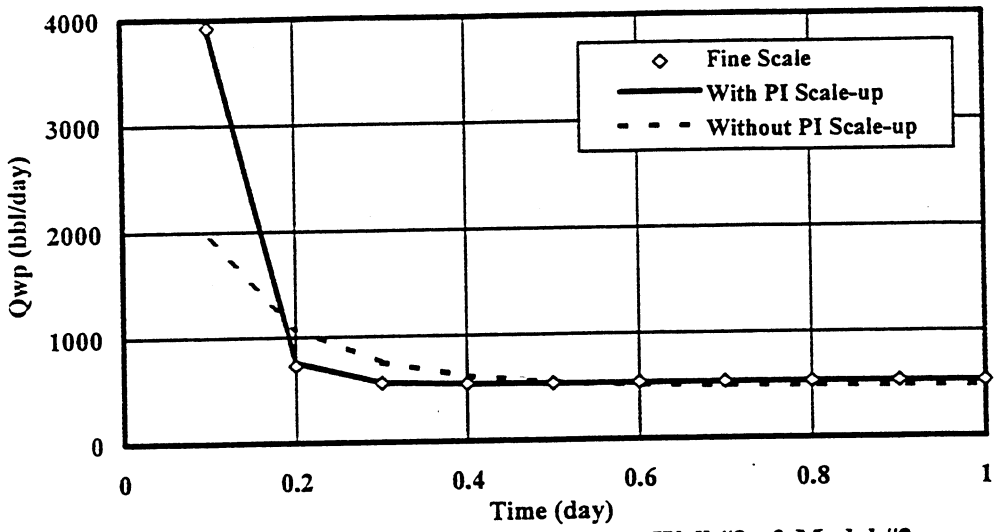

Fig. 4-58 Water Production Rate for Well #2 of Model #2

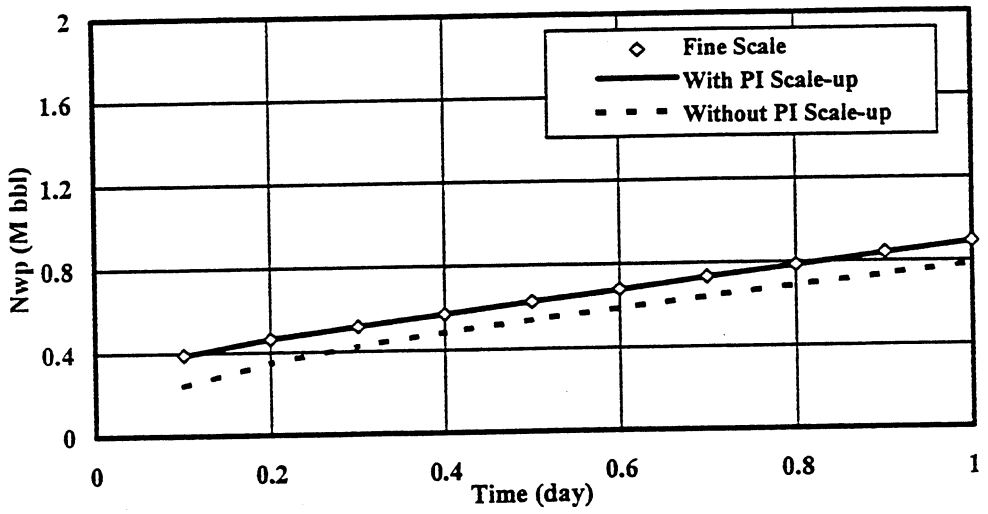

Fig. 4-59 Cum. Water Production for Well #2 of Model #2

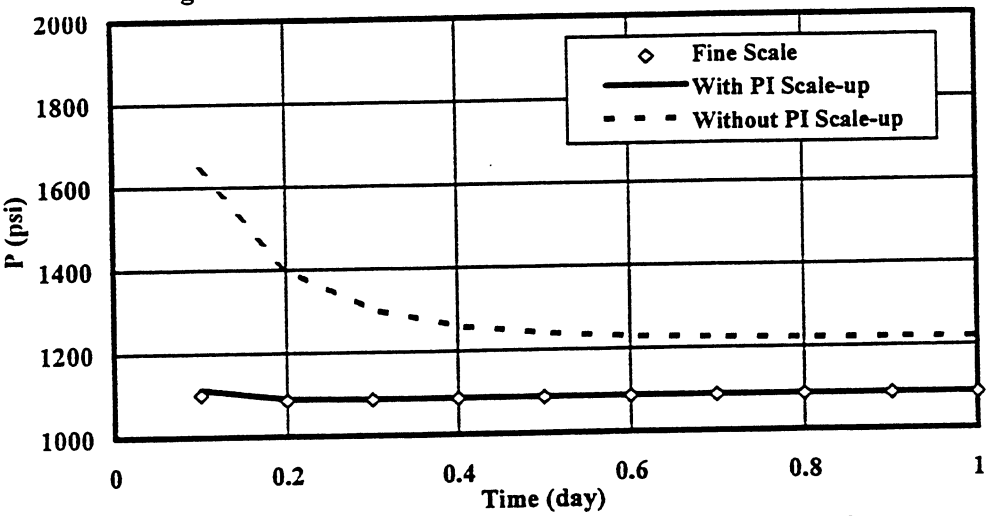

Fig. 4-60 Well Block Pressure for Well #2 of Model #2

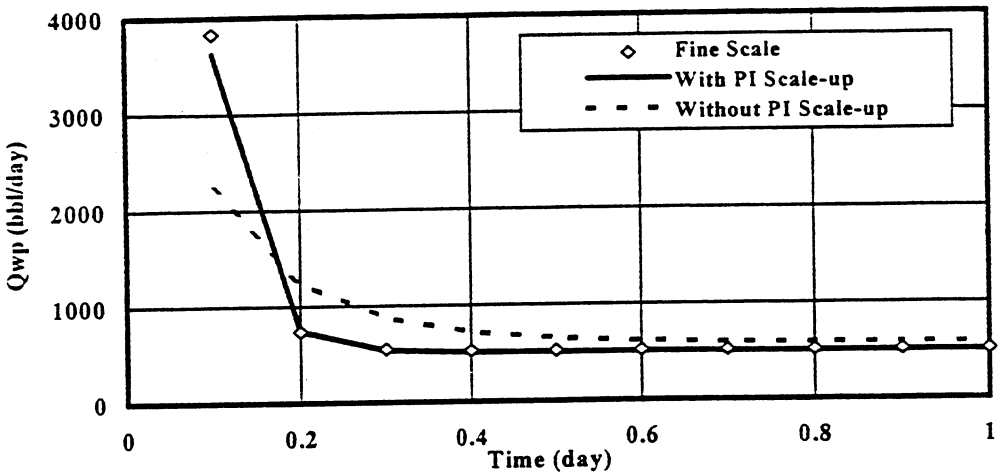

Fig. 4-61 Water Production Rate for Well #3 of Model #2

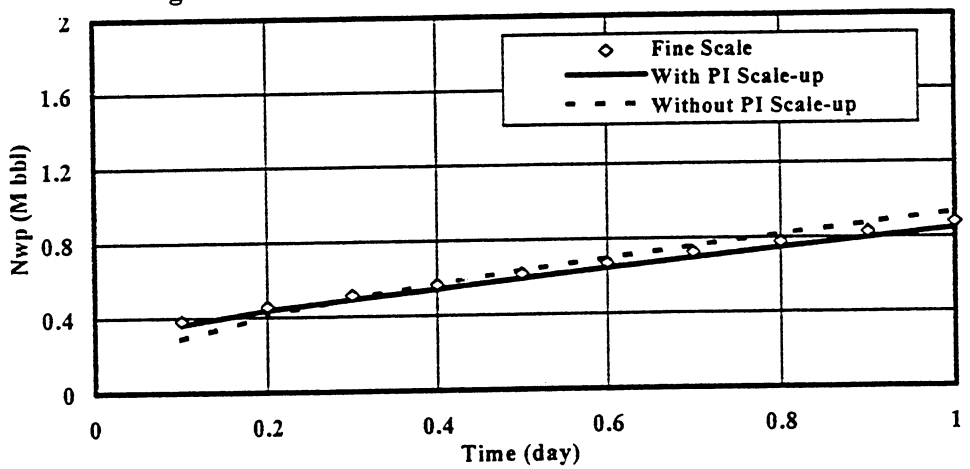

Fig. 4-62 Cum. Water Production for Well #3 of Model #2

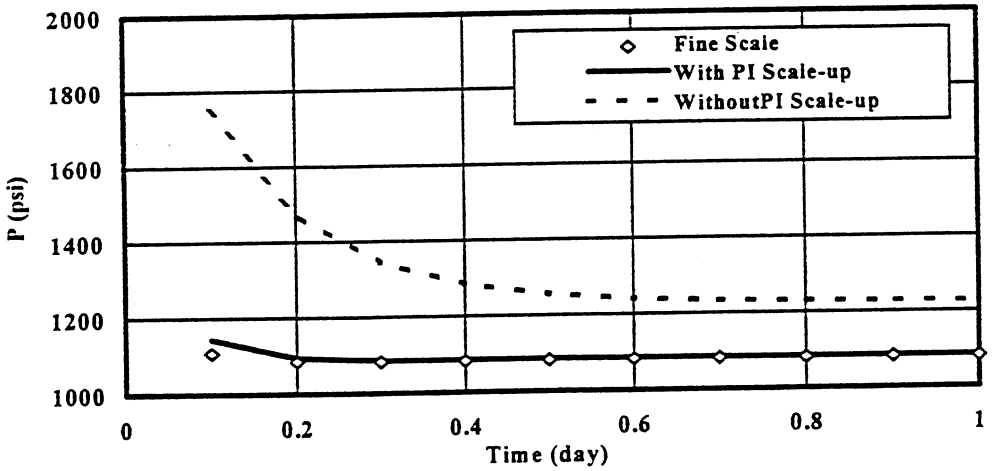

Fig. 4-63 Well Block Pressure for Well #3 of Model #2

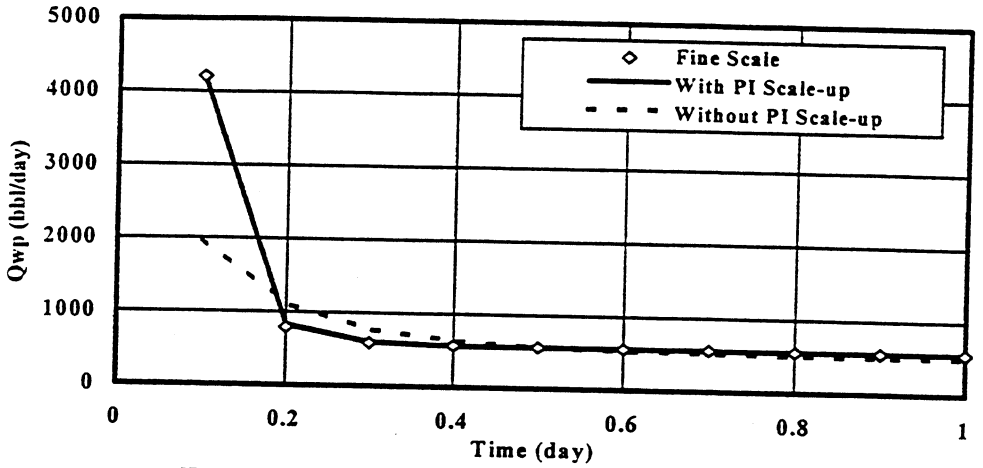

Fig. 4-64 Water Production Rate for Well #4 of Model #2

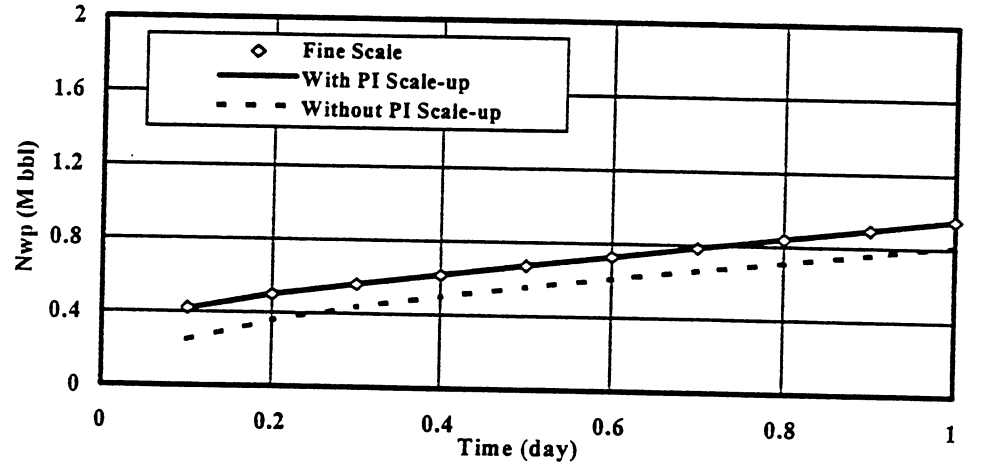

Fig. 4-65 Cum. Water Production for Well #4 of Model #2

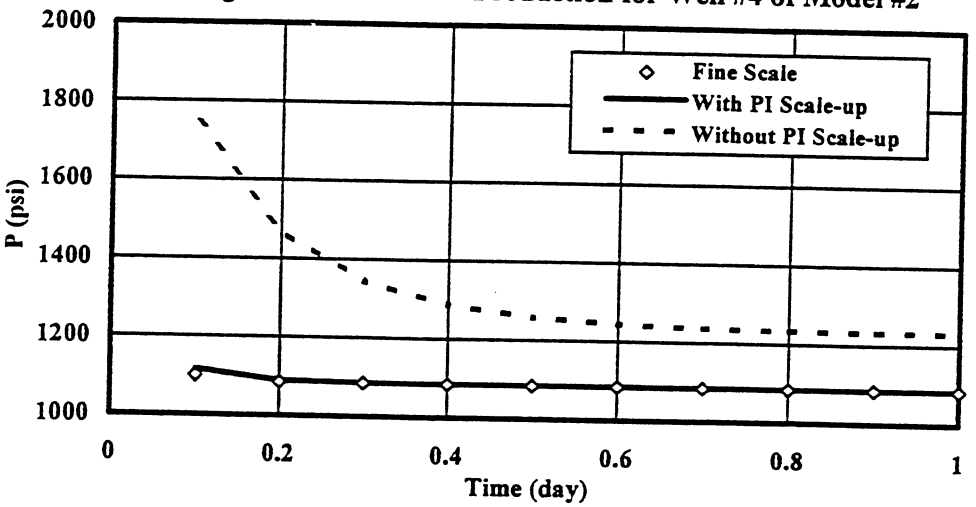

Fig. 4-66 Well Block Pressure for Well #4 of Model #2

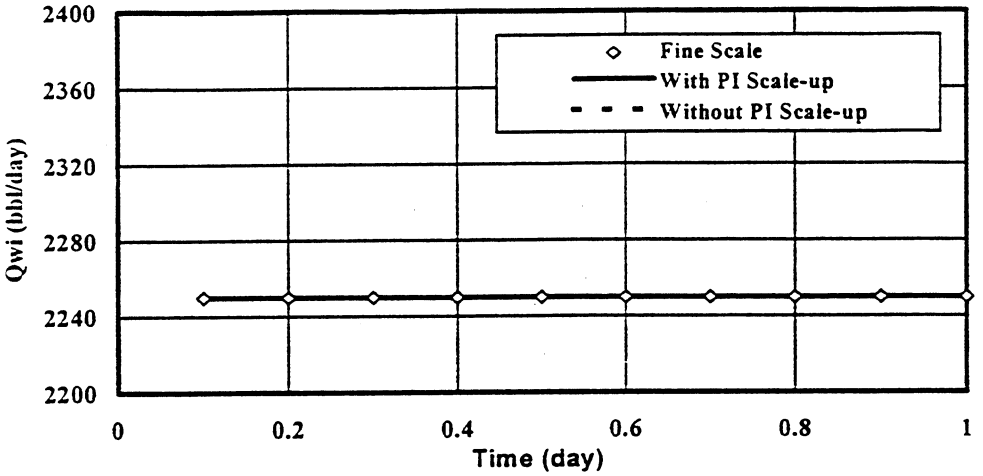

Fig. 4-67 Water Injection Rate for Well #5 of Model #2

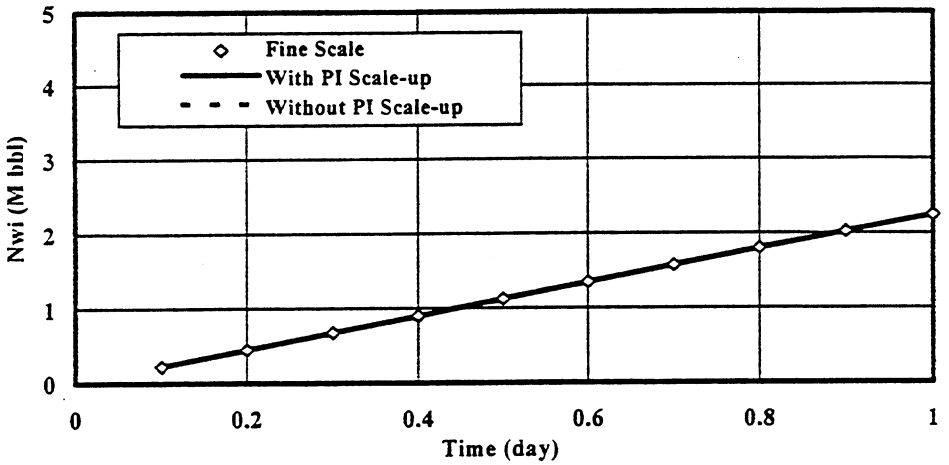

Fig. 4-68 Cum. Water Production for Well #5 of Model #2

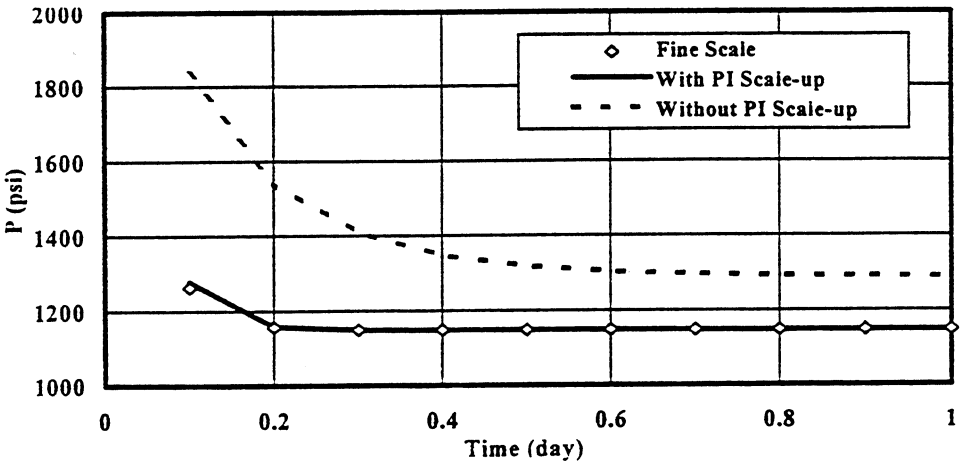

Fig. 4-69 Well Block Pressure for Well #5 of Model #2

CHAPTER V

SCALE-UP ON GYPSY FORMATION

In Chapter IV, the scale-up technique was introduced, illustrated and validated for two hypothetical models. Successful scale-up results were obtained after a PI scale-up technique was applied. In this chapter, the scale-up technique was applied to three Gypsy models developed in Chapter III to study the effects of geological modeling on scale-up.

5.1 Fine-Scale Gypsy Models

Three coarse-scale geological models were developed and described in Chapter III. To perform the scale-up, fine-scale Gypsy models were developed based on three coarse-scale models presented in Chapter III. Fine-scale models were obtained by dividing each permeable layer in the coarse-scale model into layers with one foot thickness. The layers in the fine-scale model are parallel to the bottom surface of the coarse-scale layer. The six shale layers, representing impermeable layers, were kept intact in all three models. This leads to a total of 125 layers in the channel model, 198 layers in the lithofacies model, and 136 layers in the flow unit model. The properties of the models, including permeability and porosity, were determined using the deterministic method based on the available data in the previously identified 22 drilled wells.

To efficiently perform the scale-up, instead of modeling the entire volume of the reservoir, only the area where detailed information was available was simulated, as shown in Fig. 5-1. The grid system that was simulated was 23 by 29 grid blocks in the x and y directions. A 3-D view of the permeability distribution for the three fine-scale models used in scale-up are presented in Figs. 5-2 to 5-4.

The top of the Gypsy formation was initially located at the surface with an average elevation of about 885 ft, which was obtained by averaging the elevations of 22 wells. To perform the simulation, Gypsy formation was assumed to be moved vertically 9500 ft down. The elevation of the new surface of the model was assumed to be zero.

Similar to model #1 and #2, a five-spot well pattern was used in the simulation as shown in Fig. 5-1. All five wells were assumed fully perforated in all of the permeable layers. For the production wells, a maximum production of 10,000 STB/day and a minimum bottom hole pressure of 1,000 psi at elevation of -8,500 feet were assumed. For the injection well, a maximum injection rate of 2,250 STB/day and maximum bottom hole pressure of 10,000 psi at elevation of -8,500 feet were assumed.

The process simulated was single-phase water flow. Reservoir fluid properties were the same values used for the hypothetical models in Chapter IV. No-flow boundary condition was assumed. Reservoir was assumed in equilibrium condition with an initial pressure 2500 psi at a elevation of -8,000 feet.

To simulate pinch-out in various models, the technique presented and used for model #2 in Chapter IV was used, producing an error of 0.39% in reservoir pore volume in channel model, 0.53% in lithofacies model, and 0.35% in flow unit model.

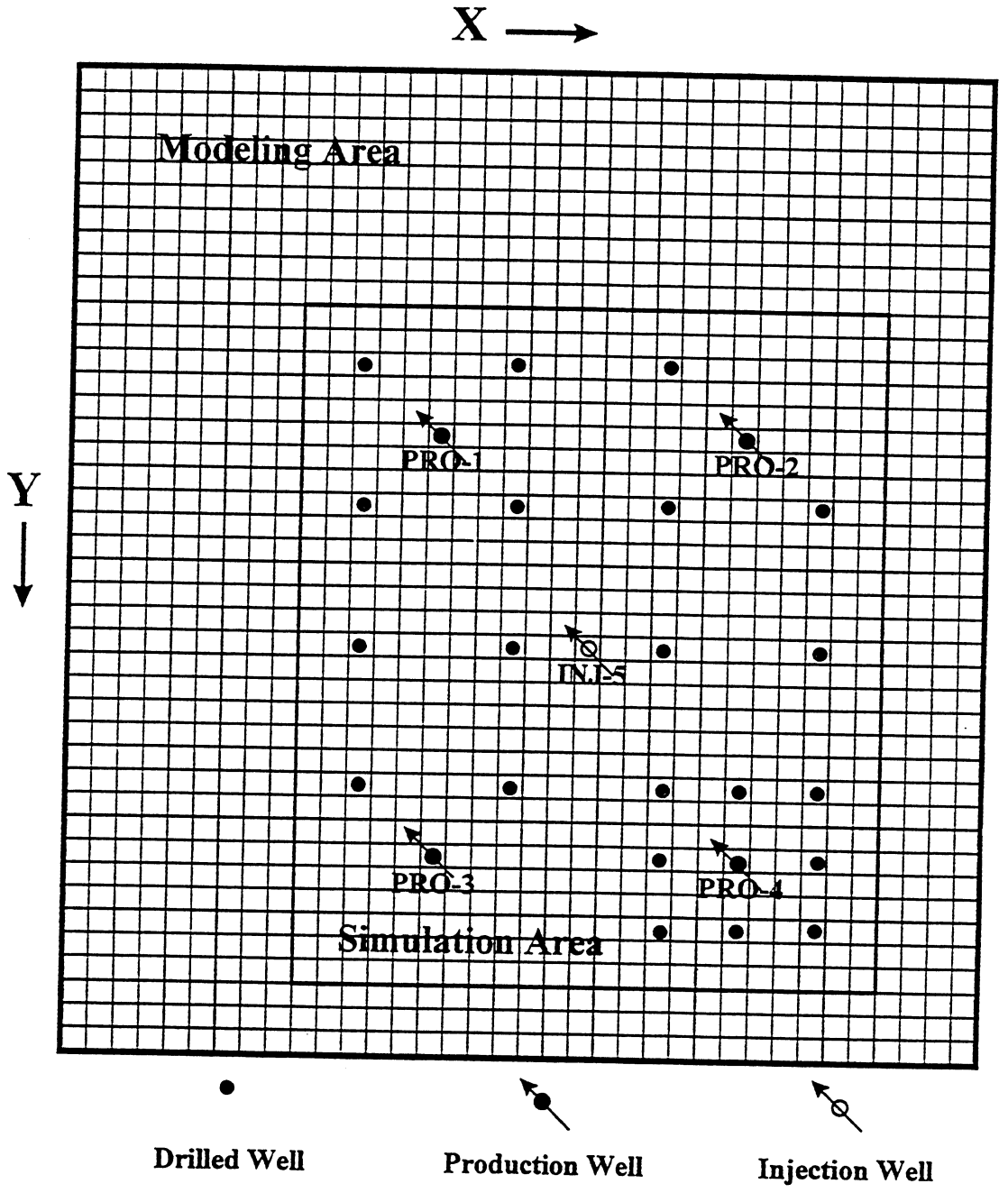

Fig. 5-1 Illustration of Geological Modeling and Simulation Area

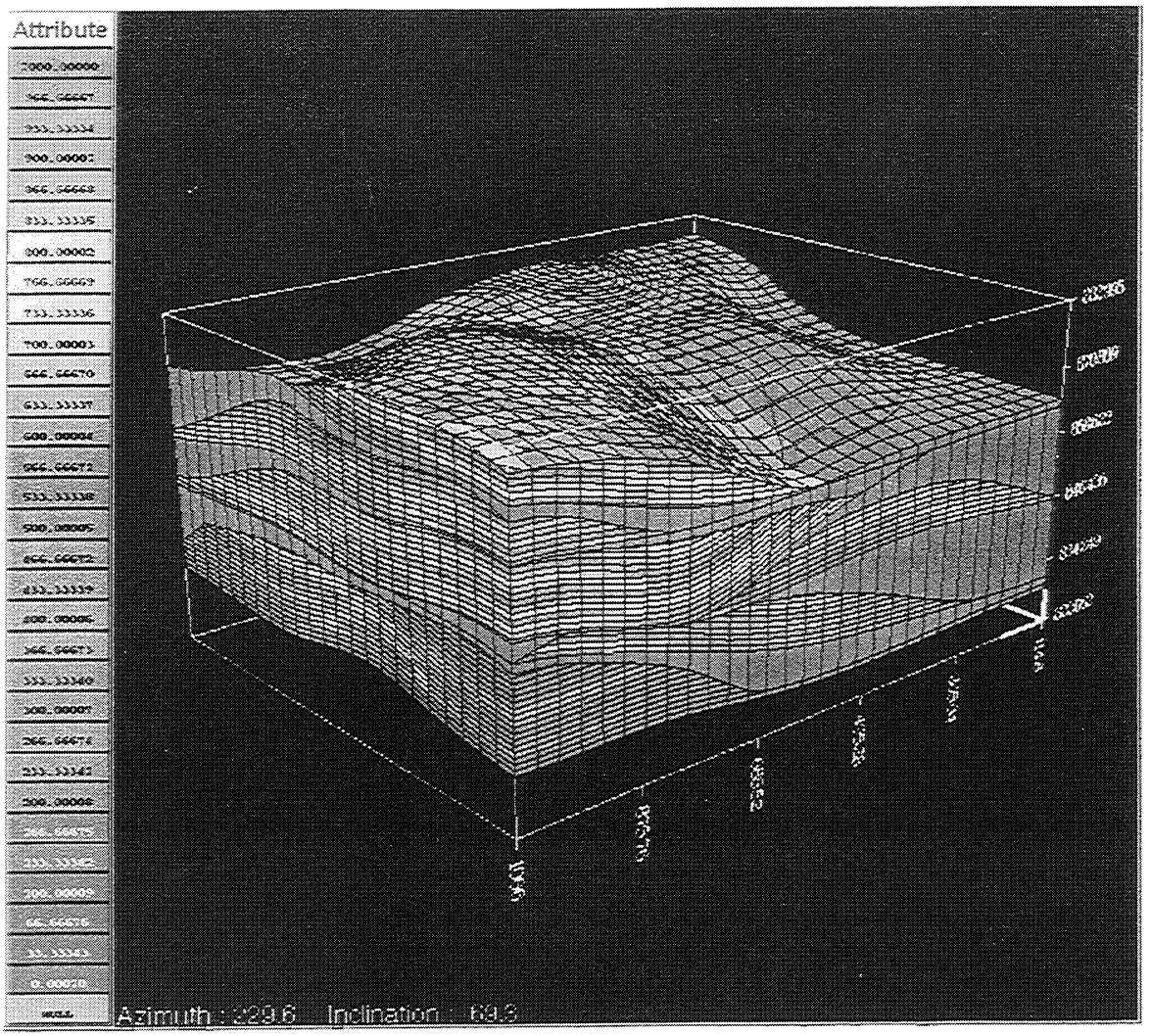

Fig. 5-2 3-D View of Permeability Distribution of Fine-Scale Channel Model

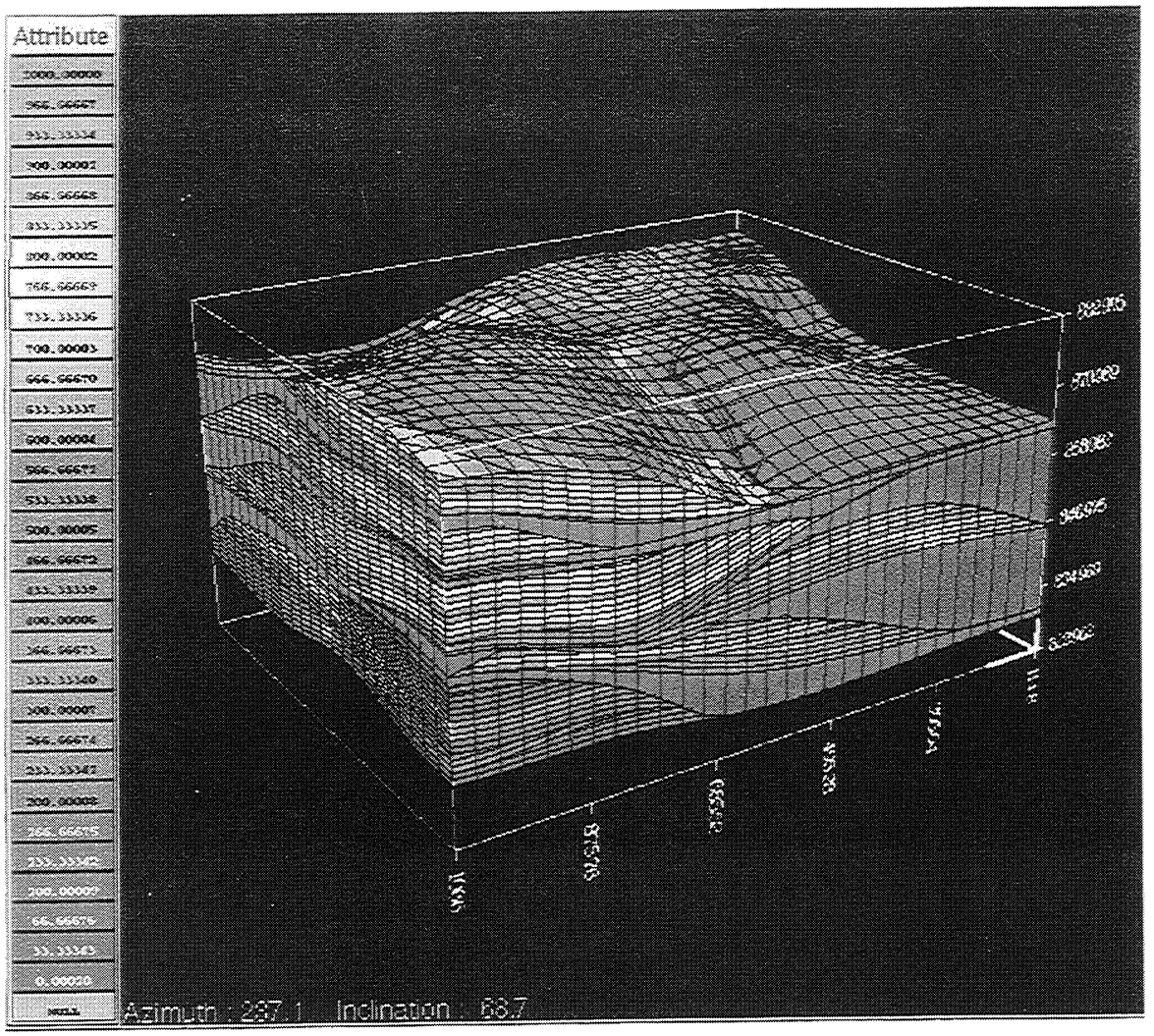

Fig. 5-3 3-D View of Permeability Distribution of Fine-Scale Lithofacies Model

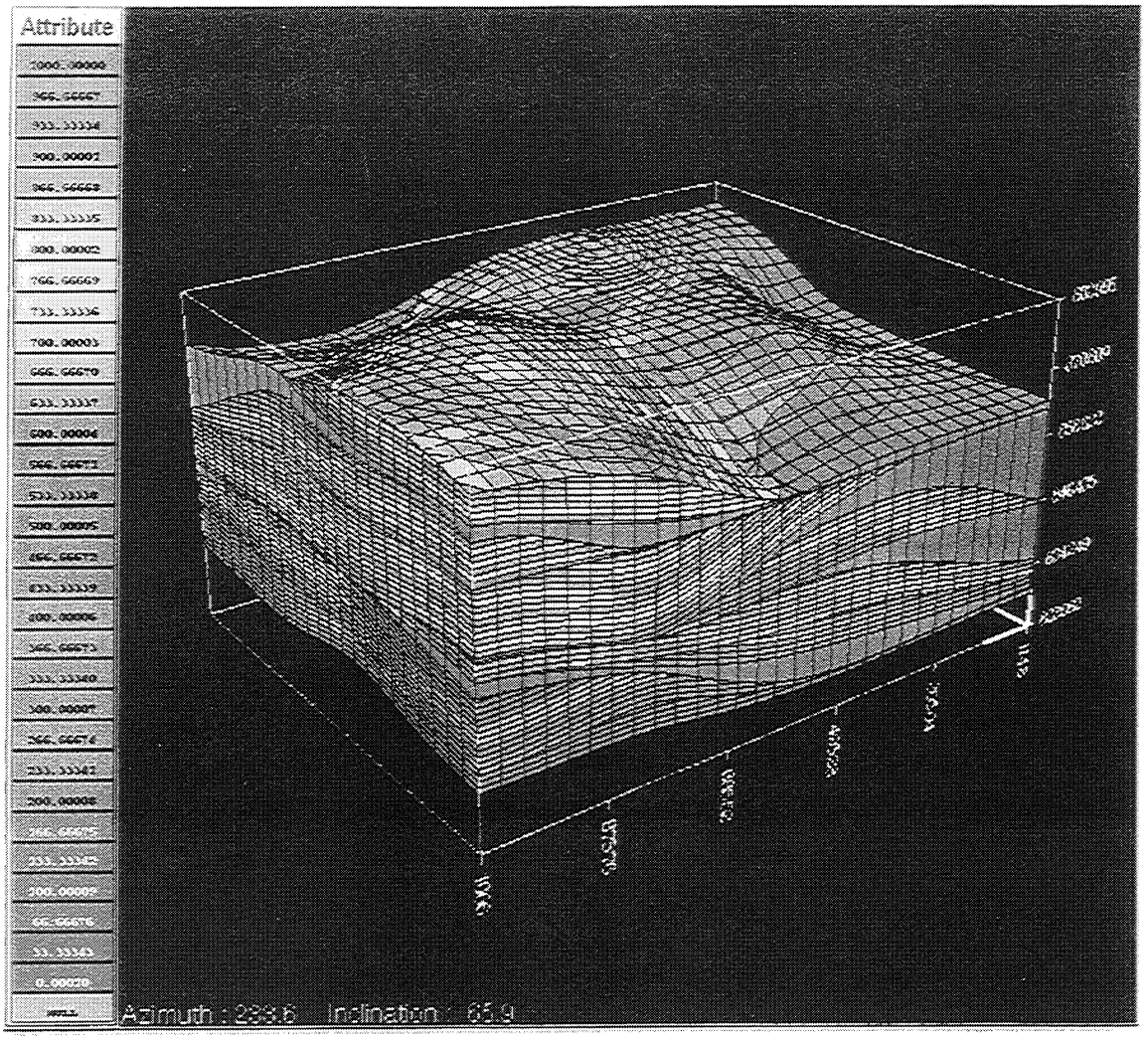

Fig. 5-4 3-D View of Permeability Distribution for Fine-Scale Flowunit Model

These errors were considered to be small enough to have negligible effect on the simulation results.

Simulation was run for 10 days of flow until a stabilized condition was obtained. As in model #1 and model #2, pressure and flowrate in three dimensions were produced in an output map file. Transmissibility, thickness, and pore volume were calculated using the program developed in Chapter IV. Because of the complex structure of the model, in fine-scale model, some layers present only in a few grid blocks. This could cause errors in the calculation of pore volume when 0.01 ft thickness was assumed for the pinch-out grid blocks. To reduce this error, layers that only occurred in a few grid blocks that had similar reservoir properties were combined to form one layer. The combination of these layers also served to reduce the computational time mainly because the memory of the available computer could not handle so many layers, especially in the lithofacies model. Table 5-1 is a summary of the three models.

Table 5-1 Summary of the Three Gypsy Models

Model	Channel	Lithofacies	Flowunit
Layers of Initial Fine-Scale Model	125	198	136
Layers of Combined Fine-Scale Model	98	107	87
Layers of Coarse-Scale Model (1)	13	28	16
Layers of Coarse-Scale Model (2)	13	13	13
Actual Pore Volume of the Model(MRB)	1001.50	906.78	967.24
Pore Volume with Pinch-out Thin Layers (MRB)	1005.37	911.57	970.63
Error Caused by Thin Layers (%)	0.39	0.53	0.35

5.2 Scale-up of the Three Gypsy Models

To be comparable for the scale-up results, three models were all scaled up to 13-layer coarse-scale channel model. To study the effects of layering on scale-up, lithofacies model and flowunit model were also scaled up to 28-layer and 16-layer coarse-scale models. Scale-up were first conducted without PI scale-up using 10 as an input for the well injectivity index in all five wells for both fine-scale models and coarse-scale model. PI scale-up was then conducted. Table 5-2 shows the scaled productivity indices used for the three models. Figs. 5-5 to 5-58 illustrate the scale-up results for the three models, including the results with and without PI scale-up.

Table 5-2 Scaled Productivity Index for the Three Gypsy Models

Well	PI Channel Model	PI Lithofacies Model	PI Flowunit Model
PRO-1	272.70	229.32	346.89
PRO-2	339.15	260.23	296.18
PRO-3	124.02	123.46	151.12
PRO-4	264.17	322.05	333.19
INJ-5	190.36	189.38	181.84

The characteristics of the simulation results for the three geological models can be summarized as follows:

1. Due to the limited volume of the reservoir and its high permeability, equilibrium condition for production and injection was obtained in only five days.
2. Production initially experienced depletion process for the first 2 to 3 days and then went through a process of displacement, in which total water production rate for the reservoir was equal to the water injection rate.
3. Without PI scale-up, both production rate and pressure are significantly different between fine scale and coarse scale at the beginning. Production rate tends to matched after three days. Pressure stabilized at a constant pressure difference after about ten day's production period.
4. After considering PI scale-up, satisfactory matches were obtained between fine scale and coarse scale for both water production and pressure. At the resolution of the plots, the difference between fine scale and coarse scale for scale-up with PI scale-up is not apparent. In fact, there exist small differences in the set of results. The differences will be discussed in next section using relative errors.

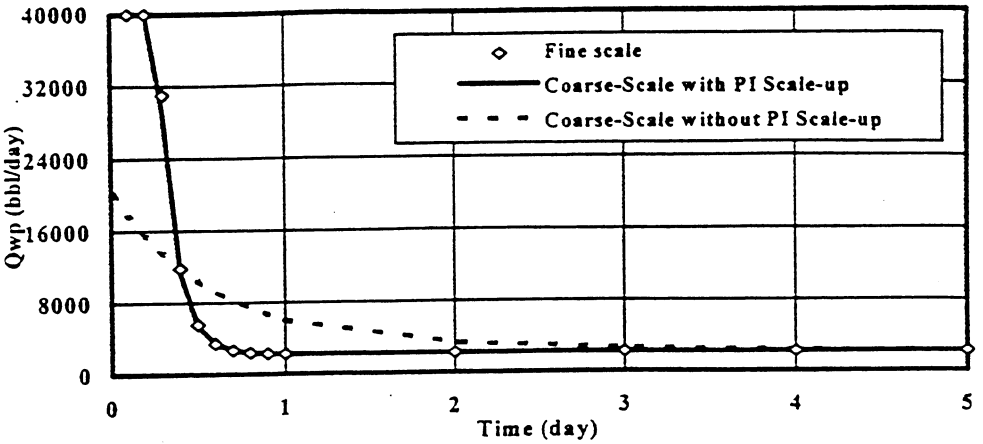

Fig. 5-5 Water Production Rate of Channel Model

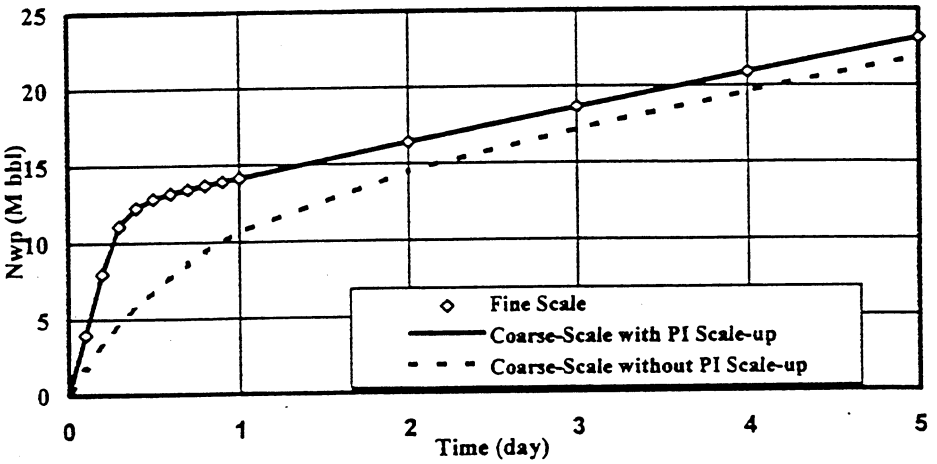

Fig. 5-6 Cum. Water Production of Channel Model

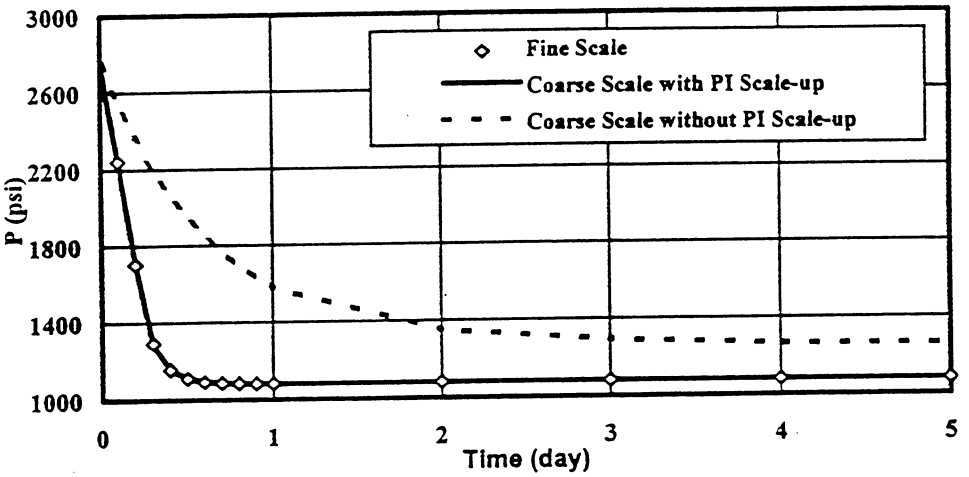

Fig. 5-7 Average Reservoir Pressure of Channel Model

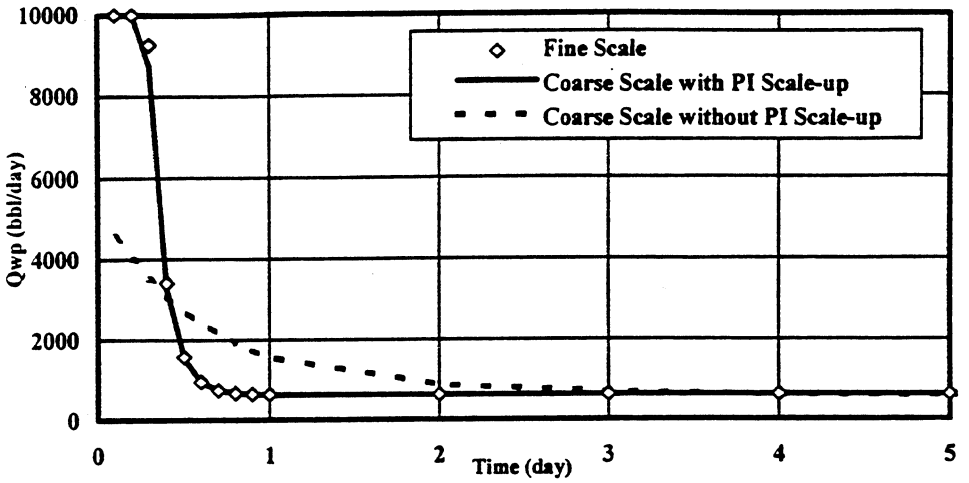

Fig. 5-8 Water Production Rate for Well #1 of Channel Model

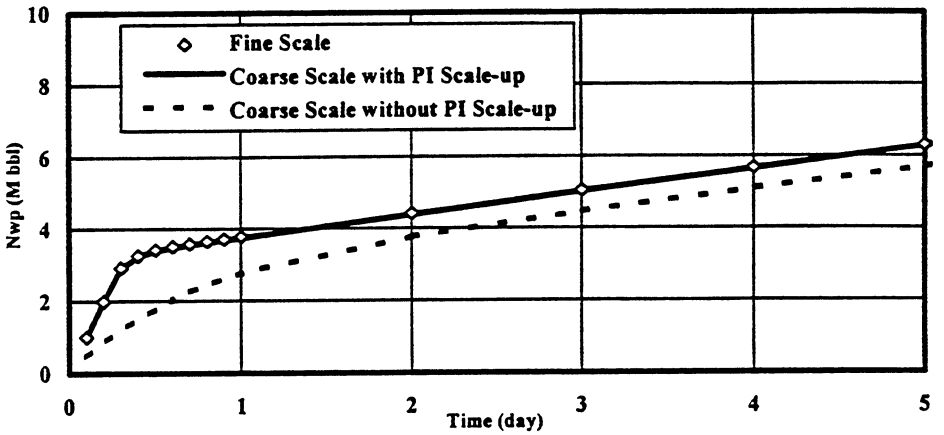

Fig. 5-9 Cum. Water Production for Well #1 of Channel Model

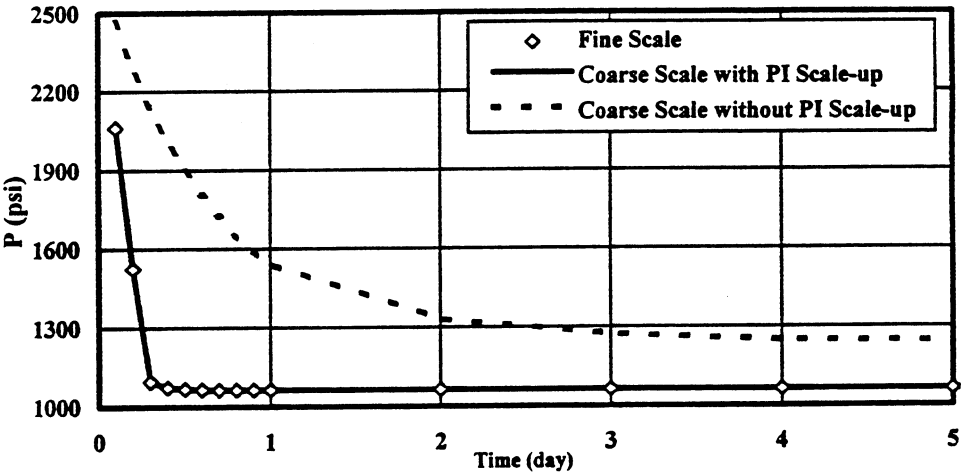

Fig. 5-10 Well Block Pressure for Well #1 of Channel Model

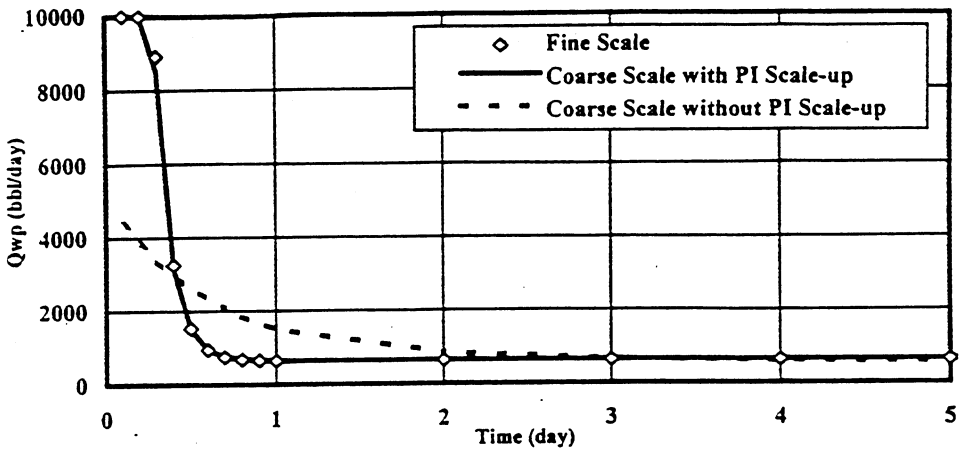

Fig. 5-11 Water Production Rate for Well #2 of Channel Model

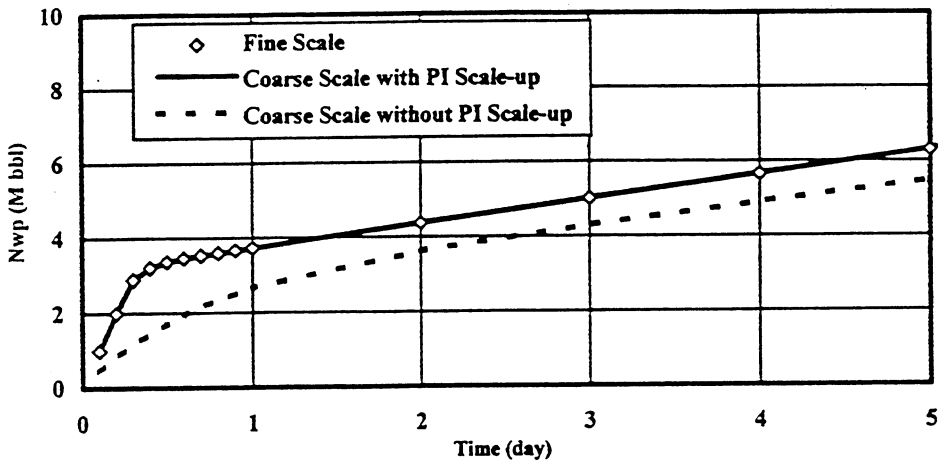

Fig. 5-12 Cum. Water Production for Well #2 of Channel Model

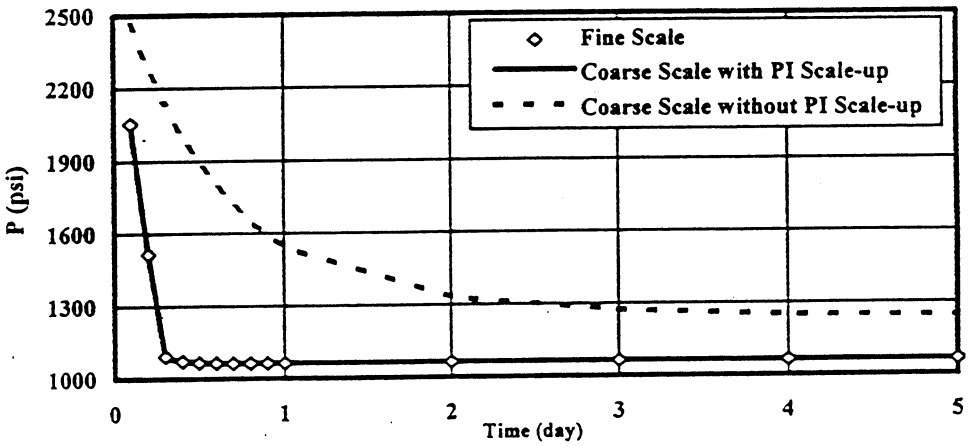

Fig. 5-13 Well Block Pressure for Well #2 of Channel Model

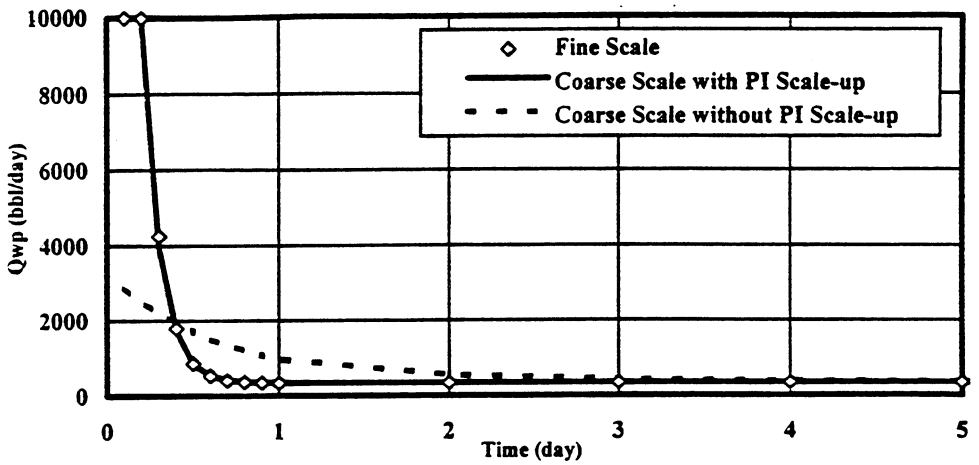

Fig. 5-14 Water Production Rate for Well #3 of Channel Model

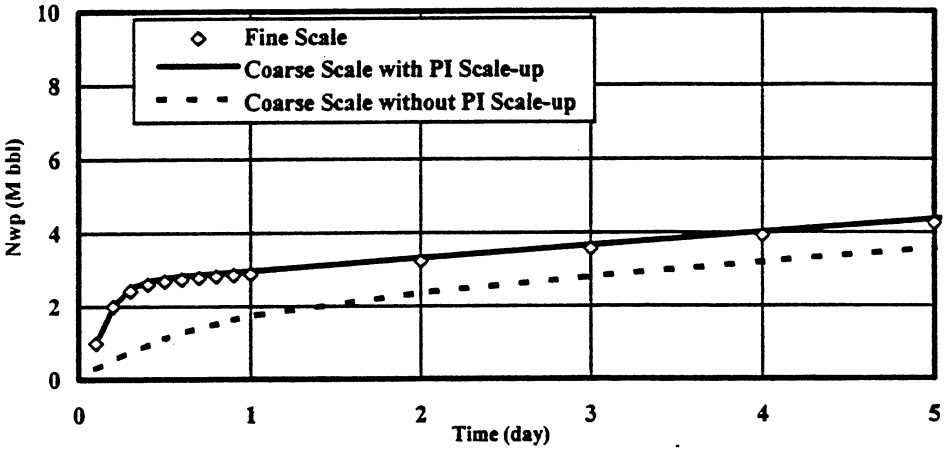

Fig. 5-15 Cum. Water Production for Well #3 of Channel Model

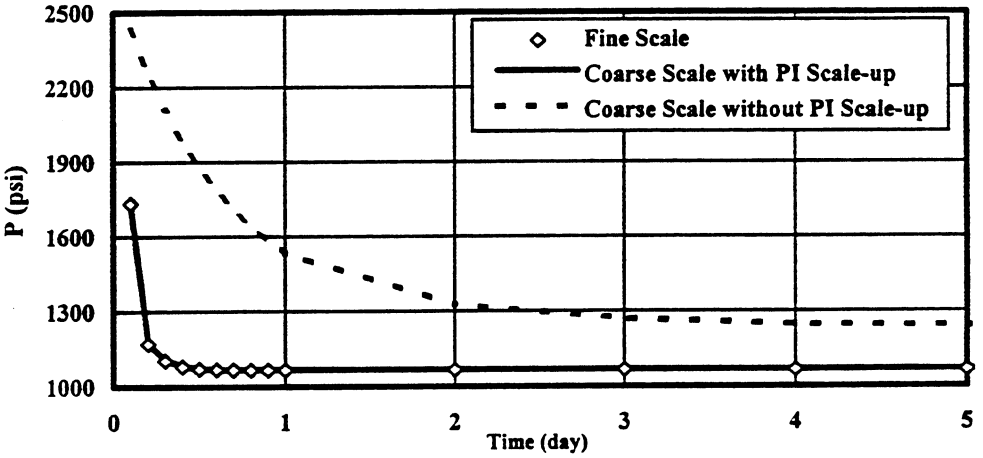

Fig. 5-16 Well Block Pressure for Well #3 of Channel Model

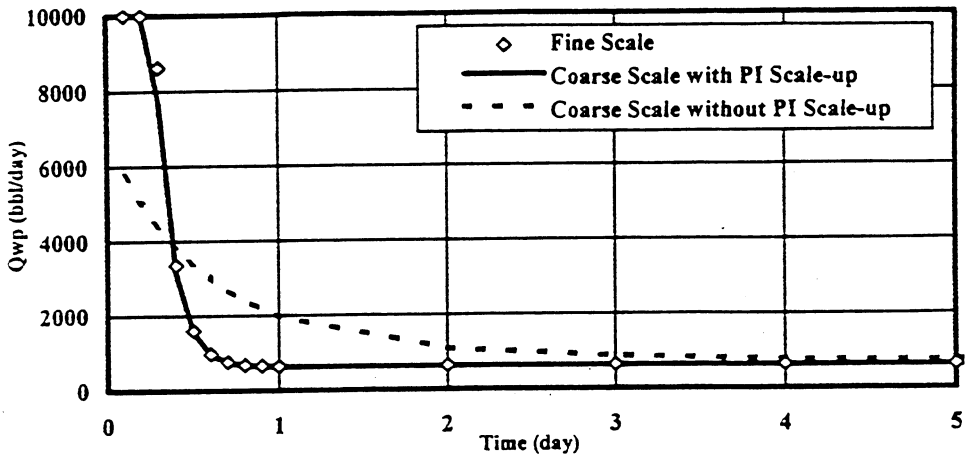

Fig. 5-17 Water Production Rate for Well #4 of Channel Model

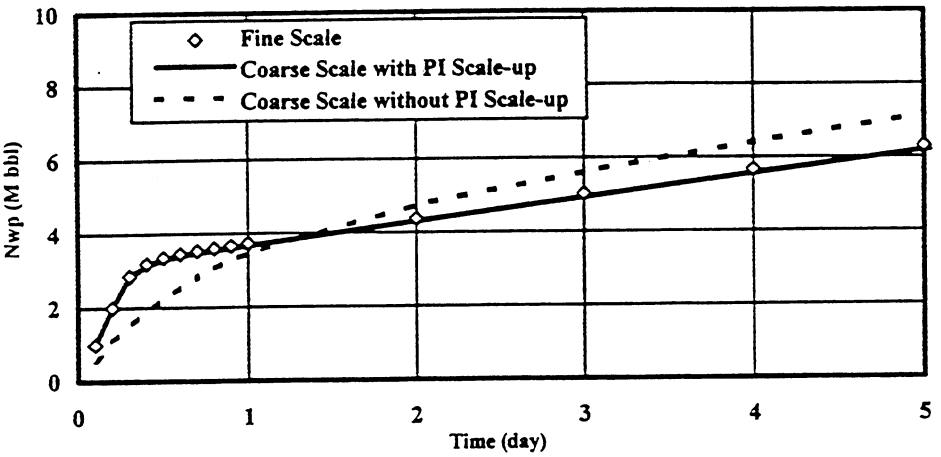

Fig. 5-18 Cum. Water Production for Well #4 of Channel Model

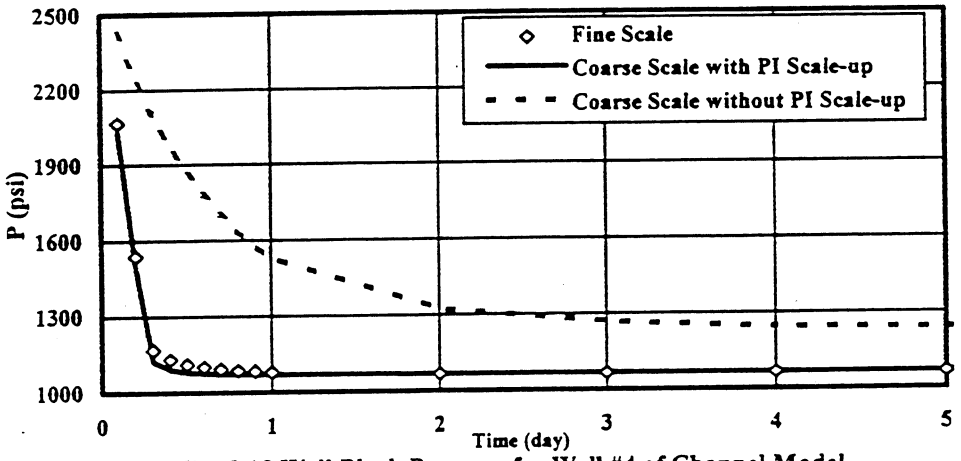

Fig. 5-19 Well Block Pressure for Well #4 of Channel Model

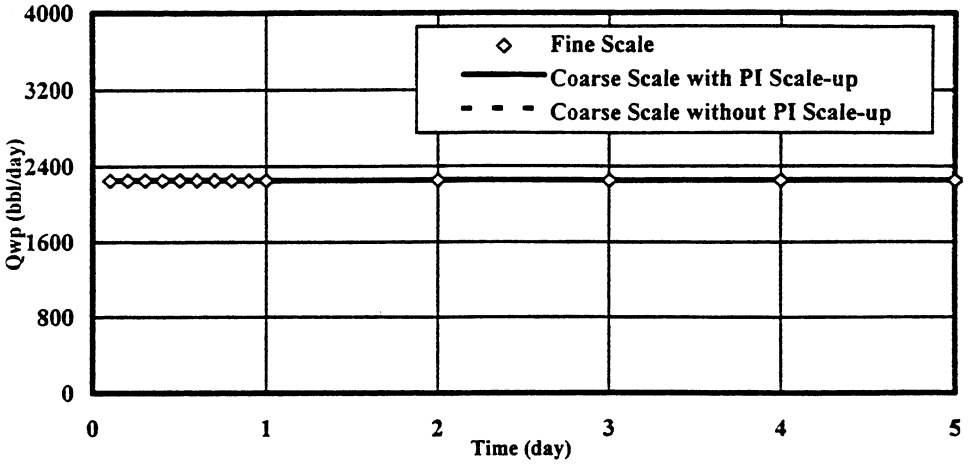

Fig. 5-20 Water Injection Rate for Well #5 of Channel Model

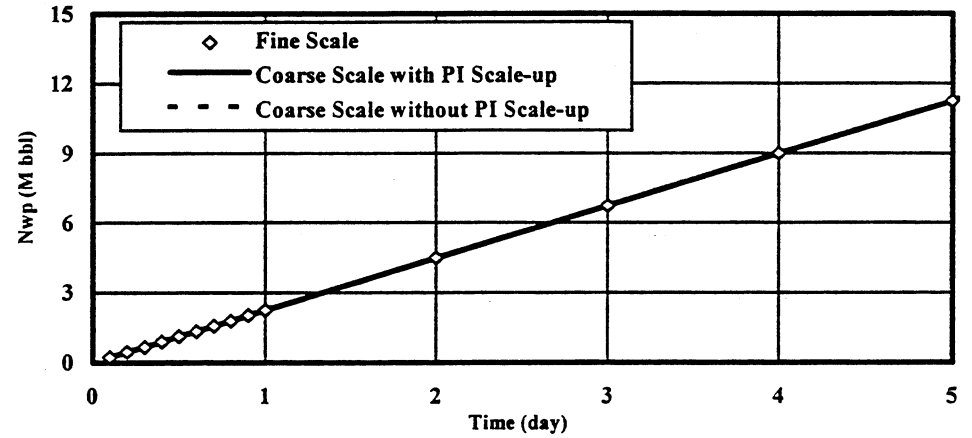

Fig. 5-21 Cum. Water Injection for Well #5 of Channel Model

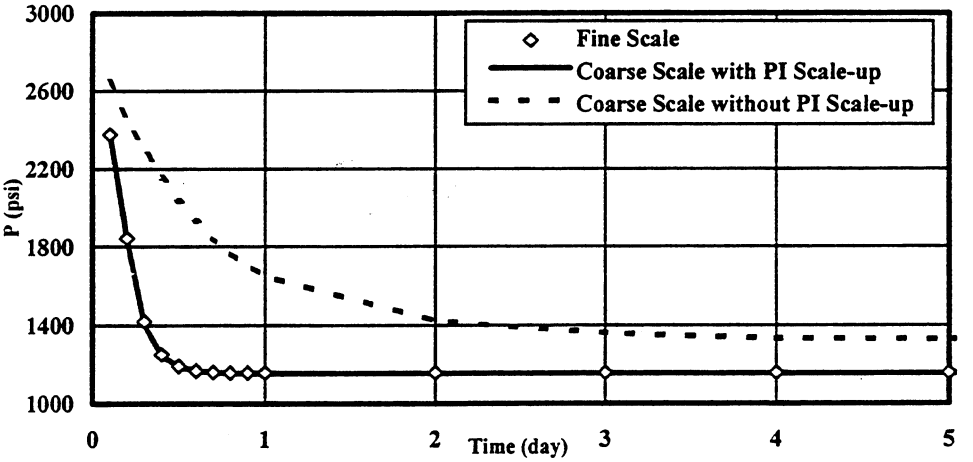

Fig. 5-22 Well Block Pressure for Well #5 of Channel Model

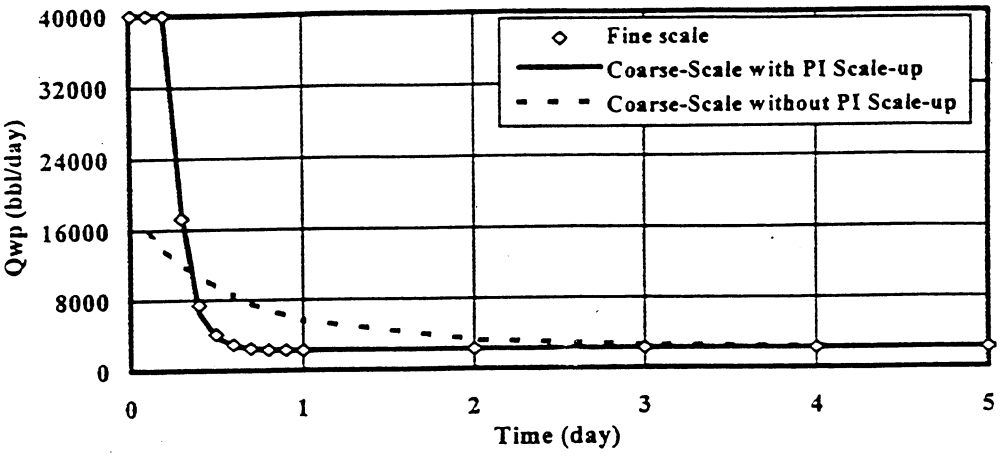

Fig. 5-23 Water Production Rate of Lithofacies Model

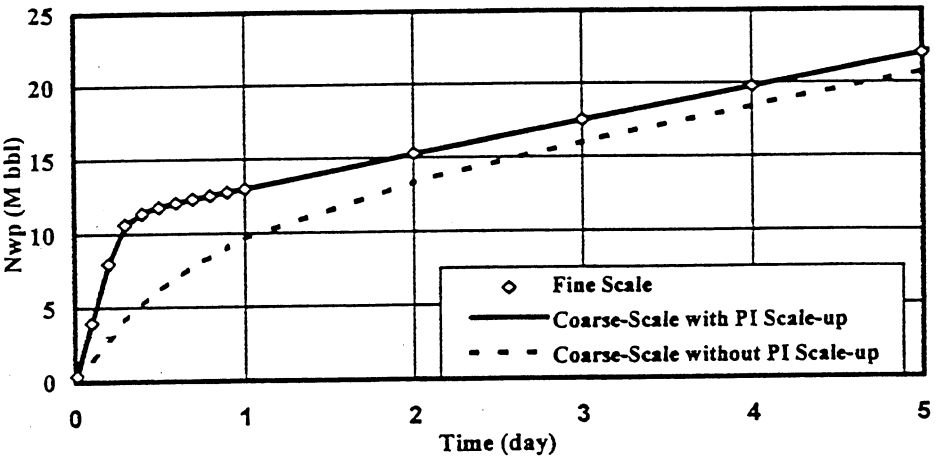

Fig. 5-24 Cum. Water Production of Lithofacies Model

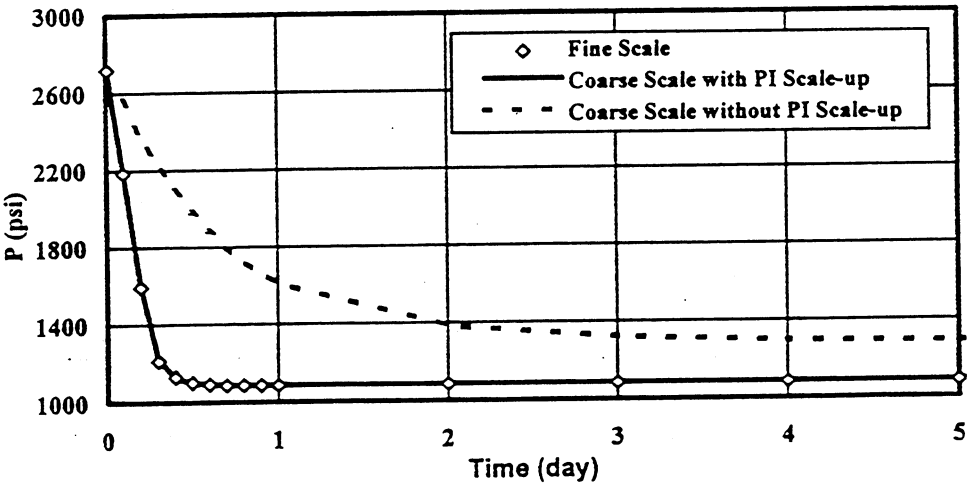

Fig. 5-25 Average Reservoir Pressure of Lithofacies Model

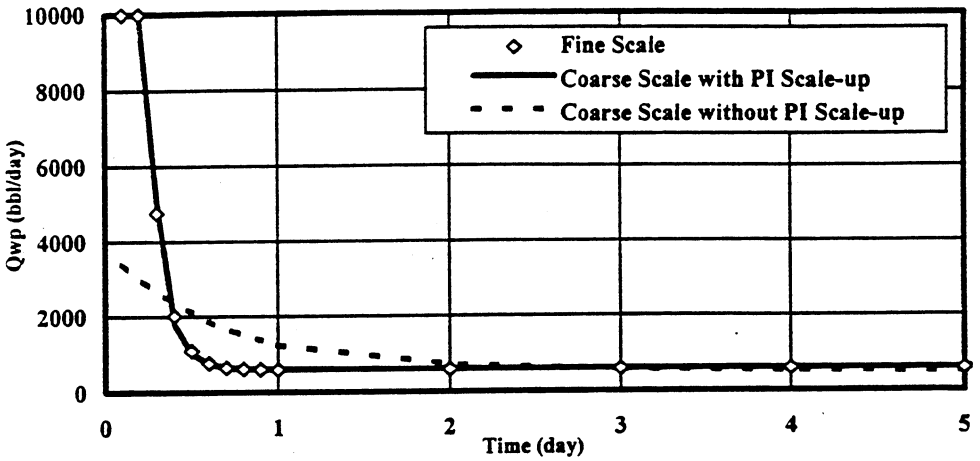

Fig. 5-26 Water Production Rate for Well #1 of Lithofacies Model

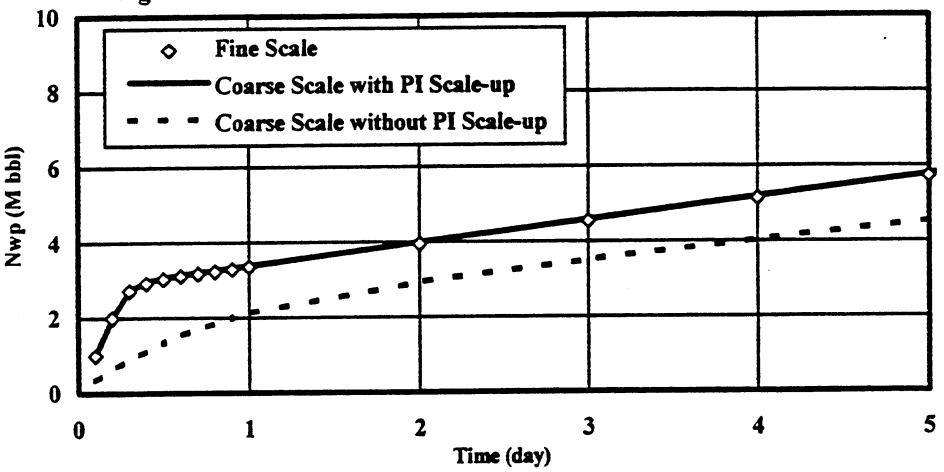

Fig. 5-27 Cum. Water Production for Well #1 of Lithofacies Model

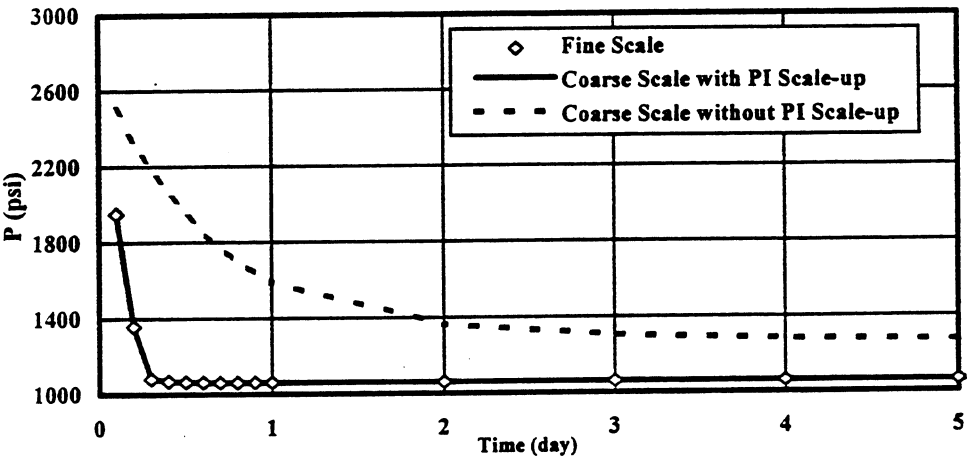

Fig. 5-28 Well Block Pressure for Well #1 of Lithofacies Model

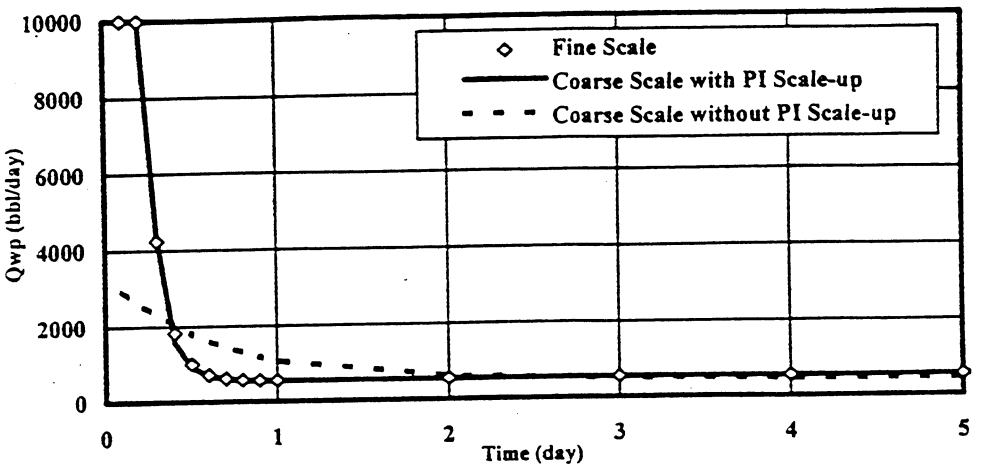

Fig. 5-29 Water Production Rate for Well #2 of Lithofacies Model

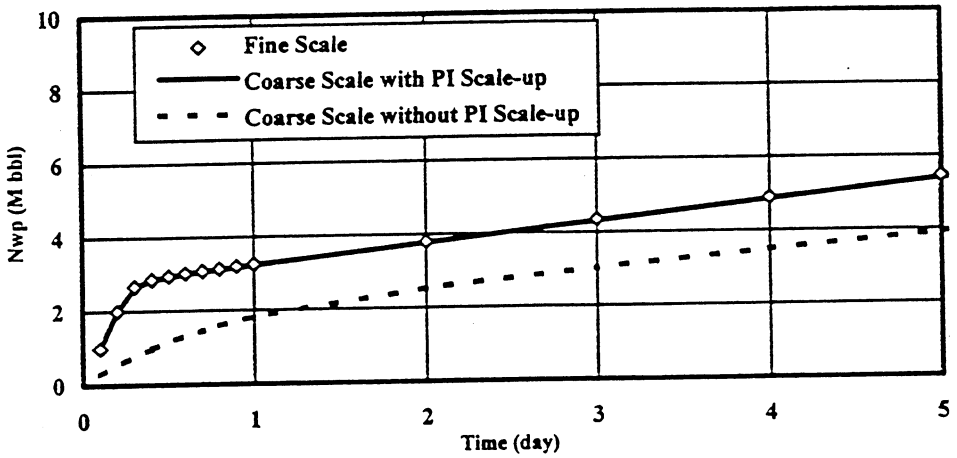

Fig. 5-30 Cum. Water Production for Well #2 of Lithofacies Model

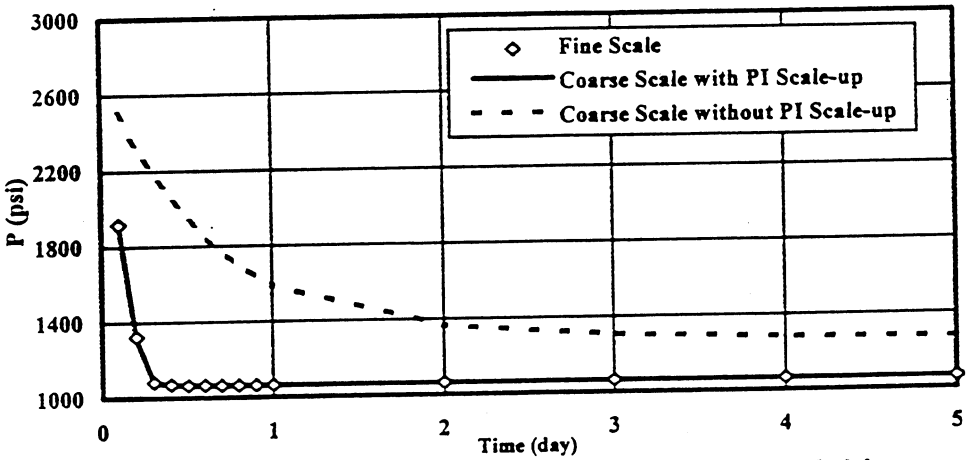

Fig. 5-31 Well Block Pressure for Well #2 of Lithofacies Model

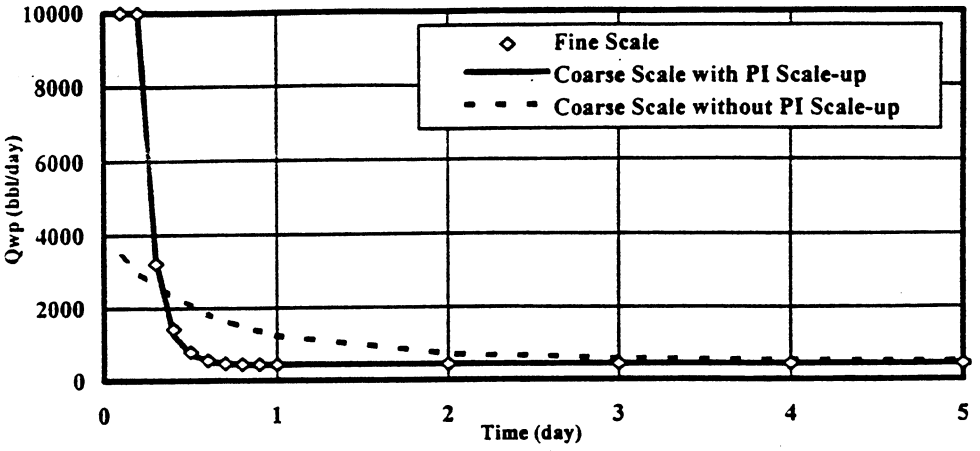

Fig. 5-32 Water Production Rate for Well #3 of Lithofacies Model

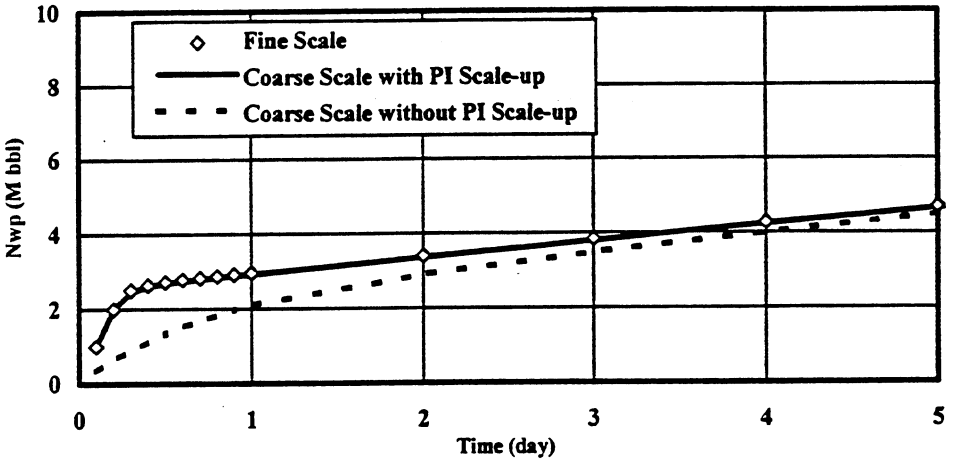

Fig. 5-33 Cum. Water Production for Well #3 of Lithofacies Model

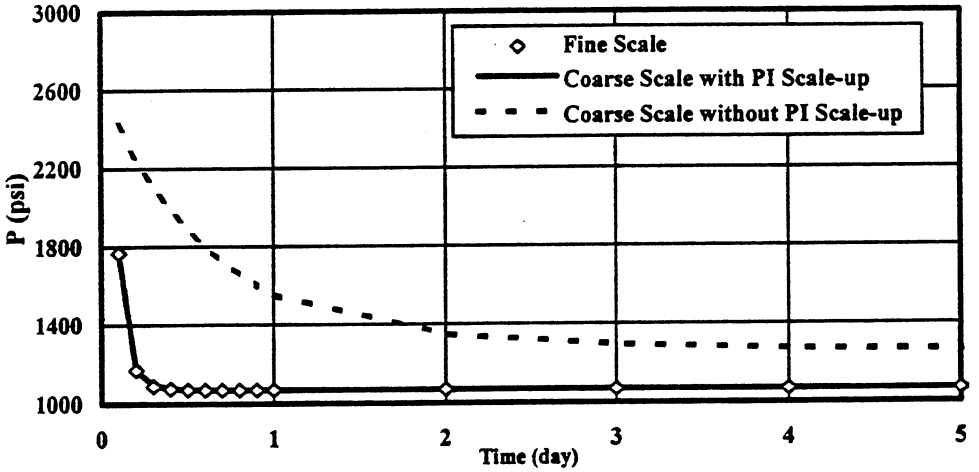

Fig. 5-34 Well Block Pressure for Well #3 of Lithofacies Model

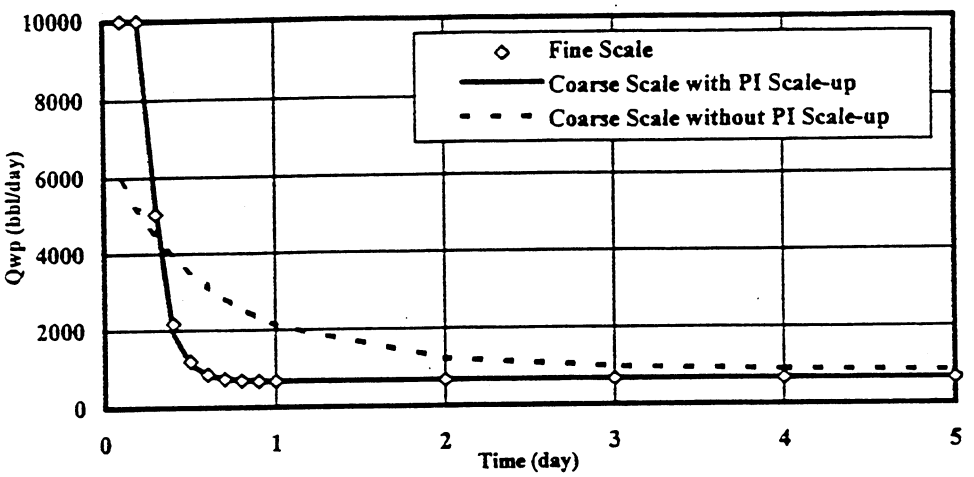

Fig. 5-35 Water Production Rate for Well #4 of Lithofacies Model

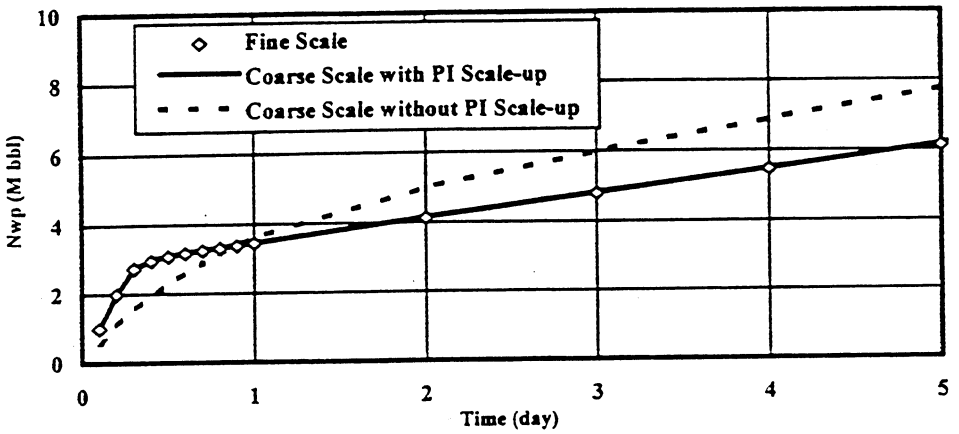

Fig. 5-36 Cum. Water Production for Well #4 of Lithofacies Model

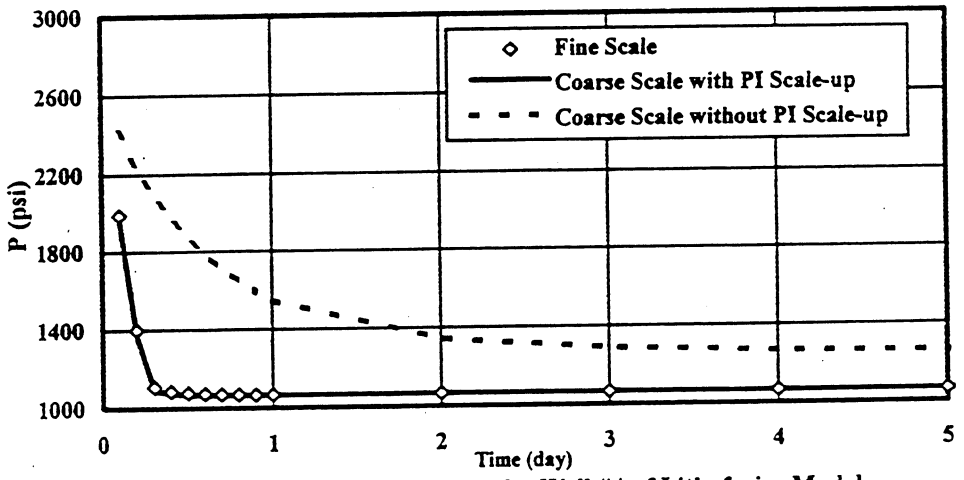

Fig. 5-37 Well Block Pressure for Well #4 of Lithofacies Model

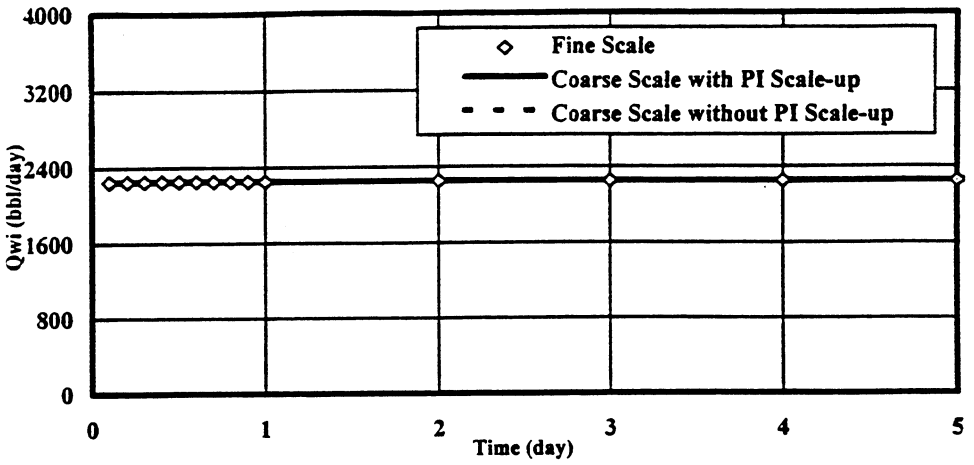

Fig. 5-38 Water Injection Rate for Well #5 of Lithofacies Model

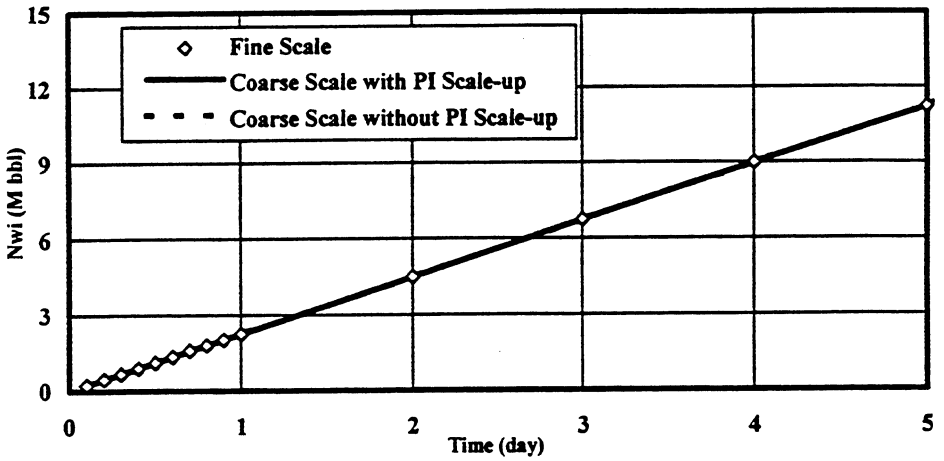

Fig. 5-39 Cum. Water Injection for Well #5 of Lithofacies Model

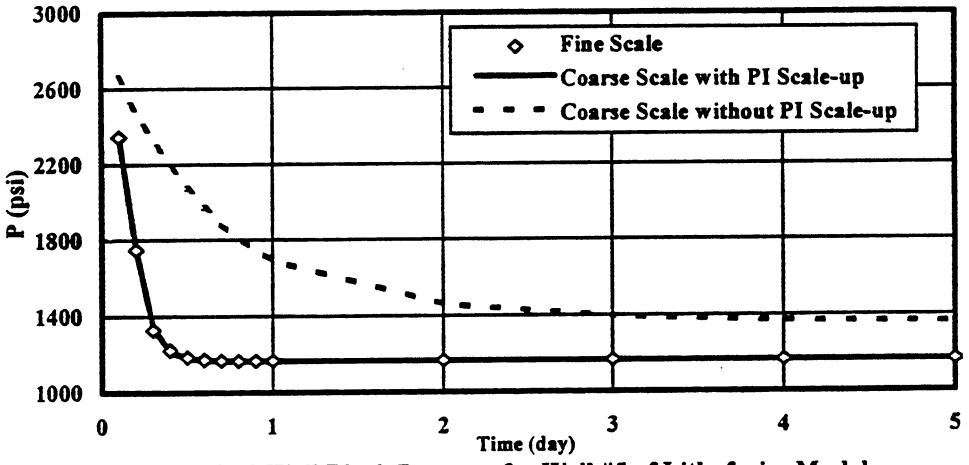

Fig. 5-40 Well Block Pressure for Well #5 of Lithofacies Model

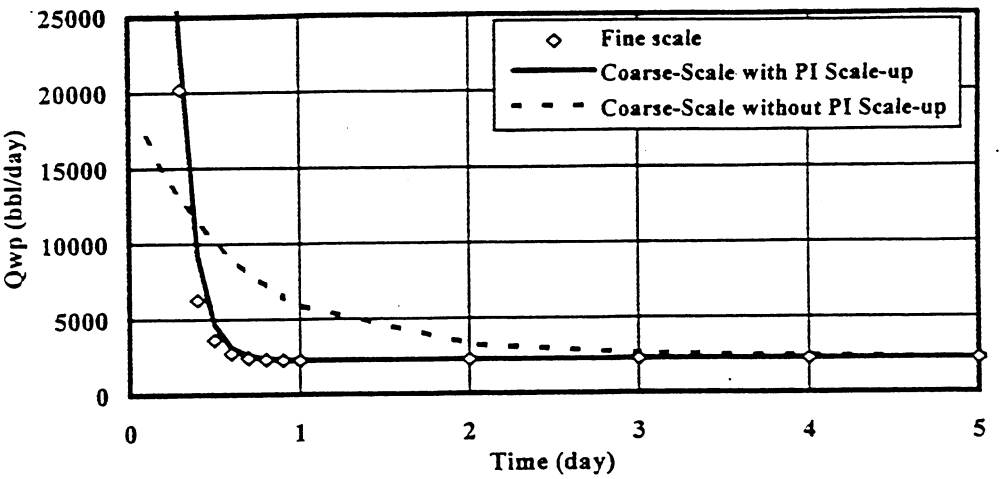

Fig. 5-41 Water Production Rate of Flow Unit Model

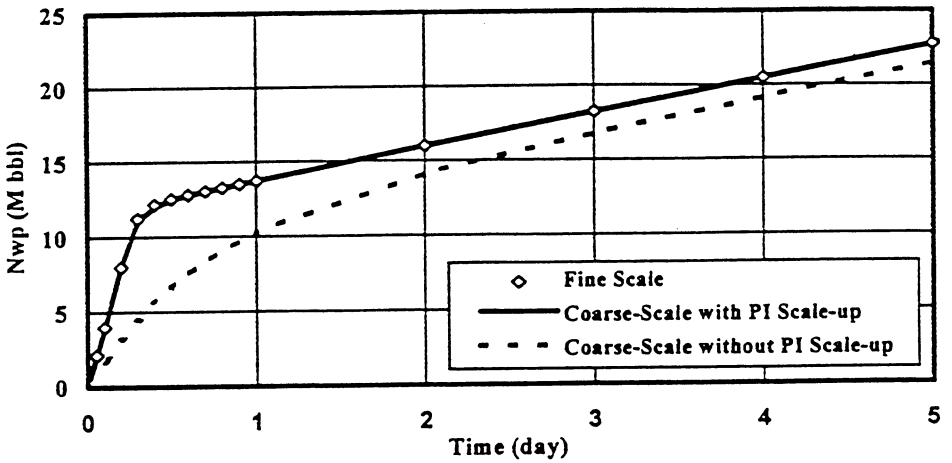

Fig. 5-42 Cum. Water Production of Flow Unit Model

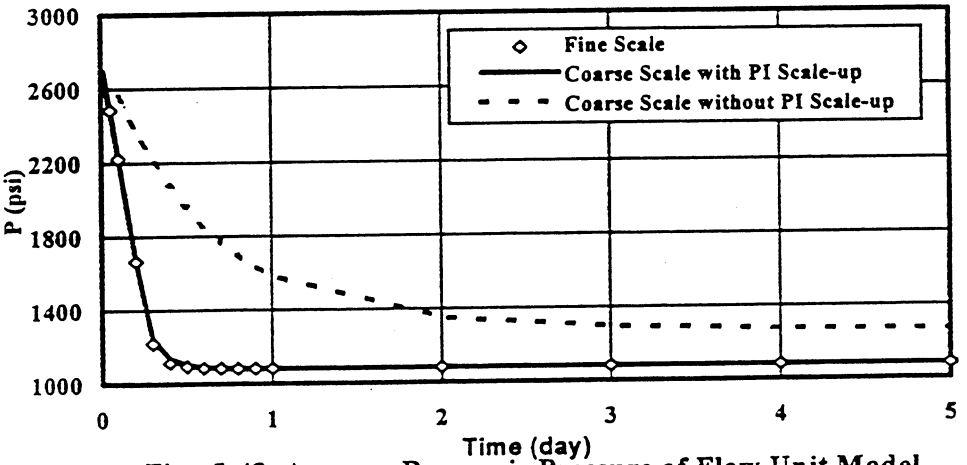

Fig. 5-43 Average Reservoir Pressure of Flow Unit Model

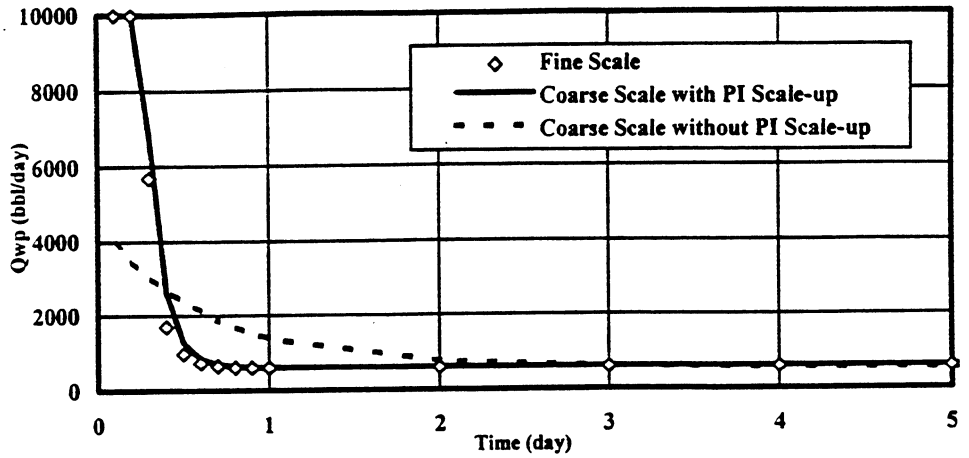

Fig. 5-44 Water Production Rate for Well #1 of Flow Unit Model

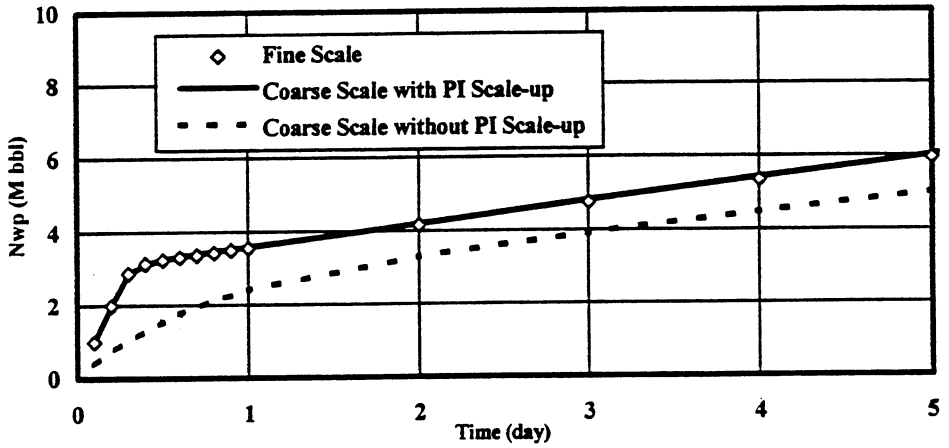

Fig. 45 Cum. Water Production for Well #1 of Flow Unit Model

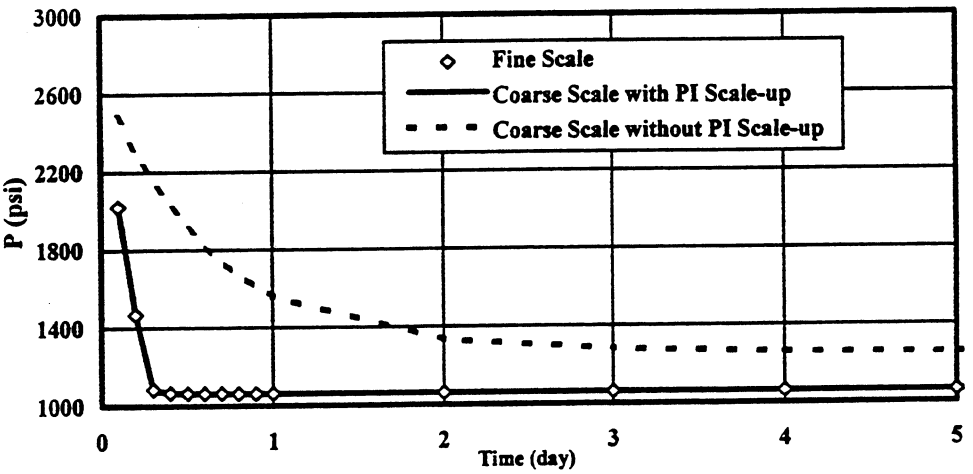

Fig. 5-46 Well Block Pressure for Well #1 of Flow Unit Model

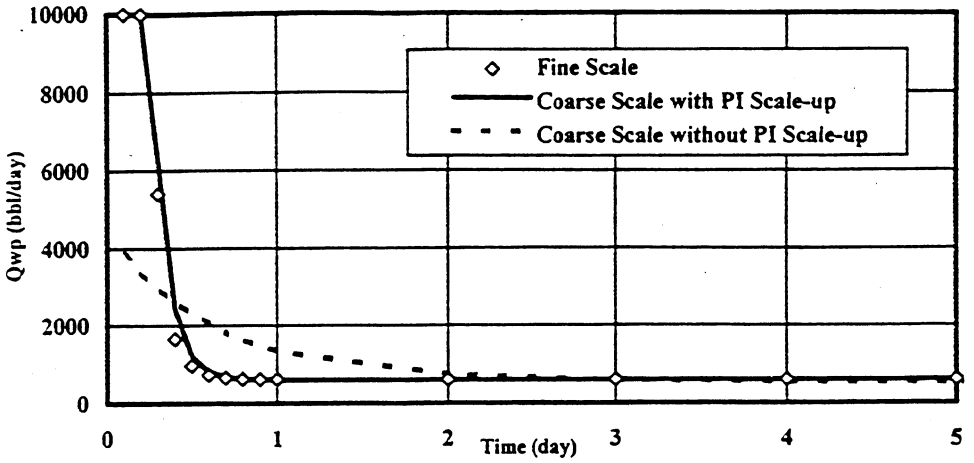

Fig. 5-47 Water Production Rate for Well #2 of Flow Unit Model

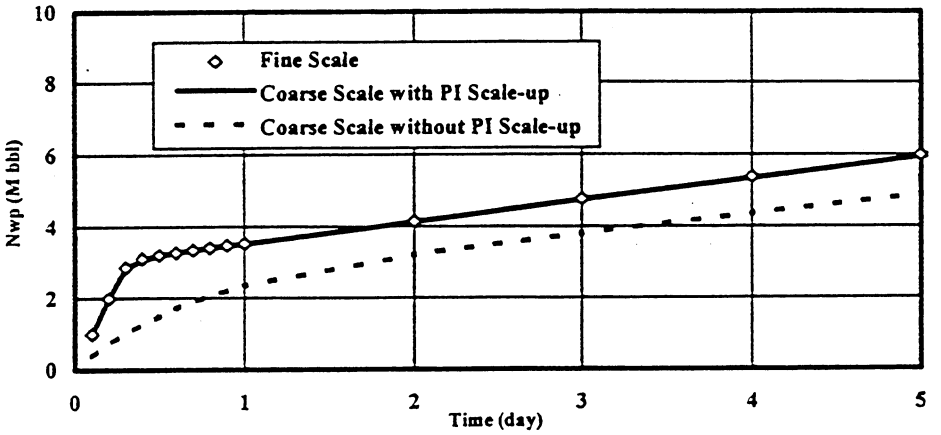

Fig. 5-48 Cum. Water Production for Well #2 of Flow Unit Model

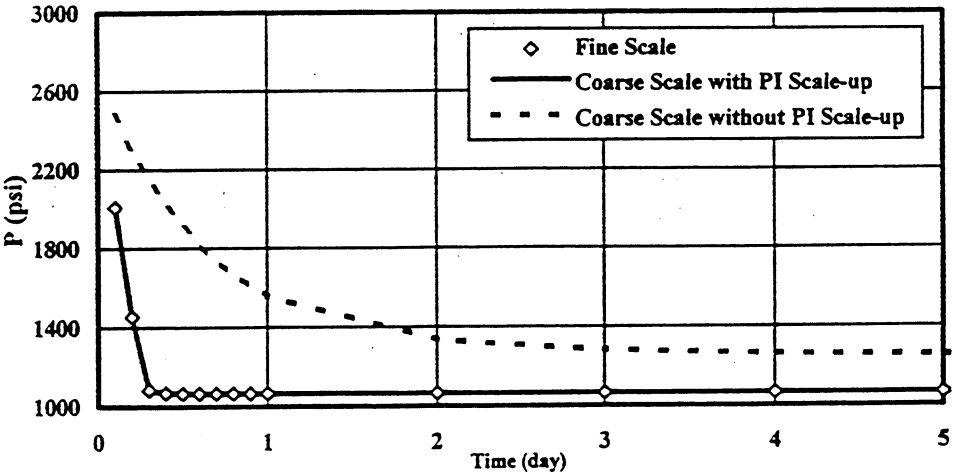

Fig. 5-49 Well Block Pressure for Well #2 of Flow Unit Model

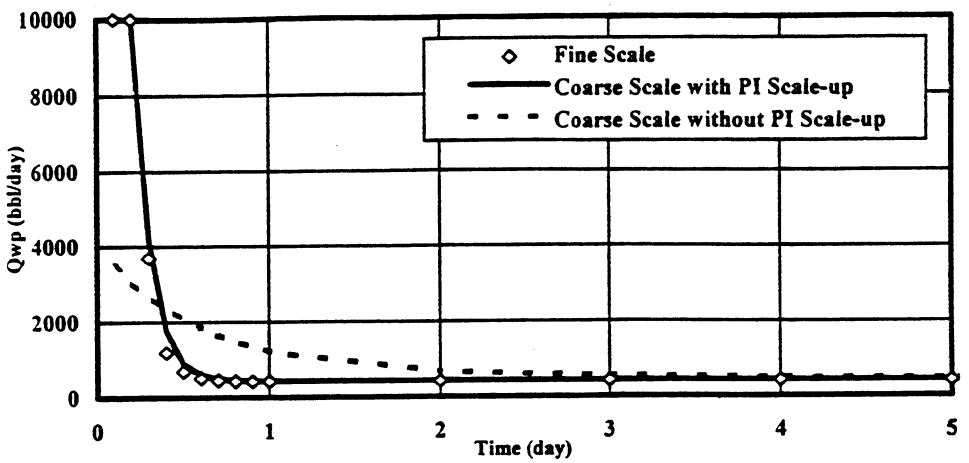

Fig. 5-50 Water Production Rate for Well #3 of Flow Unit Model

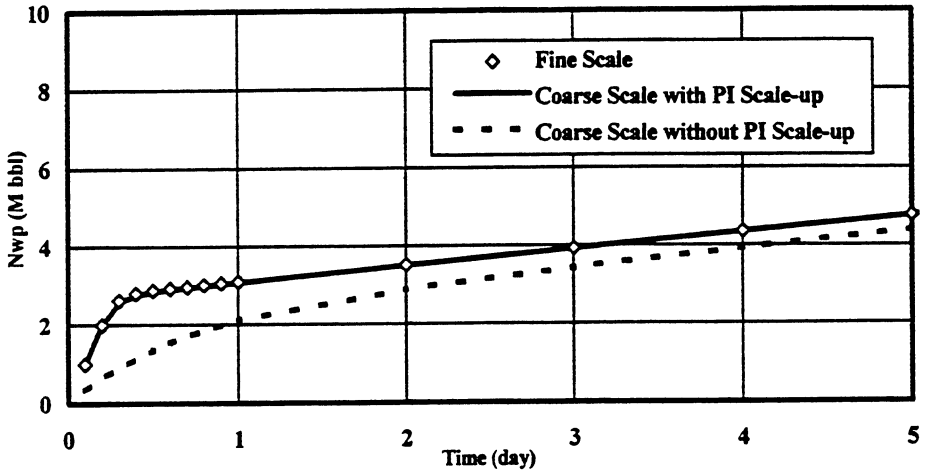

Fig. 5-51 Cum. Water Production for Well #3 of Flow Unit Model

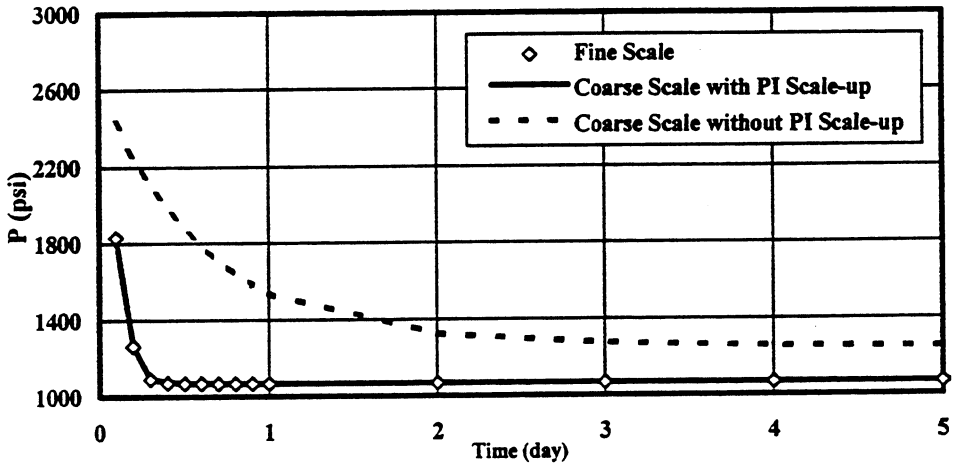

Fig. 5-52 Well Block Pressure for Well #3 of Flow Unit Model

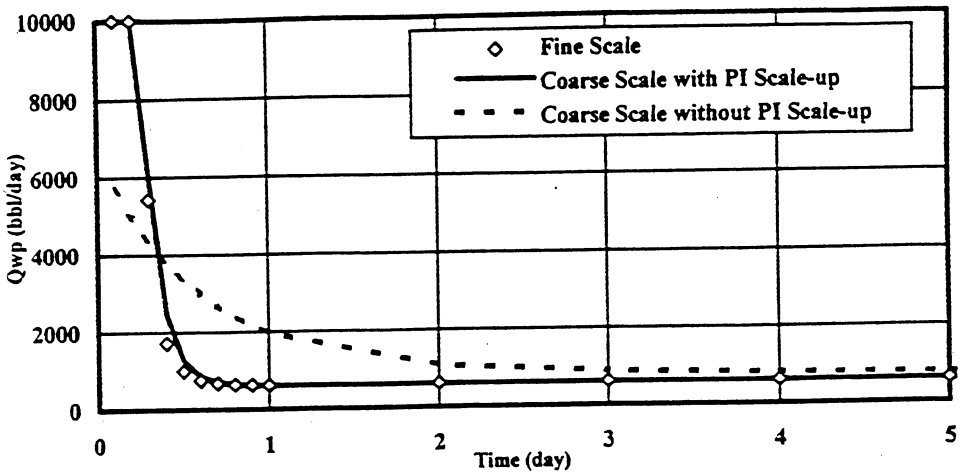

Fig. 5-53 Water Production Rate for Well #4 of Flow Unit Model

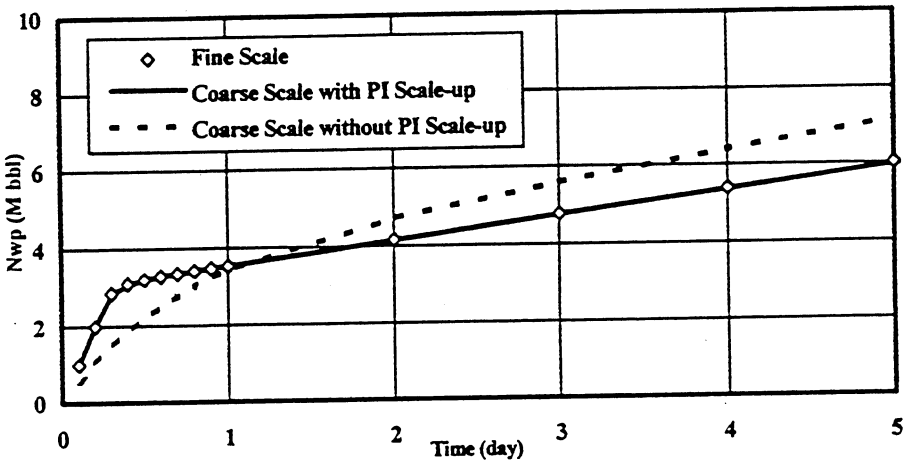

Fig. 5-54 Cum. Water Production for Well #4 of Flow Unit Model

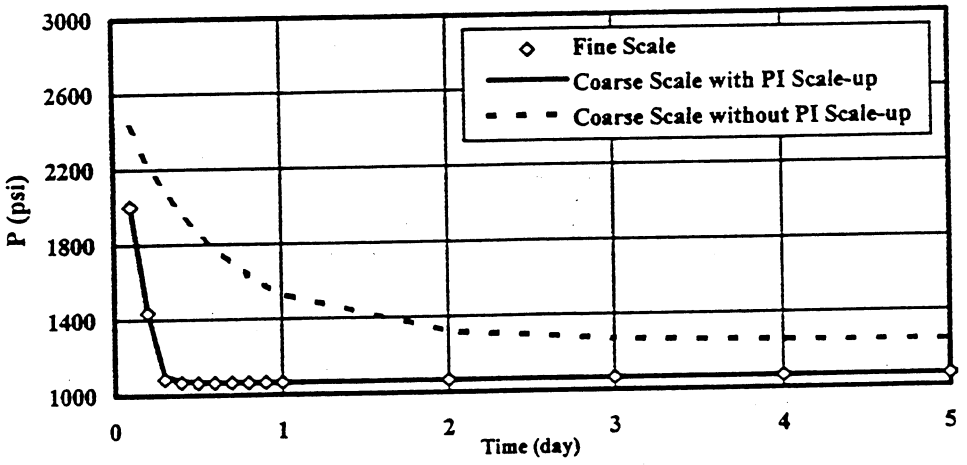

Fig. 5-55 Well Block Pressure for Well #4 of Flow Unit Model

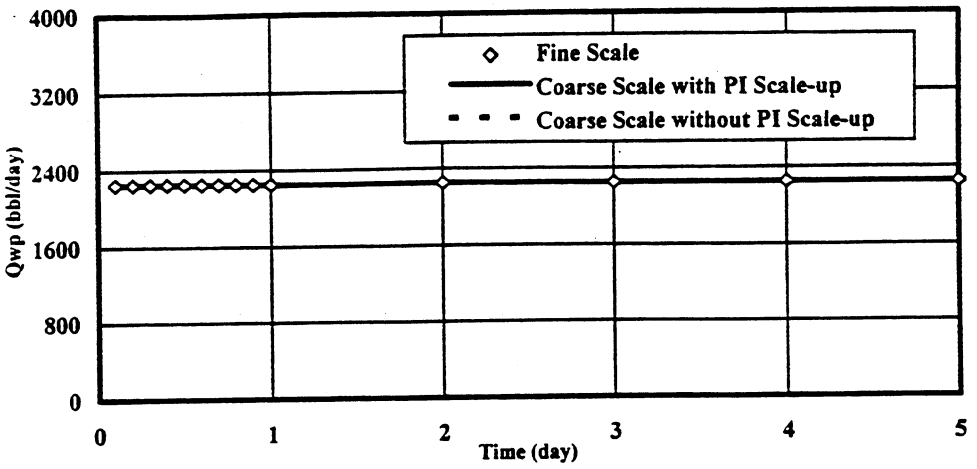

Fig. 5-56 Water Injection Rate for Well #5 of Flow Unit Model

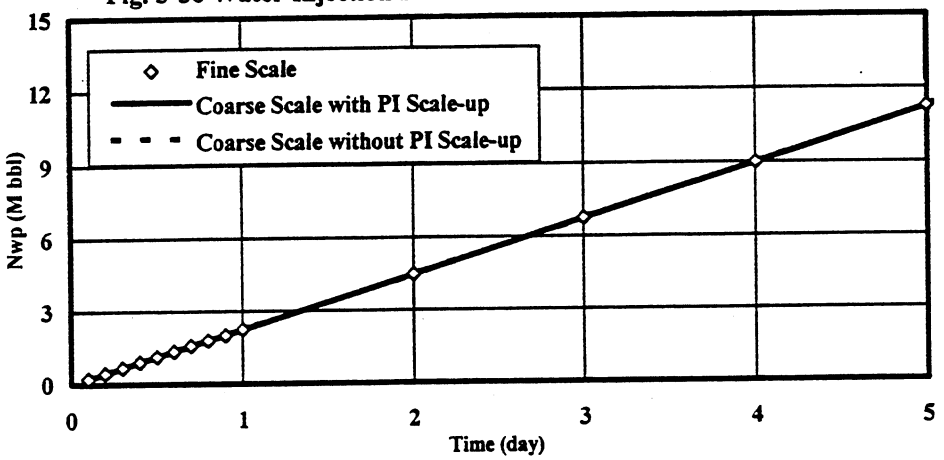

Fig. 5-57 Cum. Water Injection for Well #5 of Flow Unit Model

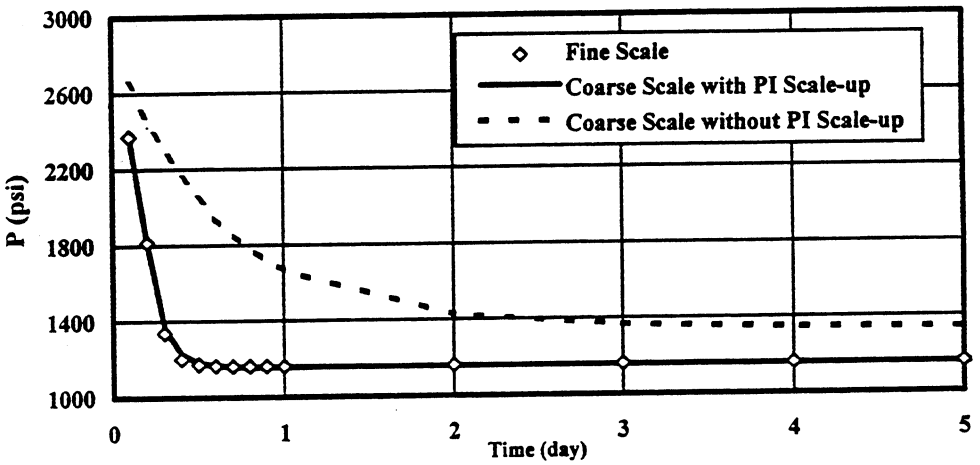

Fig. 5-58 Well Block Pressure for Well #5 of Flow Unit Model

5.3 Effects of Geological Modeling on Scale-up

The scale-up results for three Gypsy models were discussed and provided in section 5.2. In this section, the results are compared and evaluated using relative error method.

The relative error defined and used in this study is as follows:

$$\delta = \frac{V_C - V_F}{V_F} \tag{5-1}$$

where:

δ = relative error,

V_C = value obtained from coarse scale,

V_F = value obtained from fine scale.

Figs. 5-59 to 5-64 show the comparisons of water production rate, cumulative water production, and reservoir pressure for fine scale and coarse scale of the three models with and without PI scale-up. In order to study the effects of geological modeling on scale-up, the comparisons of 28-layer and 13-layer coarse-scale lithofacies models, and 16-layer and 13-layer coarse-scale flowunit models are also presented in Figs. 5-91 to 5-102.

Figs. 5-59 to 5-61 show the comparison of water production rate, cumulative water production, and reservoir pressure without PI scale-up for three 13-layer upscaled models. It can be observed that without PI scale-up, the error caused by scale-up is unacceptably large. Therefore, it must be emphasized that the scale-up of productivity

index is very important in scale-up. It can be observed that, without PI scale-up, three models produced comparable results.

Figs. 5-62 to 5-64 show the comparison of water production rate, cumulative water production, and reservoir pressure for three models with PI scale-up for three 13-layer models. Significant improvements were obtained after considering PI scale-up. The largest error for water production, which occurred in flowunit model, is 47%. Other errors calculated were 6.7% for cumulative production, and 2.1% for reservoir pressure, which are much lower than the errors in Figs. 5-59 to 5-61. The lithofacies and channel models obtained comparable results, while the flowunit model produced the worst scale-up result in the three models.

The scale-up results for four production wells without PI scale-up were provided in Figs. 5-65 to 5-76. When PI scale-up was not performed, the lithofacies model obtained better matches in wells #1 and 2 for water production rate, and the channel model obtained better matches in wells #3 and 4. The largest error calculated is 300%, which occurred in well #4. For cumulative production, the flowunit model obtained better matches in wells #1, #2 and #3, but the channel model obtained a better match in well #4. The largest error for cumulative production was -73% which occurred in well #3. For wellblock pressure, all three models produced similar matches in four production wells. The largest error for wellblock pressure was 103%, which occurred in well #1.

The scale-up results with PI scale-up for four production wells are shown in Figs. 5-77 to 5-88. Significant improvements were obtained in all four wells and shown in all

three plots. For water production rate, the channel model obtained the best match in all four wells, while the flowunit model gave the worst. The largest error for water production rate was 55% in well #1. For cumulative water production, the lithofacies model obtained the best match and the flowunit model again obtained the worst. The largest error was only 9% in well #1. Wellblock pressure again obtained similar matches in all four wells. The largest error for wellblock pressure was only 4% in well #4.

The water injection rate and cumulative water injection were exactly the same for fine scale and coarse scale in all three models, so only the results of wellblock pressure are shown in Figs. 5-89 to 5-90. Without PI scale-up, the channel model obtained the best match, with the largest error at 80%. With PI scale-up, the lithofacies model obtained the best match. The largest error was only 2.2% in the flowunit model.

Figs. 5-91 to 5-96 show the scale-up results for 28-layer and 13-layer lithofacies models with and without PI scale-up. Without PI scale-up, two models produced basically the same matches in water production rate. The 13-layer model obtained better matches in cumulative production and reservoir pressure than the 28-layer model. With PI scale-up, the 28-layer model produced a better result in water production, but the 13-layer model produced better results in cumulative water production and reservoir pressure.

Figs. 5-97 to 5-102 show the results for two flowunit models. Without PI scale-up, the 13-layer model produced better results than the 16-layer model in water production rate, cumulative water production, and reservoir pressure. With PI scale-up,

the 13-layer model still produced significantly better results than the 16-layer model in all plots.

Based on the scale-up results on three geological models presented in Figs. 5-5 to 5-56, 5-59 to 5-102, and the discussion above, the following statements can be made:

1. When scale-up of transmissibility is conducted, PI scale-up must be included. Without PI scale-up, the results are unacceptable, especially at onset of the production. The highest relative error produced without PI scale-up was up to 230% in water production rate.
2. Strategies of geological modeling have significant effects on scale-up. With PI scale-up, the channel model and the lithofacies model produced comparable matches. However, the flowunit model produced the worst matches in both water production and reservoir pressure. This is not consistent with expectations that the lithofacies model should produce the best match, and the channel model produce the worst.
3. When analyzing the process of geological modeling, the lithofacies unit is the smallest and most homogenous unit obtainable. However, when the lithofacies unit was divided into many layers to develop the fine-scale model, many grid blocks in the same layer in fine-scale model did not connect to each other horizontally. Therefore, no horizontal flow occurred between these grid blocks in the mathematical model. In real reservoir condition, even though these grid blocks do not connect to other grid blocks in the same layer, horizontal flow would still exist in these grid blocks, i.e ., between the grid blocks belonging to different lithofacies unit. Therefore, a finer-scale model does not necessarily produce more accurate results.

There is a limit to the degree of fine-scale that the model should have as good as possible horizontal communication. If too fine a scale is used, the model may lead to wrong simulation results, because the flow configuration was changed due to the limitation of mathematical strategies in simulator.

4. In the lithofacies model, the 28-layer model did not improve the scale-up results beyond that of the 13-layer model. The same is true for the flowunit model, i.e., the 16-layer model did not show better results than the 13-layer model, in fact, the accuracy decreased. This indicates that between two flow barriers, having more homogeneous lithofacies units or flow units as the targets for scale-up may not improve modeling results, probably due to a 'horizontal pinch-out' effect. Therefore, in reservoir simulation and scale-up, optimizing results occurs when the individual layer is as homogeneous as possible and the horizontal distribution of each layer is as widely as possible.

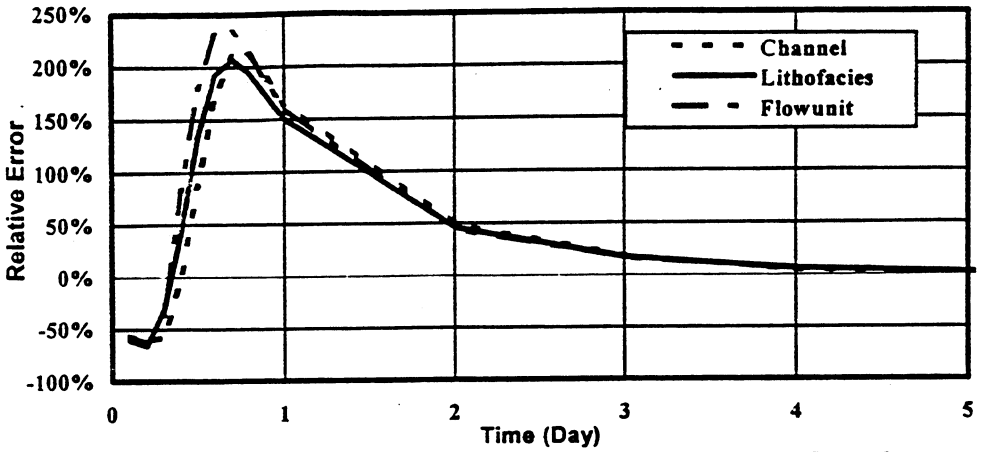

Fig. 5-59 Relative Errors of Water Production Rate for Different Models Without PI Scale-up

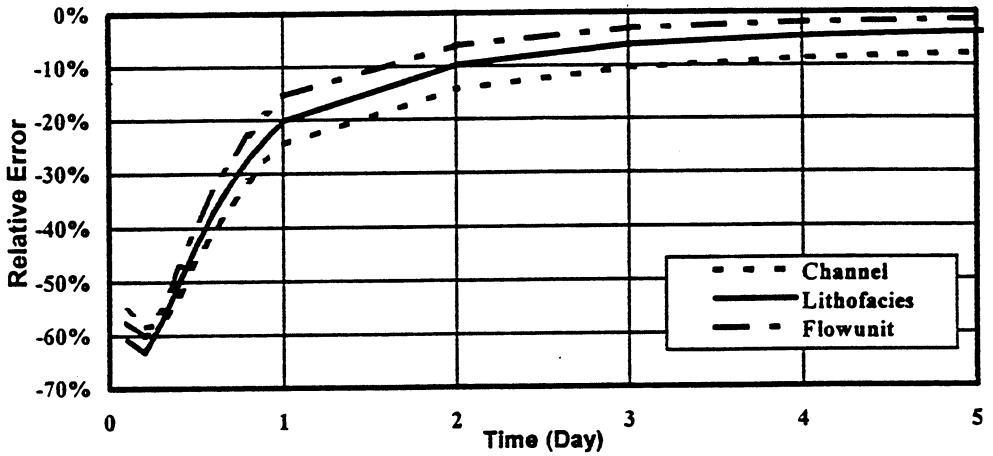

Fig. 5-60 Relative Errors of Cum. Water Production Rate for Different Models Without PI Scale-up

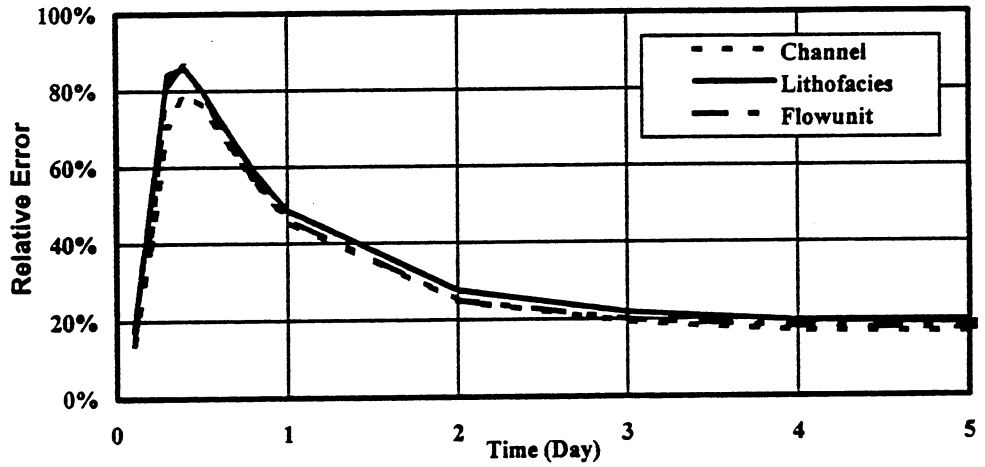

Fig. 5-61 Relative Errors of Reservoir Pressure for Different Models Without PI Scale-up

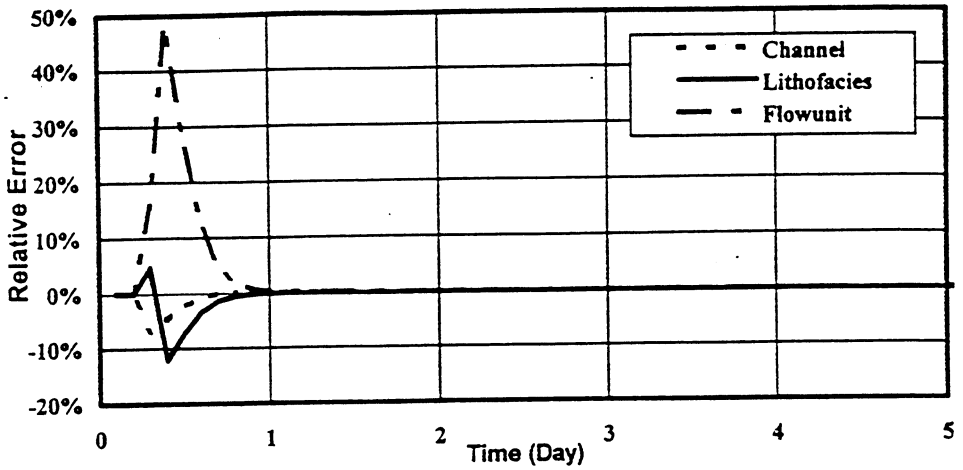

Fig. 5-62 Relative Errors of Water Production Rate for Different Models With PI Scale-up

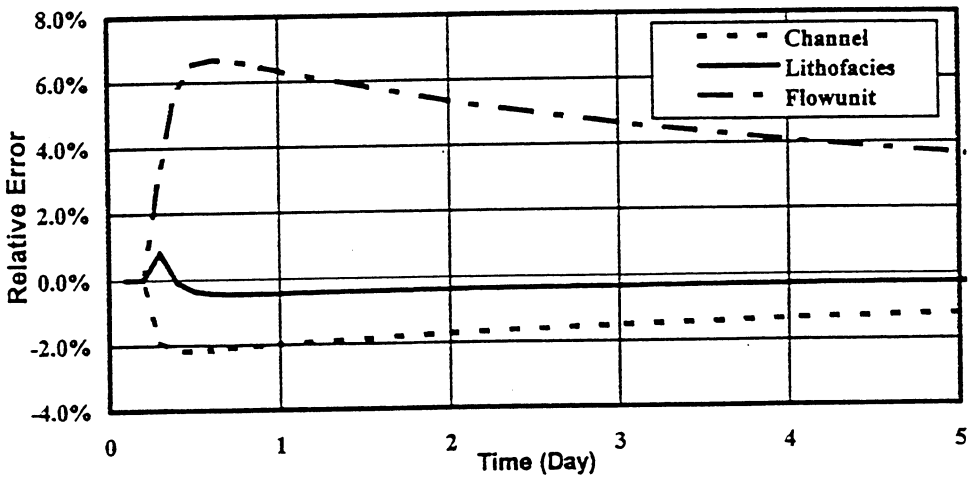

Fig. 5-63 Relative Errors of Cum. Water Production Rate for Different Models With PI Scale-up

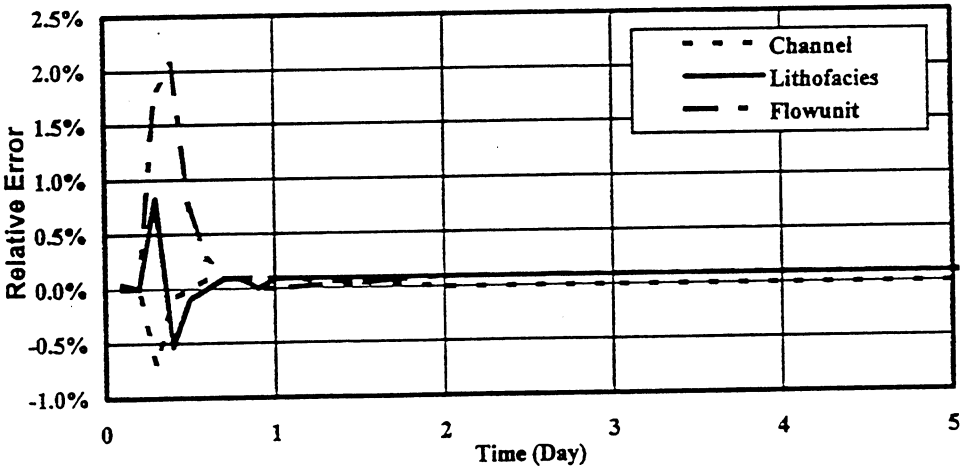

Fig. 5-64 Relative Errors of Reservoir Pressure for Different Models With PI Scale-up

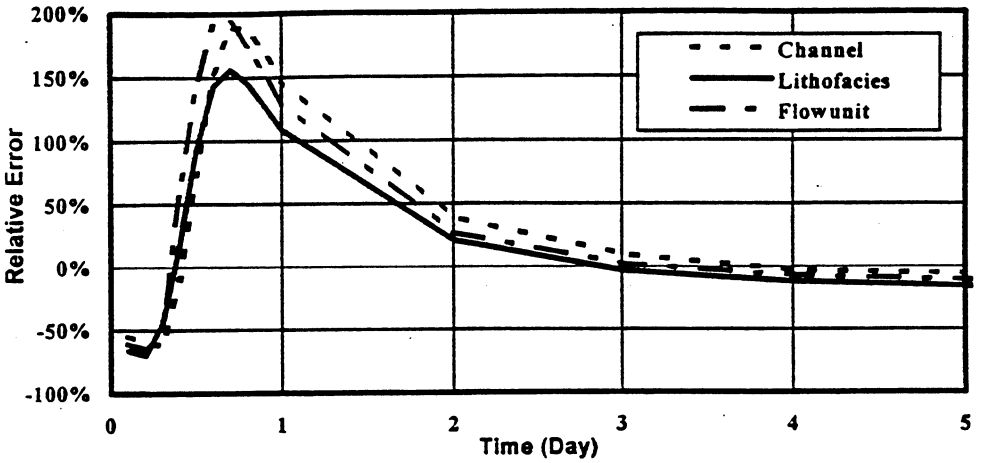

Fig. 5-65 Relative Errors of Water Production Rate Without PI Scale-up for Well #1 in Three Different Models

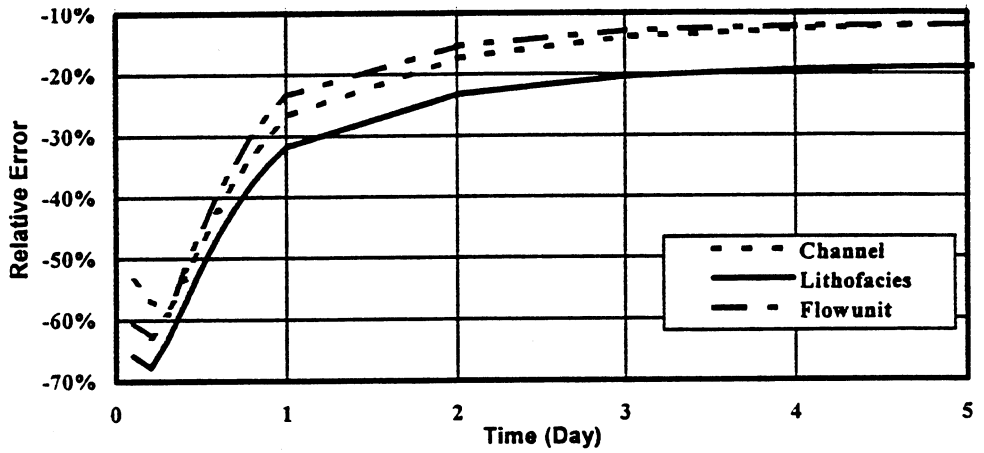

Fig. 5-66 Relative Errors of Cum. Water Production Without PI Scale-up for Well #1 in Three Different Models

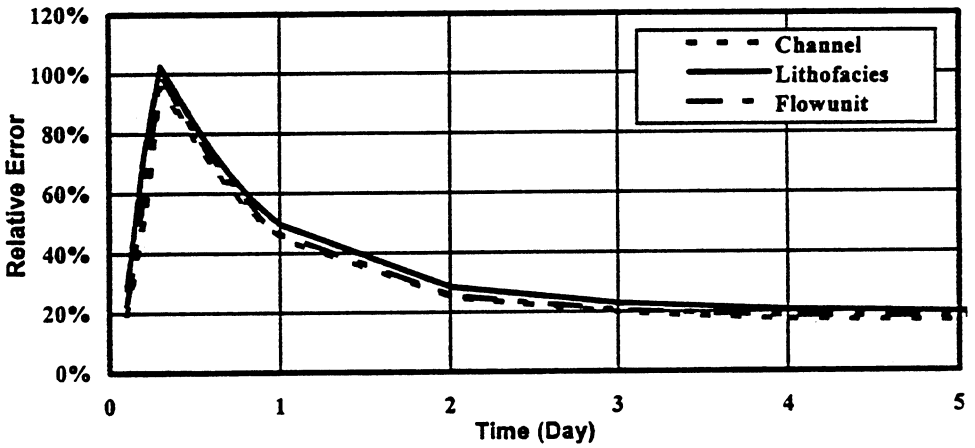

Fig. 5-67 Relative Errors of Average Wellblock Pressure Without PI Scale-up for Well #1 in Three Different Models

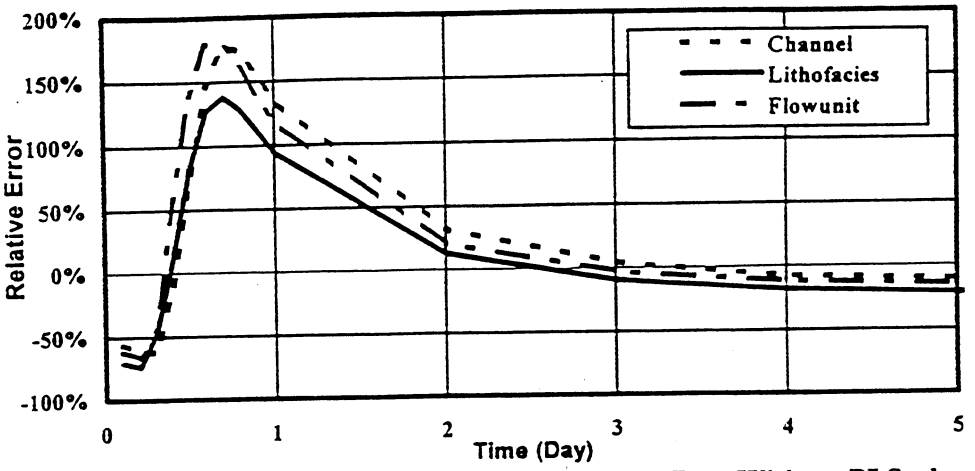

Fig. 5-68 Relative Errors of Water Production Rate Without PI Scale-up for Well #2 in Three Different Models

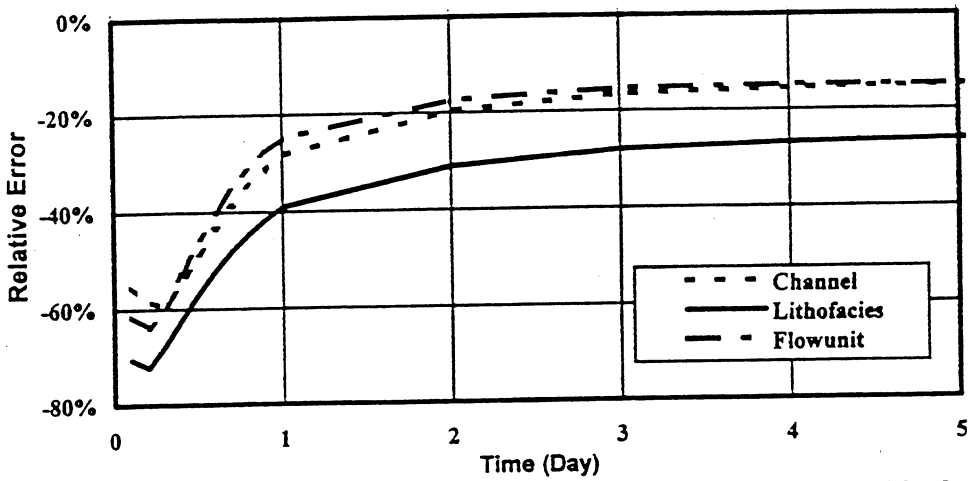

Fig. 5-69 Relative Errors of Cum. Water Production Without PI Scale-up for Well #2 in Three Different Models

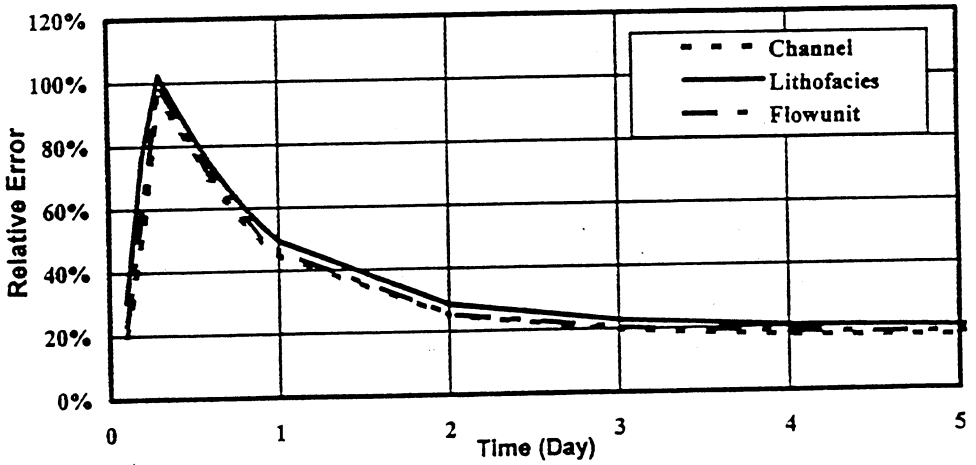

Fig. 5-70 Relative Errors of Average Wellblock Pressure Without PI Scale-up for Well #2 in Three Different Models

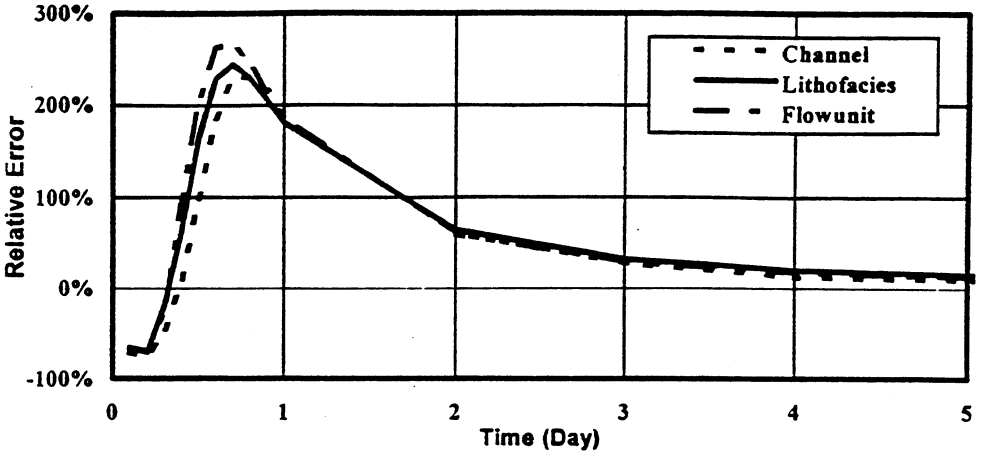

Fig. 5-71 Relative Errors of Water Production Rate Without PI Scale-up for Well #3 in Three Different Models

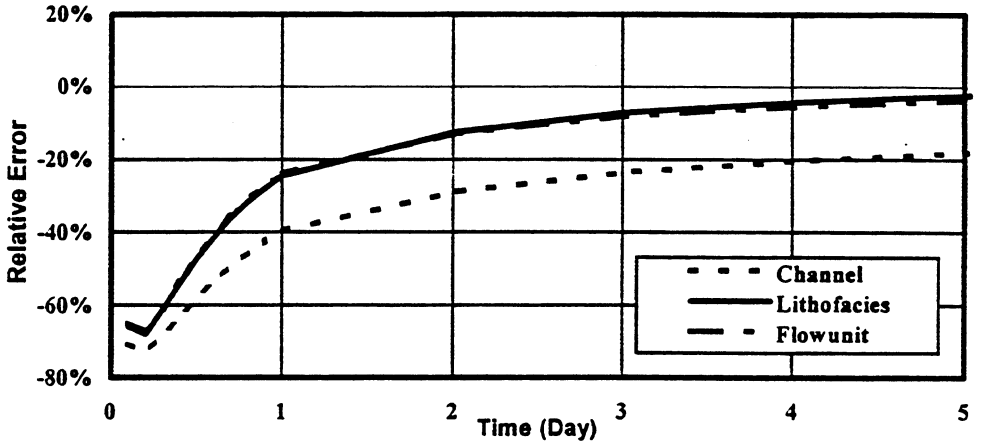

Fig. 5-72 Relative Errors of Cum. Water Production Without PI Scale-up for Well #3 in Three Different Models

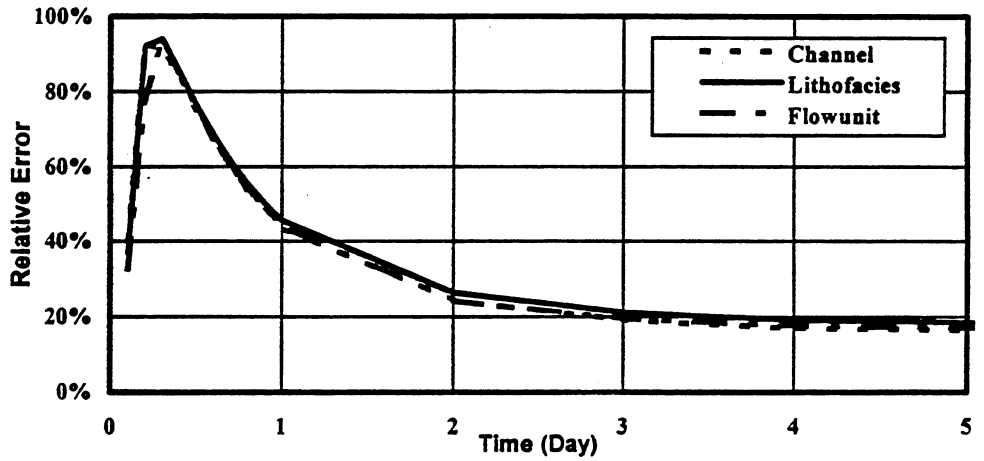

Fig. 5-73 Relative Errors of Average Wellblock Pressure Without PI Scale-up for Well #3 in Three Different Models

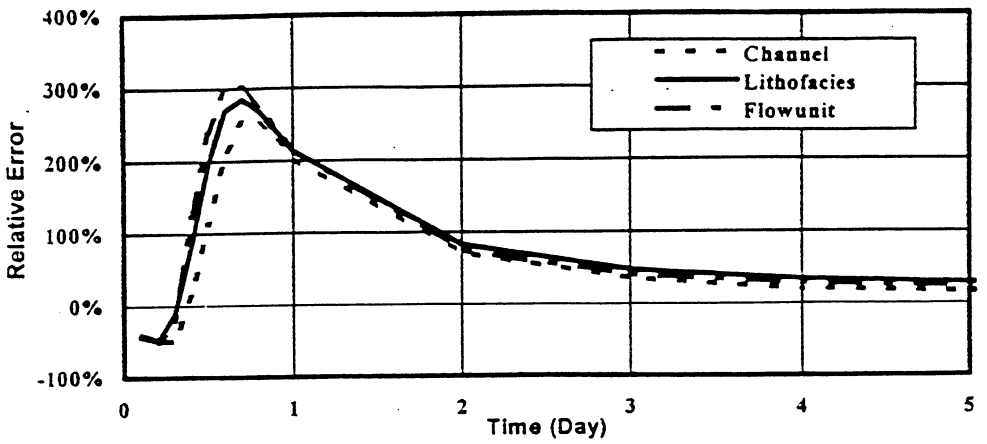

Fig. 5-74 Relative Errors of Water Production Rate Without PI Scale-up for Well #4 in Three Different Models

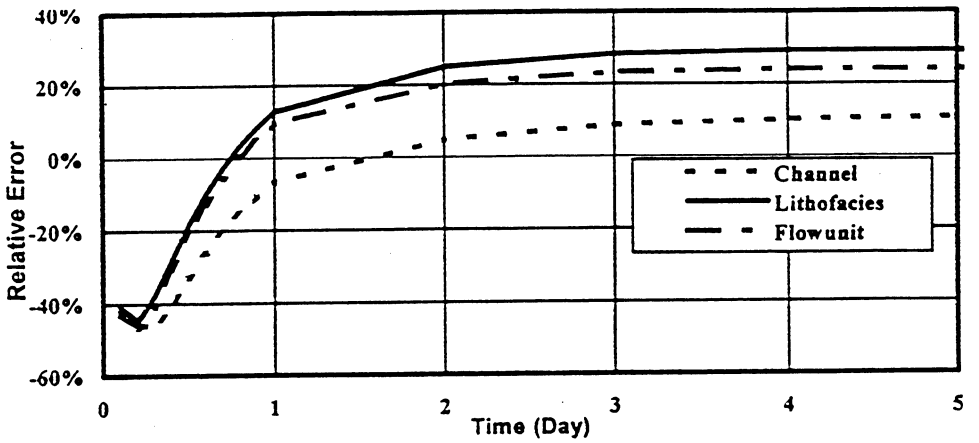

Fig. 5-75 Relative Errors of Cum. Water Production Without PI Scale-up for Well #4 in Three Different Models

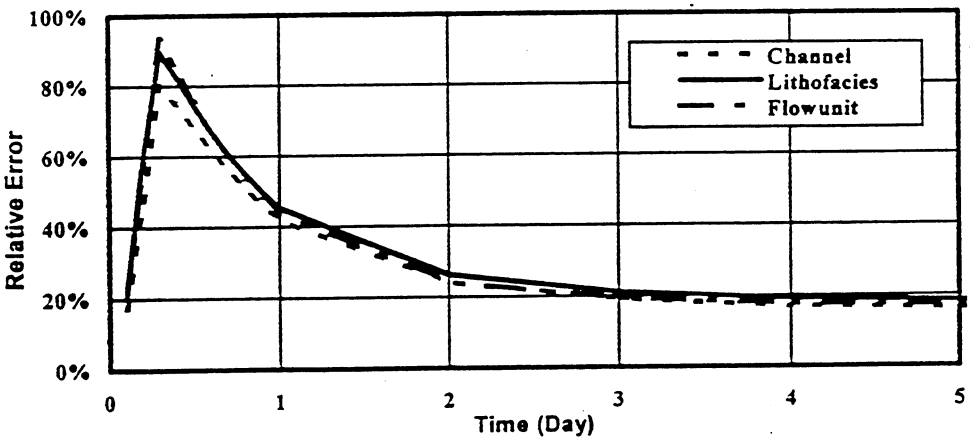

Fig. 5-76 Relative Errors of Average Wellblock Pressure Without PI Scale-up for Well #4 in Three Different Models

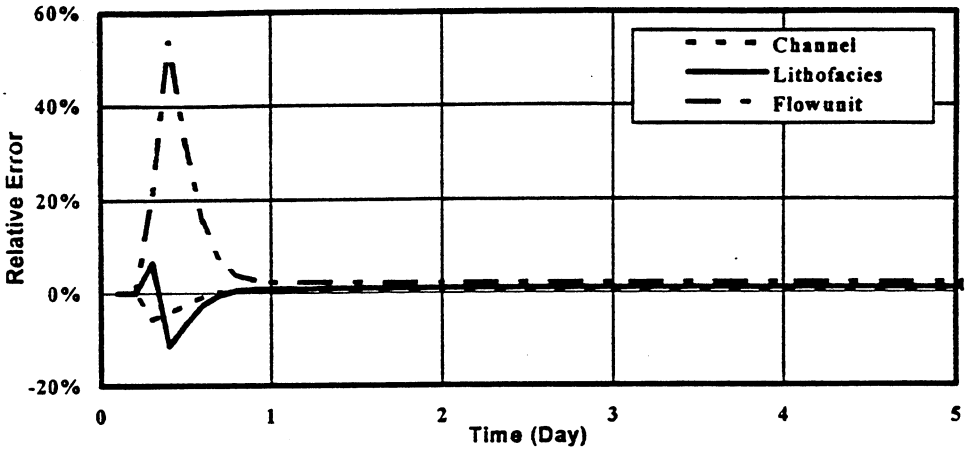

Fig. 5-77 Relative Errors of Water Production Rate With PI Scale-up for Well #1 in Three Different Models

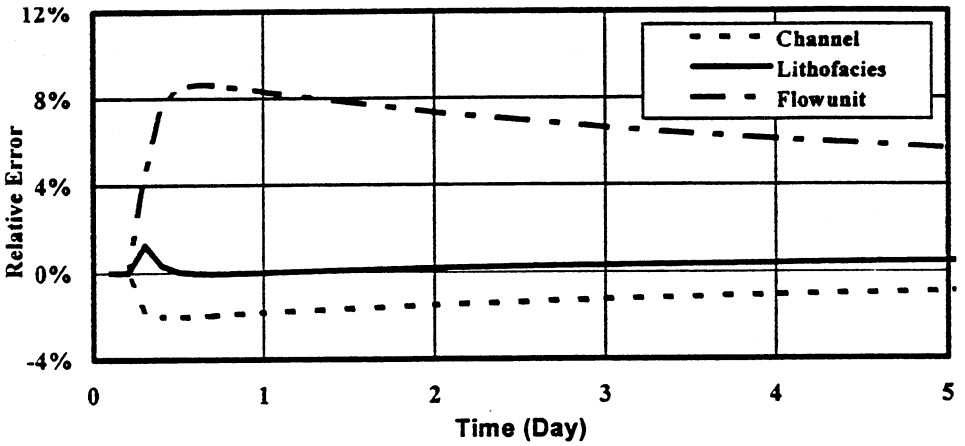

Fig. 5-78 Relative Errors of Cum. Water Production With PI Scale-up for Well #1 in Three Different Models

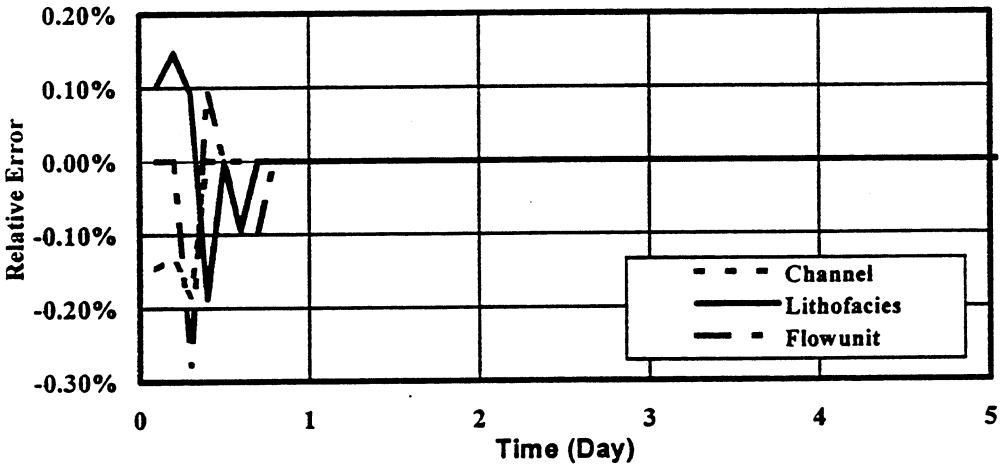

Fig. 5-79 Relative Errors of Average Wellblock Pressure With PI Scale-up for Well #1 in Three Different Models

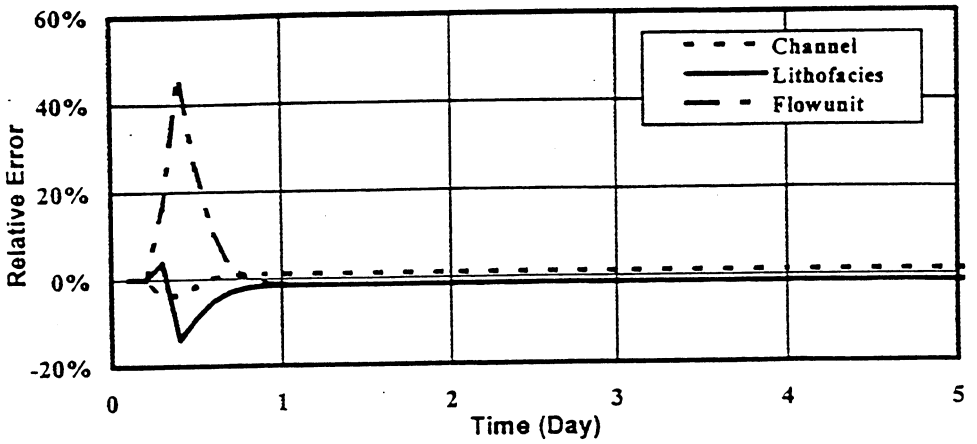

Fig. 5-80 Relative Errors of Water Production Rate With PI Scale-up for Well #2 in Three Different Models

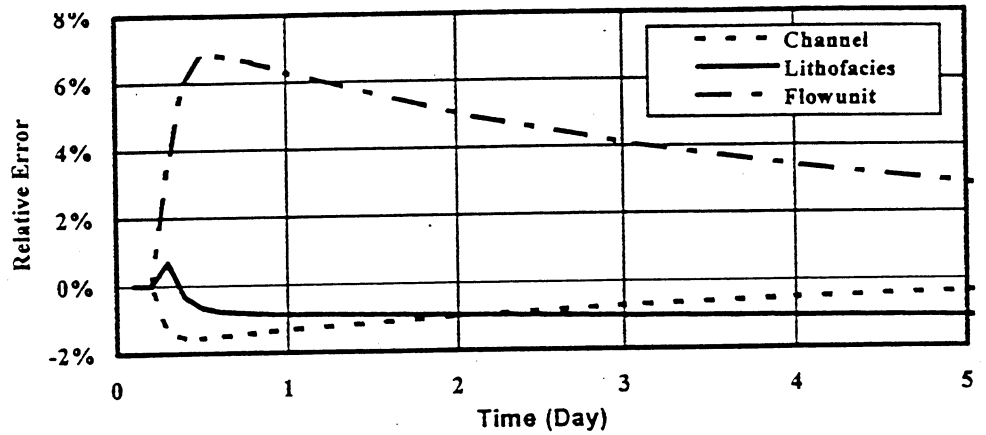

Fig. 5-81 Relative Errors of Cum. Water Production With PI Scale-up for Well #2 in Three Different Models

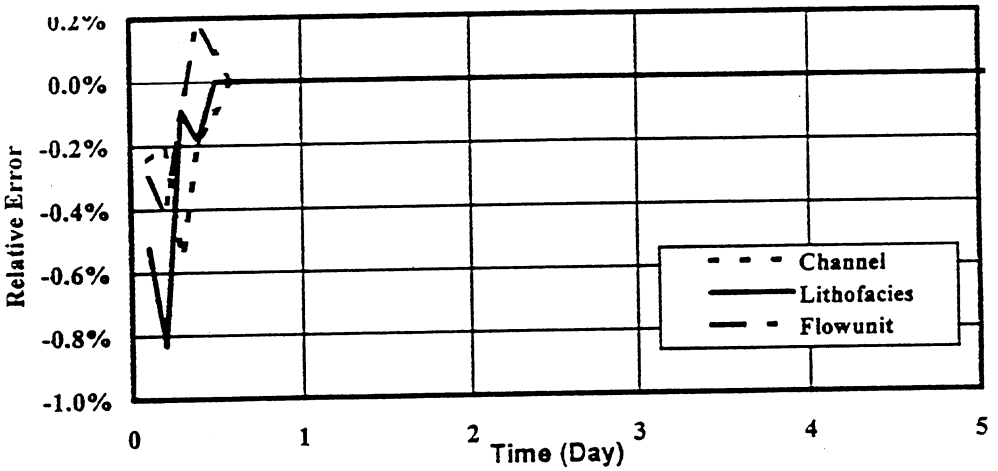

Fig. 5-82 Relative Errors of Average Wellblock Pressure With PI Scale-up for Well #2 in Three Different Models

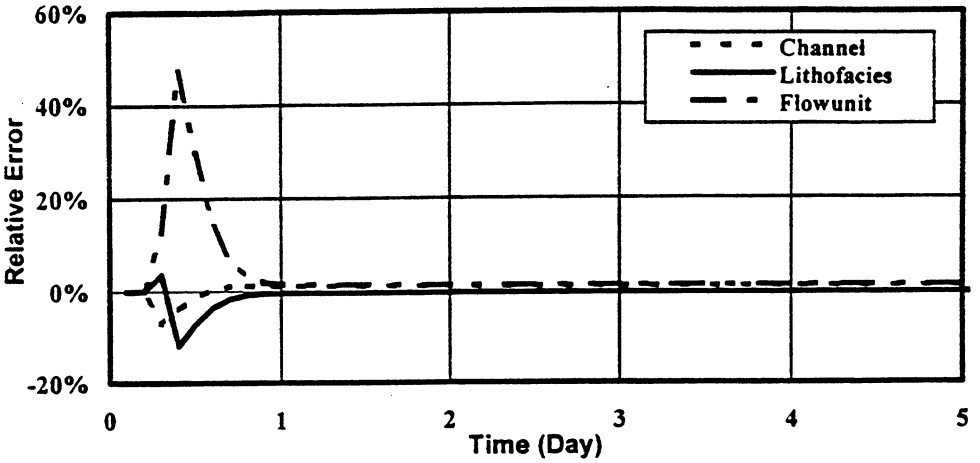

Fig. 5-83 Relative Errors of Water Production Rate With PI Scale-up for Well #3 in Three Different Models

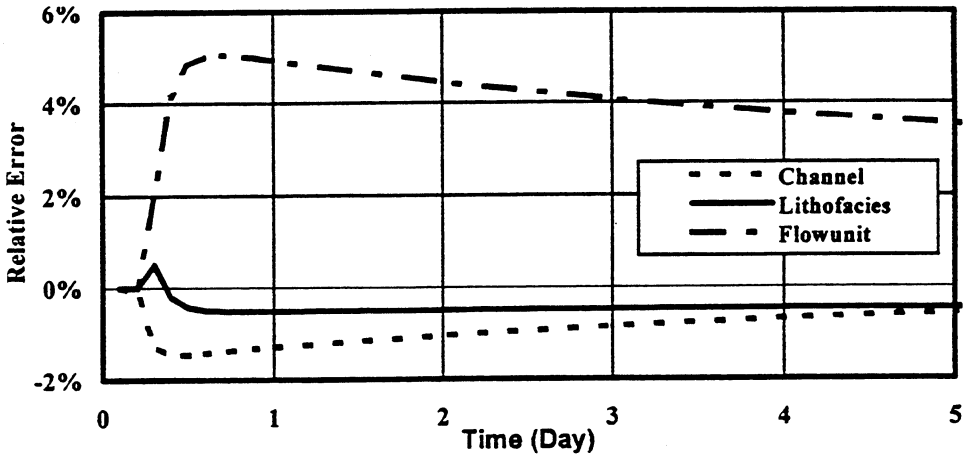

Fig. 5-84 Relative Errors of Cum. Water Production With PI Scale-up for Well #3 in Three Different Models

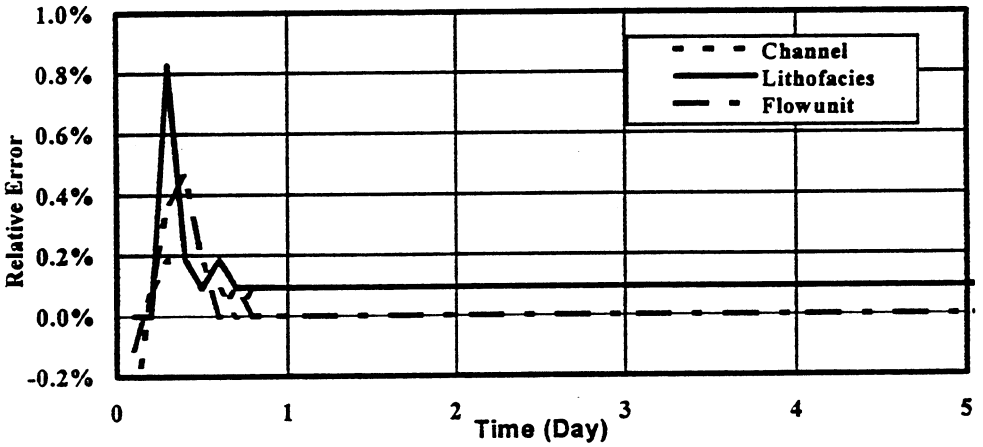

Fig. 5-85 Relative Errors of Average Wellblock Pressure With PI Scale-up for Well #3 in Three Different Models

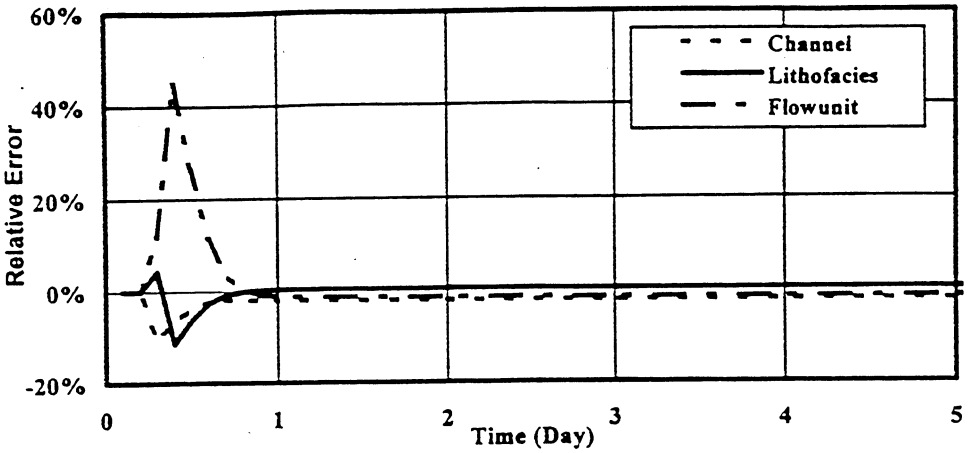

Fig. 5-86 Relative Errors of Water Production Rate With PI Scale-up for Well #4 in Three Different Models

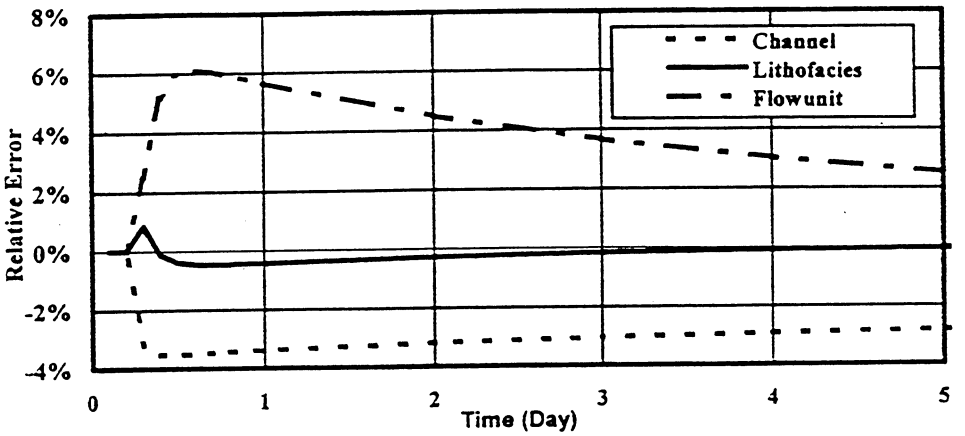

Fig. 5-87 Relative Errors of Cum. Water Production With PI Scale-up for Well #4 in Three Different Models

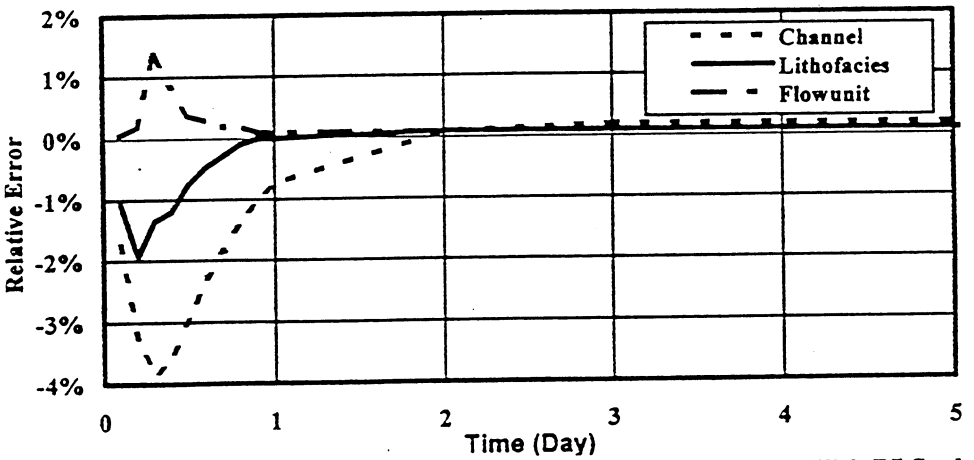

Fig. 5-88 Relative Errors of Average Wellblock Pressure With PI Scale-up for Well #4 in Three Different Models

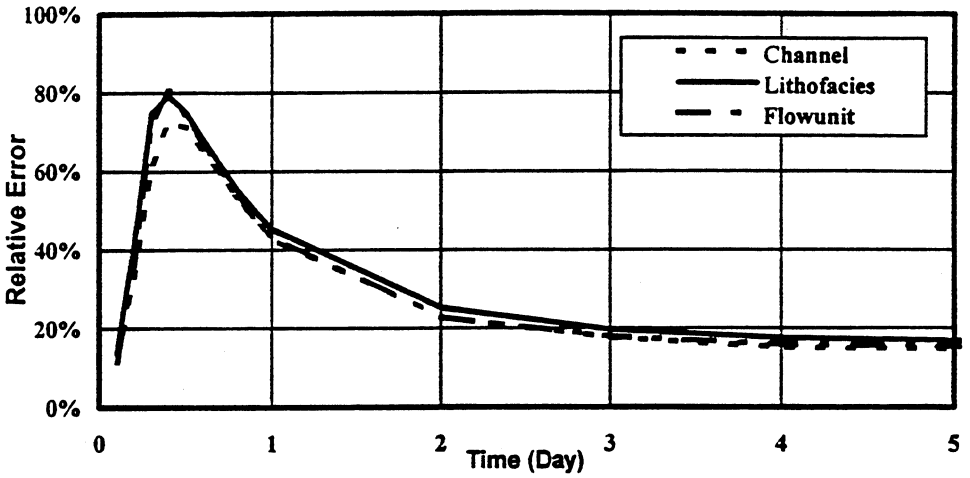

Fig. 5-89 Relative Errors of Wellblock Pressure Without PI Scale-up for Well #5 in Three Different Models

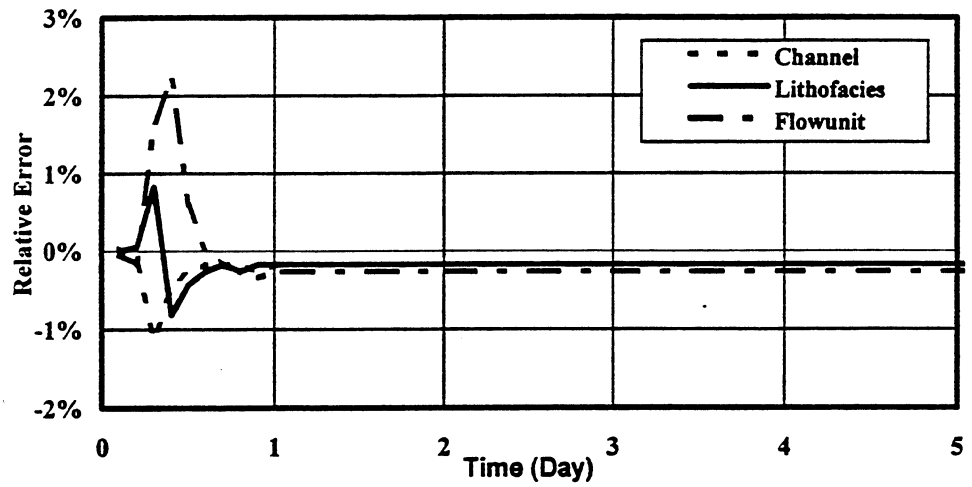

Fig. 5-90 Relative Errors of Wellblock Pressure With PI Scale-up for Well #5 in Three Different Models

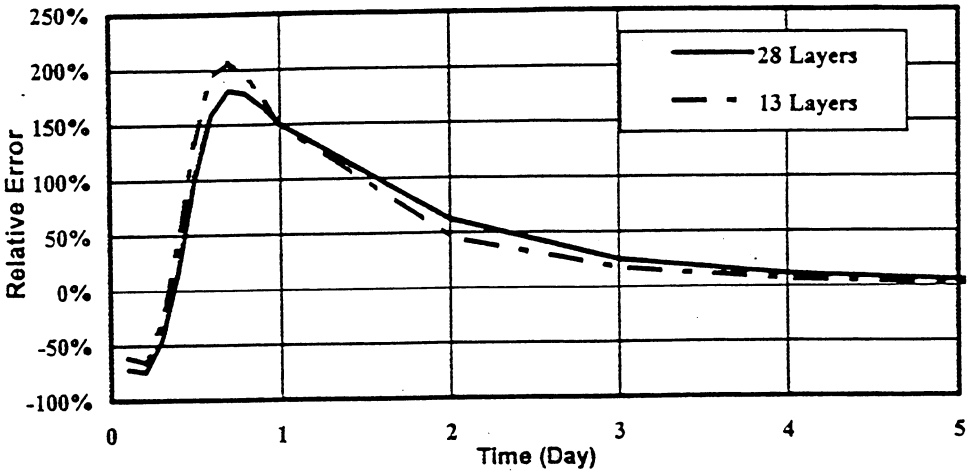

Fig. 5-91 Relative Errors of Water Production Rate Without PI Scale-up for Lithofacies Models

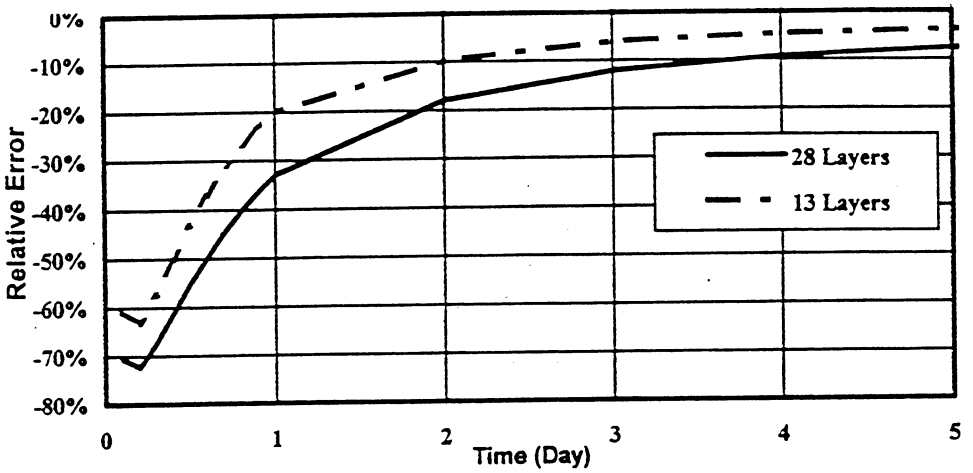

Fig. 5-92 Relative Errors of Cum. Water Production Without PI Scale-up for Lithofacies Models

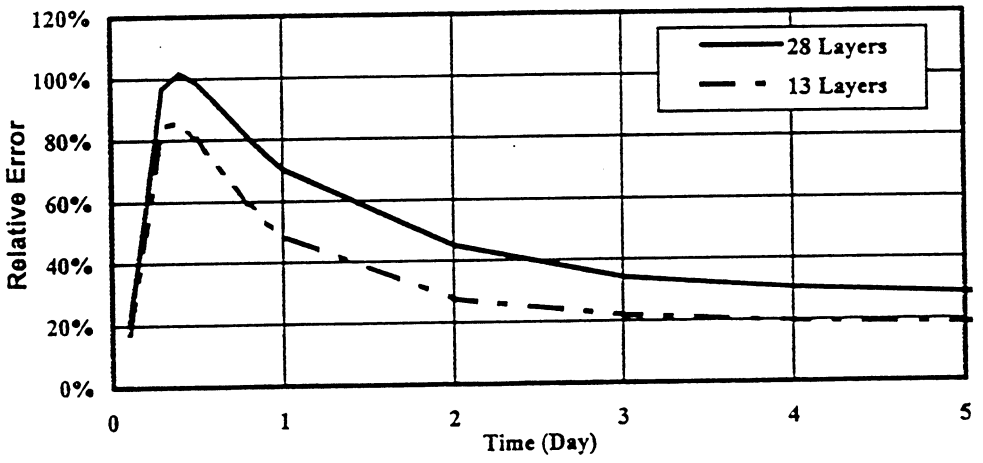

Fig. 5-93 Relative Errors of Average Reservoir Pressure Without PI Scale-up for Lithofacies Models

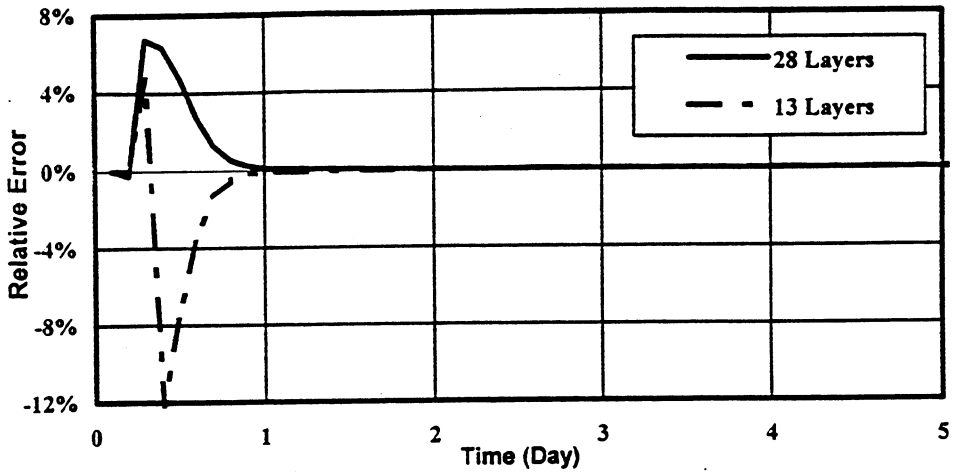

Fig. 5-94 Relative Errors of Water Production Rate Without PI Scale-up for Lithofacies Models

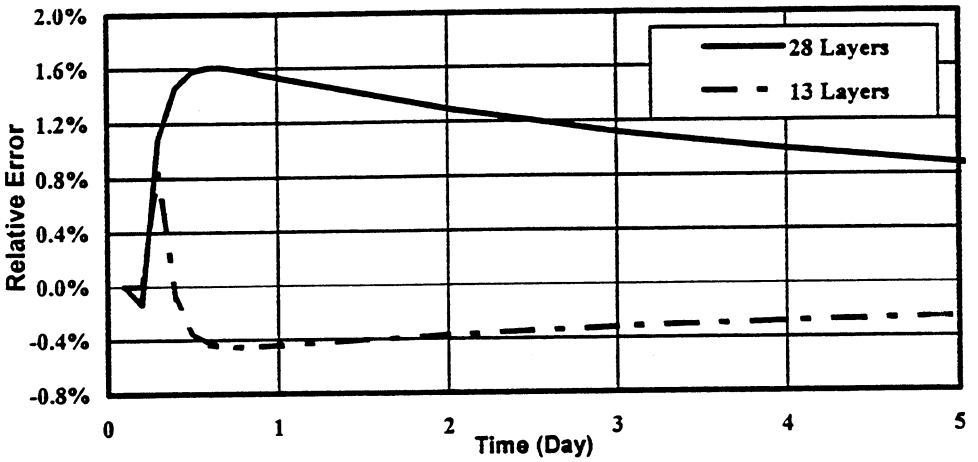

Fig. 5-95 Relative Errors of Cum. Water Production With PI Scale-up for Lithofacies Models

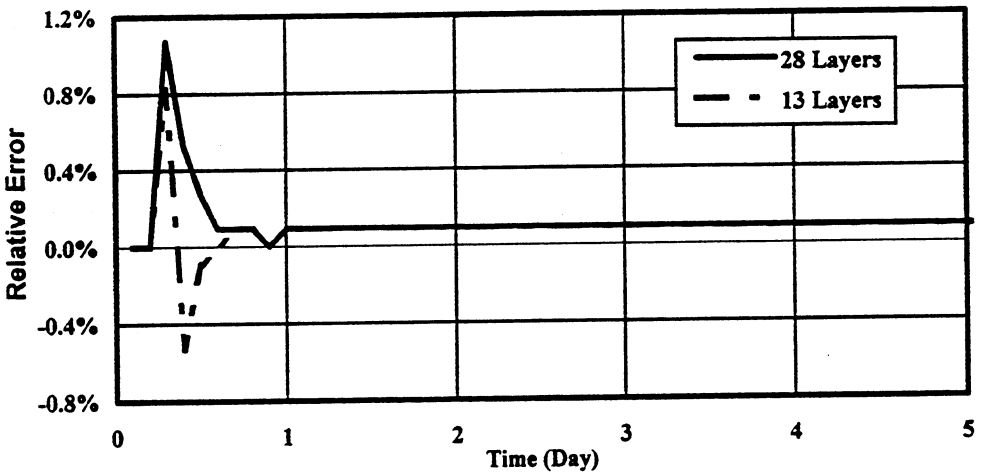

Fig. 5-96 Relative Errors of Average Reservoir Pressure With PI Scale-up for Lithofacies Models

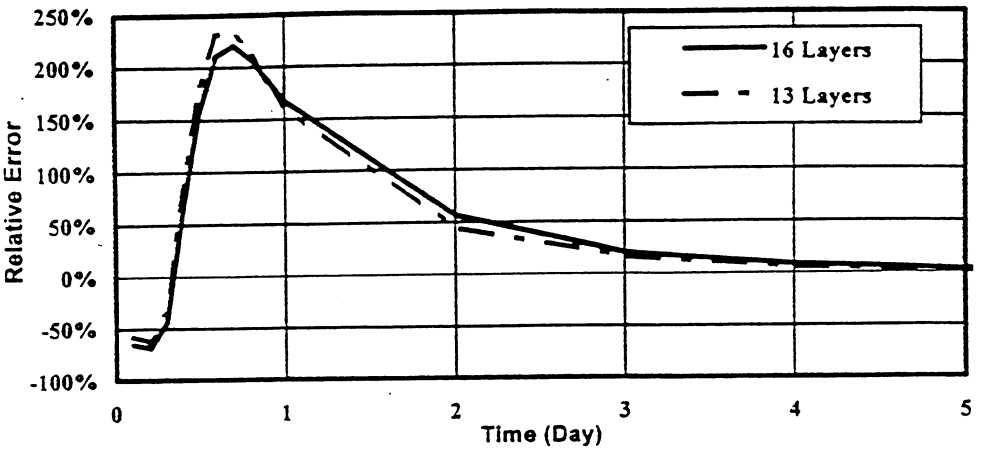

Fig. 5-97 Relative Errors of Water Production Rate Without PI Scale-up for Flowunit Models

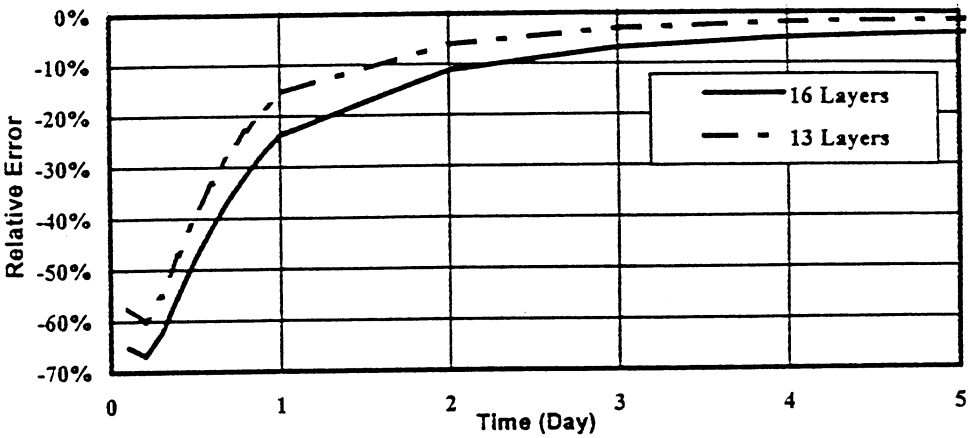

Fig. 5-98 Relative Errors of Cum. Water Production Without PI Scale-up for Flowunit Models

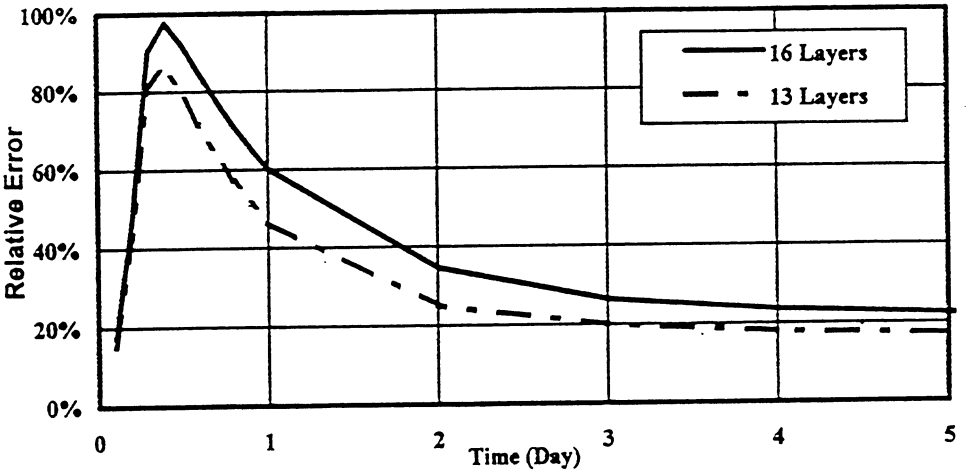

Fig. 5-99 Relative Errors of Average Reservoir Pressure Without PI Scale-up for Flowunit Models

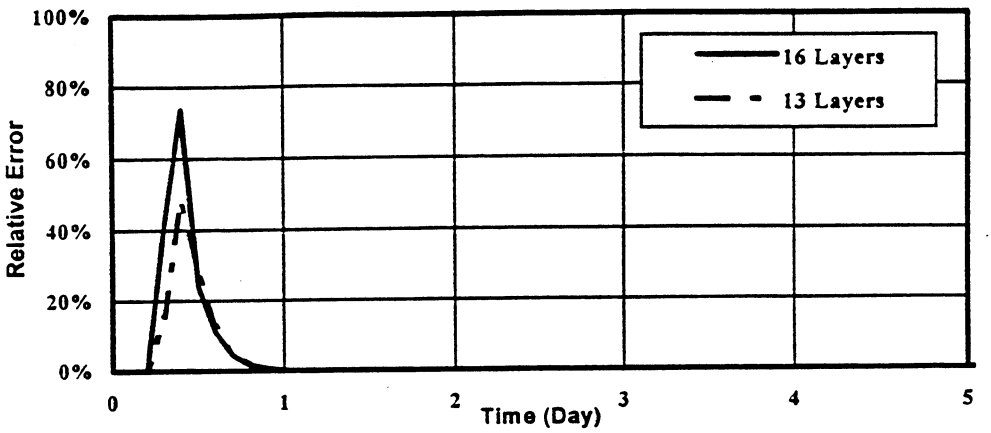

Fig. 5-100 Relative Errors of Water Production Rate With PI Scale-up for Flowunit Models

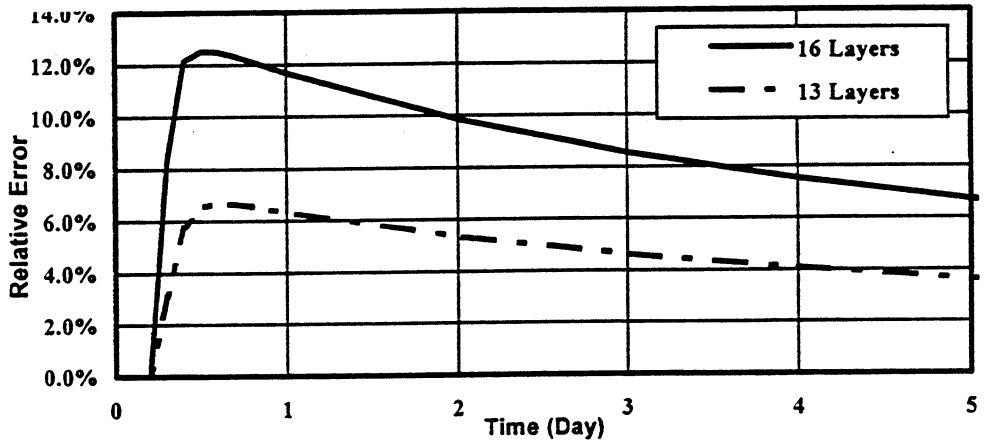

Fig. 5-101 Relative Errors of Cum. Water Production With PI Scale-up for Flowunit Models

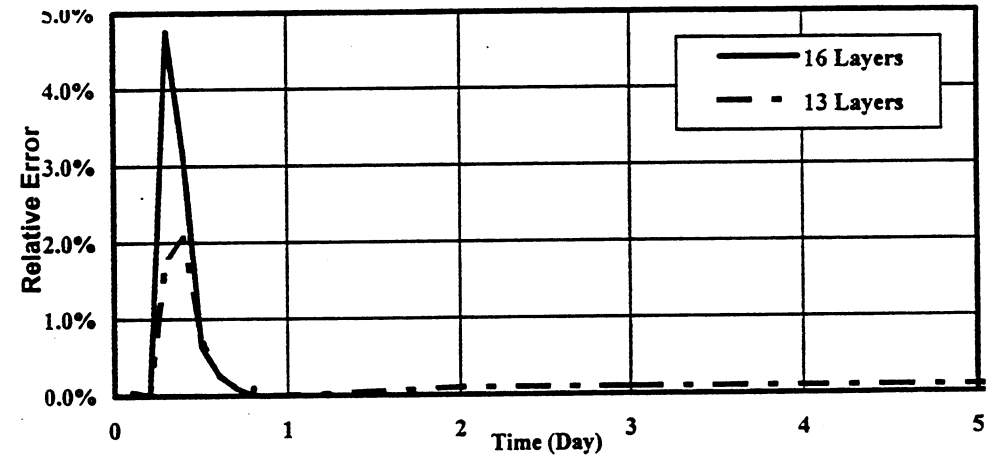

Fig. 5-102 Relative Errors of Average Reservoir Pressure With PI Scale-up for Flowunit Models

CHAPTER VI

EFFECTS OF WELL LOCATION AND BOUNDARY CONDITIONS ON SCALE-UP

In this chapter, flow in the Gypsy channel model was simulated for different boundary conditions and different production-injection scenarios. Scale-up techniques were then applied to study the effects of boundary condition, well location, and production and injection scenario on scale-up.

6.1 Effects of Well Location on Scale-up

Nine wells were designed and used to study the effects of well location on scale-up. Two production-injection scenarios were studied. Scenario #1, as shown in Fig. 6-1, is a nine-spot corner-drive production-injection scenario. Scenario #2, as shown in Fig. 6-2, is a line-drive production-injection scenario. The initial conditions for reservoir, well production, and injection controls are the same as used for three Gypsy models in Chapter V. A well injectivity index of 10 was used in the fine scale simulation. which is the same as used in previous models. The scaled productivity index used for the nine wells in the two production-injection scenarios were listed in Table 6-1 and 6-2.

A comparison of results for the three different production-injection scenarios are presented in Figs. 6-3 to 6-8. In the plots, the results for five-spot scenario are from the simulation for channel model in Chapter V.

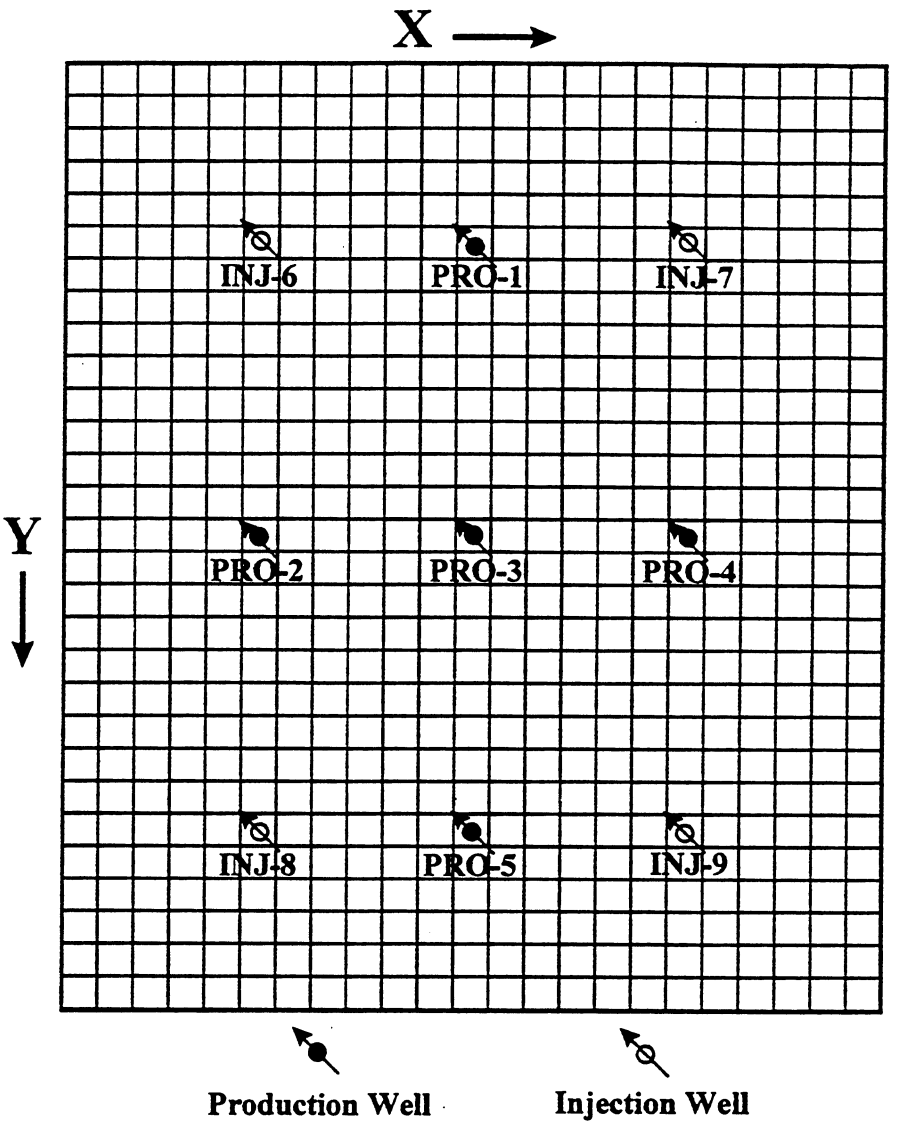

Fig. 6-1 Illustration of Nine-Spot Corner-Drive Well Pattern

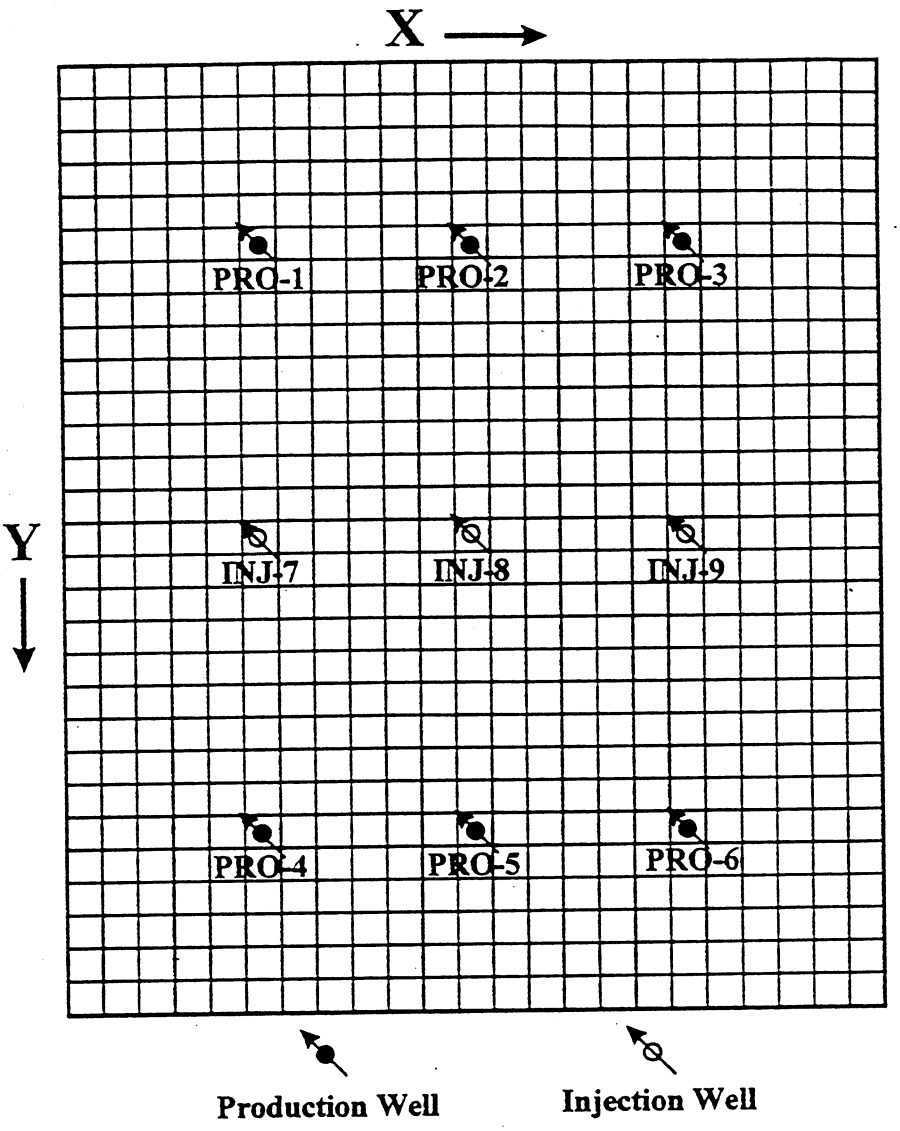

Fig. 6-2 Illustration of Line-Drive Well Pattern

Table 6-1 Scaled Productivity Index Used for Nine-Spot Corner-Drive Scenario

Well	PI
PRO-1	358.82
PRO-2	179.62
PRO-3	191.95
PRO-4	199.10
PRO-5	208.21
INJ-6	258.71
INJ-7	277.13
INJ-8	101.19
INJ-9	235.00

Table 6-2 Scaled Productivity Index Used for Line-drive Scenario

Well	PI
PRO-1	282.60
PRO-2	412.73
PRO-3	291.94
PRO-4	113.90
PRO-5	216.47
PRO-6	274.78
INJ-7	180.15
INJ-8	190.33
INJ-9	190.08

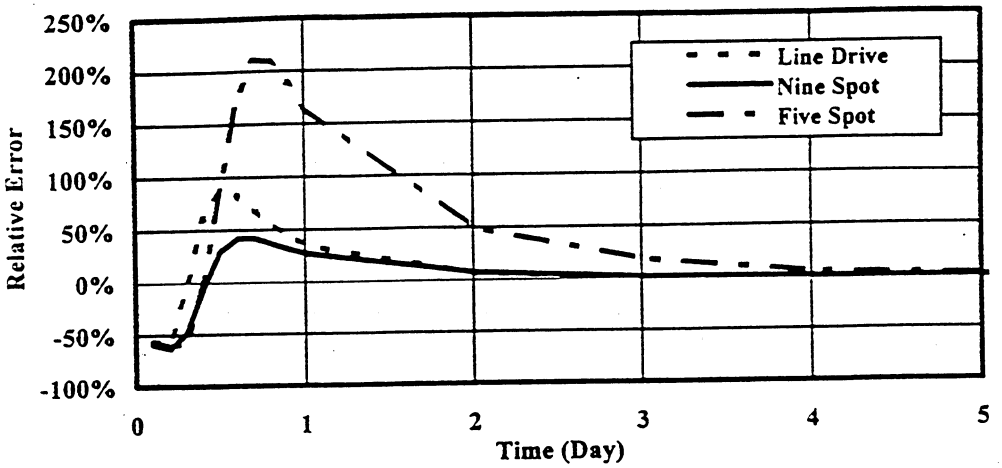

Fig. 6-3 Relative Errors of Water Production Rate without PI Scale-up for Different Production Scenarios

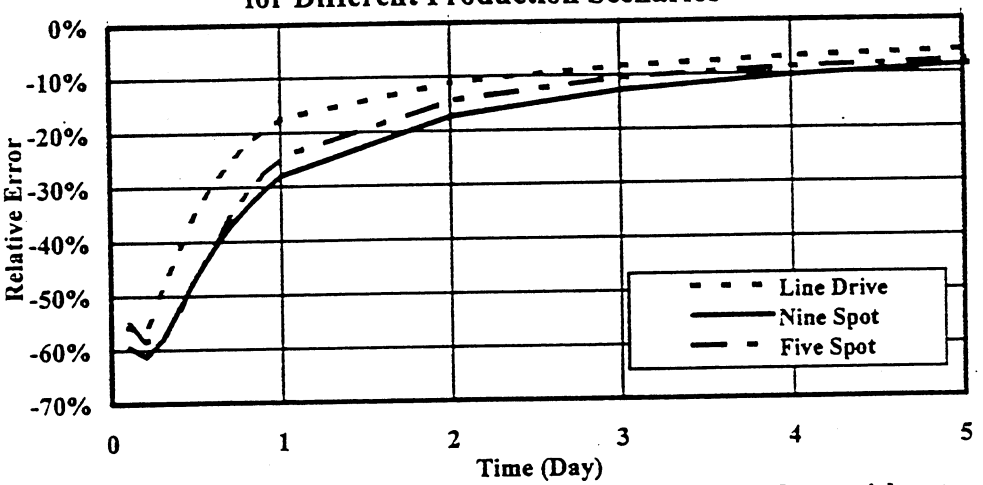

Fig. 6-4 Relative Errors of Cum. Water Production Rate without PI Scale-up for Different Production Scenarios

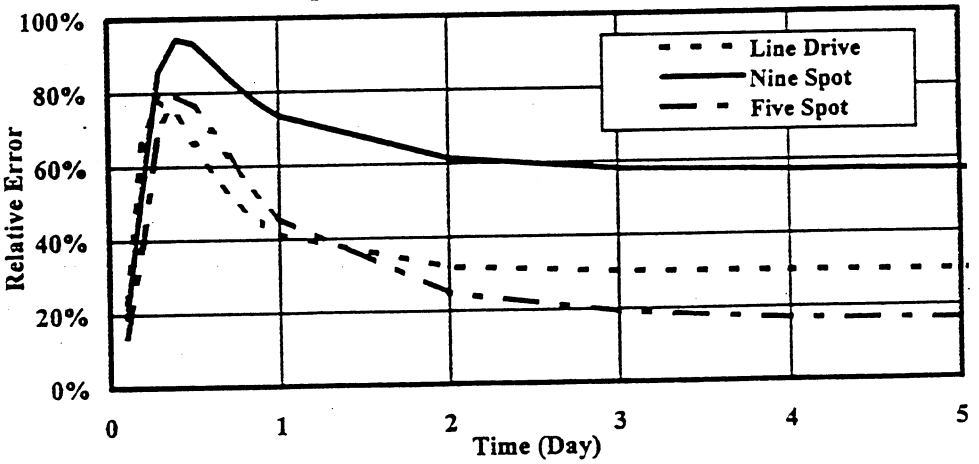

Fig. 6-5 Relative Errors of Reservoir Pressure without PI Scale-up for Different Production Scenarios

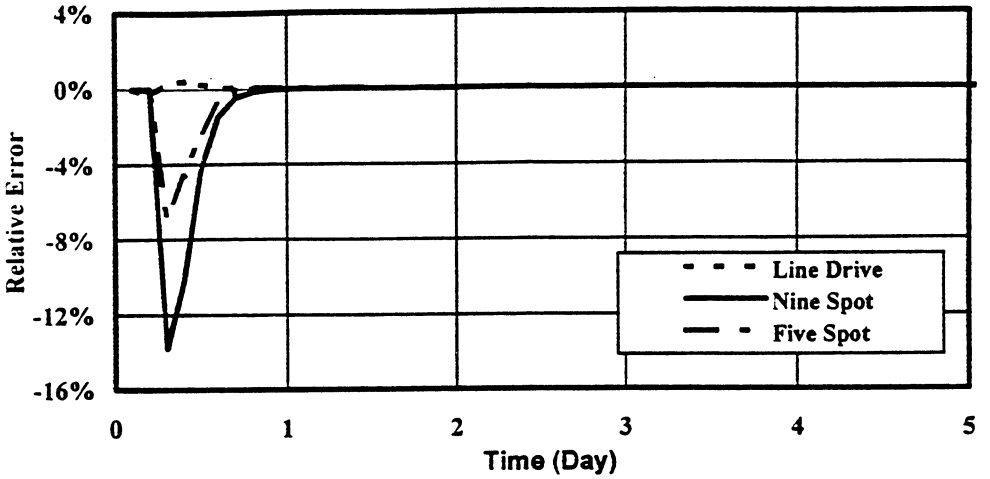

Fig. 6-6 Relative Errors of Water Production Rate with PI Scale-up for Different Production Scenarios

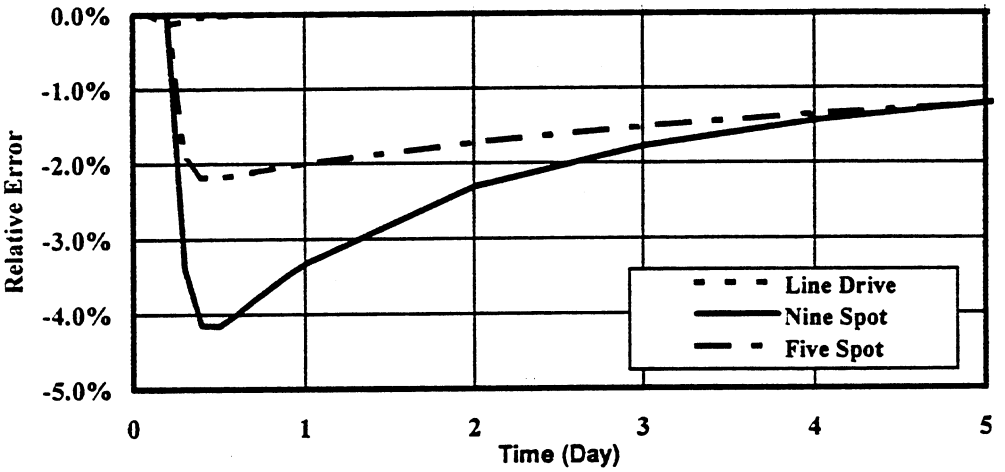

Fig. 6-7 Relative Errors of Cum. Water Production Rate with PI Scale-up for Different Production Scenarios

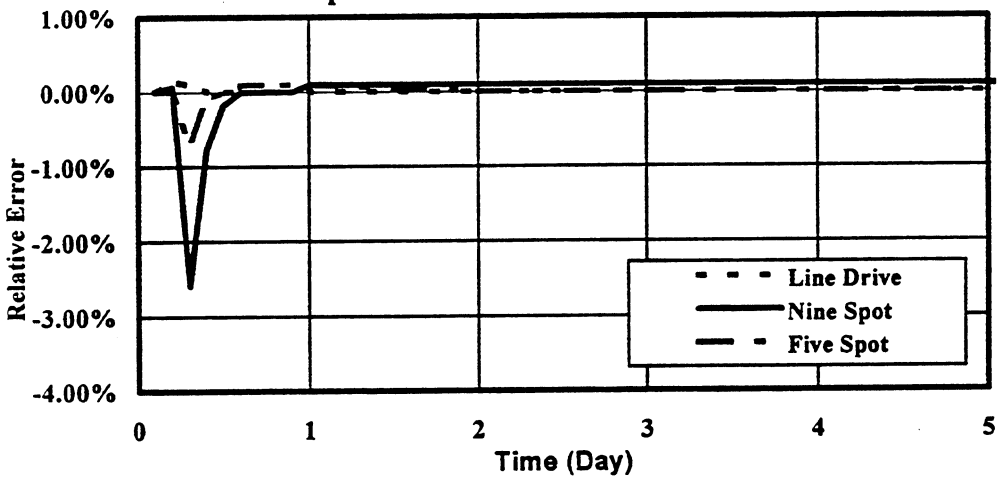

Fig. 6-8 Relative Errors of Reservoir Pressure With PI Scale-up for Different Porduction Scenarios

From the plots, the following observations are made:

1. Production-injection scenarios have significant effects on scale-up. Significant differences in scale-up results for line-drive, nine-spot drive, and fine-spot drive exist with and without PI scale-up processes.
2. Without PI scale-up, the nine-spot drive scenario produced the best result in water production rate, but showed the highest relative error in reservoir pressure and cumulative water production. In contrast, five-spot drive scenario produced the highest error in water production rate, but lowest error in reservoir pressure. Line-drive scenario produced the best matches in three production-injection scenarios.
3. After considering PI scale-up, the line-drive scenario still produced the best results in three production-injection scenarios. The nine-spot scenario produced the worst matches, probably because in line-drive scenario, the overall flow configuration of fluid in reservoir is more linear than with the nine-spot drive scenario. The nine-spot scenario has more radial flow and that may cause the larger error, because the scale-up of transmissibility is only suitable for linear flow, even though PI scale-up was conducted to reduce this effect.
4. When comparing the five-spot and nine-spot drive scenarios, the five-spot drive obtained a better match than the nine-spot drive, because more wells cause more radial flow in reservoir, and subsequently may cause the larger error in scale-up. PI scale-up significantly reduced this error in both water production and reservoir pressure, but did not completely fix the problem with the method used.

6.2 Effects of Boundary Conditions on Scale-up

Three different boundary conditions were used and simulated in order to study the effects of boundary conditions on the results of scale-up. The channel model was again used as the reservoir model. The line drive scenario used in section 6.1 was used as the only production-injection scenario, because it showed the best scale-up results in earlier study.

The first boundary condition studied was an edge-water drive, where the reservoir was assumed to be surrounded by a very large edge water that provided constant pressure at boundary. No bottom water was used in this particular model. To simulate a constant pressure around the reservoir, the equivalent diameter of the edge water should be about 10 times that of the equivalent diameter of the reservoir (Craft and Hawkins, 1989) One more grid with a size of 3,280 feet was added to the reservoir model in both X and Y directions, as shown in Fig. 6-9. This lead to a ratio of 8.8 of equivalent diameter of edge water area to the equivalent diameter of reservoir.

The second boundary condition studied was bottom-water drive, where the reservoir was assumed to have a very large bottom water with constant pressure. No water was used at the edge of the reservoir. An additional grid with a size of 3,280 feet was added to the reservoir model in the Z directions, as shown in Fig. 6-10.

The third boundary condition studied was a no flow boundary condition, in which the reservoir was sealed on all directions. The result was the same as for the line-drive scenario in Chapter V.

Scale-up was first conducted without PI scale-up, and then PI scale-up technique was applied. The productivity index values used in PI scale-up are listed in Table 6-3.

The scale-up results for these different boundary conditions are presented in Figs. 6-11 to 6-16. The discussion are summarized as follows:

1. Figs. 6-11 to 6-13 show the comparison of the scale-up results without PI scale-up for the three kinds of boundary conditions studied. Without PI scale-up, significant differences are observed between no-flow boundary and flow boundary conditions. For flow boundary condition, the bottom-water and edge-water boundary conditions produced very similar results. For no-flow boundary condition, the relative errors become smaller with time. However, for flow-boundary conditions, the errors keep remained constant or increased.

2. After PI scale-up, as shown in Figs. 6-14 to 16, significant improvements were obtained for all three cases. No-flow boundary condition provided better results than flow-boundary conditions in water production. Bottom-water boundary condition presented the largest error in water production. For reservoir pressure, edge-water drive are almost completely matched.

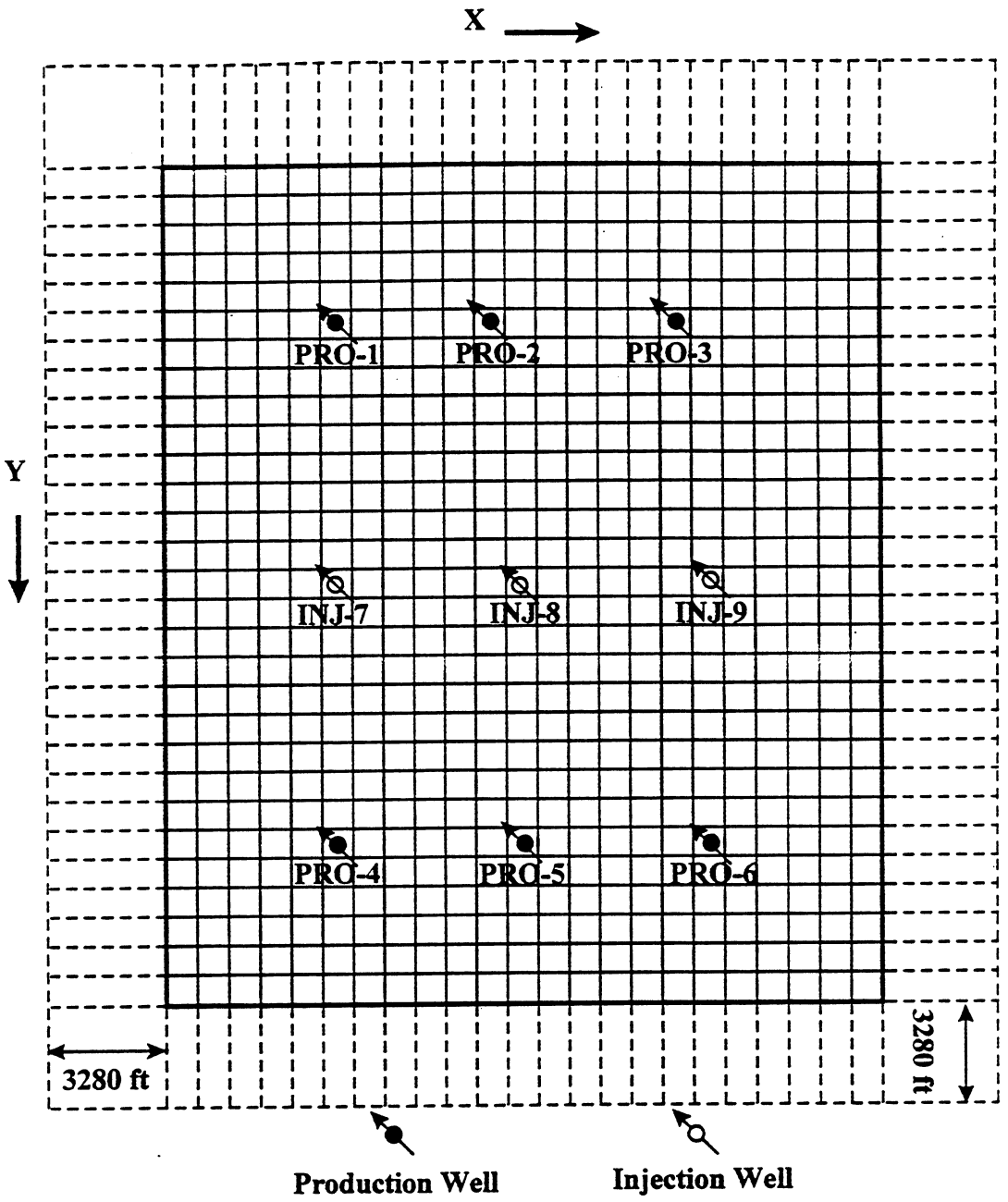

Fig. 6-9 Illustration of Reservoir Model and Well Pattern Used for Edge-Water Drive Scenario

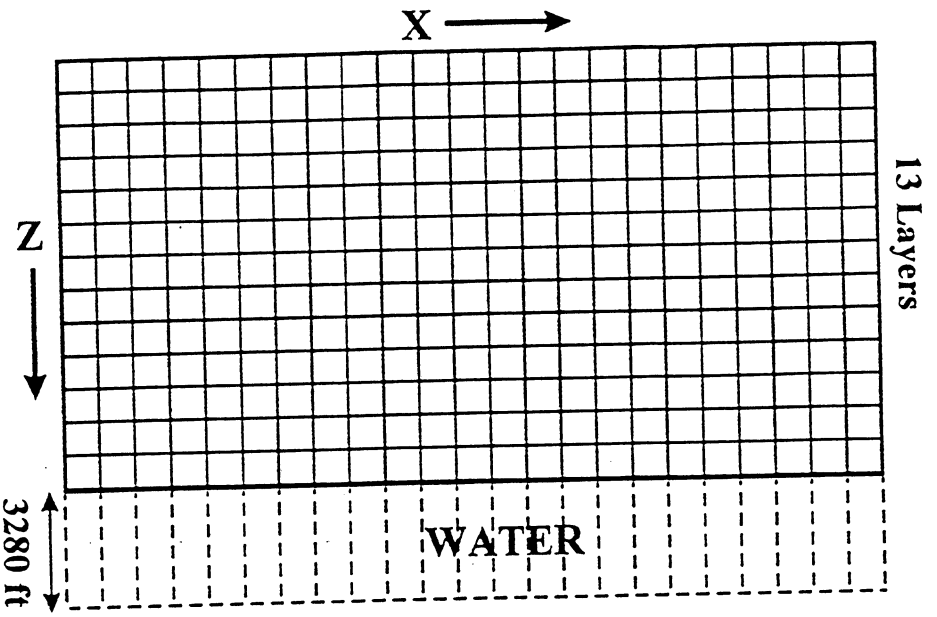

Fig. 6-10 Illustration of Reservoir Model Used for Bottom-Water Drive

Table 6-3 Scaled Productivity Index Used for Different Boundary Conditions

Well	Bottom Water	Edge Water	No Flow
PRO-1	249.91	261.08	282.60
PRO-2	324.80	329.38	412.73
PRO-3	254.44	286.69	291.94
PRO-4	103.52	106.51	113.90
PRO-5	190.23	201.01	216.47
PRO-6	224.50	241.40	274.78
INJ-7	237.10	180.15	180.15
INJ-8	207.92	207.92	190.33
INJ-9	207.62	190.08	190.08

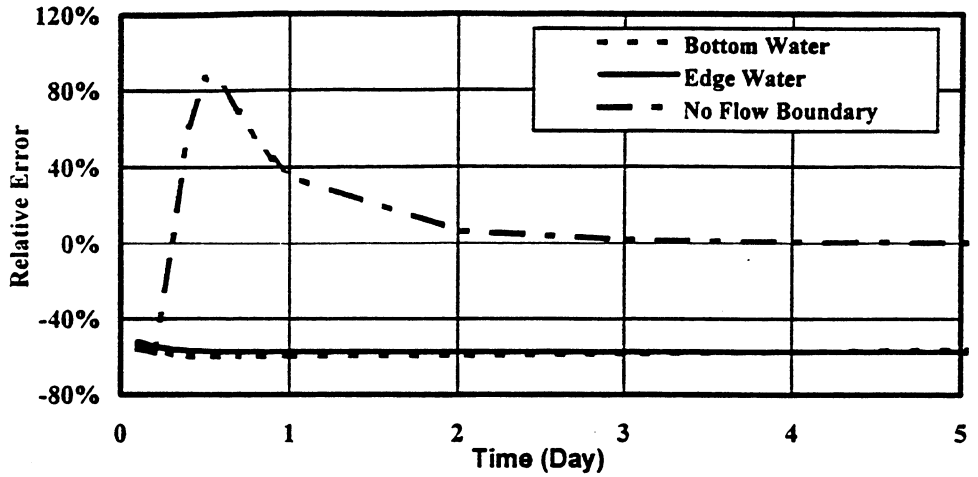

Fig. 6-11 Relative Errors of Water Production Rate without PI Scale-up for Different Boundary Conditions

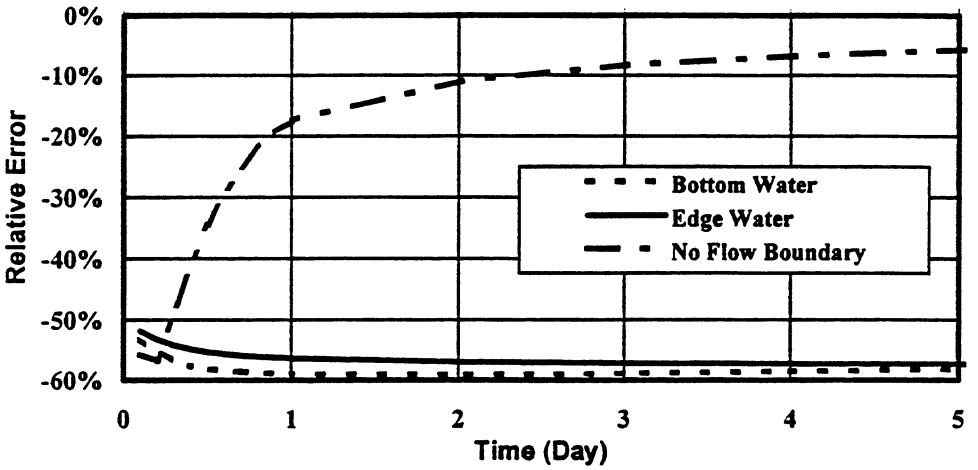

Fig. 6-12 Relative Errors of Cum. Water Production Rate without PI Scale-up for Different Boundary Conditions

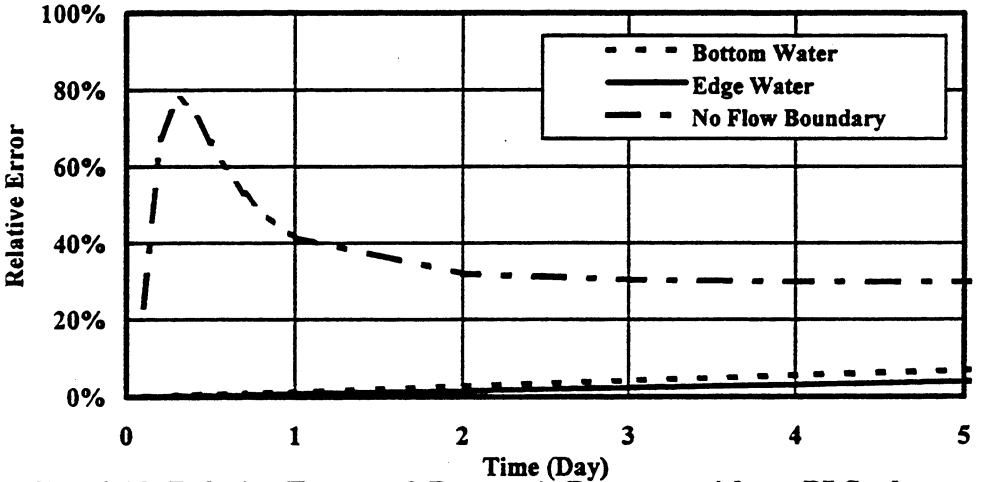

Fig. 6-13 Relative Errors of Reservoir Pressure without PI Scale-up for Different Boundary Conditions

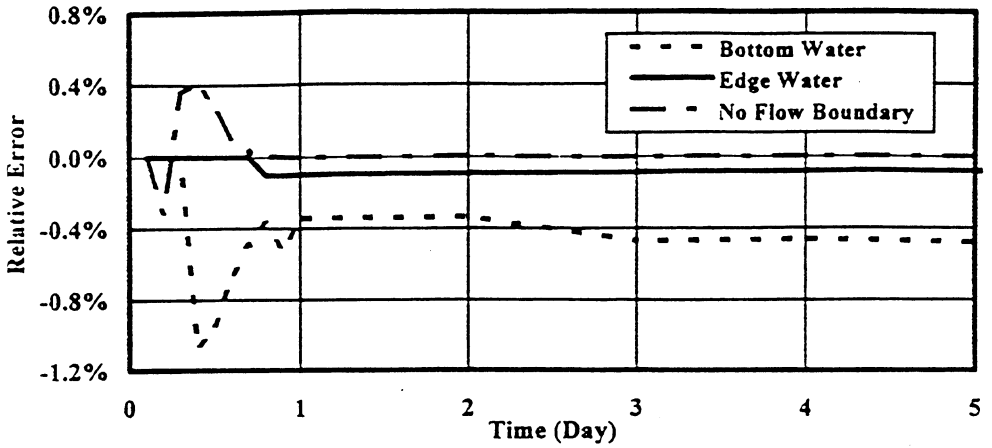

Fig. 6-14 Relative Errors of Water Production Rate with PI Scale-up for Different Boundary Conditions

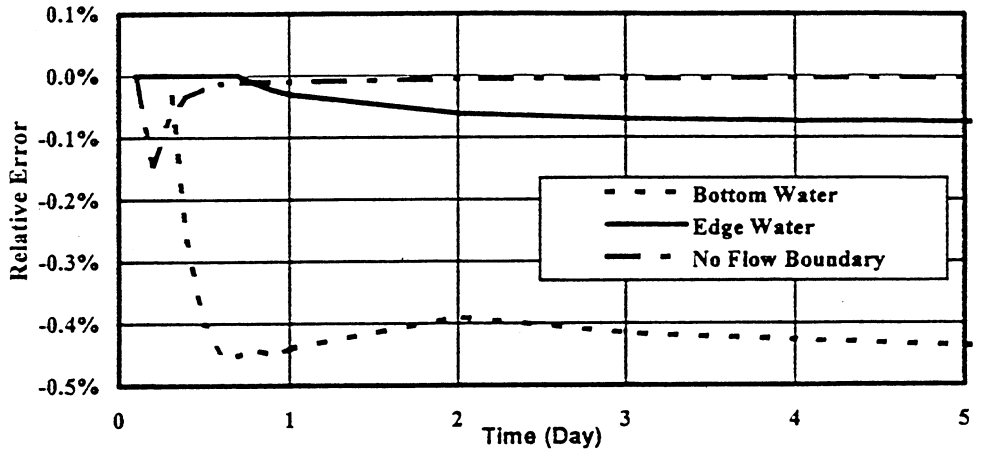

Fig. 6-15 Relative Errors of Cum. Water Production Rate with PI Scale-up for Different Boundary Conditions

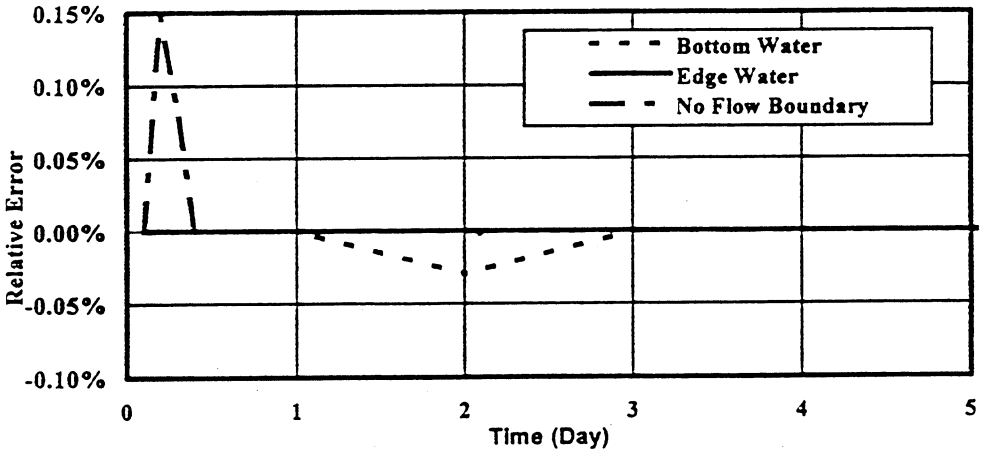

Fig. 6-16 Relative Errors of Reservoir Pressure with PI Scale-up for Different Boundary Conditions

CHAPTER VII

CONCLUSIONS AND RECOMMENDATIONS

Different strategies of geological modeling were applied as discussed in Chapter III, and three models for Gypsy formation were developed. The methodology for scale-up of transmissibility was described and illustrated in Chapter IV. Two hypothetical models were used to illustrate the application of scale-up, in which both no pinch-out and pinch-out alternatives were considered. Scale-up was conducted for the Gypsy channel, lithofacies, and flowunit models to study the effects of geological modeling process on the scale-up and performance prediction. To study the effects of well location and boundary condition on scale-up, three different production-injection scenarios and three different boundary conditions were considered for the Gypsy channel model and scale-up process were conducted.

7.1 Conclusions

Based on the analysis, modeling and simulation studies conducted in Chapter III to Chapter VI, the following conclusions are obtained:

1. Strategies of geological modeling produce significant effects on scale-up. Obvious differences in scale-up results occurred between the three Gypsy models. Based on the scale-up results obtained from this study, the channel model and the lithofacies model produce similar results, but flowunit model provides inferior results. In order to obtain a satisfactory scale-up result, the vertical variation of reservoir properties

must minimized in determining the boundary layers to be merged, and the horizontal continuity of the scale-up volume should be as wide as possible.

2. The transmissibility scale-up is only suitable for linear flow. For radial flow around the wellbore, scale-up on productivity index must be conducted in order to obtain more accurate results. The results indicated that scale-up of the productivity index (PI) is important for the overall scale-up process. Significant improvements were obtained after conducting PI scale-up.
3. The strategy of transmissibility scale-up developed in this study is a recommended approach to pursue. Special considerations must be given to pinch-out existing in the model, otherwise, incorrect simulation results occur in the fine-scale simulation.
4. When the deterministic method was used to determine the distribution of reservoir properties, the search radius, R, has a significant effect on the resulting heterogeneity of the geological model. The extent of heterogeneity decreased with increasing values of R. Improved results could be obtained if different units use different search radius values.
5. Gypsy formation was not accurately characterized using the deterministic method, because the standard deviations obtained in all three models are lower than the standard deviation obtained from core analysis. The lithofacies model provided a better description than both the channel model and the flowunit model.
6. The well location in the production-injection scenario has significant effect on scale-up. Comparing the scale-up results of nine-spot drive, line-drive, and five-spot drive, the line-drive scenario obtained the best matches for both water production and reservoir pressure. This may be attributed to the dominating of the linear flow in the

line-drive scenario. Even though PI scale-up was conducted to reduce the error caused in radial flow, radial flow effects in nine-spot drive and fine-spot drive could not be satisfactorily reduced.

7. When five-spot or nine-spot drive scenarios were used in reservoir simulation, five-spot drive produced better scale-up results.
8. Comparing the scale-up results for three different boundary conditions, no-flow boundary condition obtained a better result compared to reservoir with a flow boundary condition. When flow boundary condition is applied in scale-up, the bottom-water drive produced larger error than the edge-water drive.

7.2 Recommendations for the Future Studies

The effects of geological modeling, well location, production-injection scenario, and boundary condition on scale-up have been studied and evaluated in this study. However, there are several areas that should be further studied. The following areas are recommended:

1. This study focused on the geological modeling using the deterministic method. In Chapter III, the Gypsy models were not accurately described because the standard deviations obtained from modeling for both porosity and permeability were much lower than these obtained from core analysis. Geostatistical method should be applied to generate geological models to compare the scale-up results with the results obtained using deterministic method.

2. Only vertical scale-up was evaluated in this study. The horizontal continuity of reservoir is also very important. Therefore, scale-up including horizontal direction

should be conducted to study the effects of horizontal continuity on scale-up. When both the horizontal and vertical directions are evaluated, an optimum scale-up result could be proposed.

3. In this study, the problem of pinch-out in vertical direction was evaluated. However, fluid flow in the horizontal direction, when pinch-out exists, can also cause incorrect simulation of flow. Therefore, the effect of horizontal continuity of reservoir on scale-up should be conducted.

4. The methodology proposed in this study for scale-up produced successful scale-up results. However, the scale-up was conducted outside of the simulator, i.e., fine-scale simulation was run first. Data for flow rate and pressure for fine-scale grid blocks were obtained from an output map file. This process is cumbersome. A possible approach for streamlining the process is to incorporate the methodology into the simulator, or to develop an external program which is invoked by the simulator.

NOMENCLATURE

a	coefficient in Archie's equation
B	formation volume factor (rb/stb)
B_w	volume factor of reservoir water (rb/stb)
C_1	coefficient,
C_2	coefficient,
E_{datum}	elevation of reference datum (ft)
$E_{i,j,k}$	elevation of grid block (i,j,k) (ft)
FZI	flow zone indicator
gf	geometry factor
h	thickness of grid block (ft)
h	thickness of production layer (ft)
k	permeability (μm^2)
k	permeability of production layer (md)
K	permeability (μm^2)
k_{layer}	permeability for the layer (mD)
k_r	relative permeability of fluid
k_{ray}	permeability for the ray (mD)
k_{rw}	relative permeability of water
k_x	average permeability of the two half grid blocks (mD)

K_Y	average permeability of the two half grid blocks (mD)
k_z	average permeabilities of the two half grid blocks (mD)
L	total number of layer
m	porosity exponent
M	mobility of the fluid
n	water saturation exponent in Archie's equation
n	number of layer upscaled
n	total number of well values used
n_{ray}	total number of ray
n_{bray}	total number of block in a ray
Nwi	cumulative water injection rate (Mbbl)
Nwp	cumulative water production (Mbbl)
P	pressure (psi)
p	pressure of fine-scale grid block (psi)
P_f	wellblock pressure of fine grid (psi)
P_c	wellblock pressure of coarse grid (psi)
P_w	wellbore pressure (psi)
p_g	average pressure of wellblock (psi)
p_b	bottom hole pressure (psi)
$p_{i,j}$	wellblock pressure (psi)
PI	productivity index (stb/day-psi)
PI_c	productivity index of coarse grid (bbl/day/psi)

PI_f productivity index of fine gird (bbl/day/psi)

Δp_x pressure difference between two grid blocks in x direction

Δp_y pressure difference between two grid blocks in y direction

$q_{i+1/2,j}$ flux between two grid blocks

Q flow rate (bbl/day)

Q_t total flow rate of well (STB/day)

Qwi water injection rate (bbl/day)

Qwp water production rate (bbl/day)

Q_x flow rate in x directions (STB/day)

Q_y flow rate y directions (STB/day)

Q_z flow rate z directions (STB/day)

r radius of cylindrical tube (μm)

r distance between well and the interpolated point

r_b equivalent radius (Peaceman) of the gridblock containing the well (ft)

r_{fi} farthest point from i-th block to the well (ft)

r_{ni} nearest point from i-th block to the well (ft)

r_w wellbore radius (ft)

r_e drainage radius (ft)

R search radius

R_w resistivity of formation water (ohm-m)

R_{ti} true formation resistivity at irreducible water condition (ohm-m)

RQI reservoir quality index

s	skin factor (dimensionless)
S_{wi}	irreducible water saturation (fraction)
T_b	transmissibility between well to wellblock (ft. mD)
T_x	transmissibility in x direction (ft. mD)
T^{xx}	normal transmissibility between two grid blocks (ft. mD)
T^{yy}	cross transmissibility between two grid blocks (ft. mD)
T_y	transmissibility in y direction (ft. mD)
T_z	transmissibility in z direction (ft. mD)
v	volume of fine-scale grid block (ft^3)
V	final cell value in deterministic equation
V_C	value obtained from coarse scale
V_F	value obtained from fine scale
W	weighting function in deterministic equation
WI	well injectivity index (dimensionless)
w_{ray}	weighting coefficient of the i-th ray
x	dimension of grid block in x direction (ft)
X	power factor
Δx	length of grid block in x direction (ft)
y	dimension of grid block in y direction (ft)
Δy	length of grid block in y direction (ft)
z	dimension of grid block in z direction (ft)
Z	well value

Δz	length of grid block in z direction (ft)
ϕ	porosity (fraction)
Φ	potential of grid block (psi)
μ	viscosity (cp)
ϕ	porosity of fine-scale grid block (fraction)
ρ_f	density of fluid in reservoir (g/ cm^3)
μ_w	viscosity of reservoir water (cp)
δ	relative error

REFERENCES

Aasum, Y., Kasap, E. and Kelkar, M.: "Scale-Up of Tensional Effective Permeability to Detect Anisotropy Through MFP Measurements," *Reservoir Characterization III*, PennWell Publishing Company, 1991, p841.

Aasum, Y., Kasap, E. and Kelkar, M.: "Analytical Upscaling of Small-Scale Permeability Using a Full Tensor," SPE 25913 presented at the SPE Rocky Mountain Regional/Low Permeability Reservoir Symposium, Denver, CO, April 12-14, 1993.

Amaefule, J.O. *et al.*: "Enhanced Reservoir Description: Using Core and Log Data to Identify Hydraulic (Flow) Units and Predict Permeability in Uncored Intervals/Wells," paper SPE 26436 presented at the 1993 SPE Annual Technical Conference and Exhibition, Houston, TX, Oct. 3-6.

Begg, S.H., Carter, R.R. and Dranfield, P.: "Assigning Effective Values to Simulator Gridblock Parameters for Heterogeneous Reservoirs," *SPERE*, Nov. 1989, p. 455-463.

Begg, S.H. and King, P.R.: "Modeling the Effects of Shales on Reservoir Performance: Calculation of Effective Vertical Permeability," SPE 13529 Presented at the 1985 Reservoir Simulation Symposium held in Dallas, TX, Feb. 10-13, 1985.

Carmen, P. C.: " Fluid Flow Through Granular Beds," *Trans. AICHE* (1937) v. 15, 150-166.

Cardwell, Jr. W. T. and Parsons, R. L.: "Average Permeabilities of Heterogeneous Oil Sands," *Petroleum Technology*, March 1945, p34-42.

Chopra, A.K., Severson, C.D., and Carhart, S.R.: "Evaluation of Geostatistical Techniques for Reservoir Characterization," SPE 20734 Presented at the 65th Annual Technical Conference & Exhibition Held in New Orleans, LA, Sept. 23-28, 1990.

Christie, M. A.: "Upscaling for Reservoir Simulation," *JPT*, Nov. 1996, p1004-1010.

Christie, M. A., Mansfield, M., King, P. R. Barker, J.K. and Culverwell, I. D.: "A Renormalisation Based Upscaling Technique for WAG Floods in Heterogeneous Reservoirs," ," SPE 29127 presented at the 13th SPE Symposium on Reservoir Simulation, San Antonio, TX, Feb. 12-15, 1995.

Collins, R. E.: *Flow of Fluids Through Porous materials*, PennWell Publishing Company, Tulsa, Oklahoma, 1961.

Collins, T. M.: "Methodology for Constructing High Resolution Three Demensional Reservoir Characterization Models for Petroleum and Environmental Applications," Master's Thesis, University of Oklahoma, Norman, 1996.

Craft B.C and Terry, R.E.: *Applied Petroleum Reservoir Engineering*, prentice Hall, Englewood Cliffs, NJ, 1989.

Craig, Jr. F.F.: "Effect of Reservoir Description on Performance Predictions," *JPT*, Oct. 1970, p1239-1245.

Damsleth, E. *et al*: "Scale Consistency From Cores to Geological Description," SPE 24700 Presented at the 67th Annual Technical Conference and Exhibition of the Society of Petroleum Engineers held in Washington, DC, Oct. 4 -7, 1992.

Ding, Y.: "Scaling-up in the Vicinity of Wells in Heterogeneous Field," SPE 29137 presented at the 13th SPE Symposium on Reservoir Simulation, San Antonio, TX, Feb. 12-15, 1995.

Ding, Y. and D. Urgelli.: "Upscaling of Transmissibility for Field Scale Flow Simulation in Heterogeneous Media," SPE 38016 presented at the 14th Symposium on Reservoir Simulation held in Dallas, TX, U.S.A., June 8-11, 1997.

Doyle, J.D. ans Sweet, M.L.: "Geological Characterization of the IRD GYPSY Study Sites," BP Exploration Internal Report No. H092072, June, 1992.

Doyle, J.D., O'Meara Jr., D.J., and Witterholt, E.J.: "The "Gypsy" Field Research Program in Integrated Reservoir," SPE 24710 Presented at the 67th Annual Technical Conference and Exhibition of the Society of Petroleum Engineers held in Washington, DC, Oct. 4-7, 1992.

Dubrule, O. and Haldorsen, H.H.: "Geostatistics for Permeability estimation," *Reservoir Characterization*, 1986, p223.

Durlofsky, L.J., Milliken, W.J., Dehghani, K. and Jones, R.C.: "Application of a New Scale Up Methodology to the Simulation of Displacement Processes in Heterogeneous Reservoirs," SPE 28704 presented at the SPE International Petroleum Conference & Exhibition of Mexico, Veracruz, Mexico, Oct. 10-13, 1994.

Durlofsky, L. J. *et al.*: "Scale Up of Heterogeneous Three Dimensional Reservoir Descriptions," SPE 30709 presented at the 1995 SPE Annual Technical Conference and Exhibition, Dallas, TX, Oct. 22-25.

Ehlig-Economides, C. A.: "Engineering Application for Integrated Reservoir Characterization," SPE 29994 Presented at the Internatioal Meeting on Petroleum Engineering Held in Beijing, P.R. China, Nov. 14 -17, 1995.

Elkewidy, T. I.: "Characterization of Hydraulic (Flow) Units in Heterogeneous Clastic and Carbonate Reservoirs," Ph.D. Dissertation, The University of Oklahoma, Norman (1996).

Finley, R.J. and Tyler, N.: "Geological Characterization of Sandstone Reservoirs," *Reservoir Characterization*, 1986, p1.

Forgotson, Jr. J.M.: "Role of Reservoir Characterization in Improved Petroleum Recovery," Class Note, 1996.

Gautier, Y. and Nætinger, B.: "Preferential Flow-Paths Detection for Heterogeneous Reservoirs Using a New Renormalization Technique," Topic C: Scale Change Procedure, 1994 European Conference on the Mathematics of Oil Recovery, Røros, Norway, June, 7-10.

GeoGraphix, Inc., *GES User's Guide*, Nov., 1994.

Ghori, S.G., Ouenes, A., Pope, G.A., and et al.: "The Effect of Four Geostatistical Methods on Reservoir Description and Flow Mechanism," SPE 24755 Presented at the 67th Annual Technical Conference and Exhibition of the Society of Petroleum Engineers held in Washington, DC, Oct. 4 -7, 1992.

Guzman, R.E. *et al.*: "Evaluation of Dynamic Pseudo Functions for Reservoir Simulation," SPE 35157 presented at the 1996 SPE Annual Technical Conference and Exhibition, Denver, CO, Oct. 6-9.

Haldorsen, H. H.: "Simulator Parameter Assignment and the Problem of Scale in Reservoir Engineering," *Reservoir Characterization I* , Academic Press, INC., 1986, p293-340.

Haldorsen, H. H. and Damsleth, E.: "Stochastic Modeling," *JPT*, April, 1990, p404-412.

Harris, D.G.: "The Role of Geology in Reservoir Simulation," *JPT*, May, 1975, p625-632.

Harris, D.G. and Hewitt, C.H.: "Synergism in Reservoir Management - The Geological Perspective," *JPT*, July, 1977, p761-770.

Hearn, C.L., Ebanks, W.J., and Ranganathan, V.: "Geological Factors Influencing Reservoir Performance of the Hartzog Draw Field, Wyoming," *JPT*, August, 1984, p1335-1344.

Hearn et al.: "Reservoir Characterization for Simulation, Hartzog Draw Field, Wyoming," Reservoir Characterization, 1986, p341.

Hewett, T. A. and Archer, R.A.: "Scale-Averaged Effective Flow Properties for Coarse-Grid Reservoir Simulation," SPE 37988 presented at the 1997 SPE Reservoir Simulation Symposium held in Dallas, TX, 8-11, June 1997.

Hilchie, D.W: "Reservoir Description Using Well Logs," *JPT*, July 1984, p1067-73.

Holden, L., More, H., and Tjemeland, H.: "Integrated Reservoir Description," SPE 24261 Presented at the SPE European Petroleum Computer Conference held in Stavanger, Norway, May 25-27, 1992.

Jacks, H.H., Smith, O.J.E. and Mattax, C.C.: "The Modeling of a Three-Dimensional Reservoir with a Two-Dimensional Reservoir Simulator-The Use of Dynamic Pseudo Function," *SPEJ*, June, 1973, p. 177-185.

Jones, A. King, P., McGill, C., and Williams, J.: "Renormalization: A Multilevel Methodology for Upscaling," *Reservoir Characterization III*, PennWell Publishing Company, 1991, p823-833.

Journel, A. G.: "Geostatistics for Reservoir Characterization," Paper SPE 20750 presented at the 65th Annual Technical Conference and Exhibition of the Society of Petroleum Engineers held in New Orleans, LA, Sept. 23-26, 1990.

King, M.J.: "Application and Analysis of Tensor Permeability to Cross-Bedded Reservoir," *Proc.*, Seventh European IOR Symposium, Moscow (1993).

King, P.R.: "The Use of Renormalization for Calculating Effective Permeability," *Transport in Porous Media*, 4, 37-58 (1989).

King, P.R., Muggeridge, A.H., and Price, W.G.: "Renormalization Calcculations of Immiscible Flow," *Transport in Porous Media*, 12, 237-260 (1993).

King, P.R. and Williams, J.K.: "Upscaling Permeability: Mathematics of Renormalization," 1994 European Conference on the Mathematics of Oil Recovery, Røros, Norway, June, 7-10.

Kossack, C.A., Aasen, J.O. and Opdal, S.T.: "Scaling Up Heterogeneities with Pseudo Functions," *SPEFE*, Sept. 1990, p. 226-232.

Kumar, A.T.A. and Jerauld, G.R.: "Impacts of Scale-up on Fluid Flow from Plug to Gridblock Scale in Reservoir Rock," Paper SPE/DOE 35452 presented at the 1996 SPE/DOE 10th Symposium on Improved Oil Recovery held in Tulsa OK, 21-24, April 1996.

Kyte, J. R. and Berry D. W.: "New Pseudo Functions to Control Numerical Dispersion," *SPEJ*, Aug. 1975, p. 269-276.

Landmark Graphics Corporation: *Stratigraphic Geocellular Modeling Reference Guide*, Dec. 1995.

Lasseter, T. J., Waggoner, J. R. and lake, L. W.: "Reservoir Heterogeneity and Their Influence on Ultimate Recovery," *Reservoir Characterization I*, Academic Press, INC., 1986, p544-556.

Lee, J., Kasap, E. and Kelkar, M.G.: "Development and Applications of a New Upscaling Technique," SPE 30712 presented at the 1995 SPE Annual Technical Conference and Exhibition, Dallas, TX, Oct. 22-25.

Li. D.: "Scaling and Upscaling of Fluid Flow Through Through Permeable Media," Ph.D. Dissertation, U. of Texas, Austin (1994).

Li, D. and Lake, L.W.: "Scaling Fluid Flow Through Heterogeneous Permeable Media," SPE 26648 presented at the 1993 SPE Annual Technical Conference and Exhibition, Houston, TX, Oct. 3-6.

Li. D., Cullick, A.S. and Lake, L.W.: "Global Scale-Up of Reservoir Model Permeability with Local Grid," *J. Petro Sci. & Engir.*, 14 (Dec. 1995) 1-13.

Mattax, C. C. and Daiton, R. L.: *Reservoir Simulation*, SPE Monograph Vol 13, 1990.

O'Meara Jr., D.J. and Jiang, R.: "The Gypsy Outcrop Model for testing Geostatistical Methods," SPE 35477 presented at the European 3-D Reservoir Modeling Conference held in Stavanger, Norway, 16-17 April, 1996.

Peaceman, D.W.: "Effective Transmissibilities of a Gridblock by Upscaling - Why Use Renormalization," SPE 36722 presented at the 1996 SPE Annual Technical Conference and Exhibition, Denver, CO, Oct. 6-9.

Peaceman, D. W.: *Fundamentals of Numerical Reservoir Simulation*, Elsevier Scientific Publishing Co., Amsterdam, 1977.

Pickup, G.E. and Sorbie, K.S.: "The Scaleup of Two-Phase Flow Using Permeability Tensor," Topic C: Scale Change Procedure, 1994 European Conference on the Mathematics of Oil Recovery, Røros, Norway, June, 7-10.

Pickup, G.E. and Sorbie, K.S.: "Development and Application of a New Two-Phase Scaleup Method Based on Tensor Permeability," SPE 28586 presented at the SPE 69th Annual Technical Conference and Exhibition, New Orleans, LA, Sept. 25-28, 1994.

Pickup, G.E. *et al.* :" A Method for Calculating Permeability Tensors Using Perturbed Boundary Conditions," *Proc.*, Third European Conference on the Mathematics of Oil Recovery, M.A. Christie et al. (eds.), Delft U. Press, Delft, The Netherlands (1992) 225.

Rodriguez, A. and Maraven, S.A.: "Facies Modeling and the Flow Units Concept as a Sedimentological Tool in Reservoir Description," SPE 18154 Presented at the 63dr Annual Technical Conference and Exhibition of the Society of Petroleum Engineers held in Houston, TX, Oct. 2-5, 1988.

Saad, N., Kalkomey, C.T., and Ouenes, A.: "Optional Gridding of Stochastic Models for Scaleup," Topic A: Geometrical Characterization, 1994 European Conference on the Mathematics of Oil Recovery, Røros, Norway, June, 7-10.

Scuta, M.S.: "Flow Units and Upscaling of a Complex Carbonate Reservoir Using a 3-D Geological Model," SPE paper presented at the SPE Annual Technical Conference and Exhibition held in San Antonio, TX, Oct. 5-8, 1997.

Shedid, A.: "Influence of Stress on the Petrophysical Properties of Flow units in Clean and Shaly Heterogeneous Formation," Ph.D. Dissertation, The University of Oklahoma, Norman, 1997.

Slatt, R.M. and Hopkins, G.L.: "Scales of Geological Reservoir Description for Engineering Applications: North Sea Oilfield Example," SPE 18136 presented at the 1988 SPE Annual Technical Conference and Exhibition, Houston, TX, Oct. 2-5.

Sllseth, J.K., MavDonald, A.C., Alvestad, J. *et al.*: "Impact of Flow-Unit Reservoir Description on Simulated Waterflood Performance," SPE 20603 Presented at the Annual Technical Conference & Exhibition Held in New Orleans, Sept. 23-26, 1990.

Soeriawinata, J., and Kelkar, M.: "Permeability Upscaling for Near-Wellbore Heterogeneities," SPE 36518 presented at the 1996 SPE Annual Technical Conference and Exhibition, Denver, CO, Oct. 6-9.

Staggs, H.M. and Herbeck, E.F.: "Reservoir Simulation Models - An Engineering Overview," *JPT*, Dec. 1971, p1428-36.

Stalkup, F.I.: "Permeability Variations Observed at the Faces of Crossbedded Sandstone Outcrops," *Reservoir Characterization I,* Academic Press, Inc., 1986, p141-175.

Stone, H.L.: "Rigorous Black Oil Pseudo Function," SPE 21207 presented at the 11th SPE Symposium on Reservoir Simulation, Anaheim, CA, Feb. 17-20, 1991.

Stoudt, E. L., Thomas, A. R., Ginger, E. P. and Vinopal, R. J.: "Geologic Reservoir Characterization for Engineering Simulation, Hatter's Pond Field, Mobil County, Alabama," SPE 24713 presented at the 67th Annual Technical Conference and Exhibition of the Society of Petroleum Engineers held in Washington, DC, Oct. 4-7, 1992.

Taggart, I. L., Soedarmo, E. and Paterson, L.: "Limitations in the Use of Pseudofunctions for Up-Scaling Reservoir Simulation Models," SPE 29126 presented at the 13th SPE Symposium on Reservoir Simulation, San Antonio, TX, Feb. 12-15, 1995.

Testerman, J.D.: "A Statistical Reservoir-Zonation Technique," *JPT*, Aug. 1962, p889-893.

Tegnander, C. and Gimse, T.: "Flow Simulations To Evaluate Upscaling of Permeability," *Mathematical Geology*, Vol. 30, No. 6, 1998.

Thibeau, S. and Barker, J.W.: "Dynamical Upscaling Techniques Applied to Compositional Flows," SPE 29128 presented at the 13th SPE Symposium on Reservoir Simulation, San Antonio, TX, Feb. 12-15, 1995.

Ti. G. *et al.*: "Use of Flow Unit as a Tool for Reservoir Description: A Case Study," *SPE Formation Evaluation*, June, 1995, p122-128.

Ti, G., Ogbe, D.O., Munly, W., and Hatzignatiou, D.G.: "Use of Flow Units as a Tool for Reservoir Description: A Case Study," *SPEFE*, June 1995, p122-128.

Turpening, W.R., Chon, Y.T., and Pepper, R.E.F. *et al*: "Detection of Bed Continuity Using Crosswell Data: A Gypsy Pilot Site Study," SPE 24711 Presented at the 67th Annual Technical Conference and Exhibition of the Society of Petroleum Engineers held in Washington, DC, Oct. 4-7, 1992.

Wattenbarger, R.C., Aziz, K. and Orr, Jr. F.M.: "Optimal Scales for Representing Reservoir Heterogeneity," *Reservoir Characterization III*, PennWell Publishing Company, 1991, p195-225.

Weber, K.L. and Geuns, L.C: "Framework for Constructing Clastic Reservoir Simulation Models," *JPT*, Oct. 1990.

Willhite, G.P: *Water Flooding,* SPE Texrbook Series Vol. 3, 1986.

White, C.D. and Horne, R.N.: "Computing Absolute Transmissibility in the Presence of Fine-Scale Heterogeneity," SPE 16011 Presented at the North SPE Symposium on Reservoir Simulation held in San Antonio, TX, Feb. 1-4, 1987.

APPENDIX A

DIFINITIONS OF PARAMETERS IN THE PROGRAM FOR SCALE-UP

DPTX potential difference between two grid block of coarse-scale model in x direction (psi)

DPTY potential difference between two grid block of coarse-scale model in y direction (psi)

DPTZ potential difference between two grid block of coarse-scale model in z direction (psi)

DTM reference elevation (ft)

DX dimension of grid block in x direction (ft)

DY dimension of grid block in y direction (ft)

ELV elevation at the center of the grid block (ft)

GRA gravity of water (gm/cc)

H1 thickness of grid block for fine-scale model (ft)

H2 thickness of gird block for coarse scale model (ft)

I gird number in x direction for fine-scale model

J gird number in y direction for fine-scale model

KH1 KX1*H1 for fine-scale model

KH2 KX2*H2 for coarse scale-model

KX1 permeability of fine-scale gird block in x direction (mD)

KX2 permeability of coarse-scale gird block in x direction (mD)

KY1 permeability of fine-scale gird block in y direction (mD)

KY2 permeability of coarse-scale gird block in y direction (mD)

KZ1 permeability of fine-scale gird block in z direction (mD)

KZ2 permeability of coarse-scale gird block in z direction (mD)

L1 total grid number in z direction for coarse-scale model

L2 total grid number in z direction for fine-scale model

LL1 layer number in fine-scale model for the layers at the top boundary of coarse-scale model

LL2 layer number in fine-scale model for the layers at the bottom boundary of coarse-scale model

M total grid number in x direction for coarse-scale model

N total grid number in y direction for coarse-scale model

P1 pressure of grid block for fine-scale model (psi)

P2 pressure of grid block for coarse-scale model (psi)

PHI1 porosity of grid block for fine-scale model (%)

PHI2 porosity of grid block for coarse-scale model (%)

PHIV1 pore volume of fine-scale grid block

PRV1 PHI1*V1 for fine-scale model (ft^3)

PT potential of coarse-scale gird block (psi)

QX1 flow rate of gird block in x direction of fine-scale model (bbl/day)

QY1 flow rate of gird block in y direction of fine-scale model (bbl/day)

QZ1 flow rate of gird block in z direction of fine-scale model (bbl/day)

QX2 flow rate of gird block in x direction of coarse-scale model (bbl/day)

QY2 flow rate of gird block in y direction of coarse-scale model (bbl/day)

QZ2 flow rate of gird block in z direction of coarse-scale model (bbl/day)

TOPE elevation at top of the model (ft)

TX transmissibility of coarse-scale model in x direction (bbl-cp/day-psi)

TY transmissibility of coarse-scale model in y direction (bbl-cp/day-psi)

TZ transmissibility of coarse-scale model in z direction (bbl-cp/day-psi)

UW viscosity of water (cp)

V1 volume of gird block for fine-scale model (ft^3)

V2 pore volume of coarse-scale grid block (ft^3)

Appendix B

Strategies of Geological Modeling and Heterogeneity of Formation

by

Wei Wang and Anuj Gupta

Presented at The 3rd Young Academy Conference of Scientific Association of China, 1998

Paper for the 3rd Young Academy Conference of Scientific Association of China

Strategies of Geological Modeling and Heterogeneity of Formation

Wei Wang and Anuj Gupta
(The University of Oklahoma, USA)

Abstract

The objective of this study is to develop an effective vertical layering method for scaling of petrophysical properties used for reservoir simulation by using the available information from well logs and core analysis. Three different geological models for Gypsy formation were generated for the purpose of reservoir characterization and upscaling study by following different strategies of geological modeling. Twenty two lithofacies units were identified within seven channels in Gypsy formation based on the distribution of lithofacies from 22 wells. Ten flow units were defined using the methodology proposed by Amaefule *et al.* The statistical characteristics of heterogeneity for the generated geological models were analyzed by comparing the characteristics obtained from core measurement with one from geological modeling.

Key Words: Reservoir, Characterization, Heterogeneity

1. INTRODUCTION

One limitation of commonly available scale-up methods is that they concentrate only on the mathematics of combining petrophysical properties of fine grid blocks, but with little consideration on the geological heterogeneity and structural details. Such methods choose the coarse-grid cell boundaries while ignoring the distribution of reservoir properties. The reservoir properties are averaged within layers or channels without considering the effect of heterogeneity on fluid flow and scale-up. Such 'layer or channel" scale-up may erase the effects of extreme values of reservoir properties, such as thin continuous communicating layers, large flow barriers, or partially communicating faults. In order to obtain result for scale-up in reservoir simulation that capture the essence of flow behavior, it is very important to find an effective method to determine the boundaries of upscaled grid blocks, in addition to having a robust mathematical algorithm to obtain the average value of reservoir properties for the upscaled grid blocks. Representative scale-up result can only be obtained with both a good mathematical scale-up method and a good understanding and description of formation heterogeneity. Therefore, the objective of this study is to develop an effective vertical layering method for scaling of petrophysical properties used for reservoir simulation by using the available information from well logs and core analysis.

Gypsy Formation, which is a non-oil bearing formation and located in northeastern Oklahoma near Lake Keystone, was used as the experimental site in this study because of the extensive data available from this formation. 22 wells were drilled for the purpose of data collection and1,056 cores were obtained. Permeability, porosity, and lithofacies were measured and determined at one foot interval or at smaller spacing when there was a significant change in rock properties within one foot.

2. GEOLOGICAL ENVIROMENT OF GYPSY FORMATION

Six channels and one crevasse-splay, totally seven channels, were identified within Gypsy formation. Channel sandbodies are subparallel and trend north to northwest. They range from 6 to 21 ft thick and 150 to 560 ft wide. The lower contact of each channel sandbody is erosional, and upper contacts may be erosional with younger channels or conformable with floodplain deposits. All of the channels are surrounded or partially subdivided by floodplain deposits which are dominantly composed of impermeable mudstone and siltstone. Five sandstone lithofacies were identified within Gypsy sandbodies. They are mudclast, cross-beds, plane-beds, ripple, and overbank. The lateral extent of lithofacies is commonly less than 100 ft.

Mudclast sandstone is more extensively developed in the lower three channels. The characteristic grains of this facies are cobble stones to medium sand-size intraclasts of red, green, and/or grey mudstone. The individual facies is typically 1 to 3 ft thick. Cross-bed sandstone is composed of 0.3 to 3 ft thick sets of cross-bedding. The grain size is very fine to medium sand with some coarse sand and granule-size intraclasts being present on foreset laminations. Plane-beds sandstone is fine to very fine grained sandstone with a planar bedding ranging from 0.5 to 3 ft thick. Ripple sandstone is fine to very fine sandstone and often interlaminated with mudstone and siltstone. Overbank is mainly composed of impermeable mudstone and siltstone ranging 4.5 to 13 ft thick[1].

3. DEVELOPMENT OF 3-D GEOLOGICAL MODELS

Three geological models, channel model, lithofacies model, and flow unit model, were developed in this study to characterize Gypsy sandstone formation and will be used to conduct the scale-up study. Landmark's Stratigraphic Geocellular Modeling[3] (SGM) was used as the modeling tool in this study, which models heterogeneous rock and fluid properties in three dimensions for geological analysis and visualization. SGM uses stratigraphic pattern to generate a three-dimensional framework for geological models. The surface maps representing the distribution of layers in space were generated by GeoGraphix Exploration System[4] (GES). The modeling area is 1,627,083 ft^2 with a grid of 36 by 42.

3.1 Channel Model

During BP's Integrated Reservoir Description Project between 1989 to 1992, 1,056 cores from 22 wells were obtained and described, and seven channels were identified. Based on these information, fourteen surface maps were generated to build up a 3-D channel model for Gypsy formation.

Deterministic method was used to determine the distribution of reservoir properties, including permeability and porosity. One of the important parameters, which effects the heterogeneity of geological model, is the characteristic radial correlation length, R. There exist a minimum and a maximum value of R. The minimum allowable value of R is the one using which no null values will be created. The maximum allowable value of R is the one that allows the best characterization of reservoir heterogeneity. To determine a value of R applicable for Gypsy formation, several R values were used to generate 3-D models. The statistical characteristics of the heterogeneity of the models were then compared with the one obtained from core analysis. Statistical mean and standard deviation were used to evaluate the R values used. Figures 1 to 4 illustrate the statistical characteristics of channel models, when three different R values were used, compared with the statistical characteristics from core analysis. 534 ft was found to be the minimum R for the channel model of Gypsy formation, because some null values will be observed when a smaller R than 534 ft was used. The geological models become more homogeneous as R increases, as is apparent from the smaller values of standard deviations for the porosity and permeability with increasing R values. This is consistent with the principle of deterministic algorithm. In fact, 534 ft is still not a good value enough to characterize the heterogeneity of Gypsy formation. However, null values occurs if a smaller R value is used. Therefore, 534 ft was determined to be the R value for Gypsy channel model. It can be observed that the mean and standard deviation of porosity are not very sensitive to R values, but the mean and standard deviation of permeability are.

Fig. 5 is a cross-sectional view of the channel model. There are in total thirteen layers in the channel model, including the six layers between seven channels, in which each channel was taken as one layer. The lower or the upper contacts of some of the channels are erosional. All of the channels are surrounded or partially subdivided by floodplain deposits which are dominantly composed of impermeable mudstone and siltstone.

3.2 Lithofacies Model

Five sandstone lithofacies were mainly identified within Gypsy formation based on the analysis on 1,056 cores. Based on these data, the cross-plot of porosity and permeability for Gypsy sandstone is shown in Fig. 6. It was observed that cross-beds, plane-beds, and mudstone are more homogeneous compared with ripple and mudclast. Cross-beds and plane-beds have the best and similar properties. Mudstone presents the lowest values of porosity and permeability. The properties of ripple are between cross-beds, plane-beds and mudstone. Mudclast is the most heterogeneous lithofacies in Gypsy sandstone formation, which shows a wide distribution of properties in Fig. 7.

To develop a lithofacies model, initial identification of lithofacies' layers is necessary. The boundaries of channel may not be crossed by such lithofacies' layers, because floodplain or mudstone layers exist which act as flow barriers between channels, even though they are not continuous over the whole formation area. It is very important that a lateral correlation for each lithofacies unit between wells exists and this correlation is mappable. Therefore, it is required that each individual lithofacies within a channel must occur at least in two wells. If it exists only in one well and its thickness is less than one foot, it will be ignored and combined with the lithofacies unit which is neighbor and has similar properties. Observing the distribution of lithofacies in 22 wells, it is apparent that five kinds of lithofacies are present and follow the sequence of overbank, ripple, planebeds, crossbeds, and mudclast, from top to bottom, except planebeds and crossbeds occur interchangeably in some wells. Because crossbeds and planebeds possess similar rock properties, as shown in Fig. 6, they were combined to be treated as one lithofacies unit. Hence, there were only four significant lithofacies units in each individual channel in lithofacies model. The top and bottom positions of each lithofacies unit in the study area were determined by observing the distribution of lithofacies given in 22 wells.

Based on the correlation of lithofacies obtained, another fifteen surface maps were generated, which formed another fifteen subunits in seven channels, This leads to totally twenty eight layers in lithofacies model, including 22 lithofacies layers. The characteristic radial correlation length, R, used for lithofacies model was 890 ft. Fig. 7 is a cross- sectional view of the lithofacies model.

3.3 Flow Unit Model

Channel model has only thirteen layers, including both channels and barriers between channels. Lithofacies model is probably the most homogeneous model we can obtain. However, the number of layers is twice that in channel model. In a practical reservoir simulation study, it is of significant benefit to develop a geological model which has less layers than lithofacies model, yet provide a satisfactory results in reservoir simulation and scale-up. Flow unit concept offers a possible approach that may accomplish such a geological model.

Flow unit has been defined in different ways in previous studies. Generally speaking, flow unit is defined as a volume of reservoir rock that is continuous laterally and vertically and has similar average petrophysical properties that affect fluid flow. Flow unit can be classified at megascopic scale based on the distribution of reservoir properties. It can be also defined based on the pore-throat geometry or structure at microscopic scale.

Amaefule et al.[5] proposed a methodology to identify and characterize hydraulic flow units based on a modified Kozeny-Carmen equation and the concept of mean hydraulic radius. According to their proposed method, a log-log plot of RQI ($0.0314\sqrt{\frac{k}{\phi}}$) versus ϕ_z ($\frac{\phi}{1-\phi}$) for the same flow unit with an idea pore geometry should follow a straight line. Shedid[6] extended the method to represent a real porous medium system in a generalized form. Based on his study, a log-log plot of RQI versus ϕ should form a straight line with a slope of $\frac{(C_2+1)m-1}{2}$ and an intercept of $\left(0.0314\sqrt{C_1} * \sqrt{\frac{R_{ti}}{aR_w}}\right)$. Here, C_1 and C_2 are the coefficients in permeability equation and in porosity exponent, respectively; m is porosity exponent; a is the coefficient in Archie's equation; R_t is the true formation resistivity at irreducible water condition; and R_w is formation water resistivity. Therefore, for a real porous medium system, the slope of the plot is not unit, but a function of coefficient and porosity exponent. The intercept of the plot is a function of coefficient in permeability equation, formation water resistivity, coefficient in Archie's equation, and true formation resistivity.

Overbank occurs on the tops of channel 1, 2, 4, and 6 only in Gypsy. It mainly consists of mudstone and siltstone which has an average permeability of 0.52 md. The rock with such low permeability offers significant resistance to fluid flowing through it. It acts as a flow barrier between two lithofacies. Floodplain deposits bound and partially subdivide the Gypsy sandstone. They are dominantly mudstone and siltstone, but include lenticular, fine-grained sandstones as well. To efficiently conduct reservoir simulation, it was combined with floodplain between-channels to reduce the number of active grid blocks in simulation model.

Only three kinds of lithofacies units need to be considered after combining overbanks with floodplain deposits in channels 1, 2, 4, and 6. Plotting RQI versus ϕ for each lithofacies unit on log-log plots, ten flow units were identified in the seven channels. The characteristic radial correlation length, R, used for flowunit model was 928 ft. Fig. 8 is a cross-sectional view of flow unit model.

4. ANALYSIS OF HETEROGENEITY

The statistical characteristics for lithofacies model and flowunit model are presented in Figs. 9 to 12, respectively. Comparing the statistical characteristics of porosity and permeability for the three models, it was observed that the characteristics of porosity were better characterized than these of permeability, because the means of porosity from three models are very close to that obtained from core measurements, and the differences in standard deviations from core measurement and models for porosity are smaller than that for permeability. This is because porosity has more homogeneous characteristic than permeability in Gypsy formation. Comparing three models, it was indicated that lithofacies model obtained better description than other two models, except the permeability of mudstone in lithofacies model has a greater deviation in both its mean and standard deviation. This was caused by its spare distribution and limiting data. In all three models, the heterogeneity of Gypsy formation was still not sufficiently described, even though an optimal characteristic radial correlation length, R, has been used in each model. In SGM, only one characteristic radial correlation length, R, can be used for all layers in each model. Because of the different distribution for different channels, lithofacies, or flowunits, this may lead to the homogenization during the generation of the geological models. Therefore, a better description may be obtained if different characteristic radial correlation length, R, could be used for different units in the generation of geological models when deterministic method is used.

5. CONCLUSIONS

1. Different strategies of geological modeling lead to different heterogeneity characteristics for the models generated. Lithofacies model has more homogeneous characteristics than channel model and flowunit model.
2. Deterministic method can be used to determine the distribution of reservoir properties. The characteristic radial correlation length, R, has a significant effect on the heterogeneity of geological model generated. The extent of heterogeneity decreases with the increase of value, R.
3. Improved results could be obtained by using different characteristic radial correlation length, R, for different units when deterministic method is used to determine the properties of model.

NOMENCLATURE

k = permeability, md; ϕ = porosity, %; m = porosity exponent; C_1, C_2 = coefficients;
R_w =formation water resistivity, ohm-m; a = coefficient in Archie's equation;
R_t = true formation resistivity at irreducible water condition, ohm-m.

REFERENCES

1. Doyle, J.D. and Sweet, M.L.: "Geological Characterization of the IRD GYPSY Study Sites," BP Exploration Internal Report No. H092072.

2. Doyle, J.D., O'Meara Jr., D.J., and Witterholt, E.J.: "The "Gypsy" Field Research Program Integrated Reservoir," SPE 24710 Presented at the 67th Annual Technical Conference and Exhibition of the Society of Petroleum Engineers held in Washington, DC, Oct. 4-7, 1992.
3. Stratigraphic Geocellular Modeling Reference Guide, Landmark Graphics Corporation, Dec. 1995.
4. GES User's Guide, GeoGraphix, Inc., Nov. 1994.
5. Amaefule, J.O. *et al.*: "Enhanced Reservoir Description: Using Core and Log Data to Identify Hydraulic (Flow) Units and Predict Permeability in Uncored Intervals/Wells," Paper SPE 26436 presented at the 1993 SPE Annual Technical Conference and Exhibition, Houston, TX, Oct. 3-6.
6. Shedid, A.: "Influence of Stress on the-Petrophysical Properties of Flow units in Clean and Shaly Heterogeneous Formation," Ph.D. Dissertation, The University of Oklahoma, Norman, 1997.
7. O'Meara Jr., D.J. and Jiang, R.: "The Gypsy Outcrop Model for Testing Geostatistical Methods," SPE 35477 presented at the European 3-D Reservoir Modeling Conference held in Stavanger, Norway, 16-17 April 1996.
8. Collins, T.M.: "Methodology for Constructing High Resolution Three Dimensional Reservoir Characterization Models for Petroleum and Environmental Application," Master's Thesis, The University of Oklahoma, Norman, 1996.

ACKNOWLEDGMENTS

The authors would like to thank The Institute for Reservoir Characterization and The School of Petroleum and Geological Engineering at the University of Oklahoma for the financial and technical supports.

AUTHORS

Wei Wang is a Ph.D. candidate of the School of Petroleum and Geological Engineering at the University of Oklahoma, U.S.A. She holds a BS in Petroleum Engineering from the Petroleum University of China (Huadong) in 1982 and a MS, from the University of Oklahoma, USA in 1993. Dr. Anuj Gupta is an assistant Professor in the School of Petroleum and Geological Engineering at the University of Oklahoma, USA He holds a Ph.D. and MS in Petroleum Engineering from the University of Texas at Austin, USA and a Bachelor of Engineering in Mechanical Engineering from the Delhi University, India. His research interests include rock-fluid interactions, petrophysics, reservoir characterization, wettability, fracturing fluids, and coiled tubing hydraulics.

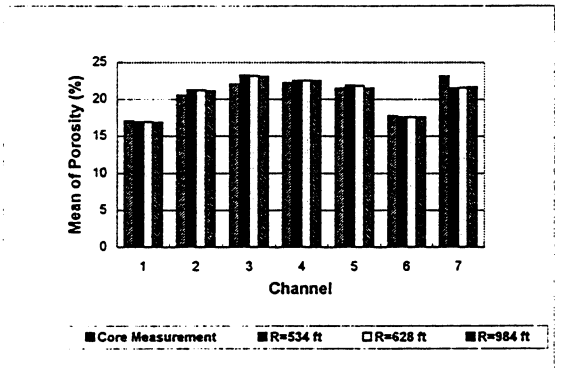

Fig. 1 Statistical Mean of Prosity for Channel Model

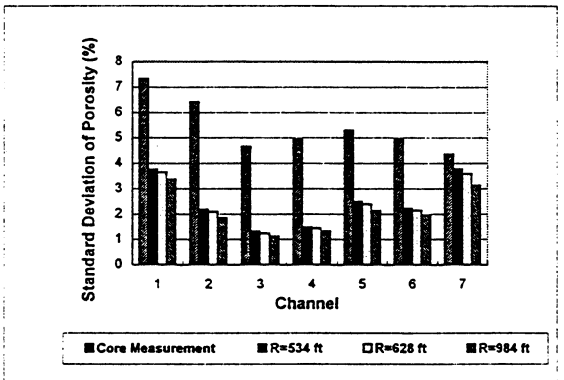

Fig. 2 Standard Deviation of Prosity for Channel Model

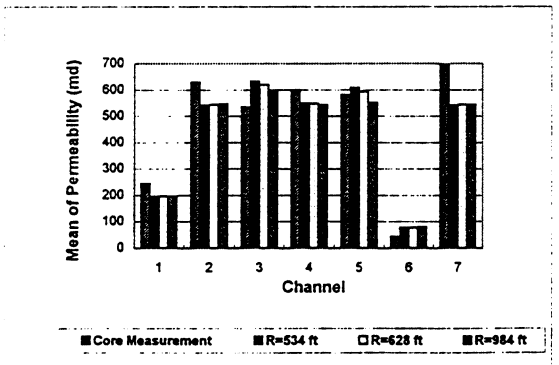

Fig. 3 Statistical Mean of Permeability for Channel Model

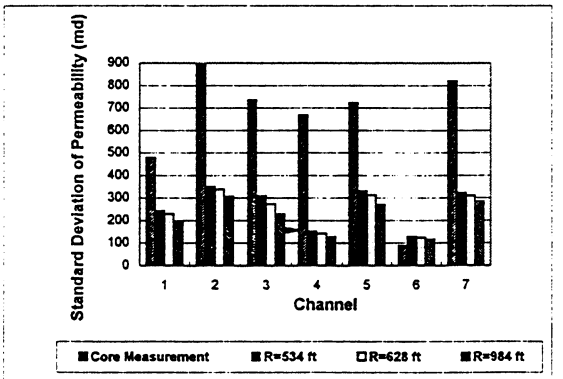

Fig. 4 Standard Deviation of Permeability for Channel Model

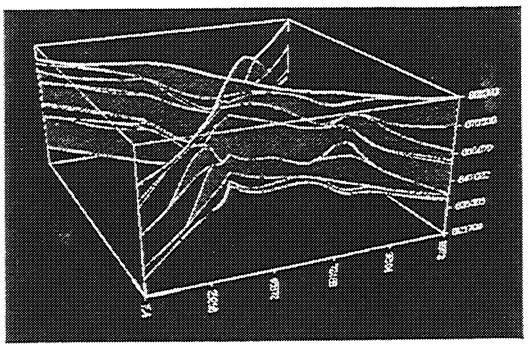

Figure 5. Cross-Sectional View of Channel Model

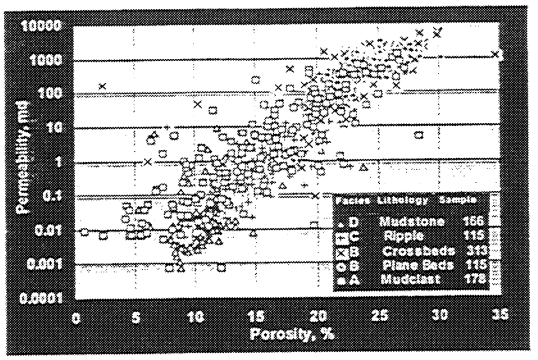

Figure 6. Cross-Plot of Porosity and permeability for Gypsy Formation

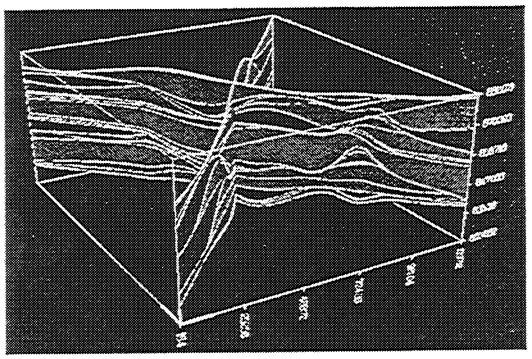

Figure 7. Cross-Sectional View of Lithofacies Model

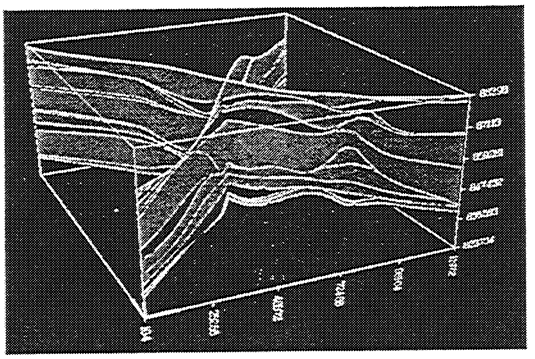

Figure 8. Cross-Sectional View of Flowunit Model

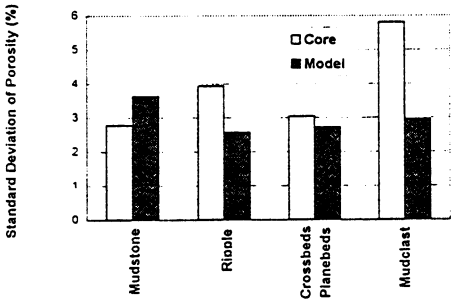

Fig. 9 Standard Deviation of Porosity for Lithofacies Model

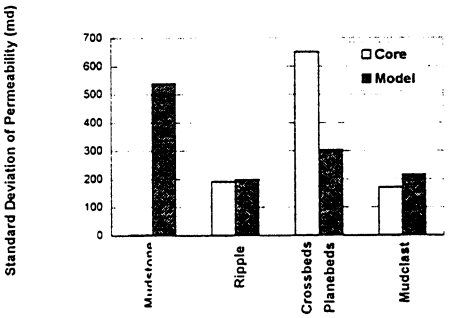

Fig. 10 Standard Deviation of Permeability for Lithofacies Model

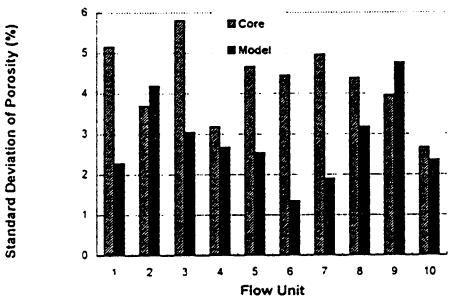

Fig. 11 Standard Deviation of Porosity for Flow Unit Model

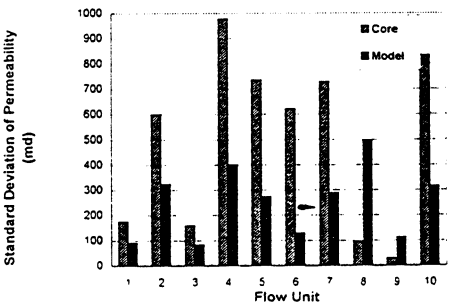

Fig. 12 Standard Deviation of Permeability for Flow Unit Model

Appendix C

Geophysical Site Characterization for 3-D Flow Simulation at the Gypsy Outcrop Site, Oklahoma

by

Roger A. Young, Zhenghan Deng, Zhi-Ming Liu, Matthias Mueller, J.M. Forgotson, Steve Danborn, Kurt Marfurt, Susan Nissen

Presented at the Society of Exploration Geophysicists Annual Convention, 1998

Geophysical site characterization for 3-D flow simulation at the Gypsy Outcrop Site, Oklahoma

Roger A. Young, Zhenghan Deng, Zhi-Ming Liu, Matthias Mueller, J.M. Forgotson, University of Oklahoma; Steve Danbom, Conoco; Kurt J. Marfurt, Susan Nissen, Amoco.*

Summary

Multiple surveys by different geophysical methods define upper channel boundaries and a fracture set in a sequence of stacked, fluvial-deltaic channels of Pennsylvanian age. Borehole lithology logs show that ground penetrating radar and seismic refraction profiles image the same boundary between two sandstone channels. 3-D dip filtering and coherence of a migrated 3-D radar survey map clearly a channel boundary between a depth of 2 and 6 m. Depth slices of instantaneous frequency for this 3-D survey show a prominent fracture set that correlates with the orientation of fractures measured in a nearby highway cut.

The radar-defined fractures have been included in a 3-D earth model constructed by upscaling matrix properties defined by laboratory porosity and permeability measurements of core from shallow boreholes. Matrix and fracture flow are made to occur in separate, interacting cells. Waterflood simulations show that fracture-assisted permeability can either improve or impede remediation depending upon the placement of wells.

Introduction

The OCAST Project is a multidisciplinary study of a fluvial-deltaic sequence of channel sands of Pennsylvanian age. The objective of the project is to demonstrate that non-invasive geophysical surveys are effective in mapping shallow, sedimentary boundaries. The study area is the Gypsy Outcrop Site, 20 mi NW of Tulsa, Oklahoma. A grid of EM 31 lines guided subsequent radar profiling (Young and others, 1995). Conductivity, ground penetrating radar, and seismic refraction and reflection profiles have been conducted to link a grid of shallow boreholes (Figure 1). Integration of these geophysical results has mapped several channel boundaries in the interborehole volume (Deng and others, 1996). Radar profiles were successful in providing structure and isopach maps of these uppermost channels.

Radar lines COS4 and COS5 and a seismic refraction profile collected between BH26 and BH28 (Figure 1) both image the channel 6/channel 4 boundary. The dielectric contrast between sandstones and an intervening mudstone generates the radar reflection, and the higher velocity of channel 4 propagates a seismic refraction (Deng and others, 1996).

3-D radar survey

A 3-D radar survey was positioned to image in detail the surfaces of the upper channel boundaries over a small area. A secondary target was an area of unusual radar appearance showing a high concentration of diffractors organized both vertically and horizontally (Young and others, 1995)

The survey used a pulseEKKO IV system with antennas having 50 MHz center frequency, 1000 V transmitter, and antennas oriented perpendicular to the survey lines. Antenna separation was 6 ft and station and line spacing 2 and 4 ft, respectively.

Conventional processing

2-D processing of each line in the 3-D survey consisted of timezero correction, spherical spreading and exponential attenuation compensation, and bandpass filtering. The time axis has been converted to depth using a velocity of .10 m/ns established from constant velocity panels for several CMP gathers in the 3-D survey area.

Unmigrated Line 1 (Figure 2) shows the east half of channel 6 plunging from a depth of 2 to 5.5 m The yellow dashed lines (Figure 1) show the channel 6/channel 4 and the channel 4/channel 3 boundaries, which are tied to the borehole lithology logs at the ends of Line 1.

The radar character of the channel 4/channel 3 and the base channel 3 boundaries (Figure 2) are jumbled in contrast to the distinct channel 6/channel 4 boundary. We interpret the former to be a superposition of overlapping hyperbolas, occurring mostly in two bands from trace 50 to trace 100 at depths of approximately 5 and 7 m. The bands do not cut channel 6. The apexes (small green arrows) of these rows of hyperbolas are grouped also in columns (F's on Line 1). A particular diffraction occurs on lines 1-5 at a depth of 4.25 m (red arrows) indicating that scatterers also occur in groups perpendicular to the lines. We explain this extremely regular distribution of scatterers as the intersection of an open fracture set with the lithological changes at boundaries between channels.

3-D geophysical characterization

A roadcut approximately 1000 ft from the 3-D survey shows fractures striking N/S and dipping steeply. These fractures do not cut channel 6 (Young and others, 1997) and correspond closely in orientation to the fractures inferred from the radar data.

3-D filtering and display

Reverse-time migration of each line was performed. Then a gentle 3-D dip filter using a Radon transform rejected all dips greater than 4.0 ns/ft. 3-D coherence and dip/azimuth were calculated for each point in the volume. Dip/azimuth timeslices at 40 and 70 ns (Figure 3) give an extremely detailed pixel-by-pixel picture of the magnitude and direction of dip along the channel boundary. The two plus signs (circled in white) in Figure 3 give a south dip of 2 ns/ft at 40 and 70 ns, respectively, along Line 6 at trace 54 (arrows). In vertical section, Line 6 (green dots in Figure 2) shows an apparent dip of 1 ns/ft agreeing closely with the true dip of 2 ns/ft when one considers that the former is measured at an angle of approximately 45 deg to the true dip.

Figure 2 (Line 1) shows that diffraction apexes fall at approximately 100 ns. Figure 4 shows an instantaneous amplitude timeslice at 100 ns. The diffraction apexes line up N/S (F symbols) strongly suggesting that diffractions are associated with the N/S striking fracture set.

Flow simulation

A 3-D earth model for the entire site was built using the program SGM. Boundaries in the model are from Collins (1996) using outcrop and borehole data, and matrix attributes of permeability (200 to 8,000 mD) and porosity (1 to 20%) were distributed according to laboratory measurements on cores from the site. Fractures were oriented N/S in agreement with the radar result and were represented as a separate attribute grid with permeability up to 16,000 mD. Several different combinations of permeability and porosity and permeability anisotropy values were assigned in an attempt to approximate actual properties. Fractures were confined to channels. Planar sets of cells represent the fractures.

Flow simulation in this model tested the effect of natural fractures and well location and producer pressures on water and oil production. In these scenarios, oil was considered a pollutant to be remediated by waterflood. Due to the unusually high permeabilities measured at Gypsy, a model with matrix permeability reduced 10-fold and fracture permeability of 8,000 mD was chosen as a more representative model for Pennsylvanian reservoirs.

Figure 5 shows pollutant saturation in the representative model for a five-spot waterflood with producer in the center. Four years have elapsed. Water breakthrough occurred after 2.2 years. Fractures are visible parallel to the edge of the model.

Conclusions

Geophysical probing can assist in the construction of a geological model, including fractures, in the area between boreholes. Multiple methods provide complementary results. The presence of fractures can either improve remediation by waterflood or reduce recovery by limiting sweep depending upon the relationship between well positions and fracture orientation.

Acknowledgments]

We are thankful to A. Peter Annan and Bill Jones for field assistance, to Dan O'Meara for guidance to M. Mueller in the flow simulations, and to Chris Liner for merging radar data at different frequencies. We are grateful to The Institute for Reservoir Characterization at the University of Oklahoma for providing radar data and site access. The Oklahoma Center for the Advancement of Science and Technology provided funding for this work through Project AR4-039.

References

Young, R.A., Forgotson, J., White, L., O'Meara, D., Deng, Z., Liu, Z-M., Liner, C.L., Weindel, R., and Danbom, S., 1995, The OCAST Project: Integrated geophysical characterization assisting flow simulation, Expanded Abstracts of the 65th International Meeeting of the Soc. of Expl. Geophys., Houston, 406-410.

Young, R.A., Deng, Z., Marfurt, K. J., Nissen, S.E., 1997, 3-D dip filtering and coherence applied to GPR data:A study, The Leading Edge, 921-928.

Deng, Zhenghan, and Young, R.A., 1996, Correspondence of a radar reflector and a seismic refractor in a fluvial-deltaic channel sequence, Expanded Abstracts of the 66th Annual Meeting of the Society of Exploration Geophysicists, Denver, 859--864.

Collins, T.M., 1996, Methodology for constructing high resolution three dimensional reservoir characterization models for petroleum and environmental application, unpublished MS thesis, University of Oklahoma.

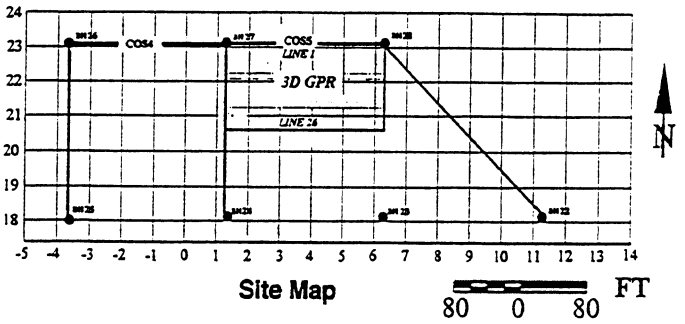

Figure 1 Northern end of Gypsy Outcrop Site. Dots show borehole locations. Radar profiles join boreholes.

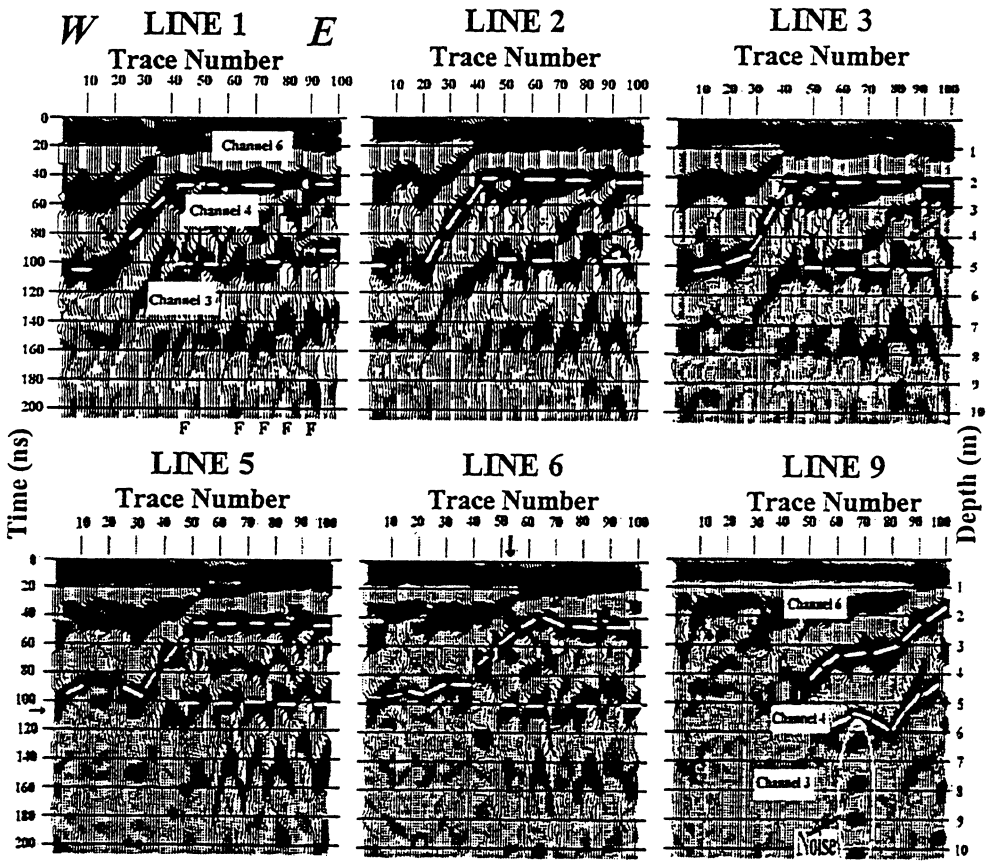

Figure 2 Unmigrated GPR lines from the 3-D survey. Water table is below radar section. ***Yellow*** dashes show channel boundaries which move eastward across successive profiles. ***Large green*** arrow corresponds to black arrow on timeslice in Fig. 4. ***Small green*** arrows on Line 1 point to apexes of diffractions generated by fractures, F. **Blue** arrows on Line 6 indicate a channel boundary apparent dip of 1 ns/ft. ***Red*** arrows point out a particular diffraction seen on Lines 1-5 at a depth of 4.25 m.

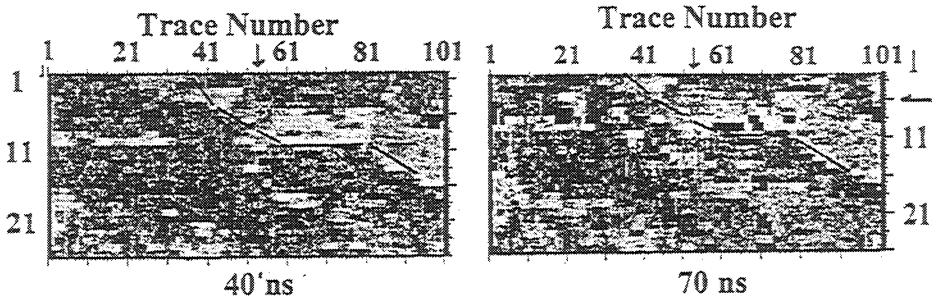

Figure 3 Dip/azimuth map at times 40 and 70 ns. Dip magnitude is shown by greater color intensity; dip direction by hue. Black plusses correspond to green dots on Line 6 (Fig. 2) and show a SW dip of 2 ns/ft. Black dashes show northern edge of channel.

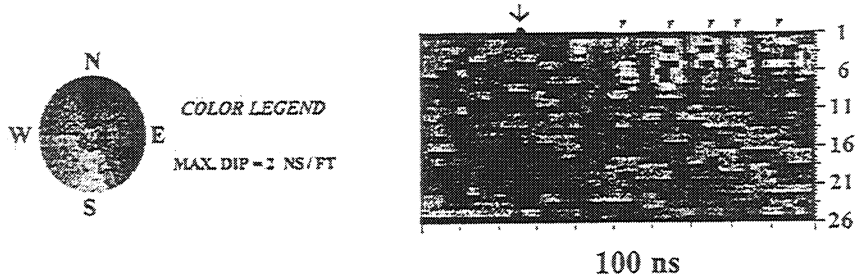

Figure 4 Instantaneous amplitude map at 100 ns after dip filtering. High amplitudes emphasize linear trends, interpreted as fractures (F's at top). Channel boundary (dashed line) is not penetrated by fractures.

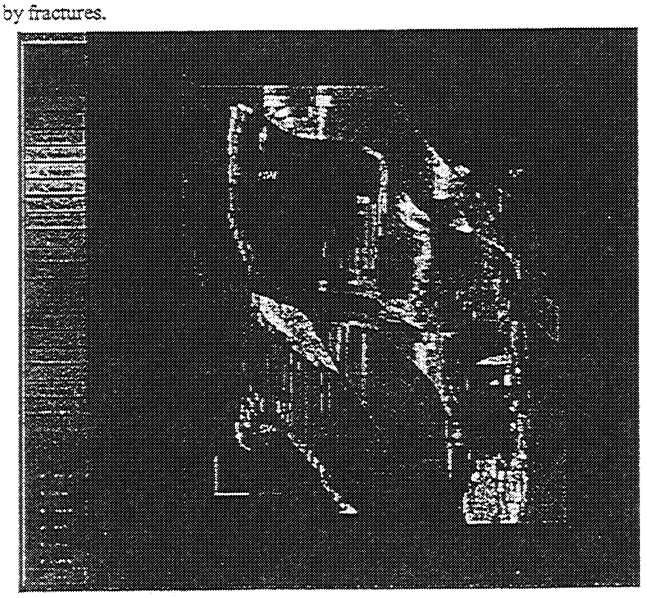

Figure 5 View of channel units from above. Reduced matrix permeability model with five-spot waterflood. Redder areas show unswept pollutant. Extractor well is in the center. Lineations are fluid-filled fractures.

Appendix D

3-D Dip Filtering and Coherence Applied to GPR Data: A Study

by

Roger A. Young, Zhenghan Deng, Kurt Marfurt, Susan Nissen

3-D dip filtering and coherence applied to GPR data: A study

ROGER A. YOUNG and ZHENGHAN DENG, University of Oklahoma, Norman, Oklahoma
KURT J. MARFURT and SUSAN E. NISSEN, Amoco EPTG, Tulsa, Oklahoma

Three-dimensional seismic data are now used routinely in hydrocarbon exploration and reservoir exploitation. Poststack processing of 3-D seismic data often includes the application of 2-D filters to the stacked data one line at a time (so-called 2-D by 2-D filtering). In this application, 2-D filtered data are sorted into cross line ensembles before a second pass of 2-D filtering. Alternatively, local three-dimensional filters may be applied to a volume of seismic data, true 3-D filtering. These filters can be either local, operating only on neighboring traces and samples of an output position, or global, depending on every trace and time sample in the data cube. Local filtering has proven successful at improving the signal-to-noise ratio and thereby the stratigraphic resolution over a wide range of depths typical for hydrocarbon accumulation, 200-7000 m.

Another geophysical exploration technique analogous to the seismic reflection method is ground penetrating radar (GPR). GPR uses radar reflections to produce high resolution stratigraphic images of the near surface from depths of 2 to perhaps 200 m. The ability of GPR 2-D profiles to image near-surface stratigraphy has been demonstrated convincingly by many authors (see "Suggestions for further reading"). As with seismic data, multifold common midpoint (CMP) data could, in principle, improve the imaging possible from single-fold profiles alone. An attractive feature of the GPR method, however, is its cost-effectiveness in small field efforts using a single transmitter/receiver pair. Multichannel GPR systems are not used widely today. Experimentation with multifold CMP radar data is in its infancy, and the conventional method of radar profiling today is single-channel, common offset surveying. These 2-D data may be moveout corrected to normal incidence, or the correction may not be applied at all because it is small. In any case, the data are processed to give single-fold coverage at closely spaced subsurface points.

Radar profiles collected along closely spaced, parallel lines are commonly termed a 3-D radar survey even though multiazimuth raypaths have not been combined to give a normal incidence radar trace as in the seismic case. A 3-D radar survey is, therefore, analogous to a 3-D seismic survey with only one prestack trace per bin.

The improvement in interpretation made possible by 3-D visualization of radar data following 2-D processing is now widely appreciated. It is also realized that crossline filtering can be very effective in attenuating noise trains. Yet, the use of three-dimensional filtering of radar surveys has not been exploited at a level approaching its use with seismic data.

Coherence filters using semblance have long been used successfully with 2-D seismic data to define local continuity in selected dip directions. Because a sudden decrease in coherence indicates a loss of lateral heterogeneity, coherence is also an effective edge detector. Algorithms have recently been developed to map seismic coherence as a 3-D seismic attribute. Results show that faults, seen unclearly in time slices, can be resolved much more accurately by coherence mapping.

The purpose of the present paper is to show an example of applying 3-D dip filtering and 3-D seismic coherence processing methods to a 3-D radar survey. Conventional 2-D processing and 3-D display of the radar survey reveal the boundary of a sand channel and a fracture set beneath the channel sand, but the images are poorly resolved because radar energy is attenuated in the clay-bearing sandstone channels. The application of 3-D coherence methods and novel 3-D displays make interpretation much easier. The present paper is, to our knowledge, the first published account of the application of 3-D coherence techniques to GPR data. It suggests that advanced seismic processing methods can be applied successfully in 3-D analog outcrop studies in order to resolve stratigraphic and structural features at a scale of several feet.

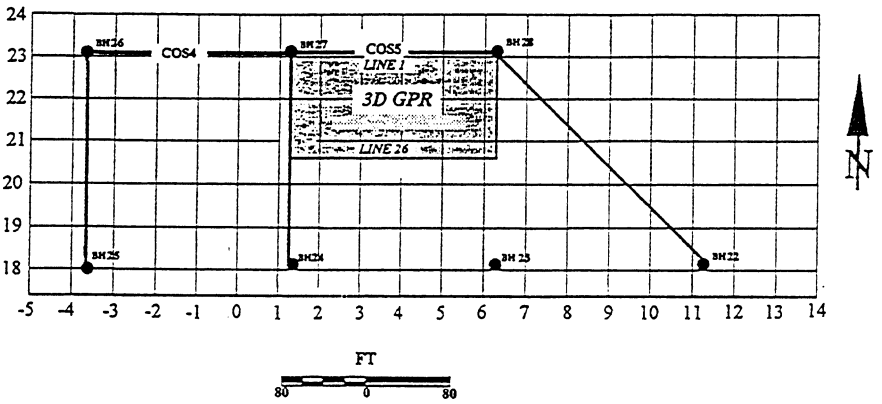

Figure 1. Northern end of Gypsy Outcrop Site. GPR profiles (dark lines), grid coordinates, and borehole numbers are from the earlier BP study by Doyle and Sweet. COS4 and COS5 are recent 2-D radar profiles used to establish the optimal location for the present 3-D GPR study.

The Oklahoma Center for the Advancement of Science and Technology (OCAST) sponsored the acquisition of the present radar data by the University of Oklahoma at the Gypsy Outcrop Site near Tulsa. This

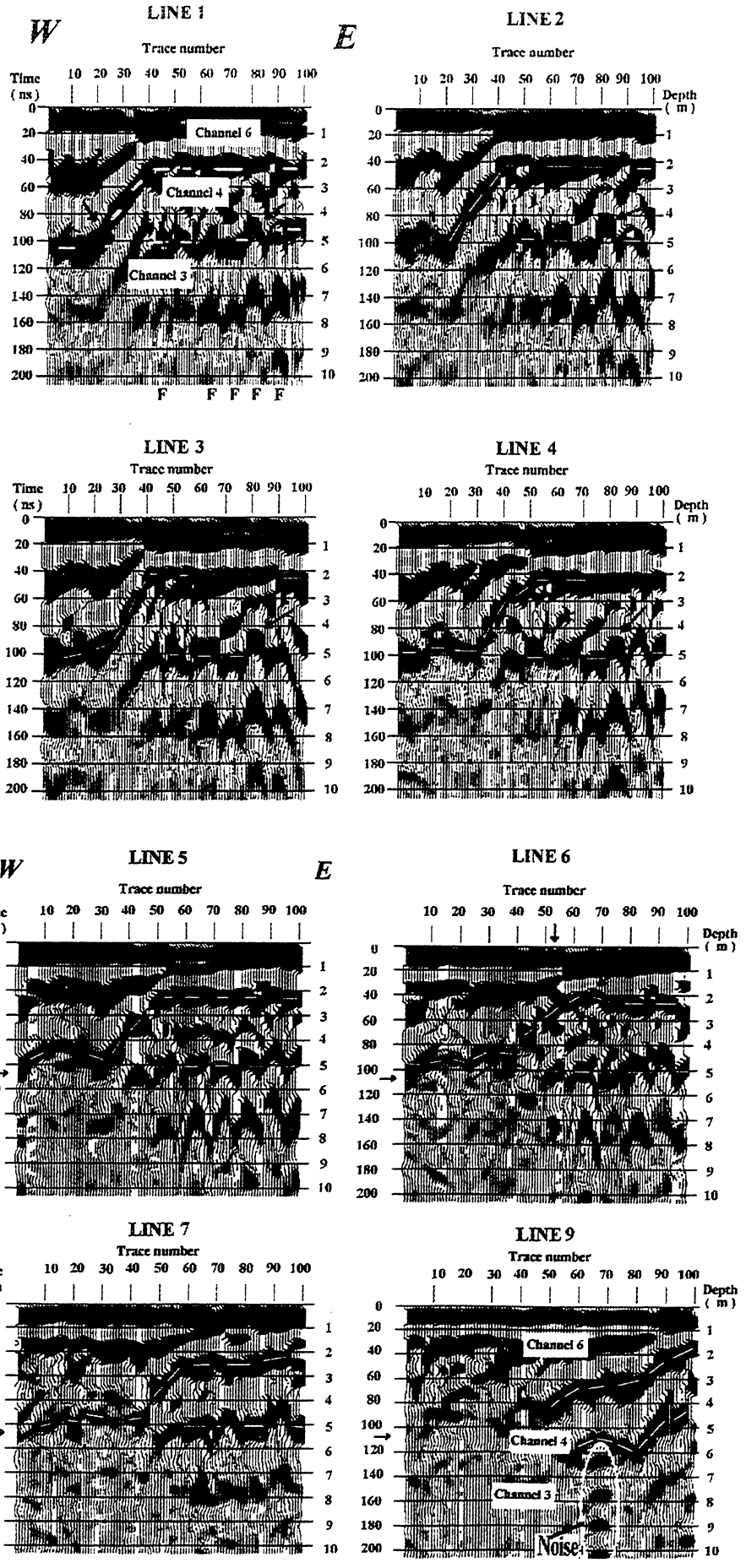

Figure 2. Unmigrated GPR profiles 1-7 and 9 from the 3-D survey. Velocity used in time-to-depth coversion is .1m/ms (.32 ft ns). Water table is below radar section.

Yellow picks indicate the channel 6/channel 4 and channel 4/channel 3 boundaries. Note that the 6/4 boundary moves eastward across successive profiles.

Large green arrow corresponds to the arrow on timeslices shown in Figures 5, 7, and 9.

Small green arrows on line 1 point to apexes of diffractions generated by fractures, F.

Blue arrows on line 6 indicate that channel 6/channel 4 boundary has an apparent west dip of 1 ns/ft.

Red arrows on lines 1-5 point out a particular diffraction that occurs at a depth of 4.25 m.

25-acre tract was used by British Petroleum in its reservoir studies, including extensive geological characterizations of Pennsylvanian fluvial-deltaic channel sands. The tract is now being studied further by its present owner, the University of Oklahoma. A grid of 22 boreholes to depths of 100 ft defines the boundaries of lithofacies units within 5 channels, and the 3-D architecture of these channels has been established by BP geologists.

2-D radar surveys and interpretation. A network of radar profiles, collected in large part before the present study, tie the boreholes at the northern end of the Gypsy Outcrop Site (Figure 1). By comparing the lithology log at BH27 to the depth-converted radar profiles on either side, it was established that a mudstone intervening between sandstone facies in channel 6 and channel 4 generates a radar reflection throughout the site. This reflection can be used to interpolate the location of the channel 6/channel 4 boundary between boreholes. Then, using all lines together, an isopach map of channel 6 throughout the interborehole volume was formed.

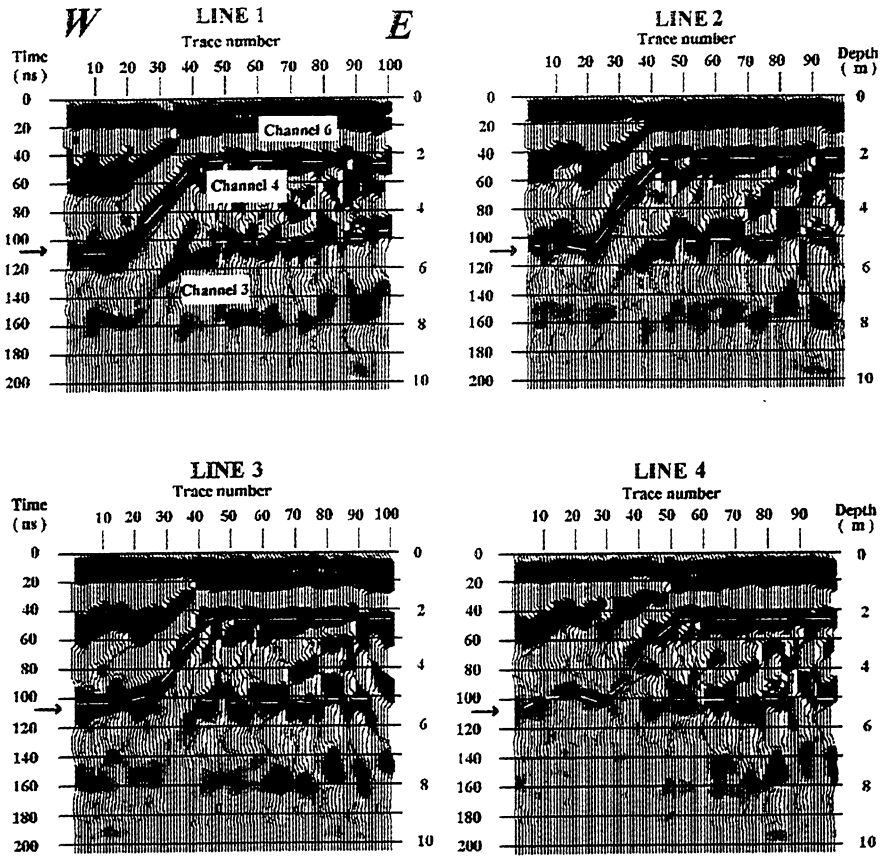

Figure 3. Migrated GPR profiles 1-4 from the 3-D survey. Diffraction energy seen in Figure 2 has been migrated to the fracture intersections with lithologic boundaries. (Colors explained in Figure 2.)

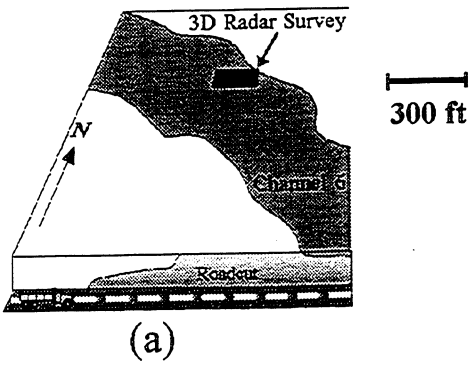

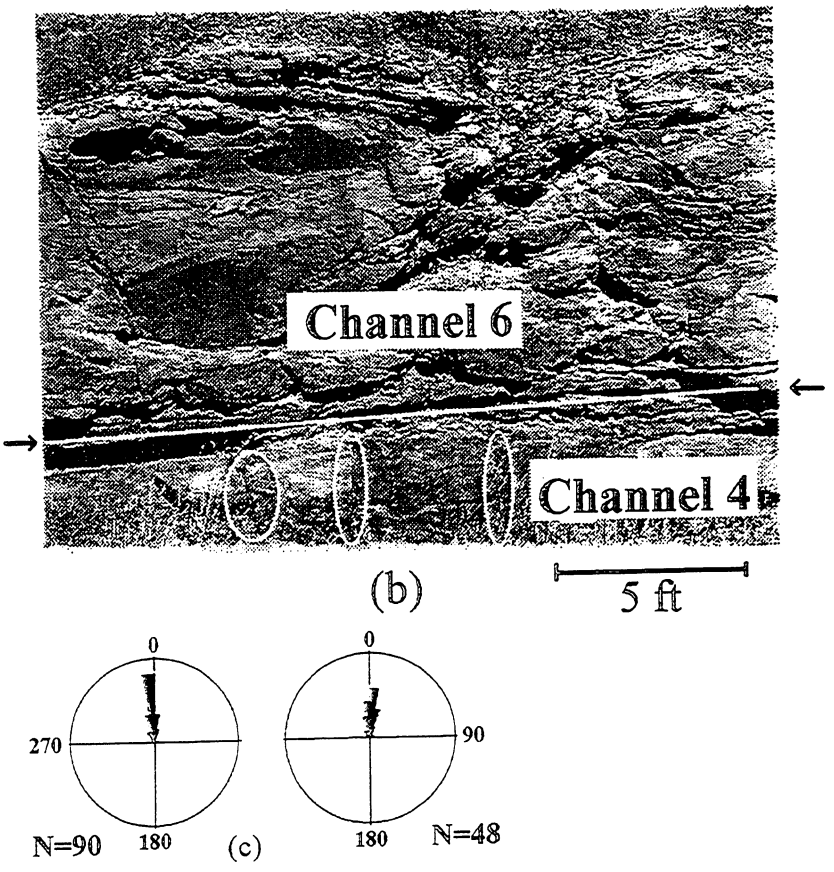

Figure 4. (a) Location of the roadcut and the 3-D radar survey at the Gypsy Outcrop Site. (b) Roadcut through uppermost channels 6 and 4. White line and black arrows show the thin mudstone at the channel 6/channel 4 boundary. Ellipses enclose fractures in channel 4. (c) Strike directions for two populations of fractures in channel 4. Circle represents 50% of N. The strike direction of fractures at the roadcut trends nearly north-south (after French).

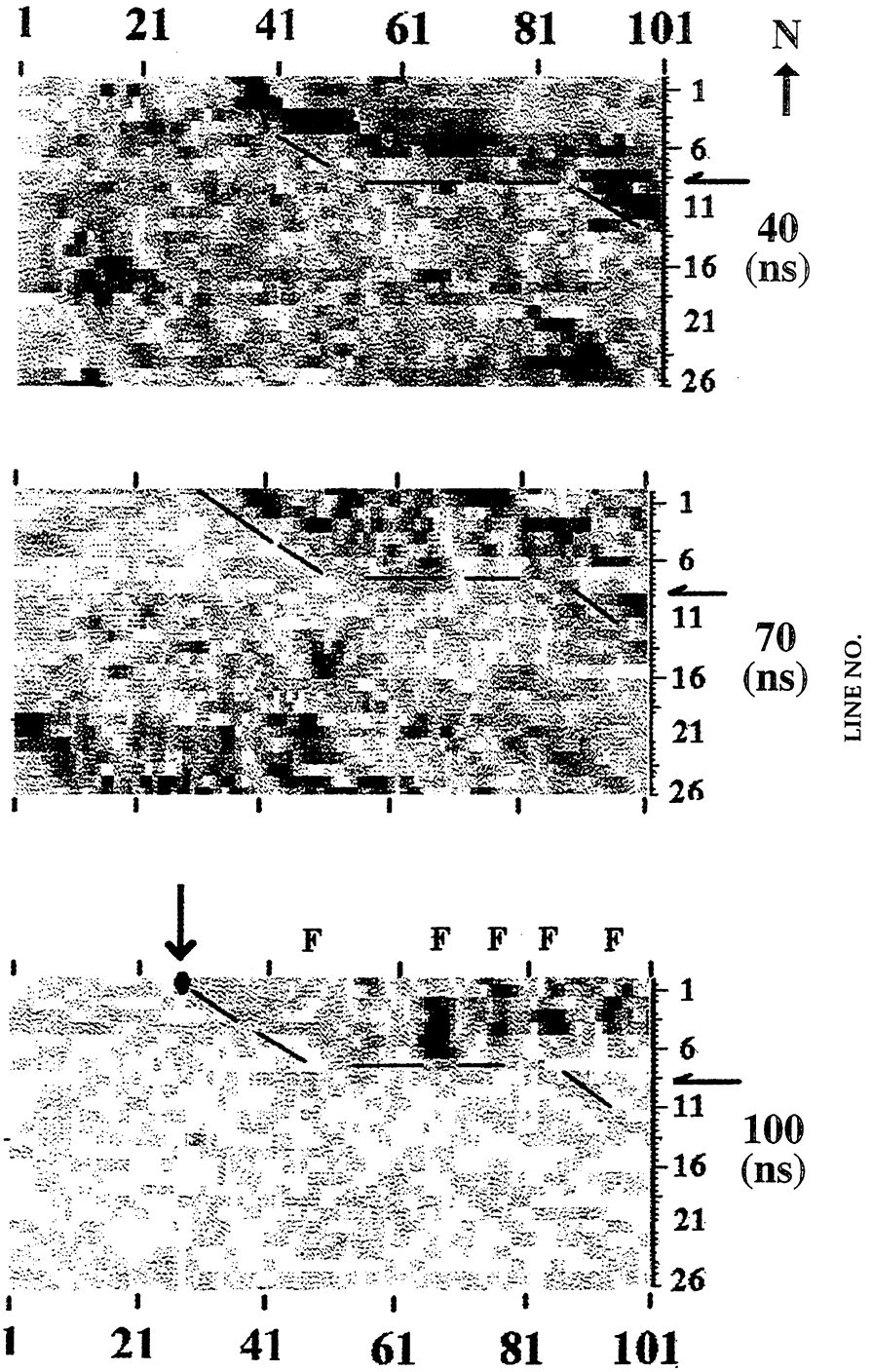

Figure 5. Timeslices of the 3-D, unmigrated radar volume at 40, 70, and 100 ns following 2-D processing. Dot (on 100 ns timeslice) locates reference point (Figure 2) on channel 6/channel 4 boundary, and dashed lines indicate the interpreted northern edge of the channel boundary. Dark lines oriented north-south in northeast corner of 100 ns timeslice result from cutting diffractions (Figure 2) just below their apexes. Blue corresponds to peaks in Figure 2. Fractures are shown by F.

The isopach map, in itself, represents a major contribution provided by the radar data: the interpolation between boreholes of the thickness of the upper channel. This is crucial information needed to construct an accurate 3-D earth model for flow simulation. But a geophysical challenge of greater significance is to image channel boundaries at every point throughout a volume. This requires a 3-D radar survey.

3-D radar survey and conventional 2-D processing. A 3-D radar survey was conducted in order to detail the bases of channel 6 and channel 4 and to investigate, throughout a small volume, a zone of numerous diffractions seen on line COS5. A pulseEKKO IV system using 50 MHz center frequency, 1000 V transmitter, and antenna orientation perpendicular to the line were employed. An earlier EM 31 conductivity survey revealed that average conductivity along the present profiles is 10-20 mS/m, relatively low attenuation for a location in the U.S. midcontinent, but one requiring us to use, nonetheless, low frequency antennas and a high-power transmitter. The separation between the transmitter and the receiver was 6 ft; station spacing and line separation were, respectively, 2 and 4 ft. A characteristic wavelength for a 50 MHz signal (given a velocity of .32 ft/ns) is, therefore, approximately 6.6 ft. This means that crossline noise will be aliased. This possibility was realized before the survey was acquired, but limited time for the survey and the need to cover a substantial area required this compromise.

Reflections from channel boundaries. Line 1 of this 3-D survey is coincident with COS5. It shows the east half of channel 6 (Figure 2). The yellow dashed line shows the channel 6/channel 4 and the channel 4/channel 3 boundaries, which are tied to the borehole lithology logs at the ends of line 1. A velocity survey established an average velocity for channels 6 and 4 of .32 ft/ns, and this was used to convert the time axis to depth in Figure 2. The appearance of reflection discontinuity across adjacent traces is an indication that stratigraphic features are changing laterally over a span of several feet. It also testifies to the detailed lateral resolution that radar data alone can provide. A smaller trace spacing would have been helpful to capture this detail.

Scattering from open fractures. The radar character in channels 4 and 3 is jumbled and is unlike the distinct layering in channel 6. We interpret the former to be a superposition of overlapping hyperbolas, occurring mostly in two bands from trace 50 to trace 100 at depths of approximately 5-7 m. The apexes of these rows of hyperbolas are grouped also in columns (Fs on line 1). Only line 1 points out the apexes (small green arrows), but the hyperbolas occur on adjacent lines. This reg-

ular pattern in vertical section indicates that the scattering points causing the diffractions are organized systematically in the subsurface and are not randomly distributed, as would be expected for unrelated scatterers. A particular diffraction occurs on lines 1-5 at a depth of 4.25 m (red arrows) which indicates that the scattering points are also organized in groups perpendicular to the lines.

The extremely regular pattern in three dimensions of the scatterers causing the diffractions can be explained as the intersection of an open fracture set with horizontal contrasts in dielectric constant within sand channels, and at the boudaries between sand channels. In fact, the upper row of diffractions at a depth of 5 m has been interpreted as the channel 4/channel 3 boundary, based on lithologic control from nearby borehole BH28. High amplitudes may also be caused by water from surface runoff filling the fractures. The diffractions become less distinct with distance from line 1, and they disappear altogether on line 9 (Figure 2). The diffractions in channels 4 and 3 do not appear to cut channel 6 on the west side of the survey.

Figure 3 shows that 2-D time migration of the profiles in Figure 2 is partially successful in collapsing the diffractions and increasing the continuity of the reflections, particularly the channel 4/channel 3 boundary.

Geological control. The channel 6/channel 4 boundary is exposed in a highway cut approximately 1000 ft south of the radar survey (Figure 4a). Structural mapping shows that fractures in channel 4 strike approximately north-south (Figure 4b). This contrasts with the regional fracture direction which is generally N30W-S30E but agrees very well with the strike direction shown by the radar data. Figure 4 also shows that the fractures in channel 4 are nearly vertical, and that they do not cut into channel 6. These geological observations support our inference that the cause of the diffractions is the intersection of a fracture set with lithology changes at the channel boundaries.

Conventional 3-D display. A seismic reflection interpretation package (Halliburton's SEISTAR) was used to view time slices through the unmigrated radar data volume. Figure 5 shows time slices at 40, 70, and 100 ns.

The channel 6/channel 4 boundary is indistinct, and the northwest-

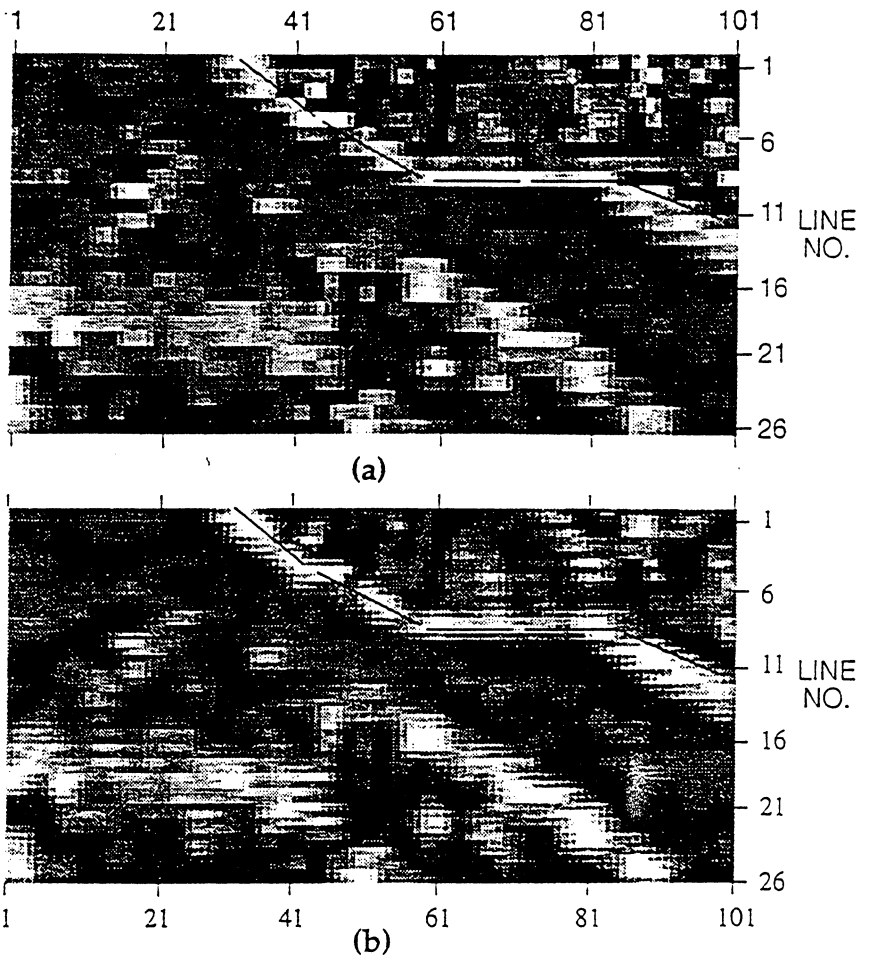

Figure 6. Timeslice at 70 ns through the migrated radar volume. Dashed line is the interpreted edge of the channel boundary which appears more continous after dip filtering (bottom) than before (top).

southeast trend appears only on the 40 and 70 ns time slices. The 100 ns timeslice cuts the diffractions at the channel 4/channel 3 boundary just below their apexes (Figure 2, line 1) and shows clearly the north-south trend of the fractures.

3-D filtering and display: channel boundaries. The channel 6/channel 4 boundary is difficult to discern on the time slices of Figure 5 for several reasons. The data are unmigrated. The low signal-to-noise ratio of the data and the fact that the data are spatially aliased in the crossline direction also contribute to poor continuity. We, therefore, began with the 2-D migrated data (Figure 6a shows a representative time slice) and applied a very gentle 3-D dip filter using a running window, discrete, Radon tranform to reject all dips greater than 4.0 ns/ft. We then interpolated to a 2-ft crossline spacing during the reverse transform (Figure 6b). Even though some flat-lying, coherent events were inadvertently attenuated due to operator aliasing, the channel boundaries appear to be more continuous after migration and dip filtering.

Following migration and dip filtering, 3-D coherence and dip/azimuth (described below) were calculated for each point in the volume. These calculations used 13 traces falling within a window having a radius of 4 ft. The vertical analysis window was + 20 ns, or + 24 samples in length. For each of the 61 solid angles, we calculated the semblance. It is postulated that the dip with the highest semblance is the dip of an assumed coherent reflector. For high coherency reflectors (c~1.0), this estimate is quite accurate. For low coherency events (c~0.5), the dip estimate is less reliable. Low values of coherence occur at disruption of reflections; consequently, low coherence values map the channel boundary. Three-dimensional filtering, coherence calculations, and display

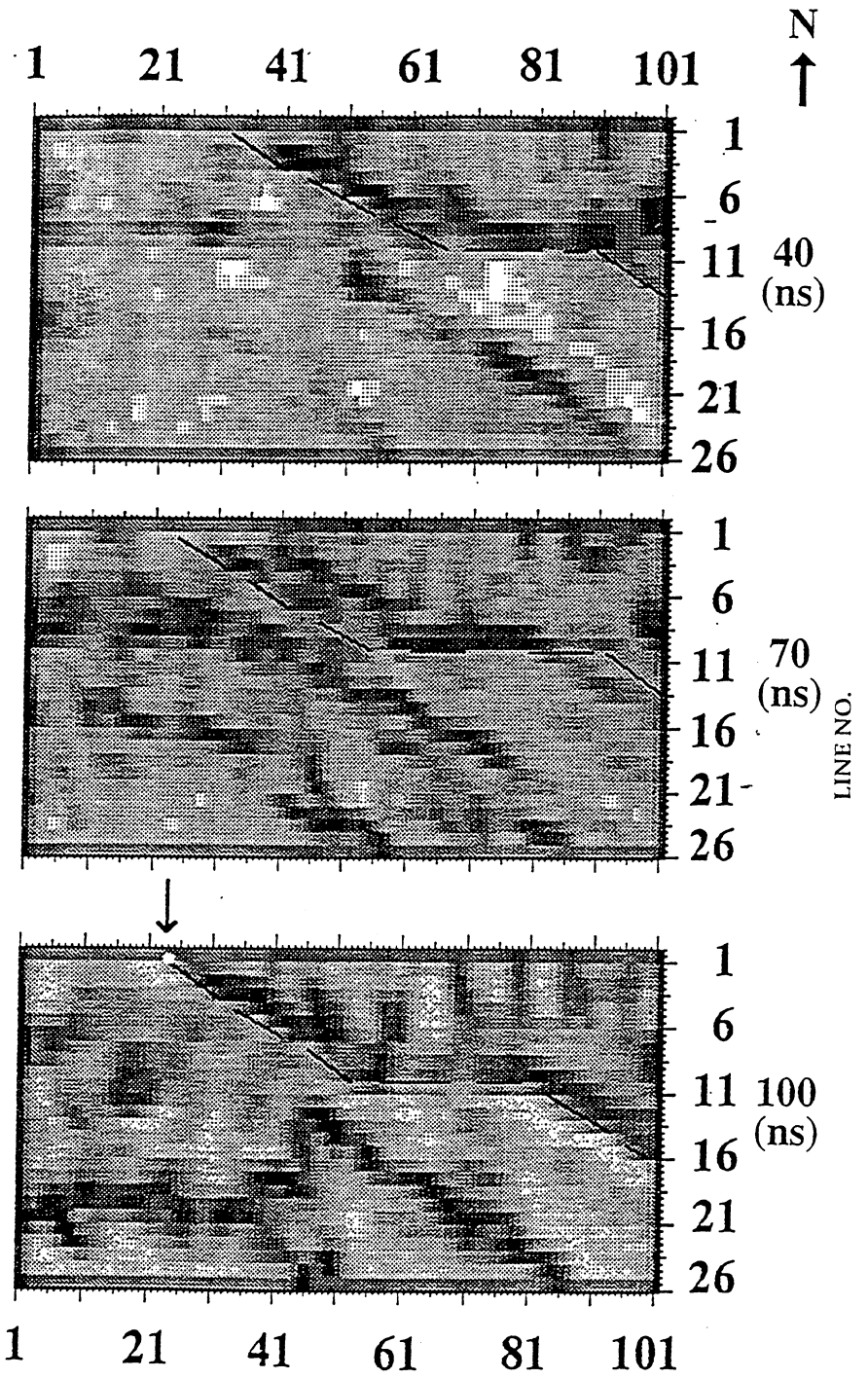

Figure 7. Timeslices progressing from 40 ns (2 m depth) to 100 ns (5 m depth) through the coherence volume. White dot (on 100 ns timeslice) locates reference point (Figure 2) on the channel 6/channel 4 boundary, and dashed lines show the northern edge of the channel boundary. Strike is approximately northwest-southeast but is locally east-west.

were done at Amoco EPTG in Tulsa, Oklahoma.

The increase in continuity due to the 3-D filtering is shown in Figure 7. Timeslices through the coherence volume mark the channel 6/channel 4 boundary much more clearly than did the timeslices through the 2-D processed volume (Figure 5). The channel boundary trends northwest-southeast (dashes in Figure 7) but it is sinuous. It strikes east-west locally, and varies in strike with depth. The irregular feature in the southwest corner is within the channel and is not the southern flank of the channel itself. The dip of the channel boundary is, by definition, perpendicular to the local strike direction in Figure 7; i.e., southeast to south and changes with depth at the eastern edge of the timeslices.

A far more detailed analysis of dip direction of coherent reflections is displayed using the instantaneous dip/azimuth attribute. In this method, a 3-D search of dip gives the dip direction and magnitude for every point within the data volume. Timeslices at 40 ns (Figure 8, top) and 70 ns (Figure 8, middle) through the dip/azimuth volume give an ex-tremely detailed picture point-by-point of the magnitude and direction of dip along the channel boundary. The two plus signs (circled in white) in Figure 8 give a south dip of 2 ns/ft at 40 and 70 ns, respectively, along line 6 at trace 54 (arrows). Line 6 (green dots in Figure 2) shows these same points in vertical section. The apparent dip in vertical section of 1 ns/ft agrees closely with the true dip in timeslice, 2 ns/ft, when one considers that the former is measured at an angle of approximatly 45° to the true dip.

3-D filtering and display: fractures. The timeslice following conventional processing (Figure 5) reveals the pattern of fractures in the northeast portion of the survey area. Figure 9 shows the instantaneous amplitude after dip filtering, displayed on the 100 ns timeslice. The north-south trend of the fractures (the F symbols in Figure 9) is much clearer than in Figure 5 because of the increased continuity of the instantaneous amplitude attribute. It is also aided by the collapsing of the diffractions by migration and by 3-D dip filtering of surface-scattered noise.

Average fracture spacing appears to be approximately 18 ft, based on the radar data, although the highway cut (Figure 4) shows small, more closely spaced fractures in the same fracture set. The highway cut also suggests that the fractures are confined to channel 4 and do not extend into channel 6. Figure 9 shows that the channel 6/channel 4 boundary (dashed line) is not penetrated by the fractures. This finding will be important to flow simulation studies because it suggests that communication between channels 6 and 4 will not be enhanced by fractures.

Conclusions. 3-D dip filtering and coherence display of radar data from a fluvial-deltaic sequence of Penn-

sylvanian age in the U.S. midcontinent has clarified interpretation of an upper sand channel boundary and of fractures in underlying channels. The strike of a channel sand boundary and its local dip are shown by timeslices through the coherence cube and the dip/azimuth volume. A fracture set of intersecting channel boundaries produces a distinctive pattern of diffractions which are enhanced by an instantaneous amplitude display.

The present 3-D radar data is sampled coarsely in space and is subject to relatively rapid attenuation, which is characteristic of the U.S. midcontinent. A more closely sampled survey conducted in a drier climate and in geological units with a lower clay content would have the potential to image boundaries at greater depth and to detail stratigraphic variation at scales of less than a foot. This present study, however, shows that 3-D processing and display markedly improve the resolution of radar images to be used in geological model building for analog reservoir simulation.

Suggestions for further reading. A good example of 2-D GPR profiling is "Ground penetrating radar of lakeshore spits in northwestern, Saskatchewan, Canada: variable internal structure" by Jol et al. (*Proceedings of the 5th International Conference on GPR*, 1994). BP's earlier work in this area is described in "Three dimensional distribution of lithofacies, bounding surface, porosity, and permeability in a fluvial sandstone — Gypsy Sandstone of Northern Oklahoma" by Doyle and Sweet (AAPG *Bulletin*, 1995). Material on specific topics includes:

Gypsy Outcrop Site: "The application of ground penetrating radar for geological characterization in three dimensions at Gypsy Outcrop Site, Northeastern Oklahoma, USA" by Z. Deng (Master's thesis, University of Oklahoma, 1996). "Fracture analysis of the Gypsy Outcrop and the surrounding area to determine the susceptibility of fluvial deltaic reservoirs to natural fractures that will effect waterflood recovery of oil" by V. French (unpublished report, School of Geology and Geophysics, University of Oklahoma, 1995). "The OCAST project: Integrated geophysical characterization assisting flow simulation" by Young et al. (SEG *1995 Expanded Abstracts*).

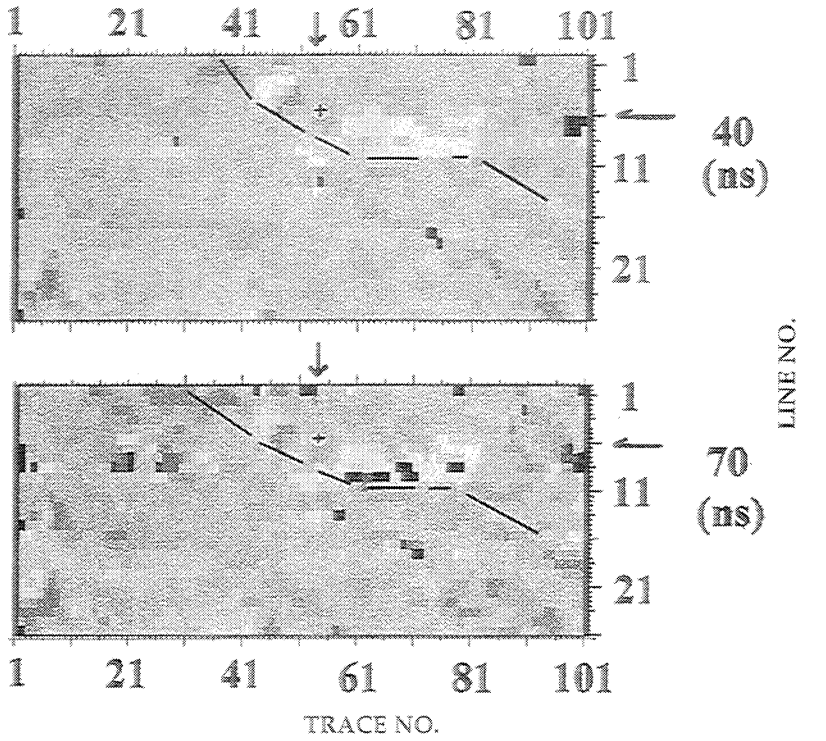

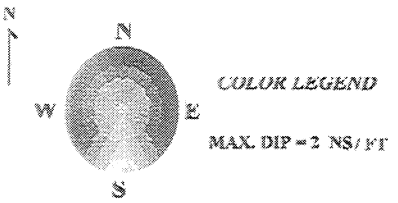

Figure 8. Dip/azimuth map at times (a) 40 ns and (b) 70 ns. Increasing dip is shown by greater color intensity, and the direction of dip is shown by hue. Plus signs (circled in white) show southwest dip above and below channel 6/channel 4 boundary and correspond to the green dots on line 6 (Figure 2). Dashed lines show the northern edge of the channel.

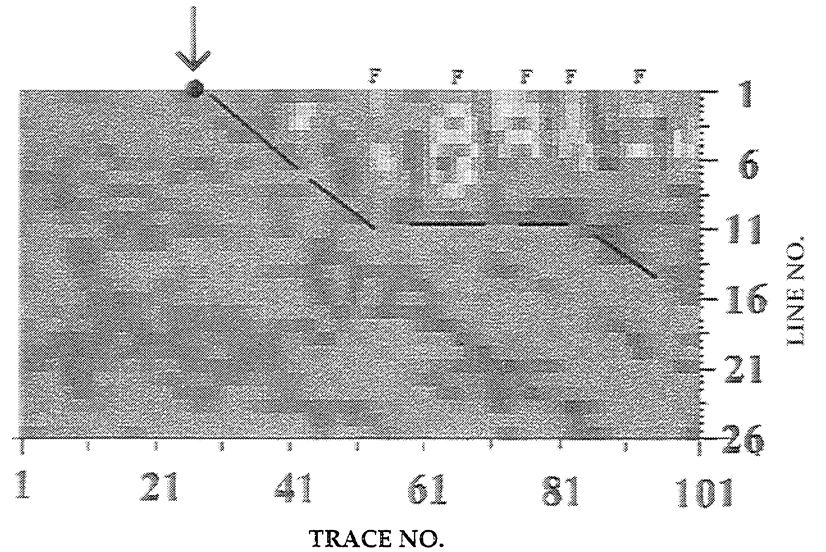

Figure 9. Instantaneous map at 100 ns after dip filtering. High amplitudes (red and yellow) emphasize linear trends, interpreted as fractures. Positions of fractures are shown by Fs at the top. The channel 6/channel 4 boundary (dashed line) is not penetrated by the fractures.

GPR: "Processing ground penetrating radar data" by Fisher et al. (*Proceedings of the 5th International Conference on GPR*, 1994). "Recognizing surface scattering in ground-penetrating radar data" by Sun and Young (GEOPHYSICS, 1995). "Unraveling lithology from stratigraphy in ground penetrating radar data" by Young and Sun (submitted to GEOPHYSICS). "Extracting a radar reflection from a noisy experiment using 3-D interpretation" by Young and Sun (submitted to *Journal of Environmental and Engineering Geophysics*).

Multifold radar: "Acquisition and processing of wide-aperture ground penetrating radar data" by Fisher et al. (GEOPHYSICS, 1992). "3-D ground penetrating radar applied to fracture imaging in gneiss" by M. Grasmueck (GEOPHYSICS, 1996); "Velocity variations and water content estimated from multi-offset, ground-penetrating radar" by Greaves et al. (GEOPHYSICS, 1996).

3-D visualization: "Experiments on the detection of organic contaminants in the vadose zone" by Grumman and Daniels (*Journal of Environmental and Engineering Geophysics*, 1995); "3-D ground penetrating radar imaging of a shallow aquifer at Hill Air Force Base, Utah" by Young and Sun (*Journal of Environmental and Engineering Geophysics*, 1996).

Correlation, semblance, and eigenstructure: "3-D seismic discontinuity for faults and stratigraphic features: the coherence cube" by Bahorich and Farmer (*TLE*, 1995); "3-D seismic attributes using a running window multitrace coherency algorithm" by Marfurt et al. (SEG *1995 Expanded Abstracts*). "Coherence computations with eigenstructure" by Gersztenkorn and Marfurt (EAGE Abstracts, 1996). "A nonlinear signal detector for enhancement of noisy seismic record sections" by Kong et al. (GEOPHYSICS, 1985). TLE

Acknowledgments: Peter Annan, Sensors and Software, kindly lent us the pulseEKKO system used in this study. Bill Jones of the B.R. Jones Instrument Company has been helpful with logistics throughout this study. Steve Danbom has been the source of many insights. Richard Weindel and Chris Liner of the University of Tulsa assisted in data collection. The authors are grateful to the Institute for Reservoir Characterization of the University of Oklahoma Energy Center for its contribution of Gypsy field data and use of the site. The authors thank Amoco EPTG for permission to publish this contribution.

Corresponding author: R.A. Young, fax 405-325-3140.

Appendix E

Fracture Analysis of the Gypsy Outcrop and Surrounding

Area to Determine the Susceptibility

of Fluvial Deltaic Reservoirs to

Natural Fractures That will Effect Waterflood Recovery of Oil

by

Victoria French

Fracture Analysis of the Gypsy Outcrop and Surrounding Area to determine the susceptibility of fluvial deltaic reservoirs to natural fractures that will effect waterflood recovery of oil

Victoria L. French

Introduction

A study of fracturing within the Gypsy Sandstone and outcrops within the surrounding area has been undertaken to determine the susceptibility of fluvial deltaic reservoirs to natural fractures and their possible effect on waterflood recovery of oil. This study is designed to determine the dominance of any probable flow orientations for the proposed tracer test (contrasting salinity flood) which is planned in conjunction with the Gypsy project. Knowledge of natural fractures and understanding their effect on primary production and secondary recovery within a reservoir prior to reservoir development can greatly increase economical field development. The Gypsy Field Project presents an excellent opportunity to study all aspects of reservoir development, including the influence of a regional fracture pattern on improved recovery of conventional oil.

Fracture Orientation

Field evidence indicates the presence of a regional fracture trend in the Gypsy outcrop site and surrounding area. Fractures were mapped at 21 outcrop locations over a 270 square mile area (T 19-22 N; R 8-11 E), including the Gypsy surface site. These outcrops indicate a regional orthogonal fracture pattern extending across the area. The most dominant fracture set (systematic) within the study area trends approximately N 65-75 E (065-075), with the less dominant set (nonsystematic) trending approximately N 25-35 W (325-335). The systematic set is aligned with the present day in-situ state of stress N 65 E (1995, Sumner; verbal communication). Other studies collaborate the existence of this trend in north-central Oklahoma and south-central Kansas (Melton, 1929; Ward, 1968; Hagan, 1972; Rizer and Queen, 1986; Rizer, 1988; and Bevan, 1989). Recent research also suggests that these orthogonal sets extend eastward onto the western margin of the Ozark Uplift. In addition, normal faults within the proximity of the Gypsy site and in north-central Oklahoma have been described (Fath, 1920, Foley, 1926; Melton, 1929; and Carl, 1957) to exhibit the same orientation (325-335) as the nonsystematic set of fractures mapped within the area.

Figure 1 is a Rose Diagram showing the main orthogonal fracture sets observed at all outcrop locations. The northerly fracture set seen occurring between the two dominant sets

reflects fractures from the Gypsy outcrop site. While the outcrop along the dip section, just to the northwest of the main Gypsy outcrop site, exhibits the orthogonal trend seen predominately throughout the area of study (fig. 2), fracture data from the Gypsy outcrop site strike section was seen to vary considerably from the main orthogonal sets mapped at other localities (figs. 3 and 4). Fractures at this location trend predominately N 10 W to N 15 E (350-015). Several factors may be responsible for the variation in fracture orientation seen at the Gypsy outcrop strike section. This particular outcrop is a roadcut along the Cimarron Turnpike and was extensively dynamited during road construction. In addition, the dominant fracture orientation (065-075) is oriented subparallel to the strike of the outcrop. Fractures exhibiting the two main orthogonal orientations are recorded at the Gypsy outcrop strike location, however, they were seen to form some of the larger faces and occurred much less frequently. Subsequently, during the process of fracture mapping they are considerably overshadowed by the northerly orientated fracture group. Because the Gypsy outcrop strike location is the primary area of ongoing research, the greatest intensity of fracture data was recorded at that locality. This explains the magnitude of the northerly orientation seen on Figure 1.

Fracture Characteristics

Lithology seemed to directly influence fracture density in several units. This was seen to occur primarily in the mudclast-rich sandstone, shale, and large scale, high-angle cross-bedded sandstone lithofacies. At the Gypsy outcrop strike location, fractures tended to terminate at the contact between the overlying plane-bedded sandstone facies and the mudclast-rich sandstone facies. Where fractures were observed within the mudclast facies, they tended to be highly irregular and die out quickly. This same observation was seen to occur within shale units occurring between sandstone intervals, particularly on the exposure located on the southern side of the Gypsy site roadcut.

At outcrop localities where large scale, cross-bedding was observed (cross-bedding forsets of several feet or larger), fractures were observed to be highly irregular and to die out within the sand bodies. It is believed that high-angle, large scale cross-bedding has influenced the propagation of fractures at these localities. It is important to note that small scale cross-bedding (less than a foot) did not appear to affect the occurrence or influence the planar nature of fractures.

Only minor mineralization was seen to occur along fracture planes within the study area. Most mineralized fractures were observed at the Gypsy outcrop strike location and occurred predominately within the mud-clast facies. It is interesting to note that the average trend of mineralized fractures was seen to be approximately N 39 W, along the nonsystematic orthogonal set. This is somewhat contradictory to what might be expected considering the present day in-situ stress. As mentioned previously, fractures within this lithofacies occurred

infrequently, tended to have highly irregular surfaces and died out quickly. It is not certain whether or not the mineralization within these fractures may be a recent event. The small number of mineralized fractures seen to occur in facies overlying the mud-clast facies suggests the possibility that this mineralization may be the result of more recent weathering and solution from above.

Fracture Spacing versus Bed Thickness

A direct relationship between fracture spacing and bed thickness was observed at all outcrops (fig. 5). While spacing between individual fractures within beds was not seen to be highly predictable, a direct linear relationship is seen to occur when fracture occurrence is averaged over an interval for a given bed thickness. Spacing versus bed thickness data (fig. 5) for the study area suggests that fracture spacing can be predicted, especially in the thinner bedded units where fracture spacing is nearly proportional to bed thickness. A good correlation is seen even though measurements reflect a wide range of variability in lithofacies occurring within individual beds.

Applications to Waterflood Recovery of Oil

The implications of fracturing on waterflood recovery of oil are probably best illustrated in the masters study of the North Burbank Field completed by Hagen (1972). Waterflood development within the North Burbank Field, located approximately forty miles northwest of the Gypsy outcrop site, was found to be significantly influenced by the same orthogonal fracture set seen throughout the study area. Shortly after initiation of the waterflood program at North Burbank, "large quantities of water appeared in oil-producing wells both east and west of the pilot flood area, apparently channeling through open joints. Evidence for a subsurface joint system at the depth of the reservoir has been the frequent early breakthrough of water from the injection to the recovery wells in an east-northeast direction parallel to the orientation of the primary surface joint set" (Hagen, 1972). Taking into consideration the present day in-situ state of stress, the systematic fracture set seen throughout northern Oklahoma and southern Kansas would tend to be the open set. Even if fracturing did not significantly influence primary production, pressures exerted during waterflooding combined with the in-situ stress state, would most likely enlarge the fracture apertures of the systematic set during the flooding process. As seen at the Burbank Field, all reservoir waterflood, as well as primary recovery programs, should include fracture analysis prior to field development.

References

Bevan, T. G., 1989, A fracture analysis of the BPX IRD Exposure (Gypsy Sandstone) near Tulsa, Oklahoma, USA: BP internal report, No. EXT 53950.

Carl, J. B., 1957, Geology of the Black Dog area, Osage County, Oklahoma: unpublished Masters thesis, The University of Oklahoma, 82 p.

Fath, A. E., 1920, The origin of the faults, anticlines and buried "Granite Ridge" of the northern part of the Mid-Continent oil and gas field: U. S. Geological Survey Professional Paper 128-C, p. 75-84.

Foley, L. L., 1926, The origin of the faults in Creek and Osage Counties, Oklahoma: American Association of Petroleum Geologists Bulletin, volume 10, No. 3, p. 293-303.

Hagen, K. B., 1972, Mapping of surface joints on air photos can help understand waterflood performance problems at North Burbank Unit, Osage and Kay Counties, Oklahoma: unpublished Masters thesis, The University of Tulsa, 85 p.

Melton, F. A., 1929, A reconnaissance of the joint-systems in the Ouachita Mountains and Cental Plains of Oklahoma: The Journal of Geology, volume 37, No. 8, p. 729-746.

Ward, J. R.,1968, A study of the joint patterns in gently dipping sedimentary rocks of south-central Kansas: Kansas State Geological Survey Bulletin 191, part 2, 23 p.

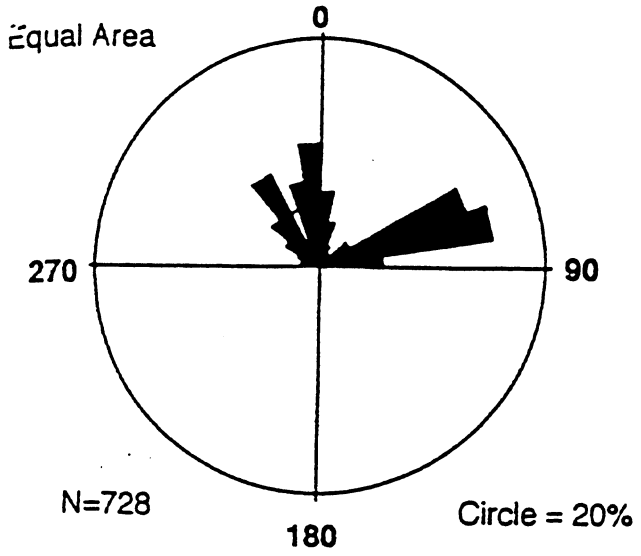

Figure 1

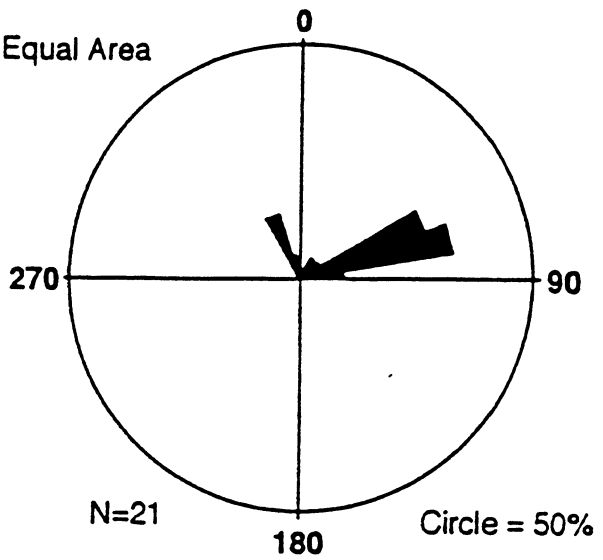

Figure 2

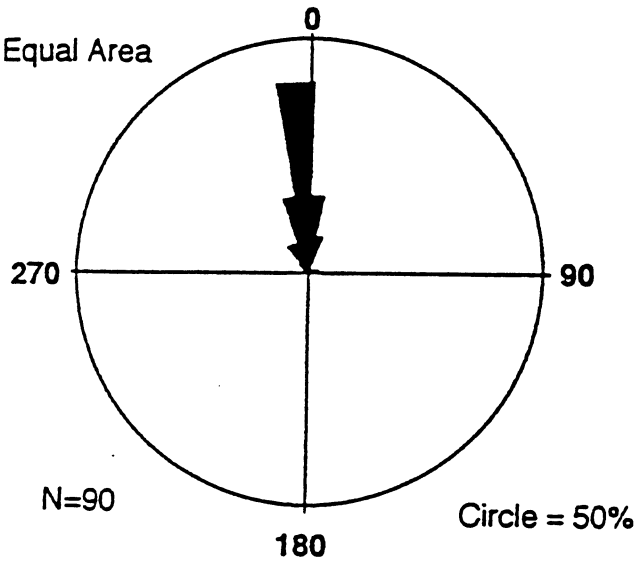

Figure 3

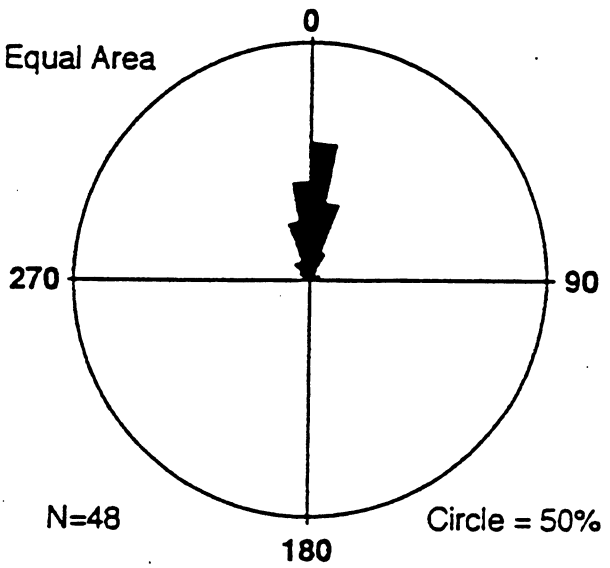

Figure 4

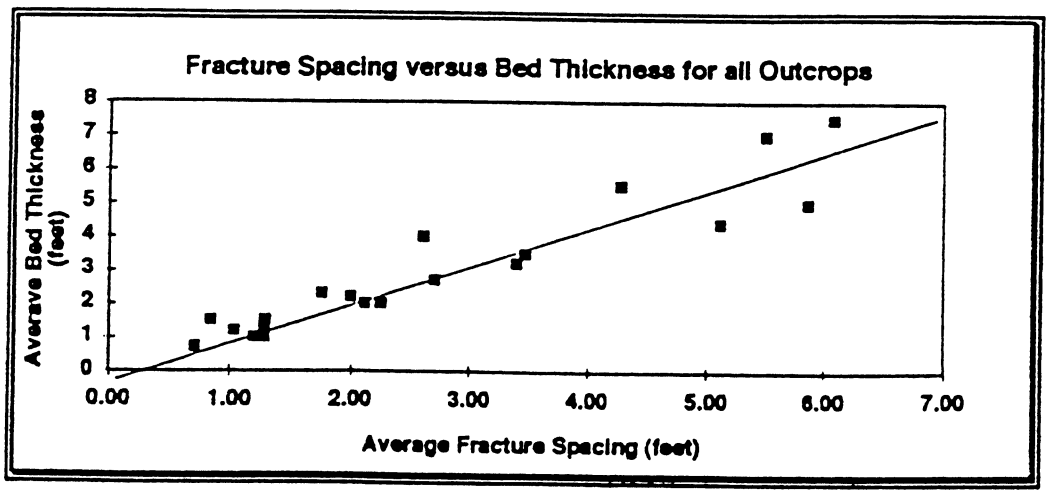

Figure 5

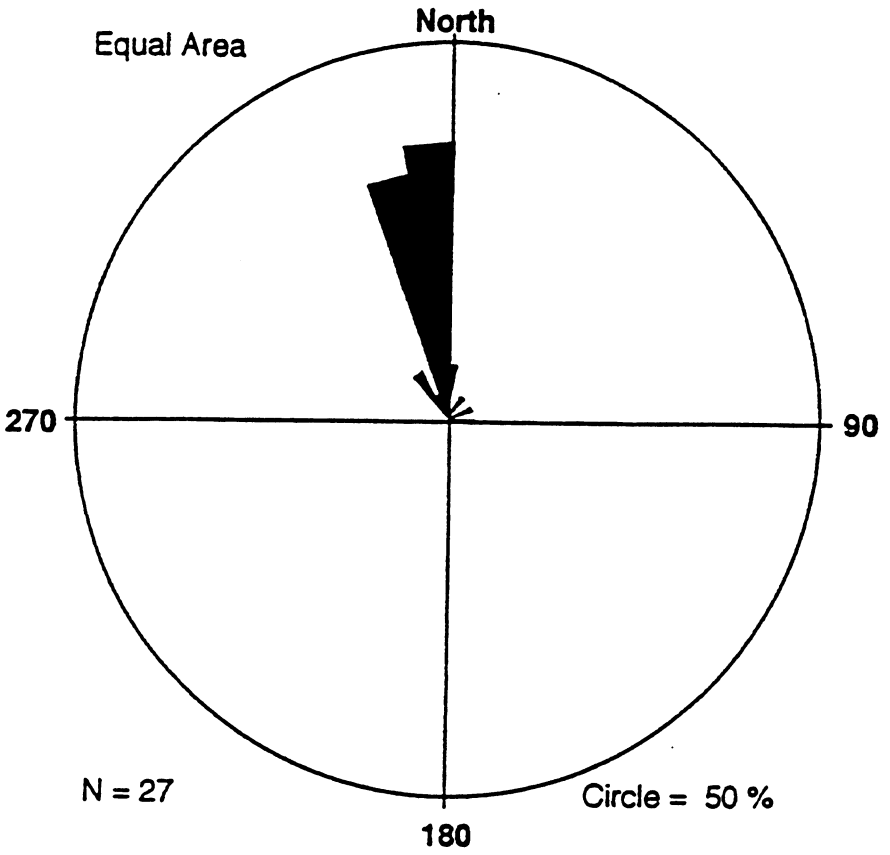

Rose Diagram: Gypsy roadcut site on Hwy 64, Keystone Dam Quadrangle (location 1A north face - uppermost level of outcrop along frontage road).

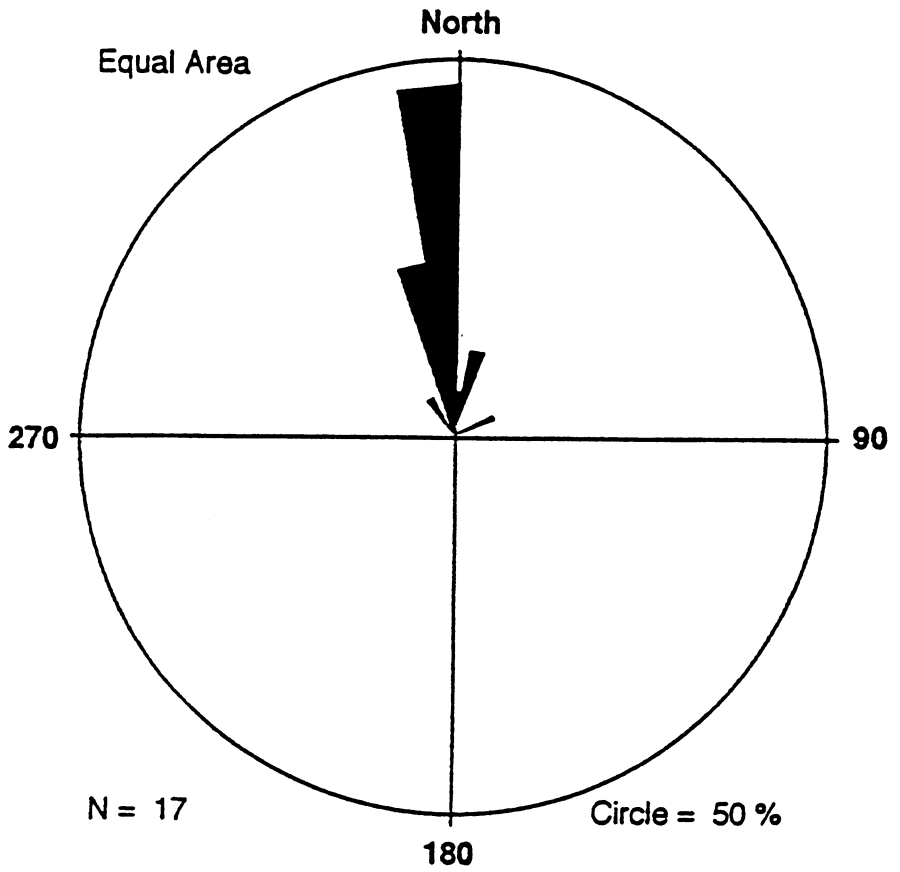

Rose Diagram: Gypsy roadcut site on Hwy 64, Keystone Dam Quadrangle (location 1A north face - middle level of outcrop).

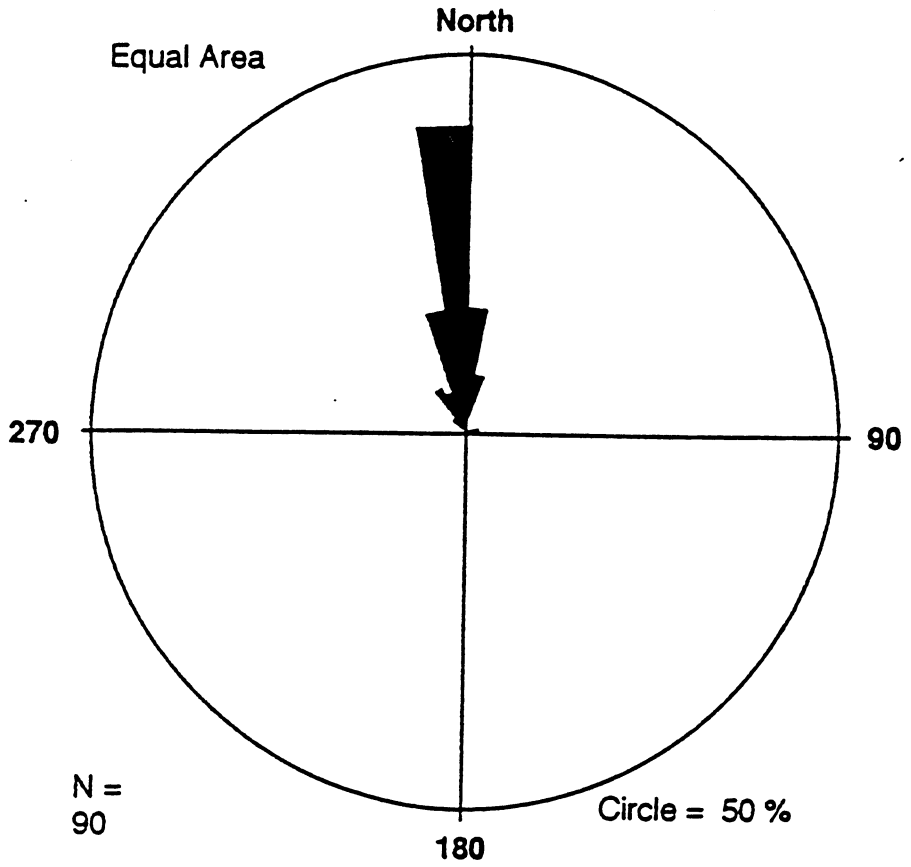

Rose Diagram: Gypsy roadcut site on Hwy 64, Keystone Dam Quadrangle (location 1A north face -lower level of outcrop).

Appendix F

Excerpts from "The Application of Ground Penetrating Radar for the Geological Characterization in Three Dimensions at the Gypsy Outcrop Site, Northeastern Oklahoma, USA"

by

Zhengan Deng

Master's Thesis, University of Oklahoma, 1997

ABSTRACT

Ground Penetrating Radar (GPR) has been widely applied to high-resolution mapping of soil and rock stratigraphy, and fracture detection. GPR is successful in defining stratigraphic boundaries and fractures in three dimensions at the Gypsy Outcrop Site, near Tulsa, Oklahoma. The dielectric contrasts between lithofacies and within a lithology both cause radar reflections at the Gypsy Outcrop Site. The boundary reflection is caused by the difference in clay content and/or porosity of the lithofacies across the boundary. The reflection within a facies is caused by the change of grain size and/or the change of porosity. Fractures can be detected at the Gypsy Outcrop Site because the place where fracture intersects with dielectric contrasts can cause radar diffractions. These diffractions are different from the diffractions caused by subsurface heterogeneity because they form regular patterns.

Some GPR data processing techniques have been used in order to increase the S/N ratio and to attenuate air wave reflections. techniques for 2-D data processing include: time-zero shift, bandpass filtering, amplitude recovery, spectral balancing, domain filtering and migration. Since 3-D radar data require much higher S/N ratio, the following special processing techniques have been applied after applying 2-D data processing techniques mentioned above: 3-D dip filtering and 3-D coherence.

GPR 2-D data were interpreted with the help of borehole information at the ends of radar lines forming a grid. The interpreted radar boundaries were digitized and isopach maps of the upper two channels were then made based on the digitized data. Isopach maps with and without adding radar information between boreholes show that the composite map adds detail to the shape of the channel and its horizontal extent. The pinchout of the channel is seen to be more abrupt after adding GPR information.

3-D coherence processing is a new technique applied to seismic reflection data. This is the first time for this method to be applied to radar data. The 3-D coherence processing at the Gypsy Outcrop Site has shown a much clearer view of the stratigraphic boundaries and fractures. The fractures detected by radar data have a 90^{o} dip, N/S strike and regular spacing.

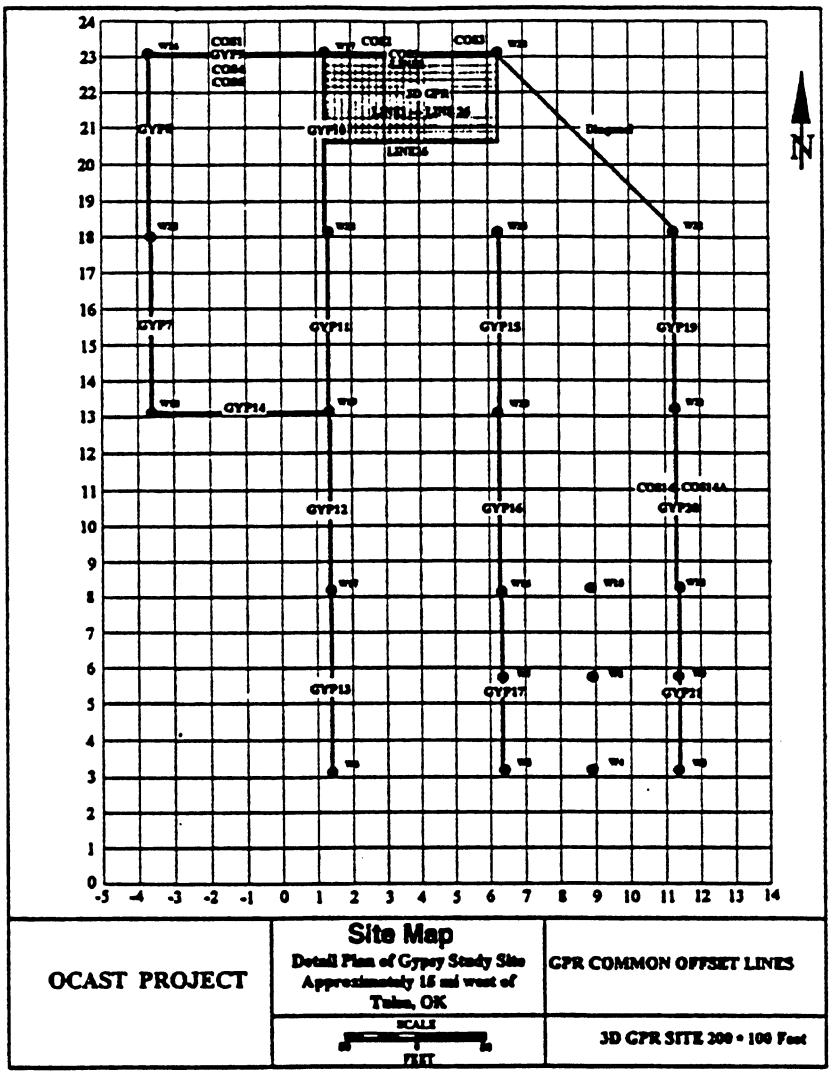

Figure 1.3 GPR 2-D and 3-D survey location at the Gypsy Outcrop Site. Coordinates use BP grid.

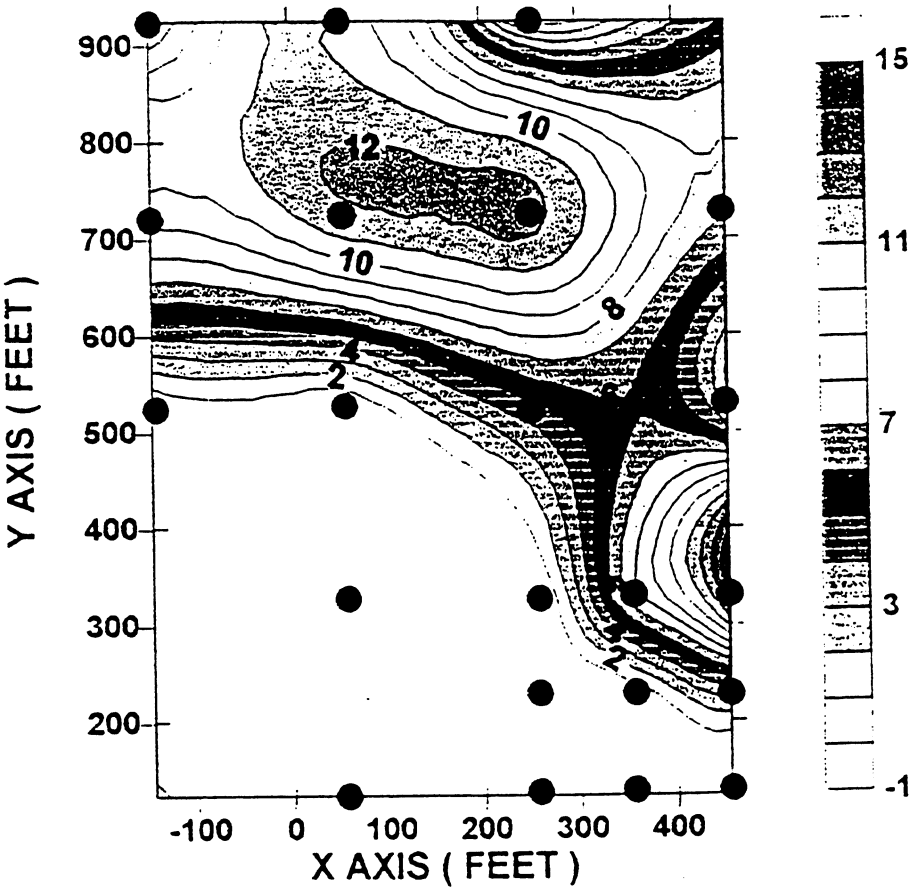

Figure 3.12 Isopach map of channel 6 using core information only.

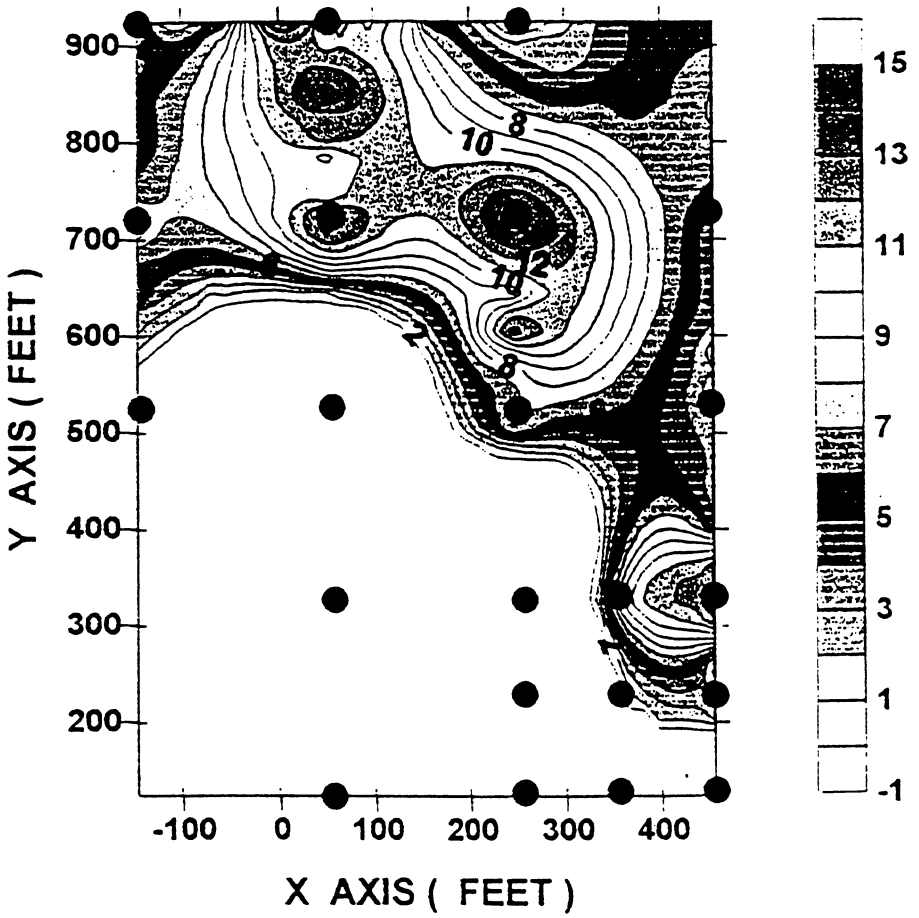

Figure 3.13 Isopach map of channel 6 using core and radar results together. Channel 6 is more contained in northeast region, shows more abrupt pinchout, and has a clearer trend after adding GPR information.

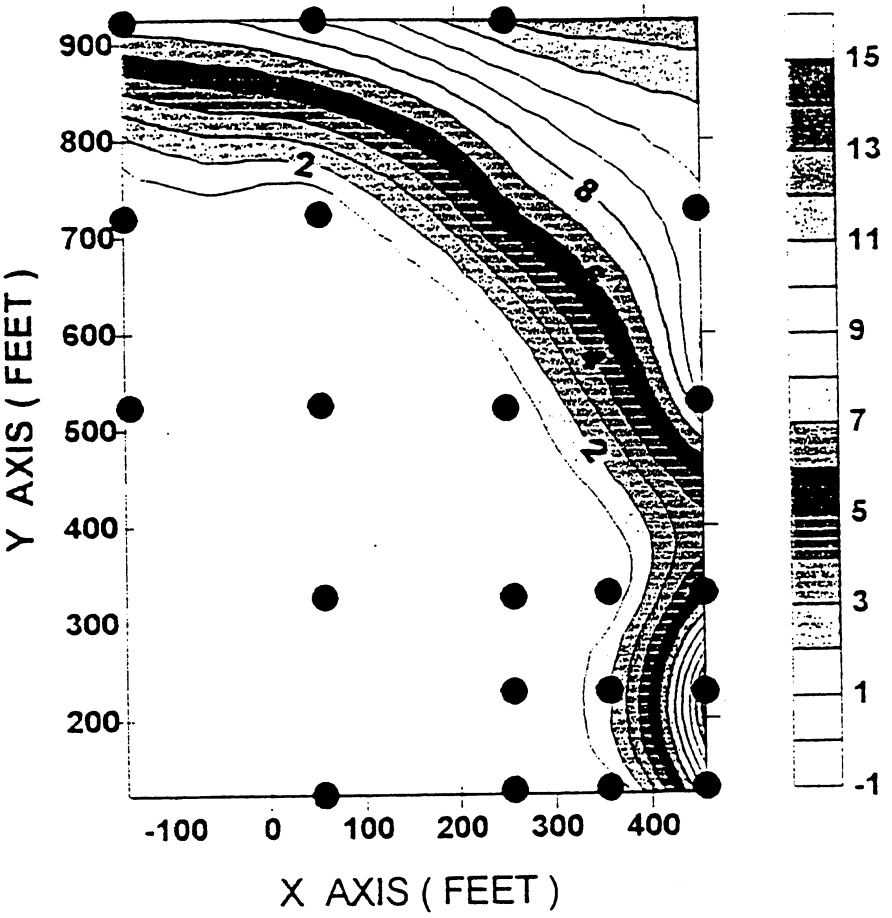

Figure 3.14 Isopach map of channel 4 using core information only.

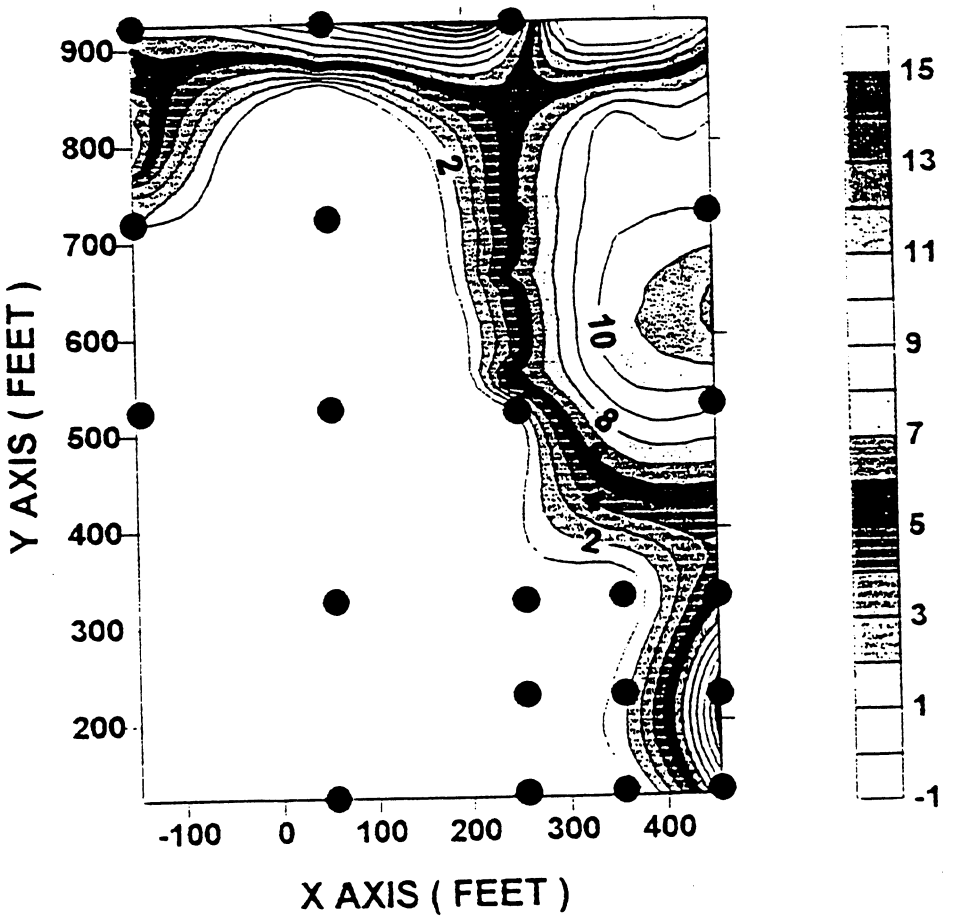

Figure 3.15 Isopach map of channel 4 using core and radar result together. The direction of channel in the northeast is more clearly defined. A thickening in the channel at the edge of the area is revealed between borehole, and the channel pinches out more abruptly than expected from borehole data only.

CONCLUSIONS

GPR was successful in defining stratigraphical boundaries and fractures in three dimensions at the Gypsy Outcrop Site. The dielectric contrasts between lithofacies and within a lithology cause radar reflections at the Gypsy Outcrop Site. The comparison between GPR data and borehole information at borehole 27 shows that the boundary reflection was caused by the difference in clay content and/or porosity of the lithologies above and below the boundary, while the reflection within a layer was caused by the change of grain size in a lithology.

Fractures can be detected at the Gypsy Outcrop Site because fracture intersections with dielectric contrasts cause radar diffractions. These diffractions can be distinguished from the diffractions caused by subsurface heterogeneity because of their regular patterns.

The conductivity measurement at the Gypsy Outcrop Site shows that the conductivity is low (less than 20 mS/m) in north and northeast region. This region is ideal for the GPR survey. The water content may not play an important role in the GPR survey at the area since the water table there is below the penetration limit of GPR.

GPR 2-D tests show that at the low conductivity region, 100 MHz data can image the inner boundary of channel 6 and penetrate the bottom boundary of channel 6. So, it should be applied at the low conductivity region. At the high conductivity region, due to the penetration limit of 100 MHz data, 50 MHz data should be applied. In order to obtain the best penetration, 50 MHz and 1000 V pulsar voltage GPR system should be applied for 3-D data collection.

Since there are a number of man-made and natural obstacles existing at the Gypsy Outcrop Site and GPR data have a low S/N ratio, some GPR data processing techniques have been applied before data interpretation. These techniques include: time-zero shift, bandpass filtering, SEC, spectral balancing, migration, domain filtering, dip filtering (for 3-D data only), and 3-D coherency (for 3-D data only). These techniques have successfully increased S/N ratio and attenuated the direct and reflected air wave.

GPR and seismic refraction comparison shows that both dielectric contrast and seismic velocity change at the channel boundary. The boundary interpreted by radar reflection method and the boundary interpreted by seismic refraction method coincide.

Isopach maps based on borehole data with and without adding radar information between boreholes, show that GPR adds detail to the shape of the channel and its horizontal extent. The pinchout of the channel is seen to be more abrupt after adding the GPR interpretation results.

Appendix G

Excerpts from "Detection and Modeling of Fractures and Their Influence on Flow Simulation at the Gypsy Site, Oklahoma"

by

Matthias Mueller

Master's Thesis, University of Oklahoma, 1997

Contents

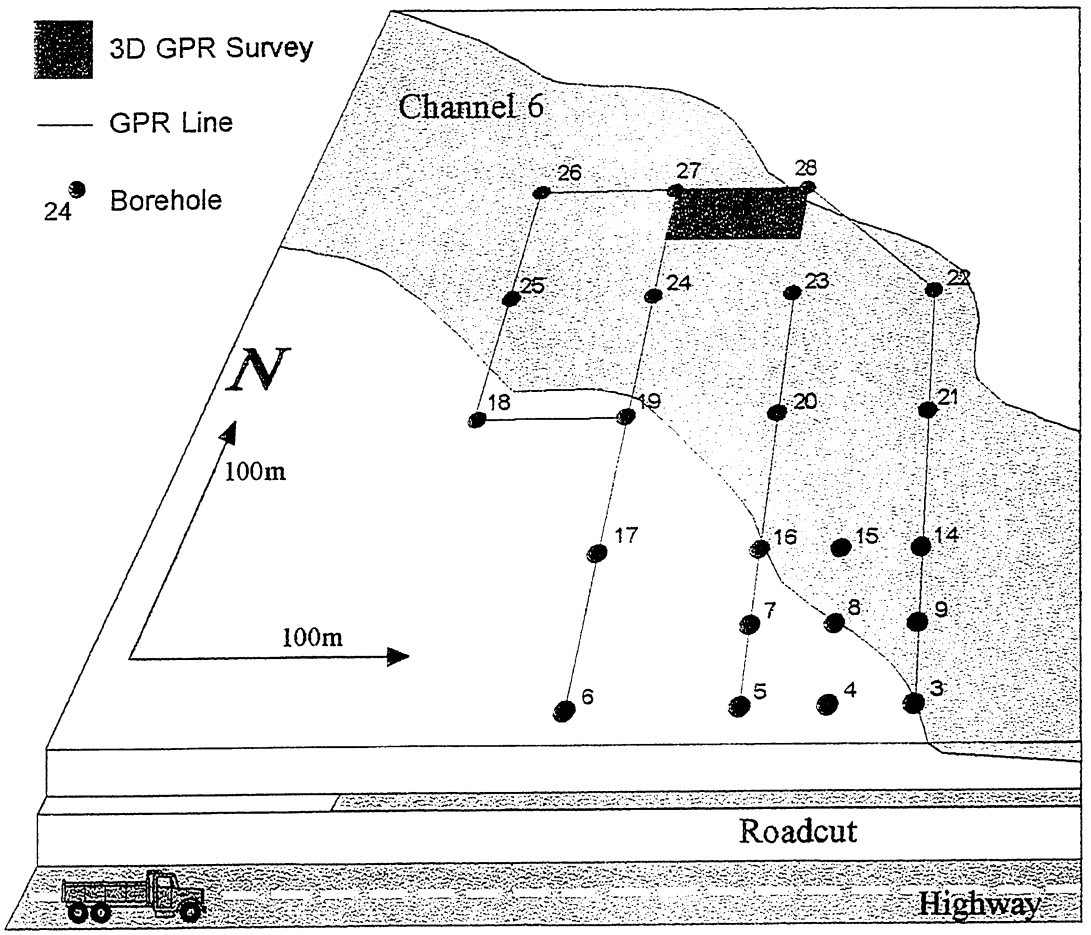

Figure 1: The outcrop of the Gypsy sandstone at the study site.
The rocks are exposed at the roadcut, the general channel trend is represented by the uppermost channel 6. The seismic refraction data have been acquired within the 3D GPR area (see also Figure 3)

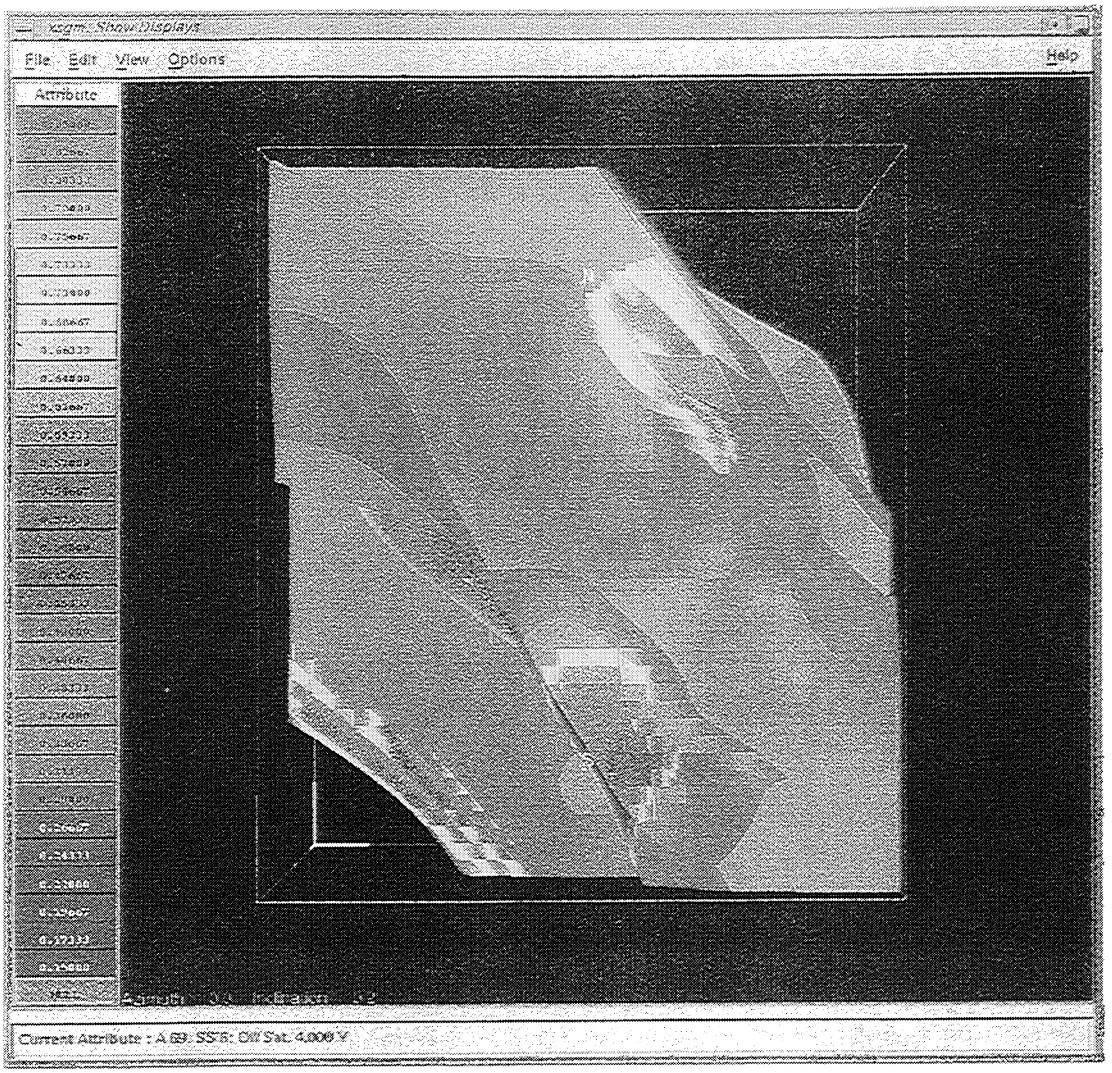

Figure 37: Non - fractured model.
View of channels from top. Waterflood from S to N. Displayed attribute is oil saturation after 4 years.

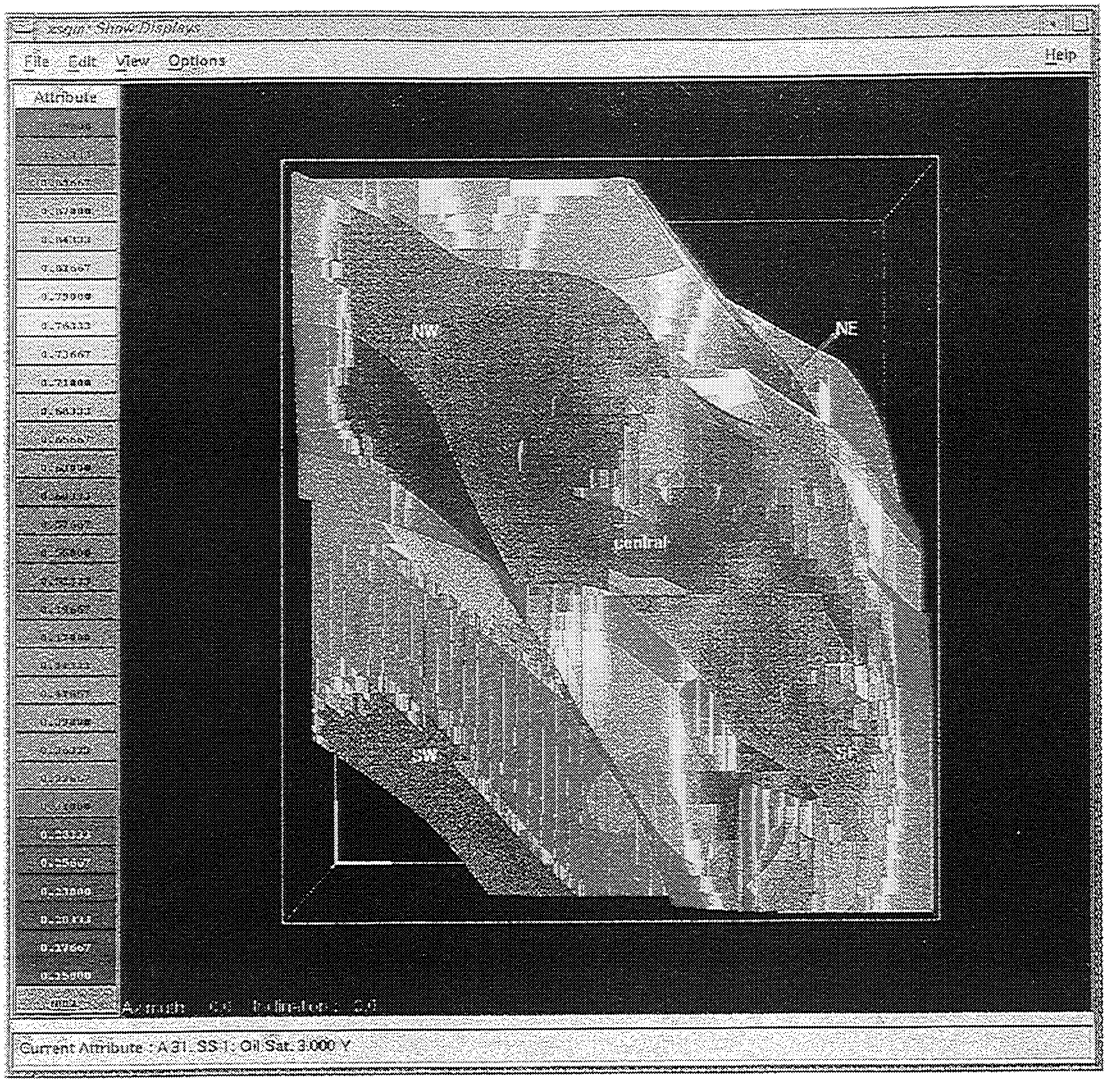

Figure 39: Five spot waterflood with the original permeability.
Fractured model. The Simulation reached the water cut limit (0.9) after 3 years. Displayed attribute is oil saturation after 3 years.

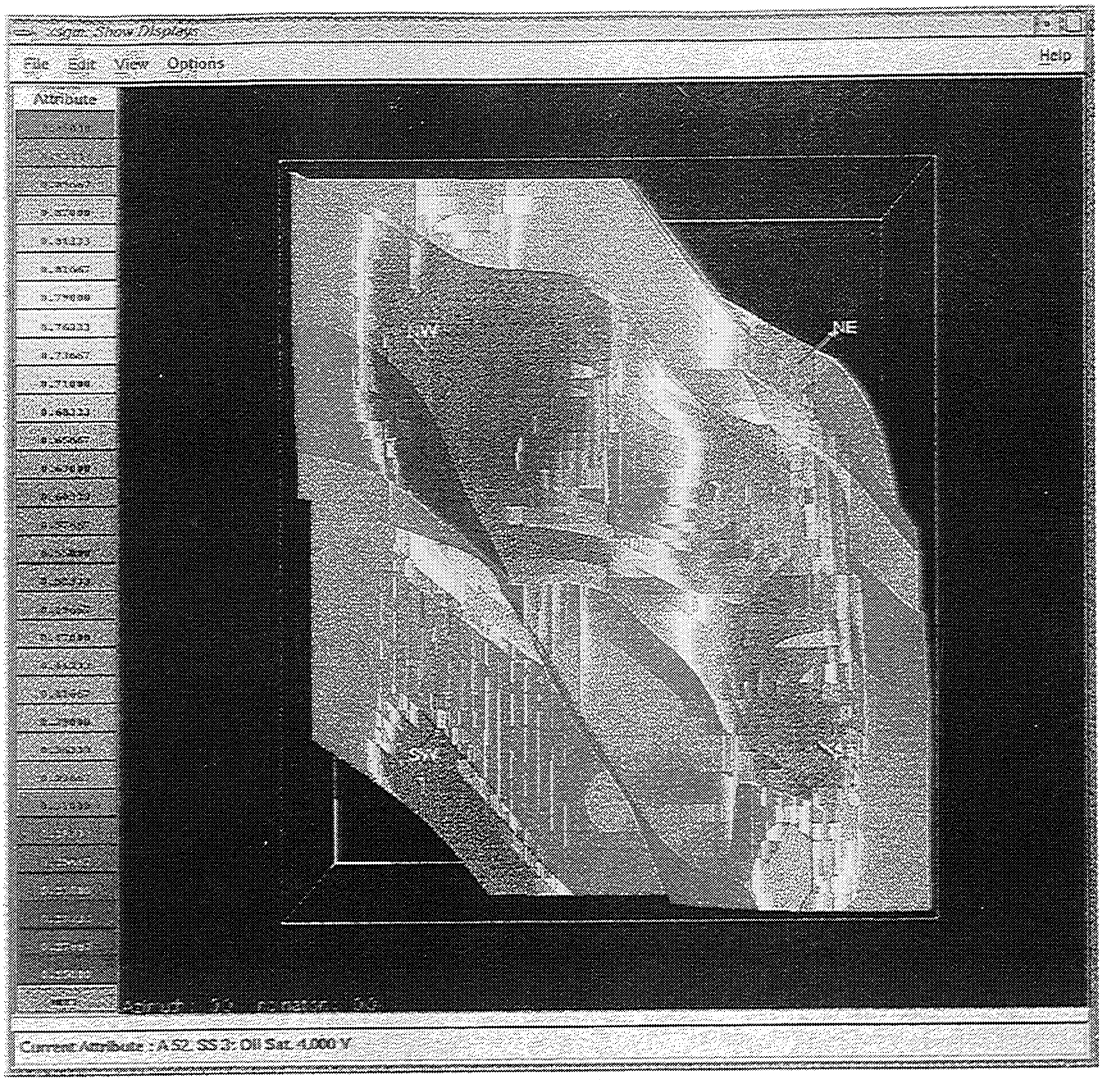

Figure 41: View of the channel units from above.
Fracture model - five spot waterflood after 4 years. Reduced matrix permeability is assigned to this model. The water breakthrough occurred after 2.2 years. Compare with Figure 38 and Figure 39.

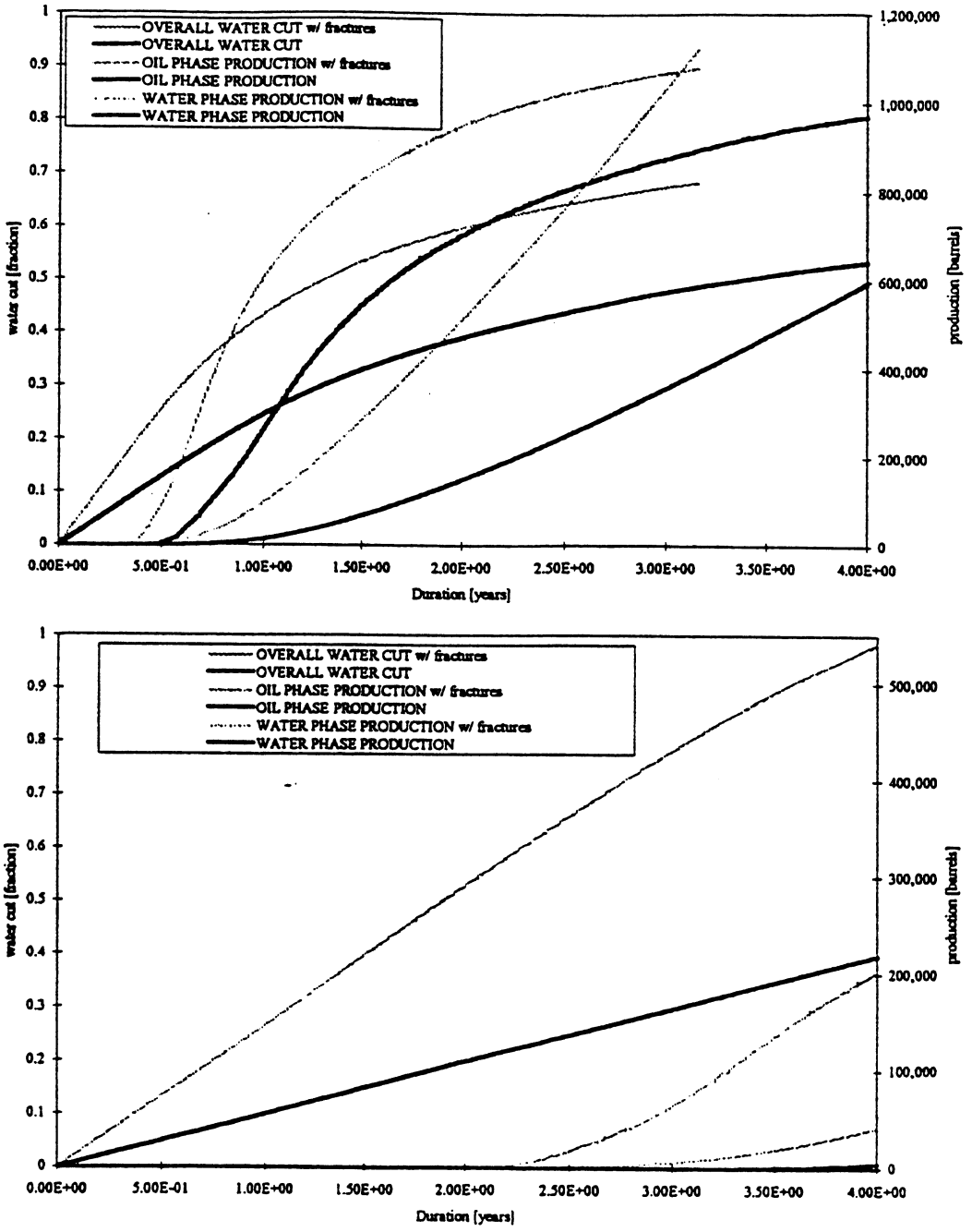

Figure 38: 5 spot waterflood.
Cumulative production and water cut for the five spot waterflood simulation using permeability obtained from the well cores (above) and the reduced permeability (below). The fractured high permeability model reaches a water cut of 0.9 after 3 years and is halted. Production from the low permeability model without fractures is very low, the water breakthrough begins after 4 years.

3.3.4 Results Of A Five Spot Waterflood

A standard five spot waterflood was simulated using parameters for fluid flow and saturation identical to the two spot pilot flood,. Four wells were placed at the corners of a rectangle with the producing well in the center. The injection wells in each simulation had a pressure of 40psi (276kPa) and the producer a pressure of 10psi (69kPa, at the top of the model elevation).

The average permeability of the channels used for this study is very high. To show a more realistic picture, the five spot waterflood was also performed in a low permeability model. To obtain a permeability distribution typical of other Pennsylvanian fluvial reservoirs the permeability was reduced by approximately the factor 10, using Equation 9. The permeability of the fractures was reduced to 8,000mD. The porosity, the oil saturation and OIP are identical to the pilot flood simulation parameters.

$$k_{reduced} = 2 \cdot k_{measured}^{0.62}$$

Equation 9: Reducing the permeability in the channel sands.

The water input achieved with a given pressure is reflecting the permeability in the model. The fractured model provides higher permeability in both cases. In the high permeability model the water input doubles with fractures, in the low permeability model the input triples.

4. Conclusions

Fractures at the Gypsy study site, observed at the roadcut and detected by 3D Ground penetrating radar can be significant for fluid flow. Refraction seismic has the potential to identify velocity anisotropy which can provide information to characterize fractures. It had been successful in other studies, especially in limestone with regular spaced large fractures. The seismic refraction survey in this work could not reach the targeted depth. An irregular refractor, low acoustic velocities and data scatter prevented the detection of velocity anisotropy.

The fractures measured at the roadcut are open, the dominant fracture set strikes at 345° to 005°. Most fractures terminate at shale or shale/silt beds and layers. The entire flow properties of the fractures are not known, no actual pump test have been conducted so far.

Fractures were modeled, using a high resolution geological model. Flow properties assigned to the fractures support the fluid flow in fracture direction. Simulations represented a reservoir of Nelson's (1993) type 3: fractures assist permeability. Using different well arrangements, flow rates, ranges of permeability and comparisons to a non fractured model it was shown that natural fractures can either improve waterflood performance or reduce recovery by limiting sweep depending on the relationship between well positions and fracture orientation.

This work shows that detailed reservoir characterization studies for simulation should include fracture characterization, even in reservoirs with good matrix permeability. Techniques to detect seismic velocity anisotropy can aid fracture characterization, if the conditions are favorable.

Appendix H

Application of Ricker Wavelet in Wavelet Transform

by

Xia Li

Application of Ricker Wavelet in Wavelet Transform

by Xia Li

As we all know, a signal may have two sets of representations in two different domains. One is in time domain, and the other is in frequency domain. The two representations, with different patterns, are the projection of the same signal from one domain to the other. Thus spectral analysis is an important tool for many processing procedures. There are many ways to do the frequency transform. Here the application of wavelet transform to spectral analysis is studied and compared to traditional Fourier methods.

Traditionally, the 1-D Fourier transform is used to get an average frequency spectrum of the whole signal within a time window. However, it includes no time localization information, thus it provides a poor representation for a seismogram that has many local features. However, we usually think of a seismogram using a convolution model or some model quite similar to it, i.e., a reflection series convolved with a wavelet (which is very compacted in time.) Thus reflection seismograms have many local features in time. Also, seismic signal attenuate with distance and high frequency energy attenuates more rapidly than low frequency energy. Thus, the reflection seismogram usually has a spectral content variant with time. Short time Fourier transform(STFT) is commonly used to improve the time –localization of the frequency content.

In STFT, moving windows are used to compute the Fourier spectrum under the assumption that the spectrum is stationary within the window. However, this method lacks theoretical proof that it is a valid time-frequency representation of the signal. Also because it uses a boxcar to window the signal, the spectrum display is the convolution of the sinc function (Fourier transform of the boxcar) with the true spectrum of the signal within the window. Thus it causes side lobe problem. What's more, it works well only when the major structures are localized over an interval whose size are close to the size of the window. It can not give a good spectrum analysis if the size of the main structure is much bigger or smaller than the size of the window. Thus it suffers from limited frequency resolution, and always has the problem of time resolution because of the invariant window length. Flexible methods are needed to represent signal components whose localization in time and frequency varies widely.

Wavelet analysis expands signals over a family of functions, which we call kernel atoms or time-frequency atoms. Because the atom has compact support both in time and in frequency domain, we keep good time and frequency resolution flexibly with the different choice of kernel atoms from the wavelet family. A general family of time-frequency atoms can be generated by scaling, translating and modulating a single atom W(t).

Here we discuss a flexible wavelet analysis method, matching pursuit decomposition, with Ricker wavelets for kernel atom family. Obvious advantages of the method and the choice of ricker wavelets are a much-improved time and frequency resolution.

Matching Pursuit Decomposition

We use matching pursuit decomposition(Mallat S. and Zhang Z., 1993; Avijit Chakraborty and David Okaya, 1995)to expand the signal over a set of band-limited wavelets. At each iteration, we decompose the residue by a wavelet that matches the residual signal best. This procedure is repeated each time on the following residue that is obtained. The choice of the wavelet reflects the correspondent characteristics of the signal both in time domain and in frequency domain.

Let f denote the seismic signal. We use a band-limited family of wavelet to decompose the signal. Let D denote the wavelet family. With $W\gamma_0 \in D$, the signal f can be decomposed into

$$f = \langle f, W\gamma_0 \rangle W\gamma_0 + Rf$$

where Rf is the residual signal after approximating f in the direction of $W\gamma_0$. The algorithm chooses $W\gamma_0 \in D$ such that $|\langle f, W\gamma_0 \rangle|$ is maximum. When we have computed the n^{th} order residue $R^n f$, for n>=0, the algorithm chooses, $W\gamma_n \in D$, which closely matches the residue $R^n f$.

The residue $R^n f$ is subdecomposed into

$$R^n f = \langle R^n f, W\gamma_n \rangle W\gamma_n + R^{n+1} f$$

We continue the procedure for m times until it meets a selected threshold. We decompose f into the sum

$$f = \Sigma_{n=0}^{n-1} \langle R^n f, W\gamma_n \rangle W\gamma_n + R^m f$$

By this procedure, we decompose the signal into a set of wavelets concentrated on both time and frequency. We keep both the high time and frequency resolution.

Ricker Wavelet Family

Our kernel atom is the Ricker Wavelet, given by

$$W(t) = (1-2\pi^2 \hat{f}^2 t^2)\exp(-\pi^2 \hat{f}^2 t^2)$$

In the matching pursuit decomposition, a family of wavelet functions is generated by scaling, translating, modulating a single wavelet function as,

$$W(s, \tau,\xi,\theta) = s^{-1/2} W((t-\tau)/s, \xi)e^{i\theta}$$

Where s is the scale, τ is the translation, ξ is the frequency modulation and θ is the phase modulation.

The basic functions are called "time-frequency" atoms because it contains both time and frequency component. We use the Ricker wavelet(Figure 1a and 1b) because it is one of the most fundamental wavelet patterns in reflection seismograms and because it satisfies the admissibility conditions (Shensa, 1992; Goupilland etc. 1985).

1. W(t) should be absolutely integrable and square integrable(i.e. its energy is finite);
$$\int W(t)\, dt < \infty \text{ and}$$
$$\int |W(t)|^2 dt < \infty$$

2. W(t) is band limited and has zero mean;
$$\int |W(\omega)/\omega|^2 d\omega < \infty$$

Comparison Of The STFT And The MPD

We use a synthetic digitized seismic signal to study the time-frequency resolution properties of STFT and MPD methods. Then we invert the time-frequency analysis back to the frequency domain and compare the result with the 1-D Fourier transform. Also the reconstructive signal from the extracted wavelets is compared with the original signal.

Figure 2 is a synthetic digitized trace produced by the convolution of Ricker wavelet of different center frequencies with a reflectivity series. The reflectivity series has a positive spike at n=16(n is the No. of the sample)(A), a positive spike at n=92 (B), a set of 2 (positive-positive)spikes at n=141(c), a set of 2(positive-positive)spikes at n=176(D) and a set of 3(positive-negative-positive)spikes at n=246(E).

Reflection A is created using a 40 Hz Ricker wavelet. The STFT(Figure 3) of this reflection produces a rectangular region centered at 40 Hz and 16th sample. Although it detects the frequency distribution of the reflection, it has a poor time resolution. However, the same reflection is well resolved both in time and frequency in the F-T plot(Figure 4), produced by MPD.

Reflection B is created using a 40 Hz Ricker wavelet and a 10 Hz wavelet. They are superposed at the same time. The STFT of the event produce a rectangular region with the maximum amplitude centered at 10 Hz and 45Hz. However, they are well resolved by MPD with the maximum amplitude centered at 11Hz and 43 Hz. They are both detected

at the 92th sample.

Event C is composed of two individual reflections. The source is a 30Hz ricker wavelet. The STFT of the event has the maximum amplitude centered at 17Hz and 47Hz, while MPD shows the maximum amplitude is centered at 39Hz and 32Hz, with the time centered at 141th and 146 th sample respectively.

Event D is composed of two individual reflections. The source is a 30Hz ricker wavelet and a 20Hz ricker wavelet. The STFT of the event has the maximum amplitude centered at 19Hz and 46Hz, while MPD shows the maximum amplitude is centered at 40Hz and 29Hz, with the time centered at 176th and 182 th sample respectively.

Event E is composed of three individual reflections. The source is a 30Hz ricker wavelet. The STFT of the event has the maximum amplitude centered at 19Hz and 46Hz, while MPD shows the maximum amplitude is centered at 30Hz, 33Hz and 29Hz, with the time centered at 244th , 246th and 253 th sample respectively.

Finally, when we convert the wavelet transform from time-frequency domain to frequency domain(Figure 5), an excellent match with the traditional 1-D Fourier transform is achieved. This is difficult to achieve with the STFT. Thus the wavelet transform provides a convenient and flexible method to project to and from time and time-frequency domain.

Application of Wavelet transform To an Arbitrary Trace

A trace of 64 samples(Figure 6) was used which comes from the first part of the horizontal component of a seismogram. It's highly variable with the amplitude lying within a wide range from less than one to almost two hundred. It may consist mainly of noise.

From the 1-D Fourier transform(Figure 7), it shows that the frequencies higher than 60 Hz are the dominant component. After wavelet transform(Figure 8), we see the change of frequency content with the time clearly. It shows that there is some low single-frequency(about 4-6 Hz) noise throughout the whole trace. There is also an obvious reflection pattern.

Conclusion

The wavelet transform is another way to do time-frequency analysis. It provides a better estimate of the frequency change with time than the STFT, and it also has the advantage of time localization of the frequency content. The STFT can only give us an average representation depending on the length of the moving window. It is better than STFT theoretically and potentially.

There are many potential applications of the wavelet transform, relating velocity analysis, Q inversion, reflectivity analysis, noise reduction, etc. These are left as objectives of future research.

Plot Index

- Figure 1a, plot of a Ricker wavelet with the central frequency 40 Hz.
- Figure 1b, plot of the 1-D Fourier transform of the wavelet.
- Figure 2, a synthetic trace composed of Ricker wavelets.
- Figure 3, plot of STFT of the trace.
- Figure 4, plot of wavelet transform of the trace.
- Figure 5, Comparation of inverted 1-D Fourier transform with the traditional 1-D Fourier transform.
- Figure 6, a arbitrary trace coming from the horizontal component of the seismogram.
- Figure 7, traditional 1-D Fourier transform of the trace.
- Figure 8, plot of wavelet transform of the trace.

Reference

1. Mallat S. and Zhang Z. , 1993, Matching Pursuit with time frequency dictionaries: IEEE Trans. , Signal proc., 41, 3397-3415.
2. Avijit Chakraborty and David Okaya , 1995, Frequency-time Decomposition of Seismic Data using wavelet-based methods : Geophysics, 1906-1915.
3. Barnes, A., 1991 , Instataneous Frequency and Amplitude at the Evelope peak of a constant-phase wavelet: Geophysics, 56, 1058-1060.
4. Bosman c. and Reiter, E., 1993, Seismic Data Compression using wavelet transforms: 63rd Ann. Internat. Mtg., Soc. Expl. Geophysics Expanded Abstracts.
5. Stephene Mallat, 1997, a Wavelet Tour of Signal processing.
6. Mladen Victor Wickerhauser, 1993, Adapted Wavelet Analysis from Theory to Software.

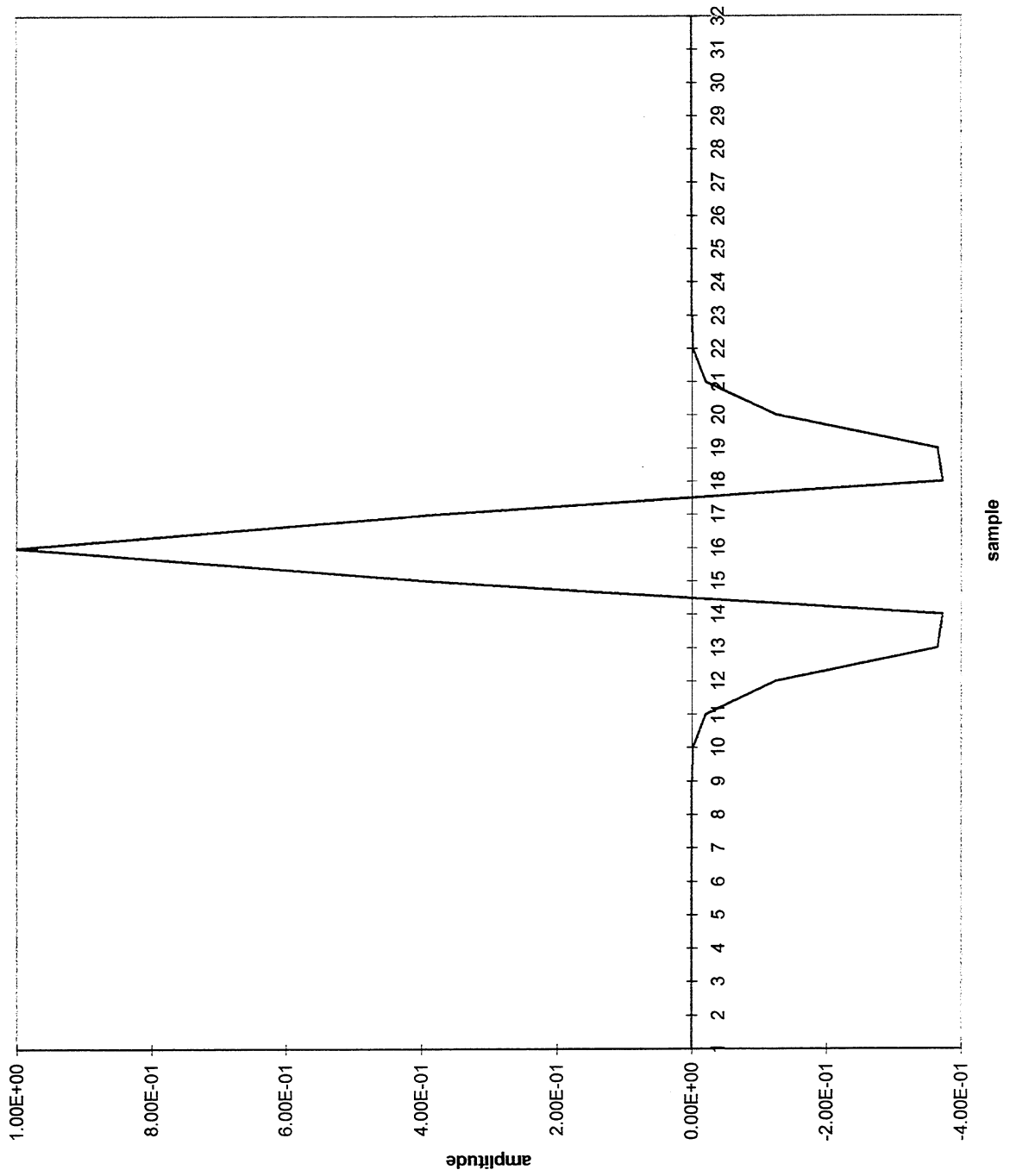
1.00E+00
8.00E-01
6.00E-01
4.00E-01
2.00E-01
0.00E+00
-2.00E-01
-4.00E-01
amplitude
1 2 3 4 5 6 7 8 9 10 11 12 13 14 15 16 17 18 19 20 21 22 23 24 25 26 27 28 29 30 31 32
sample

Figure 1a

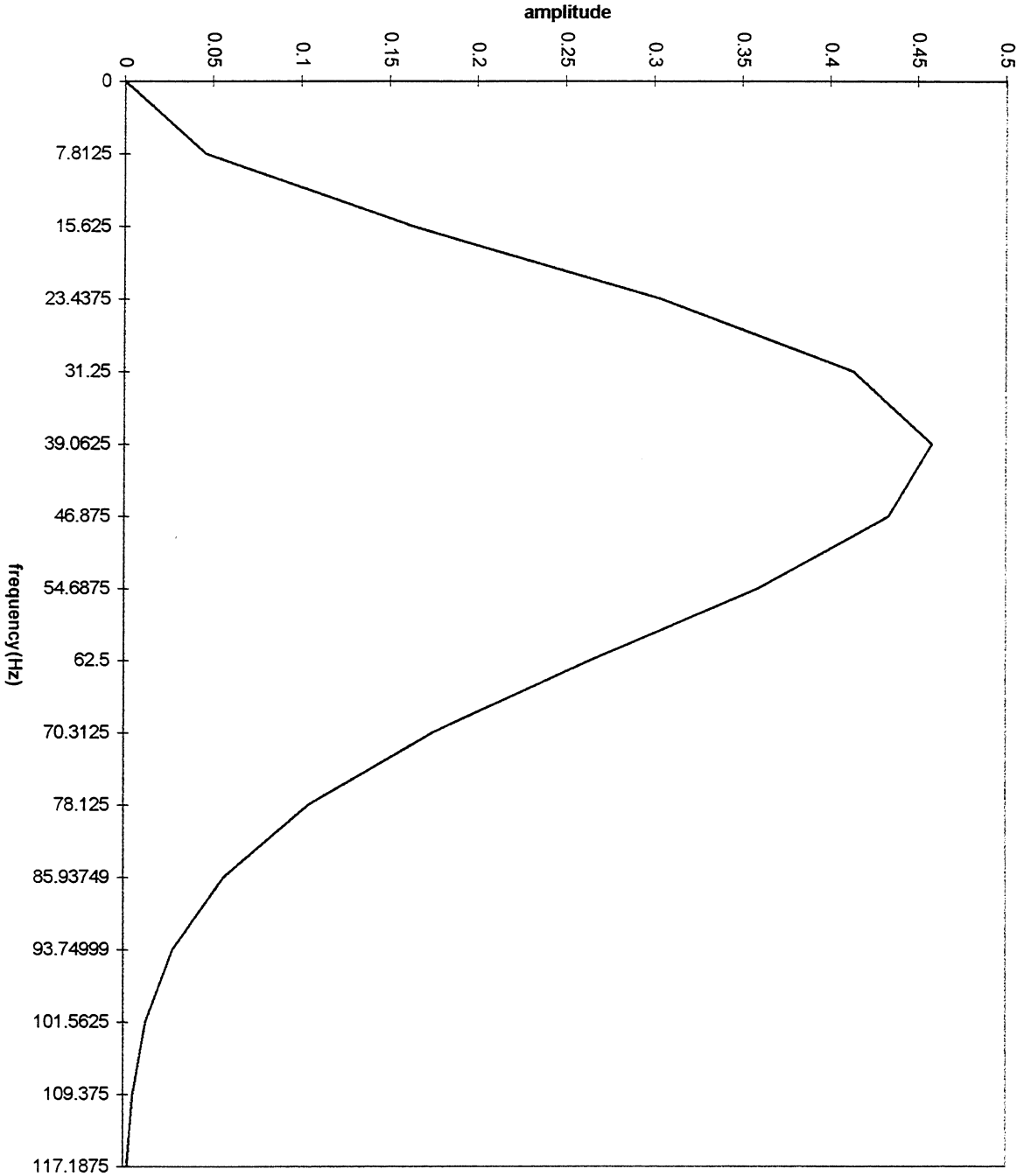
amplitude
0
0.05
0.1
0.15
0.2
0.25
0.3
0.35
0.4
0.45
0.5
frequency(Hz)
0
7.8125
15.625
23.4375
31.25
39.0625
46.875
54.6875
62.5
70.3125
78.125
85.93749
93.74999
101.5625
109.375
117.1875

Figure 1b

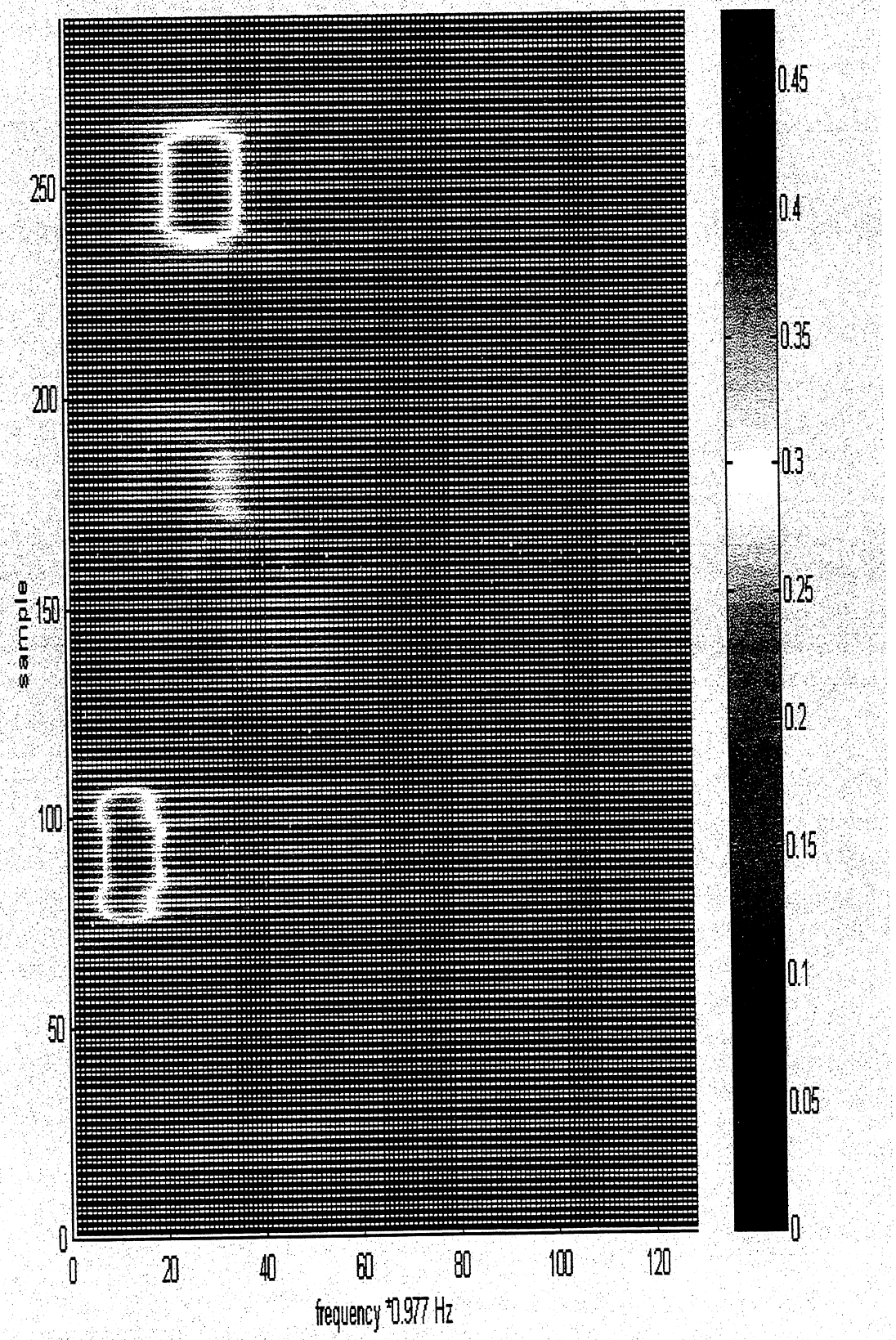
sample
250
200
150
100
50
0
0
20
40
60
80
100
120
frequency *0.977 Hz
0.45
0.4
0.35
0.3
0.25
0.2
0.15
0.1
0.05
0

Figure 3

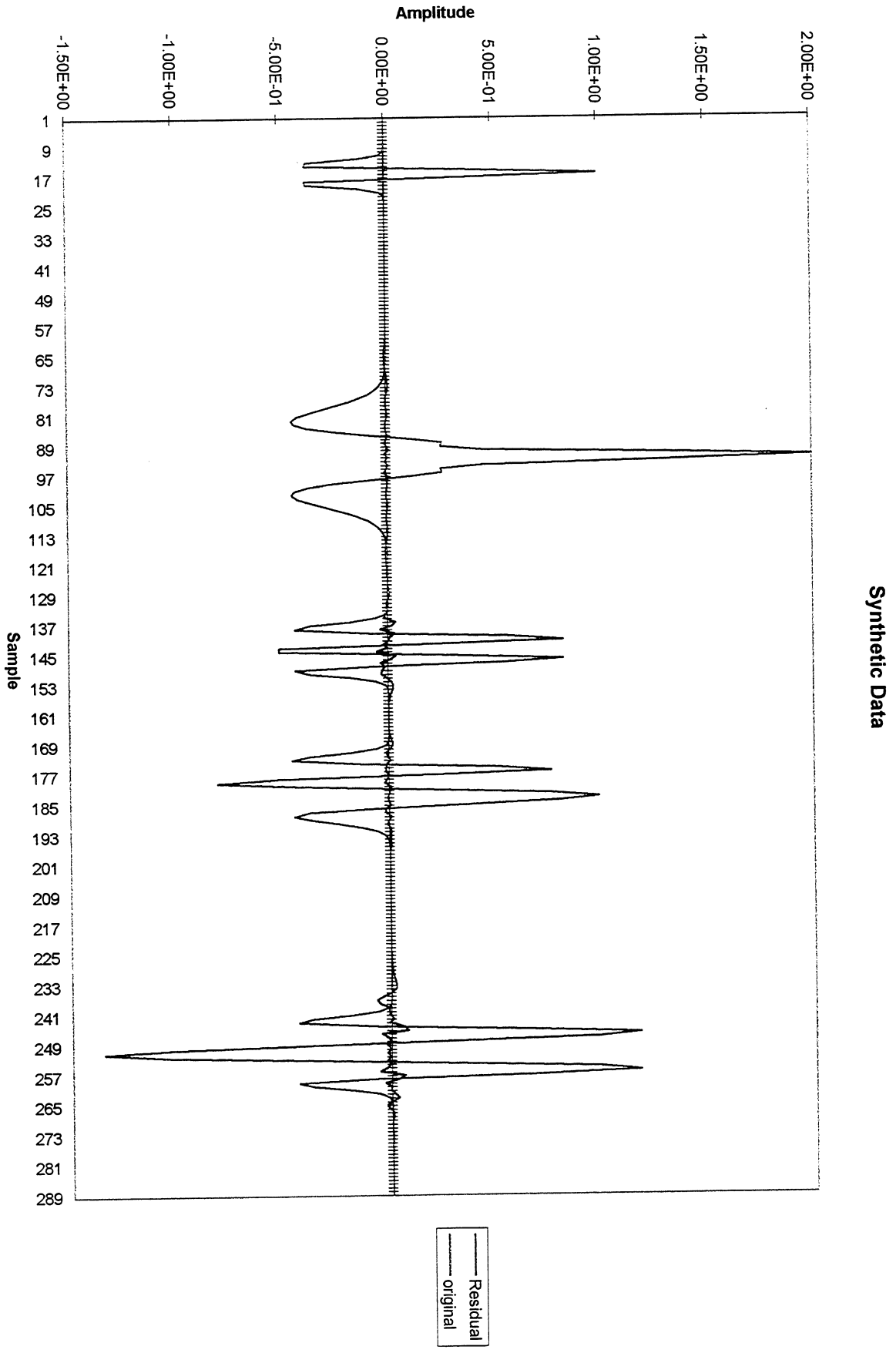
Amplitude
-1.50E+00
-1.00E+00
-5.00E-01
0.00E+00
5.00E-01
1.00E+00
1.50E+00
2.00E+00
Sample
1
9
17
25
33
41
49
57
65
73
81
89
97
105
113
121
129
137
145
153
161
169
177
185
193
201
209
217
225
233
241
249
257
265
273
281
289
Synthetic Data
Residual
original

Figure 3a

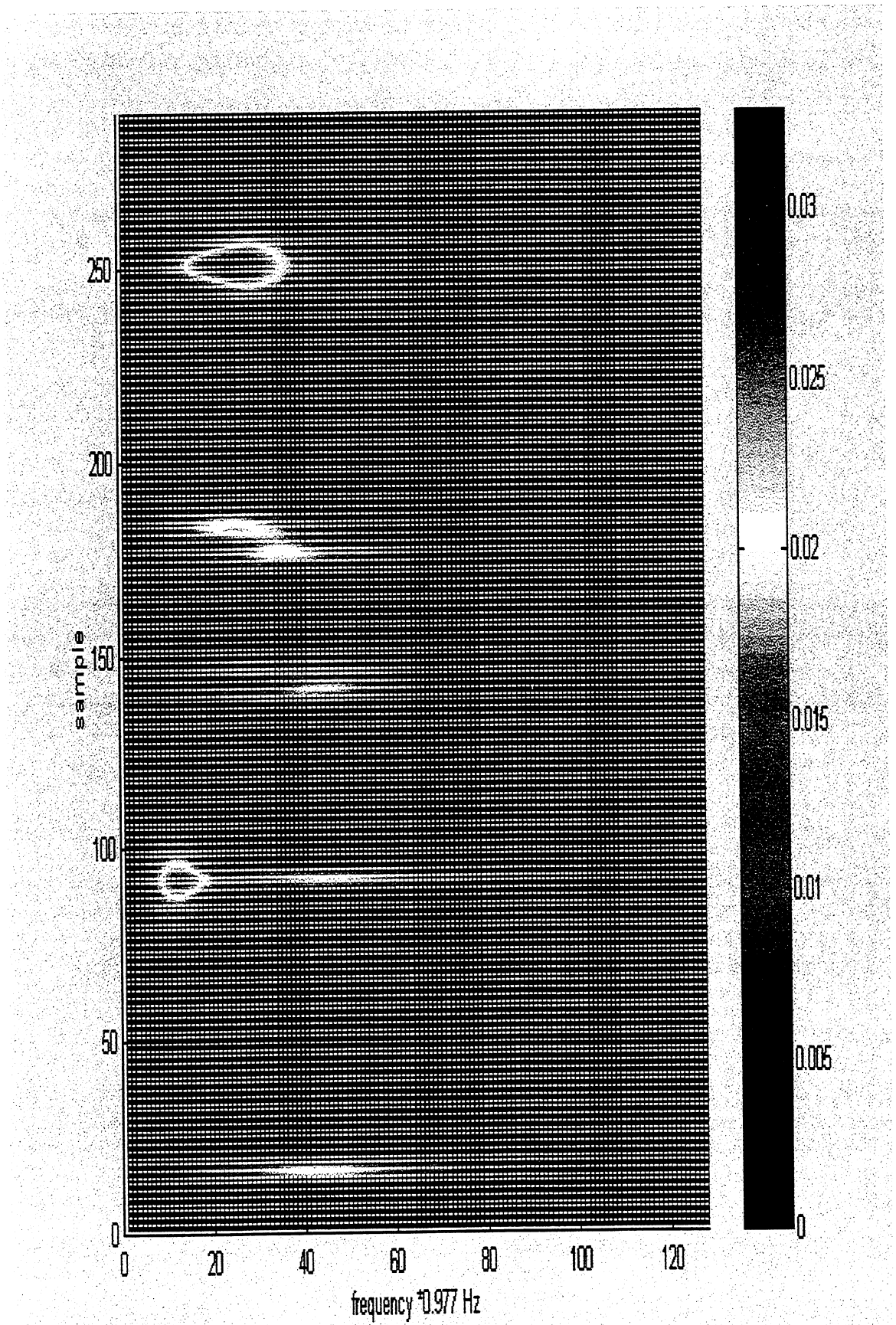
sample
0
50
100
150
200
250
0
20
40
60
80
100
120
frequency *0.977 Hz
0.03
0.025
0.02
0.015
0.01
0.005
0

Figure 4

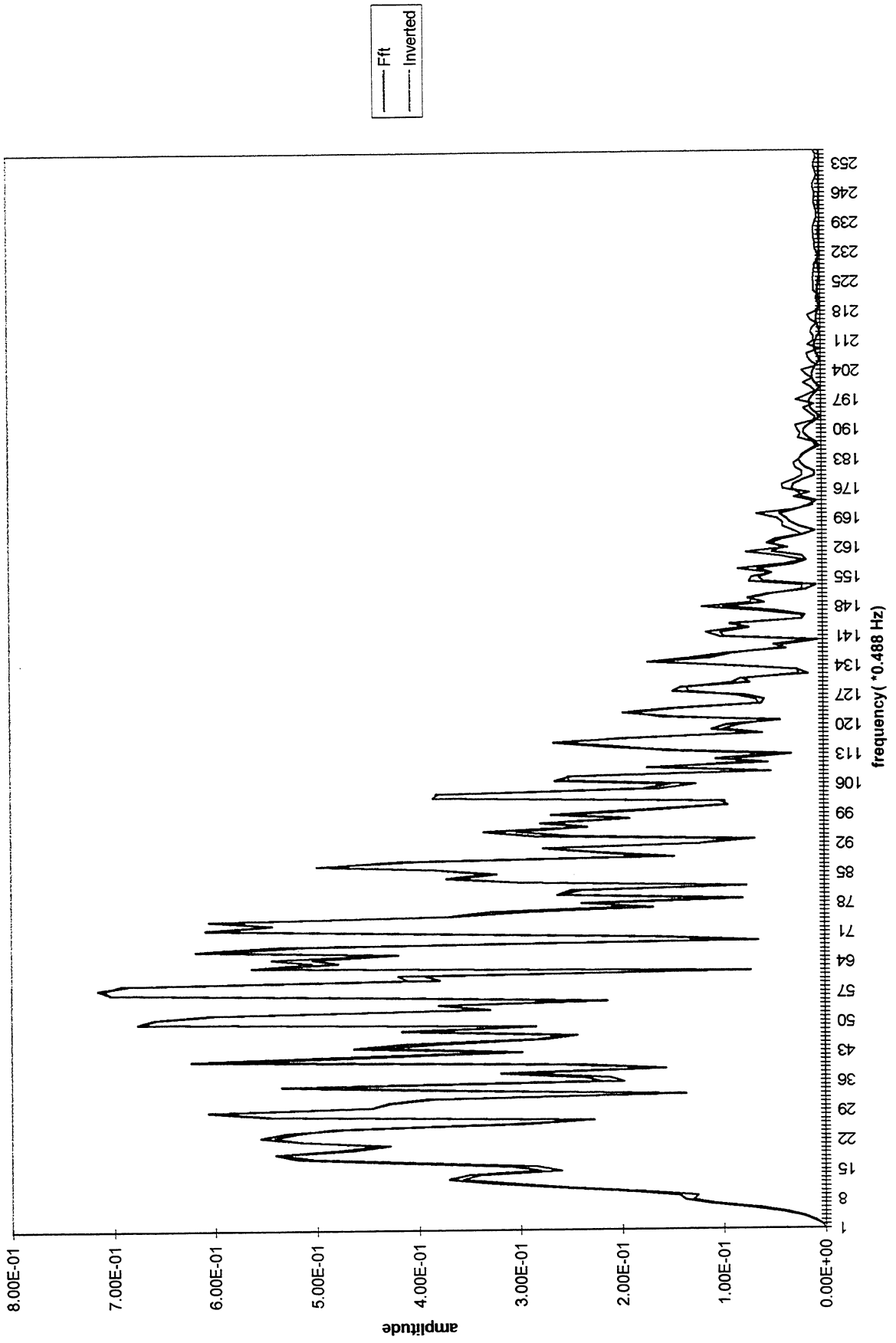
Fft
Inverted
amplitude
8.00E-01
7.00E-01
6.00E-01
5.00E-01
4.00E-01
3.00E-01
2.00E-01
1.00E-01
0.00E+00
frequency(*0.488 Hz)
1
8
15
22
29
36
43
50
57
64
71
78
85
92
99
106
113
120
127
134
141
148
155
162
169
176
183
190
197
204
211
218
225
232
239
246
253

Figure 5

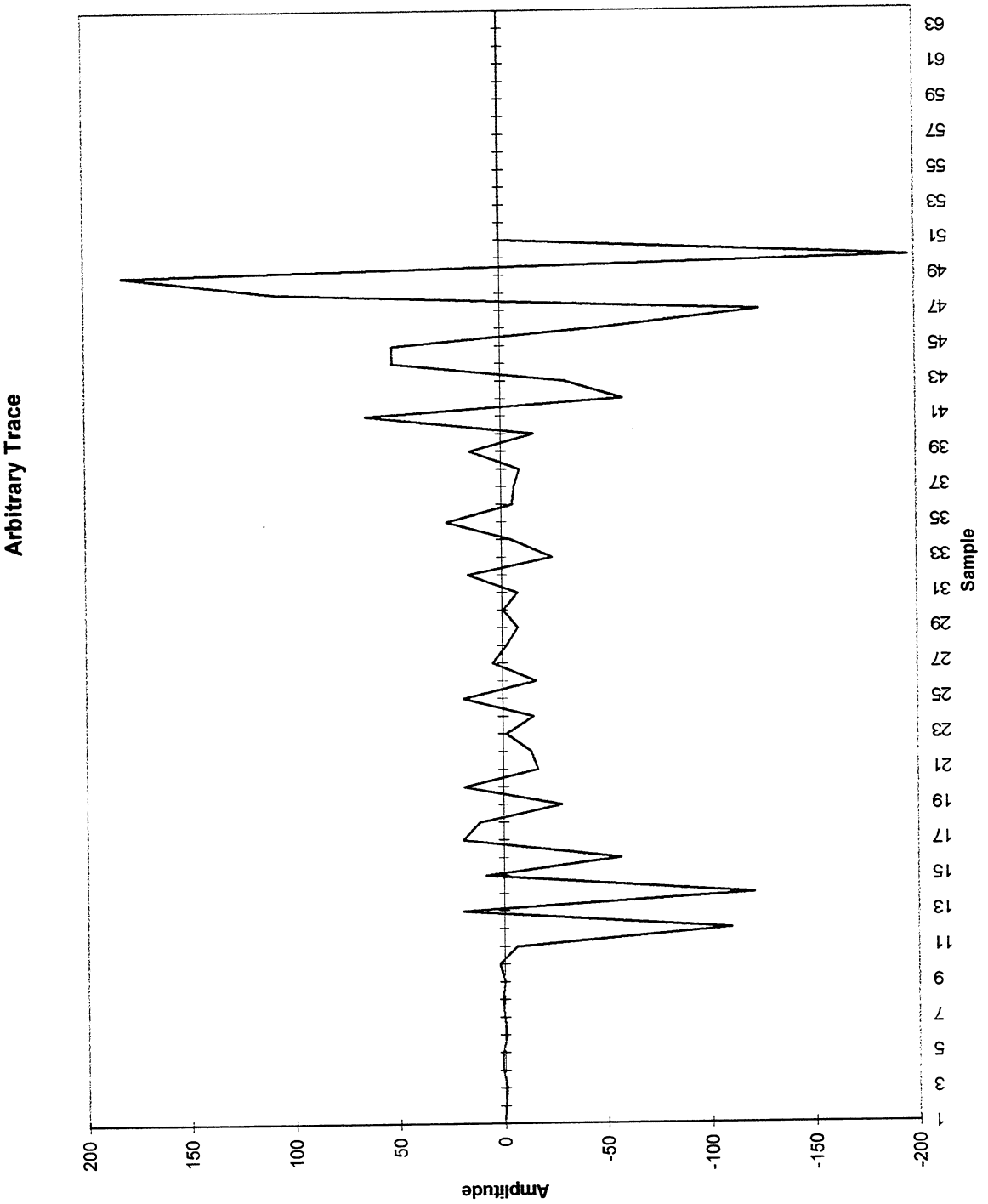
Arbitrary Trace
Amplitude
200
150
100
50
0
-50
-100
-150
-200
Sample
1
3
5
7
9
11
13
15
17
19
21
23
25
27
29
31
33
35
37
39
41
43
45
47
49
51
53
55
57
59
61
63

Figure 6

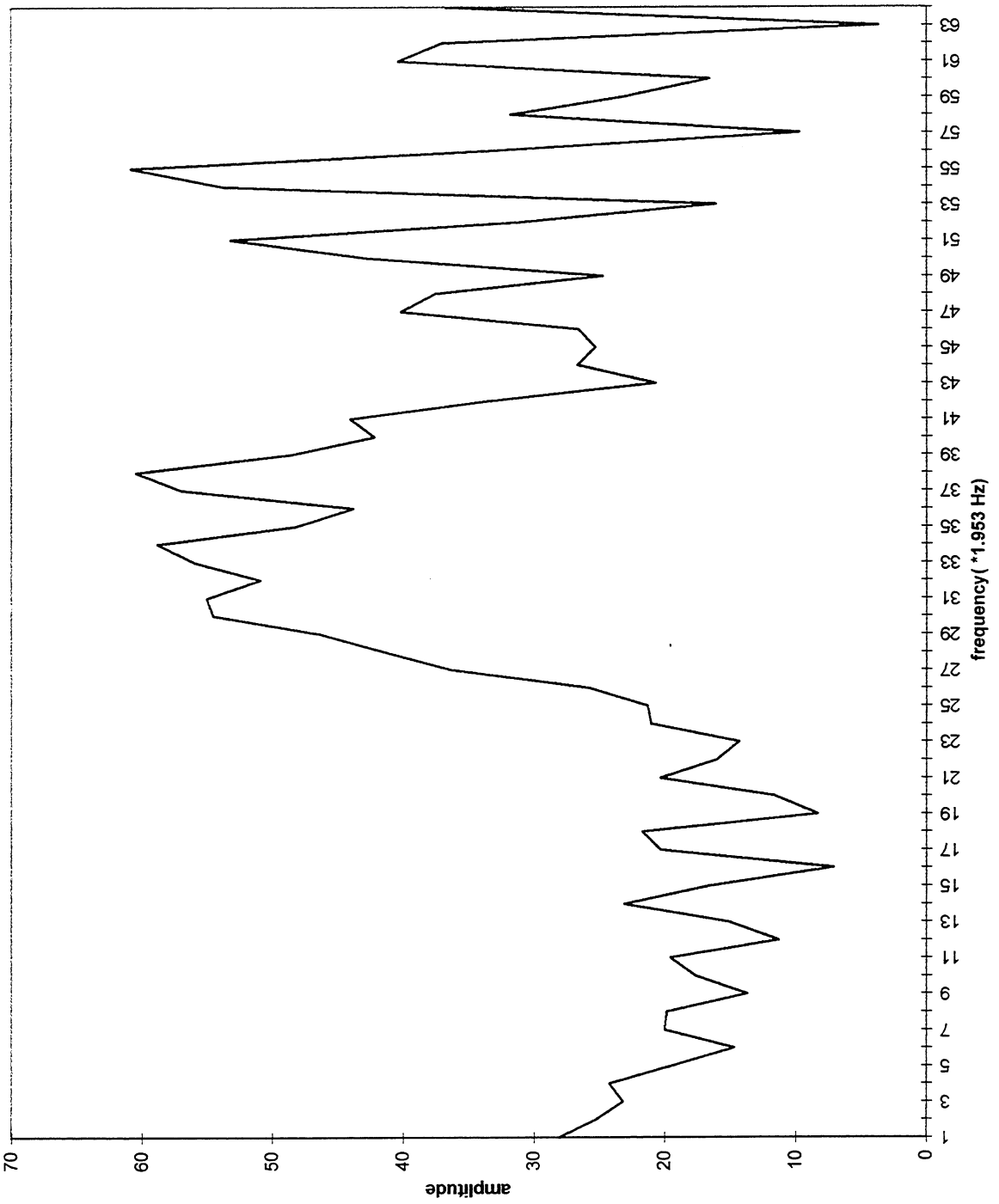
amplitude
0
10
20
30
40
50
60
70
frequency(*1.953 Hz)
1
3
5
7
9
11
13
15
17
19
21
23
25
27
29
31
33
35
37
39
41
43
45
47
49
51
53
55
57
59
61
63

Figure 7

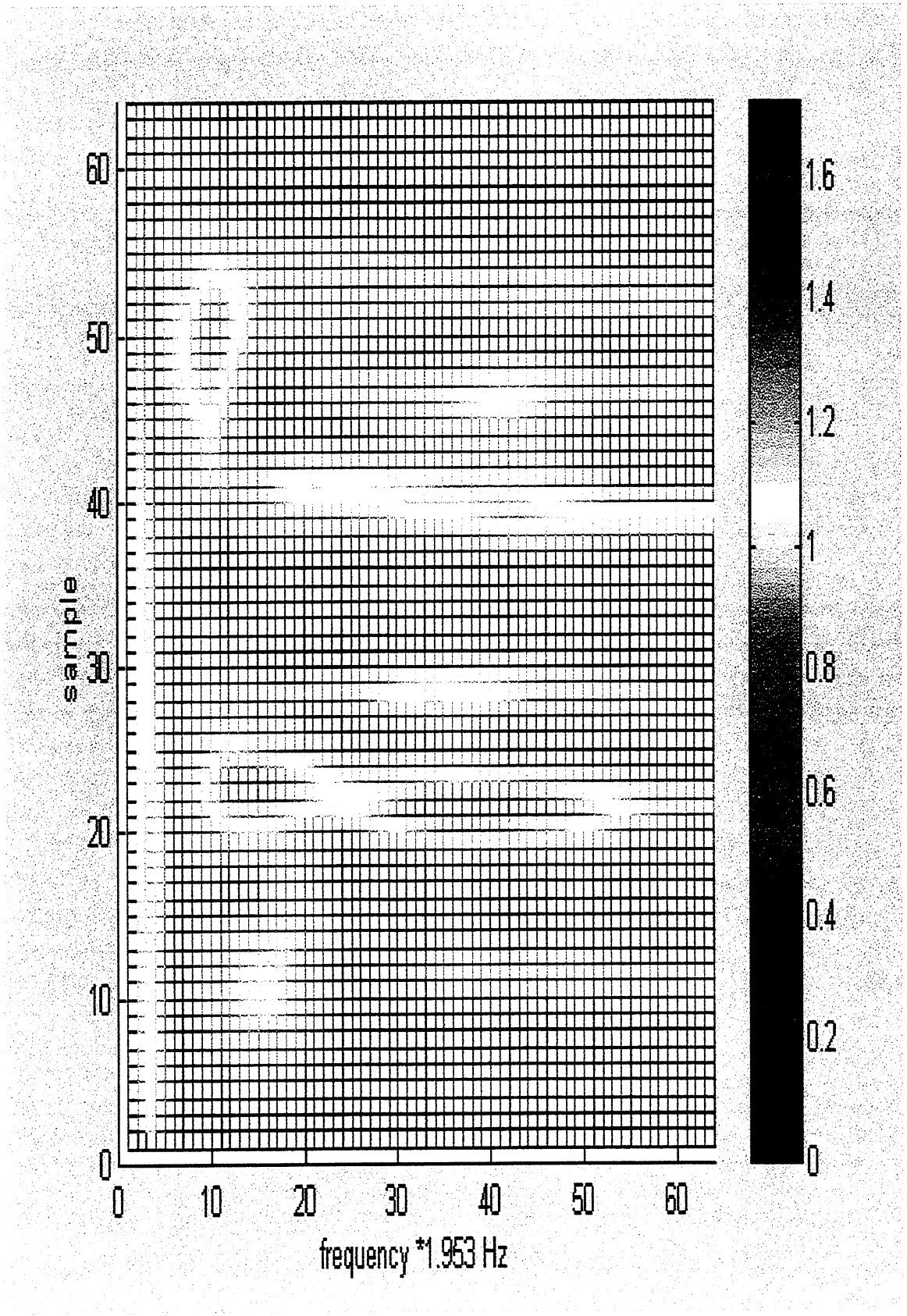
sample
0
10
20
30
40
50
60
frequency *1.953 Hz
1.6
1.4
1.2
1
0.8
0.6
0.4
0.2
0

Figure 8

Appendix I

Absorption and Dispersion from Gypsy Data

by

Bill Lamb

Progress Report
Absorption and Dispersion from Gypsy Data

William J .Lamb

Introduction

Recently, there has been substantial new laboratory evidence to substantiate the widely held view that there can be substantial velocity dispersion between seismic and well logging frequencies (Batzle et. al., 1996 and 1997, Parker, 1998). Moreover, the experiments indicate that the dispersion is related to the fluid content of the rocks. Theoretically, there are mechanisms such as squirt flow, (e.g. Dvorkin et. al., 1993) and partial gas saturation (e. g. Dutta et. al, 1979 a & b), which predict behavior of this type and magnitude. Unfortunately, experiment and theory are not yet in detailed agreement. For a lengthy discussion see Lamb 1998.

One consequence of this is that sonic logs will have to be corrected to account for dispersion when making synthetic seismograms. This problem has been known for a long time, and empirical corrections have been applied to generate an acceptable travel time to depth curve. We now have the hope that soon we will be able to do this correction in a theoretically justifiable manner.

A second consequence is that information about the viscosity - permeability ratio of the pore fluid may be available, if dispersion can be measured. This is very valuable information for exploration and production. While direct measurement of dispersion within the seismic band does not appear feasible , one should be able to detect it indirectly, since dispersion implies a corresponding absorption (Futterman 1962). This absorption will decrease the amplitude of each frequency component of the seismic signal, with the higher frequencies being attenuated more. Complicating the issue is scattering from heterogeneities, which have somewhat similar behavior.

We propose to look for absorption in the seismic frequency range by doing precision wavelet extractions on a series of short windows. Now, the wavelet is the filter which, when convolved with the log derived reflection coefficients, best matches the resulting synthetic seismogram with the seismic data. Since absorption effects are not included in the reflection coefficients, but do affect the seismic data, whatever absorption there is should be reflected in the wavelet. It will have decreasing amplitude with time, with the high frequency components decreasing most rapidly. To insure robustness against processes which slowly vary the amplitude scaling (spherical spreading, AGC, etc.), only the *relative* strength of high to low frequencies should be considered.

This procedure would measure both the real (fluid related) and apparent (scattering related) absorption. Also, various seismic processing options (especially Q compensation) will affective the relative spectral strength. Our hope to extract true absorption resides in the fact that the apparent absorption in an effect of the total overburden, so should change slowly, as will the effects of processing, while the true absorption can change rapidly due to changes in fluid type or permeability.

Theory of Wavelet Extraction

Convolutional model

The starting point for the theory of wavelet extraction is called the convolutional model, which is written as

$$S_i = \sum_{j=-N_w}^{N_w} R_{i-j} W_j \qquad \text{for } 1 <= i <= N_t \qquad (1)$$

where the time series S is called a synthetic seismogram. It is intended to model a real (processed) seismic trace. N_t is the number of elements in the time series. R is the reflection coefficient series (expressed in time). W is the wavelet. It has a length of $2\ N_w + 1$.

The theoretical basis for (1) begins with the observation that any solution to the elastic wave equation can be expressed as the convolution of the impulse response with the time signature of the source. By definition, the impulse response is the response to a delta function source in time. Equation (1) is just the discretized version of this. For the case of a plane layered earth model, and an incident compressional plane wave source, ignoring transmission losses and multiple scattering, the reflection coefficients are given by

$$R_i = \{(\rho\ Vp)_{i+1} - (\rho\ Vp)_i\} / \{(\rho\ Vp)_{i+1} + (\rho\ Vp)_i\} \qquad (2)$$

where ρ is the density and Vp is the compressional velocity. Equation (2) computes R_i at the depth $z = (i - 1)\ \Delta z$. It must be posted at the time required for the plane wave to travel from the surface to z. This time can be computed by summing the reciprocal velocities from the surface to z.

$$T(z) = \Delta z \sum (1/Vp) \qquad (3)$$

Now, a seismic experiment does not have a plane wave source, but is closer to a point source. The same model prevails, after amplitude corrections for spherical spreading, for a seismic trace with source and receiver at the same location. Now high energy sources and delicate receivers do not coexist easily, so coincident source receiver experiments are

seldom attempted. Moreover, real elastic wave propagation produces many types of waves besides primary reflections. To minimize the effect of these other types of waves (called shot generated noise), multiple experiments are done with varying source and receiver positions, but with the same midpoint, half way between source and receiver. The experiments are then averaged. The process is called stacking. The classical stacking process assumes that the subsurface geometry consists of horizontal plane layers. Various processing techniques (dip moveout, pre and post stack migration) attempt to correct for more complicated geometries.

Now, the reflection strength depends on the angle of incidence of the incident wave. In the early days this effect was just ignored. In fact, a stacked (or migrated) section corresponds to the averaged reflection coefficient over the range of angles used in the actual experiment. This range of angles will vary with depth.

The computation of the reflectivity series occurs in two stages. First the reflectivity is computed at each depth and over the relevant angle range in depth. We use the approximation , (Spratt et. al., 1993):

$$R_i = A_i + B_i \sin^2(\theta) \tag{4}$$

where θ is the incidence angle. A is given by (2), and

$$B_i = A_i - 8\ (Vs/Vp)^2\ Rs_i \tag{5}$$

and

$$Rs_i = \{(\rho\ Vs)_{i+1} - (\rho\ Vs)_i\} / \{(\rho\ Vs)_{i+1} + (\rho\ Vs)\,i\} \tag{6}$$

where Vs is the shear velocity. This approximation is adequate for small incident angles and small changes across interfaces. Then the reflectivity is transformed from depth to time using the travel time at depth function T(z). In practice, the calculation of T(z) is somewhat more complicated that the simple sum of transit times (equation(3)). Determination of T(z) is discussed in Appendix A. Because the reflection coefficients are very spiky, this transformation must be done very carefully.

Because of the stacking (or migration) process, the processed trace is an average over the incident angles which result from the acquisition geometry. The corresponding average over angles in (4) must be made in estimating the reflection coefficients. Calculation of this average is discussed in Appendix B.

Deconvolution, another common seismic processing technique, attempts to attain greater resolution by attempting to transform the actual experiment to one with a broader band source. Now the proper wavelet is not the source signature, but the signature of the hypothetical broadband experiment.

The key point is this: *most seismic processing attempts to produce output which corresponds to the convolutional model*, albeit with a somewhat altered interpretation of both the reflection coefficients and the wavelet. The wavelet is the key to qualitative seismology because it connects the reflectivity time series (determined by the geological model or well log data) and the processed seismic data.

Estimating the Wavelet

Given the reflection coefficient time series and the processed seismic at the well position, D, we can attempt to find the wavelet. We define the objective function:

$$O\{W\} = \sum_{i=1}^{N_t} (S_i - D_i)^2 \ \omega_i \tag{7}$$

where S is defined by (1), and set

$$\frac{dO}{dW_j} = 0 \qquad -N_w < j < N_w \tag{8}$$

to get a least squares solution to the problem. The $\{\omega\}$ are user assigned weight functions. Equation (8) implies the set of linear equations for W:

$$\sum_{k=-N_w}^{N_w} \left\{ \sum_{i=1}^{N_t} R_{i-j} \ \omega_i R_{i-k} \right\} W_k = \sum_{i=1}^{N_t} D_i \ \omega_i \ R_{i-j} \tag{9}$$

By rearranging indices (and ignoring the weights), the term in brackets becomes

$$\sum_{i=1+j}^{Nt+j} R_i \ R_{i-(k-j)} \tag{10}$$

Note that if we ignore the limits of the sum, the expression depends only on k-j, so would be a Toeplitz matrix. Traditionally, this approximation was made in order to use the Levinson algorithm (see Press et. al., 1992, pp 85-89), which is quadratic in the order of the matrix, instead of methods like LU decomposition or Gaussian elimination, which are cubic in the order, in order to save computer time. This worked reasonably well if the extraction interval (Nt) was very large, or if it started and ended in zones of little energy. We cannot assume this for this work, so we solve (9) by LU decomposition.

The use of the Levinson algorithm today is a historically conditioned anomaly, since the computation is trivial for modern computers.

Software

A flow chart for the software is given in Figure 1 . The first stage is data preparation. Well log data (assumed in LAS format) is read from one or several wells. We need compressional transit time, compressional and shear velocities and densities to proceed. In the absence of a shear sonic, one will have to be generated. This will require a lithology estimate, which will be made from gamma ray log or neutron - density cross plots. The log preparation step will produce first a lithology estimate. This will be used with Vp/Vs trend curves (Castagna, 1993) to produce a Vs log. Seismic data is read from one or several lines and traces near the well are saved. The next stage is to estimate the travel time to depth curve T(z), as discussed in Appendix A.

We are now ready to do wavelet extractions. First the seismic traces near the well are interpolated to give an estimate what a seismic trace would be at the exact well position. Then the reflection coefficients are computed. Finally, we loop over time, creating a series of closely spaced short windows. The wavelet is extracted and its spectrum taken and characterized.

Data

For seismic data, there is a 3D survey. The parameters are summarized in Figure 2.It is processed to 52 lines each with 52 depth points. The spacing between lines equals the CDP spacing of 25 Ft. The survey extends to 3 Seconds. The instrument filters were set to pass frequencies from 9 – 250 Hz.

The processing was done by Western Geophysical according to the flow in Figure 3. A base map of the survey is shown in Figure 4. Figures 2-4 are taken from Seifert 1993, which contains a clear introduction to the Gypsy data. There are 4 sets of processed data sets (T123443, T125856,T126328,T126339). The first contains only the central 3 cross lines (#27-#29). The others contain all 52 cross lines (#2-#54). They all contain data to 3 seconds, except the second which goes only to 1 second.

The first .3 seconds of data will be our primary focus, since we wish to compare the data to synthetics derived from log data, and our shallow wells will only produce synthetics to about this time. Even after processing, the data contain significant energy to nearly 250 Hz. in this zone.

The first .3 seconds of cross line 28 for each of the processed data sets are shown in Figures 5a - 5d. Presumably they differ only in cosmetic processing after undergoing the

processing flow of Figure 3, although the author has not yet fully sorted this out. All figures were made using the SU plotting program suxwigb, and taking the default parameters..

The most obvious difference is that the time decay of amplitude is large in T123443, small in T125856, and intermediate in the other two. The general appearance of all lines is that of good quality, high frequency data. They typically show the same events. However, looking closely at times before .1 sec show considerable divergence. Ordinarily, this would be of little interest, but since only the first .3 seconds are relevant to our study, this means that one third of the useful range is questionable.

There are 5 wells within the imaged area., Dallas 1-7,5-7,7-7,8-7,9-7 and 11-7. Their positions relative to the seismic grid are indicated in Figure 4. All have density logs and full waveform sonic logs. There are no shear logs but gamma ray and neutron logs are available. This should be sufficient to produce a synthetic shear velocity log. There are also a variety of electrical and other logs. The logs go to about 1400 Ft., corresponding roughly to the .3 seconds of seismic data quoted earlier.

Status

The software described in the previous section is written, and testing nearly complete. For our first attempt to work with the data, we chose to use the logs and processed seismic as we received them. On the basis of past experience, we had reason to expect that either or both of these might cause problems, but it is the right place to start for a quick look. This naïve approach has not yet produced good enough ties between the rough synthetics and seismic data needed to complete the T(z) estimate. It is possible that some further changes of processing parameters will resolve the problem, but the author suspects that the log data is at fault. With so many logs available, there is a good prospect for successful log editing. Seifert, 1994, also had problems getting good ties, and resorted to log editing. Even so, the quality of his ties was not outstanding. Since our software is more sophisticated than that which Seifert had available, we expect ultimately to get better ties.

Another avenue to attack the T(z) estimate is to use the VSP data, which exists for several wells. It may well prove desirable to estimate absorption directly from the VSP data, as well as from the 3D seismic.

When the tie problem is resolved, and a good estimate of T(z) is available, the wavelet extractions proper may begin. The high frequency content of the data give reason for optimism. On the other hand, the short span of time (~.2 Sec.) available for wavelet extractions may complicate removing heterogeneous scattering and processing effects. It may turn out that the seismic data needs to be reprocessed, to obtain tight control of processing effects.

Appendix A
Time to Depth Conversion

Since well logs are measured in depth, while seismic traces are recorded in time, comparing the two requires some kind of conversion between depth and time. In our process, this step occurs when the reflection coefficients are transformed from depth to time prior to the convolution with the wavelet to produce synthetic seismograms.

To do this transformation requires knowledge of the function T(z), where T is the normal incidence travel time and z is the depth. The first approximation to this function is obtained by cumulative summing of the transit times from a sonic log, (Equation (3)). In addition to doing the sum it is also necessary to determine a single tie point. Simplicity would suggest T(0) = 0. Unfortunately, seismic processing usually contains an unknown global time shift. The well logs often pose a problem as well, when the sonic log is not recorded all the way to the surface.

Many years of experience in trying to tie synthetic to real seismic data using the cumulative sum approximation have shown that usually the sonic transit time is faster than the seismic transit time, typically by about 5%. This is too much error when trying to tie seismograms over long time windows. It is also too much for the precision wavelet extractions that are needed to estimate dispersion. To further complicate matters, when the processing flow includes Q (attenuation) compensation, this error may be partially compensated for. Unfortunately, knowledge of the processing parameters is not easily transformable into a correction function for T(z).

There are many causes of this error, including the neglect of short period multiples and frequency dependence of the velocity between seismic and sonic logging frequencies. The effect of short period multiples can be fairly well approximated. Backus, 1962, has shown that all the effects of multiples can be accounted for in the long wavelength limit. In this case the effective propagation velocity V_{bav} is given by

$$V_{bav} = 1 / \{ < \rho >< 1 / (\rho V^2) > \}^{1/2} \qquad (A1)$$

The delicate part of using this formula is to decide what exactly what exactly is the long wavelength limit, or, alternatively, what is the separation point between short and long period multiples. One way to accomplish this would to build a suitably blocked model and use (A 1) on the blocks. Alternatively, one could use a moving window technique. This is what is done here. At each depth z, a window of constant time thickness is chosen, and the depth z0 at the start of the window is determined. Then the transit tine is computed from T(z0) and the Backus average time over the window. The window length is chosen to be some fraction of the period for a wave with a frequency characteristic of the seismic

data. The code permits user control of the parameter which specifies the fraction. The results are not very sensitive to (reasonable) variations in this parameter.

Despite a lot of work, there is not at present a reliable way to correct velocities measured at sonic logging frequencies to the corresponding velocities at seismic frequencies. There is really not much else to do, but to introduce an empirical stretch factor to account for frequency dispersion and all other neglected effects.

A block diagram of our approach to obtaining this empirical stretch factor is given in Figure A1.We begin by creating (crude) synthetic seismograms. They are zero phase and 90 degree phase shifted seismograms with a spectrum which is a bandpass filter with linear rolloff. The spectrum should be a good match to the seismic data. To estimate the spectrum, the seismic data undergoes a discrete Fourier transform. Then a cumulative sum of the spectrum is performed. Then for frequencies above some cumulative percentage, the spectrum is set to zero. This is done in the anticipation that such spectral content is noise, but would have a significant effect on computation of spectral moments. Limited experience suggests 90% - 95% works well. From the first four spectral moments the four frequencies to define the (preliminary) wavelet are derived.

From both the synthetic and real traces, an attempt is made to find events (high energy, well defined reflections). To do this, choose a window of fixed time length, approximately the reciprocal of the low cut in the spectrum. Then compute the energy within the window for each point along the trace. Choose the time of the largest value. This is the first event. Exclude this event and repeat. Continue until there are enough events picked.

Now that we have some events picked on the synthetic and real traces, we attempt to find a subset of these events which can be pared. We search all possible combinations and eliminate those which predict unreasonable stretch. For each hypothetical pair, the phase which provides the best correlation is computed. Some refining of the time at the center of the event is also performed. All combinations of pairs which do not meet a phase coherence criteria are eliminated, as unphysical. Then all combinations of pairs which do not have a sufficiently long time separation between first and last events are eliminated, as not useful. The largest total coherence of the remaining collections of pairs becomes our working tie. Not that this procedure is robust in the presence of bogus events such as multiples in the seismic and glitches in the well logs.

From the working ties, we derive a correction $\delta T(z)$ to $T(z)$. its form is piecewise linear, with some smoothing:

$$\delta T(z) = A + \Sigma\ B_i\ (z - C_i)\ \ S\{G_i\ (z - C_i)\} \qquad \text{(A2a)}$$

$$S(x) = (1/2) + TAN^{-1}(x) / \pi \qquad \text{(A2b)}$$

The coefficients {C} are determined chosen as the (seismic) tie points, while the smoothing parameters {G} are user defined. Finally, equating δT to the time differences at the tie points, permits A and the {B} to be determined by linear algebra.

Appendix B
Average over Incidence Angles

To estimate the angle of incidence from the offset, we do ray tracing through a plane layered medium. Snell's law can be written

$$p = \sin(\theta_1) / v_1 = \sin(\theta_2) / v_2 = \ldots = \sin(\theta_n) / v_n \qquad \text{(B1)}$$

where θ is the incident angle and v the velocity. P is called the ray parameter, and is constant, independent of the layer. The horizontal and vertical segments of the ray path in a layer are related by

$$\Delta x_i / \Delta z_i = \tan(\theta_i) \qquad \text{(B2)}$$

The offset is given by

$$X = \Sigma \Delta x_i = \Sigma \{ (\Delta z_i \; p v_i) / (1 - (p v_i)^2)^{1/2} \} \qquad \text{(B3)}$$

the depth by

$$Z = \Sigma \Delta z_i \qquad \text{(B4)}$$

and the travel time by

$$T = \Sigma (\Delta z_i / v_i) / (1 - (p v_i)^2)^{1/2} \qquad \text{(B5)}$$

To estimate the reflection coefficient, we need the average, over the traces in the gather, the square of the sine of the incident angles at depth

$$S = \Sigma \sin^2(\theta_n) / \Sigma (1) \qquad \text{(B6)}$$

Assuming constant close spacing in x the sum becomes an integral. After some manipulation, we get

$$S \cong \{ v_n^2 / (X_f - X_n) \} \; \Sigma \; (\Delta z_i / v_i^2) \{ \sin^{-1}(p v_i) - (p v_i) / (1 - (p v_i)^2))^{1/2} \} \; |^{pf}_{pn} \qquad \text{(B7)}$$

where X_f and X_n are the far and near offsets. P_f and p_n are the corresponding ray parameters. The sum is over layers.

To evaluate S, we first solve (B3) for p_f and p_n, then evaluate (B7). Since this must be done for each layer, and the exact solution of (B3) must be iterative, this will result in considerable computation.

Since we are using a small angle approximation for the reflection coefficient, we may as well investigate small angle approximations to (B3) and (B7). The small parameter here will be (p v). Doing Taylor series expansions of (B3) and (B7) produce polynomial equations whose coefficients depend on depth only through (easily computed) running sums of powers of the velocity.

An even simpler procedure is to look for the lowest order correction to the straight ray approximation. Using (B1) and (B2) in (B7) gives:

$$S \cong \{(v_n^2\ Z)/ (X_f - X_n)\} < (\tan^{-1}(\Delta x_i / \Delta z_i) - \Delta x_i / \Delta z_i) / v_i^2 > |^{Xf}_{Xn} \qquad (B8)$$

Where <...> indicates and average from the surface to depth Z. (B8) is still exact. Ignoring the correlation of the Δx and v, and taking the average operator through the arctangent gives

$$S \cong (v_n^2 / \langle v^2 \rangle) \{(Z / (X_f - X_n)) (\tan^{-1}(X_f / Z) - \tan^{-1}(X_n / Z)) - 1\} \qquad (B9)$$

This result differs only from the straight ray (constant velocity) result, by first term in parentheses. It is simple and robust, and probably as accurate as needed, given the rest of our approximations.

References

Backus, G. E., 1962, Long-wave elastic anisotropy produced by horizontal layering, J. Geophys. Res., 67, 4427-4440.

Batzle, M., Han, De-Hua and Castagna, J. P., (1996) Attenuation and Velocity Dispersion at Seismic Frequencies, SEG Expanded Abstract RP 1.3, p. 1687-1690

Batzle, M., Han, De-Hua, and Castagna, J. P., (1997) Seismic Frequency Measurements of Velocity and Attenuation, SEG Workshop

Castagna, J. P., Batzle, M. l., and Kan, T. K., 1993, Rock-Physics -- The Link Between Rock Properties and AVO response, in Offset-Dependent Reflectivity - Theory and Practice of AVO Analysis, Soc. of Expl. Geophys.

Dutta, N. C., and Ode', H., 1979, Attenuation and Dispersion of Compressional Waves in Fluid-Filled Porous Rocks with partial Gas saturation (White Model) --Part I: Biot Theory, Geophys., v. 44, p. 1777-1788

Dutta, N. C., and Ode', H., 1979, Attenuation and Dispersion of Compressional Waves in Fluid-Filled Porous Rocks with partial Gas saturation (White Model) -- Part I: Results, Geophys., v. 44, p. 1789-1805

Dvorkin, J., and Nur, A., 1993, Dynamic Poroelasticity: A Unified Model with the Squirt and the Biot Mechanisms, Geophys., v. 58, p. 524-533

Futterman, W., I., Dispersive Body Waves, 1962, J. Jeoph. Res. v. 67, p .5279-5291

Lamb, W., Dispersion, A Tool to Identify Fluids and Determine Permeabilities?, Gas Research Institute Report, Submitted, 1998

Parker, D., Thesis, Colorado School of Mines, 1998

Press, W.H., Teukolsky, S. A., Vettering, W. T. and Flannery, B. P., 1992, Numreical Recipes in Fortran, Second edition, Cambridge University Press, New York

Seifert, D., 1994, Reservoir Development Scale Modeling Based on Integration of High Resolution 3-D Seismic Data, Well-Logs and Core Data: Gypsy site, Pawnee County, Oklahoma, USA, Masters Thesis, University of Oklahoma

Spratt, R.S., Goins, N. R. and Fitch, T. J., 1993, Pseudo-Shear – The analysis of AVO, in Offset-Dependent Reflectivity - Theory and Practice of AVO Analysis, Soc. of Expl. Geophys.

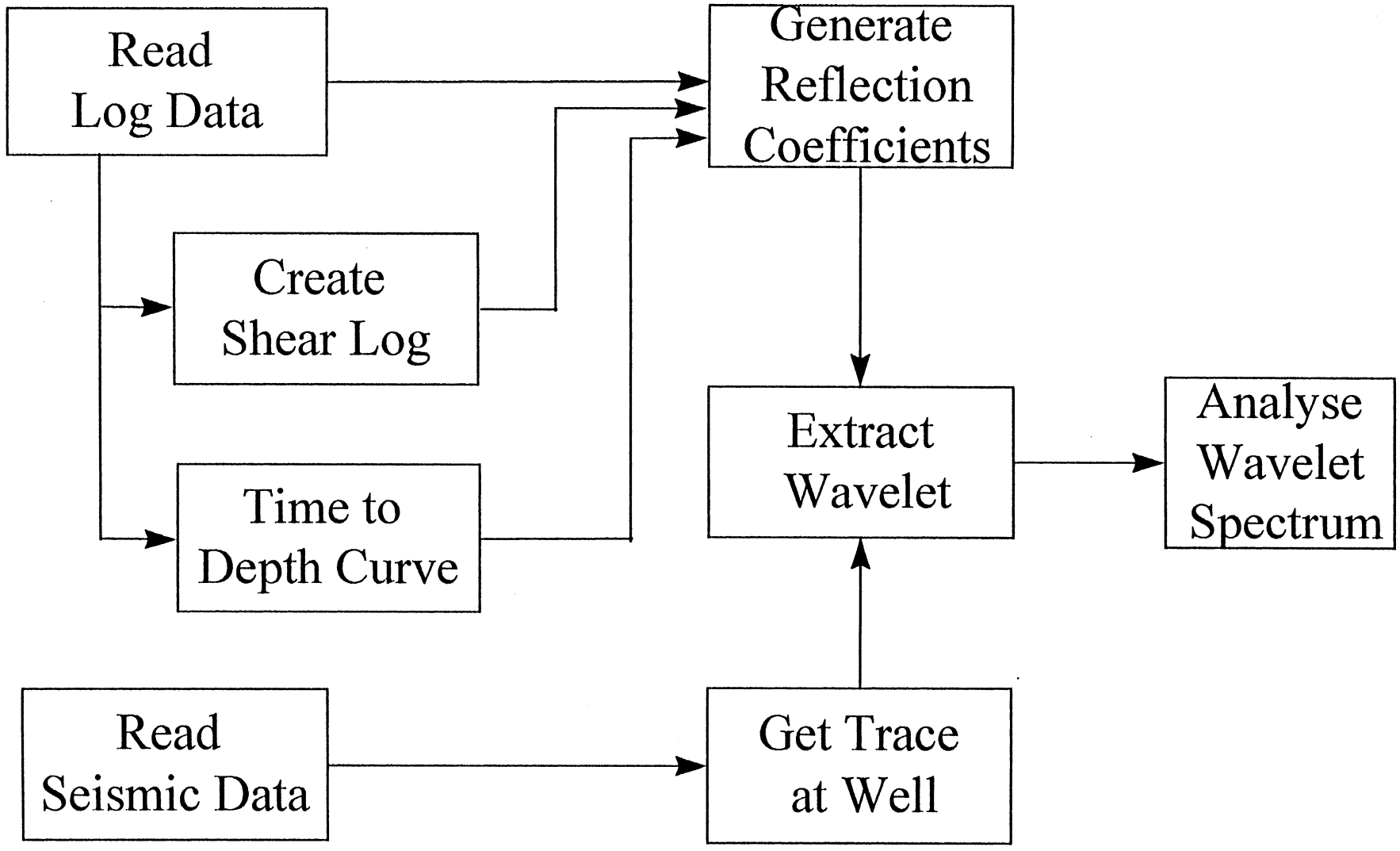

Figure 1. Block Diagram for Wavelet Spectrum Software

SURVEY DIMENSIONS

SURFACE	: 0.06 SQ. MILES
TOTAL N. - S. LINES	: 52
TOTAL E. - W. LINES	: 52
INLINE CELL DIMENSION	: 25 FEET
CROSSLINE CELL DIMENSION	: 25 FEET

RECORDING PARAMETERS

RECORDED BY	: WESTERN GEOPHYSICAL
PARTY NUMBER	: 702
DATE RECORDED	: JANUARY, 1990.

SOURCE

ENERGY SOURCE	: DYNAMITE
CHARGE SIZE	: 1 LB.
HOLE DEPTH	: 120, 110, 100 & 90 FEET
NUMBER OF SOURCES	: MULTIPLE SHOTS/HOLE
SHOT INTERVAL	: APPROX. 140 FEET

INSTRUMENTS

SYSTEM	: MDS-16
FORMAT	: SEG B
FILTER	: 9 - 250 HZ.
SLOPES	: 24 DB/OCT. - 90 DB/OCT.
NOTCH FILTER	: OUT
GEOPHONE TYPE	: LRS 1011 (28 HZ.)
FIELD SAMPLING INTERVAL	: 1 MS.
RECORD LENGTH	: 3 SECONDS
NO. OF DATA TRACES	: 243 (27 PER LINE)

ACQUISITION GEOMETRY

SOURCE

NUMBER OF SHOT LINES	: 7 (45 DEG. TO RCVR LINES)
DISTANCE BETWEEN LINES	: APPROX. 250 FEET
SHOT INTERVAL	: APPROX. 140 FEET
SHOTS PER SWATH	: 40

RECEIVERS

NUMBER OF SWATHS	: 3 (9 LINES PER SWATH)
NUMBER OF RECEIVER LINES	: 27
DISTANCE BETWEEN LINES/ SWATH	: 150 FEET
MOVEUP BETWEEN SWATHS	: 50 FEET
GROUP INTERVAL	: 50 FEET
NUMBER OF GEOPHONES	: 12
GEOPHONE ARRAY	: 25' CIRCLE ARRAY

Figure 2 . Survey dimensions, recording parameters, and acquisition geometry of the 3-D seismic survey. Data acquired by Western Geophysical.

PROCESSING SEQUENCE

PROCESSING SAMPLING INTERVAL: 1 MS.

1. DEMULTIPLEX AND DISPLAY ALL SHOTS
2. COMPUTE SUB-SURFACE GEOMETRY AND STATICS
3. GEOMETRIC SPREADING COMPENSATION
4. TRACE BALANCE
5. ZONE ANOMALY PROCESSOR (Z.A.P.)
6. SORT TO CDP ORDER
7. RESIDUAL AMPLITUDE DECAY COMPENSATION
   (OFFSET DEPENDANT RACS)
8. MISER® (AUTO STATICS)
9. SURFACE CONSISTANT DECONVOLUTION
   THREE WINDOWS
   OPERATOR LENGTH 120 MS.
   PREDICTION DISTANCE: 1 MS.
10. TIME VARIANT SPECTRAL WHITENING
    5 - 260 HZ.
11. VELAN® (VELOCITY ANALYSIS)
12. MISER® (AUTO STATICS)
13. VELAN® (VELOCITY ANALYSIS)
14. 3-D DMO STACK
15. CALC. AND APPLY SPATIAL VARIANT SCALARS TO THE SURVEY EDGES
16. TIME VARIANT FILTER

TIME	HZ./DB	- HZ./DB
0	OUT	- 250/72
700	OUT	- 250/72
1000	OUT	- 200/72
3000	OUT	- 200/72

17. MIGRATION - EXTENDED STOLT INLINE
18. CROSSLINE SORT
19. MIGRATION - EXTENDED STOLT CROSSLINE
20. INLINE SORT
21. RANDOM NOISE ATTENUATION
    0 % FEEDBACK OF ORIGINAL DATA
22. TIME VARIANT FILTER

TIME	HZ./DB	- HZ./DB
0	OUT	- 250/72
700	OUT	- 250/72
1000	OUT	- 200/72
3000	OUT	- 200/72

23. CROSSLINE SORT

Figure 3. Processing sequence for the 3-D seismic survey. Data processed by Western Geophysical.

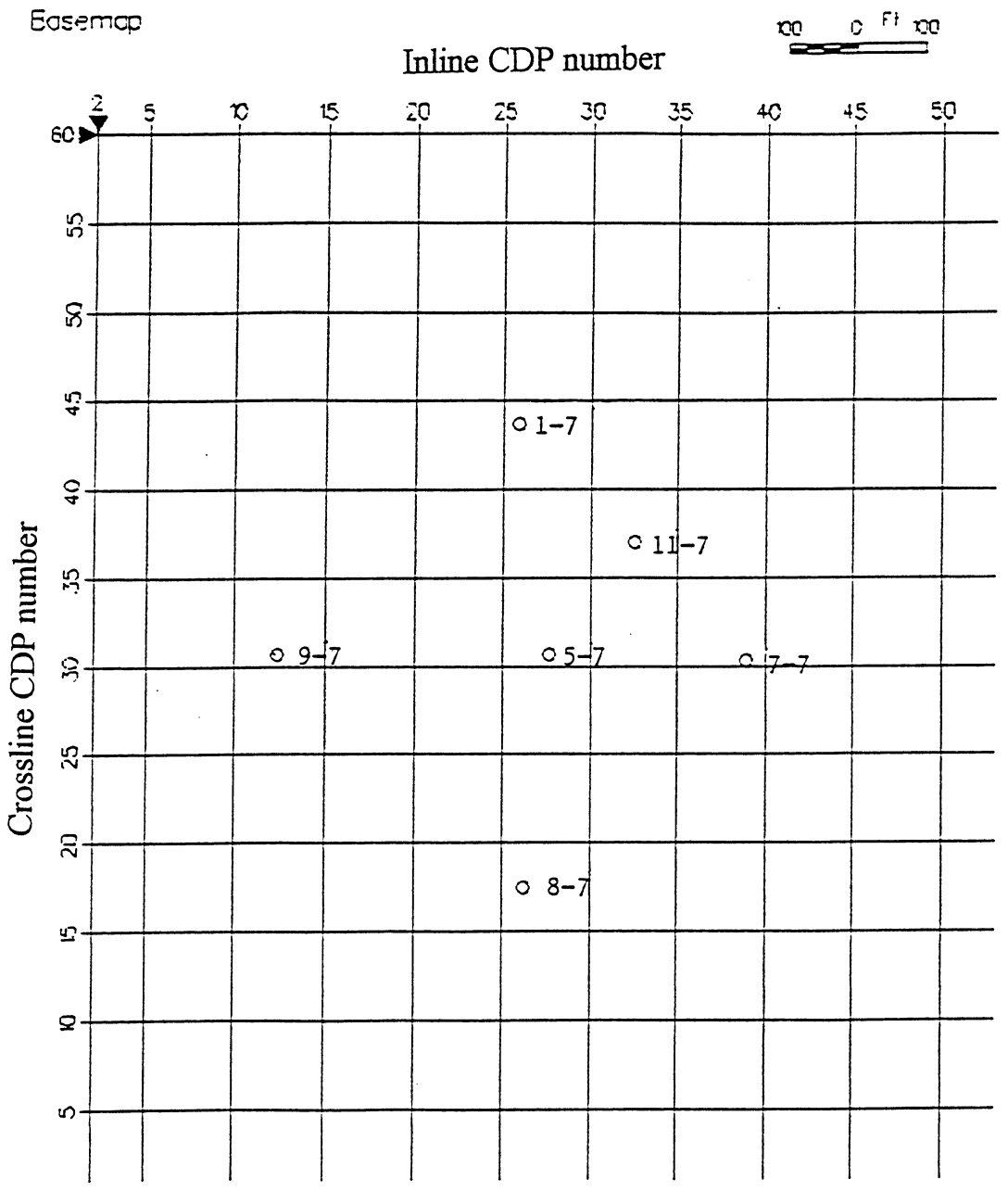

Figure 4. Seismic Basemap of the Gypsy site, 44 miles west of Tulsa.

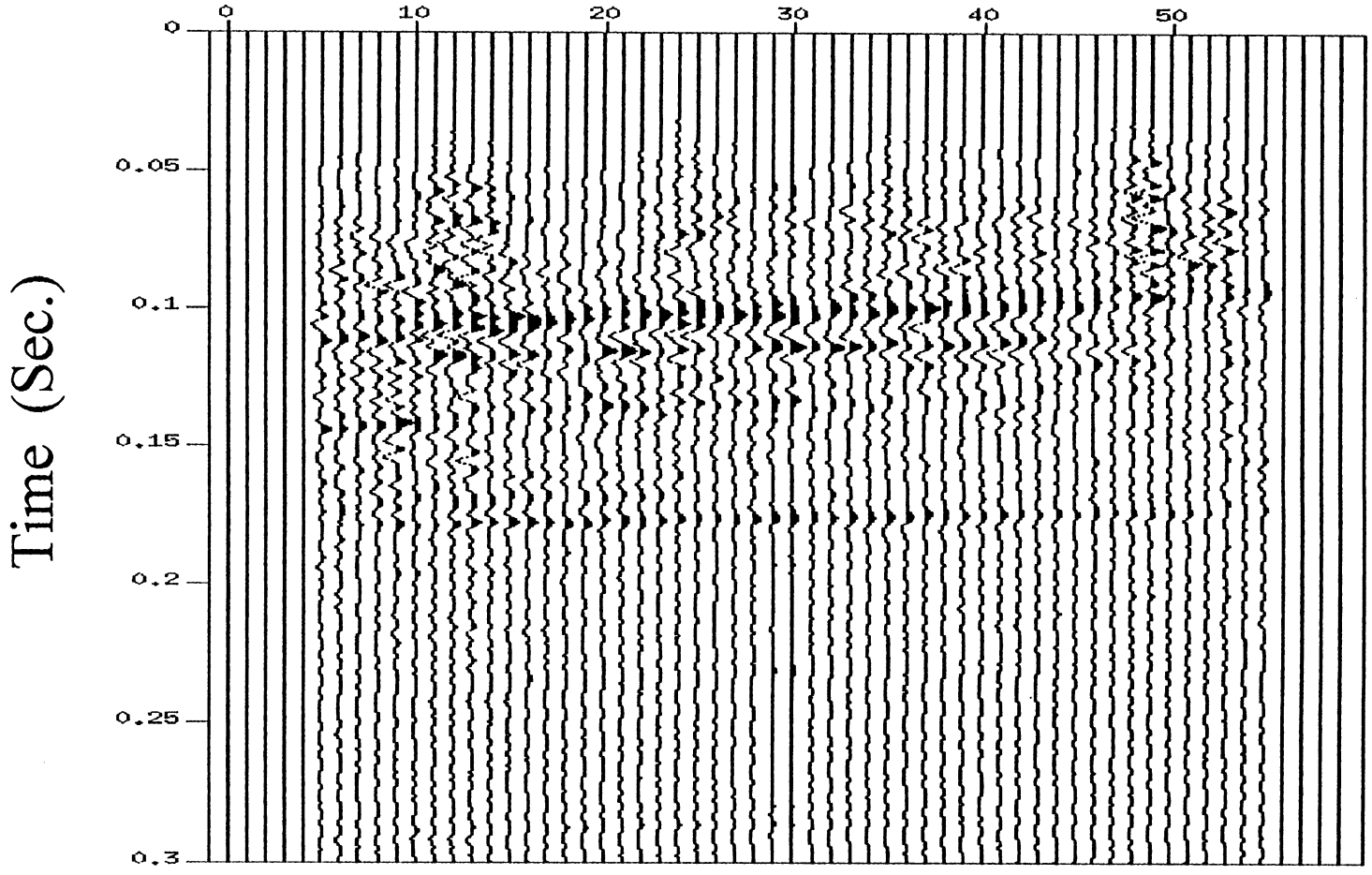

Figure 5a Cross Line 28 (T123443)

Inline CDP Number

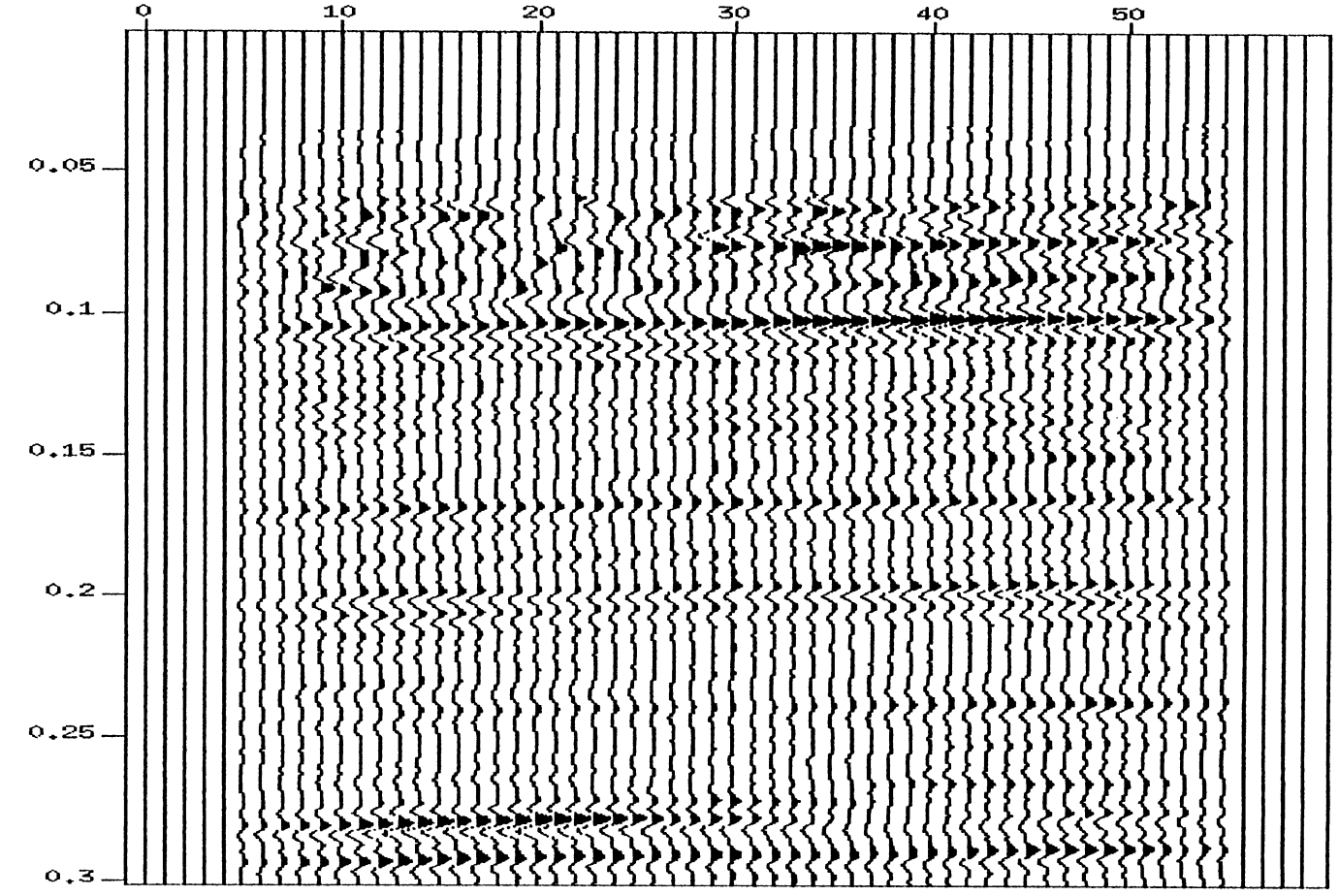

Figure 5 b Cross Line 28 (T125856)

Inline CDP Number

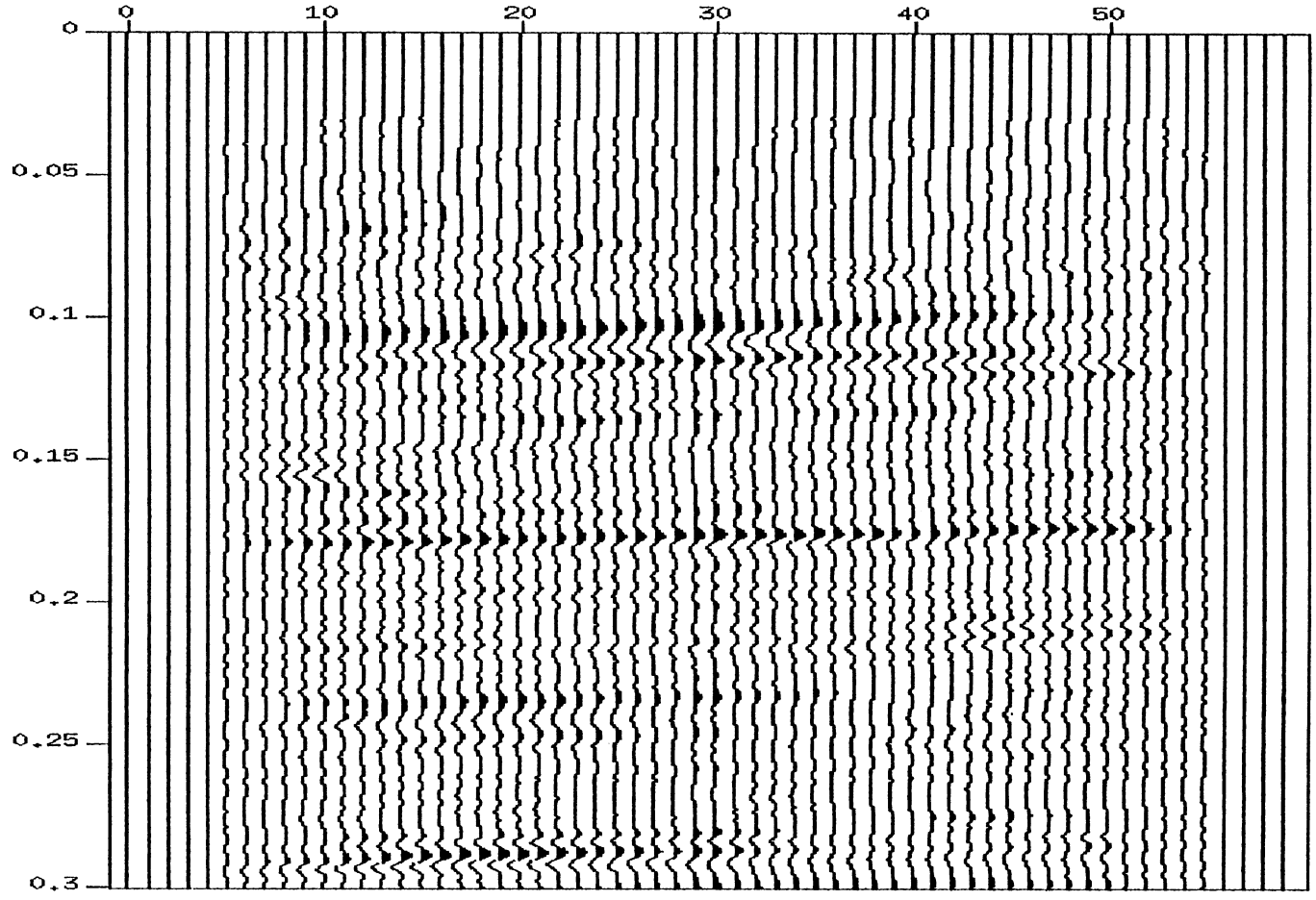

Figure 5c Cross Line 28 (T126328)

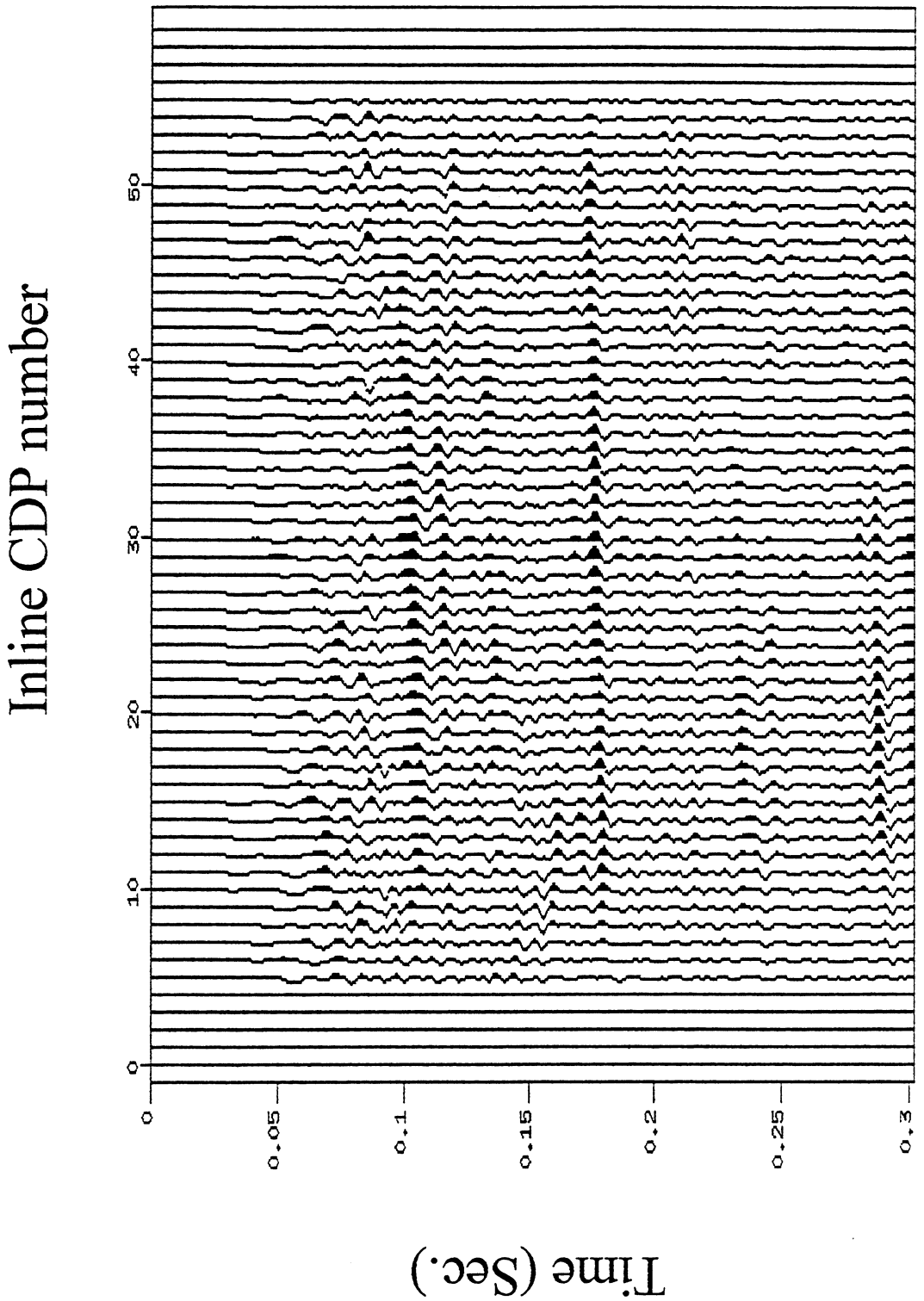

Figure 5d Cross Line 28 (T126339)

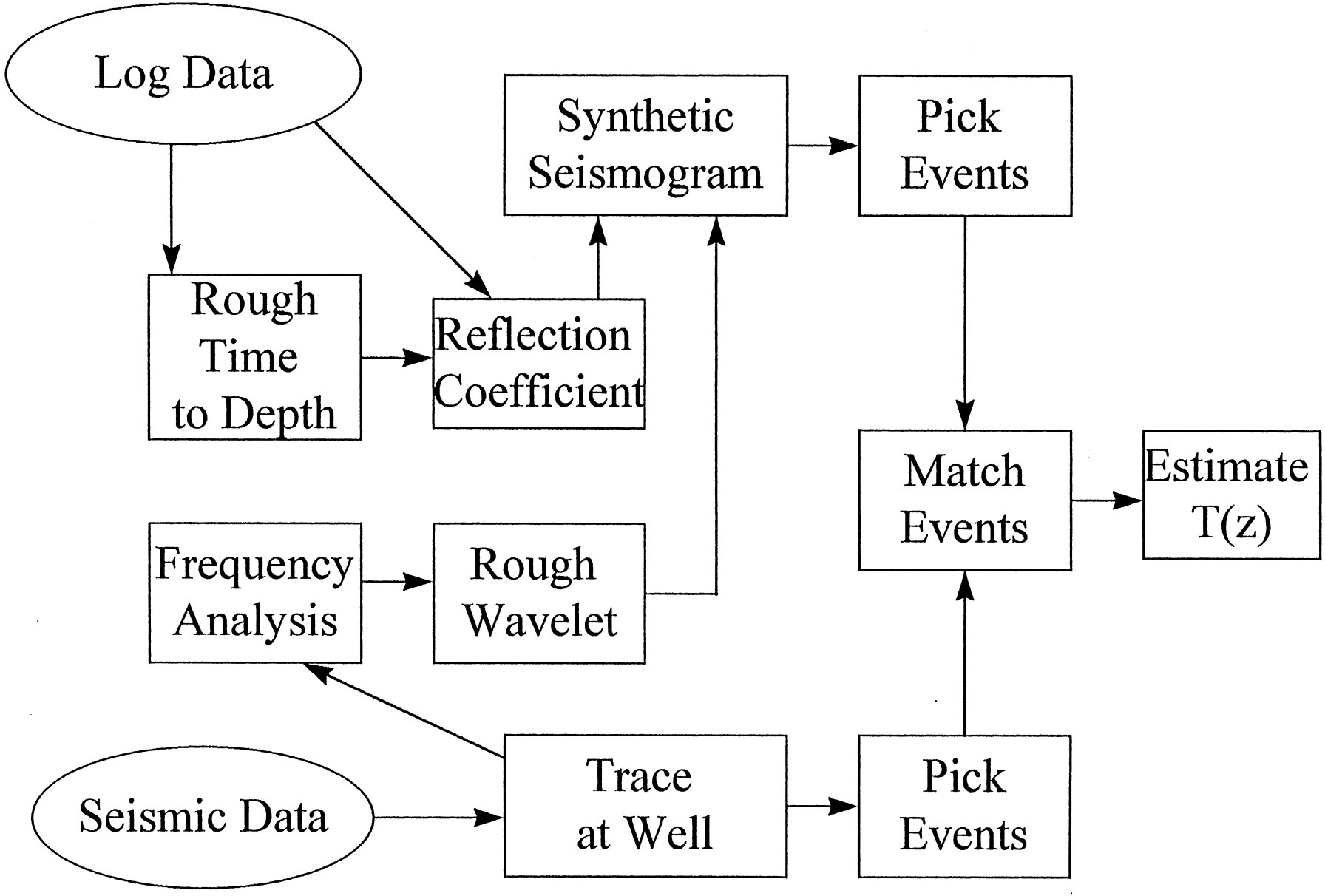

Figure A1. Block Diagram for Time to Depth Estimate

Appendix J

Velocity Dispersion: A Tool for Characterizing Reservoir Rocks

by

Raymon L. Brown and Dirk Seifert

from Geophysics, 1997, V. 62, No. 2, pp.477-486

GEOPHYSICS, VOL. 62, NO. 2 (MARCH-APRIL 1997); P. 477–486, 8 FIGS., 5 TABLES.

Velocity dispersion: A tool for characterizing reservoir rocks

Raymon L. Brown* and Dirk Seifert‡

ABSTRACT

Apparent discrepancies between velocity measurements made with different frequencies in a formation at the Gypsy test site are explained in terms of elastic scattering and intrinsic attenuation. The elastic scattering component of the dispersion (38%) in a marine interval above the Gypsy sandstone is estimated via simple models constructed from well log information. Any dispersion above the predicted value for elastic scattering in this interval is assigned to intrinsic attenuation (62%). Using the vertical measurements in the well, the marine interval directly above the Gypsy sandstone has an estimated intrinsic $Q_I = 51$ and an effective Q because of the scattering of $Q_{SC} = 85$. The total Q of the combined mechanisms is 32. The dispersion of the vertical measurements through the heterogeneous sands and shales of the Gypsy formation can be explained using an intrinsic $Q_I = 30$ and neglecting the effects of scattering. The horizontal observations require a more detailed modeling effort to unravel the relative roles of path and volume effects, elastic scattering, attenuation, and intrinsic anisotropy. Thin layers barely resolvable on the sonic logs play a significant role in modifying the crosswell response. Potentially, the dispersion can be a key to mapping reservoir properties using crosswell and surface seismic data.

INTRODUCTION

Several velocity measurements (including sonic and crosswell data) across the same interval at the Gypsy test site (Doyle et al., 1992) in Oklahoma appear to be contradictory as recognized in the recent MS thesis work of Seifert (1994) at the University of Oklahoma. This paper is devoted to an interpretation of the differences between these interval-velocity measurements.

The paper begins by describing the velocity measurements and the approach used in the interpretation and modeling of these measurements. Finally, we interpret the velocity measurements in terms of scattering and attenuation in a thin-layer model of the formation.

One of the lessons learned in this study is that velocity anisotropy should not be determined using signals with different frequencies. Velocity measurements in different directions using different frequencies require consideration of (1) elastic scattering (Melia et al., 1984; Marion et al., 1994), (2) intrinsic attenuation (e.g., De et al., 1994), (3) volume effects (Brown and Seifert, 1995), and (4) path effects (Mukerji et al., 1995). Separation of these effects is the key to reservoir characterization studies using multifrequency signals.

APPARENT VELOCITY CONTRADICTIONS

Apparent discrepancies in some of the velocity measurements at the Gypsy test site were first recognized by us during the MS thesis work of Seifert (Seifert, 1994; Brown et al., 1994) at the University of Oklahoma. Seifert's thesis involved an integrated geological, geophysical, and reservoir engineering study of the data available at the Gypsy test site (Doyle et al., 1992). The velocity discrepancies faced during that study are described in this section.

One of our first problems with the interpretation of the 3-D surface seismic data was the identification of reflectors using synthetic seismograms generated from the sonic logs. In an effort to see if the problem of identifying the reflectors using synthetic seismograms could be caused by problems with the sonic logs, a comparison of the sonic logs, vertical seismic-profiles (VSPs), and crosswell measurements was made with the hope that any major problems with the data could be identified. However, the comparison of the crosswell and sonic data only led to the confusion described below.

Figure 1 illustrates a series of crosswell seismic traces in the form of a horizontal-path log. The term "horizontal-path log" or HPL is used here to describe data from a crosswell survey in

Manuscript received by the Editor April 3, 1995; revised manuscript received May 16, 1996.
*Oklahoma Geological Survey, University of Oklahoma, Energy Center Building, Room N-131, 100 East Boyd Street, Norman, Oklahoma 73019-0628.
‡Formerly University of Oklahoma, Norman, Oklahoma; presently Heriot-Watt University, Riccarton EH14 4AS, Scotland, United Kingdom.

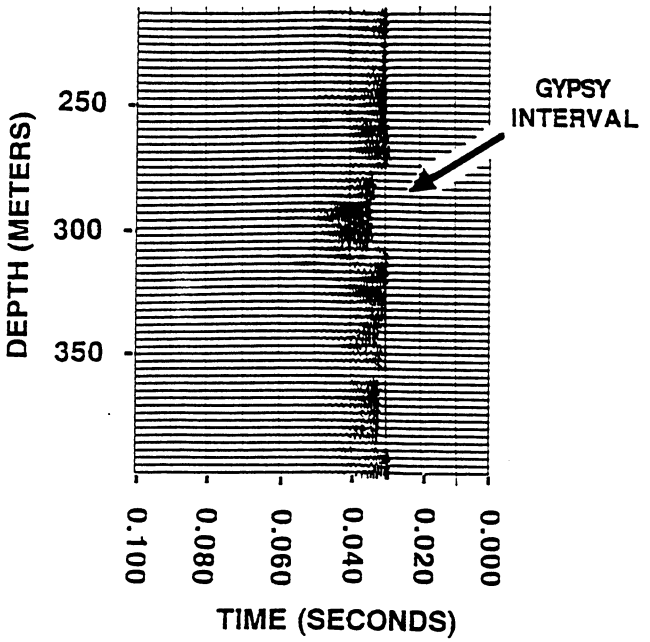

FIG. 1. Horizontal path log (HPL) traces recorded between two wells at the Gypsy test site. The salient low-velocity zone corresponds to the Gypsy sandstone interval.

which a receiver is in one well and the source is in a second well at the same depth as the receiver. In very thick homogeneous intervals where the effects of neighboring beds are not a problem, the HPL traveltimes can be used to compute the horizontal velocity for a layer. For beds of intermediate thickness (e.g., the Gypsy sandstone interval discussed below), critically refracted signals can be distinguished easily from the direct body waves through the center of the interval. In this case, the measurements of a horizontal velocity can still be obtained from the HPL. Finally, for thin beds where the wavefront does not seem to be disturbed by their presence, the scattering, intrinsic attenuation, volume and path effects (away from horizontal) need to be considered in the evaluation of horizontal velocities. This type of crosswell logging is sometimes referred to as "zero-vertical-offset logging" and offers an alternative approach to crosswell studies via effective media concepts. Figure 1 displays the seismic traces for an HPL taken between two wells at the Gypsy test site. The salient low-velocity feature in comparison to the surrounding strata that is visible clearly on this crosswell data is the Gypsy sandstone interval.

Figure 2 shows a comparison of the velocities estimated from the HPL and the sonic log in one of the wells. Surprisingly, the HPL velocity profile is the antithesis of the velocity curves determined from the sonic log. Although it is tempting to describe any differences between the vertical and horizontal propagation to anisotropy, we have chosen to consider below some of

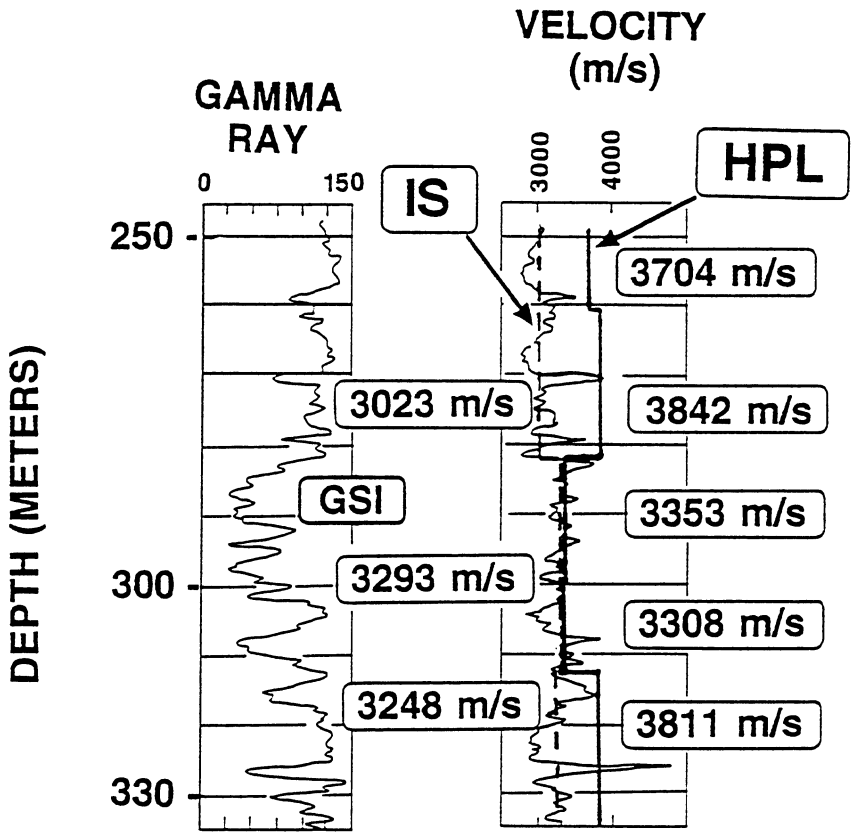

FIG. 2. Gamma ray and sonic velocities in one of the two wells used for the HPL shown in Figure 1. The depth interval includes the Gypsy sandstone interval (GSI). The velocity values determined from the HPL are plotted on the right side of the plot where straight lines are used to approximate the structure of the first-arrival times. The straight lines through the sonic curves represent the interval velocities determined by integrating the sonic log (IS) over the interval covered by the straight lines. The velocity values for these intervals are indicated in boxes on the left side of the plot.

the mechanisms affecting wave propagation before using intrinsic anisotropy as an explanation.

MODELING VELOCITY DISPERSION

Scattering and intrinsic attenuation are assumed to be responsible for most of the observed velocity dispersion and the directional dependence of the observations at the Gypsy test site. In our treatment of the data, we make the assumption that the two mechanisms can be treated as if their respective effects are additive (Richards et al., 1983). Although this is not a correct assumption in the strictest sense, it is used here to provide a simplified interpretation of the observed dispersion. Using this assumption, simple models of elastic scattering (e.g., Melia and Carlson 1984; Marion et al., 1994) and intrinsic attenuation (De et al., 1994) can be used to estimate the range of velocities expected.

Ray theory (V_{RT})

Following papers by Marion et al.(1994) and Mukerji et al. (1995), we shall refer to a velocity measured with a high-frequency signal whose wavelength is short compared to the geological length scales as a ray-theory velocity, V_{RT}. Figure 3 illustrates vertical and horizontal raypaths of high-frequency signals through a layered formation. The V_{RT} (vertical) for the vertical raypath can be computed by simply summing the travel segments in the individual layers to obtain

$$\frac{1}{V_{RT}} = \sum_k \frac{f_k}{V_k}, \qquad (1)$$

where the f_k are the volume fractions of the layers, and V_k are the interval velocities within each layer (Marion et al., 1994). We will use the above ray-theory formula to estimate the high-frequency limit for the vertical transmission of waves

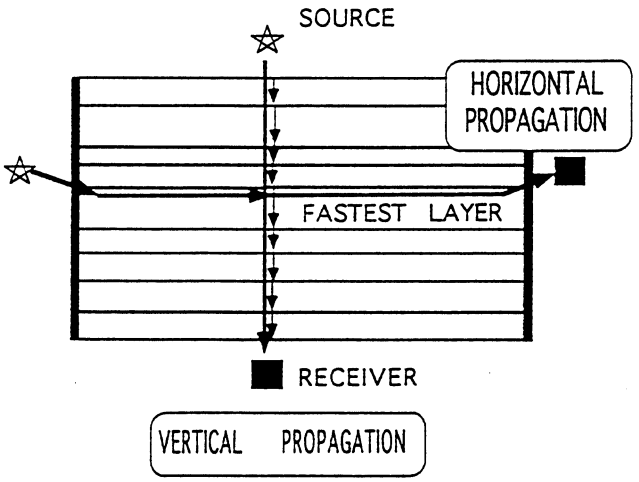

FIG. 3. V_{RT}. Vertical and horizontal raypaths are illustrated, and represent minimum-time travel through a horizontally layered medium for very high-frequency signals whose wavelengths are short compared to the dimensions of the layers. The vertical propagation velocity is simply the thickness of the total interval divided by the sum of individual traveltimes in each layer. Horizontal propagation is assumed to be the result of critical refraction through the fastest layer in the stack of layers.

through the layers. Equation (1) yields the vertical interval velocity one would measure by integrating a sonic log over an interval and dividing into the thickness of the interval. Each measurement of the sonic log is assumed to be over a homogeneous layer. Of course this assumption is not always true for sonic measurements (Sams, 1995). As a side note, any further references to sonic velocity measurements in this paper imply an interval velocity determined by dividing the thickness of the interval by the integrated time of the sonic log over the interval.

Horizontal propagation for the high-frequency limit is assumed to be via critical refraction through the fastest layer in the group of layers being considered (Figure 3). If we assume further that the vertical offset of the bed responsible for the critical refraction is small compared to the total horizontal propagation distance, then the horizontal value of V_{RT} (horizontal) can be approximated by the velocity of the fastest layer in the layered sequence. The value of both of the ray-theoretical velocities is that they can be used as upper bounds on the velocity for high-frequency propagation through a formation. The computation of V_{RT} for any angle of propagation depends upon knowledge of the high-frequency velocities (sonic in this case) for the individual components of a multicomponent formation.

Effective media theory (V_{EMT})

At the other end of the spectrum, i.e., when the wavelengths are long compared to the distances over which the geology varies, the effective response can be treated again as if the wave behavior is independent of frequency [e.g., see the classic papers by Postma (1955), Backus (1962), Berryman (1979), and Helbig (1984)]. Following Melia and Carlson (1984) and Marion et al. (1994), we refer to this velocity limit as the effective media velocity, V_{EMT}, and use the long-wavelength-averaging formulas derived by Backus (1962) to estimate the effective elastic properties of a layered medium. *The elastic properties computed are then used along with the average density of the formation to compute the directionally-dependent values of V_{EMT}, the effective media velocity for a sequence of layers.* In this paper, we restrict the discussion to calculations of V_{EMT} for cases of vertical and horizontal propagation.

The term "effective media" in general usage can imply a frequency dependence based upon combined physical mechanisms for attenuation and dispersion (Jones, 1986). In this paper, the V_{EMT} velocity is restricted to the long-wavelength estimate of velocity that accounts for elastic scattering only and is independent of frequency. The V_{EMT} velocities will be slower than the ray-theory velocities because of interfering energy that follows the shortest path through the medium. However, the estimated V_{EMT} velocities will be faster than the actual velocity measurements across such beds since the intrinsic attenuation of the beds has not been taken into account.

For vertical propagation, the interbed multiples that affect signal amplitudes (O'Doherty and Anstey, 1971) act to introduce a delay in the waveform. The apparent signal delay caused by these multiples makes V_{EMT} (vertical) smaller than V_{RT} (vertical). The scattering effects, i.e., the multiples for vertical propagation, responsible for the delay are strictly elastic.

A slightly different phenomenon occurs for horizontal propagation. In this case, the trailing seismic energy behind the

minimum-time raypath is governed by normal and leaky modes that can be viewed as a special type of multiple. The trailing energy, although in a different form, again makes V_{EMT} (horizontal) smaller than V_{RT} (horizontal).

Marion et al. (1994) and Melia and Carlson (1984) have used V_{RT} and V_{EMT} as estimates of the velocity limits for vertical propagation through layered media. In fact, Marion et al. (1994) point out that when the wavelengths are approximately ten times longer than the thickness of the layers, the velocities they measure in the laboratory approach the values computed using the Backus (1962) averaging. Some numerical studies have indicated a different range of transition (e.g., Carcione et al., 1991), but the value of ten will be used in this paper as a part of the interpretation.

Although there are some fundamental differences in the physics of horizontal-wave propagation, we suggest turning the idea of Marion et al. (1994) for vertical propagation over on its side. In this case, we use the horizontal values of V_{EMT} and V_{RT} as estimates of the long wavelength and short wavelength velocities for horizontal propagation. However, we do not expect to see the same frequency transition from V_{RT} to V_{EMT} for horizontal propagation as observed for vertical propagation in the paper by Marion et al. (1994). In spite of the expected differences, vertical and horizontal propagation will be treated as if they behave or scale in essentially the same manner from the ray theoretical (V_{RT}) to the effective media limits (V_{EMT}). The problem of understanding the differences between the propagation directions through a formation is one of the reasons the topic of scaling is drawing so much theoretical attention in the literature (e.g., Shapiro and Zien, 1993).

Wave theory (V_{WT})

For intermediate frequencies, where the wavelengths become comparable to the scale of the heterogeneity within a formation, the velocity will be referred to as the wave theory velocity, V_{WT}. The velocity V_{WT} is the frequency-dependent velocity that accounts for elastic scattering. The values of V_{WT} range between V_{RT} and V_{EMT}. In spite of recent contributions to the goal of computing the wave theory velocity V_{WT} (e.g., Shapiro and Zien, 1993; Kerner et al., 1994), there are many issues remaining to be resolved before a simple formula capable of predicting the wave theory velocity V_{WT} for a general model of the medium will be available. Until such a theory is available, numerical methods will have to be used to estimate the wave response at frequencies between those where V_{RT} and V_{EMT} are thought to apply.

Since numerical methods can be used to estimate the V_{WT} for a formation, it would seem that all of the basic problems are solved. We merely have to build a model of the geology from the small scale, i.e., from the ray theoretical scale, and solve for the wave motion in the model. The effective wave response can be estimated for all frequencies. However, the approximation of the length scales associated with various geological formations is, in our opinion, one of the formidable tasks remaining to accomplish a scaling relationship for all frequencies. In spite of all the studies on depositional environments, the quantitative aspects of the heterogeneities, i.e., the length scales for different depositional environments, are poorly documented. Still another problem is the treatment of intrinsic attenuation described below.

Intrinsic attenuation

The ray theory (V_{RT}), effective media theory (V_{EMT}), and wave theory velocities (V_{WT}) described above account for the elastic propagation of signals without intrinsic attenuation. Intrinsic attenuation of sound waves causes an additional velocity dispersion that is not predicted by elastic scattering. Since intrinsic attenuation is thought to be related to the viscosity of the fluids filling the pores (Jones, 1986), this component of dispersion is important for mapping reservoir fluids. However, identifying the roles of scattering and intrinsic attenuation separately is a major task when faced with velocity measurements at different frequencies. We simplify this task by making the assumption that the intrinsic attenuation effect upon the velocity dispersion can simply be subtracted from the velocity estimate accounting only for elastic scattering. The justification for this assumption will be given below.

The approximate relationship used to account for attenuation (Aki and Richards, 1980) relates the velocities V_H and V_L measured at frequencies f_H and f_L ($f_H > f_L$) in the form

$$\frac{V_H}{V_L} = 1 + \left(\frac{1}{\pi Q}\right) \ln\left(\frac{f_H}{f_L}\right), \tag{2}$$

where subscripts indicate high-frequency (H) and low-frequency (L) measurements. The equation is derived using the assumption that plane waves are propagating in an infinite homogeneous medium with a nearly constant Q. The dispersion described in equation (2) is an artifact of the popular Fourier transform representation of signals and the condition of causality for those signals. The results are strictly phenomenological and do not represent any particular physical mechanism for attenuation such as local flow (Jones, 1986). The dispersion predicted in equation (2) with respect to a reference low velocity of 2896 m/s measured at a frequency of 30 Hz is shown in Figure 4 for different values of Q.

Combined effects

The total attenuation of a medium can be represented approximately by the sum of the effective attenuation caused by scattering ($1/Q_{SC}$) and the intrinsic attenuation ($1/Q_I$) (Richards and Menke, 1983)

$$\frac{1}{Q_{TOTAL}} = \frac{1}{Q_{SC}} + \frac{1}{Q_I}. \tag{3}$$

This equation for total attenuation is used below to consider the relative dispersions resulting from these two mechanisms. Substituting the above expression for the total attenuation into equation (2) leads to the following prediction for the dispersion:

$$\frac{V_L + \Delta V_{SC} + \Delta V_I}{V_L} = 1 + \left(\frac{1}{\pi}\right)\left(\frac{1}{Q_{SC}} + \frac{1}{Q_I}\right) \ln\left(\frac{f_H}{f_L}\right), \tag{4}$$

where ΔV_{SC} and ΔV_I represent the individual contributions to dispersion caused by scattering and intrinsic attenuation with respect to the low-frequency velocity V_L. The high-frequency and low-frequency velocity measurements are related via the following expression:

$$V_H = V_L + \Delta V_{SC} + \Delta V_I. \tag{5}$$

The scattering and intrinsic relative dispersions can be computed from the respective attenuations using

$$\frac{\Delta V_{SC}}{V_L} = \left(\frac{1}{\pi Q_{SC}}\right) \ln\left(\frac{f_H}{f_L}\right) \tag{6}$$

for scattering and

$$\frac{\Delta V_I}{V_L} = \left(\frac{1}{\pi Q_I}\right) \ln\left(\frac{f_H}{f_L}\right) \tag{7}$$

for intrinsic attenuation.

The dispersion predicted by equation (2) has been used in VSP studies by De et al. (1994) to estimate the intrinsic attenuation using the drift of high-frequency log measurements from VSP measurements. Implicit in their approach is either (1) the neglect of elastic scattering effects or (2) the assumption that scattering and intrinsic attenuation can be treated collectively as described in equation (4). As will be pointed out later in the discussion of the Gypsy sandstone interval, the neglect of the scattering component to dispersion is sometimes justifiable for vertical propagation through some sand/shale environments such as those studied by De et al. (1994). In general, the scattering component of dispersion in equations (4) and (5) cannot be neglected (Richards and Menke, 1983). Both components of dispersion are used in the interpretation described below.

INTERPRETATION OF MEASUREMENTS IN THE UPPER MARINE SECTION

Although the sonic velocities in the wells at the Gypsy test site seemed at first to be erratic with large variations over short distances, there was no indication on the caliper log that hole conditions were a problem. The velocity comparison in Figure 2 indicates that the sections directly above and below the Gypsy sandstone interval are responsible for the large discrepancies in the velocity profiles obtained using the sonic and HPL. The rapid changes in the sonic were identified using petrophysical analysis of logs as dolomitic streaks in the marine environments surrounding the Gypsy sandstone interval. Figure 5 illustrates the respective depositional environments interpreted for the logged interval shown in Figure 2. Since the marine sections above and below the Gypsy formation represent shales and/or sands with intermittent dolomite streaks, thin-layer and intrinsic-attenuation effects in the marine sections are interpreted to be responsible for the major differences in the velocity profiles. To justify this conclusion, a layered model of the upper marine section (depth range 248–312 m in Figure 2) was made and is compared with the observations in the discussion below.

The pertinent velocity measurements in the upper marine section are tabulated in Table 1. Included in Table 1 are the

a)

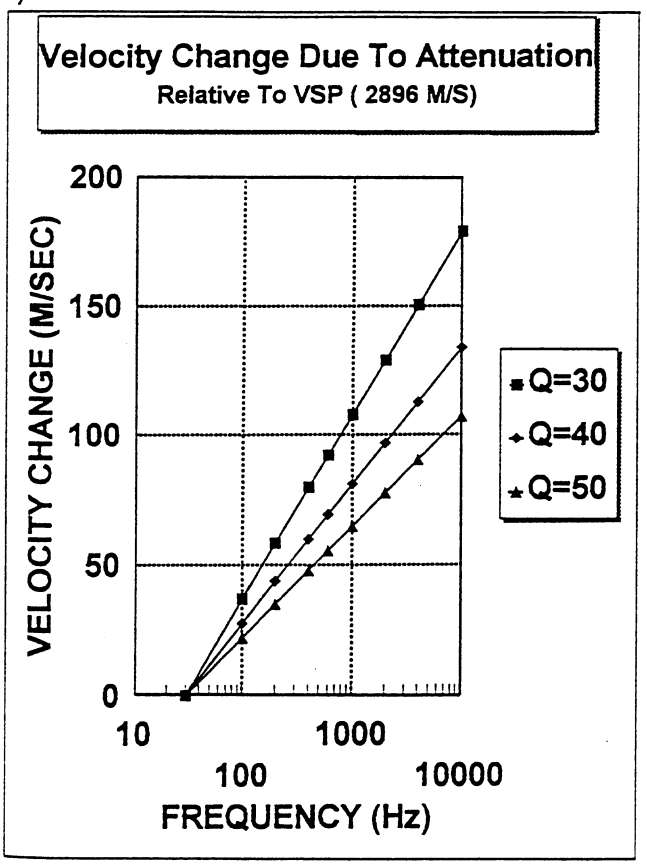

b)

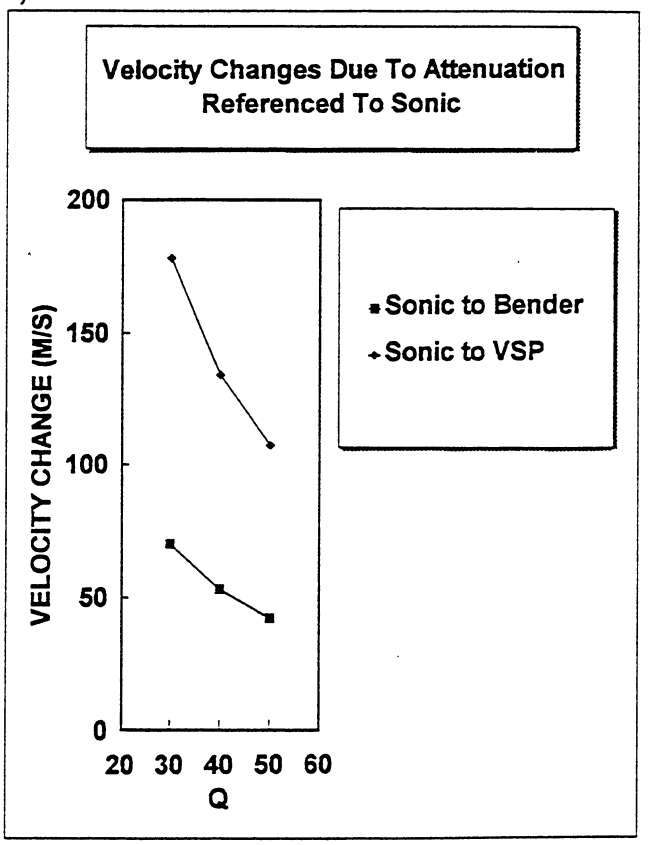

FIG. 4. Attenuation. (a) The velocity increase as a function of frequency is shown for a plane wave in a homogeneous-attenuating medium. The computation is made using equation (2) assuming a reference velocity of 2896 m/s for V_L at a frequency (f_L) of 30 Hz. This particular value was chosen as a reference to approximate the VSP interval velocity estimate for the upper marine interval listed in Table 1. (b) Plot showing the velocity decrease caused by attenuation (taken from the plot shown in (a) for different values of Q. The bottom curve represents the drop in velocity from a sonic-log measurement (10 000 Hz) to a Bender log or HPL measurement at 1000 Hz. The top curve represents the velocity change from a sonic-log measurement to a VSP measurement at 30 Hz.

integrated sonic-log, the Bender log, the HPL and the VSP estimates of the interval velocity. The Bender and VSP measurements were made by Burns et al. (1992, personal communication). The frequencies used for subsequent calculations and the directions of the measurements are also listed in Table 1. The shale-prone measurements listed in Table 1 represent only a portion of the upper marine interval from 250–260 m (see Figure 2).

To approximate the velocity errors, we estimated the timing accuracy for the different measurements (Table 1). The estimates are referenced to an assumed VSP timing accuracy of 1 ms. The timing error for the other measurements were scaled with respect to the VSP measurement using the respective frequencies shown in Table 1. To estimate the relative velocity errors shown in Table 1, the interval-distance error for each of the measurement intervals listed was neglected. The relative velocity error is then obtained using

$$\frac{V_M - V_A}{V_A} = \frac{\Delta V}{V_A} = \frac{\Delta T}{T}, \tag{7}$$

where V_M is the measured velocity, V_A is the actual velocity, ΔT is the timing error, ΔV is the velocity measurement error, and T is the traveltime across the interval of measurement. The velocity errors (ΔV) listed in Table 1 have been computed using equation (7). Note that the Bender log is essentially a low-frequency sonic log with a source-receiver spacing of approximately 10 m.

Table 1. Velocity measurements. Marine section above the Gypsy sandstone interval.

Measurement-direction	Frequency (HZ)	Estimated timing error (dt in s)	Measurement interval (m)	Velocity (m/s)	Estimated velocity error (m/s)
Sonic Vertical	10 000	3.00×10^{-6}	.6	3038	45
Sonic (shale-prone) Vertical	10 000	3.00×10^{-6}	.6	2994	44
HPL Horizontal	1000	3.00×10^{-5}	105.5	3841	4
HPL (shale-prone) Horizontal	1000	3.00×10^{-5}	105.5	3704	4
Bender log (shale-prone) Vertical	1000	3.00×10^{-5}	10.0	2927	26
VSP Vertical	30	1.00×10^{-3}	34.1	2896	246

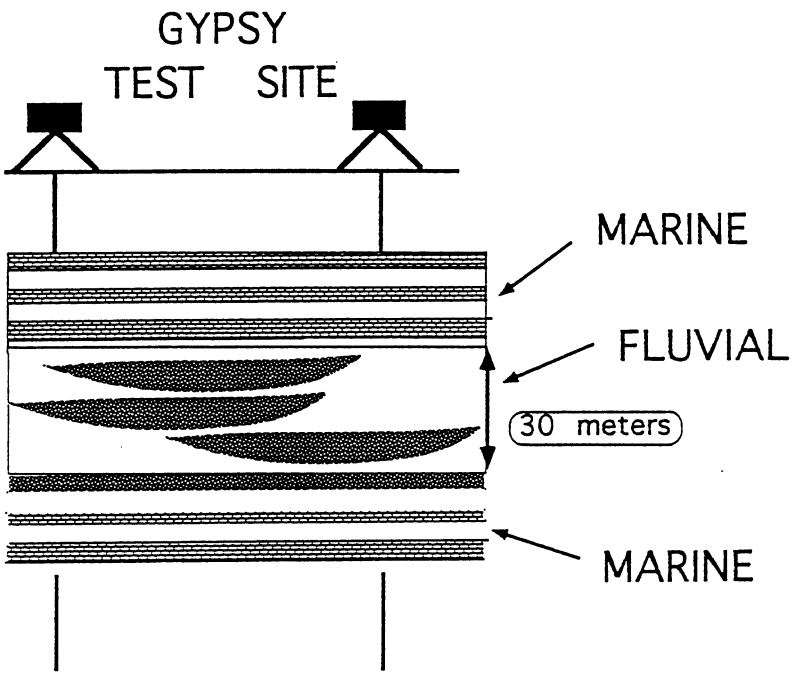

FIG. 5. Schematic of the types of depositional environments for the log interval shown in Figure 2. The strata above and below the Gypsy sandstone are cyclic marine sequences, while the Gypsy interval is a heterogeneous fluvial environment. The upper marine sequence consists of shales and dolomitic streaks while the lower marine sequence contains sands, shales, and dolomitic streaks.

In a homogeneous isotropic interval, all of the measurements presented in Table 1 should agree since they were all made in the same upper marine section. Given the errors involved, the VSP measurement could be considered to be in agreement with all of the other measurements. However, the HPL and Bender velocities are significantly different from the sonic velocity for the interval. To interpret the differences between the measurements listed in Table 1, we will follow the work of Marion et al. (1994) as a guide. They used the ratio of the wavelength of the seismic signals to the thickness of the beds as an indicator of when the respective velocities defined above should be applied, i.e., ray theory, wave theory, and effective media theory. When the ratio is less than one, the ray theory velocity applies. When the ratio is greater than approximately 10 (Marion et al., 1994), effective-media-theory velocities are used. We will use this value, although other ratios have been suggested (e.g., Carcione et al., 1991), to estimate the signal frequencies where the effective media velocity applies.

To estimate the wavelengths associated with the different signals, we assume a velocity of 4000 m/s that is intermediate between the vertical and horizontal velocities measured in the upper marine section. Using this velocity and a bed thickness of $d = .6$ m, the wavelength-to-thickness ratios in Table 2 were computed. The bed thickness was chosen to approximate the thin dolomite streaks distributed throughout the marine sections. Following Marion et al. (1994), these values are assembled into the plot of scaled velocities versus the ratio (λ/d) of the wavelength (λ) to the bed thickness (d) shown in Figure 6. The actual transition curve describing the frequency-dependent velocities, V_{WT}, will depend on a number of factors including the spectrum of bed thicknesses, the contrasts between the beds, the spectrum of the signal, and the direction of propagation through the formation. In spite of all of the physical distinctions between vertical and horizontal propagation in the upper marine section, we assume that both directions of propagation can be treated using the scaling relationship shown in Figure 6. Specifically, the HPL and Bender log measurements are treated as if they have a λ/d of 7 and an estimated wave-theory velocity of

$$V_{WT} = \tfrac{1}{2}(V_{RT} + V_{EMT}), \qquad (8)$$

where V_{RT} for an interval is approximated by the integrated sonic measurements, and V_{EMT} represents the low-frequency measurements at VSP frequencies. The V_{WT} and V_{EMT} represent only the elastic scattering effects at different frequencies that act to lower the velocity below the V_{RT} value.

Armed with the above elastic scaling relations, we are now ready to interpret the velocity measurements in the upper marine section in terms of a layered model. The upper marine section is assumed to consist of layers of shale and dolomite with the properties described in Table 3. The densities and P-wave velocities were obtained from logs. The shear velocities were estimated from V_P/V_S ratios for the particular lithologies involved. Curves of V_{RT} and V_{EMT} for vertical and horizontal propagation through the model are shown in Figures 7 and 8, respectively as a function of the percentage of dolomite. These curves will be used as a foundation for the interpretation of the velocities through the upper marine interval.

Table 2. Frequencies, wavelengths, and wavelength/bed-thickness ratios assumed for measurements.

Measurement	Frequency (Hz)	Wavelength (λ) meters	λ/d
VSP	30	133	222
HPL,Bender	1000	4	7
Sonic	10 000	0.4	0.7

Vertical measurements

VSP measurement.—To interpret the VSP measurement through the upper marine section, we begin by finding a layered model with a V_{RT} (Figure 7) for vertical propagation through the upper marine section that agrees with the interval velocity estimate of 3023 m/s obtained by integrating the sonic log through the upper marine section (Figure 2). The basic idea is to vary the relative percentages of dolomite and shale for the layered model until the model value of V_{RT} agrees with the sonic estimate of the velocity for the interval. The layer parameters are fixed as listed in Table 3. A fractional volume of dolomite rounded to 28% yields a V_{RT} of 3063 m/s, which is an approximation to the integrated sonic. Therefore our layered model for the total upper marine section (248–312 m) consists of 28% dolomite and 72% shale. The effective elastic constants (Backus, 1962) for this model listed in Table 4 were used to compute V_{EMT} (vertical) and V_{EMT} (horizontal).

The layered model with 28% dolomite has a V_{EMT} (vertical) of 3000 m/s which is the predicted VSP velocity in the absence

Table 3. Layer parameters for the model of the marine section above the Gypsy sandstone interval.

Component	Density (g/cm^3)	P-wave velocity (m/s)	S-wave velocity (m/s)
Shale Layers	2.5	2713	1219
Dolomite Layers	2.5	4573	2540

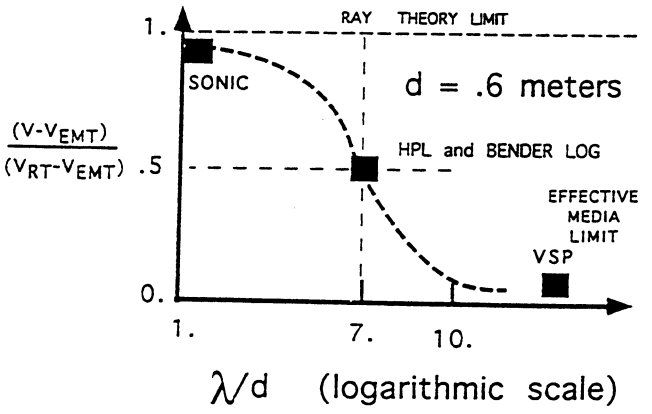

FIG. 6. Schematic illustration of the assumed scaling relationship (accounting only for elastic scattering) in the upper marine section. The integrated-sonic velocity (IS in Figure 2 and listed as a sonic measurement in Table 1) is used as an estimate of V_{RT}, while the value of V_{EMT} is expected to represent the VSP measurement if the intrinsic attenuation is negligible. The beds are assumed to have a thickness of .6 m for the marine section above the Gypsy sandstone. The dispersion caused by elastic scattering is assumed to scale (approximately) along the curve shown (Marion et al., 1994).

Table 4. Effective elastic constants (GPa) for layered models.

	C11	C33	C13	C44	C66
Upper marine interval (248–312 m) 28% dolomite	27.50	22.48	12.06	4.74	7.19
Shale-prone interval (250–260 m) 23% dolomite	25.86	21.62	11.83	4.51	6.57

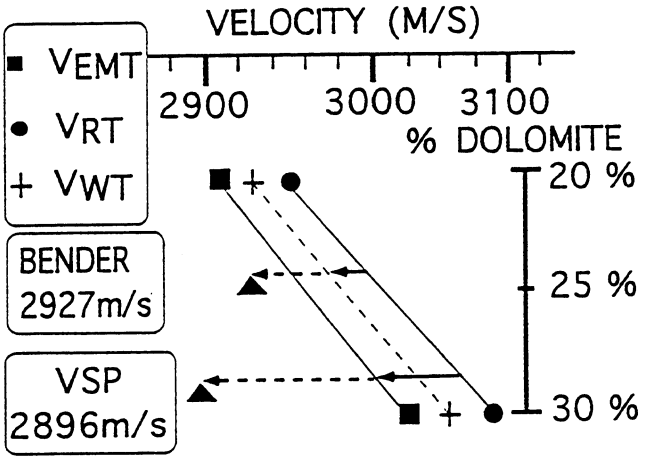

FIG. 7. Layered-model velocities predicted for vertical propagation through the marine section above the Gypsy sandstone interval. The three computed velocities V_{RT}(sonic), V_{WT}(Bender) and V_{EMT}(VSP) are shown for different percentages of isotropic shale and dolomite layers (see Table 2). The values of V_{WT} (1000 Hz) and V_{EMT} (30 Hz) account for the elastic scattering component of dispersion away from the sonic log measurements (V_{RT}). The differences between the vertical measurements can be explained in terms of dispersion caused by an elastic scattering component (solid arrows), intrinsic attenuation ($Q_I = 51$, dashed arrows) and measurement errors (see Table 1).

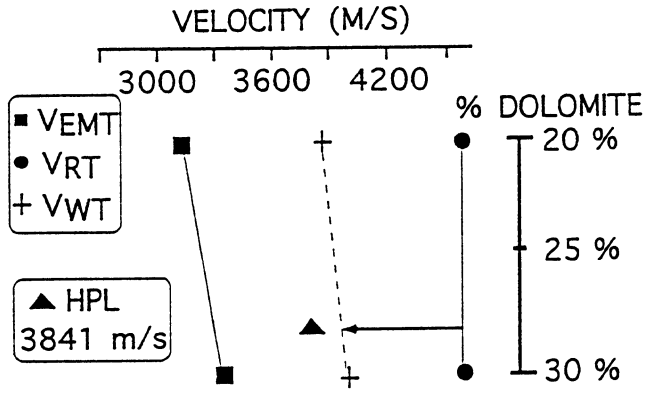

FIG. 8. Layered-model velocities predicted for horizontal propagation through the marine section above the Gypsy sandstone interval. The three computed velocities V_{RT}(sonic), V_{WT}(crosswell at 1000 Hz), and V_{EMT}(crosswell at 30 Hz) are shown for different percentages of isotropic shale and dolomite layers (see Table 2). The values of V_{WT} and V_{EMT} account for the elastic scattering component of dispersion away from the sonic log measurements predicted by V_{RT}. The crosswell measurement (the HPL at 1000 Hz) differs significantly from the sonic log measurement because of elastic scattering (solid arrow), intrinsic attenuation and possibly a component of intrinsic anisotropy.

of intrinsic attenuation. The difference between this value of V_{EMT} and the actual VSP measurement (2896 m/s) can be explained by the effects of intrinsic attenuation ($Q = 51$). Since the errors for the sonic measurement and the VSP overlap, the significance of this interpretation is a moot point (see the listed measurement errors in Table 1).

Both the VSP and Bender measurements were made by New England Research (Burns et al., 1992, personal communication) in a more shale-prone portion of the upper marine interval (depth interval approximately 250–260 m in Figure 2). Notice that we have chosen to interpret the VSP measurement made over this restricted interval as if it represents the complete upper marine section (248–312 m in Figure 2) because of the larger volume affected by the VSP signals. In other words, measurements of velocities over short intervals with signals that have long wavelengths are affected by the surrounding formations.

Bender log.—The Bender log measurements, unlike the VSP measurements, should be representative of the more shale-prone interval (250–260 m in Figure 2) because of the shorter wavelengths. The value of the integrated sonic for this interval is 2994 m/s. In this case, the respective measurement errors listed in Table 1 indicate that the sonic and the Bender log velocity differences are significant over the interval. By allowing the volume of dolomite to vary, we find that a layered model with 23% dolomite yields a value of V_{RT} in agreement with the sonic measurement for the shale-prone interval. The values of V_{RT} and V_{EMT} for a model with 23% dolomite can be used in equation (8) to predict V_{WT}, the velocity expected for the Bender log measurement (2969 m/s) accounting only for elastic scattering. The intrinsic attenuation effect for a $Q_I = 51$ is approximately an additional 42 m/s drop in the velocity and puts the velocity estimate close to the observed velocity for the Bender measurement of 2927 m/s (Figure 7). Thus the differences between the vertical measurements through the upper marine section can be interpreted using scattering, attenuation, measurement errors, and some juggling to account for the effective volumes influencing the different wavelengths. Approximately 38% of the dispersion between the sonic and VSP is caused by elastic scattering with a computed Q_{SC} of 85 using equation (6). The remaining 62% of the dispersion is assumed to be caused by intrinsic dispersion with a Q_I of 51. The total Q computed using equation (3) for vertical propagation through the upper marine interval caused by scattering and intrinsic attenuation is 32.

Horizontal measurement

We now interpret the horizontal measurement, the HPL, through the upper marine interval using the same ideas. The model used for the interpretation will be the same one used for the complete upper marine section from 248–312 m (28% dolomite). The model predictions and the measurement of the horizontal propagation velocity through the upper marine section are indicated in Figure 8. The V_{RT} (horizontal) is the velocity of the fastest layer (the dolomite streaks in this case). V_{EMT} is the model velocity (Backus, 1962), accounting only for elastic scattering, for an HPL measurement at frequencies comparable to the VSP (no HPL measurements were made at these frequencies). At higher frequencies around 1000 Hz, the elastic velocity estimate, V_{WT}, for the HPL is 3945 m/s using

equation (8) and the assumption that the model for the interval has 28% dolomite. The higher percentage of dolomite (28% rather than 23% in the shale-prone interval) is used to account (approximately) for the volume and/or horizontal path effects that occur during crosswell propagation versus the vertical propagation over a smaller more shale-prone interval for the Bender measurements. The shift from the elastic value indicated for the HPL measurements to the measured value of 3841 m/s is more than can be explained by a $Q_I = 51$ used for vertical propagation. We are not bothered by this discrepancy for several reasons:

1) The scaling relationship between V_{WT} and V_{EMT} is approximate and is not expected to be the same for vertical and horizontal propagation as we have assumed.
2) The effect of attenuation may act differently in a horizontal direction because the mode of propagation is distinctly different from vertical propagation.
3) The geology between the two wells may have average properties that differ from the Bender and sonic measurements in the well. This includes both the volume effects described earlier and the path effects (Mukerji et al., 1995).
4) The effects of intrinsic anisotropy have not been considered.

INTERPRETATION OF MEASUREMENTS IN THE GYPSY SANDSTONE INTERVAL

Although we have not emphasized the Gypsy sandstone interval since the vertical and horizontal differences were not as dramatic, the basic ideas still apply. A brief discussion of the Gypsy sandstone interval is given here since it is what was treated as the reservoir for the integrated studies conducted at the Gypsy test site (Doyle et al., 1992). Complimenting our own velocity data, we have used measurements reported in Burns et al. (1992, personal communication) for the VSP and Bender log measurements in this interval. The velocities are listed in Table 5. The errors in Table 5 were computed just as they were for the errors in Table 1.

Indications of reservoir heterogeneity

Bender log and HPL.—The difference between the integrated sonic measurements and the HPL are within the measurement errors. However, the Bender log measurement differs significantly from both the HPL and sonic measurements. Anisotropy is one possible explanation, but a heterogeneous shaley-sand interval is not expected to exhibit very much anisotropy. Instead, we interpret the difference between the Bender log and the HPL as being the result of volume and/or path effects since both measurements have the same dominant frequency. *We suggest that the recognition of volume and/or path effects between wells is an important clue to predicting reservoir heterogeneity.* An indication of the reservoir heterogeneity in the Gypsy sandstone has been recognized by the difference between vertical and horizontal velocity measurements through the reservoir made using the same frequencies. The question of how to interpret the differences between these measurements remains to be solved. In the case of the Gypsy sandstone, the fluvial channels embedded in flood plain deposits represent the heterogeneity in the reservoir.

Sonic, Bender log, and VSP.—The differences between the vertical measurements in the Gypsy sandstone interval can be explained by neglecting elastic scattering and assuming an intrinsic attenuation ($Q_I = 30$). Neglecting elastic scattering seems to work for vertical propagation in sand/shale environments (e.g., De et al., 1994). Note that only the Bender log and integrated sonic measurements in this study show a vertical difference that exceeds the measurement errors listed in Table 5.

DISCUSSION AND CONCLUSIONS

Simple models of elastic scattering and intrinsic attenuation have been used to interpret the velocity differences observed at the Gypsy test site in terms of dispersion. At this point, all of the observations can be explained without the need to introduce intrinsic anisotropy. The explanation for the diversity of the velocity measurements within the same interval has been in terms of

1) elastic scattering,
2) intrinsic attenuation,
3) volume differences,
4) path effects, and
5) measurement errors.

The elastic component of the dispersion (38%) has been estimated from a model of the upper marine interval constructed from well logs and subtracted from the total dispersion to estimate the portion of the dispersion (62%) caused by the intrinsic attenuation. A $Q_I = 51$ was obtained for the upper marine interval accounting for scattering. A $Q_I = 30$ was obtained for the Gypsy sandstone interval by neglecting scattering. The horizontal observations require a more detailed modeling effort to unravel the relative roles of path and volume effects, elastic scattering, attenuation, and intrinsic anisotropy. However, based upon the results at hand, it is unlikely that a large intrinsic anisotropy will be required in the final model.

Although the fit to the models worked, the interpretation presented is expected to be modified by a more detailed study of the data involved. Our goal here has been to simply explain the measurements in terms of components of scattering and intrinsic attenuation in layered media using single frequencies and single bed thicknesses. A more robust approach to well log data is required (e.g., see Kerner et al., 1994) which accounts for the spectra of frequencies and bed thicknesses. One of the biggest problems for scaling velocity measurements is defining the volume contributing to the received signal. The volumes affected and the path effects (Mukerji et al., 1995) for signals can be quantified potentially by using multidirectional velocity measurements through a formation using the same frequency signals. In this study, the difference between the HPL and the

Table 5. Velocity measurements. Gypsy sandstone interval.

Measurement-direction	Frequency (Hz)	P-wave Velocity (m/s)	Estimated velocity error (m/s)
Sonic-vertical	10 000	3313	54
HPL	1000	3353	3
Bender log	1000	3226	31
VSP	30	3143	289

Bender log measurements at the same dominant frequency gave an indication of the heterogeneity in the Gypsy reservoir interval.

Next, after identifying the volumes affected, comes the even harder task of quantifying the important length scales of seismic properties within the representative volume that control the scattering component of dispersion. A sonic log is not very useful for the recognition of length scales (Sams, 1995). For example, our assumed bed thickness (.6 m or 2 ft) is on the limit of sonic resolution. These thin beds, although barely resolvable on the sonic data, are critical in the interpretation of the crosswell data. Their dimensions place crosswell measurements in the wave-theory domain where velocity changes caused by elastic scattering are frequency dependent (Figure 6). Thus assembly of a velocity model, especially for crosswell studies, requires a higher resolution estimate of velocity variations than is available directly from sonic logs. Even with higher resolution measurements in the well, the lateral length scales cannot be characterized easily by measurements in the available well control. The problem of geological scale is not a small one since it affects the coherence and mode of propagation of signals traveling in different directions through a formation. As a result, the "trailing energy" is expected to have a directional character that is dependent upon the length scales of the geology.

One of the important aspects to be concluded from this work is that velocity-dispersion logging can potentially be used to estimate important properties of reservoirs. For example, the difference in frequency between the sonic (10 kHz) and the Bender (1 kHz) was sufficient to cause an observable shift of the velocities beyond the respective measurement errors. Since the elastic scattering effects upon dispersion can be neglected in some formations the observed dispersion can sometimes be used to infer the intrinsic attenuation directly. Since intrinsic attenuation is indicative of important reservoir properties, e.g., the presence of gas, cracks, and permeability, velocity-dispersion logging should be a useful tool for recognizing and characterizing pay zones (especially gas reservoirs) where conventional logging methods have failed. In addition, the elastic scattering component of velocity dispersion can contribute to the prediction of depositional environments since the scale and degree of heterogeneity within formations controls the amount of elastic scattering. In this study, the difference between the Bender and HPL velocity measurements was interpreted to be the result of reservoir heterogeneity. Reconciliation of these types of measurements can be used to monitor reservoir variations between wells.

ACKNOWLEDGMENTS

The data for this project were furnished by the Institute for Reservoir Characterization at the University of Oklahoma. Dr. A. Gorody, Universal Geosciences Inc., kindly provided the abstract of the work by New England Research, Inc. D. Seifert was supported by the Institute for Reservoir Characterization during his thesis work. R. Brown received support from the Department of Energy-Bartlesville (Contract No. DE-FG22-94BC14970) and the Gas Research Institute (Contract No. 5093-260-2618). R. Brown also received a number of useful papers and input on topics related to this study from Dr. S. Raikes, British Petroleum, and Dr. D. Ebrom, University of Houston. Dr. J. Parra, Southwest Research Institute, provided input to the portion of the project related to guided waves, while Dr. H. Collier provided a petrophysical analysis of the logs. Appreciation is also expressed to T. Mukerji, G. Mavko, D. Mukerji and N. Lucet for sharing a preprint of their paper on this topic. Constructive reviews by G. Mavko and G. Towle improved the final version of the paper.

REFERENCES

Aki, K., and Richards, P. G., 1980, Quantitative seismology, Vol. 1: W. H. Freeman and Co.

Backus, G. E., 1962, Long-wave elastic anisotropy produced by horizontal layering: J. Geophys. Res., **67**, 4427–4440.

Berryman, J. G., 1979, Long-wave elastic anisotropy in transversely isotropic media: Geophysics, **44**, 896–917.

Brown, R. L., Parra, J. O., and Seifert, D., 1994, Reconciled surface and borehole measurements: A case history: 64th Ann. Internat. Mtg., Soc. Expl. Geophys., Expanded Abstracts, 467–470.

Brown, R. L., and Seifert, D., 1995, Velocity dispersion: a problem and a solution: 65th Ann. Internat. Mtg. Soc. Expl. Geophys., Expanded Abstracts, 663–666.

Carcione, J. M., Kosloff, D., and Behle, A., 1991, Long-wave anisotropy in stratified media: Geophysics, **56**, 245–254.

De, S. G., Winterstein, D. F., and Meadows, M. A., 1994, Comparison of P-wave and S-wave velocities and Q's from VSP and sonic log data: Geophysics, **59**, 1512–1529.

Doyle, J. D., O'Meara, D. J., and Witterholt, E. J., 1992, The "Gypsy" field research program in integrated reservoir characterization, SPE 24710, 67th Ann. Technical Conference and Exhibition: Soc. Petr. Eng.

Helbig, K., 1984, Anisotropy and dispersion in periodically layered media: Geophysics, **49**, 364–373.

Jones, T., 1986, Pore fluids and frequency-dependent wave propagation in rocks: Geophysics, **51**, 1939–1953.

Kerner, C., and Harris, Peter E., 1994, Scattering attenuation in sediments by ARMA processes-validation of simple Q models: Geophysics, **59**, 1813–1826.

Marion, D., Mukerji, T., and Mavko, G., 1994, Scale effects on velocity dispersion: From ray to effective medium theories in stratified media: Geophysics, **59**, 1613–1619.

Melia, P. J., and Carlson, R. L., 1984, An experimental test of P-wave anisotropy in stratified media: Geophysics, **49**, 374–378.

Mukerji, T., Mavko, G., Mujica, D., and Lucet, N., 1995, Scale-dependent seismic velocity in heterogeneous media: Geophysics, **60**, 1222–1233.

O'Doherty, R. F., Anstey, N. A., 1971, Reflections on amplitudes: Geophys. Prosp., **19**, 430–458.

Postma, G. W., 1955, Wave propagation in stratified medium: Geophysics, **20**, 780–806.

Richards, P. G., and Menke, W., 1983, The apparent attenuation of a scattering medium, Bull., Seis. Soc. of Am., **73**, 1005–1021.

Sams, M. S., 1995, Attenuation and anisotropy: The effect of extra fine layering: Geophysics, **60**, 1646–1655.

Seifert, D., 1994, Reservoir development scale modeling based on integration of high-resolution 3-D seismic data, well logs and core data: Gypsy Site, Pawnee County, Oklahoma, U.S.A.: M.Sc. Thesis, University of Oklahoma.

Shapiro, S. A., and Zien, H., 1993, The O'Doherty-Anstey formula and localization of seismic waves: Geophysics, **58**, 736–740.

Appendix K

Modeling Depositional Environments

by

Luther White

PROJECT 1 - MODELING DEPOSITIONAL ENVIRONMENTS

1. Statement of Purpose - Modeling Depositional Environments

The purpose of this project is to identify, evaluate, and develop methods for constructing geological models of oil and gas reservoirs. Of particular interest are reservoirs for which fluvial processes are dominant. The Gypsy formation serves as a useful prototype for such reservoirs.

The goals for our study are as follows:

1. Include multiresolution analysis in inverse and geostatistical methods.

2. Couple multiresolution analysis with the sensitivity and resolution techniques to investigate, in a more precise way, the detail in estimated reservoir mappings supported by various types of data.

The data base in the Gypsy Project provides a unique test bed for the comparison of different types of data. We propose to investigate the application of wavelet and multiresolution analysis techniques using the notion of the sensitivity and resolution developed in the third year of the project in order to ascertain the detail obtainable through estimation and geostatistical procedures for various types of data.

2. Introduction.

A goal of the Gypsy Project is to determine reservoir mappings from data collected from various types of measurements. Of particular interest is the extention of kriging methods to estimate geological mappings with possible discontinuities using core and model-related data. A method set forth in the second year's work uses a regularized-output-least-squares (ROLS) estimation procedure to detect possibly discontinuous behavior using permeability and pressure measurements. A discontinuous map is determined by isolating a region in which there is anomalous behavior and to estimate its magnitude. One then seeks to determine perturbations of the discontinuous map by the ROLS procedure. If there is an additional indication of discontinuous behavior, then again it is estimated. The procedure continues until the ROLS method no longer obtains coefficients with sudden changes.

The success of the above method (or any such similar procedure) depends on the detection step. Thus, the study of the resolution of estimation methods (ROLS or kriging) arises natually. This requires the calculation of derivatives of various mappings with respect to possible reservoir functions. Consequently, in the third year of the project, the resolution and sensitivity of estimation procedures are investigated. Moreover, such an analysis leads to information on how much can be discerned from a given method and data. These notions may allow us to assess quantitatively different estimation techniques to determine explicitly classes of geological models that are not discernable from the data. In turn

these characterizations may be used to generate simulations and to formulate admissible sets over which further estimation procedures may be posed using additional information. Finally, these ideas may be applied to facilitate in the design of experiments, the selection of observation locations, and the determination of the value of additional data in posing problems.

In order to assess the sensitivity of the estimation procedure mentioned above, it is desireable to have at hand sets of component basis functions that possess multiresolution properties with which to describe the reservoir. Essentially, what is needed is the ability to refine estimates of reservoir properties spatially. While this can be done with finite element methods, wavelet methods yield a convenient system of accounting, well estabablished approximation properties, and efficient computational procedures. Hence, the class of wavelet functions and wavelet transforms fulfill just such a need. Moreover, the use of the orthonormal bases in finite element formulations may lead to fast and more efficient codes for solving reservoir models. Finally, multiresolution analysis has applications to the inversion of seismic data and upscaling. These techniques may well offer a powerful package of tools with which the analysis of of reservoir properties may be undertaken.

3. Resolution, Sensitivity, and Multiresolution Bases.

Suppose that data $\{K_i\}_{i=1}^{N_0}$ and $\{p_j\}_{j=1}^{N_1}$ are obtained for a given system in which $K_i =< \phi_i, K >$ and $p_j =< \psi_j, p >$ correspond to measurements of the parameter functions K and a function p, respectively that are related through a model equation

$$L(K,p) = f. \tag{1}$$

Further, suppose that it is known that for each K belonging to an admissible set Q_{ad} there exists a unique solution $p = p(K)$ to equation (1). Thus, (1) determines p as a function of K. The estimation method seeks to determine that parameter K in Q_{ad} minimizing the fit-to-data criterion $J(K)$. Usually the criterion is quadratic, and the problem is a least squares minimization comparing observations of the parameters and the state with those obtained through solving numerical approximations of the model equations.

$$J(K) \;=\; \gamma_0 \sum_{i=1}^{N_0} (< \phi_i, K > - K_i)^2 \;+\; \gamma_1 \sum_{i=1}^{N_1} (< \psi_i, p(K) > - p_i)^2 \;+\; N(K) \tag{2}$$

over Q_{ad} where N represents a seminorm that serves as a regularizing term and γ_0 and γ_1 are nonnegative numbers. It is well known that under suitable conditions an optimal solution of (1)-(2) exists although it may not be unique. Furthermore, it is worth noting that geostatistical kriging techniques fall under this formulation where $\gamma_1 = 0$ and K is expressed as an expansion involving chosen covariance functions.

The analysis of sensitivity with respect to data focuses on the behavior of estimators with respect to perturbation of the data. The concept of resolution involves the differentiability of the estimated parameter with respect to perturbations of the actual parameter. Since

the actual parameter is unknown, we consider model-based problems. That is, we suppose a parameter K_0 is given (here a priori knowledge of the type of parameter can be used in giving a physically meaningful formulation). This parameter is used to calculate a corresponding solution $p(K_0)$ to (1). Appropriate data is taken by means of the measurement operators. One then attempts to recover K_0, ie. K_0', through the estimation procedure. If the estimator is unique, then the estimation method defines a mapping $K_0 \mapsto K_0'$. The mapping thus defined is thus a function of the model used to generate the data, the observation operators used in collecting the data, the approximation method, and the estimation procedure. The study of the differentiability of this mapping and its properties constitutes the analysis of the resolution of the method.

To investigate further the resolution supported by an estimation procedure, its approximation, and the problem data, it would be useful to have at one's disposal approximating subspaces with which one may easily express finer scale properties. While this may be accomplished with finite element bases, it is desirable to be able to easily generate basis functions without having to refine the finite element mesh. Fourier series provides a basis that are easily refinable. However, such sine=cosine functions do not have compact support and are known not to resolve detail in the spatial domain adequately. However, it has been shown that wavelet bases are orthonormal bases that are easily generated without redefining meshes. Moreover, the wavelet basis functions have compact support that allow multiple scales and give rise to a multiresolution analysis. It is the capability of easily generating new orthonormal basis functions that have the ability of refining spatial variations that make wavelets and multiresolution analysis so attractive in these applications.

4. Applications.

As pointed out in the third year proposal, resolution of an estimation technique involves the analysis of certain mappings associated with the problem. It depends on the model, the data, and the approximation. Wavelet bases and multiresolution analysis provide a rech source of test elements with which we may explicitely dtermine spatial resolution properties. The analysis of the recovery mapping provides a tool with which to assess various estimation and kriging techniques. Explicit characterizations of indistinguishable perturbations to estimated reservoir properties may be used to generate simulations in order to gain insight into the model and to aid in the formulation of further estimation and control strategies by restricting the class possible geological models. Determining the resolution of the problem should also aid by providing information to avoid unnecessary refinement of geological models not supported by the data. The analysis will also provide a tool with which we may design problems with desireable resolution properties. For example, one might use this information to place observation wells that collect data which maximize the information collected.

For a given reservoir on which various types of measurements have been made an issue that arises naturally is to what extent does different data actually add to our knowledge concerning the reservoir properties. For example, can one quantitatively determine the

value that pressure data or tracer data add to core measurements. If one can determine a functional relationship between the geological parameters and the data, then it is expected that resolution analysis should help in assessing the value of the data. Quantitatively characterizing resolution properties allows us to gain insight into the value of additional data with regard to increasing the ability of the estimation method to refine detail in reservoir properties.

5. Deterministic Model of the Gypsy Outcrop.

An important aspect of the second and third years of effort was the construction of a single "determinisitic" reservoir model of the Gypsy Outcrop. This is described by O'Meara and Jiang (1996). This model honors all existing data as closely as possible. As such, the model represents our "best guess" for describing the Outcrop. We have adopted this model as our "ground truth" description. Granted, it cannot be an exact description for what actually exists. However, the model contains real data and will represents a realistic geological interepretation. It is as representative of the Outcrop as any model of a producing reservoir is ever likely to be. The deterministic model will be a valuable asset in the testing and evaluating of a range of both present and future reservoir characterization methods.

One can think of the deterministic model as a reservoir description for which everything is known. We have built the model using Stratamodel's Stratigraphic Geocellular Modeling software, using in excess of 200K cells (or gridblocks). Every cell is assigned properties such as porosity, permeability, lithology, etc. This model was built from the existing Gypsy Outcrop database. The primary Gypsy outcrop site is offered by the north face of a roadcut twenty-two core holes were drilled on an 18 acre tract behind the primary strike oriented outcrop. A nearby dip oriented outcrop was also examined.

6. Tasks-Modeling Depositional Environments.

Generally, we purpose to introduce multiresolution analysis and wavelets as bases in order to determine resolution for inverse and kriging methods. Model-based resolution criteria are to be used for the assessment of methods and the determination of realizations supported by the data. These resolution considerations are to be applied to a theoretical analysis of the design of experiments to determine reservoir mappings and the value of different types of data. In addition Gypsy related models (perhaps simplified versions with fewer layers) along with simulated flow data are to be used to determine the the resolution of data based from flow models. For example, given the layered structured from the geological model of the Gypsy outcrop but without the permeability values (or with only a limited number of values) along with simulated pressure or tracer data determine the extent the permeability can be estimated and the resolution. By analyzing the resolution properties, we will also seek explicit characterization of geological mappings that are equivalent with respect to the data. These characterizations will be used in related estimation and control problems.

Appendix L

Differentiability of Interior Regularized Output Least Square Estimators with Respect to Data for Parabolic Systems

by

Luther White

Differentiability of Interior Regularized Output Least Squares Estimators with Respect to Data for Parabolic Systems

by

Luther W. White
Department of Mathematics
University of Oklahoma
Norman, Oklahoma 73019

1. Introduction. We consider a problem to estimate the permeability from core measurements and transient pressure data. Of particular interest is the dependence of the estimated permeability on pressure measurements. In this report we establish mathematical conditions under the estimated permeability is determined as a function of the pressure data that varies smoothly with respect to small changes in that data. This investigation is a key step in the study of the resolution properties of model-based estimation test problems.

2. The Semidiscrete Formulation of the Parabolic Problem. In this section we present the formulation for the parabolic models. To fix ideas, let Ω be an open bounded domain in $\mathbf{R}^n$ with a Lipschitz boundary $\partial\Omega$. Let $H = L^2(\Omega)$ and $V = H^1(\Omega)$. Let

$$f \in L^2(0,T;H) \text{ and } a \in Q \subset L^\infty(\Omega).$$

We assume that there is a positive constant ν such that

$$a(x) \geq \nu \text{ almost everywhere in } \Omega.$$

Consider the initial boundary value problem given by

$$\frac{\partial u}{\partial t} - \nabla \cdot (a \nabla u) = f \text{ in } \Omega x(0,T) \tag{2.1}$$

$$\frac{\partial u}{\partial n} = 0 \text{ on } \partial\Omega, \tag{2.2}$$

and

$$u(\cdot,0) = u_0 \in H \tag{2.3}$$

with $f \in L^2(0,T;H)$ and $a \in Q \subset L^\infty(\Omega)$. For ease we will take $u_0 = 0$. It is well known [2] that there exists a unique solution $u \in L^2(0,T;V)$. Furthermore, if $a_n \to a$ in Q for $a_n \geq \nu$, then the sequence of associated solutions $u(a_n)$ converges weakly to $u(a)$ in $L^2(0,T;H)$, [2]. In formulating a ROLS estimation problem, we suppose that Q is a Hilbert space that compactly imbeds into $L^\infty(\Omega)$.

We study systems of initial value problems obtained from the finite element approximations [2]. Suppose that $\{B_i\}_{i=1}^N$ and $\{b_i\}_{i=1}^M$ are linearly independent functions in U and Q, respectively. Express u and a as sums

$$u(t) = \sum_{i=1}^{N} c_i(t) B_i$$

and

$$a = \sum_{j=1}^{M} a_j b_j,$$

respectively. Given the coefficient a, we seek $u = u(a)$ such that

$$\frac{\partial}{\partial t} \int_\Omega u(t) B_i dx \; + \; \int_\Omega a \nabla u(t) \cdot \nabla B_i dx \; = \; \int_\Omega f(t) B_i dx \tag{2.4}$$

for $i = 1, ..., N$. Introducing the representation of a as the above sum and collecting terms, we define component stiffness matrices as the N x N matrices $G^{(k)}$ with entries

$$G_{ij}^{(k)} = \int_\Omega b_k \nabla B_i \cdot \nabla B_j dx$$

for $k = 1, ..., M$ and

$$G_{0ij} = \int_\Omega B_i B_j dx.$$

Define the column N-vector valued function $t \mapsto F(t)$ with entries

$$F(t)_i = \int_\Omega f(t) B_i dx$$

for $i = 1, ..., N$, and set

$$\mathbf{a} \; = \; \begin{bmatrix} a_1 \\ a_2 \\ \cdot \\ \cdot \\ \cdot \\ a_M \end{bmatrix}$$

and

$$c \; = \; c(t) \; = \; \begin{bmatrix} c_1(t) \\ c_2(t) \\ \cdot \\ \cdot \\ \cdot \\ c_N(t) \end{bmatrix}.$$

We also write $c = c(\mathbf{a})$ when it is desirable to emphasize the dependence of c on $\mathbf{a}$. The stiffness matrix is given as the linear combination of the component matrices

$$G = G(\mathbf{a}) = \sum_{k=1}^{M} a_k G^{(k)}.$$

and the discrete version of the boundary value problem (2.4) is thus given by the equation

$$G_0 \frac{d}{dt} c + G(\mathbf{a})c = F \tag{2.5}$$

with initial condition

$$c(0) = 0 \tag{2.6}$$

Setting

$$S(a)(t) = \exp[G_0^{-1} G(\mathbf{a})t]$$

The solution to (2.5) may be represented by

$$c(t) = \int_0^t S(\tau - t) G_0^{-1} F(\tau) d\tau. \tag{2.7}$$

Remark 2.1. The elliptic case is given by

$$G(\mathbf{a})c = F$$

where the vectors c and F no longer depend on t.

Suppose there are given continuous linear functionals $\{\Delta_n\}_{n=1}^{N_0}$ on V and $\{\Theta_n\}_{n=1}^{N_1}$ on Q to serve as observation functionals, [3]. From these functionals we construct the operators

$$C_0 : L^2(0,T;V) \mapsto Z_0 = L^2(0,T;\mathbf{R}^{N_0})$$

and $C_1 : Q \mapsto Z_1 = \mathbf{R}^{N_1}$ as

$$C_0 v(t) = \begin{bmatrix} < \Delta_1, v(t) > \\ \cdot \\ \cdot \\ \cdot \\ < \Delta_{N_0}, v(t) > \end{bmatrix}$$

and

$$C_1 \psi = \begin{bmatrix} < \Theta_1, \psi > \\ \cdot \\ \cdot \\ \cdot \\ < \Theta_{N_1}, \psi > \end{bmatrix},$$

respectively.

The minimization problem is formulated by introducing a fit-to-data functional

$$J(a) = \int_0^T \sum_{k=1}^{N_0} (< \Delta_k, u(t) > - z_k(t))^2 \; + \; \sum_{k=1}^{N_1} (< \Theta_k, a > - K_k)^2 \; +$$

$$+ \; \int_\Omega [\gamma_2 \mid D^2 a \mid^2 \; + \gamma_1 \mid \nabla a \mid^2] dx$$

where γ_1, and $\gamma_2 \; \geq \; 0$. The functional $J(a)$ is to be minimized over an admissible set $Q_{ad} \; \subset \; Q$. For example, Q_{ad} may be taken to be

$$Q_{ad} \; = \; \{a \in H^2(\Omega) : \; a \geq \nu > 0\}. \tag{2.8}$$

The finite dimensional formulation of the fit-to-data functional is obtained by introducing the N_0 x N matrix Φ

$$\Phi_{ij} = < \Delta_i, B_j >$$

for $i = 1, ..., N_0$ and $j = 1, ..., N$, the M x M matrix

$$H_{ij} = \int_\Omega [\gamma_1 \nabla b_i \cdot \nabla b_j + \gamma_2 D^2 b_i D^2 b_j] dx$$

for $i, j = 1, ..., M$, the N_1 x M matrix

$$\Psi_{ij} = < \Theta_i, b_j >$$

for $i = 1, ..., N_1$ and $j = 1, ..., M$, the N_0 column vector

$$\mathbf{z} \; = \; \begin{bmatrix} z_1 \\ . \\ . \\ . \\ z_{N_0} \end{bmatrix},$$

the N_1 column vector

$$\mathbf{K} \; = \; \begin{bmatrix} K_1 \\ . \\ . \\ . \\ K_{N_1} \end{bmatrix}.$$

Let

$$\Phi_2 = \Phi^* \Phi \text{ and } \Psi_2 = \Psi^* \Psi$$

where * denotes transposition. The functional $J(\cdot)$ may thus be viewed as being defined on $\mathbf{R}^M$ and is expressed as

$$J(\mathbf{a}) = \int_0^T [c^*\Phi_2 c - 2\mathbf{z}^*\Phi c + \mathbf{z}^*\mathbf{z}]dt + \mathbf{a}^*(H + \Psi_2)\mathbf{a} - 2\mathbf{K}^*\Psi\mathbf{a} + \mathbf{K}^*\mathbf{K} \tag{2.9}$$

where $\mathbf{a} \in Q_{ad}^M$ and Q_{ad}^M serves as an appropriate admissible set in $\mathbf{R}^M$.

To study the effect of perturbations of the data on interior optimal estimators, our starting point is the system of equations characterizing optimal estimators. Note the Frechet derivative of c at a with increment $\mathbf{a}'$, $Dc(\mathbf{a})\mathbf{a}'$, satisfies the equation

$$G_0 \frac{d}{dt}[Dc(\mathbf{a})\mathbf{a}'] \; + \; G[Dc(\mathbf{a})\mathbf{a}'] = -G(\mathbf{a}')c(\mathbf{a}). \tag{2.10}$$

with initial condition

$$[Dc(\mathbf{a})\mathbf{a}'](0) \; = \; 0$$

so that

$$[Dc(\mathbf{a})\mathbf{a}'](t) \; = \; -\int_0^t S(\tau - t)G_0^{-1}G(\mathbf{a}')c(\mathbf{a})(\tau)d\tau.$$

Defining the column N-vectors

$$d_0^{(k)}(\mathbf{a})(t) \; = \; \int_0^t S(\tau - t)G_0^{-1}G^{(k)}c(\mathbf{a})(\tau)d\tau$$

and the N x M matrix

$$\mathcal{D}_0(\mathbf{a})(t) \; = \; [d_0^{(1)}(\mathbf{a})(t), ..., d_0^{(M)}(\mathbf{a})(t)],$$

we may write

$$[Dc(\mathbf{a})\mathbf{a}'](t) \; = \; -\mathcal{D}_0(\mathbf{a})(t)\mathbf{a}'.$$

It follows then that

$$\frac{1}{2}DJ(\mathbf{a})\mathbf{a}' \; = \; \int_0^T (\Phi_2 c(\mathbf{a}) - \Phi^*\mathbf{z})^* \; [Dc(\mathbf{a})\mathbf{a}'] \; dt \; + \; ((H \; + \; \Psi_2)\mathbf{a} \; - \; \Psi^* \; \mathbf{K})^* \; \mathbf{a}' \tag{2.11}$$

Introducing the vector $\pi \; = \; \pi(\mathbf{a}, \mathbf{z})$ as the solution of the system,

$$-\frac{d}{dt}G^{(0)}\pi \; + \; G(\mathbf{a})\pi = \Phi_2 c(\mathbf{a}) - \Phi^*\mathbf{z}, \tag{2.12}$$

$$\pi(T) = 0,$$

we see that

$$\int_0^T (\Phi_2 c(\mathbf{a}) - \Phi^*\mathbf{z})^* G[Dc(\mathbf{a})\mathbf{a}'] \; dt = \; -\int_0^T \pi^* G(\mathbf{a}')c(\mathbf{a})dt$$

holds. The solution of (2.12) may be represented by the formula

$$\pi(\mathbf{a},\mathbf{z})(t) = -\int_t^T S(t-\tau)G_0^{-1}(\Phi_2 c(\mathbf{a})(\tau) - \Phi^*\mathbf{z}(\tau))d\tau.$$

Define the column M-vector $\mathcal{X} = \mathcal{X}(\mathbf{a},\mathbf{z})$ with entries,

$$\mathcal{X}_k = \int_0^T \pi(\mathbf{a},\mathbf{z})^* G^{(k)} c(\mathbf{a})dt. \tag{2.13}$$

The derivative of J may now be expressed by the formula

$$\frac{1}{2}DJ(\mathbf{a})\mathbf{a}' = [(H+\Psi_2)\mathbf{a} - \Psi^*\mathbf{K} - \mathcal{X}]^*\mathbf{a}' \tag{2.14}.$$

Thus, the optimality conditions statisfied by an interior solution are given by the following.

Proposition 2.2. If a is an interior local minimum for the estimation problem, then a satisfies the system

$$G_0\frac{d}{dt}c(\mathbf{a}) + Gc(\mathbf{a}) = F \tag{2.15}(i)$$

$$c(\mathbf{a})(0) = 0$$

$$-G_0\frac{d}{dt}\pi(\mathbf{a},\mathbf{z}) + G\pi(\mathbf{a},\mathbf{z}) = \Phi_2 c(\mathbf{a}) - \Phi^*\mathbf{z} \tag{2.15}(ii)$$

$$\pi(\mathbf{a},\mathbf{z})(T) = 0$$

$$(H+\Psi_2)\mathbf{a} - \Psi^*\mathbf{K} - \mathcal{X}(\mathbf{a},\mathbf{z}) = 0. \tag{2.15}(iii)$$

The optimality system in (2.15) establishes a relationship between the data vectors $\mathbf{z}$ and $\mathbf{K}$ and an optimal estimator $\mathbf{a}$. We next obtain conditions such that the relation given by the optimality conditions of Proposition 2.2 determines a function $\mathbf{z} \mapsto \mathbf{a}(\mathbf{z})$ from $\mathbf{R}^{N_0}$ into $\mathbf{R}^M$. To this end, define the function

$$\mathcal{F} : \mathbf{R}^M \text{ x } Z_0 \text{ x } \mathbf{R}^{N_1} \mapsto \mathbf{R}^M$$

by

$$\mathcal{F}(\mathbf{a},\mathbf{z},\mathbf{K}) = (H+\Psi_2)\mathbf{a} - \Psi^*\mathbf{K} - \mathcal{X}(\mathbf{a},\mathbf{z}). \tag{2.16}$$

For the time being we are interested only in the dependence of $\mathbf{a}$ on $\mathbf{z}$. Hence, we view $\mathbf{K}$ as a constant vector and set

$$\mathcal{F}(\mathbf{a},\mathbf{z}) = \mathcal{F}(\mathbf{a},\mathbf{z},\mathbf{K}).$$

Of course, existence of an interior solution for data $\mathbf{z}$ implies that the relation

$$\mathcal{F}(\mathbf{a},\mathbf{z}) \;=\; 0 \tag{2.17}$$

holds. At a pair $(\mathbf{a}_0,\mathbf{z}_0)$ for which $\mathcal{F}(\mathbf{a}_0,\mathbf{z}_0) \;=\; 0$, the implicit function theorem asserts that if the Frechet partial derivatives, $D_a\mathcal{F}(\mathbf{a}_0,\mathbf{z}_0)$ and $D_z\mathcal{F}(\mathbf{a}_0,\mathbf{z}_0)$, of $\mathcal{F}$ exist and $D_a\mathcal{F}(\mathbf{a}_0,\mathbf{z}_0)^{-1}$ exists, then $\mathbf{z}\mapsto\mathbf{a}(\mathbf{z})$ is determined as a Frechet differentiable function in a neighborhood of $\mathbf{z}_0$, [1].

For any $\mathbf{a}'$, with $D_a\pi \;=\; D_a\pi(\mathbf{a},\mathbf{z})$, and $Dc = Dc(\mathbf{a})$,

$$-G_0\frac{d}{dt}[(D_a\pi)\mathbf{a}'] + G(\mathbf{a})[(D_a\pi)\mathbf{a}'] \;=\; -G(\mathbf{a}')\pi \;+\; \Phi_2[(Dc)\mathbf{a}']. \tag{2.18}$$

and initial condition

$$[D_a\pi)\mathbf{a}'](T) \;=\; 0.$$

Defining the N x M matrix $P(t)$ with columns

$$P_k(t) = \int_t^T S(t-\tau)G_0^{-1}G^{(k)}\pi(\mathbf{a},\mathbf{z})(\tau)d\tau$$

for k=1,...,M, and the N x M matrix

$$\mathcal{D}(t) = \int_t^T S(t-\tau)G_0^{-1}\Phi_2\mathcal{D}_0(\mathbf{a})(\tau)d\tau,$$

we may respresent $D_a\pi$ by the formula

$$[D_a\pi(\mathbf{a},\mathbf{z})\mathbf{a}'](t) \;=\; -(P(t)+\mathcal{D}(t))\mathbf{a}'$$

In addition, it easy to see that for $D_z\pi \;=\; D_z\pi(\mathbf{a},\mathbf{z})$

$$-G_0\frac{d}{dt}[(D_z\pi)\mathbf{z}'] \;+\; G(\mathbf{a})[(D_z\pi)\mathbf{z}'] \;=\; -\Phi^*\mathbf{z}'. \tag{2.19}$$

$$[(D_z\pi)\mathbf{z}'](T) = 0,$$

and

$$[(D_z\pi)\mathbf{z}'] \;= -\int_t^T S(t-\tau)G_0^{-1}\Phi^*\mathbf{z}'(\tau)d\tau.$$

It follows from equations (2.6) and (2.13) that

$$D_a\mathcal{X}_k(\mathbf{a},\mathbf{z})\mathbf{a}' \;=\; \int_0^T \{[D_a\pi(\mathbf{a},\mathbf{z})\mathbf{a}']^*G^{(k)}c(\mathbf{a}) + \pi(,\mathbf{z})^*G^{(k)}[Dc(\mathbf{a})\mathbf{a}']\}dt$$

and

$$D_z\mathcal{X}_k(\mathbf{a},\mathbf{z})\mathbf{z}' \;=\; \int_0^T [D_z\pi(\mathbf{a},\mathbf{z})\mathbf{z}']^* G^{(k)} c(\mathbf{a})dt.$$

Hence, we obtain the expressions

$$D_a\mathcal{X}_k(a,\mathbf{z})\mathbf{a}' \;=\; -[\int_0^T \{c(\mathbf{a})(t)^* G^{(k)}(P(t)+\mathcal{D}(t)) + \pi(\mathbf{a},\mathbf{z})(t)G^{(k)}\mathcal{D}_0(\mathbf{a})(t)\}dt]\mathbf{a}'$$

and

$$D_z\mathcal{X}_k(\mathbf{a},\mathbf{z})\mathbf{z}' \;=\; \int_0^T [\int_0^\tau c(\mathbf{a})(t)^* G^{(k)} S(t-\tau)dt G_0^{-1}\Phi^*]\mathbf{z}'(\tau)d\tau.$$

Setting

$$\mathbf{X}(\mathbf{a},\mathbf{z})(t) \;=\; -\begin{bmatrix} \int_0^t c(\mathbf{a})(t)^* G^{(1)} S(\tau-t)d\tau \\ \cdot \\ \cdot \\ \cdot \\ \int_0^t c(\mathbf{a})(t)^* G^{(M)} S(\tau-t)d\tau \end{bmatrix} G_0^{-1}\Phi^*,$$

we may write

$$D_z\mathcal{F}(\mathbf{a},\mathbf{z})\mathbf{z}' \;=\; \int_0^T \mathbf{X}(\mathbf{a},\mathbf{z})(t)\mathbf{z}'(t)dt$$

Furthermore, define the MxN matrices $\mathcal{K}_1$ and $\mathcal{K}_2$ in which the k-th rows are given by

$$\mathcal{K}_1 \;=\; \int_0^T c(\mathbf{a})(t)^* G^{(k)}(P(t)+\mathcal{D}(t))dt$$

and

$$\mathcal{K}_2 \;=\; \int_0^T \pi(\mathbf{a},\mathbf{z})(t)G^{(k)}\mathcal{D}_0(\mathbf{a})(t)dt,$$

respectively, and set

$$\mathcal{K} \;=\; \mathcal{K}_1 \;+\; \mathcal{K}_2.$$

From (2.16), we see that

$$D_a\mathcal{F}(\mathbf{a},\mathbf{z}) \;=\; H \;+\; \Psi_2 \;+\; \mathcal{K},$$

and from the implicit function theorem [1] we have the following.

Proposition 2.3. Suppose that $\mathcal{F}(\mathbf{a}_0,\mathbf{z}_0) \;=\; 0$. If matrix $H \;+\; \Psi_2 \;+\; \mathcal{K}$ is invertible, then there is a neighborhood $\mathcal{N}(\mathbf{z}_0)$ such that $\mathbf{z} \mapsto \mathbf{a}(\mathbf{z})$ is defined as a function on $\mathcal{N}(\mathbf{z}_0)$, and

$$Da(\mathbf{z})\mathbf{z}' \;=\; (H+\Psi_2+\mathcal{K})^{-1}\int_0^T \mathbf{X}(\mathbf{a},\mathbf{z})(t)\mathbf{z}'(t)dt. \tag{2.20}$$

It is also of interest to calculate the second derivatives of $\mathbf{z} \mapsto \mathbf{a}(\mathbf{z})$. The following is a consequence of a straight forward calculation.

Lemma 2.4. The second derivatives of c and π satisfy the following equations.

$$(2.21)(i) \qquad G_0 \frac{d}{dt}[(D^2c)(\mathbf{a}',\mathbf{a}')] + G(\mathbf{a})[(D^2c)(\mathbf{a}',\mathbf{a}')] = -2G(\mathbf{a}')[(Dc)\mathbf{a}', (Dc)\mathbf{a}']$$

$$[(D^2c)(\mathbf{a}',\mathbf{a}')](0) = 0$$

$$-G_0 \frac{d}{dt}[(D^2_{aa}\pi)(\mathbf{a}',\mathbf{a}')] + G(\mathbf{a})[(D^2_{aa}\pi)(\mathbf{a}',\mathbf{a}')] =$$

$$(2.21)(ii) \qquad = \Phi_2[(D^2c)(\mathbf{a}',\mathbf{a}') - 2G(\mathbf{a}')[(D_a\pi)\mathbf{a}'],$$

$$[(D^2_{aa}\pi)(\mathbf{a}',\mathbf{a}')](T) = 0$$

$$-G_0 \frac{d}{dt}[(D_{az}\pi)(\mathbf{a}',\mathbf{z}')] + G(\mathbf{a})[(D_{az}\pi)(\mathbf{a}',\mathbf{z}')] = -\mathbf{G}(\mathbf{a}')[(\mathbf{D_z}\pi)\mathbf{z}'], \mathbf{(2.21)(iii)}$$

$$[(D^2_{az}\pi)(\mathbf{a}',\mathbf{z}')](T) = 0$$

and

$$2.21(iv) \qquad D_{zz}\pi = 0.$$

We note from (2.13) that the second Frechet derivative of $\mathcal{X}_k$ is given by

$$D_{zz}\mathcal{X}_k(\mathbf{a},\mathbf{z})(\mathbf{z}',\mathbf{z}') = \int_0^T [D_{zz}\pi(\mathbf{a},\mathbf{z})(\mathbf{z}',\mathbf{z}')]^* G^{(k)}c(\mathbf{a})dt$$

Hence, by (2.21)(iv)

$$D_{zz}\mathcal{X}_k(\mathbf{a},\mathbf{z}) = 0$$

from (2.16), we see that

$$D_{zz}\mathcal{F}(\mathbf{a},\mathbf{z}) = 0.$$

Other second partial derivatives of $\mathcal{F}$ may be calculated similarly. From (2.16) and (2.17), we see that

Proposition 2.5. The second derivative of $\mathbf{z} \mapsto \mathbf{a}(\mathbf{z})$ with respect to $\mathbf{z}$ is given by

$$D^2a(\mathbf{z})(\mathbf{z}',\mathbf{z}') = -(H+\Psi_2+\mathcal{K})^{-1}\{D_{aa}\mathcal{F}(\mathbf{a},\mathbf{z})(\mathbf{Da}(\mathbf{z})\mathbf{z}', \mathbf{Da}(\mathbf{z})\mathbf{z}') +$$

$$+ 2D_{za}\mathcal{F}(\mathbf{a},\mathbf{z})(\mathbf{z}', Da(\mathbf{z})\mathbf{z}')\}.$$

Remark 2.6. Extending the above argument, it easy to see that if $H+\Psi_2+\mathcal{K}$ is invertible, then any derivative of $\mathbf{a}$ exists.

Suppose that $\mathbf{z}'$ is such that $D\mathbf{a}(\mathbf{z})\mathbf{z}' = 0$. That is, denoting the null space of $D\mathbf{a}(\mathbf{z})$ by $N(D\mathbf{a}(\mathbf{z}))$, suppose that

$$\mathbf{z}' \in N(D\mathbf{a}(\mathbf{z})).$$

From Propositions 2.3 and 2.6, we have the following.

Corollary 2.7. If $\mathbf{z}'$ is such that $\mathbf{z}' \in N(Da(\mathbf{z}))$, then

$$D^{(n)}\mathbf{a}(\mathbf{z})(\mathbf{z}', ..., \mathbf{z}') = 0$$

for any n. For such vectors $\mathbf{z}'$ we see that

$$\mathbf{a}(\mathbf{z} + \mathbf{z}') = \mathbf{a}(\mathbf{z}).$$

Remark 2.8. It follows that the estimated coefficient $\mathbf{a}(\mathbf{z})$ is insensitive to any perturbation (no matter how large) $\mathbf{z}' \in N(Da(\mathbf{z}))$. Note this is a consequence of the fact that the fit-to-data functional is quadratic in the data $\mathbf{z}$.

We next examine sufficient conditions underwhich the matrix $H + \Psi_2 + \mathcal{K}$ is invertible. To this end we introduce the following assumptions. Recalling that $G_0, G(a), G^{(k)}$ for $k = 1, ..., M$ are NxN symmetric matrices and that H and Ψ_2 are MxM symmetric matrices, we suppose there positive real numbers β, μ_0, ν_0, μ_1, and μ such that

(2.22)(*i*) $$H + \Psi_2 \geq \beta I$$

(2.22)(*ii*) $$\mu_1 I \geq G_0 \geq \mu_0 I$$

(2.22)(*iii*) $$G(a) \geq \nu_0 I$$

and for any $k = 1, ..., M$

(2.22)(*iv*) $$G^{(k)} \geq \mu I$$

where I represents the identity matrix on $\mathbf{R}^N$ or $\mathbf{R}^M$ which ever is appropriate. From straight forward estimates, we obtain

$$\|c(\mathbf{a})\|_{L^2(0,T,\mathbf{R}^N)} \leq \frac{1}{\nu_0}\|F\|_{L^2(0,T,\mathbf{R}^N)}$$

$$\|\pi(\mathbf{a}, \mathbf{z})(t)\|_{L^2(0,T,\mathbf{R}^N)} \leq \frac{1}{\nu_0}\|\Phi_2 c(\mathbf{a})(t) - \Phi^* \mathbf{z}\|_{L^2(0,T,\mathbf{R}^N)}$$

$$\|\pi(\mathbf{a}, \mathbf{z})\|_{L^2(0,T,\mathbf{R}^N)} \leq \frac{|\Phi|}{\nu_0}\{\frac{|\Phi|}{\nu_0}(\|F\|_{L^2(0,T,\mathbf{R}^N)} + \|\mathbf{z}\|_{L^2(0,T,\mathbf{R}^{N_0})}$$

$$\|Dc(\mathbf{a})\mathbf{a}'\| \leq \frac{\mu}{\nu_0^2}\|F\||\mathbf{a}'|$$

$$\|D_a\pi(\mathbf{a},\mathbf{z})\mathbf{a}'\| \leq [\frac{\mu}{\nu_0^2}(\|\Phi_2 c(\mathbf{a}) - \Phi^*\mathbf{z}\|_{L^2(0,T,\mathbf{R}^N)} + \frac{\mu_0|\Phi|^2}{\nu_0^3}\|F\|_{L^2(0,T,\mathbf{R}^N)}\|]|\mathbf{a}'|$$

It follows then that for

$$K(\mathbf{a},\mathbf{z},F) = \mu\{[\frac{\mu}{\nu_0^2}(\|\Phi_2 c(\mathbf{a}) - \Phi^*\mathbf{z}\|_{L^2(0,T,\mathbf{R}^N)} +$$

$$+ \frac{\mu_0|\Phi|^2}{\nu_0^3}\|F\|_{L^2(0,T,\mathbf{R}^N)}\|][\frac{1}{\nu_0}\|F\|_{L^2(0,T,\mathbf{R}^N)}] +$$

$$+ [\frac{1}{\nu_0}\|\Phi_2 c(\mathbf{a})(t) - \Phi^*\mathbf{z}\|_{L^2(0,T,\mathbf{R}^N)}][\frac{\mu}{\nu_0^2}\|F\|]\},$$

we have

$$\|D_a\mathcal{X}_k(\mathbf{a},\mathbf{z})\mathbf{a}'\|_{L^2(0,T)} \leq K|\mathbf{a}'|$$

and

$$\|D_a\mathcal{X}(\mathbf{a},\mathbf{z})\mathbf{a}'\|_{L^2(0,T,\mathbf{R}^M)} \leq K|\mathbf{a}'|$$

Proposition 2.9. If

$$K(\mathbf{a},\mathbf{z},F) < \beta,$$

then $H + \Psi_2 + \mathcal{K}$ is invertible.

References

[1] K. Deimling, *Nonlinear Functional Analysis,* Springer-Verlag, New York, 1980.
[2] J.L. Lions, *Optimal Control of Systems Governed by Partial Differential Equations,* Springer-Verlag, New York, 1971.
[3] R.L.Parker, *Geophysical Inverse Theory,* Princeton University Press, Princeton, New Jersey, 1994.

Appendix M

Resolution of Regularized Output Least Squares Estimators for Elliptic and Parabolic Problems

by

Ying-jun Jin and Luther White

Resolution of Regularized Output Least Squares Estimators for Elliptic and Parabolic Problems

by

Ying-jun Jin
and
Luther W. White
Department of Mathematics
University of Oklahoma
Norman, Oklahoma 73019

Abstract

The sensitivity of interior optimal regularized output least squares estimators with respect to perturbations of coefficients used in posing numerical test problems for finite element approximations of parabolic problems is studied. By determining the null space of a sensitivity operator we may determine spaces of perturbations that are not observable. This information may be used in designing experiments. Numerical examples are given comparing results for elliptic systems to those for parabolic.

1. Introduction. We consider the dependence of interior optimal regularized output least squares estimators of elliptic coefficients on perturbations of measurements on the state and the coefficients themselves. In particular, we study the sensitivity of the estimated elliptic coefficient to perturbations of the test coefficient used in posing numerical test problems for finite element approximations of a parabolic initial value problem. The mapping taking the test coefficient to the resulting estimated coefficient is referred to as the recovery mapping. Conditions are given to assure that this mapping is well-defined. The recovery mapping is determined by the mathematical model, the observation model, the approximation procedure, and the estimation technique. Its Frechet derivative is an indicator of the resolution properties that can be expected. By determining the null space (or range) of the Frechet derivative, it is possible to determine the space of perturbations that are not detectible by the method. This information may then be used, for example, in posing experiments in such away as to enhance their ability to detect perturbations in the parameters.

In Section 2 we formulate problems based on the systems that are obtained as finite element approximations to parabolic initial value problems. We also consider the differentiability of estimated parameters with respect to state observations. The material in this section is contained in a previous report, but it is included here for completeness and to establish notation.

Section 3 applies these results to the so called recovery mapping to develop the sensitivity matrix. Section 4 applies the tools developed in Section 3 to a problem to determine the best location of a state measurement. In Section 5 results are included for the anal-

ogous elliptic case in order to contrast with the parabolic results. The data arising from the time dependence significantly contributes to the ability to detect perturbations by making the sensitivity matrix of full rank for just a single observer location while multiple observers must be used to obtain a similar result for the elliptic case.

2. The finite dimensional problem. In this section we present the formulation for the parabolic models. In Section 5 we will remark on elliptic models as well, for the purpose of comparison. A detailed discussion of finite dimensional approximations to elliptic problems is included in [6]. To fix ideas, let Ω be an open bounded domain in $\mathbf{R}^n$ with a Lipschitz boundary $\partial\Omega$. Let $H = L^2(\Omega)$ and $V = H^1(\Omega)$. Let

$$f \in L^2(0,T;H) \text{ and } a \in Q \subset L^\infty(\Omega).$$

We assume that there is a positive constant ν such that

$$a(x) \geq \nu \text{ almost everywhere in } \Omega.$$

Consider the initial boundary value problem given by

$$\frac{\partial u}{\partial t} - \nabla \cdot (a \nabla u) = f \text{ in } \Omega \text{x} (0,T) \tag{2.1}$$

$$\frac{\partial u}{\partial n} = 0 \text{ on } \partial\Omega, \tag{2.2}$$

and

$$u(\cdot, 0) = u_0 \in H \tag{2.3}$$

with $f \in L^2(0,T;H)$ and $a \in Q \subset L^\infty(\Omega)$. For ease we will take $u_0 = 0$. It is well known [2] that there exists a unique solution $u \in L^2(0,T;V)$. Furthermore, if $a_n \to a$ in Q for $a_n \geq \nu$, then the sequence of associated solutions $u(a_n)$ converges weakly to $u(a)$ in $L^2(0,T;V)$, [2]. In formulating a regularized output least squares estimation problem, we suppose that Q is a Hilbert space that imbeds compactly into $L^\infty(\Omega)$, [2].

We study systems of initial value problems obtained from finite element approximations [4]. Suppose that $\{B_i\}_{i=1}^N$ and $\{b_i\}_{i=1}^M$ are linearly independent functions in V and Q, respectively. Express u and a as sums

$$u(t) = \sum_{i=1}^{N} c_i(t) B_i$$

and

$$a = \sum_{j=1}^{M} a_j b_j,$$

respectively. Given the coefficient a, we seek $u = u(a)$ such that

$$\frac{\partial}{\partial t}\int_\Omega u(t)B_i dx \; + \; \int_\Omega a\nabla u(t)\cdot\nabla B_i dx \; = \; \int_\Omega f(t)B_i dx, \; t \in (0,T) \tag{2.4}$$

for $i = 1, ..., N$. Introducing the representation of a as the above sum and collecting terms, we define component stiffness matrices as the N x N matrices $G^{(k)}$ with entries

$$G^{(k)}_{ij} = \int_\Omega b_k \nabla B_i \cdot \nabla B_j dx$$

for $k = 1, ..., M$ and

$$G_{0ij} = \int_\Omega B_i B_j dx.$$

Define the column N-vector valued function $t \mapsto F(t)$ with entries

$$F(t)_i = \int_\Omega f(t)B_i dx$$

for $i = 1, ..., N$, and set

$$\mathbf{a} \; = \; \begin{bmatrix} a_1 \\ a_2 \\ \cdot \\ \cdot \\ \cdot \\ a_M \end{bmatrix}$$

and

$$c \; = \; c(t) \; = \; \begin{bmatrix} c_1(t) \\ c_2(t) \\ \cdot \\ \cdot \\ \cdot \\ c_N(t) \end{bmatrix}.$$

We also write $c \; = \; c(\mathbf{a})$ when it is desirable to emphasize the dependence of c on $\mathbf{a}$. The stiffness matrix is given as the linear combination of the component matrices

$$G \; = \; G(\mathbf{a}) \; = \; \sum_{k=1}^{M} a_k G^{(k)}.$$

and the discrete version of the boundary value problem (2.4) is thus given by the equation

$$G_0 \frac{d}{dt}c \; + \; G(\mathbf{a})c = F \tag{2.5}(i)$$

with initial condition

$$c(0) = 0 \tag{2.5}(ii)$$

Setting

$$S(a)(t) = \exp[tG_0^{-1}G(\mathbf{a})] \tag{2.6}$$

The solution to (2.5) may be represented by

$$c(t) = \int_0^T S(\tau - t)G_0^{-1}F(\tau)d\tau. \tag{2.7}$$

Suppose there are given continuous real-valued linear functionals $\{\Delta_n\}_{n=1}^{N_0}$ on V and $\{\Theta_n\}_{n=1}^{N_1}$ on Q to serve as observation functionals, [3]. From these functionals we construct the operators

$$C_0 : L^2(0,T;V) \mapsto Z_0 = L^2(0,T;\mathbf{R}^{N_0})$$

and $C_1 : Q \mapsto Z_1 = \mathbf{R}^{N_1}$ as

$$C_0 v(t) = \begin{bmatrix} < \Delta_1, v(t) > \\ \cdot \\ \cdot \\ \cdot \\ < \Delta_{N_0}, v(t) > \end{bmatrix}$$

and

$$C_1 \psi = \begin{bmatrix} < \Theta_1, \psi > \\ \cdot \\ \cdot \\ \cdot \\ < \Theta_{N_1}, \psi > \end{bmatrix},$$

respectively.

The minimization problem is formulated by introducing a fit-to-data functional

$$J(a) = \int_0^T \sum_{k=1}^{N_0} (< \Delta_k, u(t) > - z_k(t))^2 + \sum_{k=1}^{N_1} (< \Theta_k, a > - K_k)^2 +$$

$$+ \int_\Omega [\gamma_2 \mid D^2 a \mid^2 + \gamma_1 \mid \nabla a \mid^2] dx$$

where γ_1, and $\gamma_2 \geq 0$. The functional $J(a)$ is to be minimized over an admissible set $Q_{ad} \subset Q$. For example, Q_{ad} may be taken to be

$$Q_{ad} = \{a \in H^2(\Omega) : \ a \geq \nu > 0\} \tag{2.8}$$

cf. [5].

The finite dimensional formulation of the fit-to-data functional is obtained by introducing the N_0 x N matrix Φ

$$\Phi_{ij} =< \Delta_i, B_j >$$

for $i = 1, ..., N_0$ and $j = 1, ..., N$, the M x M matrix

$$H_{ij} = \int_\Omega [\gamma_1 \nabla b_i \cdot \nabla b_j + \gamma_2 D^2 b_i D^2 b_j] dx$$

for $i, j = 1, ..., M$, the N_1 x M matrix

$$\Psi_{ij} =< \Theta_i, b_j >$$

for $i = 1, ..., N_1$ and $j = 1, ..., M$, the N_0 column vector

$$\mathbf{z} = \begin{bmatrix} z_1 \\ . \\ . \\ . \\ z_{N_0} \end{bmatrix},$$

the N_1 column vector

$$\mathbf{K} = \begin{bmatrix} K_1 \\ . \\ . \\ . \\ K_{N_1} \end{bmatrix}.$$

Let

$$\Phi_2 = \Phi^* \Phi \text{ and } \Psi_2 = \Psi^* \Psi$$

where * denotes matrix transposition. The functional $J(\cdot)$ may thus be viewed as being defined on $\mathbf{R}^M$ and is expressed as

$$J(\mathbf{a}) = \int_0^T [c^* \Phi_2 c - 2\mathbf{z}^* \Phi c + \mathbf{z}^* \mathbf{z}] dt + \mathbf{a}^* (H + \Psi_2)\mathbf{a} - 2\mathbf{K}^* \Psi \mathbf{a} + \mathbf{K}^* \mathbf{K} \tag{2.9}$$

where $\mathbf{a} \in Q_{ad}^M$ and Q_{ad}^M serves as an appropriate admissible set in $\mathbf{R}^M$.

To study the effect of perturbations of the data on interior optimal estimators, our starting point is the system of equations characterizing optimal estimators. Note the Frechet derivative of c at a with increment $\mathbf{a}'$, $Dc(\mathbf{a})\mathbf{a}'$, satisfies the equation

$$G_0 \frac{d}{dt}[Dc(\mathbf{a})\mathbf{a}'] \; + \; G[Dc(\mathbf{a})\mathbf{a}'] = -G(\mathbf{a}')c(\mathbf{a}). \tag{2.10}$$

with initial condition

$$[Dc(\mathbf{a})\mathbf{a}'](0) \; = \; 0$$

so that

$$[Dc(\mathbf{a})\mathbf{a}'](t) \;=\; -\int_0^t S(\tau-t)G_0^{-1}G(\mathbf{a}')c(\mathbf{a})(\tau)d\tau.$$

Defining the column N-vectors

$$d_0^{(k)}(\mathbf{a})(t) \;=\; \int_0^t S(\tau-t)G_0^{-1}G^{(k)}c(\mathbf{a})(\tau)d\tau$$

and the N x M matrix

$$\mathcal{D}_0(\mathbf{a})(t) \;=\; [d_0^{(1)}(\mathbf{a})(t),...,d_0^{(M)}(\mathbf{a})(t)],$$

we may write

$$[Dc(\mathbf{a})\mathbf{a}'](t) \;=\; -\mathcal{D}_0(\mathbf{a})(t)\mathbf{a}'.$$

The derivative of J satisfies

$$(2.11)\quad \frac{1}{2}DJ(\mathbf{a})\mathbf{a}' \;=\; \int_0^T (\Phi_2 c(\mathbf{a})-\Phi^*\mathbf{z})^*\,[Dc(\mathbf{a})\mathbf{a}']\,dt \;+\; ((H\;+\;\Psi_2)\mathbf{a}\;-\;\Psi^*\,\mathbf{K})^*\;\mathbf{a}'$$

Introducing the vector $\pi \;=\; \pi(\mathbf{a},\mathbf{z})$ as the solution of the system,

$$(2.12)\qquad -\frac{d}{dt}G_0\pi \;+\; G(\mathbf{a})\pi = \Phi_2 c(\mathbf{a})-\Phi^*\mathbf{z},$$

$$\pi(T)=0,$$

we see that

$$\int_0^T (\Phi_2 c(\mathbf{a})-\Phi^*\mathbf{z})^*[Dc(\mathbf{a})\mathbf{a}']\,dt = \;-\int_0^T \pi(\mathbf{a},\mathbf{z})^*G(\mathbf{a}')c(\mathbf{a})dt$$

holds. The solution of (2.12) may be represented by the formula

$$\pi(\mathbf{a},\mathbf{z})(t) = -\int_t^T S(t-\tau)G_0^{-1}(\Phi_2 c(\mathbf{a})(\tau)-\Phi^*\mathbf{z}(\tau))d\tau.$$

Define the column M-vector $\mathcal{X} \;=\; \mathcal{X}(\mathbf{a},\mathbf{z})$ with entries,

$$(2.13)\qquad \mathcal{X}_k(\mathbf{a},\mathbf{z}) \;=\; \int_0^T \pi(\mathbf{a},\mathbf{z})^*G^{(k)}c(\mathbf{a})dt.$$

The derivative of J may now be expressed by the formula

$$(2.14).\qquad \frac{1}{2}DJ(\mathbf{a})\mathbf{a}' \;=\; [(H+\Psi_2)\mathbf{a}\;-\;\Psi^*\mathbf{K}\;-\mathcal{X}]^*\mathbf{a}'$$

Thus, the optimality conditions statisfied by an interior solution are given by the following, cf [5].

Proposition 2.1. If $\mathbf{a}$ is an interior local minimum for the estimation problem, then $\mathbf{a}$ satisfies the system

$$(2.15)(i) \qquad G_0 \frac{d}{dt} c(\mathbf{a}) + G(\mathbf{a})c(\mathbf{a}) = F \text{ in } (0,T)$$

$$c(\mathbf{a})(0) = 0$$

$$(2.15)(ii) \qquad -G_0 \frac{d}{dt} \pi(\mathbf{a},\mathbf{z}) + G(\mathbf{a})\pi(\mathbf{a},\mathbf{z}) = \Phi_2 c(\mathbf{a}) - \Phi^* \mathbf{z} \text{ in } (0,T)$$

$$\pi(\mathbf{a},\mathbf{z})(T) = 0$$

$$(2.15)(iii) \qquad (H + \Psi_2)\mathbf{a} - \Psi^* \mathbf{K} - \mathcal{X}(\mathbf{a},\mathbf{z}) = 0.$$

where the components of $\mathcal{X}(\mathbf{a},\mathbf{z})$ are given by (2.13).

The optimality system in (2.15) establishes a relationship between the data vectors $\mathbf{z}$ and $\mathbf{K}$ and an optimal estimator $\mathbf{a}$. We next obtain conditions such that the relation given by the optimality conditions of Proposition 2.2 determines a function $\mathbf{z} \mapsto \mathbf{a}(\mathbf{z})$ from $\mathbf{R}^{N_0}$ into $\mathbf{R}^M$. To this end, define the function

$$\mathcal{F} : \mathbf{R}^M \text{ x } Z_0 \text{ x } \mathbf{R}^{N_1} \mapsto \mathbf{R}^M$$

by

$$(2.16) \qquad \mathcal{F}(\mathbf{a},\mathbf{z},\mathbf{K}) = (H + \Psi_2)\mathbf{a} - \Psi^* \mathbf{K} - \mathcal{X}(\mathbf{a},\mathbf{z}).$$

For the time being we are interested only in the dependence of $\mathbf{a}$ on $\mathbf{z}$. Hence, we view $\mathbf{K}$ as a constant vector and set

$$\mathcal{F}(\mathbf{a},\mathbf{z}) = \mathcal{F}(\mathbf{a},\mathbf{z},\mathbf{K}).$$

Of course, existence of an interior solution for data $\mathbf{z}$ implies that the relation

$$(2.17) \qquad \mathcal{F}(\mathbf{a},\mathbf{z}) = 0$$

holds. At a pair $(\mathbf{a}_0,\mathbf{z}_0)$ for which $\mathcal{F}(\mathbf{a}_0,\mathbf{z}_0) = 0$, the implicit function theorem asserts that if the Frechet partial derivatives, $D_a\mathcal{F}(\mathbf{a}_0,\mathbf{z}_0)$ and $D_{\mathbf{z}}\mathcal{F}(\mathbf{a}_0,\mathbf{z}_0)$, of $\mathcal{F}$ exist and $D_a\mathcal{F}(\mathbf{a}_0,\mathbf{z}_0)^{-1}$ exists, then $\mathbf{z} \mapsto \mathbf{a}(\mathbf{z})$ is determined as a Frechet differentiable function in a neighborhood of $\mathbf{z}_0$, [1].

For any $\mathbf{a}'$, with $D_a\pi = D_a\pi(\mathbf{a},\mathbf{z})$, and $Dc = Dc(\mathbf{a})$,

$$(2.18) \qquad -G_0 \frac{d}{dt}[(D_a\pi)\mathbf{a}'] + G(\mathbf{a})[(D_a\pi)\mathbf{a}'] = -G(\mathbf{a}')\pi + \Phi_2[(Dc)\mathbf{a}'].$$

and initial condition

$$[(D_a\pi)\mathbf{a}'](T) \;=\; 0.$$

Defining the N x M matrix $P(\mathbf{a},\mathbf{z})(t)$ with columns

$$P_k(t) \;=\; P_k(\mathbf{a},\mathbf{z})(t) \;=\; \int_t^T S(t-\tau)G_0^{-1}G^{(k)}\pi(\mathbf{a},\mathbf{z})(\tau)d\tau$$

for k=1,...,M, and the N x M matrix

$$\mathcal{D}(\mathbf{a})(t) = \int_t^T S(t-\tau)G_0^{-1}\Phi_2\mathcal{D}_0(\mathbf{a})(\tau)d\tau,$$

we may respresent $D_a\pi$ by the formula

$$[D_a\pi(\mathbf{a},\mathbf{z})\mathbf{a}'](t) \;=\; -(P(\mathbf{a},\mathbf{z})(t)+\mathcal{D}(\mathbf{a})(t))\mathbf{a}'$$

In addition, it easy to see that for $D_z\pi \;=\; D_z\pi(\mathbf{a},\mathbf{z})$

$$-G_0\frac{d}{dt}[(D_z\pi)\mathbf{z}'] \;+\; G(\mathbf{a})[(D_z\pi)\mathbf{z}'] \;=\; -\Phi^*\mathbf{z}'. \tag{2.19}$$

$$[(D_z\pi)\mathbf{z}'](T) = 0,$$

and

$$[(D_z\pi)\mathbf{z}'] \;= -\int_t^T S(t-\tau)G_0^{-1}\Phi^*\mathbf{z}'(\tau)d\tau.$$

It follows from equation (2.13) that

$$D_a\mathcal{X}_k(\mathbf{a},\mathbf{z})\mathbf{a}' \;=\; \int_0^T\{[D_a\pi(\mathbf{a},\mathbf{z})\mathbf{a}']^*G^{(k)}c(\mathbf{a})+\pi(\mathbf{a},\mathbf{z})^*G^{(k)}[Dc(\mathbf{a})\mathbf{a}']\}dt$$

and

$$D_z\mathcal{X}_k(\mathbf{a},\mathbf{z})\mathbf{z}' \;=\; \int_0^T[D_z\pi(\mathbf{a},\mathbf{z})\mathbf{z}']^*G^{(k)}c(\mathbf{a})dt.$$

Hence, we obtain the expressions

$$D_a\mathcal{X}_k(a,\mathbf{z})\mathbf{a}' \;=\; -[\int_0^T\{c(\mathbf{a})(t)^*G^{(k)}(P(\mathbf{a},\mathbf{z})(t)+\mathcal{D}(\mathbf{a})(t))+\pi(\mathbf{a},\mathbf{z})^*(t)G^{(k)}\mathcal{D}_0(\mathbf{a})(t)\}dt]\mathbf{a}'$$

and

$$D_z\mathcal{X}_k(\mathbf{a},\mathbf{z})\mathbf{z}' \;=\; \int_0^T[\int_0^\tau c(\mathbf{a})(t)^*G^{(k)}S(t-\tau)dt]G_0^{-1}\Phi^*\mathbf{z}'(\tau)d\tau.$$

Setting

$$\mathbf{X}(\mathbf{a},\mathbf{z})(t) \;=\; -\begin{bmatrix} \int_0^t c(\mathbf{a})(\tau)^* G^{(1)} S(\tau - t)d\tau \\ \cdot \\ \cdot \\ \cdot \\ \int_0^t c(\mathbf{a})(\tau)^* G^{(M)} S(\tau - t)d\tau \end{bmatrix} G_0^{-1}\Phi^*,$$

we may write

$$D_z\mathcal{F}(\mathbf{a},\mathbf{z})\mathbf{z}' \;=\; \int_0^T \mathbf{X}(\mathbf{a},\mathbf{z})(t)\mathbf{z}'(t)dt. \tag{2.20}$$

Furthermore, define the MxN matrices $\mathcal{K}_1$ and $\mathcal{K}_2$ in which the k-th rows are given by

$$\mathcal{K}_1(\mathbf{a},\mathbf{z})_k \;=\; \int_0^T c(\mathbf{a})(t)^* G^{(k)}(P(\mathbf{a},\mathbf{z})(t) + \mathcal{D}(\mathbf{a})(t))dt$$

and

$$\mathcal{K}_2(\mathbf{a},\mathbf{z})_k \;=\; \int_0^T \pi(\mathbf{a},\mathbf{z})(t) G^{(k)} \mathcal{D}_0(\mathbf{a})(t)dt,$$

respectively, and set

$$\mathcal{K} \;=\; \mathcal{K}(\mathbf{a},\mathbf{z}) \;=\; \mathcal{K}_1(\mathbf{a},\mathbf{z}) \;+\; \mathcal{K}_2(\mathbf{a},\mathbf{z}).$$

From (2.16), we see that

$$D_a\mathcal{F}(\mathbf{a},\mathbf{z}) \;=\; H \;+\; \Psi_2 \;+\; \mathcal{K}(\mathbf{a},\mathbf{z}), \tag{2.21}$$

and from the implicit function theorem we have the following.

Proposition 2.2. Suppose that $\mathcal{F}(\mathbf{a}_0,\mathbf{z}_0) \;=\; 0$. If matrix $H \;+\; \Psi_2 \;+\; \mathcal{K}$ is invertible, then there is a neighborhood $\mathcal{N}(\mathbf{z}_0)$ such that $\mathbf{z} \mapsto \mathbf{a}(\mathbf{z})$ is defined as a function on $\mathcal{N}(\mathbf{z}_0)$, and

$$D\mathbf{a}(\mathbf{z})\mathbf{z}' \;=\; (H + \Psi_2 + \mathcal{K}(\mathbf{a},\mathbf{z}))^{-1} \int_0^T \mathbf{X}(\mathbf{a},\mathbf{z})(t)\mathbf{z}'(t)dt.$$

It is also of interest to calculate the second derivatives of $\mathbf{z} \mapsto \mathbf{a}(\mathbf{z})$. The following is a consequence of a straight forward calculation.

Lemma 2.3. The second derivatives of c and π satisfy the following equations.

$$G_0\frac{d}{dt}[(D^2c)(\mathbf{a}',\mathbf{a}')] \;+\; G(\mathbf{a})[(D^2c)(\mathbf{a}',\mathbf{a}')] \;=\; -2G(\mathbf{a}')[(Dc)\mathbf{a}'] \tag{2.22}(i)$$

$$[(D^2c)(\mathbf{a}',\mathbf{a}')](0) \;=\; 0$$

$$-G_0\frac{d}{dt}[(D^2_{aa}\pi)(\mathbf{a}',\mathbf{a}')] \;+\; G(\mathbf{a})[(D^2_{aa}\pi)(\mathbf{a}',\mathbf{a}')] \;=$$

(2.22)(*ii*)
$$= \Phi_2[(D^2c)(\mathbf{a}',\mathbf{a}')] \;-\; 2G(\mathbf{a}')[(D_a\pi)\mathbf{a}'],$$

$$[(D^2_{aa}\pi)(\mathbf{a}',\mathbf{a}')](T) \;=\; 0$$

(2.22)(*iii*)
$$-G_0\frac{d}{dt}[(D^2_{az}\pi)(\mathbf{a}',\mathbf{z}')] \;+\; G(\mathbf{a})[(D^2_{az}\pi)(\mathbf{a}',\mathbf{z}')] \;=\; -G(\mathbf{a}')[(D_z\pi)\mathbf{z}'],$$

$$[(D^2_{az}\pi)(\mathbf{a}',\mathbf{z}')](T) \;=\; 0$$

and

2.22(*iv*)
$$D^2_{zz}\pi(\mathbf{a},\mathbf{z}) \;=\; 0.$$

We note from (2.13) that the second Frechet derivative of $\mathcal{X}_k$ is given by

$$D^2_{zz}\mathcal{X}_k(\mathbf{a},\mathbf{z})(\mathbf{z}',\mathbf{z}') \;=\; \int_0^T [D^2_{zz}\pi(\mathbf{a},\mathbf{z})(\mathbf{z}',\mathbf{z}')]^* G^{(k)}c(\mathbf{a})dt$$

Hence, by (2.22)(iv)

$$D^2_{zz}\mathcal{X}_k(\mathbf{a},\mathbf{z}) \;=\; 0$$

from (2.16), we see that

$$D^2_{zz}\mathcal{F}(\mathbf{a},\mathbf{z}) \;=\; 0.$$

Other second partial derivatives of $\mathcal{F}$ may be calculated similarly. From (2.16) and (2.17), we see that

Proposition 2.4. The second derivative of $\mathbf{z} \mapsto \mathbf{a}(\mathbf{z})$ with respect to $\mathbf{z}$ is given by

$$D^2a(\mathbf{z})(\mathbf{z}',\mathbf{z}') \;=\; -(H+\Psi_2+\mathcal{K})^{-1}\{D^2_{aa}\mathcal{F}(\mathbf{a},\mathbf{z})(\mathbf{Da}(\mathbf{z})\mathbf{z}',\mathbf{Da}(\mathbf{z})\mathbf{z}') \;+$$

$$+\; 2D^2_{za}\mathcal{F}(\mathbf{a},\mathbf{z})(\mathbf{z}',Da(\mathbf{z})\mathbf{z}')\}.$$

Remark 2.5. Extending the above argument, it easy to see that if $H+\Psi_2+\mathcal{K}$ is invertible, then any derivative of $\mathbf{a}$ exists.

Suppose that $\mathbf{z}'$ is such that $D\mathbf{a}(\mathbf{z})\mathbf{z}' \;=\; 0$. That is, denoting the null space of $D\mathbf{a}(\mathbf{z})$ by $N(D\mathbf{a}(\mathbf{z}))$, suppose that

$$\mathbf{z}' \;\in N(D\mathbf{a}(\mathbf{z})).$$

From Propositions 2.2 and 2.4, we have the following.

Corollary 2.6. If $\mathbf{z}'$ is such that $\mathbf{z}' \in N(Da(\mathbf{z}))$, then

$$D^{(n)}\mathbf{a}(\mathbf{z})(\mathbf{z}', ..., \mathbf{z}') \ = \ 0$$

for any n. For such vectors $\mathbf{z}'$ we see that

$$\mathbf{a}(\mathbf{z} + \mathbf{z}') = \mathbf{a}(\mathbf{z}).$$

Remark 2.7. It follows that the estimated coefficient $\mathbf{a}(\mathbf{z})$ is insensitive to any perturbation (no matter how large) $\mathbf{z}' \in N(Da(\mathbf{z}))$. Note this is a consequence of the fact that the fit-to-data functional is quadratic in the data $\mathbf{z}$.

We next examine sufficient conditions underwhich the matrix $H + \Psi_2 + \mathcal{K}$ is invertible. To this end we introduce the following assumptions. Recalling that $G_0, G(a), G^{(k)}$ for $k = 1, ..., M$ are NxN symmetric matrices and that H and Ψ_2 are MxM symmetric matrices, we suppose there positive real numbers β, μ_0, ν_0, μ_1, and μ such that

(2.23)(*i*) $$H \ + \ \Psi_2 \geq \beta I$$

(2.23)(*ii*) $$\mu_1 \ I \ \geq G_0 \ \geq \ \mu_0 \ I$$

(2.23)(*iii*) $$G(a) \ \geq \ \nu_0 \ I$$

and for any $k = 1, ..., M$

(2.23)(*iv*) $$G^{(k)} \ \leq \ \mu I$$

where I represents the identity matrix on $\mathbf{R}^N$ or $\mathbf{R}^M$ which ever is appropriate. From straight forward arguments, we obtain estimates that are sufficient for our purposes.

(2.24)(*i*) $$\|\mathbf{c}(\mathbf{a})\|_{L^2(0,T,\mathbf{R}^N)} \ \leq \frac{1}{\nu_0}\|F\|_{L^2(0,T,\mathbf{R}^N)}$$

(2.24)(*ii*) $$\|\pi(\mathbf{a}, \mathbf{z})\|_{L^2(0,T,\mathbf{R}^N)} \ \leq \ \frac{1}{\nu_0}\|\Phi_2 c(\mathbf{a})(t) - \Phi^* \mathbf{z}\|_{L^2(0,T,\mathbf{R}^N)}$$

$$\leq \frac{|\Phi|}{\nu_0} J(\mathbf{a})^{\frac{1}{2}}.$$

We also have

$$\|\pi(\mathbf{a}, \mathbf{z})\|_{L^2(0,T,\mathbf{R}^N)} \ \leq \ \frac{|\Phi|}{\nu_0}\{\frac{|\Phi|}{\nu_0}(\|F\|_{L^2(0,T,\mathbf{R}^N)} \ + \ \|\mathbf{z}\|_{L^2(0,T,\mathbf{R}^{N_0})}\}$$

$$\|Dc(\mathbf{a})\mathbf{a}'\| \leq \frac{\mu}{\nu_0^2}\|F\||\mathbf{a}'|(2.24)(iii)$$

$$(2.24)(iv) \quad \|D_a\pi(\mathbf{a},\mathbf{z})\mathbf{a}'\| \leq [\frac{\mu}{\nu_0^2}(\|\Phi_2 c(\mathbf{a}) - \Phi^*\mathbf{z}\|_{L^2(0,T,\mathbf{R}^N)} + \frac{\mu_0|\Phi|^2}{\nu_0^3}\|F\|_{L^2(0,T,\mathbf{R}^N)}\|]|\mathbf{a}'|$$

It follows then that for

$$(2.25) \qquad K(\mathbf{a},\mathbf{z},F) = \mu\{[\frac{\mu}{\nu_0^2}(\|\Phi_2 c(\mathbf{a}) - \Phi^*\mathbf{z}\|_{L^2(0,T,\mathbf{R}^N)} +$$

$$+ \frac{\mu_0|\Phi|^2}{\nu_0^3}\|F\|_{L^2(0,T,\mathbf{R}^N)}\|][\frac{1}{\nu_0}\|F\|_{L^2(0,T,\mathbf{R}^N)}] +$$

$$+ [\frac{1}{\nu_0}\|\Phi_2 c(\mathbf{a})(t) - \Phi^*\mathbf{z}\|_{L^2(0,T,\mathbf{R}^N)}][\frac{\mu}{\nu_0^2}\|F\|_{L^2(),T,\mathbf{R}^N)}]\},$$

we have

$$|D_a\mathcal{X}_k(\mathbf{a},\mathbf{z})\mathbf{a}'| \leq K(\mathbf{a},\mathbf{z},F)|\mathbf{a}'|$$

and

$$|D_a\mathcal{X}(\mathbf{a},\mathbf{z})\mathbf{a}'| \leq K(\mathbf{a},\mathbf{z},F)|\mathbf{a}'|$$

Proposition 2.8. If

$$(2.26) \qquad K(\mathbf{a},\mathbf{z},F) < \beta,$$

then $H + \Psi_2 + \mathcal{K}$ is invertible.

2.9. Note that given $\beta > 0$, from (2.24) and (2.25) the condition (2.26) may be satisfied by choosing $\|F\|_{L^2(0,T,\mathbf{R}^N)}$ suitably small.

3. The recovery function. Given the model (2.1)-(2.3) and an estimation procedure, we consider the recovery of the parameter "a" for a test problem. To formulate the problem, data associated with a state has been obtained as the solution of the model equation for a specified function α belonging to int Q_{ad}. Using the data generated from this state, the goal is to recover α by means of the estimation procedure. This is a typical technique for posing a numerical test of an estimation algorithm [ ]. Our interest is in the effect perturbations of test coefficient (vector) $\alpha(\alpha)$ have on the estimated coefficient (vector) a (a). Toward this end, suppose that $\alpha \in Q'_{ad}$ where Q'_{ad} is in the interestion of a finite dimensional subspace with basis $\{\beta_k\}_{k=1}^{M'}$ of Q and Q_{ad}. Let

$$\alpha = \sum_{k=1}^{M'} \alpha_k\beta_k$$

and

$$\alpha \;=\; \begin{bmatrix} \alpha_1 \\ . \\ . \\ . \\ \alpha_{M'} \end{bmatrix}.$$

Define N x N matrices $\Gamma^{(k)}$ for $k = 1, ..., N'$ by

(3.1)(*i*) $$\Gamma_{ij}^{(k)} \;=\; \int_\Omega \beta_k \nabla B_i \cdot \nabla B_j dx.$$

and set

$$\Gamma(\alpha) \;=\; \sum_{k=1}^{M'} \alpha_k \Gamma^{(k)}$$

and

(3.1)(*ii*) $$(\Gamma_0)_{ij} \;=\; \int_\Omega B_i B_j dx.$$

The initial value problem used to generate data is given by

(3.2)(*i*) $$\Gamma_0 \frac{d}{dt}\zeta(\alpha) \;+\; \Gamma(\alpha)\;\zeta(\alpha) \;=\; F.$$

(3.2)(*ii*) $$\zeta(\alpha)(0) \;=\; 0.$$

Denoting by

$$S_0(t) \;=\; \exp(t\Gamma_0^{-1}\Gamma(\alpha)),$$

the solution of (3.2) is given by

(3.2)(*iii*) $$\zeta(\alpha)(t) \;=\; \int_0^t S_0(s-t)\Gamma_0^{-1} F(s) ds.$$

The data $\mathbf{z}$ is obtained from

$$\mathbf{z} \;=\; \Phi\zeta(\alpha).$$

Defining the matrices

$$\psi_{ij} \;= < \Theta_i, \beta_j >$$

for $j = 1, ..., M'$ and $i = 1, ..., N_1$ and $\psi_2 = \psi^*\psi$, the data $\mathbf{K}$ is obtained from

$$K \;=\; \psi\alpha.$$

The functional given by (2.4) becomes

$$J(\mathbf{a}) \;=\; \int_0^T (\Phi c(\mathbf{a}) - \Phi\zeta(\alpha))^*(\Phi c(\mathbf{a}) \;-\; \Phi\zeta(\alpha))dt \;+\; \mathbf{a}^*(H + \Psi_2)\mathbf{a} \;-\; 2\alpha^*\psi^*\Psi\mathbf{a} \;+\; \alpha^*\psi_2\alpha$$

or

$$(3.3)\quad J(\mathbf{a}) \;=\; \int_0^T (c(\mathbf{a})-\zeta(\alpha))^*\Phi_2(c(\mathbf{a})-\zeta(\alpha))dt + \mathbf{a}^*(H+\Psi_2)\mathbf{a} - 2\alpha^*\psi^*\Psi\mathbf{a} + \alpha^*\psi_2\alpha.$$

The optimality conditions given in Proposition 2.1 may be restated as

$$G_0\frac{d}{dt}c(\mathbf{a}) \;+\; Gc(\mathbf{a}) \;=\; F$$

$$c(\mathbf{a})(0) \;=\; 0$$

$$(3.4)(i)\qquad -G_0\frac{d}{dt}\pi(\mathbf{a},\Phi\zeta(\alpha)) \;+\; G\pi(\mathbf{a},\Phi\zeta(\alpha)) \;=\; \Phi_2(c(\mathbf{a}) \;-\; \zeta(\alpha))$$

$$\pi(\mathbf{a},\Phi\zeta(\alpha))(T) \;=\; 0.$$

and

$$(H+\Psi_2)\mathbf{a} \;-\; \Psi^*\psi\alpha \;-\; \mathcal{X}(\mathbf{a},\Phi\zeta(\alpha)) \;=\; 0$$

where the kth component of $\mathcal{X}$ is given by

$$(3.4)(ii)\qquad \mathcal{X}_k \;=\; \mathcal{X}_k(\mathbf{a},\Phi\zeta(\alpha)) \;=\; \int_0^T \pi(\mathbf{a},\Phi\zeta(\alpha))^*G^{(k)}c(\mathbf{a})dt.$$

Define the function

$$\mathcal{G}(\mathbf{a},\alpha) \;=\; \mathcal{F}(\mathbf{a},\Phi\zeta(\alpha),\psi\alpha)$$
$$=\; (H+\Psi_2)\mathbf{a} \;-\; \Psi^*\psi\alpha \;-\; \mathcal{X}(\mathbf{a},\Phi\zeta(\alpha)).$$

The derivatives satisfy the relation

$$D_a\mathcal{G}(\mathbf{a},\alpha)D\mathbf{a}(\alpha)\alpha' \;+\; D_\alpha\mathcal{G}(\mathbf{a},\alpha)\alpha' \;=\; 0.$$

In terms of $\mathcal{F}(\mathbf{a},\Phi\zeta(\alpha),\psi\alpha)$, we have

$$(3.5)\qquad D_a\mathcal{F}(\mathbf{a},\Phi\zeta(\alpha),\psi\alpha)D\mathbf{a}(\alpha)\alpha' \;+\; D_z\mathcal{F}(\mathbf{a},\Phi\zeta(\alpha),\psi\alpha)\Phi D\zeta(\alpha)\alpha' \;+$$
$$+\; D_{\mathbf{K}}\mathcal{F}(\mathbf{a},\Phi\zeta(\alpha),\psi\alpha)\psi\alpha' \;=\; 0.$$

From (2.20) and (2.21) we see that with $\mathbf{z}' \;=\; \Phi D\zeta(\alpha)\alpha'$

$$D_z\mathcal{F}(\mathbf{a},\Phi\zeta(\alpha),\psi\alpha)\Phi D\zeta(\alpha)\alpha' \;=\; \int_0^T \mathbf{X}(\mathbf{a},\zeta(\alpha))(t)\Phi[D\zeta(\alpha)\alpha'](t)dt$$

$$=\; \int_0^T \mathbf{X}(\mathbf{a},\Phi\zeta(\alpha))(t)\Phi\sum_{k=1}^{M'}\alpha_k\int_0^t S_0(t-s)\Gamma_0^{-1}\Gamma^{(k)}\zeta(\alpha)(s)dsdt$$

Define the MxM' matrix $\mathcal{I}$ in which the kth column is given by

$$\mathcal{I}_k(\mathbf{a}, \Phi\zeta(\alpha)) \;=\; \int_0^T \mathbf{X}(\mathbf{a}, \Phi\zeta(\alpha))(t)\Phi \int_0^t S_0(t-s)\Gamma_0^{-1}\Gamma^{(k)}\zeta(\alpha)(s)dsdt.$$

From (2.20) and (2.21), equation (3.5) now becomes

$$(3.6) \qquad (H \;+\; \Psi_2 \;+\; \mathcal{K}((\mathbf{a}, \Phi\zeta(\alpha)))D\mathbf{a}(\alpha)\alpha' \;+\; (\mathcal{I} \;+\; \Psi^*\psi)\alpha' \;=\; 0$$

From (3.5) and (3.6) and from calculations similar to those previously, we obtain the following.

Theorem 3.1. Let $H + \Psi_2 + \mathcal{K}(\mathbf{a}, \Phi\zeta(\alpha))$ be invertible. Then

$$(3.7) \qquad D\mathbf{a}(\alpha)\alpha' \;=\; (H + \Psi_2 + \mathcal{K})^{-1}(\mathcal{I}(\mathbf{a}, \Phi\zeta(\alpha)) + \Psi^*\psi)\alpha'.$$

We note that the null space of $D\mathbf{a}(\alpha)$ and thus of $\mathcal{I} \;+\; \Psi^*\psi$ determines the space of the test coefficient that have no effect on the optimal estimators.

Remark 3.2. It is not hard to see from performing further differentiation of equation (3.5) that $\alpha' \in N(D\mathbf{a}(\alpha))$ certainly does not imply that $D^{(n)}\mathbf{a}(\alpha)(\alpha', ..., \alpha') \;=\; 0$.

Set

$$(3.8) \qquad \mathcal{A} \;=\; \mathcal{I}(\mathbf{a}, \Phi\zeta(\alpha)) \;+\; \Psi^*\psi,$$

$$d \;=\; D\mathbf{a}(\alpha)\alpha',$$

and

$$(3.9) \qquad \mathcal{B} \;=\; H + \Psi_2 + \mathcal{K}(\mathbf{a}, \Phi\zeta(\alpha)).$$

Rewrite equation (3.7)

$$\mathcal{B}d \;=\; \mathcal{A}\alpha'.$$

The $M'xM'$ symmetric positive semidefinite matrix $\mathcal{A}^*\mathcal{A}$ is diagonalizable with nonnegative eigenvalues $\lambda_i \quad i \;=\; 1, ..., M'$ and has a set of orthonormal eigenvectors $\{\mu_i\}_{i=1}^{M'}$. Expressing α' in terms of the basis vectors μ_k by $\alpha' \;=\; \sum_{k=1}^{M'} \alpha_k^*\mu_k$, it follows that

$$|\; \alpha' \;|^2 \;=\; \sum_{k=1}^{M'} \lambda_k(\alpha_k^*)^2.$$

It is clear that the eigenvalues $\{\lambda_i\}_{i=1}^{M'}$ provide measures of the sensitivity of $\mathcal{A}$ to the components in the corresponding eigenspace of $\mathcal{A}^*\mathcal{A}$. Thus, define the matrix

$$\mathcal{M} \;=\; [\mu_1, ..., \mu_{M'}].$$

We refer to the product matrix

$$\mathcal{S} = \mathcal{A}\mathcal{M} \tag{3.10}$$

as the sensitivity matrix. Note that $D\mathbf{a}(\alpha)\alpha' = \mathcal{B}^{-1}\mathcal{S}\alpha^\star$ where

$$\alpha^\star = \begin{bmatrix} \alpha_1^\star \\ . \\ . \\ . \\ \alpha_M^\star \end{bmatrix}$$

From an elementary linear algebra argument, we have the following.

Proposition 3.3. The number of nonzero eigenvalues of $\mathcal{A}^*\mathcal{A}$ equals the rank of the matrix $\mathcal{S}$ and thus of $D\mathbf{a}(\alpha) = \mathcal{B}^{-1}\mathcal{S}$.

Remark 3.4. Proposition 3.3 is an algebraic result. Computationally, the eigenvalues may be small and thus the associated eigenvector be effectively in the null space in the sense that any perturbation by that eigenvector has little effect. Nevertheless by calculating rank and the eigenvalues, we can gain some idea of the behavior of the derivative.

The goal of testing of the estimation procedure is to recover the vector α. Indeed, as mentioned previously, one typically validates the algorithm by comparing $\mathbf{a}(\alpha)$ with α, cf [9]. Thus, it is of interest to compare $\mathbf{a}(\alpha)$ with α. We refer to the difference

$$\epsilon(\alpha) = \mathbf{a}(\alpha) - \alpha$$

as the recovery error. Suppose that the set of functions $\{\beta_i\}_{i=1}^{M'}$ coincides with the set $\{b_i\}_{i=1}^{M}$ with $M = M'$. It follows that $\Psi = \psi$, $\Psi_2 = \psi_2$, and $\Gamma^{(i)} = G^{(i)}$. Hence, we have the optimality conditions (3.4) become

$$G_0\frac{d}{dt}c(\mathbf{a}) + G(\mathbf{a})c(\mathbf{a}) = F$$

$$c(\mathbf{a})(0) = 0$$

$$-G_0\frac{d}{dt}\pi(\mathbf{a}, \Phi\zeta(\alpha)) + G\pi(\mathbf{a}, \Phi\zeta(\alpha)) = \Phi_2(c(\mathbf{a}) - \zeta(\alpha))$$

$$\pi(\mathbf{a}, \Phi\zeta(\alpha))(T) = 0$$

$$(H + \Psi_2)\mathbf{a} - \Psi_2\alpha - \mathcal{X}(\mathbf{a}, \Phi\zeta(\alpha)) = 0.$$

To estimate the recovery error, we find

$$|\,\epsilon(\alpha)\,| = |\,(H + \Psi_2)^{-1}\Psi_2\alpha - \alpha + (H + \Psi_2)^{-1}\mathcal{X}(\mathbf{a}, \Phi\zeta(\alpha))\,| \tag{3.11}$$

Hence, it follows that

$$| \epsilon(\alpha) | \leq | (\mathbf{H} + \Psi_2)^{-1} | (| \mathbf{H} || \alpha | + | \mathcal{X}(\mathbf{a}, \Phi\zeta(\alpha)) |)$$

From the estimates (2.24)(ii) we have

$$\|\pi(\mathbf{a}, \zeta(\alpha)\|_{L^2(0,T;\mathbf{R}^N} \leq \frac{| \Phi |}{\nu_0} J(\mathbf{a})^{\frac{1}{2}}.$$

Proposition 3.5. Suppose that the set of basis functions $\{\beta_i\}_{i=1}^M$ coincides with the set of basis functions $\{b_i\}_{i=1}^M$. Then

$$| \epsilon(\alpha) | \leq \frac{1}{beta}(| H || \alpha | + \frac{| \Phi || F | \mu}{\nu_0} J(\mathbf{a})^{\frac{1}{2}}). \tag{3.11}$$

Proof. Since

$$\|\mathbf{c}(\mathbf{a})\|_{L^2(0,T;\mathbf{R}^N)} \leq \frac{\|F\|_{L^2(0,T;\mathbf{R}^N)}}{\beta}.$$

the inequality (3.11) follows from (2.24)(i),(2.24)(ii), and (3.4)(ii).

Remark 3.6. The first term of (3.11) depends on $|H|$ which is usually chosen to be small, but is balanced by $\frac{1}{\beta}$. Obviously, choosing the smallest regularization possible for a fixed β is desireable. The second term involves the difference in the observations of $c(\mathbf{a})$ and $\zeta(\alpha)$ and not on $c(\mathbf{a})$ and $\zeta(\alpha)$ themselves. This allows us to involve the criterion $J(\mathbf{a})$ directly in the estimate. Hence, the recovery error is determined from the regularization and the criterion. If there is a sufficient number of observations so that Ψ_2 is invertible, then H may be taken to be zero and the recovery error depends on $J(\mathbf{a})$.

4. Application to Experimental Design. In experimental design it is of interest to determine measurement functionals that optimize various features of the results. For example, one might want to determine the "best" place to locate a pressure sensor in the test problem with the idea that it would aid in the location of sensors in the actual experimental setup. Here "best" could mean that the fit-to-data functional is smallest for a particular collection of measurement functionals as opposed to any other set of measurement functionals or that certain properties of the derivative are maximized. Our approach is to determine locations at which the sensitivity matrix has maximal rank. Among these, it is then desirable to seek locations at which the functional J is minimal while the derivative is maximal in some sense. This will be accomplished by defining a new functional

$$Jk(\Phi) = J(\mathbf{a}; \Phi) + \frac{\gamma}{|D_\alpha \mathbf{a}(\alpha, \Phi)|}$$

where γ is a positive weighting factor that is selected to balance the two terms. We seek a measurement matrix Φ_o such that

$$Jk(\Phi_o) = \text{minimum } Jk(\Phi)$$

where Φ ranges over those Φ associated with locations at which the sensitivity matrix has maximal rank. To carry out such a program, it is useful to examine differentiability with respect to the measurement matrix Φ. To emphasize dependence we include Φ as a argument where appropriate. Thus, the optimality conditions for a given Φ and α are the following.

$$G_0 \frac{d}{dt} c(\mathbf{a}) + G(\mathbf{a}) c(\mathbf{a}) = F$$

$$c(\mathbf{a}) = 0$$

$$-G_0 \frac{d}{dt} \pi(\mathbf{a}, \Phi\zeta(\alpha), \Phi) + G(\mathbf{a})\pi(\mathbf{a}, \Phi\zeta(\alpha), \Phi) = \Phi^*\Phi(c(\mathbf{a}) - \zeta(\alpha)) \tag{3.12}$$

$$\pi(\mathbf{a}, \Phi\zeta(\alpha), \Phi)(T) = 0$$

$$(H + \Psi_2)\mathbf{a} - \Psi^*\psi\alpha - \mathcal{X}(\mathbf{a}, \Phi\zeta(\alpha), \Phi) = 0$$

where the kth component of $\mathcal{X}(\mathbf{a}, \Phi\zeta(\alpha), \Phi)$ is given by

$$\mathcal{X}_k(\mathbf{a}, \Phi\zeta(\alpha), \Phi) = \pi(\mathbf{a}, \Phi\zeta(\alpha), \Phi)^* G^{(k)} c(\mathbf{a}).$$

As in the previous arguments, these equations implicitly determine the function $a = a(\alpha, \Phi)$. Consider the function where we have included dependence on Φ

$$\mathcal{G}(\mathbf{a}, \alpha, \Phi) = (H + \Psi_2)\mathbf{a} - \Psi^*\psi\alpha - \mathcal{X}(\mathbf{a}, \Phi\zeta(\alpha), \Phi), \tag{3.13}$$

From (2.21) we see

$$D_a \mathcal{G}(\mathbf{a}, \alpha, \Phi)[D_\Phi \mathbf{a}(\alpha, \Phi)\Phi'] = (H + \Psi_2 + \mathcal{K}) D_\Phi \mathbf{a}(\alpha, \Phi)\Phi'.$$

Furthermore,

$$D_\Phi \mathcal{G}(a, \alpha, \Phi)\Phi' = -D_\Phi \mathcal{X}(\mathbf{a}, \zeta(\alpha), \Phi)\Phi',$$

and that

$$D_\Phi \mathcal{G}_k(\mathbf{a}, \alpha, \Phi)\Phi' = D_\Phi \mathcal{X}_k(\mathbf{a}, \Phi\zeta(\alpha), \Phi)\Phi' = \int_0^T \{[D_\Phi \pi(\mathbf{a}, \Phi\zeta(\alpha), \Phi)(\Phi')(t)^* G^{(k)} c(\mathbf{a})(t)$$

Under the assumption that $H + \Psi_2 + \mathcal{K}$ is invertible, we conclude that

$$D_\Phi \mathbf{a}(\alpha, \Phi)\Phi' = -(H + \Psi_2 + \mathcal{K})^{-1} D_\Phi \mathcal{F}(a, \alpha, \Phi)\Phi'. \tag{3.14}$$

Furthermore, we may calculate higher derivatives. For example, $D^2_{\alpha\Phi}\mathbf{a}(\alpha, \Phi)(\alpha', \Phi')$ satisfies the equation

$$D_a \mathcal{G}(\mathbf{a}, \alpha, \Phi)[D^2_{\alpha\Phi}\mathbf{a}(\alpha, \Phi)(\alpha', \Phi')] + D^2_{\zeta\alpha}\mathcal{G}(\mathbf{a}, \alpha, \Phi)(D_\Phi \mathbf{a}(\alpha, \Phi)\Phi', D\zeta(\alpha)\alpha') + \tag{3.15}$$

$$+ D^2_{aa}\mathcal{G}(\mathbf{a}, \alpha, \Phi)(D_\Phi \mathbf{a}(\alpha, \Phi)\Phi', D_\alpha \mathbf{a}(\alpha, \Phi)\alpha') +$$

$$D^2_{\zeta\Phi}\mathcal{F}(\mathbf{a},\zeta(\alpha),\Phi)(D\zeta(\alpha)\alpha',\Phi') + D^2_{a\Phi}\mathcal{F}(\mathbf{a},\zeta(\alpha),\oplus)([\mathcal{D}\mathbf{a}(\alpha,\oplus)\alpha'],\oplus')+$$

$$+D^2_{\Phi\Phi}\mathcal{F}(\mathbf{a},\zeta(\alpha),\Phi)(\Phi',\Phi') \;=\; 0$$

and thus may be calculated in a straightforward but tedious manner.

Theorem 3.7 Under the assumption that $H+\Psi_2+\mathcal{K}$ is invertible, the partial derivatives $D_\Phi a(\alpha,\Phi)$ and $D^2_{\alpha\Phi}a(\alpha,\Phi)$ are given in terms of the expressions (3.14) and (3.15).

Even though the derivatives have been given and thus can be used to construct algorithms to determine optimal observation points, we consider the case in which there are only finitely many observation locations from which to choose. Hence, we propose the following procedure to locate observation points.

(i) Determine those locations L for which the sensitivity matrix has maximal rank.

(ii) Determine the value of the functional Jk at the locations in L.

(iii) Select the location with the minimum value Jk.

Consider the problem posed on the 2 dimensional domain $\Omega = (0,1)\text{x}(0,1)$. We suppose that the forcing function is given as

$$f(x,y) = \begin{cases} 1 \text{ if} (x,y) = (0.2,0.2) \\ 0 \text{ otherwise} \end{cases}$$

We also suppose that the pressure p is zero at the point $(0.8,0.8)$ as well. The test coefficient a is given by the following

$$a(x,y) = \begin{cases} 1.0, 0 \le y < 0.16 \\ 1.5, 0.16 \le y < 0.33 \\ 2.0, 0.33 \le y < 0.5 \\ 2.5, 0.5 \le y < 0.67 \\ 3.0, 0.67 \le y < 0.83 \\ 2.5, 0.83 \le y < 1.0 \end{cases}$$

We assume that the zones in the coefficient are known and use the appropriate step functions to approximate a. The pressure is approximated using basis functions obtained from the tensor product of piecewise linear "hat" functions on a uniform mesh with 5 subintervals on each side of Ω. Thus, 36 basis functions are used to approximate the pressure. We seek the location of the "best" observation point in the sense that we have described above.

Test Points	Rank	J(E-04)	Jk(E-04)
(0.2,0.2)	6	2.23	2.81
(0.2,0.4)	6	2.34	2.82
(0.2,0.6)	6	2.01	2.37
(0.2,0.8)	6	2.36	2.48
(0.4,0.2)	6	2.18	2.52
(0.4,0.4)	6	2.05	2.6
(0.4,0.6)	6	2.05	2.42
(0.4,0.8)	6	2.31	2.42
(0.6,0.2)	6	2.34	2.59
(0.6,0.4)	6	2.08	2.7
(0.6,0.6)	6	2.27	2.46
(0.6,0.8)	6	2.33	2.46
(0.8,0.2)	6	2.15	2.56
(0.8,0.4)	6	2.23	2.7
(0.8,0.6)	6	2.23	2.54
(0.8,0.8)	6	2.0	2.42

We observe that the rank in all cases in this example is 6 so that in every case the null space of the sensitivity matrix is trivial. The location of the observer is thus determined by choosing that location for which the functional Jk is minimum. Hence, the location $(x, y) = (0.2, 0.4)$ is chosen.

5. The Elliptic Case. By way of comparison we consider this example but with the underlying model being the time independent elliptic model. We briefly describe the derivative of the recovery mapping in this case the details of the derivation are presented in [6]. The underlying equation in given by

$$G(\mathbf{a})c(\mathbf{a}) \;=\; F$$

with the data equation

$$\Gamma(\alpha)\zeta(\alpha) \;=\; F$$

data is given by

$$K \;=\; \psi\alpha$$

and

$$\mathbf{z} \;=\; \Phi\zeta(\alpha)$$

with adjoint equation given by

$$G(\mathbf{a})\pi(\mathbf{a},\mathbf{z}) \;=\; \Phi_2 c(\mathbf{a}) - \Phi^*\mathbf{z}$$

The optimality condition for an interior optimal estimator is given by

$$\mathcal{F}(\mathbf{a},\mathbf{z},\mathbf{K}) \;=\; 0$$

where

$$\mathcal{F}(\mathbf{a}, \mathbf{z}, \mathbf{K}) \;=\; (H + \Psi_2)\mathbf{a} - \Psi^*\mathbf{K} - \mathcal{X}(\mathbf{a}, \mathbf{z}).$$

Set

$$\mathcal{G})(\mathbf{a}, \alpha) \;=\; \mathcal{F}(\mathbf{a}, \oplus\zeta(\alpha), \psi\alpha).$$

Defining the MxM matrix $\mathcal{K}$ by

$$\mathcal{K}_{ik} \;=\; \pi^* G^{(i)} G^{-1} G^{(k)} c + \pi^* G^{(k)} G^{-1} G^{(i)} c + c^* G^{(i)} G^{-1} \Phi_2 G^{-1} G^{(k)} c,$$

we find that

$$D_a\mathcal{F}(\mathbf{a}, \mathbf{z}, \mathbf{K})\mathbf{a}' \;=\; (H + \Psi_2 + \mathcal{K})a'.$$

Moreover, with

$$D_z\mathcal{F}(\mathbf{a}, \mathbf{z}, \mathbf{K})\mathbf{z}' \;=\; -D_z\mathcal{X}(\mathbf{a}, \mathbf{z})\mathbf{z}'$$

where

$$D_z\mathcal{X}_k(\mathbf{a}, \mathbf{z})\mathbf{z}' \;=\; -c^* G^{(k)} G^{-1} \Phi^* \mathbf{z}',$$

we find that

$$D_\alpha\mathcal{G}(\mathbf{a}, \alpha)\alpha' \;=\; \Psi^*\psi\alpha' - D_z\mathcal{X}(\mathbf{a}, \Phi\zeta(\alpha))D\zeta(\alpha)\alpha'.$$

Finally, the derivative of the recovery function is expressed as

$$D\mathbf{a}(\alpha)\alpha' = \{(H + \Psi_2 + \mathcal{K})^{-1} D_\alpha\mathcal{G}(\mathbf{a}, \alpha)\}\alpha'.$$

We apply these equations to the case described in Section 4 in which data is generated using the coefficient given there. We use the same basis elements in spatial approximations for both the parameter and the state. Hence, $G^(k) = \Gamma^(k)$ for k=1,...,M. The same forcing function is used and it is assumed that the pressure is zero at the point $(0.8, 0.8)$. In a similar computation as was carried out for the parabolic case we look at various locations calculating the rank of the sensitivity matrix and the values of the fit-to-data functional J and the fit-to-data functional with a sensitivity term Jk. The following table of values is obtained.

Test Points	Rank	J(E-02)	Jk(E-02)
(0.2,0.2)	3	0.0297	0.4541
(0.2,0.4)	4	0.1677	0.4741
(0.2,0.6)	4	0.1029	0.4276
(0.2,0.8)	4	1.9121	1.9264
(0.4,0.2)	4	0.1777	0.3381
(0.4,0.4)	4	0.1145	0.2916
(0.4,0.6)	4	0.0904	0.6367
(0.4,0.8)	4	0.2926	0.5888
(0.6,0.2)	4	0.2074	0.4754
(0.6,0.4)	4	0.0961	0.2831
(0.6,0.6)	4	0.0961	0.2831
(0.6,0.8)	4	0.0729	0.4338
(0.8,0.2)	4	0.2626	0.6311
(0.8,0.4)	4	0.2159	0.5603
(0.8,0.6)	4	0.0915	0.2605
(0.8,0.8)	3	0.0565	0.4703

We locate the observer at the point $(0.8, 0.6)$. Assuming now that we have a pressure observer located at the point $(0.8, 0.6)$, we now seek a second point.

Test Points	Rank	J(E-02)	Jk(E-02)
(0.2,0.2)	4	0.0721	0.2887
(0.2,0.4)	5	0.1834	0.5231
(0.2,0.6)	4	0.1084	0.4331
(0.2,0.8)	5	0.1238	0.2073
(0.4,0.2)	5	1.9351	1.9865
(0.4,0.4)	5	0.1462	0.5511
(0.4,0.6)	4	0.1089	0.6194
(0.4,0.8)	5	0.1134	0.1662
(0.6,0.2)	5	0.2925	0.6213
(0.6,0.4)	5	0.2183	0.5801
(0.6,0.6)	4	0.1117	0.2273
(0.6,0.8)	5	0.1025	0.3095
(0.8,0.2)	5	0.2629	0.6945
(0.8,0.4)	5	1.8877	2.1451
(0.8,0.6)	4	1.7642	1.9731
(0.8,0.8)	4	0.0914	0.2605

The point $(0.4, 0.8)$ is selected for the second pressure observer. To determine the third point, we fix the previous two points and look for an additional location.

Test Points	Rank	J(E-02)	Jk(E-02)
(0.2,0.2)	5	0.0972	0.1646
(0.2,0.4)	5	0.1967	0.5236
(0.2,0.6)	5	0.1049	0.5076
(0.2,0.8)	5	0.1111	0.1739
(0.4,0.2)	6	1.9458	1.9587
(0.4,0.4)	5	0.1812	0.6008
(0.4,0.6)	5	0.1184	0.4553
(0.4,0.8)	5	0.1986	0.5841
(0.6,0.2)	6	0.2761	0.5591
(0.6,0.4)	5	0.1972	0.3757
(0.6,0.6)	5	0.1162	0.6345
(0.6,0.8)	5	0.0662	0.5101
(0.8,0.2)	6	0.2612	0.6312
(0.8,0.4)	6	0.3185	0.7622
(0.8,0.6)	5	0.1249	0.4772
(0.8,0.8)	5	0.1135	0.1662

The third pressure observer is located at $(0.6, 0.2)$.

References

[1] K. Deimling *Nonlinear Functional Analysis,* Springer-Verlag, New York, 1980.

[2] J.L.Lions,*Optimal Control of Systems Governed by Partial Differential Equations,* Springer-Verlag, New York, 1971.

[3] R.L.Parker,*Geophysical Inverse Theory,* Princeton University Press, Princeton, New Jersey, 1994.

[4] M. Schultz, *Spline Analysis,* Prentice Hall, Englewood Cliffs, New Jersey, 1973.

[5] L.W.White and J. Zhou, Continuity and Uniquenesss of Regularized Output Least Squares Optimal Estimators, *J. Math. Analysis and Applications,* 196, pp 53-83, 1995.

[6] L.W.White, Resolution of Regularized Output Least Squares Estimation Procedures, *Computation and Applied Mathematics,* to appear.